

1169-40046

NASA CR-72495
TRW NO. 09588-6003-R0-00

FINAL REPORT
SPACE STORABLE
THRUSTER INVESTIGATION

BY
F. E. ARNDT AND R. M. WILLIAMS

CASE FILE
COPY

Prepared for
NATIONAL AERONAUTICS AND
SPACE ADMINISTRATION

NASA LEWIS RESEARCH CENTER
CONTRACT NAS 3-11184
P. N. HERR, PROJECT MANAGER

TRW
SYSTEMS GROUP

NOTICE

This report was prepared as an account of Government sponsored work. Neither the United States, nor the National Aeronautics and Space Administration (NASA), nor any person acting on behalf of NASA:

- a) Makes any warranty or representation, expressed or implied, with respect to the accuracy, completeness, or usefulness of the information contained in this report, or that the use of any information, apparatus, method or process disclosed in this report may not infringe privately owned rights; or
- b) Assumes any liabilities with respect to the use of, or for damages resulting from the use of any information, apparatus, method or process disclosed in this report.

As used above, "person acting on behalf of NASA" includes any employee or contractor of NASA, or employee of such contractor, to the extent that such employee or contractor of NASA or employee of such contractor prepares, disseminates, or provides access to, any information pursuant to his employment or contract with NASA, or his employment with such contractor.

Requests for copies of this report should be referred to

National Aeronautics and Space Administration
Office of Scientific and Technical Information
Attention: AFSS-A
Washington, D.C. 20546

NASA CR-72495
TRW No. 09588-6003-R0-00

FINAL REPORT
SPACE STORABLE THRUSTER INVESTIGATION

by

F. E. Arndt and R. M. Williams

TRW SYSTEMS GROUP
One Space Park
Redondo Beach, California 90278

Prepared for
NATIONAL AERONAUTICS AND SPACE ADMINISTRATION

August 1, 1969

Contract NAS 3-11184

NASA Lewis Research Center
Cleveland, Ohio
P. N. Herr, Project Manager
Liquid Rocket Technology Branch

FOREWORD

This report was prepared by the Science and Technology Division of the TRW Systems Group at One Space Park, Redondo Beach, California, under Contract NAS 3-11184. The contract was administered by the Lewis Research Center of the National Aeronautics and Space Administration, Cleveland, Ohio. This is the final report on the subject contract and summarizes the technical work conducted during the July 1967 to November 1968 period. The NASA project manager for the contract was Mr. P. N. Herr.

The following personnel at TRW Systems Group contributed to the technical effort of the program: F. E. Arndt and R. M. Williams, Program Managers; Dr. H. L. Burge and S. J. Van Grouw, Technical Advisors; L. L. Smith and J. J. King, Thermal Analysis; S. S. Cherry and C. T. Weekley, Performance Analysis; K. J. Mock and L. B. Goddard, Design; and F. E. Robinett and J. R. Augustson, Test Operations.

ABSTRACT

An analytical and experimental program was conducted with the objective of evaluating cooling techniques for space storable reaction control thrusters using the various FLOX/LPG propellant combinations. Also performed was a detailed examination of the performance characteristics of each propellant combination. Experimental studies were limited to an evaluation of the feasibility for using the LPG fuel, methane-ethane blend, for film conduction cooling.

CONTENTS

	Page
1. INTRODUCTION	1
2. SUMMARY.	3
3. THRUSTER DESIGN ANALYSIS	5
3.1 Propellant Evaluation	5
3.1.1 Equilibrium and Frozen Performance and Propellant Characterization.	6
3.1.2 Fuel Decomposition	13
3.1.3 Gas Specie Composition	13
3.1.4 Delivered Performance Estimates.	17
3.1.5 Predicted Thrust Chamber and Engine Performance. . .	26
3.1.6 Propellant Selection on Performance Criteria	35
3.2 Thruster Thermal Analysis	35
3.2.1 Propellant Heat Transfer Characteristics	38
3.2.2 Cooled Thruster Thermal Analysis	57
3.3 Other Material Design Considerations.	86
3.3.1 Heat Transfer Properties	86
3.3.2 Heat Storage Effects	88
3.3.3 Chemical Compatibility Factors	88
3.3.4 Mechanical Property Considerations	89
3.3.5 Summary of Material Property Considerations.	91
3.4 Thruster Value Selection Evaluation	91
4. HARDWARE DESCRIPTION	95
4.1 Hardware Design Summary	95
4.1.1 Injector Design.	95
4.1.2 Experimental Thrust Chamber Designs.	110
4.1.3 Altitude Thruster Designs.	115
5. EXPERIMENTAL RESULTS	121
5.1 Injector Development Cold Flow Studies.	121
5.2 Hot Firing Program.	130
5.2.1 Test Facility.	130
5.2.2 Basic Injector Development	130
5.2.3 Basic Injector Heat Transfer Characterization. . . .	137
5.2.4 Injector/Film Cooling Characterization	143
5.3 Data Evaluation	167
5.3.1 Basic Injector Tests	167
5.3.2 Film Cooling Tests	167

CONTENTS (Continued)

	Page
5.4 Bipropellant Valve Evaluation	186
6. CONCLUDING REMARKS	187
6.1 Analytical Results	187
6.2 Experimental Results	188
6.3 Analytical Reevaluation	188
6.4 Recommendations	191
REFERENCES	192
APPENDICES	
A PROPELLANT PHYSICAL PROPERTY AND THEORETICAL PERFORMANCE SUMMARY	A-1
B LPG POOL BOILING EXPERIMENTS	B-1
C HEAT TRANSFER DATA ANALYSIS PROGRAM	C-1
D CALCULATION OF C* EFFICIENCY	D-1
E CARBON DEPOSITION EFFECTS ON GAS SIDE HEAT TRANSFER COEFFICIENT.	E-1
F CHEMICAL ANALYSIS OF CARBON DEPOSITION LAYER	F-1
G COMPUTER PROGRAMS	G-1

DISTRIBUTION

ILLUSTRATIONS

	Page
3-1 Vacuum Specific Impulse (CH_4)	7
3-2 Vacuum Specific Impulse (P_c Variation)(CH_4)	7
3-3 Equilibrium Characteristic Velocity (P_c Variation)(CH_4)	7
3-4 Equilibrium Combustion Temperature (P_c Variation)(CH_4)	7
3-5 Vacuum Specific Impulse (55% CH_4 + 45% C_2H_6)	8
3-6 Vacuum Specific Impulse (P_c Variation) (55% CH_4 + 45% C_2H_6)	8
3-7 Equilibrium Characteristic Velocity (P_c Variation) (55% CH_4 + 45% C_2H_6)	9
3-8 Equilibrium Combustion Temperature (P_c Variation) (55% CH_4 + 45% C_2H_6)	9
3-9 Vacuum Specific Impulse (C_3H_8)	10
3-10 Vacuum Specific Impulse (P_c Variation)(C_3H_8)	10
3-11 Equilibrium Characteristic Velocity (P_c Variation) (C_3H_8)	10
3-12 Equilibrium Combustion Temperature (P_c Variation) (C_3H_8)	10
3-13 Effect of Chamber Pressure on Vacuum Specific Impulse (55% CH_4 + 45% C_2H_6)	11
3-14 Summary Curves of Vacuum Specific Impulse (All Fuels)	11
3-15 Performance Versus FLOX Concentration (55% CH_4 + 45% C_2H_6)	12
3-16 Carbon Deposition Mass Fraction (All Fuels)	14
3-17 Vacuum Specific Impulse of Monopropellant LPG Fuels	14
3-18 Chamber Specie Concentrations for all Propellant Combinations.	15
3-19 Effect of Engine Thrust Level and Chamber Pressure on Kinetic Efficiency	21
3-20 Combined Heat Transfer and Friction Loss.	23
3-21 Simplified Chamber/Nozzle Zonal Model	23

ILLUSTRATIONS (Continued)

	Page
3-22 Sensitivity of Mixture Ratio to Mass Fraction of Fuel in Outer Barrier Zone	25
3-23 Vacuum Specific Impulse and Combustion Temperature (CH ₄)	27
3-24 Vacuum Specific Impulse and Combustion Temperature (55% CH ₄ + 45% C ₂ H ₆)	27
3-25 Vacuum Specific Impulse and Combustion Temperature (C ₃ H ₈)	27
3-26 Specific Impulse Zonal Losses (All Fuels).	29
3-27 Vacuum Specific Impulse with Losses for all Propellant Combinations.	31
3-28 Summary Curves of Delivered Vacuum Specific Impulse for all Propellant Combinations.	32
3-29 Schematic Representation of Thruster Cooling Concepts. . .	36
3-30 Baseline Chamber Configuration	39
3-31 Mach Number Distribution	42
3-32 Gas Convection Coefficient	43
3-33 Mixture Ratio Effect on Gas Convection Coefficient	43
3-34 Effects of Recombination on Convective Heat Transfer (80% FLOX/55% CH ₄ + 45% C ₄ + 45% C ₂ H ₆)	44
3-35 Recovery Temperature Ratio Mach Number Variation	46
3-36 Functional Dependence of F _A on Atomic Ratio of Hydrogen to Carbon	47
3-37 Gas Convection Coefficient Axial Distribution.	49
3-38 Thermal Resistance Distribution with Carbon Deposition . .	49
3-39 Overall Thermal Resistance Axial Distribution.	51
3-40 LPG Fuel Vapor Pressure Curves	51
3-41 LPG Fuel Heat of Vaporization.	52
3-42 LPG Fuel Liquid Density.	52

ILLUSTRATIONS (Continued)

	Page
3-43 LPG Fuel Liquid Sensible Heat Absorption	53
3-44 LPG Fuel Specific Heat	53
3-45a. LPG Liquid Heat-Absorption Capability.	54
3-45b. Total Heat Absorption Capability	54
3-46 Baseline Temperature Distribution for Radiation-Cooled Chamber Concepts	58
3-47 Comparison of Equilibrium Throat Temperature for Refractory Radiation-Cooled Thruster	58
3-48 Comparison of Equilibrium Throat Temperature for CARB-I-TEX Radiation-Cooled Thruster	59
3-49 Effect of Recovery Temperature on Wall Temperature Distribution	59
3-50 Effect of CARB-I-TEX Throat Thickness On Throat Temperature	61
3-51 Effect of Carbon Disposition on CARB-I-TEX Wall Temperature Distribution.	61
3-52 Time Required for a CARB-I-TEX Radiation Chamber to Reach Study State	62
3-53 Transient Radiation-Cooled CARB-I-TEX Wall Temperature Response	62
3-54 Transient Radiation Cooled CARB-I-TEX Wall Temperature Response (Pulsed).	63
3-55 Transient Radiation Cooled CARB-I-TEX Wall Temperature Response (Pulsed).	63
3-56 Copper Conduction Cooled Chamber Temperature Distribution	65
3-57 Film-Conduction Cooling Thermal Model.	65
3-58 Optimum Copper Conduction-Cooled Chamber Configuration.	68
3-59 Comparison of Film Coolant Flow Rate Requirements.	68
3-60 Comparative Cooling Capability of LPG Film Coolant	69
3-61 Film Coolant Percentage Required Versus Chamber Pressure	72

ILLUSTRATIONS (Continued)

	Page
3-62 Total Heat Load Versus Characteristic Length and Chamber Pressure	72
3-63 Nondimensional Film Coolant Heat Flux Versus Chamber Pressure	73
3-64 Throat Temperature Versus Chamber Pressure	75
3-65 Effects of Chamber Geometry on Conductive Cooling Limits	75
3-66 Heat Rejection Characteristics for Conductively Cooled Thrusters	76
3-67 Effect of Chamber Thickness on Heat Flux Distribution. . .	78
3-68 Effect of Chamber Thickness on Temperature Distribution. .	78
3-69 Steady-State Isothermal Profiles	79
3-70 Film-Conduction Cooled Thruster Configuration with Isolation Slots	80
3-71 Effect of Isolation Slots on Nozzle Temperature Distribution	80
3-72 Transient Temperature Response of a Propane Cooled Thruster.	83
3-73 Effect of Initial Temperatures on Transient Response of a Propane Conductively Cooled Thruster	83
3-74 Thermal Conductivity of Candidate Conductive and Heat Sink Materials.	87
3-75 Thermal Diffusivity of Candidate Materials	87
3-76 Measure of Response of Candidate Materials	89
4-1 Basic 100-Pound-Thrust FLOX/LPG Injector Assembly.	97
4-2 Assembled 100 lbf FLOX/LPG Injector.	99
4-3 Disassembled View of 100 lbf FLOX/LPG Injector	99
4-4 Injector Orifice Configurations.	100
4-5 Close-Up View of Final Orifice Configuration	100

ILLUSTRATIONS (Continued)

	Page
4-6 100 lbf FLOX/LPG Injector Assembly with Integrated Film Coolant	103
4-7 Film Coolant Injector Body Prior to Final Assembly.	105
4-8 100 lbf FLOX/LPG Injector Assembly with External Film Coolant Manifold	107
4-9 Overall View of External Film Coolant Manifold	109
4-10 Thin Wall Copper Heat Sink Chamber Assembly (Cylindrical)	111
4-11 Thin Wall Copper Heat Sink Chamber Assembly (Tapered)	113
4-12 Overall View of Typical Heat Sink Chamber	115
4-13 Overall View of Heat Sink Chamber Showing Internal Grooving and Thermocouple Installation.	116
4-14 100 lbf FLOX/LPG Altitude Thruster Design (Thin Wall).	117
4-15 100 lbf FLOX/LPG Altitude Thruster Design (Thick Wall).	119
5-1 Oxidizer Orifice Hydraulic Characteristics.	122
5-2 Fuel Gap Hydraulic Characteristics	122
5-3 Oxidizer Passage Hydraulic Characteristics.	122
5-4 Coaxial Injector Cold Flow Collector.	123
5-5 Longitudinal Mass and Mixture Ratio Distribution.	126
5-6 Longitudinal Mass and Mixture Ratio Distribution.	126
5-7a Resulting Impingement Flow at Optimum Force Balance	127
5-7b Resulting Impingement Flow at Rated Volumetric Flow Rates	127
5-8 Film Coolant Manifold Hydraulic Characteristics	128
5-9 Film Coolant Manifold Hydraulic Characteristics	128
5-10 Film Coolant Manifold Hydraulic Characteristics	128
5-11 Film Coolant Impingement Characteristics	129
5-12 Schematic of FLOX/LPG Facility	131

ILLUSTRATIONS (Continued)

	Page
5-13 Overall View of FLOX/LPG Facility	132
5-14 Thrust Chamber Mount	132
5-15 100 Pound FLOX/LPG Thrust Stand	133
5-16 Schematic Representation of Chamber Showing Convective Heat Load Components	137
5-17 Baseline Injector Performance and Heat Transfer Data Without Film Cooling	141
5-18 Baseline Injector Performance and Heat Transfer Data Without Film Cooling	142
5-19 Baseline Injector Performance and Heat Transfer Data Without Film Cooling	142
5-20 Baseline Injector Performance and Heat Transfer Data Without Film Cooling	142
5-21 Baseline Injector Performance and Heat Transfer Data Without Film Cooling	143
5-22 Performance Data Runs (059-064) with 40% Film Cooling	147
5-23 Heat Transfer Data Runs (059-064) with 40% Film Cooling	147
5-24 Temperature Profile Run (064) (40% Film Cooling).	148
5-25 Performance Data Runs (065-066) with 50% Film Cooling	149
5-26 Heat Transfer Data Runs (065-066) with 50% Film Cooling	149
5-27 Temperature Profile Run (066) (50% Film Cooling).	150
5-28 Performance Data Runs (067-068) with 60% Film Cooling	151
5-29 Heat Transfer Data Runs (067-068) with 60% Film Cooling	151
5-30 Temperature Profile Run 068 (60% Film Cooling).	152

ILLUSTRATIONS (Continued)

	Page
5-31 Performance Data Runs (071-072) with 60% Film Cooling and Grooved Wall	153
5-32 Heat Transfer Data Runs (071-072) with 60% Film Cooling and Grooved Wall	153
5-33 Temperature Profile Run (071) (60% Film Cooling)	154
5-34 Performance Data Runs (073-074) with 60% Film Cooling. . .	155
5-35 Heat Transfer Data Run (073-074) with 60% Film Cooling . .	155
5-36 Temperature Profile Run (074)(60% Film Cooling).	156
5-37 Test Hardware with Shroud	157
5-38 Temperature Profile Run (075)(60% Film Cooling).	158
5-39 Performance Data Runs (076-077) with 60% Film Cooling and Higher ΔP_{IF}	160
5-40 Heat Transfer Data Runs (076-077) with 60% Film Cooling and Higher ΔP_{IF}	160
5-41 Temperature Profile Run (077) (60% Film Cooling)	161
5-42 Temperature Profile Run (081)(60% MMH Film Cooling). . . .	162
5-43 Performance Data Run (082-084) with 60% Film Cooling and Thick Walled Chamber	163
5-44 Temperature Profile Run (084) (60% Film Cooling)	164
5-45 Test Hardware with Splash Ring	165
5-46 Temperature Profile Run (085)(60% Film Cooling with Splash Ring)	166
5-47 Comparison of Thrust and Chamber Pressure C^* Measurements	174
5-48 Basic Injector Performance Summary (O/F Variation)	174
5-49 Basic Injector Heat Transfer Summary (O/F Variation) . . .	175
5-50 Basic Injector Performance Summary (L^* Variation)	175
5-51 Basic Injector Heat Transfer Summary (L^* Variation). . . .	176

ILLUSTRATIONS (Continued)

	Page
5-52 Basic Injector Performance Summary (P_c Variation)	176
5-53 Basic Injector Heat Transfer Summary (P_c Variation)	177
5-54 Film Cooling Performance Summary (O/F Variation)	178
5-55 Film Cooling Performance Summary (% F.C. Variation)	179
5-56 Film Cooling Heat Transfer Summary (O/F Variation)	181
5-57 Film Cooling Heat Transfer Summary (% F.C. Variation)	182
5-58 Effect of Chamber Contour and Film-Cooling on Initiation of Carbon Deposition	184
6-1 Inter-Regen Thermal Model	190
6-2 Isotherms and Accumulative Heat Load for a Steady-State Inter-Regen Thruster Test	190

TABLES

	Page
3-1 Summary of Exhaust Gas Chemical Species	17
3-2 Gaseous Species and Reactions Involved in the FLOX/Hydrocarbon Propellant Systems	20
3-3 Delivered Engine Performance Summary	32
3-4 Adiabatic Combustion Temperature FLOX/Blend, $P_o = 100$ psia	34
3-5 One-Dimensional Shifting Equilibrium Specific Impulse FLOX/Blend, $P_o = 100$ psia, $\epsilon = 60$, Vacuum	34
3-6 Design Concepts/Material Evaluated	37
3-7 Comparison of Throat Heat Flux and Gas Convection Coefficients ($P_o = 100$ psia, $T_w = 1500^\circ R$, Optimum Mixture Ratios for Each Propellant)	43
3-8 Comparison of Gas Convection Resistance at Optimum Mixture Ratio ($P_o = 100$ psia, Throat Station)	48
3-9 Physical Property Summary of Propellants.	50
3-10 Summary of Heat Absorption Capability of LPG Fuels	55
3-11 Summary of Pool Boiling Tests	56
3-12 Summary of Coefficients of Thermal Expansion	77
3-13 Comparison of LPG Fuels	84
3-14 Effective Heat Absorption Capability of LPG Fuels	85
3-15 Comparison of LPG Fuels	85
3-16 Heat Storage Effects for Several Candidate Thruster Materials	88
3-17 Summary of Thruster Material Considerations	92
4-1 Summary of Injector Design Calculations (FLOX/55% Methane-45% Ethane, O/F = 5.2)	110
5-1 Basic Injector Development Data	135
5-2 Basic Injector Characterization Data (No Film Cooling)	139

TABLES (Continued)

	Page
5-3 Film Coolant/Injector Data	145
5-4 Total Program Performance and Heat Transfer Data	169
5-5 Space Storable Thruster Corrected Performance	173
6-1 Comparison of Three Fuels	189

NOMENCLATURE

A	-	area	in^2
A	-	atomic ratio of hydrogen to carbon	-
Bi	-	Biot modulus	-
C*	-	characteristic exhaust velocity	ft/sec
C _f	-	thrust coefficient	-
C _p	-	gas specific heat	Btu/lbm-°R
D	-	diameter	inches
E	-	modulus of elasticity	lbf-in ²
F	-	momentum force	lbf
F	-	thrust	lbf
H	-	enthalpy	Btu/lbm
ΔH	-	enthalpy change	Btu/lbm
I _{sp}	-	specific impulse	lbf-sec/lbm
L	-	length	inches
L*	-	characteristic length	inches
M	-	Mach number	-
MR	-	mixture ratio	-
N	-	cycles	-
O/F	-	mixture ratio	-
P	-	pressure	lbf/in ²
Pr	-	Prandtl number	-
Q	-	heat absorption capability	Btu/lbm
Q̇	-	heat rate	Btu/sec
Q̇/A	-	heat flux	Btu/in ² -sec
q/A	-	heat flux	Btu/in ² -sec

Nomenclature (Continued)

R	-	radius	inches
R	-	gas constant	ft-lb _f /lbm-°R
R	-	thermal resistance	in ² -sec-°R/Btu
RF	-	recovery factor	-
T	-	temperature	°R
V	-	velocity	ft/sec
	-	volume	ft ³
\dot{w}	-	flow rate	lbm/sec
X	-	mass fraction	-
c*	-	characteristic exhaust velocity	ft/sec
d	-	differential	-
f	-	influence factor (chamber pressure)	-
g	-	gravitational constant	lbm-ft/lb _f -sec ²
h	-	heat transfer coefficient	Btu/in ² -sec-°R
k	-	thermal conductivity	Btu/sec-ft-°R
\dot{m}	-	flow rates	lbm/sec
q	-	heat rate	Btu/sec
r	-	radius	inches
t	-	thickness	inches
	-	time	seconds
v	-	velocity	ft/sec
\dot{w}	-	flow rate	lbm/sec
x	-	axial dimension	inches
α	-	angle	-
	-	coefficient of thermal expansion	in/in-°R
	-	thermal diffusivity	feet ² /sec

Nomenclature (Continued)

γ	-	gas specific heat ratio	-
ϵ	-	area ratio	-
	-	emissivity	-
	-	strain	inches
∂	-	partial differential	-
θ	-	time	seconds
	-	angle	
ρ	-	density	lbm/ft ³
μ	-	viscosity	lbm/ft-sec
Δ	-	finite differential	-
η	-	efficiency	-
σ	-	stress	lbf/in ²
	-	Stefan-Boltzman constant	Btu/sec-ft ² -°R ⁴
ν	-	Poisson's ratio	-
ϕ	-	influence factor (thrust)	-
Γ	-	function of γ	- -

Subscripts

a	-	ambient
am	-	arithmetic mean
c	-	contraction, chamber, combustion, gas, cold
c [*]	-	characteristic exhaust velocity
CH	-	chamber
div	-	divergence
DIS	-	discharge
e	-	exit, expansion
f	-	fuel, fracture ductility

Nomenclature (Continued)

fg	-	vaporization
FC	-	film coolant
FR	-	friction
g	-	gas, effective gas side
G	-	gas
HL	-	heat loss
i	-	inner
I_{sp}	-	specific impulse
k	-	kinetic
KE	-	kinetic
l	-	liquid
NOZ	-	nozzle
o	-	stagnation, outer, oxidizer, carbon deposition
p	-	plastic, pressure
r	-	radial
s	-	surface
SAT	-	saturated
t	-	total, throat
tc	-	thrust chamber
TR	-	throat radius
TOT	-	total
theo	-	theoretical
th	-	throat
v	-	vapor
vac	-	vacuum
vis	-	viscous

Nomenclature (Continued)

w	-	wall
W	-	wall
z	-	zonal
*	-	throat
∞	-	free stream

1. INTRODUCTION

The Space Storable Thruster Investigation, contract NAS 3-11184, was a detailed analytical and experimental evaluation of passive cooling techniques for reaction control thrusters utilizing the FLOX/LPG propellant combinations at a nominally 100 lbf thrust level.* A great deal of previous work involving both radiation and conduction (inner-regenerative) cooling has been performed on reaction control thrusters using the earth storable propellants; however, very little or no effort has been expended on the possible use of these cooling modes with the space storable propellants. The overall purpose of this effort was to determine the feasibility of the use of the FLOX/LPG propellant combinations for each of these passive cooling modes and to also determine relative ranking for three of the LPG fuels; methane, methane-ethane blend, and propane. The scope of this evaluation included detailed analytical examinations of both modes of passive cooling with each of the fuels. Corollary studies were made to determine performance maps for each propellant combination and the effects of each cooling mode on delivered performance. Additional examinations were made of certain physical properties of the LPG fuels, which were thought to be unreliable, in order to improve the accuracy of the analysis.

An early program direction decision to carry out the experimental tasks with the 55% methane/45% ethane blend was made, based on the studies described in Section 3.1, in order to ultimately take advantage of common propellant tankage in final system designs. The analytical studies showed that either a radiation cooled or conductively cooled design could be expected to operate satisfactorily with propane, whereas the blend was marginal and methane appeared to be unfeasible for inner-regenerative cooling operation. The inner-regenerative concept was selected for technology evaluation, since it appeared to offer the coolest design in a system with the potential of no throat erosion. The experimental hot firing tests were divided into two efforts: 1) achievement of the performance goal of 92% shifting equilibrium combustion characteristic velocity efficiency, and 2) a determination of the conduction cooling limits for inner-regeneratively cooled chambers.

As a conclusion to the program, a reevaluation of the analytical and experimental results was conducted to formulate design requirements and direction for future investigations into the inner-regenerative cooling applications with the LPG fuels.

* All FLOX mixtures are percentage of fluorine by weight.

2. SUMMARY

The Space Storable Thruster Investigation program effort, contract NAS 3-11184, consisted of an investigative evaluation of performance and of passive cooling techniques for reaction control thrusters employing the FLOX/LPG propellant combination, 80% FLOX blend and 55% methane/45% ethane fuel blend. The program efforts included analytical examination of several LPG propellants with respect to their potential thermal capacity to cool a thruster in an inner-regenerative cooling mode, analytical design of thruster approaches, injector design and performance evaluation, experimental thermal evaluations, and preliminary valve evaluations. The overall design goals included thruster design life goals of 1800 seconds, minimum thermal soak-back to injector/valve assemblies, lightweight, high pulse rate capability, and a goal of zero throat erosion.

The program was divided into six tasks. Task I involved analysis and preliminary design and evaluation of two basic thrust chamber cooling concepts for a nominal 100 lbf, 100 psia thruster using the space storable propellants FLOX/methane, FLOX/methane-ethane blend, and FLOX/propane. The two basic cooling concepts investigated were:

- Conductive (inner-regenerative) cooling with an internal film coolant used to accept heat
- Radiation cooling with metal conduction used to spread heat input.

Various materials evaluated in each of these concepts were copper, copper-beryllium, beryllium, nickel, graphites, and columbium. As a part of the overall thermal analysis, existing FLOX/LPG data on physical properties and carbon deposition correlations were reviewed and additional studies made where it was deemed necessary.

Three fuels, methane, 55/45 methane/ethane blend, and propane were analytically evaluated for potential use in the thruster. On the basis of the thermal analysis, the propane fuel rated as the superior fuel, primarily because of its expected superior carbon deposition behavior. Because of a desire for commonality of main propulsion and reaction control thruster propellants, the methane/ethane blend was chosen for the experimental program.

Complete performance analyses were made to determine the effects of chamber pressure, mixture ratio, film coolant percentages, and coolant schemes. The effects of kinetics and real fluid flow on performance were also calculated. Chamber material selection ratings and the effects of pulse duty cycle and steady-state operation on the overall thrust chamber durability were determined. As an additional study, thermal soakback was determined for the chamber/injector/valve arrangement.

Task II comprised the design and fabrication of an experimental copper chamber fully instrumented to obtain heat transfer and performance data during sea-level operation with FLOX/methane-ethane propellants. Also, preliminary designs of the altitude thruster were made. Certain features

of this design (i.e., chamber length, contraction angle, etc.) were left open to be selected on the basis of Task IV results.

Task III consisted of injector design and fabrication. The basic TRW coaxial injector design approach was utilized in the design. For the small thruster both a continuous slot design and discontinuous design were fabricated. The designs were made flexible to facilitate achievement of the performance goal.

The injector checkout tests were carried out during Task IV. Cold flows were made on the injectors to determine flow rate pressure drop data, mass and mixture ratio distributions, and overall impingement characteristics. Hot firing tests were made with variations in mixture ratio, chamber pressure, chamber length, and film coolant percentage to determine the thruster performance and heat transfer characteristics. The nonfilm-cooled chamber was found to have heating rates far above those necessary for successful film conduction cooling (15-20 versus 4-6 Btu/sec). Subsequent tests were performed with varying film coolant percentages and various chamber and injector modifications to reduce these heating rates. Throughout the test series, it was found that liquid fuel propellants could not be maintained on the chamber walls. To improve the film cooling efficiency, chamber geometry variations with a tapered combustion chamber geometry were investigated. With 60% film coolant and a tapered grooved chamber, nozzle heat loads near those necessary for inner-regenerative cooling were achieved; however, a hot spot in the chamber barrel prohibited conductive cooling from occurring.

The indicated difficulties in achieving properly controlled wall environments for true inner-regeneratively cooled operation resulted in a program direction to more thoroughly assess the thermal interaction environment with the exclusion of actual altitude testing in subsequent tasks. A test with MMH as the film coolant resulted in successful conduction-cooled operation, thus strongly indicating that the main problem was associated with the volatility of the space storable fuel. As a final test on the program, a splash plate was added to the injector in an attempt to isolate the main combustion from the film coolant layer. This test also resulted in steady-state operation indicating that the space storable propellant methane-ethane can be made to operate in a conduction-cooled mode. It was also noted that this was achieved with gaseous fuel on most of the wall and the possibility of liquid on only about the first 0.5 inch of the chamber.

Task V was to have been altitude tests on the final cooled thruster design. These were not run because of the extra effort required in Task IV to more thoroughly understand the requirements of a thruster capable of inner-regeneratively cooled operation with the LPG fuels.

Task VI was comprised of a design reevaluation based on all of the experimental and analytical data generated. These findings showed that two cooled thruster designs should be considered, one having a thin throat thickness if the film coolant fluid is not of marginal heat absorption capability and one having a thick throat and isolation slot if the film coolant is marginal. Also indicated is a strong possibility of LPG gaseous film cooling, provided that combustion interaction efforts are minimized.

3. THRUSTER DESIGN ANALYSIS

In this section, the basic thruster design analysis efforts are presented. Included are data on propellant performance characterization, thruster thermal analysis, material design considerations, thruster design tradeoff analyses, scaling data, and valve design selection discussion.

3.1 PROPELLANT EVALUATION

As part of the Task I cooling concept evaluation, detailed analyses were performed to characterize the three selected FLOX/LPG propellants (methane, 55/45 methane-ethane, propane) as to their performance and chemical characteristics.

This analysis effort was performed in two parts:

- Propellant performance characterization
- Delivered propellant performance estimates.

The propellant performance characterization included the frozen and equilibrium performance determination, exhaust gas chemical specie determination, and the evaluation of the fuel decomposition characteristics. Since a large quantity of data were generated during the performance characterization analysis and since it was not convenient or necessary to present all of the data in the following discussion, all data generated are presented in summary in Appendix A.

The second phase of the analysis was concerned with estimating the delivered performance of the propellant system. Included in this analysis was the determination of kinetic losses, divergence losses, and viscous losses. Zonal losses which include the effects of nonuniform mass and mixture ratio distribution within the chamber were also investigated. These loss determinations are described in Section 3.1.4.1.

The three propellant combinations evaluated were:

82.5% FLOX/ CH_4

80% FLOX/55% CH_4 + 45% C_2H_6

76% FLOX/ C_3H_8

The nominal operating parameters for the basic thruster design were:

Thrust (F)	100 lbf vacuum
Chamber Pressure (P_o)	100 psia
Nozzle Expansion Ratio (ϵ)	60

3.1.1 Equilibrium and Frozen Performance and Propellant Characterization

Shifting equilibrium and frozen propellant performance calculations were performed for each of the propellant systems at chamber pressures of 50, 100, 200, 500, and 750 psia with the Reference 1 program. These calculations were conducted over a range of mixture ratios sufficient to establish the peak equilibrium and frozen performance points for each of the pressures. A wider range of mixture ratios were covered at the 100 psia chamber pressure to better define the performance characteristics and chemical specie concentrations at off-mixture ratio conditions. Figure 3-1 presents the frozen and equilibrium specific impulse for the 82.5% FLOX/CH₄ propellant combination at a chamber pressure of 100 psia. A summary curve is shown in Figure 3-2 where the equilibrium specific impulse is compared for each chamber pressure investigated. The equilibrium characteristic velocity and equilibrium combustion temperature are presented in Figures 3-3 and 3-4 for each of the chamber pressures investigated. Similar results are presented for the 80% FLOX/55% CH₄ + 45% C₂H₆ and 76% FLOX/C₃H₈ in Figures 3-5 through 3-8 and Figures 3-9 through 3-12, respectively.

Each of the performance parameters are sensitive to mixture ratio. The specific impulse is much more sensitive, however, to mixture ratio variations that exceed the peak equilibrium, thus indicating that the real performance of the propellant system will be very dependent on mixture ratio and mass distributions in the combustion chamber. A more detailed description of the effects of mass and mixture ratio distributions is presented in Section 3.1.4

Since the peak performances of the FLOX/LPG combinations occur at the stoichiometric mixture ratio, the mixture ratios at which the performance, characteristic velocity, and combustion temperature peaks occur show no dependence on pressure. However, the magnitude of these parameters vary with pressure as indicated in the previous figures. For example, the 80% FLOX/55% CH₄ + 45% C₂H₆ propellant combination combustion temperature varies from 7300°R at 50 psia to 8250°R at 750 psia and the characteristic velocity varies from 6860 ft/sec at 50 psia to 7130 ft/sec at 750 psia. Each of the other propellant combinations have similar variations. The equilibrium specific impulse mixture ratio variation is insensitive to chamber pressure; however, the frozen specific impulse changes substantially with pressure as indicated in Figure 3-13.

A performance summary for each of the propellants investigated is presented in Figure 3-14. The FLOX/CH₄ combination exhibits the highest equilibrium performance of 424.7 seconds with FLOX/methane-ethane following at 422.6 seconds and the FLOX/C₃H₈ showing the lowest performance of 415.4 seconds. The performance values are quoted at a chamber pressure of 100 psia at their respective peak equilibrium mixture ratios of 5.75, 5.33, and 4.50 using an expansion area ratio of 60.

The sensitivity of the performance of FLOX/55% CH₄ + 45% C₂H₆ propellant combination to FLOX concentration variations from the optimum FLOX concentration was also briefly investigated. The specific impulse and characteristic velocity variations with percent FLOX concentration are shown in Figure 3-15.

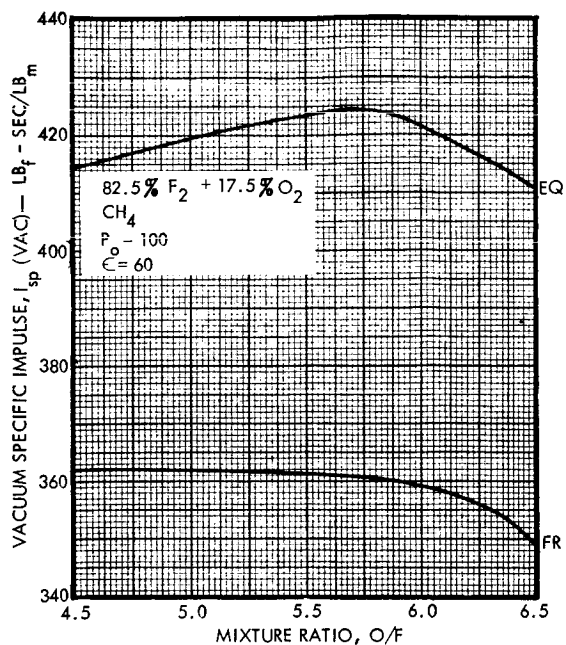


Figure 3-1. Vacuum Specific Impulse (CH_4)

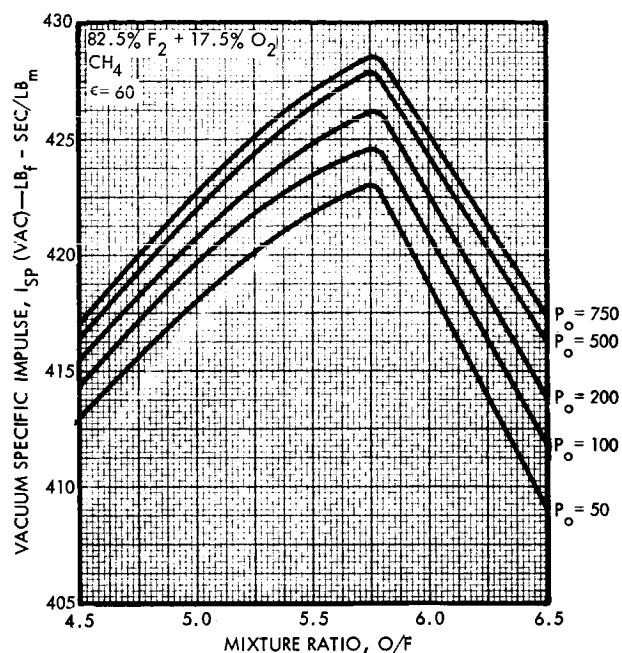


Figure 3-2. Vacuum Specific Impulse (P_c Variation) (CH_4)

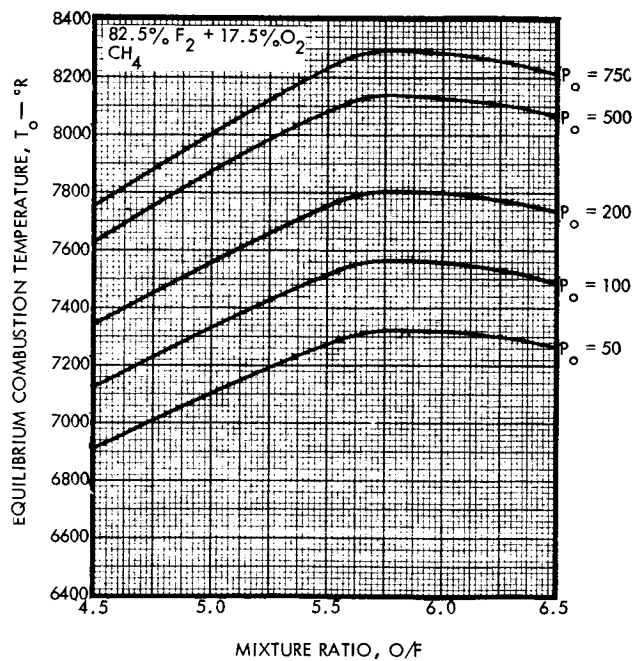


Figure 3-3. Equilibrium Characteristic Velocity (P_c Variation) (CH_4)

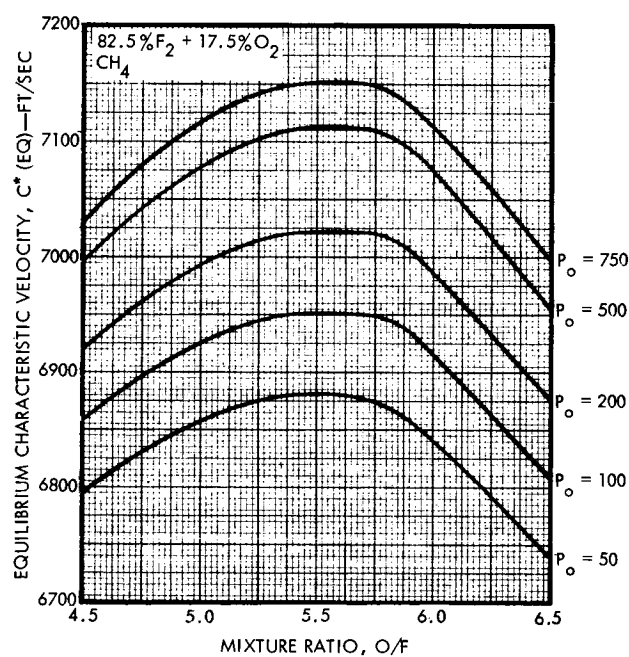


Figure 3-4. Equilibrium Combustion Temperature (P_c Variation) (CH_4)

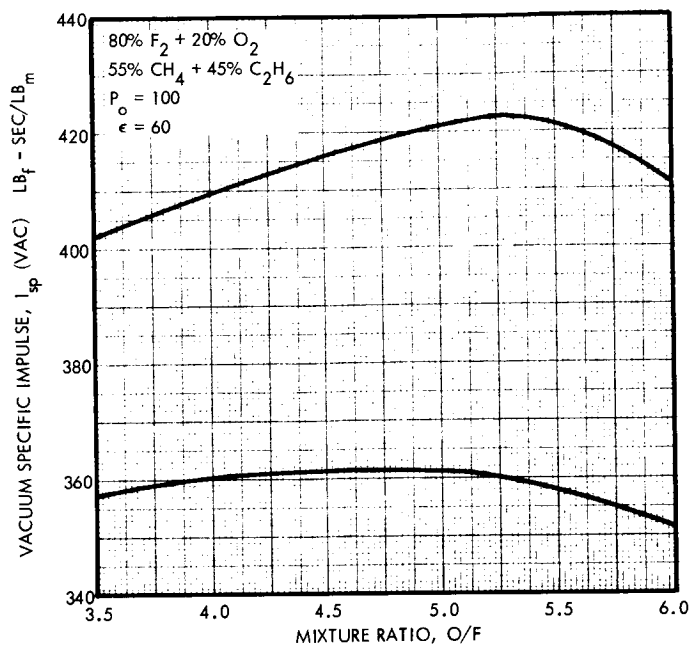
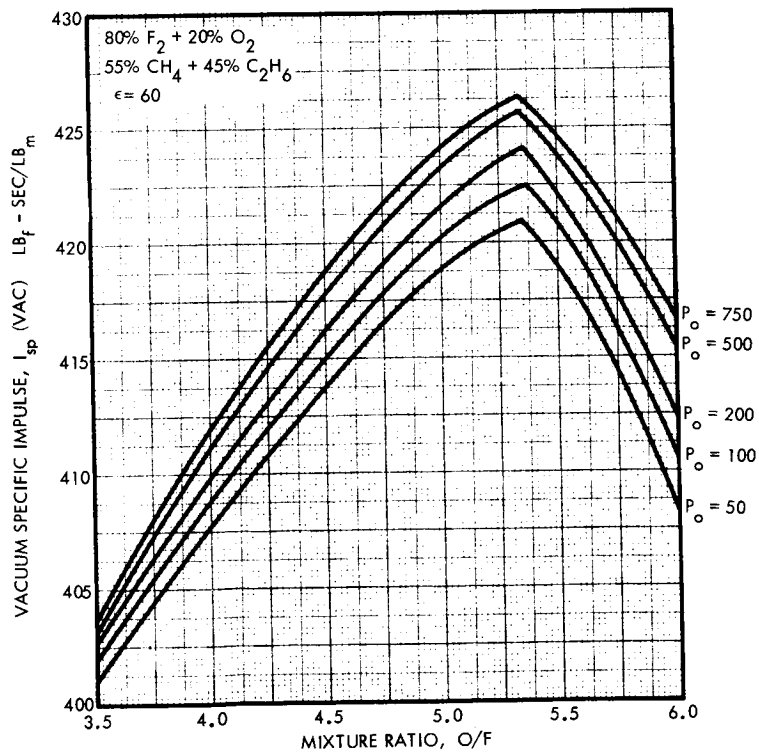


Figure 3-5
Vacuum Specific Impulse
(55% $CH_4 + 45\% C_2H_6$)

Figure 3-6
Vacuum Specific Impulse
(P_c Variation)
(55% $CH_4 + 45\% C_2H_6$)



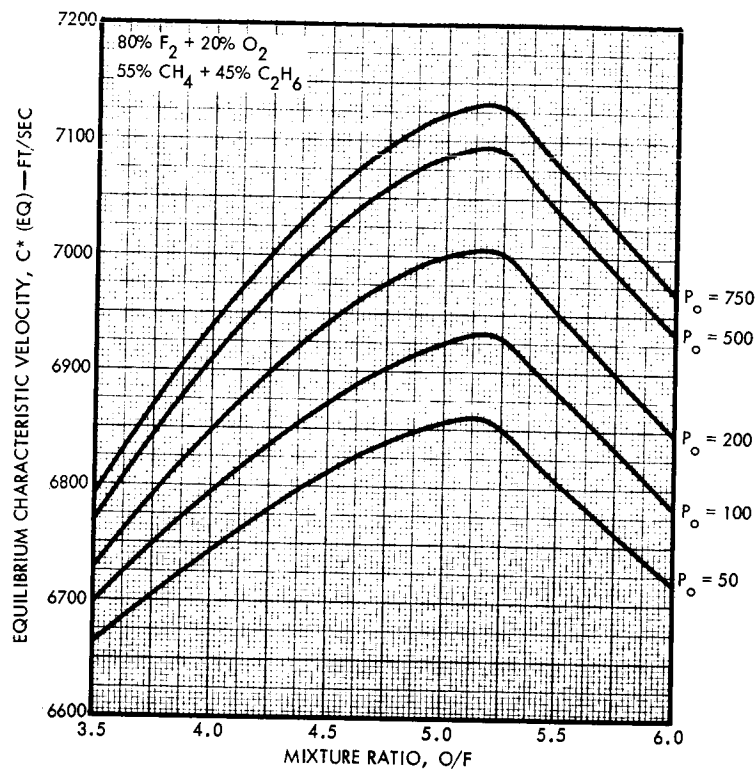
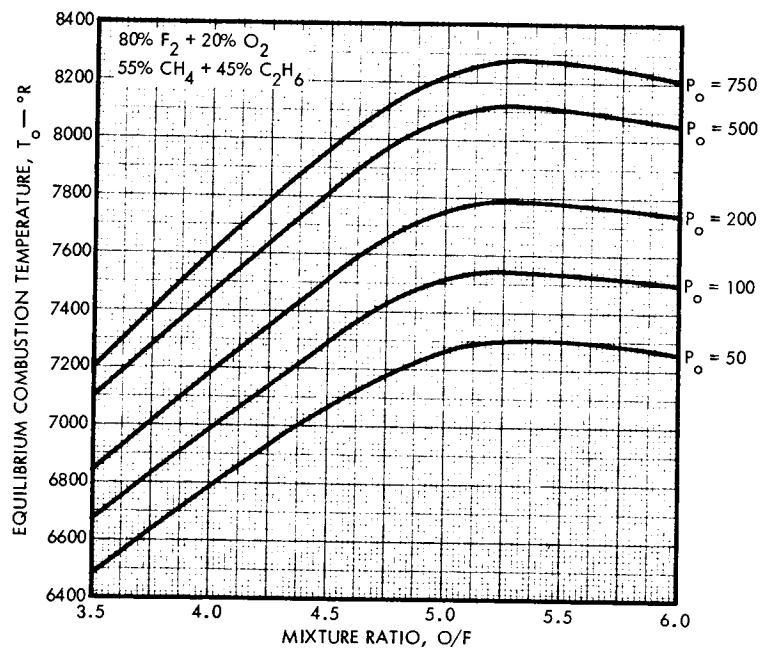


Figure 3-7
Equilibrium Characteristic
Velocity (P_c Variation)
(55% CH_4 + 45% C_2H_6)

Figure 3-8
Equilibrium Combustion
Temperature (P_c Variation)
(55% CH_4 + 45% C_2H_6)



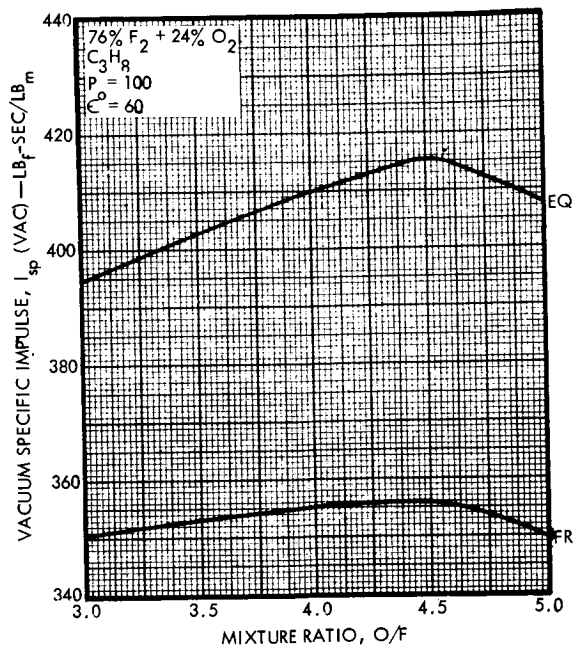


Figure 3-9. Vacuum Specific Impulse (C_3H_8)

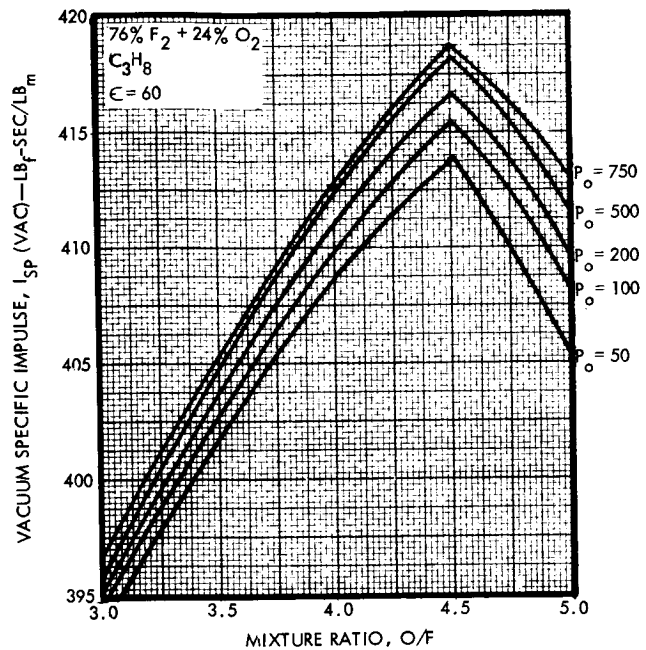


Figure 3-10. Vacuum Specific Impulse (P_c Variation) (C_3H_8)

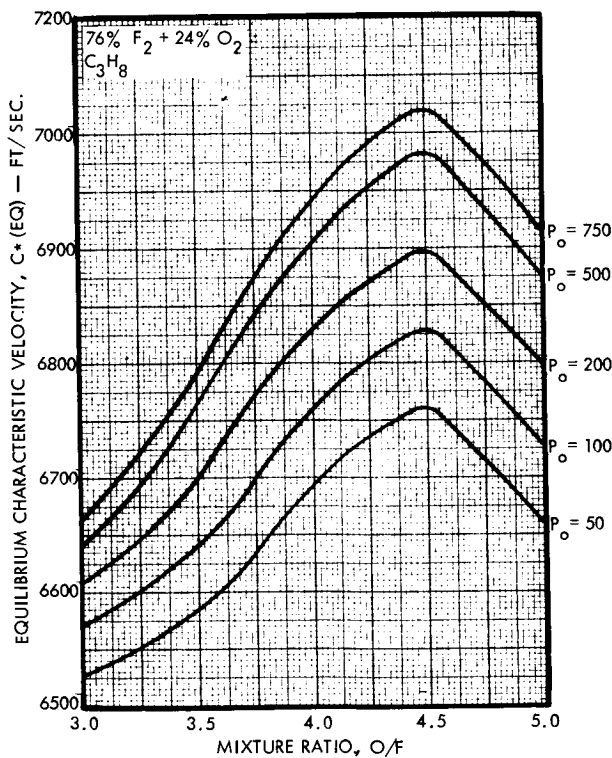


Figure 3-11. Equilibrium Characteristic Velocity (P_c Variation) (C_3H_8)

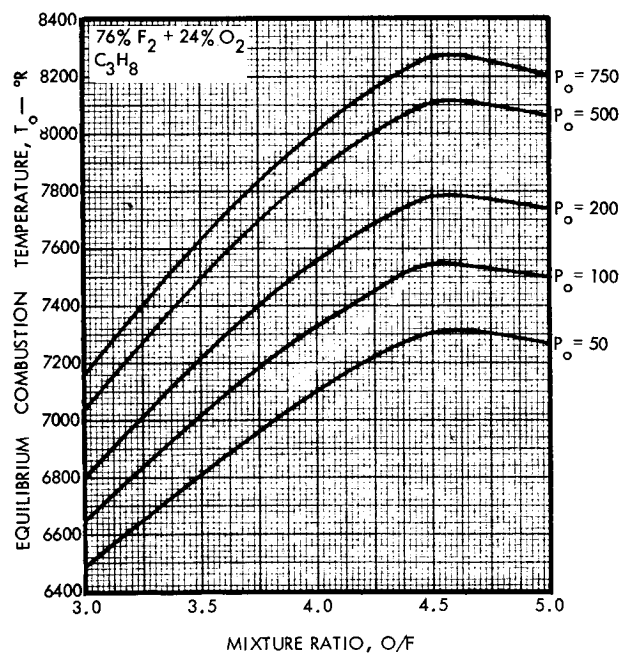


Figure 3-12. Equilibrium Combustion Temperature (P_c Variation) (C_3H_8)

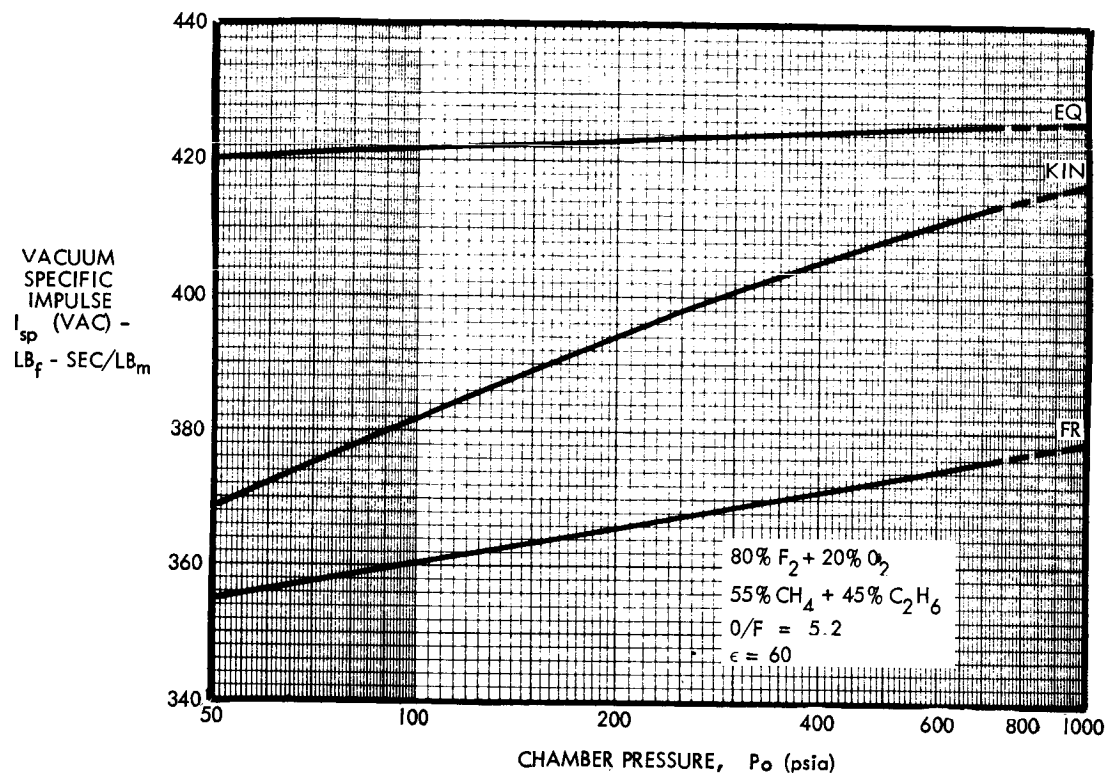


Figure 3-13. Effect of Chamber Pressure on Vacuum Specific Impulse (55% $CH_4 + 45\% C_2H_6$)

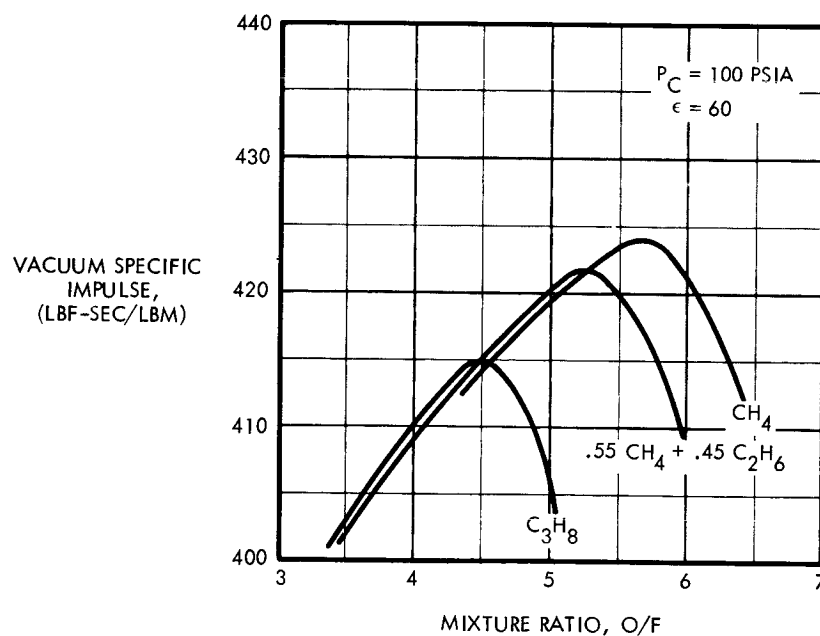


Figure 3-14. Summary Curves of Vacuum Specific Impulse (All Fuels)

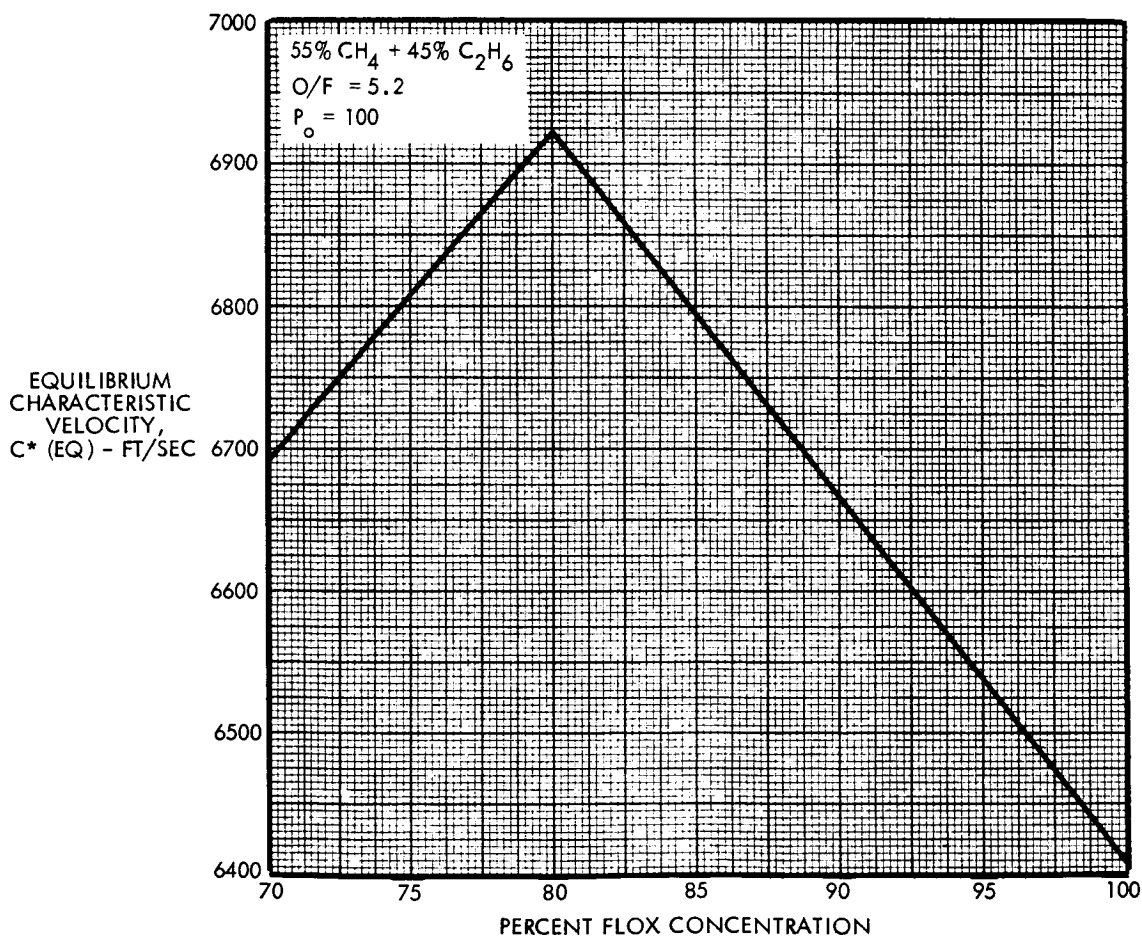
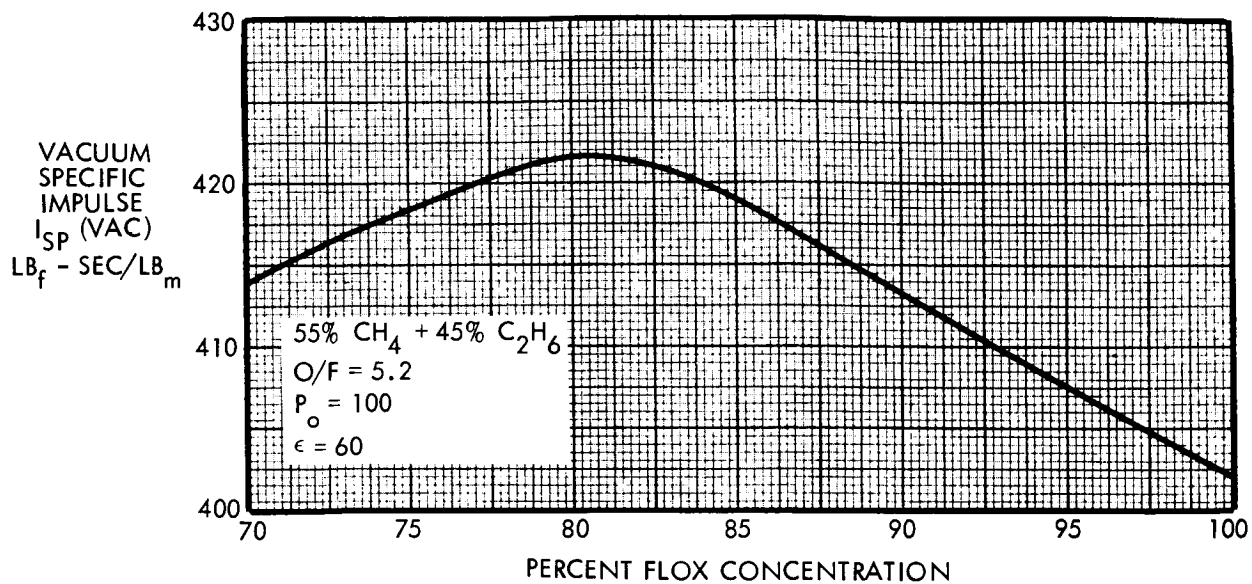


Figure 3-15. Performance Versus FLOX Concentration
(55% CH_4 + 45% C_2H_6)

3.1.2 Fuel Decomposition

The thermal decomposition of the fuels is of interest because of the cracking characteristics of the fuels and the resultant carbon yield for coking of carbon on the chamber walls. The carbon serves as a good thermal insulation layer to block the convective heat transfer to the chamber wall. Figure 3-16 compares the condensed phase carbon available from each of the fuels as a function of temperature. Each of the fuels begins decomposition at approximately 1000°R with the maximum yield of carbon occurring at approximately 3000°R . The decrease in available carbon at the higher temperatures is the result of the reaction of the carbon and hydrogen to form higher molecular weight gas constituents, such as acetylene.

The monopropellant performance (I_{sp}) for each of the fuels is shown in Figure 3-17 for each of the fuels as a function of heated gas temperature. The methane shows the highest monopropellant performance, with the methane-ethane blend and propane fuels following respectively in performance levels. These results are useful for estimating the performance degradation due to film cooling, assuming no mixing.

3.1.3 Gas Specie Composition

In addition to the general performance characteristics of the propellant system discussed above, the gas specie concentrations were determined. These are shown graphically in Figure 3-18 for each of the propellant systems investigated. The results are presented for the combustion chamber at a pressure of 100 psia. These data were generated in order that some insight could be obtained as to the gas species concentration that might exist at the combustion chamber wall. Each of the propellant systems is similar in distribution of species concentration versus mixture ratio. At mixture ratios near stoichiometry, the primary gas specie concentrations are hydrogen fluoride (HF) and carbon monoxide (CO). Low quantities of dissociated hydrogen and fluorine also exist with the free monatomic fluorine concentration increasing rapidly as the mixture ratio increases from about 4. (The free fluorine is not chemically compatible with any known materials at operating temperature levels to be experienced in most thruster applications.) With the exception of the very low mixture ratios ($O/F < 1$) where low concentrations of water vapor exist, the chemical species are compatible with graphites, copper, and nickel when used in the proper temperature range. At mixture ratios of approximately 3 and below, the condensed phase carbon concentration increases rapidly as the mixture ratio is lowered. Thus, if the barrier region of the combustion chamber is operated at these low mixture ratios considerable quantities of condensed phase carbon are available for coking on the combustion chamber wall with a resultant thermal resistance to heat transfer. It would appear from these results that the barrier region of the chamber would have to be in a relatively low fuel rich mixture ratio condition ($O/F < 3$) to insure coking on the chamber wall.

Another general guideline which may be established from these equilibrium specie concentration calculations is that from a practical point of view, because of the designer's inability to accurately control the circumferential uniformity of the barrier mixture ratio, the barrier mixture ratio must be, on the average, lower than that where free fluorine appears in order to insure chamber durability and essentially infinite chamber life.

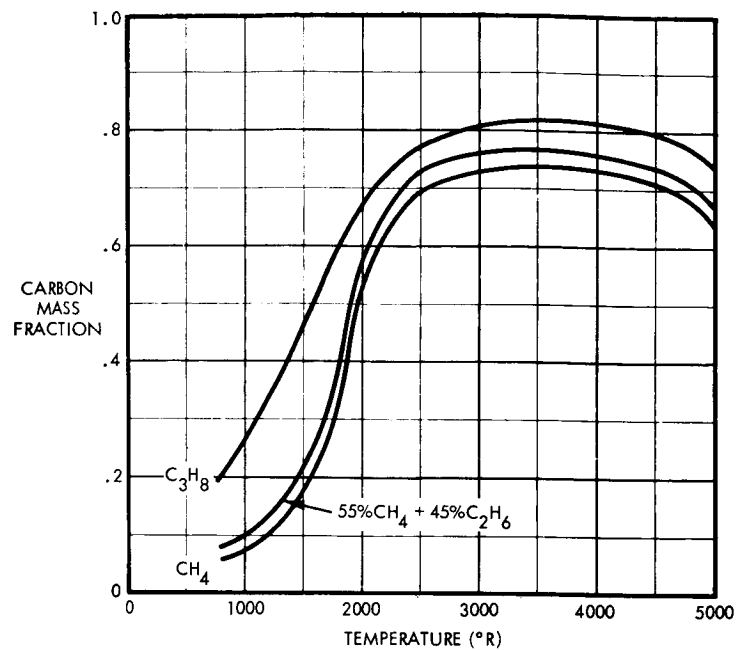


Figure 3-16. Carbon Deposition Mass Fraction (All Fuels)

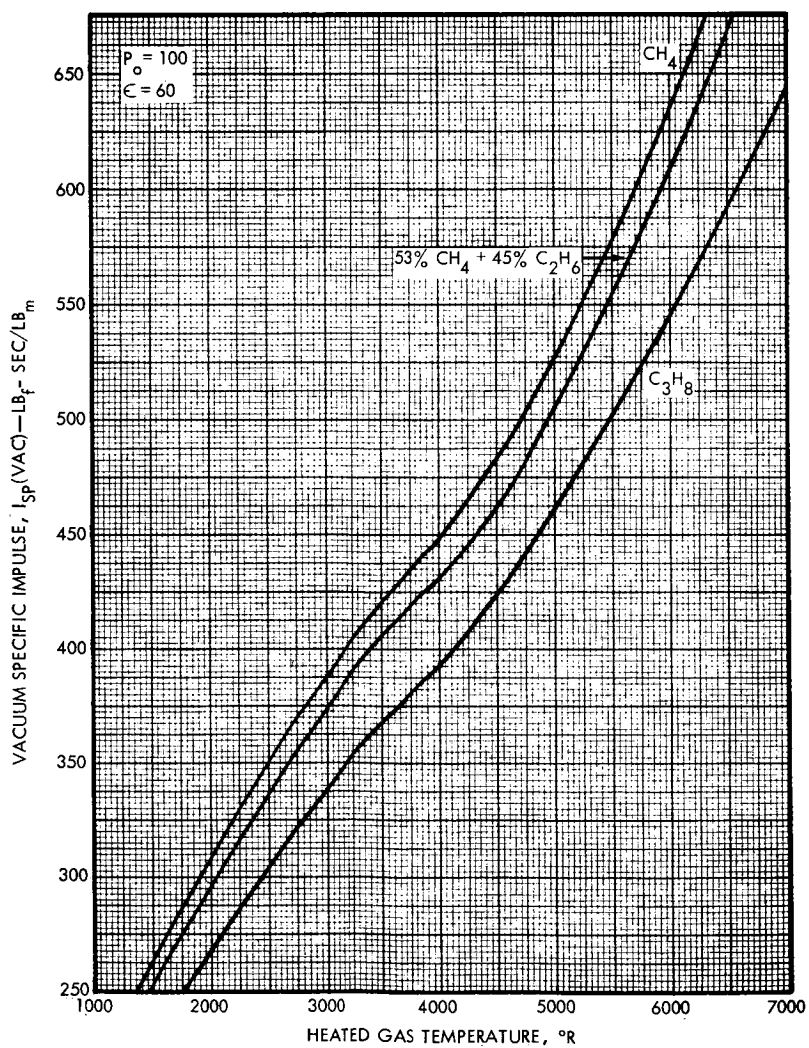


Figure 3-17
Vacuum Specific Impulse
of Monopropellant
LPG Fuels

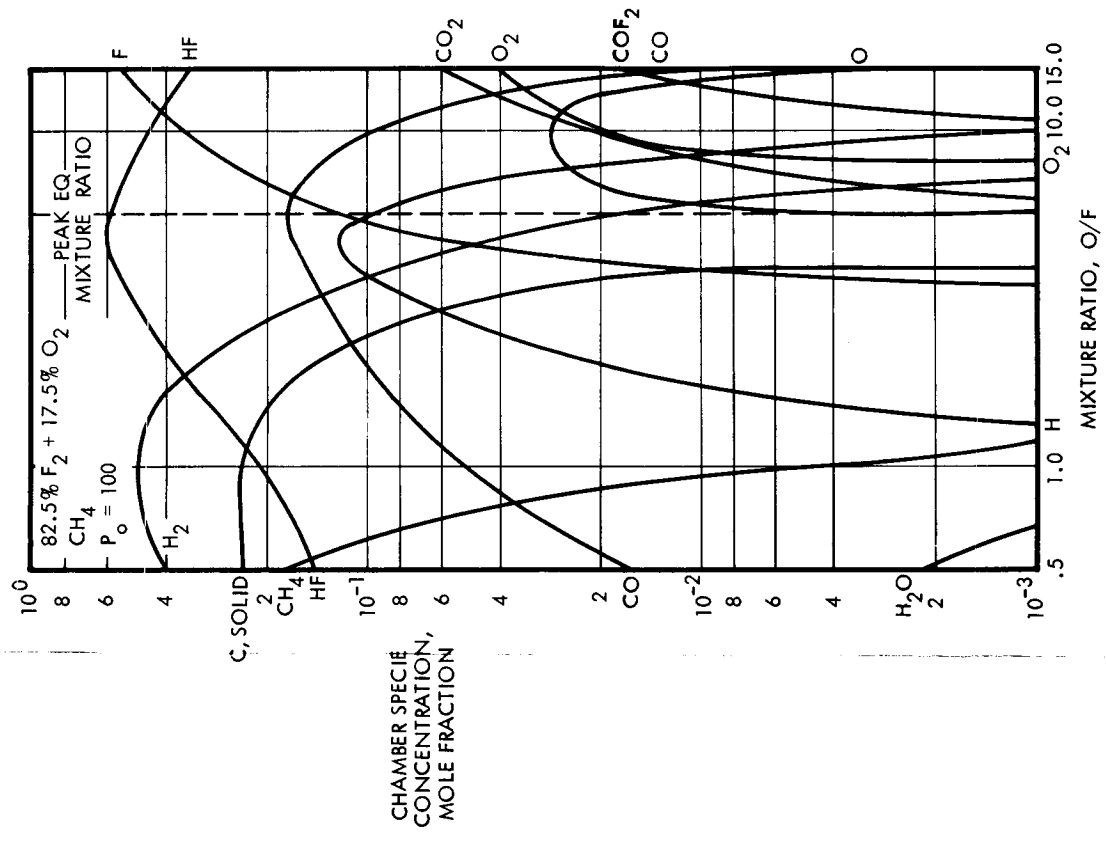
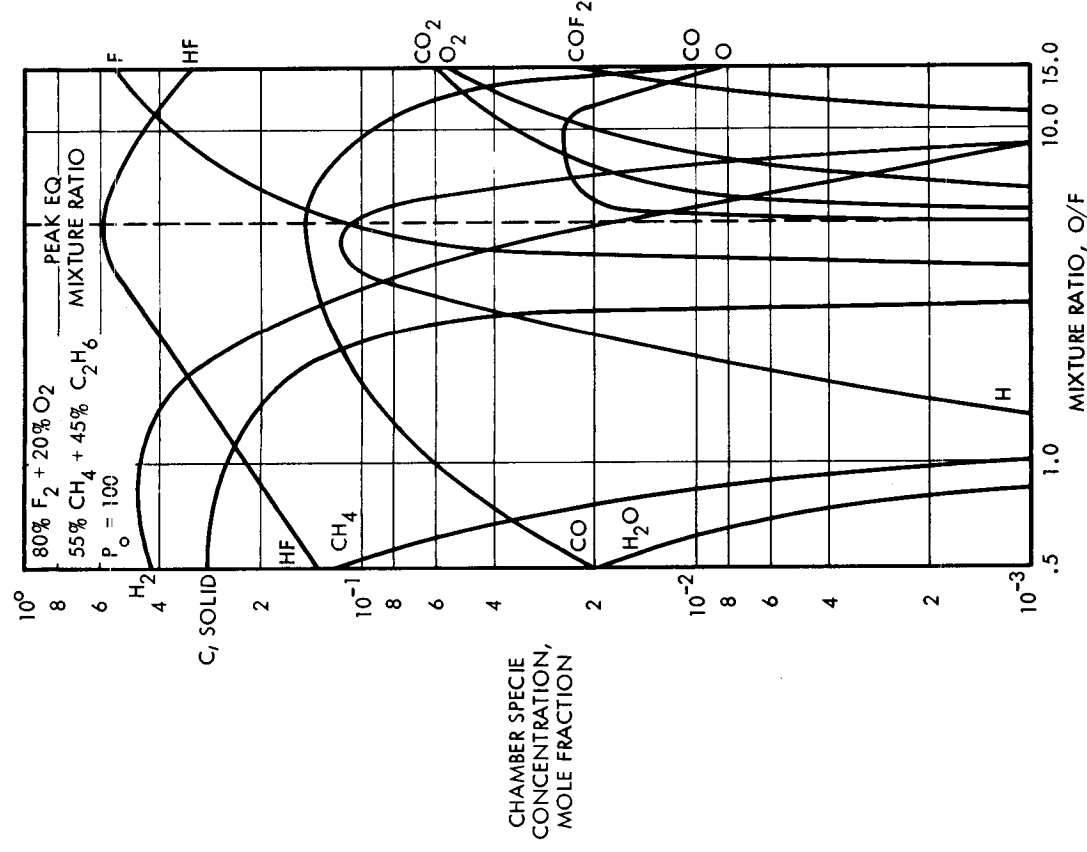
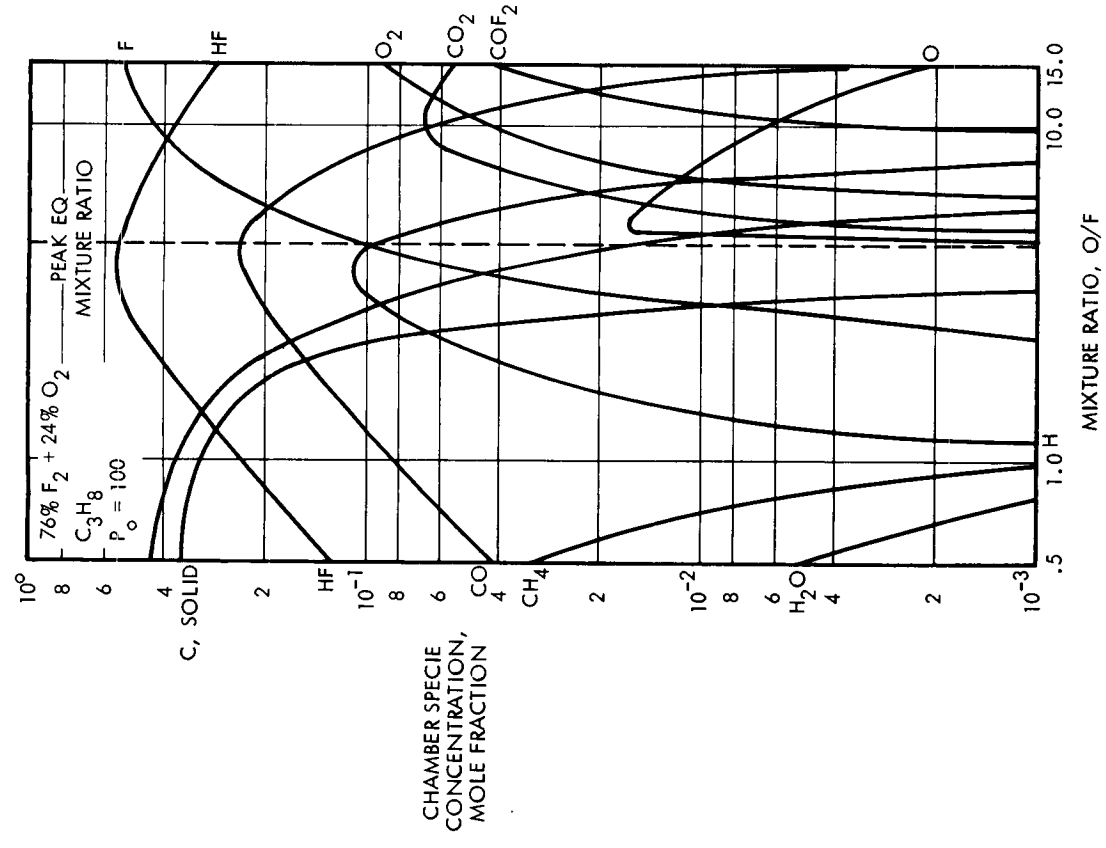


Figure 3-18. Chamber Specie Concentrations for All Propellant Combinations

To achieve this condition, some degradation of the engine performance is required. Tradeoffs can be made, however, considering heat transfer, performance, and chamber life.

The specie concentrations are relatively insensitive to chamber pressure. A summary of the specie concentrations in the chamber is given in Table 3-1 at the peak mixture ratio for the 80% FLOX/55% CH₄ + 45% C₂H₆ propellant combination. Data are presented at pressures of 100 and 750 psia and at expansion ratios of 10 and 60 for a chamber pressure of 100 psia.

Table 3-1. Summary of Exhaust Gas Chemical Species
(80% FLOX/55% CH₄ + 45% C₂H₆)

CHEMICAL SPECIE	SPECIE CONCENTRATION, MOLE FRACTION			
	P _o = 750	P _o = 100		
	CHAMBER	CHAMBER	ε = 10	ε = 60
CO	.20311	.19843	.21978	.22126
CO ₂	.00025	.00015	.00188	.00235
F	.09718	.11394	.00373	---
H	.07921	.10576	.01320	---
H ₂	.02104	.01607	.00847	.01348
H ₂ O	.00023	.00011	.00046	.00038
HF	.59671	.56320	.75207	.76247
O	.00138	.00170	.00018	---
OH	.00068	.00047	.00018	---

3.1.4 Delivered Performance Estimates

The following discussion presents the techniques used to determine the delivered performance for each of the propellant systems investigated. These calculations were performed at the nominal design conditions shown below over a range of mixture ratios.

Chamber Pressure (P _o)	100 psia
Thrust (vacuum)	100 lbf
Nozzle Expansion Ratio (ε)	60

A brief survey of the effects of chamber pressure and thrust level on the kinetic losses was performed and is given in Section 3.1.4.1.

For the purpose of this analysis, the performance loss factors are treated in two categories:

- Thrust chamber performance losses
- Injector combustion efficiency losses (including cooling losses)

Thus, it is possible to define the engine efficiency ($\eta_{I_{sp}}$) as:

$$\eta_{I_{sp}} = I_{sp} \text{ (del)} / I_{sp} \text{ (Eq)} = \eta_{C^*} \eta_{tc} \quad (3-1)$$

where

- η_{C^*} = combustion efficiency
- η_{tc} = thrust chamber efficiency
- $I_{sp} \text{ (del)}$ = delivered engine performance
- $I_{sp} \text{ (Eq)}$ = shifting equilibrium performance

The thrust chamber efficiency includes the recombination losses (kinetic losses), nozzle divergence losses, viscous losses (combined friction and heat transfer losses), and zonal losses. The thrust chamber efficiency (η_{tc}) is defined as follows:

$$\eta_{tc} = I_{sp} \text{ (TC)} / I_{sp} \text{ (Eq)} = \eta_k \eta_{vis} \eta_{div} \eta_z \quad (3-2)$$

where

- η_{tc} = thrust chamber efficiency
- $I_{sp} \text{ (TC)}$ = delivered thrust chamber performance for an ideal injector (100% combustion efficiency)
- $I_{sp} \text{ (Eq)}$ = equilibrium specific impulse
- η_{kin} = recombination losses
- η_{div} = nozzle divergence losses
- η_{vis} = viscous losses
- η_z = zonal losses

For the purpose of defining the performance losses, an 80% Bell nozzle was selected having the following characteristics. The design of the nozzle was obtained using the analysis program of Reference 2. The basic nozzle parameters were:

Nozzle expansion ratio (ϵ)	=	60
Nozzle exit radii (R_e/r_{th})	=	7.746
Nozzle length (L/r_{th})	=	20.4
Nozzle exit lip angle (α)	=	9.4°
Downstream throat blend radii (R/r_{th})	=	2

No attempt was made to investigate other nozzle geometries, but rather, the approach was to select a nozzle configuration and define the loss components for comparison with experimental data. Comparisons with various nozzle designs are presented in References 3 and 4.

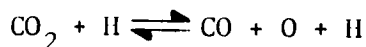
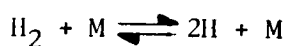
Each of the performance loss components discussed above were computed in an uncoupled mode. The analysis technique is covered in the following sections.

3.1.4.1 Performance Loss Analysis

Recombination Losses. Because of the high theoretical combustion temperatures and the resultant dissociated gas species, it was anticipated that the FLOX/LPG's would have relatively large recombination (kinetic) losses. The TRW technique (Reference 5) employed for computing the kinetic losses is an exact technique in that reaction rate equations are integrated throughout the complete expansion process. The analysis approach does not require the use of any freezing criteria and is limited only to the extent of the uncertainty in the rate constants.

The 12 gaseous species shown in Table 3-2 and related by the tabulated 23 chemical reactions were used in the calculation procedure.

The reaction rate constants were obtained from the study of Reference 6. It was also established (Reference 7) that the important reactions for the propellant system (containing C, O, and F) were:



that is, these six reactions affected specific impulse by greater than ± 0.5 lbf sec/lbm at an expansion area ratio of 40 when either their rate constants were:

- Increased to their estimated current uncertainty
- Reduced to zero (which freezes the reaction)

Kinetic calculations were performed for each of the three propellant combinations at their peak equilibrium mixture ratios, and additional calculations were performed at lower mixture ratios for the FLOX/methane-ethane blend propellant. The kinetic efficiency is shown in Figure 3-19.

Table 3-2. Gaseous Species and Reactions Involved in the FLOX/Hydrocarbon Propellant Systems

SPECIES

- | | |
|--------------------|---------------------|
| 1. C | 7. H ₂ |
| 2. CO | 8. H ₂ O |
| 3. CO ₂ | 9. HF |
| 4. F | 10. O |
| 5. F ₂ | 11. O ₂ |
| 6. H | 12. OH |

REACTIONS

- | | |
|---|--|
| 1. CO ₂ + M \rightleftharpoons CO + O + M | 13. CO + CO \rightleftharpoons CO ₂ + C |
| 2. H ₂ O + M \rightleftharpoons OH + H + M | 14. CO + H \rightleftharpoons C + OH |
| 3. CO + M \rightleftharpoons C + O + M | 15. CO + O \rightleftharpoons C + O ₂ |
| 4. F ₂ + M \rightleftharpoons 2F + M | 16. HF + F \rightleftharpoons H + F ₂ |
| 5. HF + M \rightleftharpoons H + F + M | 17. HF + H \rightleftharpoons H ₂ + F |
| 6. H ₂ + M \rightleftharpoons 2H + M | 18. HF + HF \rightleftharpoons H ₂ + F ₂ |
| 7. OH + M \rightleftharpoons O + H + M | 19. HF + O \rightleftharpoons OH + F |
| 8. O ₂ + M \rightleftharpoons 2O + M | 20. HF + OH \rightleftharpoons H ₂ O + F |
| 9. CO ₂ + H \rightleftharpoons CO + OH | 21. H ₂ + O \rightleftharpoons OH + H |
| 10. CO ₂ + O \rightleftharpoons CO + O ₂ | 22. H ₂ + O ₂ \rightleftharpoons 2OH |
| 11. H ₂ O + H \rightleftharpoons OH + H ₂ | 23. H ₂ + O ₂ \rightleftharpoons 2OH |
| 12. H ₂ O + O \rightleftharpoons 2OH | |

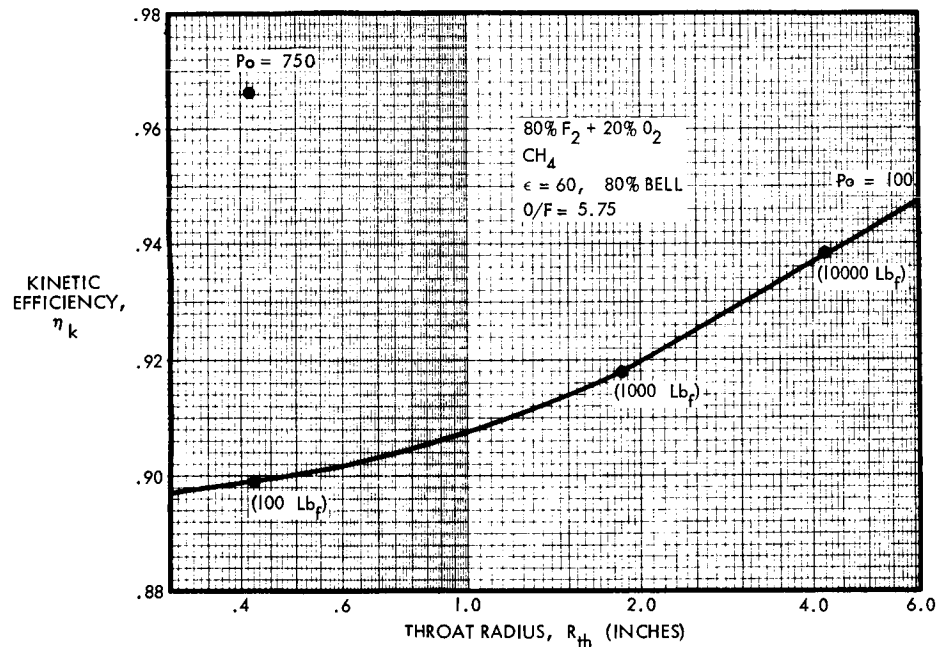


Figure 3-19. Effect of Engine Thrust Level and Chamber Pressure on Kinetic Efficiency

Divergence Losses. The divergence loss is essentially a loss due to nozzle geometry in that the gases leave the nozzle exit at some angle with respect to the nozzle axis. The momentum loss to nonaxial alignment of the exit momentum vector results in the divergence loss.

The divergence loss coefficient (η_{div}) was determined as follows:

$$\eta_{div} = \frac{C_{f2D}}{C_{f1D}} \quad (3-3)$$

where C_{f2D} is the two-dimensional inviscid thrust coefficient for the 80% Bell nozzle and C_{f1D} is the one-dimensional inviscid thrust coefficient. Both values were computed assuming constant γ expansion and expansion area ratio of 60. The computed divergence loss coefficient was used as a constant throughout the analysis and was:

$$\eta_{div} = 0.987 \quad (3-4)$$

Viscous Losses. The combined friction and heat transfer losses which are defined as the viscous losses were computed using the analysis technique of Reference 9. This technique considers the simultaneous solution of the integral momentum and integral energy equations for the turbulent boundary

layer in a rocket engine. From the solution of these equations, the momentum efficiency at the exit of the nozzle due to the boundary layer can be determined.

$$\Delta M_x = \frac{\rho U^2}{2g} 2\pi r_e \theta \cos \alpha_e \quad (3-5)$$

where

$$\begin{aligned} \Delta M_x &= \text{axial component of momentum deficiency due to boundary layer} \\ \frac{\rho U^2}{2g} &= \text{inviscid momentum flux at edge of boundary layer} \\ r_e &= \text{nozzle exit radius} \\ \theta &= \text{momentum thickness} \\ \alpha_e &= \text{nozzle exit lip angle} \end{aligned}$$

The viscous loss parameter was computed as

$$\eta_{vis} = 1 - \frac{\Delta M_x}{F} \quad (3-6)$$

where the thrust (F) is the inviscid vacuum thrust based on the equilibrium thrust coefficient.

The results of the analysis are presented in Figure 3-20. All viscous corrections were computed using a mixture ratio of 5.3 for the 80% FLOX/methane-ethane blend since the computed variations with mixture ratio are well within the accuracy of the overall analysis.

Zonal Losses. As previously discussed, the FLOX/LPG propellant combination performance levels are sensitive to variations in mass and mixture ratio distribution across the chamber. From a chamber heat rejection control and chemical compatibility point of view, some off-mixture ratio control will be required at the combustion chamber wall. The following discussion shows the sensitivity of performance to zonal effects considering variations on mass and mixture ratio distribution. The sensitivity of the specific impulse and characteristic velocity to zone effects was evaluated using a two-zone model shown schematically in Figure 3-21.

The model used is a simplification of a more generalized multi-zone model which is used to predict performance from injector cold flow hydraulic characterization results. The model consists of inner (primary combustion zone) and outer (wall zone) regions. Both the characteristic velocity and specific impulse were evaluated on a mass weighted basis.

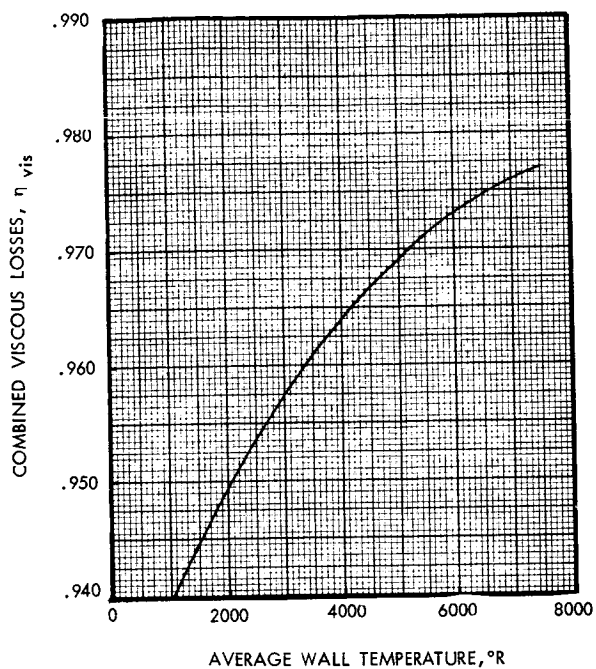


Figure 3-20
Combined Heat Transfer
and Friction Loss

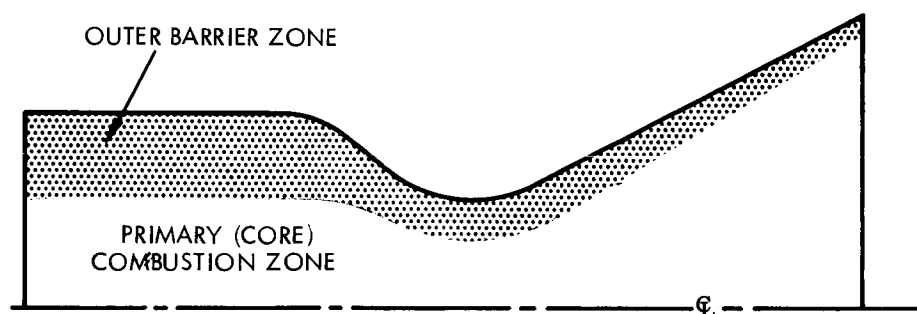


Figure 3-21. Simplified Chamber/Nozzle Zonal Model

$$C^* = X_i C_i^* + X_o C_o^* \quad (3-7)$$

$$I_{sp} = X_i I_{sp_i} + X_o I_{sp_o} \quad (3-8)$$

where

C^* is characteristic velocity
 I_{sp} is specific impulse
 X is the mass fraction of propellant in a given zone
 o & i represent the outer and inner zones, respectively

The outer zone mass fraction is written in terms of the inner zone mass fraction as:

$$X_o = 1 - X_i \quad (3-9)$$

and the inner zone mass fraction is written as

$$X_i = \frac{(1-B)(1+O/F_i)}{(1 + O/F)} \quad (3-10)$$

$$O/F_i = \frac{O/F - (B)(O/F_o)}{(1-B)} \quad (3-11)$$

where

B is the mass fraction of the total fuel in the outer zone
 O/F is the overall engine mixture ratio
 O/F_i & O/F_o are the inner and outer zone mixture ratios

Several analyses were performed to compare each of the propellant systems for the effects on performance of the outer combustion zone containing different mass and mixture ratios. The effects can be seen by examining Equation (3-11) for the case of a fixed overall mixture ratio (O/F) constraint or Equation (3-12) which follows, for the case where the core mixture ratio (O/F_i) is constrained at the peak value.

$$O/F = (O/F_i)(1-B) + (B)(O/F_o) \quad (3-12)$$

Typical results of mixture ratio and mass fraction as a function of fuel mass distribution are shown in Figure 3-22 for the 80% FLOX/55% methane + 45% ethane propellant combination. The extreme sensitivity of the core mixture ratio to percent of fuel used in the barrier region is evident for the case where the overall mixture ratio constraint is imposed. A larger percentage of the total mass flow is in the core for this case also.

In the zonal calculations that follow, two conditions were assumed. In one case, the overall engine mixture ratio was held at the peak equilibrium mixture ratio, and the delivered performance was computed assuming

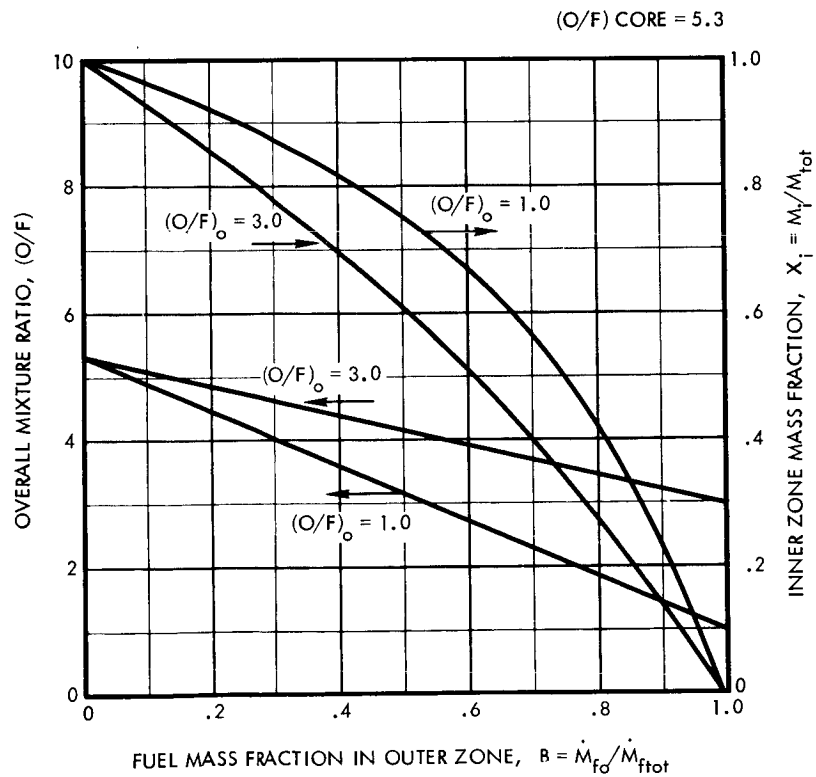
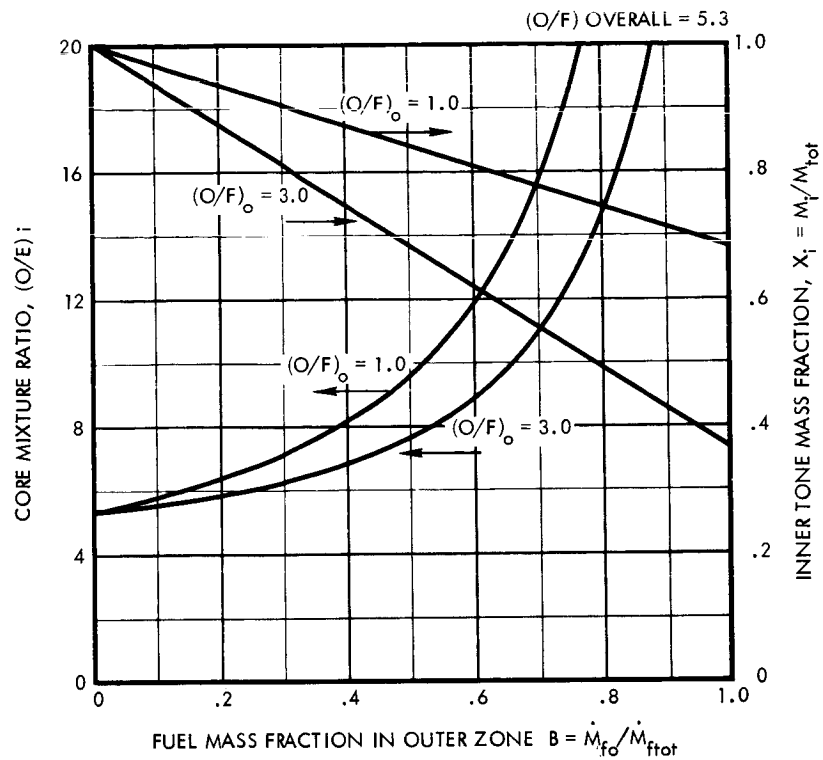


Figure 3-22. Sensitivity of Mixture Ratio to Mass Fraction of Fuel in Outer Barrier Zone

that a certain fraction of the fuel in the outer region around the combustion chamber wall was at preselected temperature (hence, mixture ratio) levels. Figures 3-23 through 3-25 present the specific impulse and combustion temperature variations over a broad range of mixture ratios used in these calculations.

For the first case, the central core mixture ratio level of the chamber was allowed to move to an oxidizer rich condition to satisfy the overall mixture ratio requirement. In the second case, it was assumed that the core region of the chamber remained at the peak equilibrium mixture ratio while the outer combustion chamber wall region ran at a mixture ratio and total propellant flow rate determined from preselected temperatures and percentages of fuel in the outer wall zone. The overall mixture ratio, in this latter analysis, was determined on the basis of the constraints imposed by the central core mixture ratio and outer annular mixture ratio (Equation 3-12). The essential results of this analysis showed that the performance of the FLOX/light hydrocarbon combination is extremely sensitive to the primary combustion zone mixture ratios and that this mixture ratio must be near the peak. Results for each of the above cases presented in Figure 3-26 for the FLOX/LPG combinations. As shown, performance losses can be limited to 4 or 5 percent provided the central core is operated at the peak equilibrium mixture ratio; however, the overall mixture ratio drops to approximately 3.5 for 40 percent of the fuel in the barrier region at an effective gas temperature of 2000° to 3000°F. These film coolant losses would be considered acceptable. On the other hand, if the overall peak equilibrium mixture ratio constraint is imposed, then large performance losses can be expected since the core mixture ratio is driven oxidizer-rich with the attendant large performance losses. Basically, this is a result of the high overall mixture ratio of the FLOX/LPG propellant systems and their sensitivity to the use of small percentages of the total fuel flow rate as either a film coolant or in low mixture ratio barrier temperature control as shown in Figure 3-22.

3.1.5 Predicted Thrust Chamber and Engine Performance

The estimated engine performance was computed using Equation (3-2). The data presented in Figure 3-27 show the thrust chamber performance for each of the propellant systems analyzed. The results do not include injector efficiency effects. These results are for a uniform mixture ratio considering no zonal effects ($\eta_z = 1$). Each of the loss components discussed in the previous sections² is identified as a separate curve on the figures. The estimated thrust chamber performance is presented for two mean wall temperature levels that are typical of a cold wall and hot wall chamber design. In the final analysis, the actual wall temperature distribution must be considered; however, the curves establish the trends for cold and hot wall chamber designs and will not change significantly with variations in the wall temperature distribution. Figure 3-28 presents a comparison of the thrust chamber performance of each of the propellant systems/investigated. Because of the lower kinetic losses of FLOX/methane-ethane blend, this propellant system shows the highest performance with the 82.5% FLOX/methane following and the 76% FLOX/propane being lowest. The thrust chamber efficiency is approximately 77 percent for each of the systems investigated. Table 3-3 gives the delivered performance summary for all propellants.

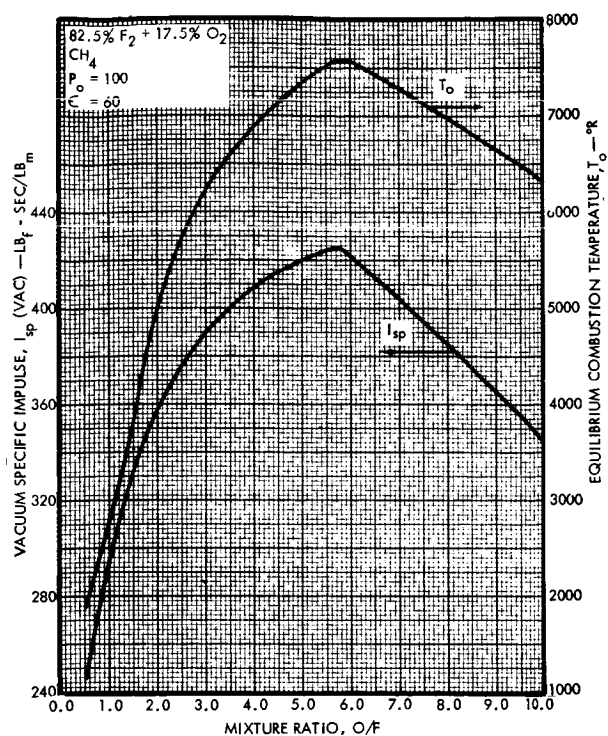


Figure 3-23. Vacuum Specific Impulse and combustion Temperature (CH_4)

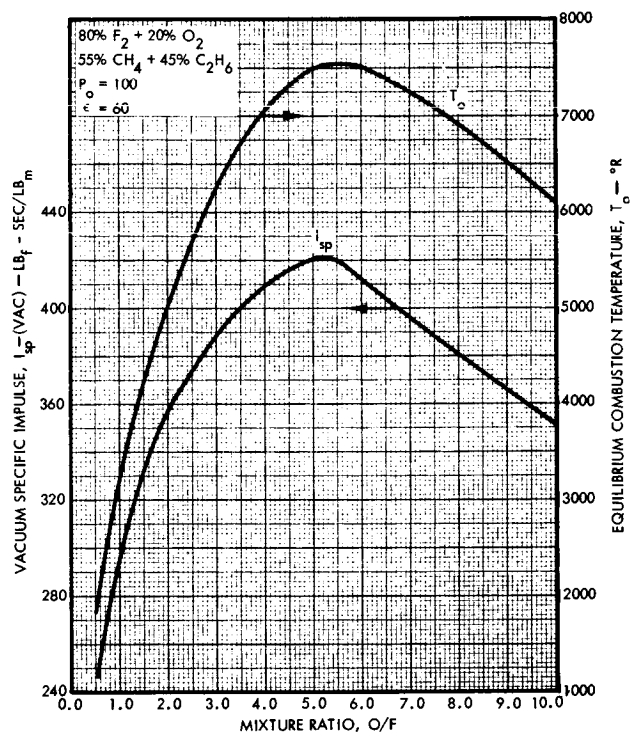


Figure 3-24. Vacuum Specific Impulse and Combustion Temperature (55% CH_4 + 45% C_2H_6)

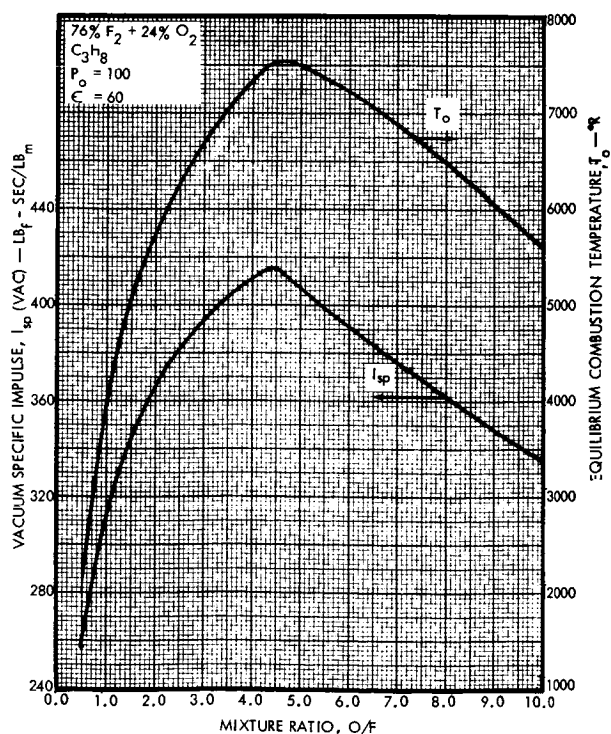
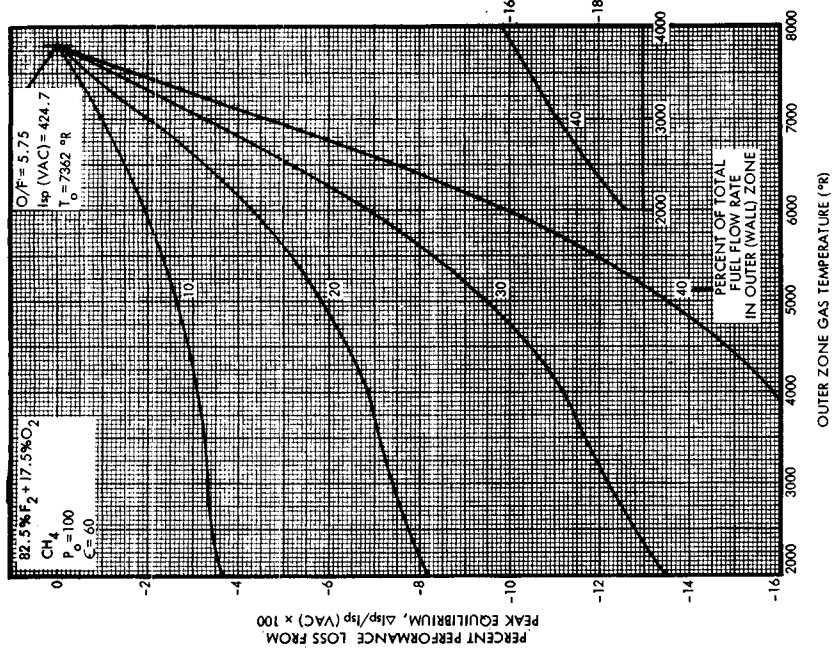
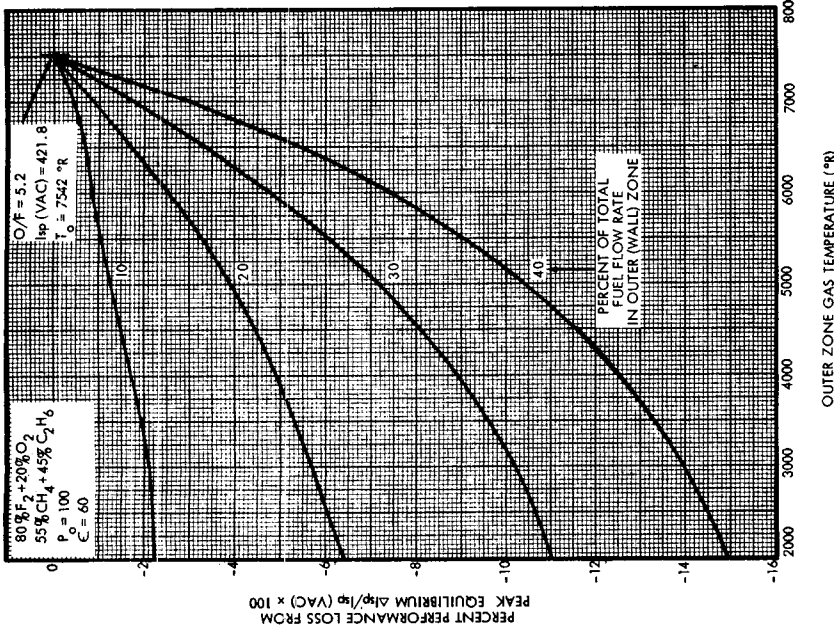


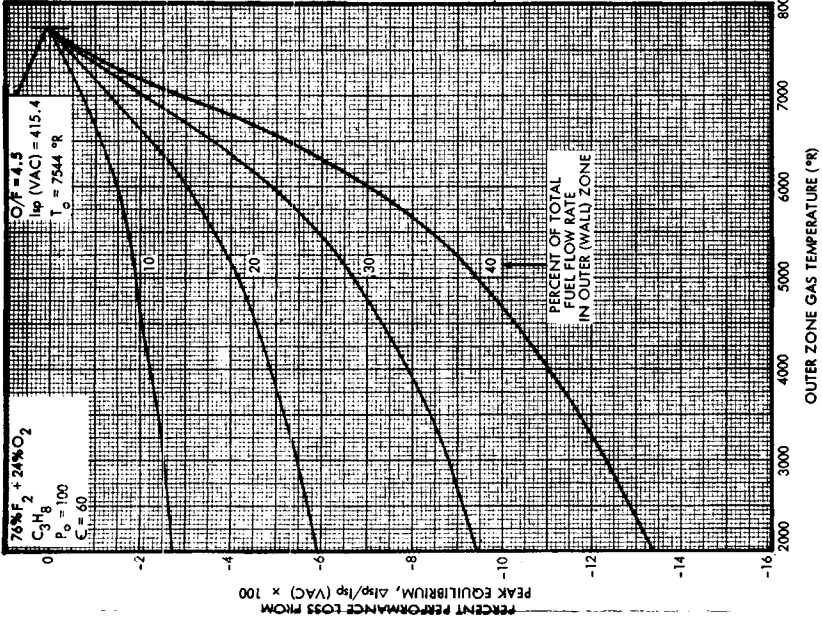
Figure 3-25
Vacuum Specific Impulse and
Combustion Temperature
(C_3H_8)



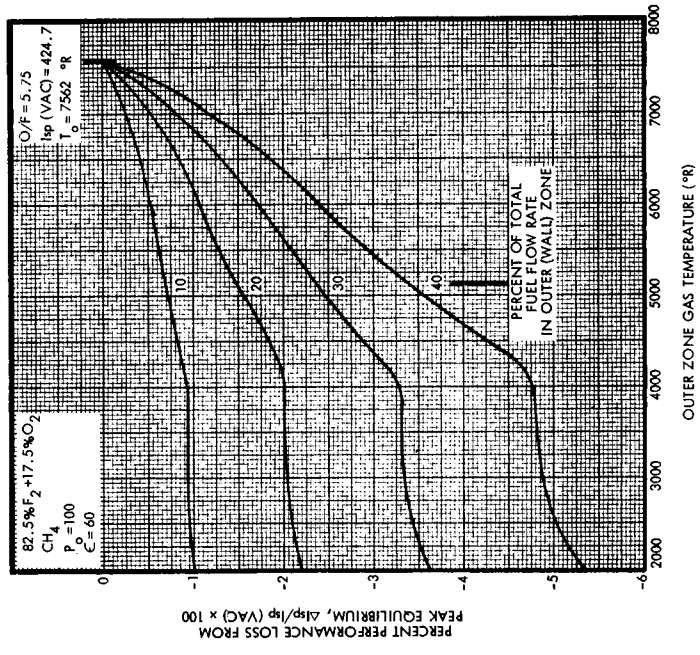
(a) Overall Mixture Ratio Maintained at Peak Equilibrium Value



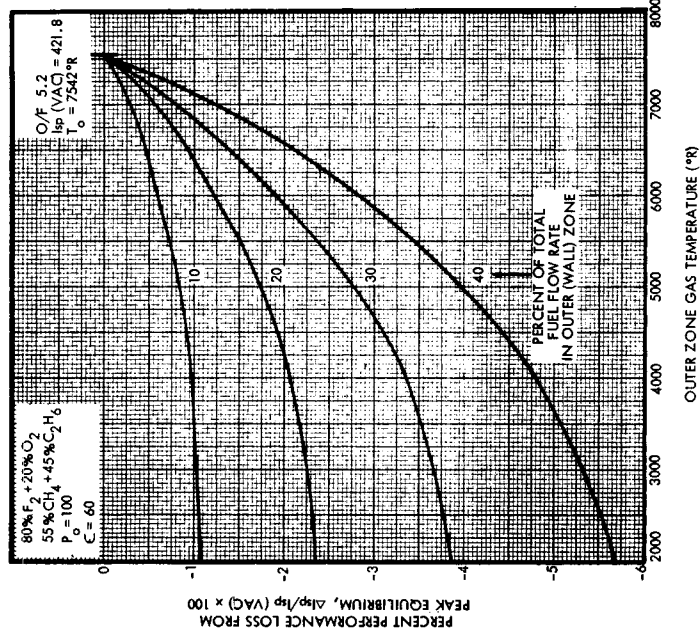
(c) Overall Mixture Ratio Maintained at Peak Equilibrium Value



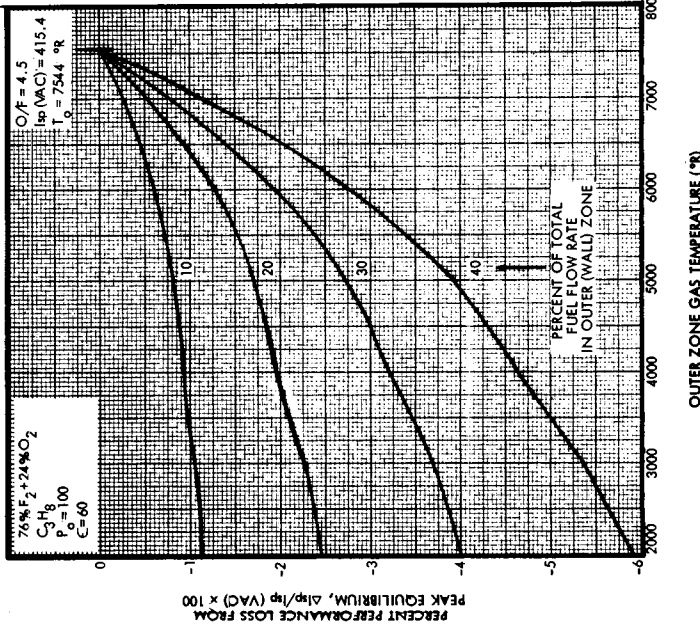
(e) Overall Mixture Ratio Maintained at Peak Equilibrium Value



(b) Core Mixture Ratio Maintained at Peak Equilibrium Value

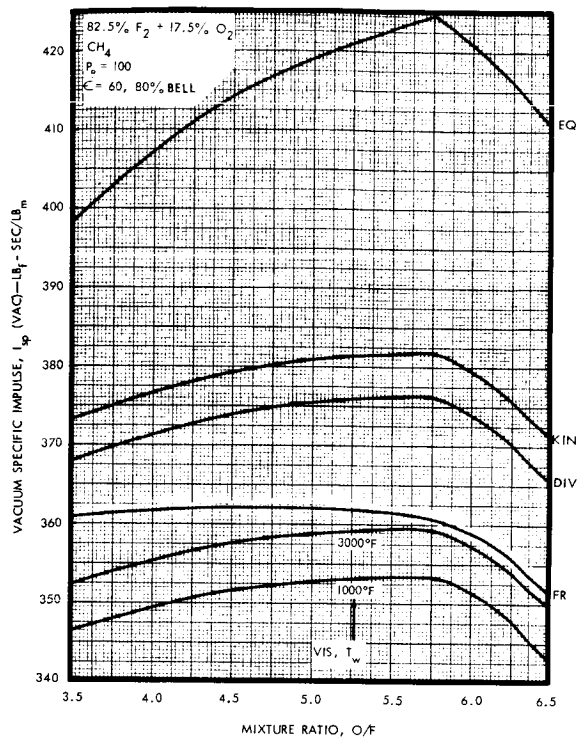


(d) Core Mixture Ratio Maintained at Peak Equilibrium Value

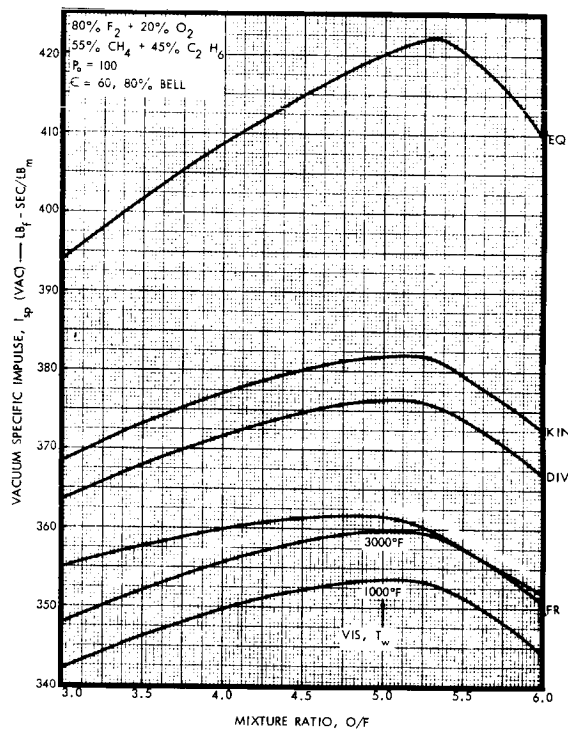


(f) Core Mixture Ratio Maintained at Peak Equilibrium Value

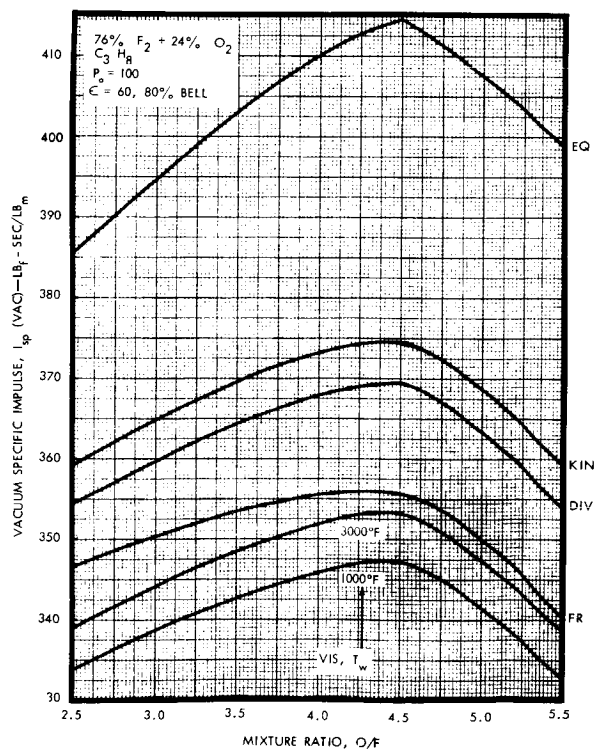
Figure 3-26. Specific Impulse Zonal Losses (All Fuels)



(a)



(b)



(c)

Figure 3-27
Vacuum Specific Impulse with
Losses for all Propellant
Combinations

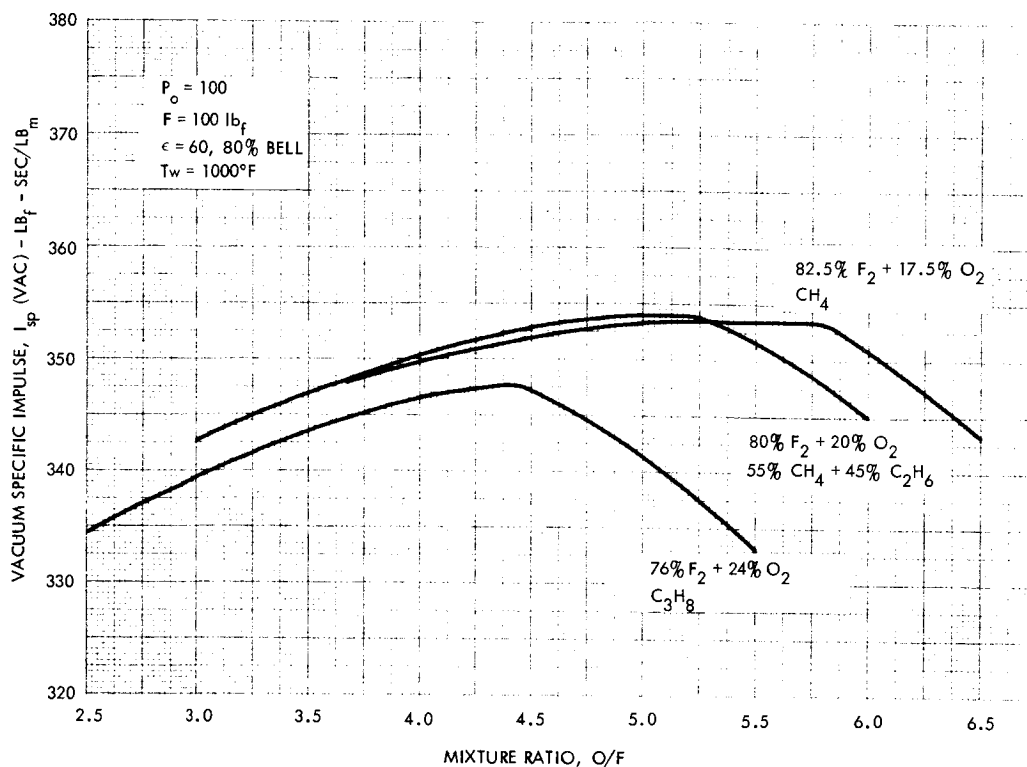


Figure 3-28. Summary Curves of Delivered Vacuum Specific Impulse for all Propellant Combinations

Table 3-3. Delivered Engine Performance Summary

O/F	DELIVERED ENGINE PERFORMANCE*					
	METHANE		PROPANE		55% METHANE/45% ETHANE	
	$T_w = 1000$	$T_w = 3000$	$T_w = 1000$	$T_w = 3000$	$T_w = 1000$	$T_w = 3000$
3.0	--	--	311.6	316.5	314.9	320.2
3.5	318.9	324.2	315.2	320.5	318.5	323.8
4.0	321.4	326.9	318.1	323.6	321.6	327.1
4.5	323.6	329.1	319.4	324.9	324.1	329.6
5.0	324.5	330.1	314.1	319.5	324.7	331.0
5.2	--	--	--	--	325.4	331.1
5.5	325.2	330.6	306.2	311.5	323.3	328.9
6.0	323.3	328.7	--	--	316.9	323.8

* Computed on the basis of $\eta_{C^*} = 92\%$

Variations of mass and mixture ratio within the combustion chamber can result from essentially two factors:

- Variations within the primary injector elements
- Controlled variations at the combustion chamber wall

The former variation which is dependent upon each element's hydraulic characteristics, number and arrangement of elements, element configuration, and element-element interaction can be assessed by detailed cold flow and hydraulic characterization. For the most part, the losses associated with these variations account for the combustion losses (reduced combustion efficiency). Other considerations must be given to mass droplet sizes to insure that evaporation losses do not occur and further reduce the combustion efficiency. The techniques and skills for accomplishing this are generally well known and have been used many times. Generally, reaction rates are not a limiting factor on combustion performance (Reference 9).

In the film-cooled chamber designs or in any chamber design that requires the sensible heat absorption capability of the coolant, such as a transpiration cooled chamber, the amount of coolant required will be relatively insensitive to the overall mixture ratio because the theoretical heat flux will not vary significantly with mixture ratio. Thus, with high mixture ratio propellant systems such as the FLOX/LPG's, where limited quantities of fuel are available and the amount of fuel required to cool the thruster is essentially a fixed value the thruster performance will be extremely sensitive to overall thruster mixture ratio for the reasons presented in Section 3.1.4.1. In the case of a conduction cooled thruster it is shown later that 60 percent of the total fuel is required to cool the thruster at an overall mixture ratio of 5.2 utilizing the methane-ethane fuel blend. This percentage of fuel would have less impact on the overall performance of the thruster at overall mixture ratios less than 5.2. In fact, higher delivered specific impulse can be realized by operating the thruster at a lower overall engine mixture ratio because of the increased quantities of fuel available to reenter the combustion process after use as a film coolant.

The validity of performance calculations is dependent upon the number of chemical species considered and engine operating conditions e.g., mixture ratio (O/F). A given species list may be sufficient for a given O/F or range of O/F's but may yield erroneous results for other conditions.

This situation is illustrated by equilibrium chamber calculations performed for the FLOX (80% F_2 + 20% O_2)/(55% CH + 45% C_2H_6) propellant system at a chamber pressure, P_o , of 100 psia. (Percentages are expressed on a weight basis.) The first series of calculations considered 24 gaseous species; C, C_2 , C_3 , CH, CH_2 , CH_3 , C_2H_2 , CO, CO_2 , CF, CF_2 , CF_3 , CF_4 , C_2F_2 , F, F_2 , H, H_2 , H_2O , HF, HCO , O, O_2 and OH. The second series of calculations considered 12 gaseous species; C, CO, CO_2 , F, F_2 , H, H_2 , H_2O , O, O_2 and OH.

The adiabatic combustion temperatures, T_o , computed with both sets of species lists is shown in Table 3-4.

Table 3-4. Adiabatic Combustion Temperature
FLOX/Blend, $P_o = 100$ psia

O/F	T_o , °R 24 Species	T_o , °R 12 Species	ΔT_o , °R
5.9	7503	7500	3
5.5	7536	7533	3
5.2	7542	7539	3
4.5	7289	7125	164
3.5	6671	5545	1126

It is apparent from Table 3-4 that chamber calculations considering 12 gaseous species are only valid in an O/F range from 5.2 to 5.9. This was verified by comparing the one-dimensional shifting equilibrium specific impulse, I_{sp} , at an expansion area ratio, ϵ , of 60. These results are noted in Table 3-5.

Table 3-5. One-Dimensional Shifting Equilibrium Specific Impulse
FLOX/Blend, $P_o = 100$ psia, $\epsilon = 60$, Vacuum

O/F	I_{sp} , $\frac{\text{lbf-sec}}{\text{lbm}}$ 24 Species	I_{sp} , $\frac{\text{lbf-sec}}{\text{lbm}}$ 12 Species	ΔI_{sp} , $\frac{\text{lbf-sec}}{\text{lbm}}$
5.9	412.94	411.33	1.61
5.5	420.44	420.22	0.22
5.2	421.77	421.72	0.05
4.5	415.12	399.06	16.06
3.5	401.82	333.45	68.37

The I_{sp} calculations shown in Table 3-5 also indicate that the 12-species list is only valid when compared to the 24-species results, for an O/F range from 5.2 to 5.9.* It is evident that kinetics calculations considering the 12 species will be, in turn, only valid for the indicated O/F range.

* A ΔI_{sp} of 0.5 lbf-sec/lbm is incurred at an O/F of approximately 5.63. This further reduces the range of validity of the 12-species list if an error of no greater than 0.5 lbf-sec/lbm is acceptable.

An examination of the computed chamber composition shows that the sum of the mole fractions of the 12 neglected species is $2.8 \times 10^{-3}\%$ at an O/F of 5.2; 1.2% at an O/F of 4.5; and 3.8% at an O/F of 3.5; i.e., the neglected species (primarily C_xH_y) become of increasing importance as the O/F is reduced.

3.1.6 Propellant Selection on Performance Criteria

Based on the preceding performance analyses the blend, methane/ethane, is selected as the most desirable fuel. The predicted performance is shown in Figure 3-28 and Table 3-3. The higher predicted performance of the fuel blend is primarily achieved through reduced kinetic losses.

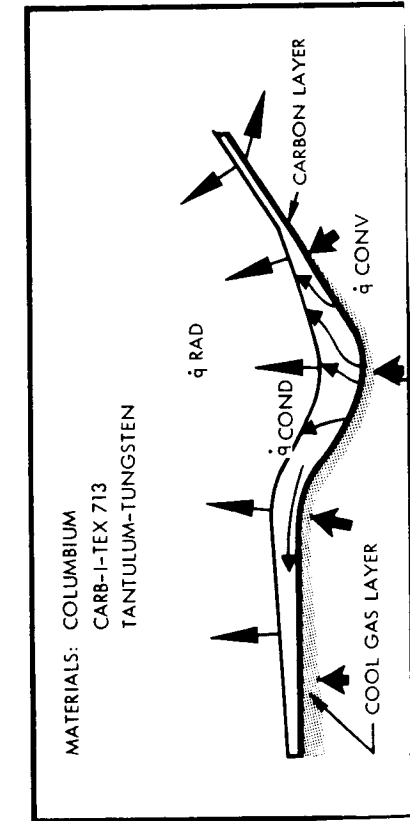
3.2 THRUSTER THERMAL ANALYSIS

During the Task I analysis activity thermal analysis was performed to characterize the basic cooling concepts listed below.

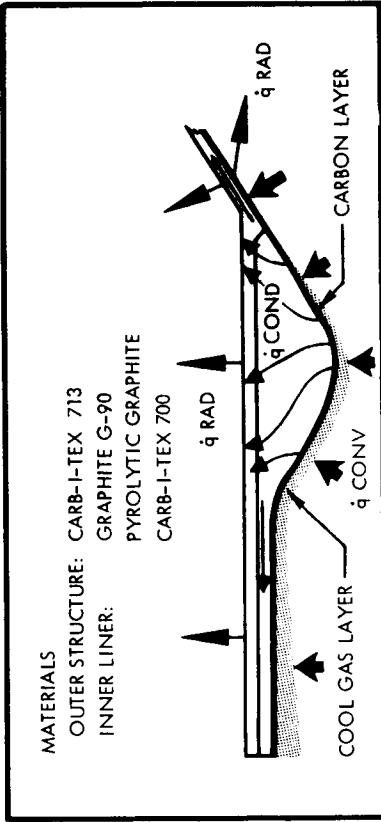
- Inner regenerative cooling where an internal film coolant is used to accept heat rejection from the throat and to conduct it back into the combustion chamber.
- Overall radiation cooling where conduction is used to spread heat from a high heat flux zone to lower temperature regions of greater surface area where it can be radiated away.

Variations of the two basic approaches coupled with conduction, radiation, and film cooling were considered during the analysis phase. Conceptual sketches of these designs are shown in Figure 3-29, and the designs are briefly described below.

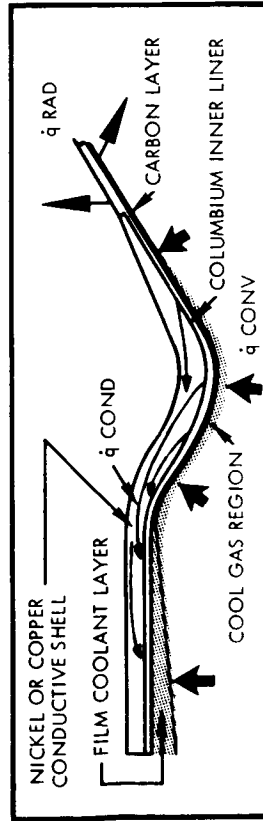
- Basic radiation-cooled chamber whereby heat is radiated to free space. Materials considered are graphites and refractory metals.
- Composite radiation-cooled chamber design whereby a heavy inner liner, contained within an outer structure, is used to distribute heat to lower temperature regions where it is radiated to space. Materials considered are reinforced graphite or pyrolytic graphite for the inner liner.
- A composite conductively cooled chamber design whereby an inner high temperature shell is surrounded by a highly conductive material used to distribute heat from high heat flux regions for rejection into a film coolant layer or radiation from regions of large surface area. Materials considered for the inner liner are nickel, high temperature nickel alloys, and refractories. Materials considered for the outer conductive layer are copper or nickel.



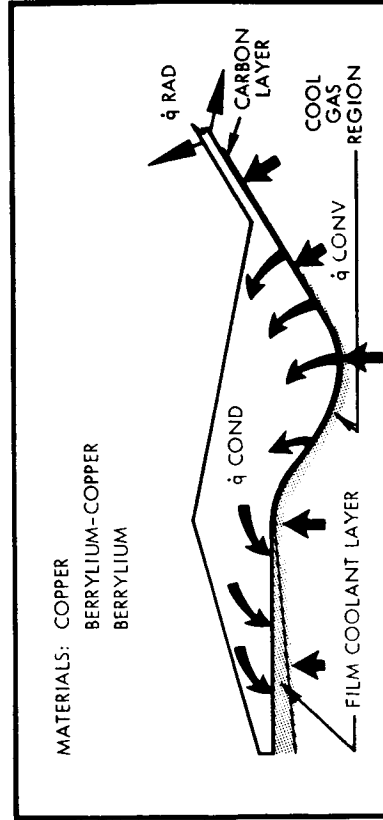
(1a) Basic Radiation Cooled Thruster



(1b) Composite Radiation Cooled Thruster



(1c) High Temperature Liner,
Conductively Cooled Thruster



(1d) Film-Conduction Cooled Thruster

Figure 3-29. Schematic Representation of Thruster Cooling Concepts

- Conductively cooled engine whereby heat is conducted from high heat flux regions and rejected to a film-coolant layer. Materials considered are copper, beryllium-copper, and beryllium.

The material selections listed above and summarized in Table 3-6 are based primarily on the chemical reactivity (chemical inertness) with gas species obtained from fluorine containing oxidizers and on temperature capability.

Table 3-6. Design Concepts/Material Evaluated

<u>Design Concept</u>	<u>Materials Evaluated</u>
Film-Conduction Cooled Thruster	Copper Beryllium-Copper Beryllium
Conductively Cooled Thruster With High Temperature Liner (Composite Design)	Columbium Liner/Copper Conductive Shell Columbium Liner/Nickel Conductive Shell Nickel Liner/Copper Conductive Shell
Basic Radiation-Cooled Thruster	Columbium Tantalum-Tungsten Reinforced Graphitized Structures (CARB-I-TEX 713)
Composite Radiation-Cooled Thruster	Reinforced Graphitized Structures for Outer Shell (CARB-I-TEX 713) Inner Conductive Liner <ul style="list-style-type: none"> . Graphite G-90 . Pyrolytic Graphite . CARB-I-TEX 700

Nickel and copper have excellent chemical reactivity characteristics with the fluorine containing oxidizers; however, these limits are at relatively low temperatures when compared with the graphites. Considering the high thermal conductivity and resultant heat distribution characteristics, coupled with the carbon deposition effects of the fuel and the resultant heat transfer blockage, these materials are attractive for the film-conduction-cooled chamber designs. Nickel and copper are relatively inert to raw fluorine (Reference 10) in either the liquid or gaseous phase, making thruster designs less susceptible to fluorine exposure during transient propellant leads or lags.

Beryllium has high thermal conductivity which makes it a possible candidate for the conduction-cooled chamber design; however, the thermal stability of the beryllium fluoride film is questionable (Reference 11) as well as are its low cycle fatigue characteristics. Coating systems for the refractory metals are available (Reference 12) for chemical protection against the HF exhaust gas species. Thus, the columbium and tantalum tungsten alloys show some promise for the basic radiation-cooled designs.

The graphite materials are particularly attractive from a chemical reactivity point of view as well as high temperature strength capability of the reinforced graphitized materials (for example, CARB-I-TEX 713). Graphite is inert to attack by hydrogen fluoride below temperatures of 5400°R (Reference 13). Carbon monoxide does not react with graphite. Hydrogen is effectively inert to graphite below 5400°R.

During the thermal characterization analysis the thermal behavior of each of the designs was determined under a variety of heat transfer environment conditions. For the film-conduction cooled design, a large number of parametric analyses were conducted to establish the film coolant flow rate as a function of heat transfer rates and geometric configuration. Only a relatively small number of parametric analyses were conducted on the radiation-cooled chamber designs. Primary analysis emphasis was placed on the film-conduction cooled designs since it was desired to experimentally evaluate this cooling concept. Most of the analyses were conducted for steady-state conditions, however some transient analyses were conducted to indicate the general transient characteristics of each basic design.

3.2.1 Propellant Heat Transfer Characteristics

The propellant heat transfer characteristic analyses were divided into several subtasks:

- Gas-side convection coefficient determination
- Carbon resistance determination
- Gas-side convection coefficient determination
- Carbon resistance determination
- Liquid fuel heat absorption capability
- Liquid fuel boiling characteristics

Each of these tasks is discussed more fully in the following paragraphs. A baseline chamber configuration was established for all analyses. The chamber is illustrated schematically in Figure 3-30. (The baseline chamber configuration was sized prior to the time when refined estimates of the delivered performance were available for the propellant systems and, therefore, the chamber is somewhat smaller than the chambers which were tested. The small difference in size does not have any significant impact on the analysis results.) The baseline chamber configuration was not intended to imply a mainline chamber design but was selected, somewhat arbitrarily, as a convenient starting point for the analysis.

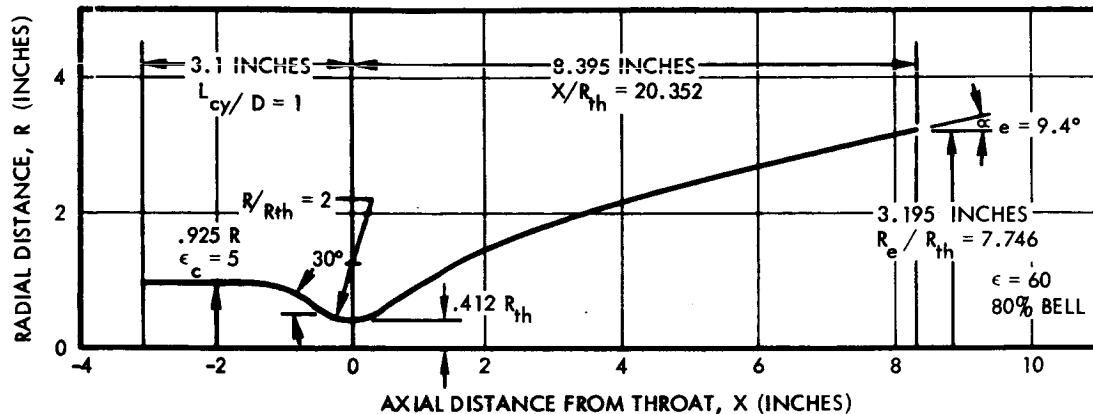


Figure 3-30. Baseline Chamber Configuration

3.2.1.1 Gas-Side Heat Transfer

Gas-side heat transfer rates were computed using an effective gas-side heat transfer coefficient which includes the thermal resistance caused by carbon deposition and temperature difference as the potential for heat transfer as shown below.

$$\dot{q}/A = hg (T_G - T_W) \quad (3-13)$$

where

\dot{q}/A = local heat flux (Btu/in²-sec)

hg = effective gas side heat transfer coefficient (Btu/in²-sec-°F)

T_G = local gas driving temperature for heat transfer (°F), including recovery effects

The effective gas-side heat transfer coefficient includes the thermal resistance caused by carbon deposition and is defined as

$$h_g = \frac{1}{\frac{1}{h_c} + R_o} \quad (3-14)$$

where

h_c = is the gas convection coefficient (Btu/in²-sec-°F)

R_o = is the gas side resistance caused by carbon deposition (in²-sec-°F/Btu)

Gas Side Convection Coefficients

The gas convection coefficient was computed using the Bartz simplified technique given in Reference 14 and shown below.

$$h_c = \left[\frac{.026 \left(\frac{\mu}{P_r} \right)^{.2} C_p}{D_*^{0.2} \left(\frac{P_o}{C^*} \right)^{0.8} \left(\frac{D_*}{r_c} \right)^{0.1}} \right] \left(\frac{A_*}{A} \right)^{0.9} \sigma \quad (3-15)$$

where

- P_r = Prandtl number
- D_* = throat diameter (in)
- μ = gas viscosity (lb/in-sec)
- C_p = gas specific heat (Btu/lb-°R)
- P_o = chamber pressure (psig)
- C^* = characteristic velocity (in/sec)
- g = gravitational constant (32.17 ft/sec²)
- A_* = throat area (in²)
- A = area at station of interest (in²)
- o = denotes stagnation chamber conditions
- r_c = throat radius of curvature (in)

The term σ accounts for the variation of properties (density ρ , and viscosity μ) with temperature. The term is dependent upon the reference condition at which the properties were evaluated.

Bartz defined σ as:

$$\sigma = (\rho_{am}/\rho)^{0.8} (\mu_{am}/\mu)^{0.2} \quad (3-16)$$

where

- ρ = density
- am = reference temperature condition based on the arithmetic mean between the gas and wall temperature

$$\sigma = \left\{ \left[\frac{1}{2} \frac{T_w}{T} \left(1 + \frac{\gamma-1}{2} M^2 \right) + \frac{1}{2} \right]^{0.8 - \frac{\gamma}{5}} \left[1 + \frac{\gamma-1}{2} M^2 \right]^{\frac{\gamma}{5}} \right\}^{-1} \quad (3-17)$$

Mass Flux Evaluation

Equation (3-15) in a more generalized form may be written as

$$h_c = \frac{.026}{D_*^{0.2}} \left(\frac{\mu_p}{Pr^{0.6}} \right)_{am} (\rho_{am} v)^{0.8} \quad (3-18)$$

Thus, it is shown that the convection coefficient is a function of the properties of the gas and the local mass flux (ρv). The two-dimensional mass flux distribution at the combustion chamber wall was used in the calculations and was determined from the method of characteristics solution for the supersonic expansion nozzle. The flow in the transonic region was determined from Hall's Second Order Approximation while the subsonic combustion chamber flow was based on one-dimensional flow. The importance of using two-dimensional mass flux at the wall is illustrated in Figure 3-31 where the one-dimensional and two-dimensional Mach number distributions are compared. Two-dimensionally, the sonic point occurs upstream of the nozzle geometric throat. The mass flux immediately downstream of the throat drops off much more rapidly than does the one-dimensional mass flux. However, on the average, the mass flux is higher throughout the nozzle extension (see Figure 3-31).

Using Equation (3-15), calculations were performed to investigate the effects of mixture ratio, reference temperature technique, and propellant system on the gas convection coefficient.

Property Reference Temperature

Three reference temperature techniques were evaluated as shown below:

$$T_{ref} = \frac{1}{2} (T_\infty + T_w) = T_{am} \quad (3-19a)$$

$$T_{ref} = T_\infty \quad (3-19b)$$

$$T_{ref} = \frac{1}{2} (T_w + T_\infty) + 0.22 RF (T_o - T_\infty) \quad (3-19c)$$

The first equation represents the arithmetic mean used by Bartz. The second equation evaluates the properties on the basis of the free stream properties while the last equation is the Eckert reference temperature technique. Results are shown in Figure 3-32 for each of the above reference temperature techniques. Reference temperatures based on the arithmetic mean give the highest gas convection coefficients in the critical design portions of the combustion chamber and were used for the analysis presented herein.

Propellant System Sensitivity

Table 3-7 presents the gas convection coefficients for each of the propellant systems investigated. For practical purposes the differences

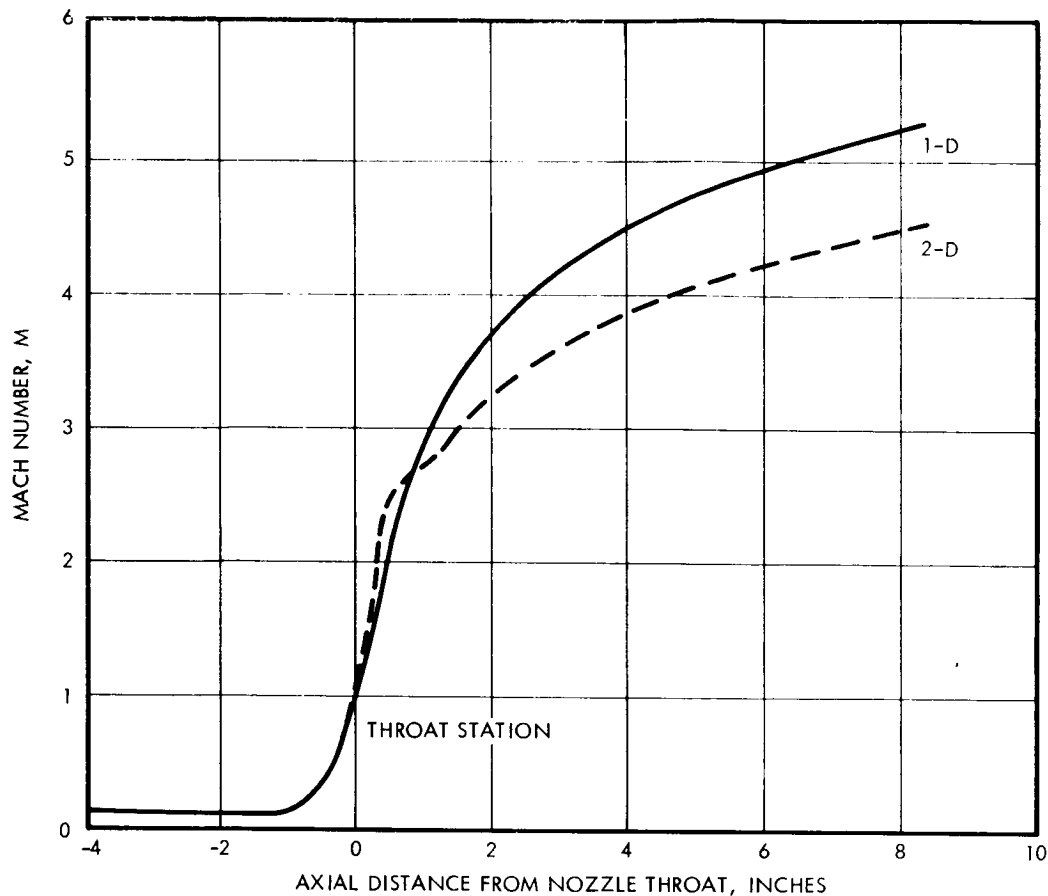


Figure 3-31. Mach Number Distribution

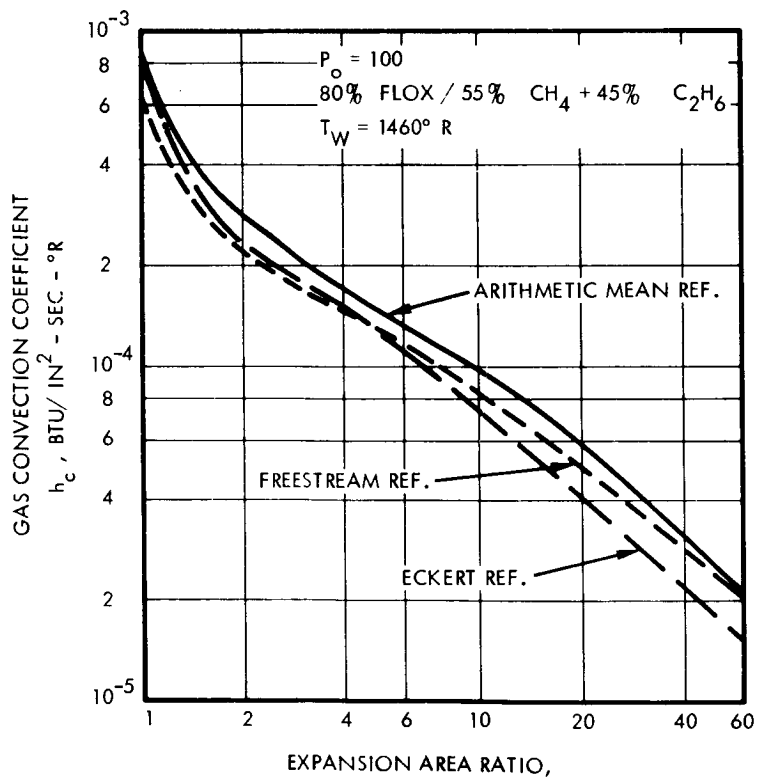


Figure 3-32
Gas Convection Coefficient

Table 3-7. Comparison of Throat Heat Flux and Gas Convection Coefficients ($P_o = 100$ psia, $T_w = 1500^\circ\text{R}$, Optimum Mixture Ratios for Each Propellant)

Propellant System	h_c Btu/in ² -sec-°R	T_o °R	\dot{q}/A Btu/in ² -sec
82.5% FLOX CH ₄	8.530×10^{-4}	7562	5.16
80% FLOX 55% CH ₄ + 45% C ₂ H ₆	8.555×10^{-4}	7542	5.17
76% FLOX C ₃ H ₈	8.440×10^{-4}	7544	5.10

are small and the analyses assumed that the gas convection coefficients were independent of propellant systems. Detailed calculations were performed using the 80% FLOX/55% CH₄/45% C₂H₆ propellant combination.

Mixture Ratio Effects

Mixture Ratio effects are shown graphically in Figure 3-33. For mixture ratios below the optimum there are large increases in the gas convection coefficient while at mixture ratios exceeding the optimum the gas convection coefficient is about the same as the values computed at the optimum conditions. Generally, because of chamber durability considerations, oxidizer-rich conditions would not be considered at the chamber wall.

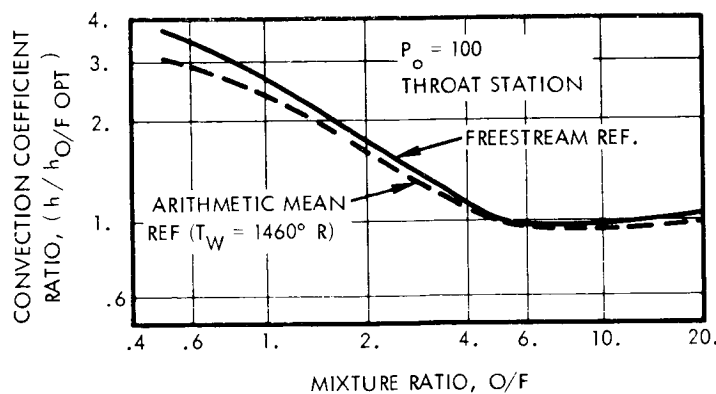


Figure 3-33
Mixture Ratio Effect on
Gas Convection Coefficient

Recombination Enhancement

Because dissociated gas species exist (monatomic hydrogen and fluorine) at mixture ratios in excess of 4 (Section 3.1.3), it would be anticipated that recombination could enhance the convective heat transfer. Recombination enhancement was estimated at the optimum mixture ratio of 5.3 for the 80% FLOX/55% CH_4 + 45% C_2H_6 propellant combination. The heat transfer based on enthalpy difference was computed as

$$\dot{q}/A/\Delta H = \dot{q}/A/\Delta T \frac{H_\infty - H_W}{C_p (T_G - T_W)} \quad (3-20)$$

where

$\dot{q}/A/\Delta H$ = heat transfer rate based on enthalpy difference

$\dot{q}/A/\Delta T$ = heat transfer rate based on temperature difference
(Equation 1)

C_p = Frozen specific heat of gases (Btu/lb-°R)

$(T_G - T_W)$ = temperature potential for heat transfer (°R)

$(H_\infty - H_W)$ = equilibrium enthalpy potential for heat transfer
based on free stream temperature and local wall
temperature (Btu/lb)

Shown in Figure 3-34 is the recombination enhancement to heat transfer (i.e., the ratio of heat transfer computed on an enthalpy basis to heat transfer computed on a temperature basis). The amount of recombination enhances is to a large extent dependent on the wall operating temperature level. Wall temperature levels for most practical designs would operate below 4000°R; therefore increases in the convective heat loads because of recombination could be as high as 100 percent. For cold wall chamber designs having operating temperatures less than 2000°R the convective heat transfer could be increased as much as 60 percent. In most cases of practical design interest, those dissociated gas species which would give rise to recombination enhancement (monatomic fluorine) are chemically incompatible with most available chamber material operating temperature levels.

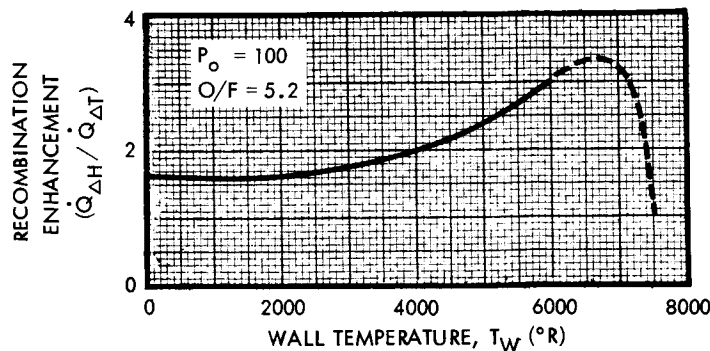


Figure 3-34. Effects of Recombination on Convective Heat Transfer (80% FLOX/55% CH_4 + 45% C_2H_6)

Gas Driving Temperature Determination

Two approaches can be used to establish the gas driving temperature (T_G) for heat transfer:

- Compute the gas driving* temperature from the aerodynamics of the nozzle and the recovery factors
- Assume a constant gas driving temperature as a function of nozzle length

The gas driving temperature as computed from the Mach number distribution and recovery factor is written as follows:

$$T_G = (T_O) \frac{\left(1 + (RF) \frac{\gamma-1}{2} M_\infty^2\right)}{\left(1 + \frac{\gamma-1}{2} M_\infty^2\right)} \quad (3-21)$$

where

T_O = total gas temperature ($^{\circ}R$)

γ = gas specific heat ratio

M_∞ = free stream Mach number at edge of boundary layer

RF = recovery factor $\sim \sqrt[3]{Pr}$

Figure 3-35 which presents the recovery temperature ratio (T_G/T_O) as a function of Mach number was computed using a constant value of recovery factor. The variation in gas temperature (recovery or adiabatic wall temperature) computed using Equation (3-21) as less than 3 percent of the total temperature (T_O) in the critical portions of the chamber and nozzle. This corresponds to 300° to 400°F reduction in the theoretical total temperature and can be substantially less at the lower barrier total temperature which is required in most practical design situations. On the basis of the above results the technique used to compute the gas recovery temperature was to assume a constant distribution as a function of length. This, of course, resulted in computed heat fluxes at the higher expansion ratios that were slightly high. This is of no real consequence when considering the overall uncertainty in computing gas side heat transfer rates.

*

The gas driving temperature discussed herein is the same as the recovery temperature or adiabatic wall temperature which is also referred to as the driving potential for heat transfer. The recovery factor is taken as the customarily given Prandtl number correction.

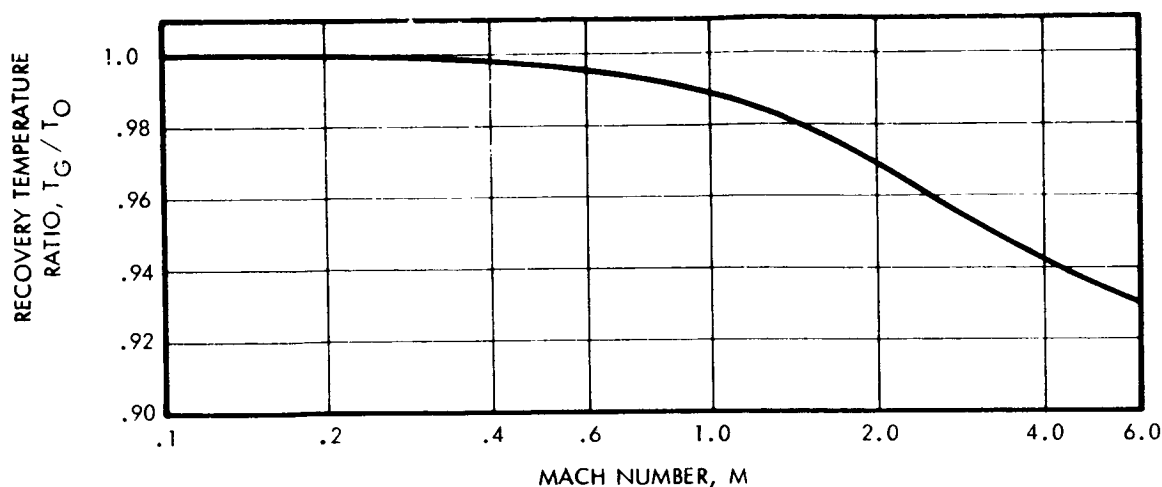


Figure 3-35. Recovery Temperature Ratio Mach Number Variation

3.2.1.2 Carbon Resistance Determination

A detailed discussion and presentation of the analysis and correlation of previously existing test data for thermal resistance caused by carbon deposition is presented in Appendix E.

The carbon deposition resistance is found to be dependent on mass flux rate, mixture ratio, and propellant combination and may be written in a more generalized form as

$$R_O = F_G F_A F_R K \quad (3-22)$$

where

F_G = function defining the mass flux rate dependents

F_A = function dependent upon the atomic ratio of hydrogen to carbon is the fuel

F_R = function defining the mixture ratio effects

K = empirical constant (2500 in²-sec-°F/Btu)

The function F_G , based on the results presented in Reference E-1 and E-2 is given by

$$F_G = e^{1.285 - 0.51 \rho v} \quad (3-23)$$

where ρv is the local mass flux in lb/in²-sec. The atomic ratio (A) of hydrogen to carbon in the fuel is represented by the function F_A .

$$F_A = \frac{[C_1 (1-C_1-C_2 (A-2))]}{(1-C_1) [C_1 + C_2 (A-2)]} \quad (3-24)$$

The constants C_1 and C_2 and empirical constants which are related to a specific injector design and its operating characteristic such as chamber cooling. Based on the data of Reference E-3 the constants C_1 and C_2 are 0.16 and 0.21, respectively. Figure 3-36 illustrates Equation (3-24) graphically.

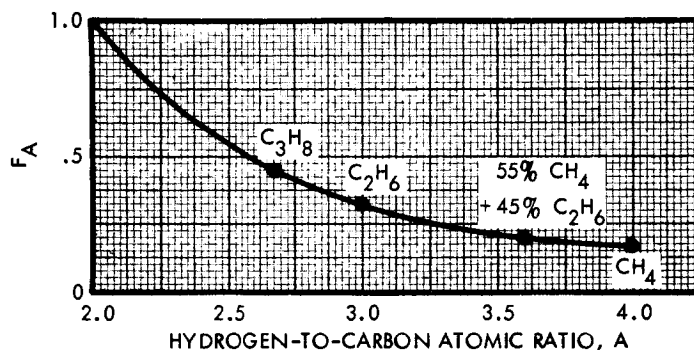


Figure 3-36. Functional Dependence of F_A on Atomic Ratio of Hydrogen to Carbon

An important point to note here is the dependence of the parameter in Figure 3-36 on the overall thruster design. The coefficients in Equation (3-24) were based primarily on the data of Reference E-3 since these data appeared more consistent than the data of Reference E-4.

Finally, the parameter F_R which includes the effects of mixture ratio for a given propellant system was evaluated using the data of Reference E-4 (at mixture ratios near the optimum). The available data were not consistent; fortunately the parameter is near unity and was therefore taken as $F_R = 1.0$.

The resultant expression for the thermal resistance for carbon deposition becomes

$$R_O = (2500) (e^{1.285 - 0.51\rho v}) F_A \quad (3-25)$$

The applicability of the above equation is subject to question at mixture ratios away from stoichiometry.

Carbon resistances computed using Equation (3-25) are presented in Table 3-8 for each of the propellant systems at their respective optimum mixture ratios. These results are compared to the gas convection resistance ($R_c = 1/h_c$).

Table 3-8. Comparison of Gas Convection Resistance at Optimum Mixture Ratio ($P_o = 100$ psia, Throat Station)

Propellant System	Thermal Resistances $\text{In}^2\text{-sec-}^\circ\text{R/Btu}$			R_c/R_g
	R_o	R_c	R_g	
82.5% FLOX CH_4	1248	1171	2419	.485
80% FLOX 55% CH_4 + 45% C_2H_6	1426	1169	2595	.450
76% FLOX C_3H_8	3275	1185	4460	.266

The reduction in heat transfer caused by carbon deposition is significant for all the propellant systems investigated. Over a 50 percent reduction in heat transfer is computed for both the CH_4 and 55% + CH_4 + 45% C_2H_6 fuel blends, while close to a 75 percent reduction is computed for the propane fuel. These results are presented for the throat station. Distribution as a function of length were based on the two-dimensional mass flux distribution computed from the Mach number distribution presented in Figure 3-31.

3.2.1.3 Effective Gas Side Resistance

Equation (3-14) of Section 3.2.1.1 defined the effective gas-side heat transfer coefficient (h_g) in terms of the gas convection coefficient (h_c) and a thermal resistance caused by carbon deposition (R_o) (Reference 15). An effective gas-side resistance (R_g) can be written as

$$R_g = \frac{1}{h_g} = \frac{1}{h_c} + R_o \quad (3-26)$$

where $1/h_c$ is the gas convection resistance (R_c).

The heat transfer coefficients were computed from Equation (3-15) using the Mach number distribution presented in Figure 3-31. Typical distributions are shown in Figure 3-37 for three wall temperature levels. The carbon resistance is shown in Figure 3-38 as a function of Mach number for each of the propellant systems. Also plotted is the gas convection resistance for a wall temperature of 1460°R . Thus with the use of the Mach number distribution presented in Figure 3-31 the effective gas side resistance distributions were determined from a crossplot of Figure 3-37. Figure 3-39 shows the overall convective resistance.

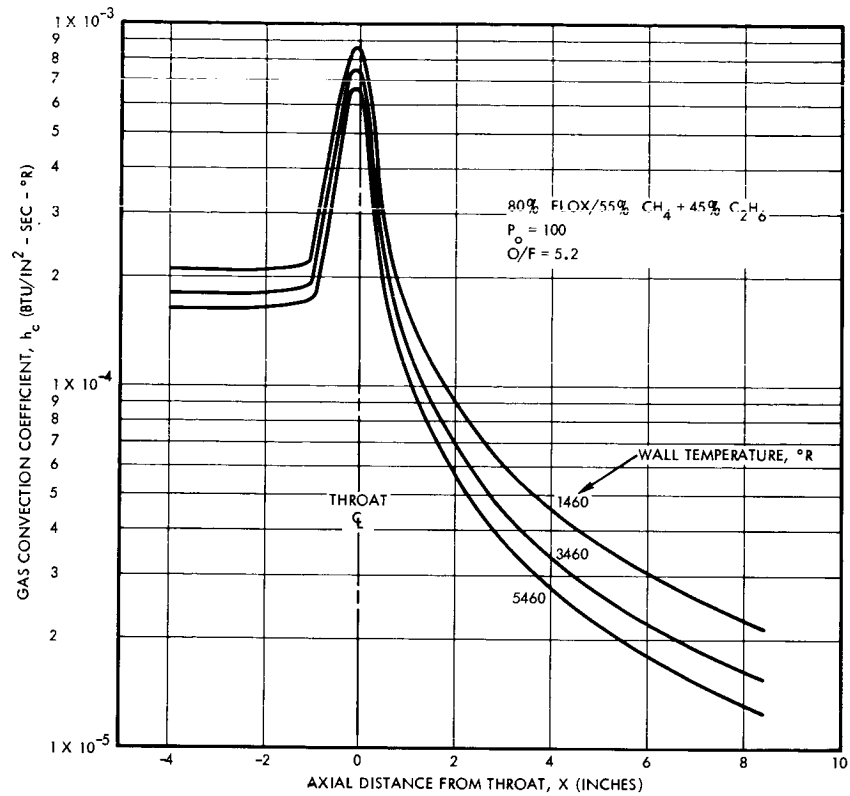


Figure 3-37. Gas Convection Coefficient Axial Distribution

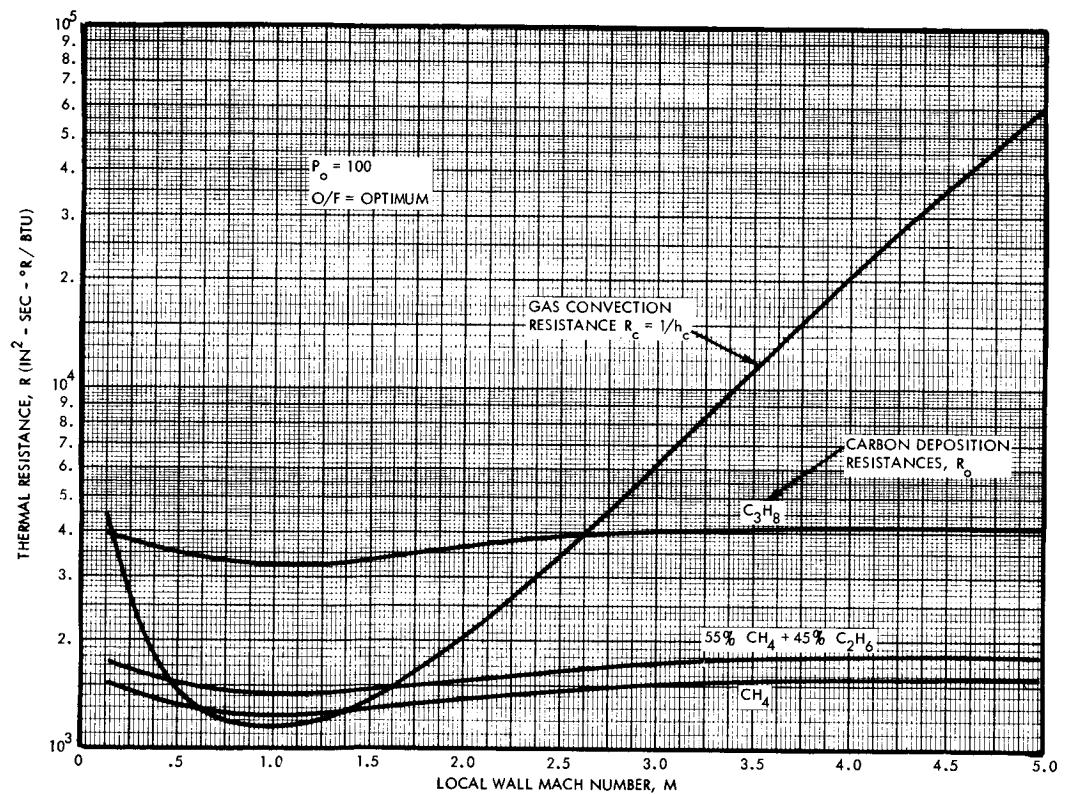


Figure 3-38. Thermal Resistance Distribution with Carbon Deposition

3.2.1.4 Fuel Heat Absorption Capabilities

The physical properties of each of the fuels are of importance to this application as coolants. The primary properties of importance are presented in Table 3-9.

Table 3-9. Physical Property Summary of Propellants

Property	Propellants					
	Fuels				Oxidizer	
	CH ₄	C ₂ H ₆	55% CH ₄ + 45% C ₂ H ₆	C ₃ H ₈	F ₂	O ₂
Molecular Weight	16.04	30.07	22.35	44.09	38.0	32.0
Freezing Point, °R	163.2	161.9	133.0	154.0	96.4	97.8
Critical Temperature, °R	343.4	549.8	-----	666.0	55.0	49.72
Critical Pressure, Psia	673.0	708.0	-----	618.7	259.1	277.8

Values for the oxidizers (fluorine and oxygen) are also presented for comparison purposes. The vapor pressure-temperature curve and the heat of vaporization-temperature curve are given in Figures 3-40 and 3-41, respectively. Liquid densities are presented in Figure 3-42.

From a film cooling standpoint methane can absorb heat to 255°R while the methane-ethane blend and the propane can absorb heat to 417 and 516°R, respectively, in a 100 psia environment. Whether a stable film layer can be achieved beyond the saturation temperature of the methane in the methane-ethane blend was subject to question, although the methane is sub-cooled with respect to the ethane. The sensible heat absorption capability of each of the fuels is presented in Figure 3-43. Here the methane-ethane blend heat capacity was determined on a component mass weight basis with adjustments made for the lower freezing point. The liquid fuel specific heats are presented in Figure 3-44. As a film coolant (or transpiration coolant) the vaporized fuel is heated by the combustion gases. The heat absorption capability of the gases is presented in Figure 3-45. Thus, the total heat absorption capability of a given fuel is

$$H_T = \bar{C}_p (T_{SAT} - T_{INLET}) + \Delta H_{fg} + \Delta H_G \quad (3-27)$$

where

H_T = total heat absorption capability of the fuel (Btu/lb)

T_{SAT} = saturation temperature of the fuel (based on P_0) (°F)

T_{INLET} = inlet temperature of fuel (°F)

Figure 3-39
Overall Thermal Resistance
Axial Distribution

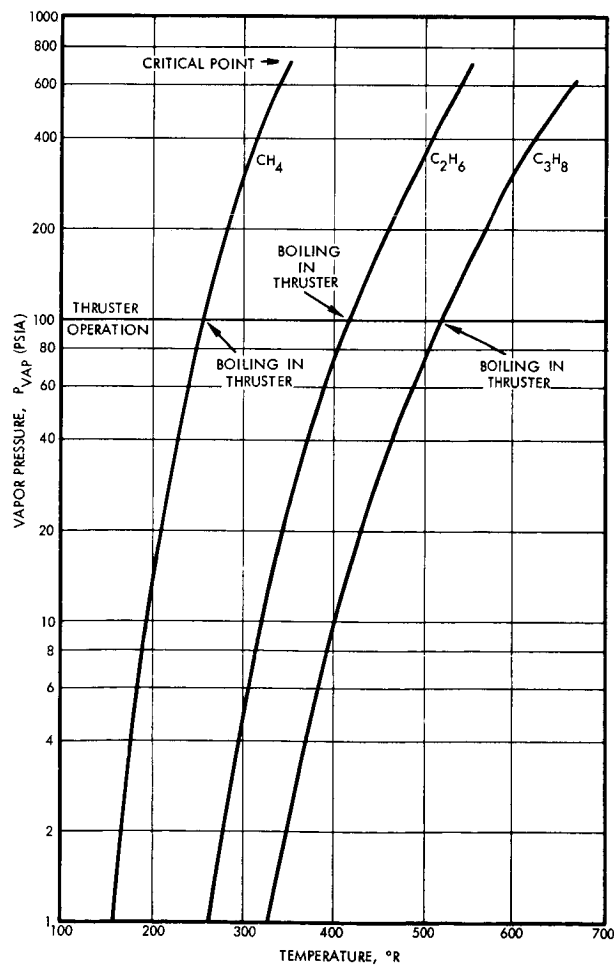
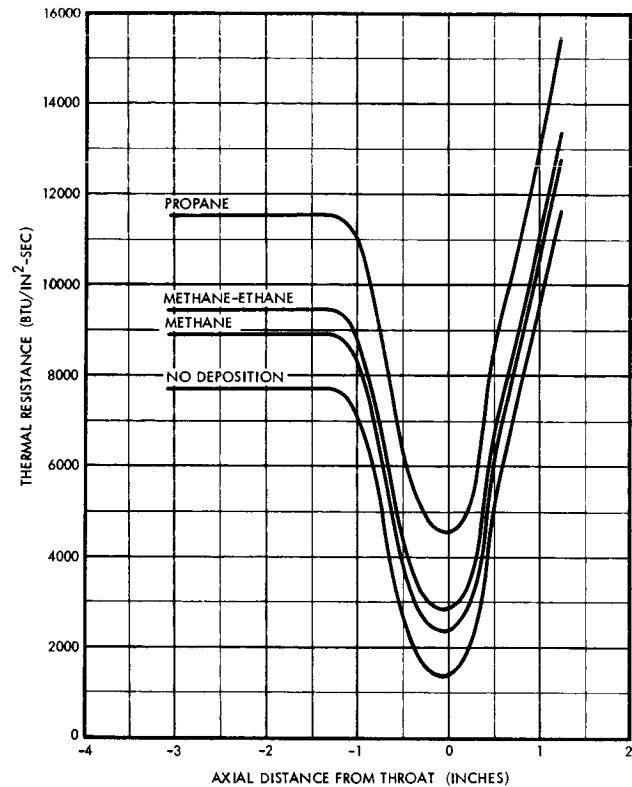


Figure 3-40
LPG Fuel Vapor Pressure Curoes

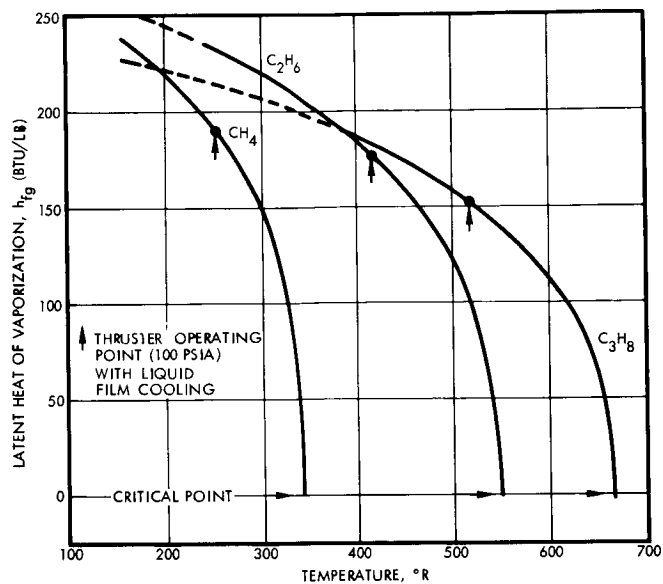


Figure 3-41
LPG Fuel Heat of Vaporization

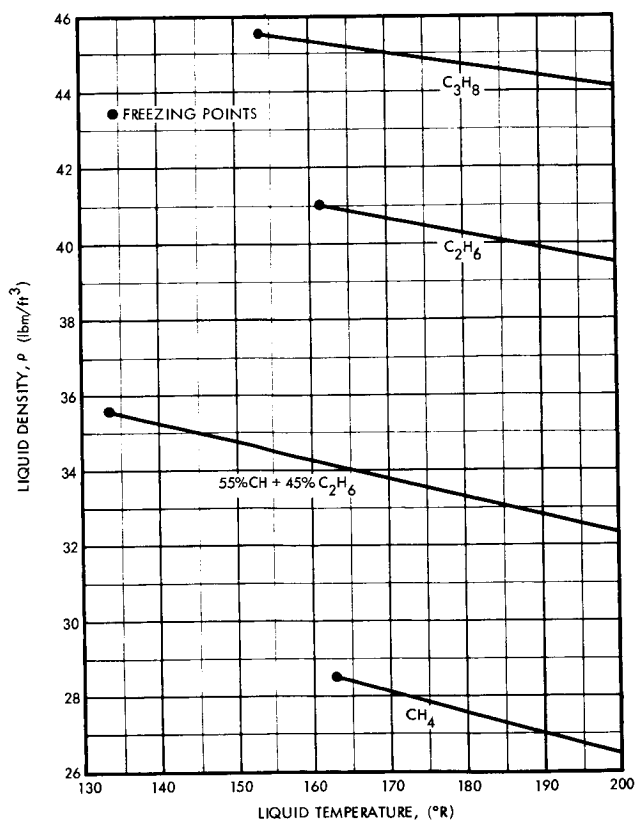


Figure 3-42
LPG Fuel Liquid Density

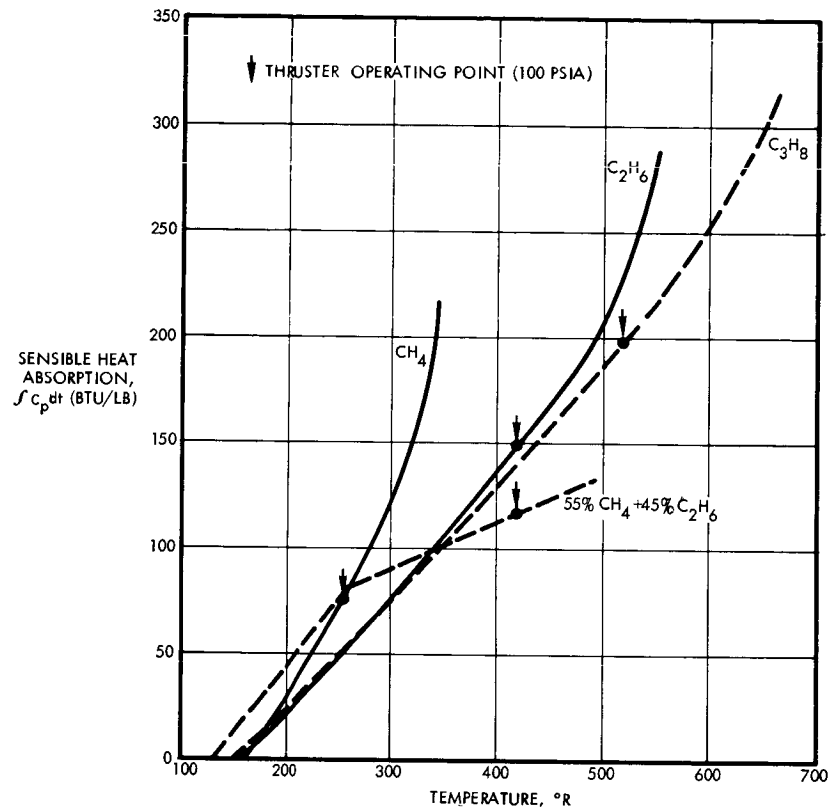


Figure 3-43. LPG Fuel Liquid Sensible Heat Absorption

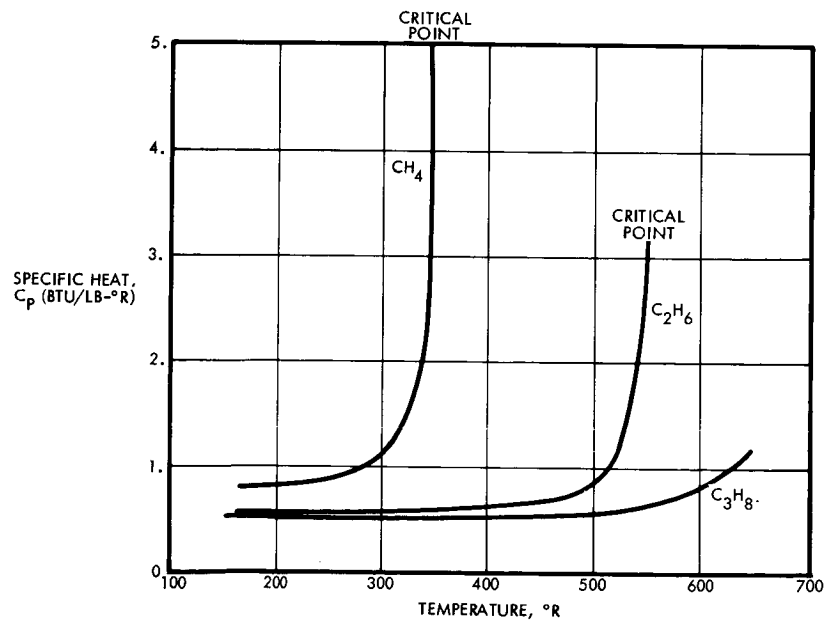


Figure 3-44. LPG Fuel Specific Heat

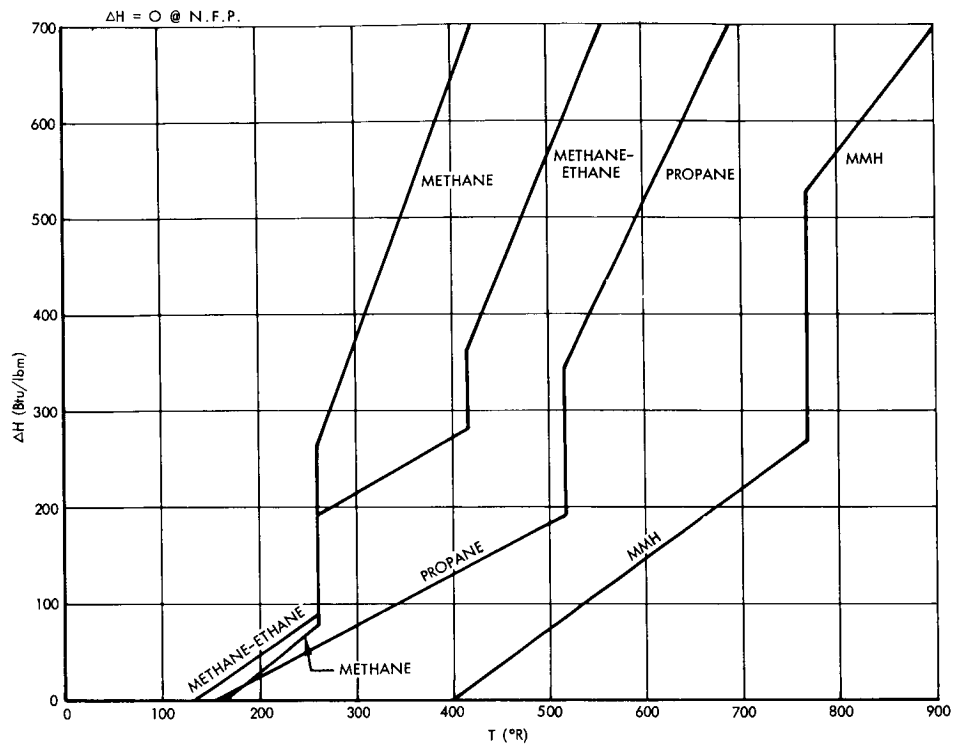


Figure 3-45a. Liquid Heat-Absorption Capability

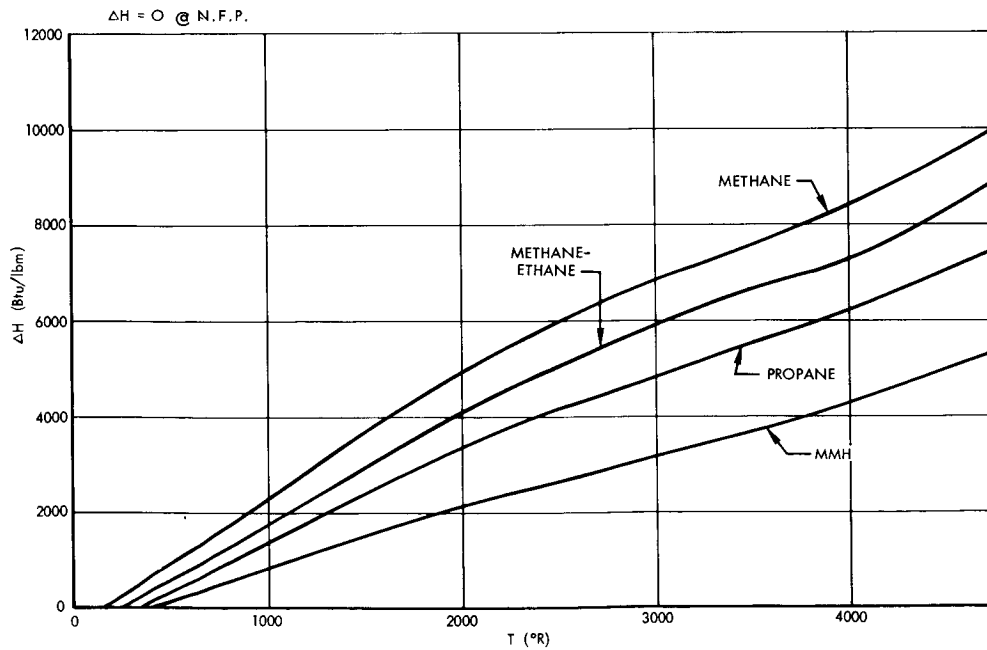


Figure 3-45b. Total Heat Absorption Capability

ΔH_{fg} = heat of vaporization of fuel at saturation temperature (Btu/lb)

ΔH_G = heat absorption capabilities of gaseous coolant which includes decomposition energies

Table 3-10 summarizes the total heat absorption capability for each of the fuels heated to 3000°R, which is above the decomposition temperature, and therefore includes the decomposition energies.

Table 3-10. Summary of Heat Absorption Capability of LPG Fuels

Fuel	$\int C_p dT$	ΔH_{fg}	ΔH_G	H_T
CH ₄	79	188	6634	6900
C ₂ H ₆	149	176	----	----
55% CH ₄ + 45% C ₂ H ₆	177	183	5633	6000
C ₃ H ₈	192	155	4553	4900

All fuels having freezing points that are sufficiently low such that propellant freezing should not generally be a problem. Close attention would, however, have to be given to propellant freezing in the injector and valves should system analyses indicate that temperatures are in the freezing point ranges.

The low saturation temperature of the fuels indicate the potential problems in the thruster startup could occur if the injector is not sufficiently chilled at the time of fuel admittance. Soackback in the injector may be a problem.

3.2.1.5 Fuel Boiling Characteristics

Because of the uncertainty in the nucleate boiling characteristics of the fuels, a brief experimental program was conducted to obtain the necessary data for subsequent analysis. A complete discussion of the experimental results of the fuel boiling characteristics are presented in Appendix B. Some typical results and their influence on the thermal analysis are presented in this section.

Ambient experimental boiling results were obtained for the three fuels at several degrees of subcooling. These results are tabulated in Table 3-11. As can be seen the experimental values of the peak heat fluxes when extrapolated to a pressure of 100 psia agreed with the values assumed for the preliminary thermal analysis, except for the case of the methane-ethane fuel blend where the measured peak heat fluxes were twice those previously assumed. The impact of this result is to allow twice as much heat absorption before the onset of film boiling (Reference 15). As will be seen the final result of this is that methane-ethane fuel blend is comparable in overall film coolant capabilities to propane.

Table 3-11. Summary of Pool Boiling Tests

Fuel	Bulk Temperature F	Measured (Q/A) _{MAX} at 14.7 psia Btu/in ² -sec	Estimated (Q/A) _{MAX} at 100 psia Btu/in ² -sec	Assumed For Previous Analysis (Q/A) _{MAX} Btu/in ² -sec
55% Methane/ 45% Ethane	-313	.32 - .38	**	**
	Saturated	.24 - .33	.48 - .66	.26 - .31
Propane	-140	.35 - .45	**	**
	- 80	.24 - .28	**	**
	Saturated	.14 - .21	.28 - .42	.33 - .40
Methane	-300	.28 - .35	**	**
	Saturated	.14 - .23	.28 - .46	.26 - .31

3.2.1.6 Fuel Wetting Characteristics

A basic test was also performed to determine the wettability of the methane-ethane blend with copper. This was necessary to insure good thermal contact of the film coolant with the chamber walls. A visual examination on the meniscus formed when copper was immersed into methane-ethane revealed that wetting was indeed occurring.

3.2.2 Cooled Thruster Thermal Analysis

Each of the designs shown in Figure 3-29 was analyzed for its equilibrium temperature distributions considering no carbon deposition and the full theoretical gas driving temperature of approximately 7550 R (Reference 17). These results established a reference for comparison with the calculations when carbon deposition is considered. The columbium thruster temperature shown exceeds its melting temperature, although it has a more uniform and lower temperature distribution. This is because of its relatively high thermal conductivity which distributes the heat from the throat region of the thruster into the cooler chamber and nozzle extension regions. The amount of heat distribution is also affected by the wall material thickness distribution; however, if the wall is increased much beyond 0.3 inch, very little temperature relief is obtained. Two factors affect this result: (1) the reduced axial temperature gradients, and (2) the increased temperature gradient across the wall. The composite chamber design offers no significant reduction in temperature due to axial conduction and operates at a temperature approximately 300°F lower than a reinforced graphitized chamber fabricated of a material such as CARB-I-TEX 713. The composite chamber design has the disadvantage that the wall is relatively thick thus giving rise to large temperature gradients across the wall and the susceptibility of cracking of the thick inner wall. A free-standing pyrolytic graphite chamber would have a temperature distribution similar to the CARB-I-TEX curve shown in Figure 3-46.

3.2.2.1 Radiation Cooled Thruster Analysis

More detailed analysis of a refractory metal chamber and a graphite chamber was performed to determine the equilibrium throat temperature as a function of heat rejection rate (gas recovery or driving temperature). These results are shown in Figures 3-47 and 3-48. The effects of carbon deposition for all fuels is shown to be significant; however, the carbon deposition effects for the propane fuel are clearly superior.

The major differences between the columbium and the CARB-I-TEX chambers are a result of the differences in thermal conductivity of the two chamber materials. CARB-I-TEX, with the lower thermal conductivity, is not as effective in conducting the heat away from the throat region. Consequently, it results in a throat temperature as much as 500°F higher than that for the columbium chamber. In the expansion cone and the cylindrical chamber section, where conduction is relatively unimportant, there is little difference in wall temperatures between the two materials. This can be seen in Figure 3-49, which is a comparison between the columbium and CARB-I-TEX chambers for propane carbon deposition at various recovery temperatures.

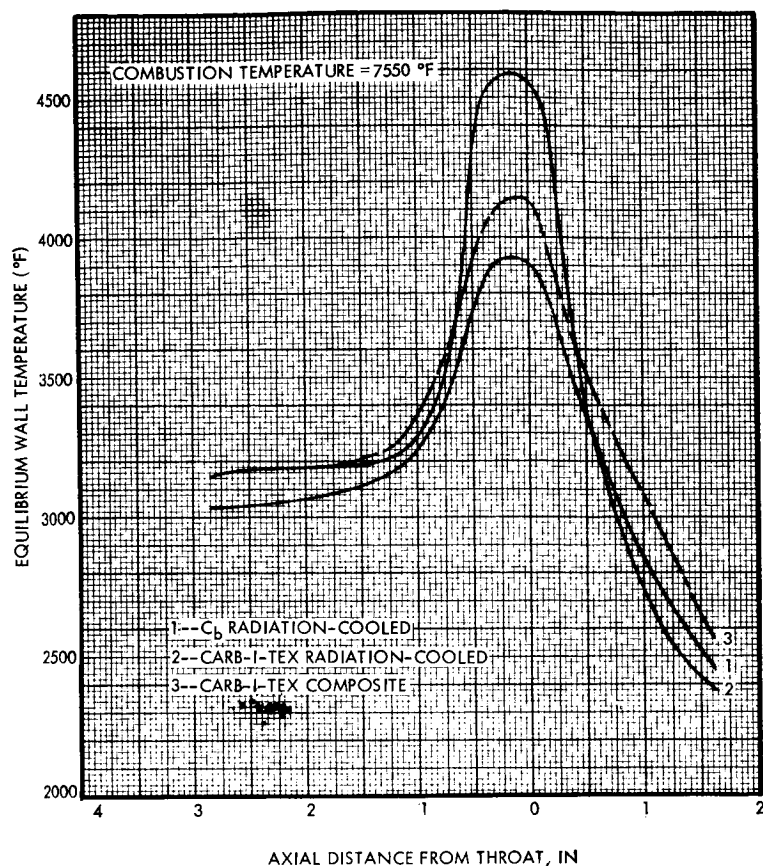


Figure 3-46. Baseline Temperature Distribution for Radiation-Cooled Chamber Concepts

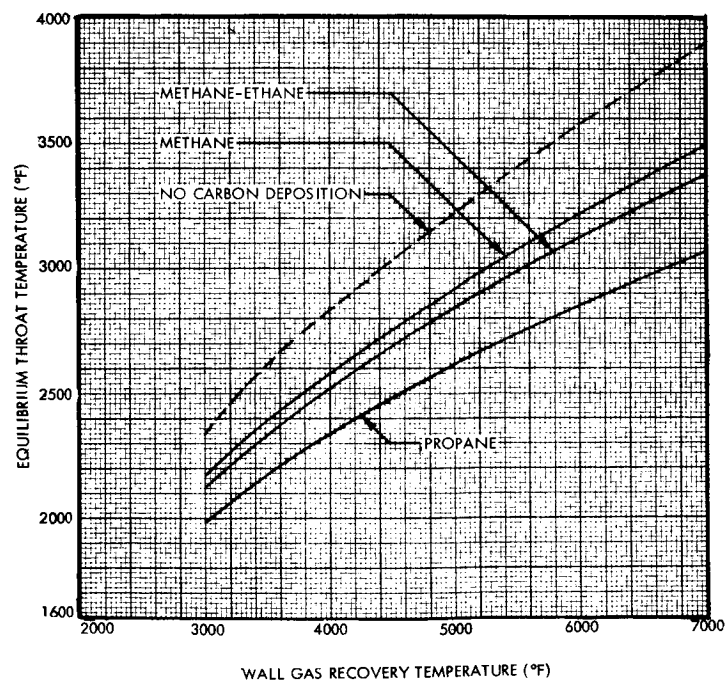


Figure 3-47. Comparison of Equilibrium Throat Temperature for Refractory Radiation-Cooled Thruster

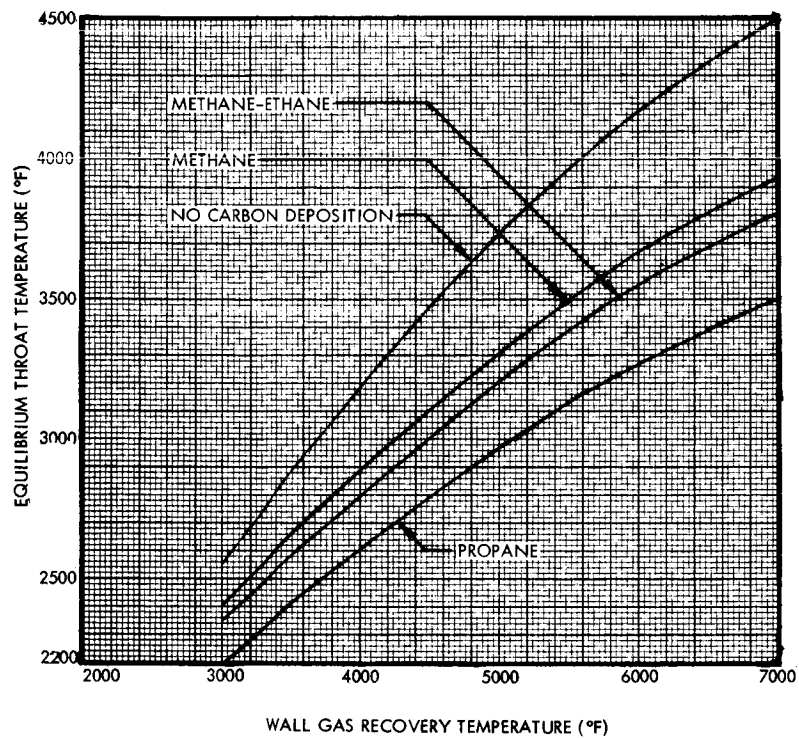


Figure 3-48. Comparison of Equilibrium Throat Temperature for CARB-I-TEX Radiation-Cooled Thruster

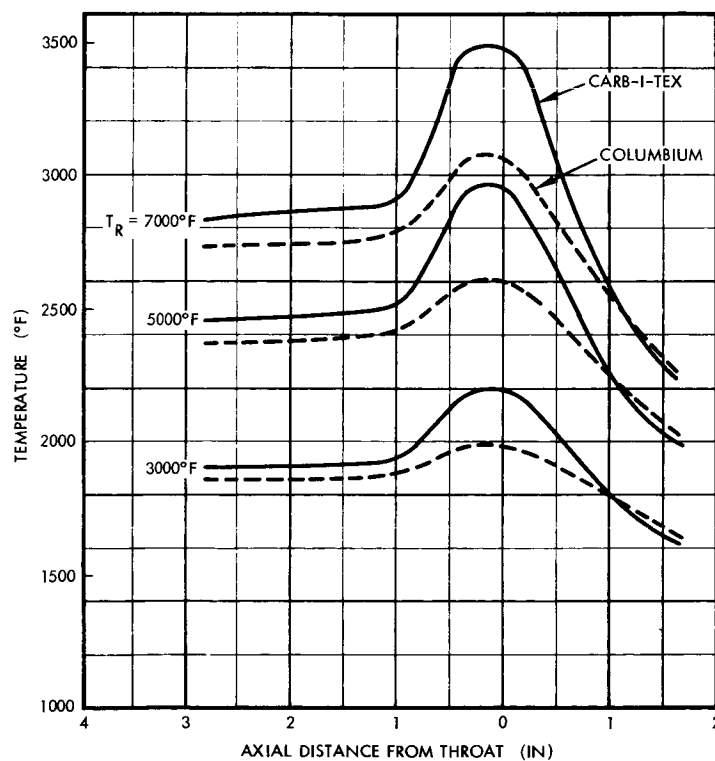


Figure 3-49. Effect of Recovery Temperature on Wall Temperature Distribution

A tradeoff analysis was performed between wall thickness and reduction in the maximum throat temperature due to a redistribution of heat from axial conduction for the CARB-I-TEX chamber design. The results of these analyses are shown in Figure 3-50 and indicate that because of the low thermal conductivity of the CARB-I-TEX material, the temperature relief because of axial conduction is offset by the inner wall temperature increase due to increased thermal resistance across the thicker wall.

The axial wall temperature variation in the CARB-I-TEX chamber is shown in Figure 3-51 for the three fuels. This shows that the lowering of the wall temperatures is a maximum in the throat region and diminishes considerably in the chamber and expansion areas, as would be expected from the values of the resistances.

It can be generally concluded that a graphite radiation-cooled chamber will operate with little or no heat rejection control required in the throat region of the nozzle. However, considerable heat rejection control is necessary in the region of the injector-chamber attachment to minimize injector heat soakback and high temperature sealing problems. Also, because of its insensitivity to heat rejection control and the high temperature limits of operation of the wall, the chamber design cannot be operated in a buried installation. Consideration must be given to thermal interaction of the thruster with the spacecraft or vehicle on which it is installed. This would usually require the use of more sophisticated thermal isolation devices such as reflective radiation shields and/or insulation schemes.

Since CARB-I-TEX can withstand a higher wall temperature than columbium, this chamber was used for analyses of the transient temperature response. Three duty cycles were used: a 100% burn duty cycle, a 33% burn duty cycle with 1.0 second on and 2.0 seconds off, and a 33% burn duty cycle with 0.1 second on and 0.2 seconds off. Each of the analyses was performed using carbon deposition from the various fuels.

For the 100% burn duty cycle, the major differences between the results for the different fuels was the wall temperature level at steady state. This is illustrated in Figure 3-48 for the steady-state condition. The other important difference was the time for the throat to reach steady state which is shown in Figure 3-52 as a function of gas recovery temperature for each of the fuels. The maximum variation in the time to reach steady state at a given recovery temperature is 10 seconds.

The temperature response of the CARB-I-TEX chamber at a recovery temperature of 5000°F for the FLOX-propane propellant combination is shown in Figure 3-53 for the 100% burn duty cycle. The responses are shown for the cylindrical chamber section, the throat, and the divergent section at an expansion area ratio of approximately nine.

The results for the two 33% burn duty cycles are shown in Figures 3-54 and 3-55. The responses for the remaining two propellant combinations are similar to those shown in Figures 3-53 through 3-55, although somewhat more rapid.

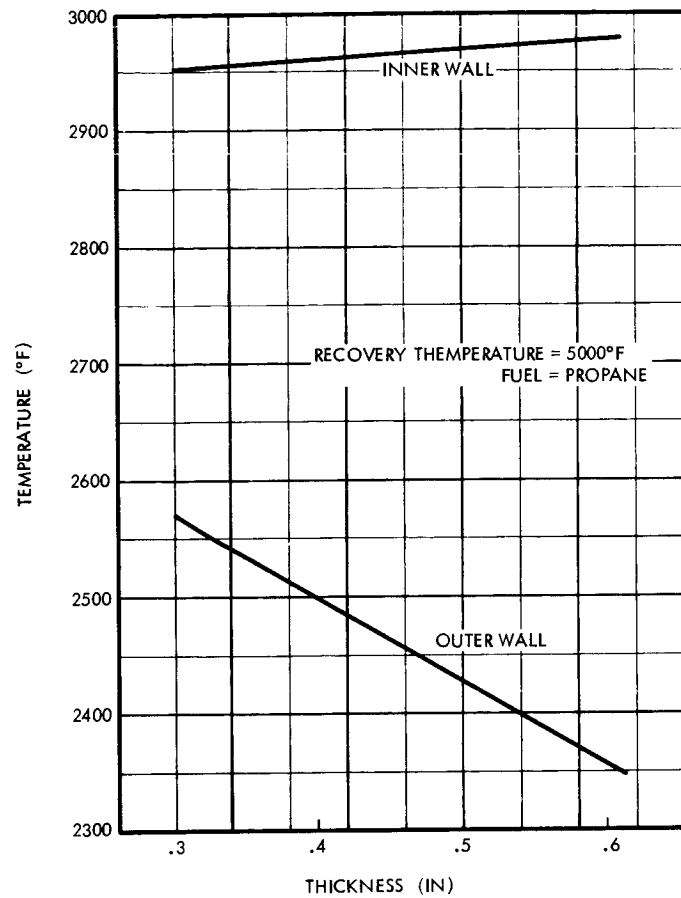


Figure 3-50. Effect of CARB-I-TEX Throat Thickness On Throat Temperature

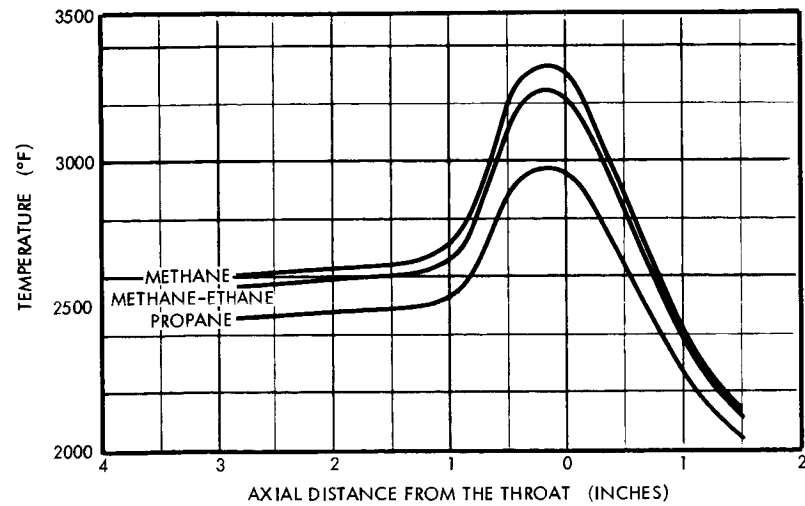


Figure 3-51. Effect of Carbon Disposition on CARB-I-TEX Wall Temperature Distribution

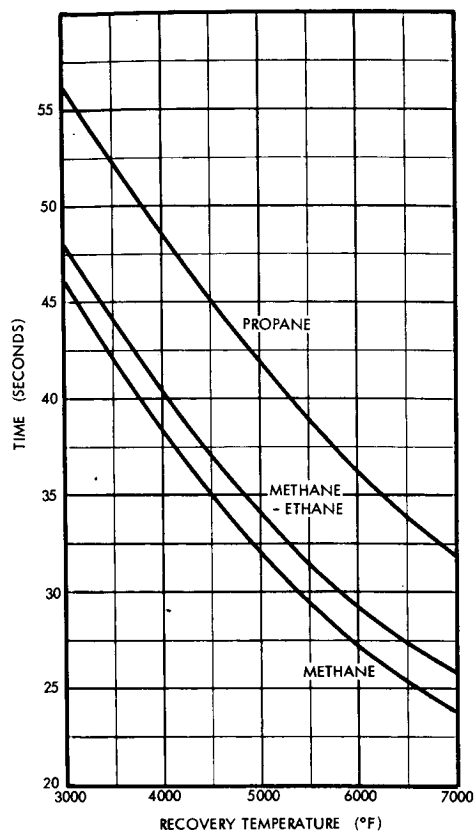


Figure 3-52. Time Required for a CARB-I-TEX Radiation Chamber to Reach Study State

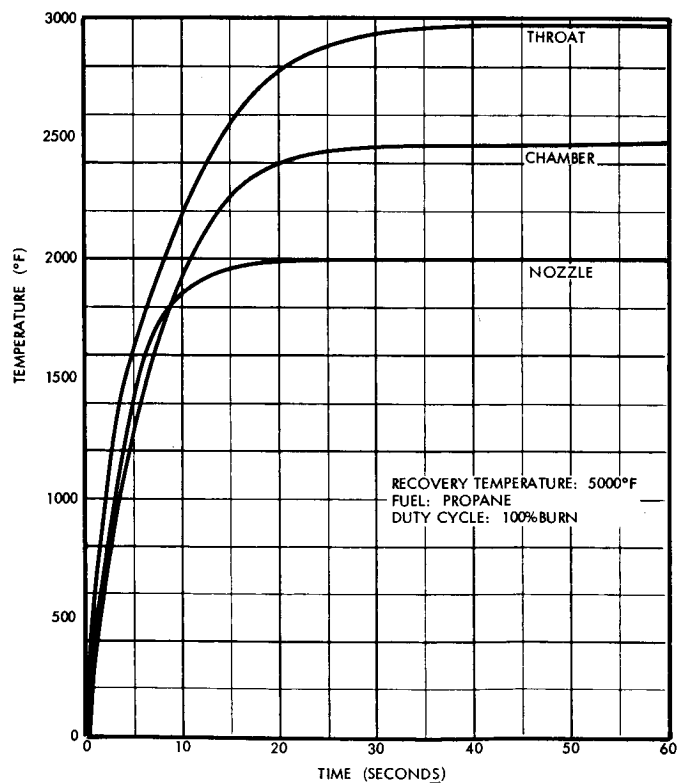


Figure 3-53. Transient Radiation-Cooled CARB-I-TEX Wall Temperature Response

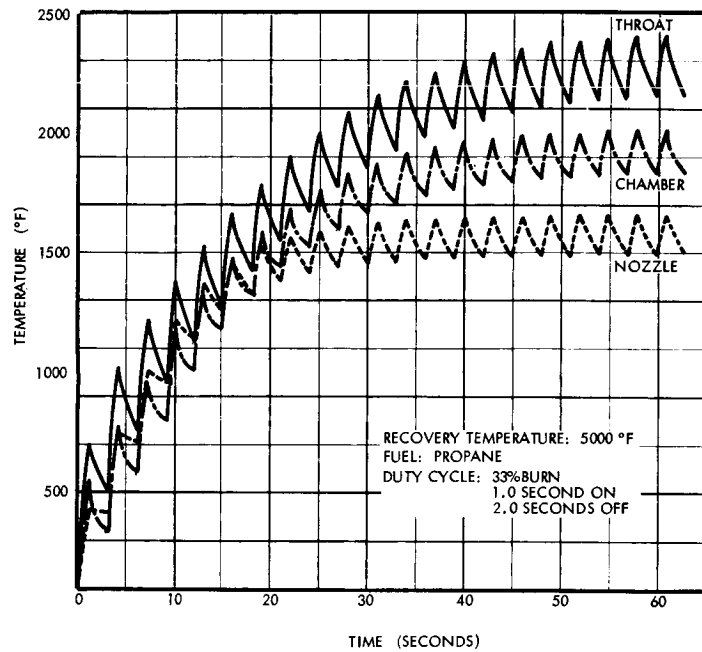


Figure 3-54. Transient Radiation Cooled CARB-I-TEX Wall Temperature Response (Pulsed)

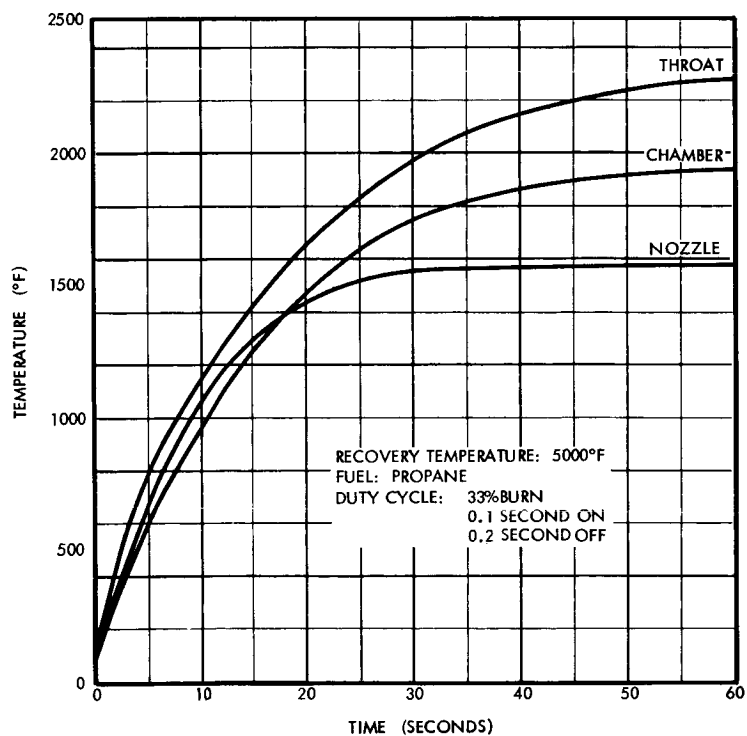


Figure 3-55. Transient Radiation Cooled CARB-I-TEX Wall Temperature Response (Pulsed)

The important difference between the three duty cycles is the steady state throat temperatures; the wall temperature was reduced by 500 degrees for the 33% burn duty cycles over the 100% burn duty cycle. It is interesting to note that the average temperature responses for the two 33% burn duty cycles were very nearly equal. This would indicate that all 33% burn duty cycles with burn pulses between 0.1 and 1.0 second would yield approximately the same temperature response.

3.2.2.2 Film-Conduction Cooled Thruster Analysis

Analyses were conducted on the copper film-conductively cooled chamber configuration shown in Figure 3-29d. As with the basic radiation-cooled chamber studies discussed previously, analyses were conducted for various total heat rejection rates by varying the local wall gas recovery temperatures. Three recovery temperature levels were selected: 3000°, 5000°, and 7000°F, and were used with the gas-side thermal resistance shown in Figure 3-39 for the propane fuel. The resultant temperature distributions from these analyses are shown in Figure 3-56. For the design shown as the preliminary chamber configuration, insufficient fuel was available to cool the chamber for the wall thickness distribution initially assumed. Subsequent analyses were performed with various wall thickness distribution which indicated the optimal temperature distribution would be nearly parabolic as shown in Figure 3-56. It was also determined that, in order to conductively cool the throat section using the minimum possible fuel coolant flow rate, the wall temperature distribution must be maximized for a given gas-side recovery temperature. This can be done by determining the wall material thickness distribution from the assumed temperature distribution.

The wall thickness distributions can be computed from the assumed parabolic temperature distribution by integrating the convective heat flux input along the uncooled portion of the chamber wall and setting it equal to the sum of the conduction heat transfer along the wall and the radiation heat loss from the outer wall. The thermal model developed for determining the thickness distribution is shown in Figure 3-57.

It is assumed that the liquid coolant is capable of absorbing all of the energy conducted to the liquid cooled area. While this may not be physically possible from the standpoint of the limiting allowable heat flux to the coolant, it allows the calculation of a required minimum coolant flow rate to cool the thruster. In addition, the assumption is made that at a specified expansion area ratio, a material of relatively low conductivity is attached such that the conduction heat loss across the boundary is small compared to the conductivity of the film-conduction cooled chamber material. Also, the maximum wall temperature is assumed to occur at the end of the high conductivity section of the expansion cone, while the temperature of the chamber at the end of the liquid-cooled section is assumed to be slightly above the saturation temperature at the chamber pressure.

The temperature distribution along the wall is approximated by

$$T_{\text{wall}} = ax^2 + bx + c \quad (3-28)$$

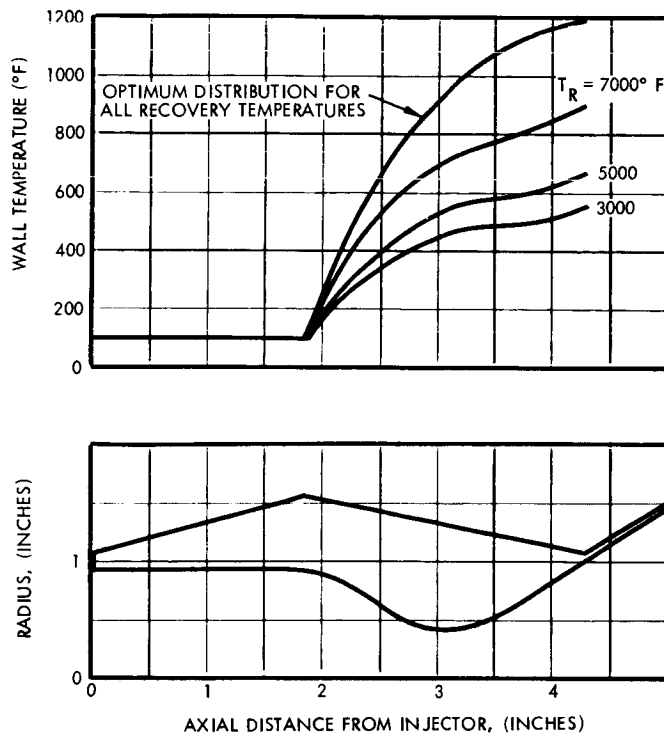


Figure 3-56. Copper Conduction Cooled Chamber Temperature Distribution

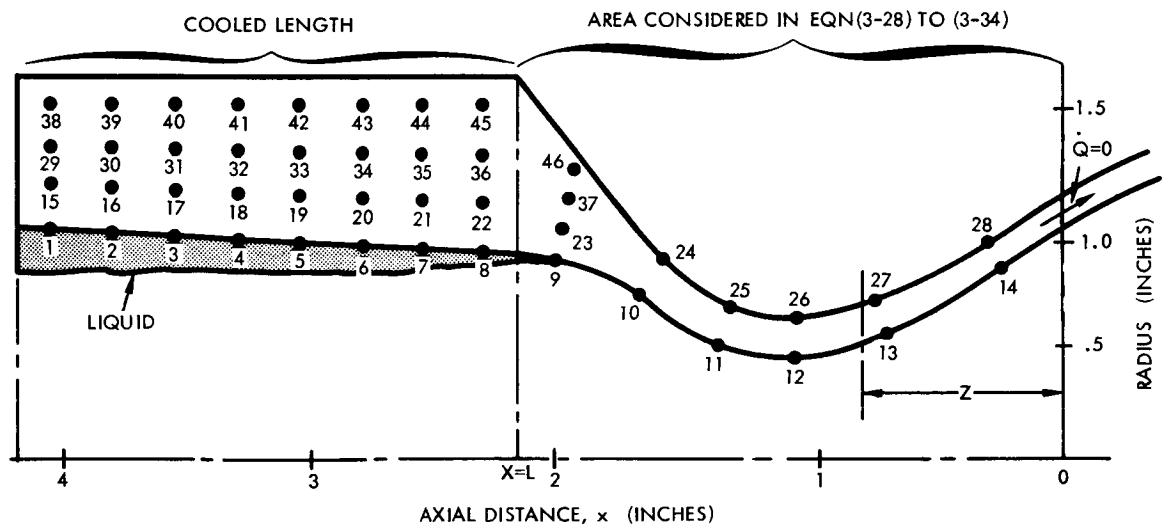


Figure 3-57. Film-Conduction Cooling Thermal Model

where $x = 0$ corresponds to the end of the high-conductivity region of the expansion cone. Using the assumptions,

$$\left. \frac{dT}{dx} \right|_{x=0} = 0 \quad (3-29)$$

$$T_{\text{wall}} = T_{\text{max}} \text{ at } x = 0 \quad (3-30)$$

$$T_{\text{wall}} = T_{\text{sat}} + \Delta T \text{ at } x = L \quad (3-31)$$

the temperature distribution then becomes

$$T_{\text{wall}} = T_{\text{max}} - \frac{T_{\text{max}} - (T_{\text{sat}} + \Delta T)}{L^2} x^2 \quad (3-32)$$

If the conduction heat transfer is considered to be one-dimensional and the outside surface area is considered to be approximately equal to the inside surface area, the heat loss at any position down the chamber at some distance z is given by

$$\dot{Q}_L|_z = (T_R - T_{\text{max}}) \int_0^z h_g dA_s + \frac{T_{\text{max}} - (T_{\text{sat}} + \Delta T)}{L^2} \int_0^z h_g x^2 dA_s - \sigma \epsilon F \int_0^z T_w^4 dA_s \quad (3-33)$$

Since the conduction heat loss was considered to be essentially one-dimensional, the heat transferred across z can also be given by

$$\dot{Q}_L|_z = -kA_c \left. \frac{dT}{dx} \right|_z = 2kA_c \frac{T_{\text{max}} - (T_{\text{sat}} + \Delta T)}{L^2} x|_z \quad (3-34)$$

From this the cross-sectional area, A_c , can be determined and consequently the thickness distribution in the uncooled portion can be calculated. Subsequent detailed two-dimensional analyses based upon the thicknesses derived from Equation (3-34) substantiated the one-dimensional conduction assumption.

The coolant flow rate necessary to absorb the heat conducted from the uncooled section is determined by the following heat balance

$$\dot{w}_{liq} = \left[\frac{1}{\Delta H_L} \dot{Q}_L \Big|_{x=L} + \frac{1}{\Delta H_T} \int_L^x h_g (T_R - T_{sat}) dA_s \right] \frac{1}{\eta_{FC}} \quad (3-35)$$

The integral term accounts for the heat absorbed by the fuel caused by convection from the combustion gases. Entrainment losses due to mechanical action between the liquid and the main core gases are taken into account by the film coolant efficiency, η_{FC} . This is defined as the ratio of the coolant available to absorb heat to the total coolant flow rate. For the purpose of comparing the three coolant fuels, a typical efficiency of 0.4 was assumed.

It is interesting to note that by examining Equations (3-33), (3-34), and (3-35) one concludes that no single configuration will yield to the minimum fuel coolant flow rate for all gas recovery temperatures.

Selecting the maximum allowable wall temperature of 1200°F for copper at a point in the expansion cone ($x = 0$) of a film-conductively cooled chamber, an optimum thickness configuration was computed for the propane film-cooled chamber with a gas recovery temperature of 5000°F. This chamber configuration is shown in Figure 3-58. It is noted that the thickness for these conditions are relatively thin. The result, however, is not surprising considering the high thermal conductivity of copper. Thickness distributions for other materials would be proportional to the thermal conductivity of the material, i.e., a beryllium chamber would be approximately three times as thick as a copper chamber.

Taking the maximum allowable copper wall temperature as 1200°F and the temperature distribution given by Equation (3-32), a series of parametric analyses were performed on the baseline chamber configuration to determine the minimum fuel coolant flow rate as a function of gas recovery temperature, cooled expansion area ratio, cooled length of combustion chamber wall, and film coolant flow rate. In all analyses it was assumed that the wall temperature at the end of the liquid film-cooled section was 40°F above the saturation temperature of the fuel at 100 psia. It was also assumed that at the end of the liquid-cooled section, the liquid immediately diffused into the main core gases. The recovery temperature downstream of the liquid-cooled section was assumed to be invariant with axial distance.

Shown in Figure 3-59 are the film-coolant flow rate requirements for each of the fuels investigated as a function of the wall gas recovery temperatures for a copper conductively cooled chamber which is cooled to an expansion area ratio of 6:1. The film-coolant length was equal to the length of the cylindrical chamber (1.85 inches).

From the results of these analyses, it can be seen that the propane fuel is clearly the superior coolant, with the methane-ethane blend showing some possibility. However, the preceding analyses do not account for the peak nucleate boiling heat flux of the fuels. The superior cooling capability of the propane fuel is due to its superior carbon deposition characteristics.

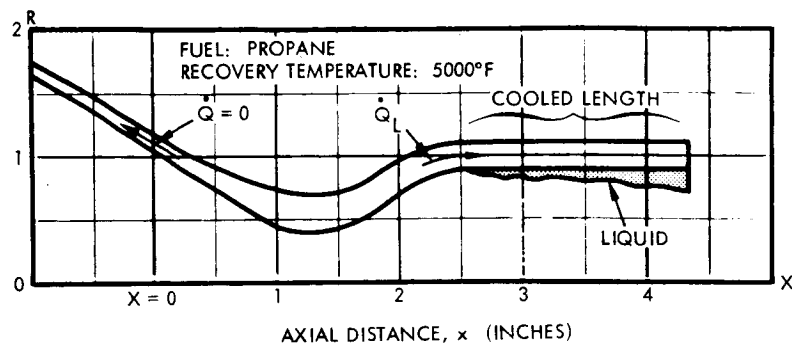


Figure 3-58. Optimum Copper Conduction-Cooled Chamber Configuration

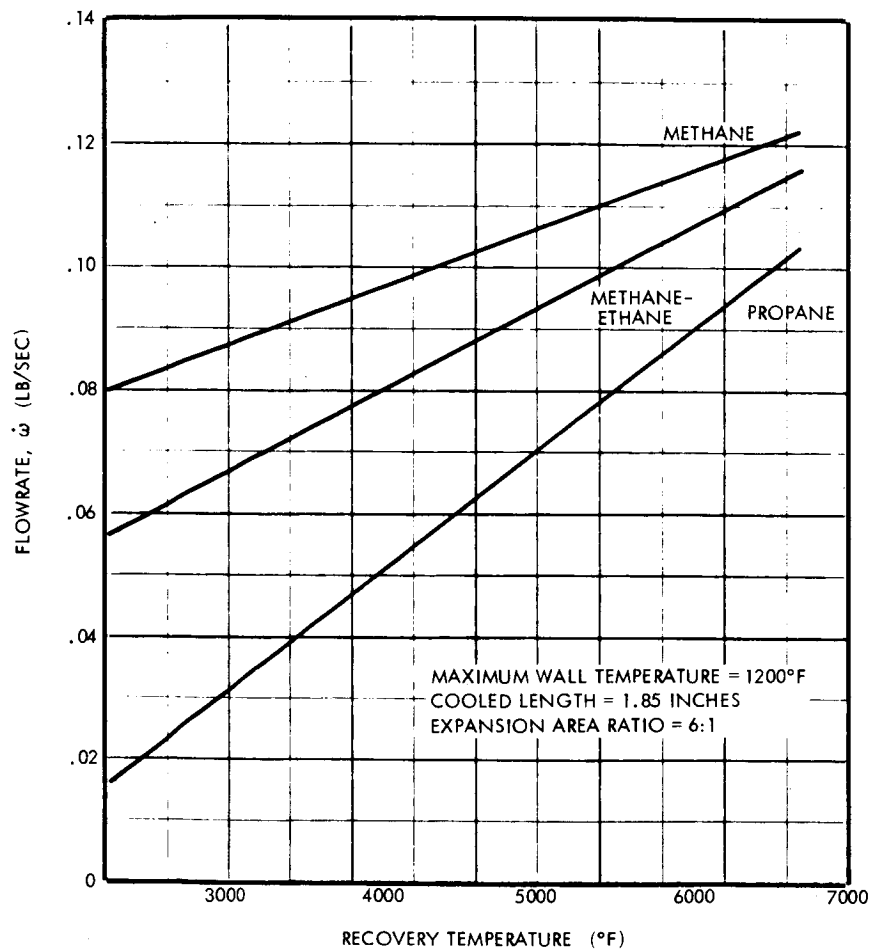


Figure 3-59. Comparison of Film Coolant Flow Rate Requirements

When the fuels are compared on the basis of an optimum tradeoff between the total heat rejection rate and the film coolant layer burnout heat flux (i.e., the point where the film coolant layer film binds), the methane-ethane fuel blend is shown to be the best, as in Figure 3-60.

Thus propane appears best on the basis of a fixed-film coolant flow rate while methane-ethane is best on the basis of total heat rejection capability.

The effects of operating pressure and scalable dimension have been investigated analytically to determine the limits of inter-region thruster operation. In order for the thruster to operate successfully three conditions must be satisfied. These include:

- (1) The film coolant flow rate must be sufficient to absorb the total heat load into the thrust chamber.
- (2) The heat flux of the rejected heat into the liquid-film coolant layer must be less than the fuel peak nucleate boiling heat flux.
- (3) The thermal resistance due to conduction length must be small enough such that the throat temperature remains below a material limit.

With these three limitations considered expressions can be derived which indicate the effects of chamber pressure and scalable dimensions.

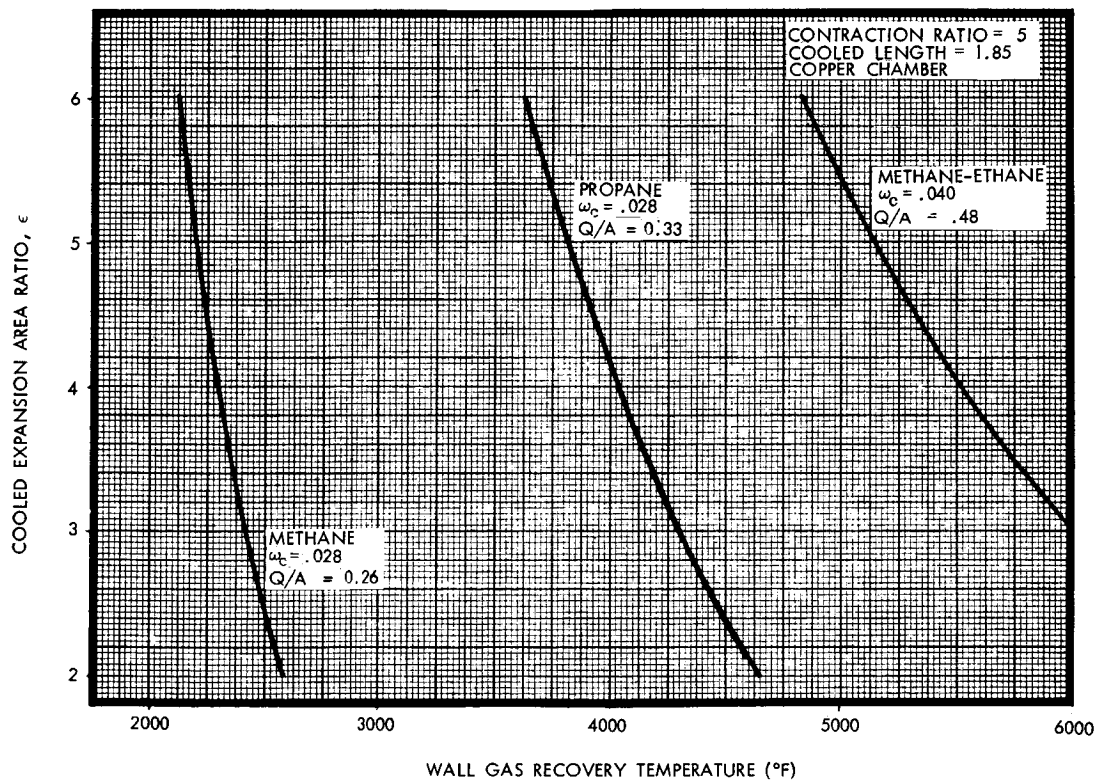


Figure 3-60. Comparative Cooling Capability of LPG Film Coolants

The basic assumptions made are that the film coolant is a liquid covering a certain portion of the chamber, the chamber characteristic length is constant, the chamber length is proportional to the chamber diameter, and the "core" mixture ratio is fixed.

The total propellant flow rate is proportional to the thrust and for a fixed "core" mixture ratio the film coolant flow rate is proportional to the thrust.

$$\dot{w}_{fc} \sim F \quad (3-36)$$

the throat area and chamber area are given by

$$A_t \sim \frac{F}{P_c} \quad (3-37)$$

$$A_c \sim \epsilon \frac{F}{P_c} \quad (3-38)$$

the area associated with heat input to the chamber is

$$A_h \sim D_c L_c \quad (3-39)$$

But for $L_c \sim D_c$

$$A_h \sim D_c^2 \sim A_c \quad (3-40)$$

The Bartz heat transfer coefficient is given by

$$h_g \sim \frac{P_c^{.8}}{A_t^{.05} \epsilon^{.9}} \sim \frac{P_c^{.85}}{F^{.05} \epsilon^{.9}} \quad (3-41)$$

For a constant driving temperature potential $(T_r - T_w)$

$$\begin{aligned} \dot{q}_{in} &\sim h_g A_h \\ &\sim \frac{F^{.95} \epsilon^{.1}}{P_c^{.15}} \end{aligned} \quad (3-42)$$

But for $L^* = \epsilon L_c = \text{constant}$ and $L_c \sim D_c$

$$\epsilon \sim \frac{P_c^{.33}}{F^{.33}} \quad (3-43)$$

Thus,

$$\dot{q}_{in} \sim \frac{F^{.92}}{P_c^{.12}} \quad (3-44)$$

This expression relates the effect of chamber pressure and thrust on the chamber heat input.

However, the fuel heat absorption capability is also related to the thrust by

$$\dot{q}_{\text{absorb}} \sim \dot{w}_{fc} \sim F \quad (3-45)$$

Using those two expressions (Equations 3-44 and 3-45) the required film coolant percentage can be determined for various thrust and chamber pressure levels. This result is shown in Figure 3-61.

As noted, increases in both chamber pressure and thrust have a positive effect on the percentage of film coolant required to absorb the heat loads. This is because of the more rapid decrease in the heat input area than the increase in heat transfer coefficient and also because of the increase in film coolant flow rate with thrust level.

For the cases to be examined experimentally the chamber and throat diameter are fixed and either the chamber length (L^*) or the chamber pressure (also thrust) is varied. For this condition it is found that the heat input is given by

$$\dot{q}_{in} \sim P_c^{.8} L^* \quad (3-46)$$

Using this expression the variation of the total chamber heat input is determined as a function of chamber pressure and characteristic chamber length. These results are shown in Figure 3-62. These results can be compared with the experimental results shown in Figure 5-51 and 5-53. As is noted the agreement is excellent.

The heat flux into the film coolant is determined from the heat input to the chamber divided by the area covered by the film coolant, as given below.

$$(q/A)_{fc} = \frac{\dot{q}_{in}}{A_{fc}} = \frac{\dot{q}_{in}}{\pi D_c L_{fc}} \quad (3-47)$$

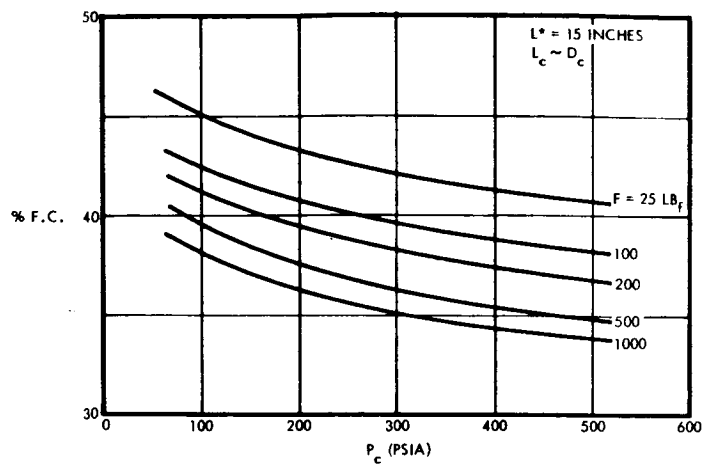


Figure 3-61. Film Coolant Percentage Required Versus Chamber Pressure

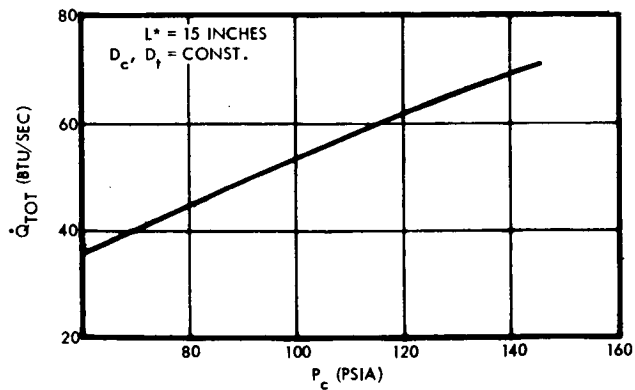
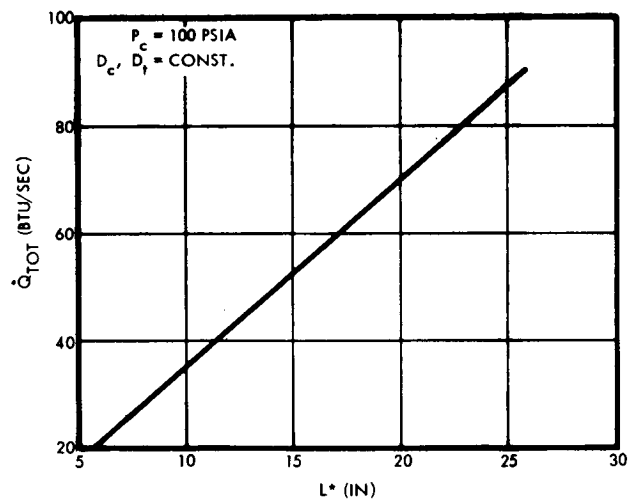


Figure 3-62. Total Heat Load Versus Characteristic Length and Chamber Pressure

The length of the film coolant layer, L_{fc} , is primarily a function of the film coolant flow rate or

$$L_{fc} \sim w_{fc} \sim F \quad (3-48)$$

Thus

$$(q/A)_{Fc} \sim \frac{P_c^{.21}}{F^{.41}} \quad (3-49)$$

The peak nucleate boiling heat flux is also a function of the operating pressure and is related by

$$(q/A)_{\text{peak}} \sim P_c^{.36} \quad (3-50)$$

The ratio of the heat flux into the film coolant and the peak heat flux gives a measure of where film binding of the film coolant layer will occur. For ratios greater than 1.0 film binding will occur and hence inter-regen operation is severely limited. Figure 3-63 shows the results of the calculation for various chamber pressure and thrust levels. As seen for a chamber pressure of 100 psia the thrust level must be greater than about 75 lbf in order to avoid film binding. However, it should be noted that this is for a liquid film coolant. With a gaseous film coolant there would be no such limit.

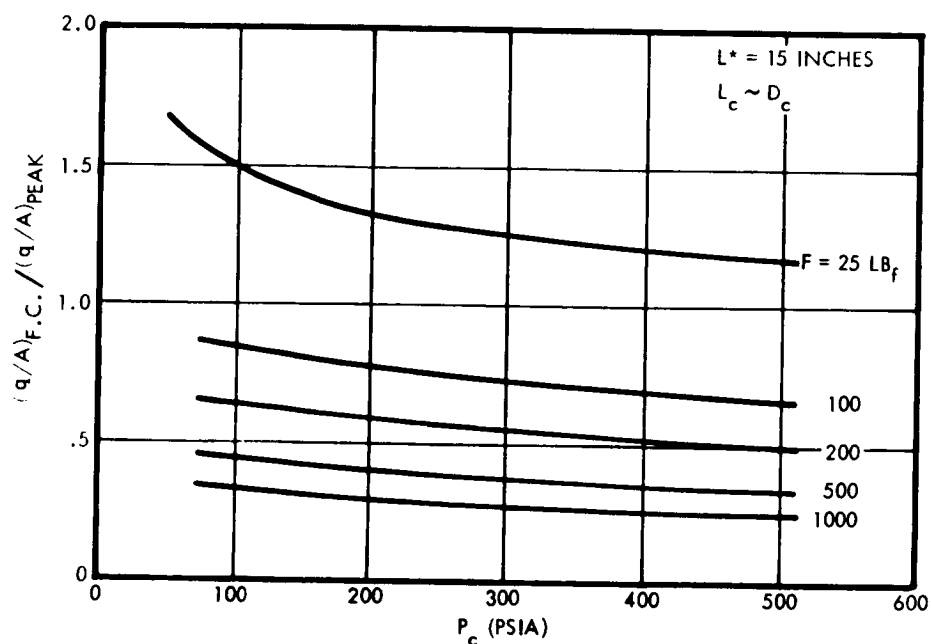


Figure 3-63. Nondimensional Film Coolant Heat Flux Versus Chamber Pressure

The final possible limitation is due to a limitation on the material temperature at the thrust. This means that there will be some limit on the conduction length between the thrust and the film coolant. However, the length limitation only arises as a result of two dimensional effects (radial temperature gradients). In an ideal one-dimensional case the chamber thickness (or conduction area) can be increased as the conduction length is increased. A calculation was made for the one-dimensional case with a constant conduction area. The result of this is shown in Figure 3-64 which indicates that for a chamber pressure of 100 psia the thrust level must remain below about 120 lbf if the maximum safe material temperature is 1500°F. In an actual situation the conduction area should be a scalable dimension and the thrust limit would be higher than this. Unfortunately the two-dimensional limit was not determined, however, it can be stated that the limit would be much less severe for higher conductivity materials.

Both the contraction area ratio and the combined effects of the convergence angle and the throat radius of curvature were investigated for the copper film-conduction cooled thruster using propane as the coolant. The cylindrical portion of these chambers remained constant at 1.85 inches and was considered to be covered by liquid propane. Figure 3-65 summarizes the contraction ratio effects as well as the effects of changes in convergent angle and the upstream throat blend radius. These curves are for the lower limit of the peak flux for propane (0.33 Btu/in²-sec). As would be expected, the smaller the contraction area ratio, the higher the allowable recovery temperature at which the chamber can be operated. Between contraction area ratios of 6:1 and 2:1 the increase in operating limits is as much as 1000°F. Similarly, the larger the convergent angle and the smaller the throat blend radius, the higher the operating recovery temperature. Reducing the throat blend radius from 2 to 1 radius and increasing the convergent angle from 35 to 60 degrees results in an increase in the operating recovery temperature of approximately 1400°F.

Figure 3-66 compares film-conduction cooled thrusters fabricated of copper, beryllium, and composite designs having a columbium liner with a copper outer conductive shell and columbium liner with a nickel outer conductive shell (designs shown in Figure 3-29). A thruster having a nickel inner liner with a copper outer conductive shell would have essentially the same characteristics as the beryllium and columbium-copper design shown in Figure 3-66. This is because the temperature limits of the outer conductive shell establish the design criteria. However, a conductive design with a nickel inner liner would have better chemical resistance to the gas environment. Each of the results shown in this figure has utilized propane as the film coolant; however, the trends are valid for each fuel. The beryllium chamber has a design temperature of 1600°F as compared to the 1200°F design temperature for the copper. Only a small amount of increased heat rejection capability is gained by operating at the higher temperature offered by the beryllium. On the other hand, if the beryllium fluoride layer is unstable at temperatures in excess of 800°F, as indicated in Reference 11, then beryllium offers no advantages over copper. The composite designs having a columbium inner liner and a copper outer shell have

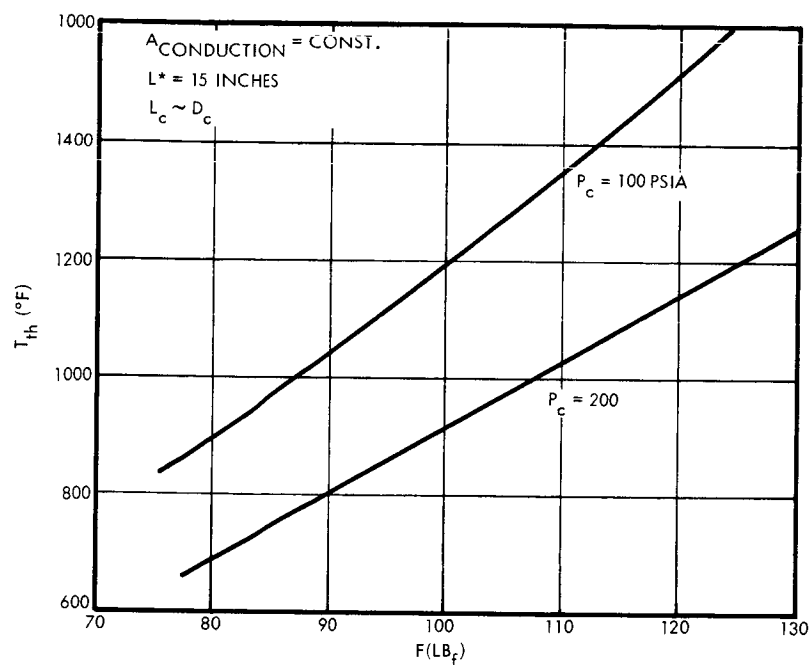


Figure 3-64. Throat Temperature Versus Chamber Pressure

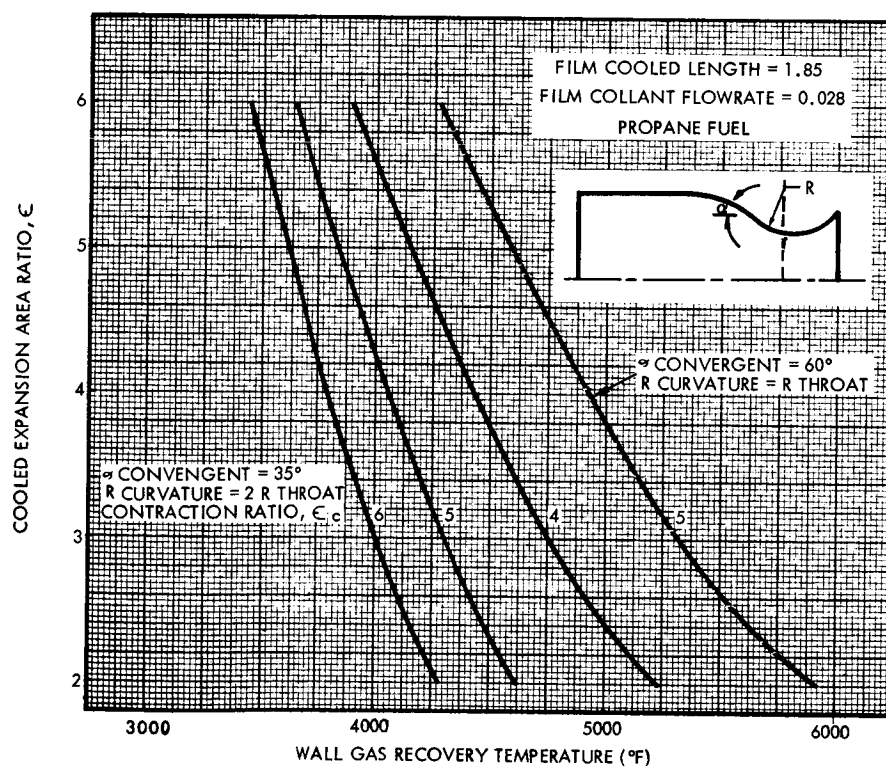


Figure 3-65. Effects of Chamber Geometry on Conductive Cooling Limits

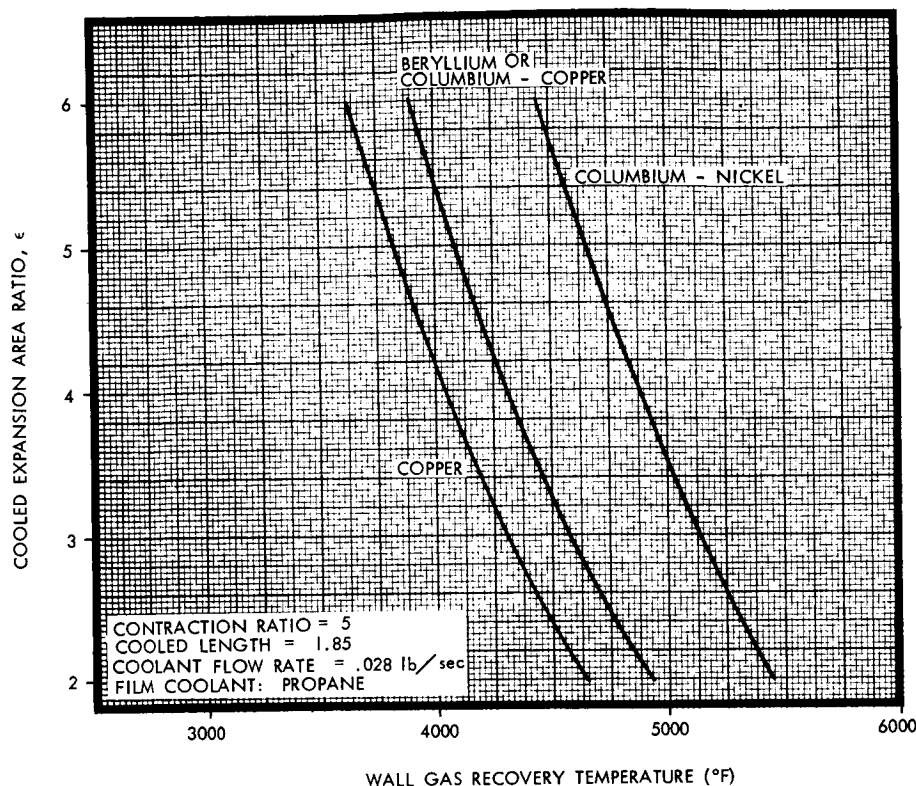


Figure 3-66. Heat Rejection Characteristics for Conductively Cooled Thrusters

essentially the same characteristics as a beryllium chamber, while a composite design consisting of columbium with a nickel outer shell (design temperature of 2000°F) offers more heat rejection capability than a copper design. Although the composite designs offer some advantages in increased heat rejection capability, two disadvantages exist:

- (1) Differential thermal expansion between copper and columbium, nickel and columbium, and copper and nickel will pose a problem of separation at the material interfaces which would increase the thermal resistance resulting in a hot spot and subsequent burnout of the inner liner. A comparison of the thermal expansion coefficient for each of the materials is presented in Table 3-12.
- (2) The second disadvantage lies in the fact that for the higher operating temperatures associated with the composite designs as well as with the beryllium design, more heat is stored in the liner thereby resulting in more severe injector soakback problems as well as chamber design that is more sensitive to film binding during pulse duty cycles.

Table 3-12. Summary of Coefficients of Thermal Expansion

Material	Coefficient of Thermal Expansion α , in/in-°F x 10 ⁶
Copper	9.8
Nickel	7.4
Columbium	3.8
Tungsten	2.5
Beryllium	6.4
Beryllium-Copper	9.8

A series of detailed two-dimensional analyses were performed to determine the actual heat flux distribution in the film-cooled length. The analyses showed that in order to reduce the heat flux at the end of the film-cooled length, the required thickness distribution over the film-cooled length would be considerably thicker than that indicated in Equation (3-34).

Some typical heat flux distributions in the film-cooled length are shown in Figure 3-67 for three geometries in this area. The thickness, t , in this area is the thickness derived by Equation (3-34). It is obvious from an inspection of this figure that the thickness must be many times the so called optimum thickness in order to limit the heat flux to less than the peak nucleate boiling heat flux ($Q/A = 0.4$ for propane). Extrapolation of the data indicates that a thickness in the order of five times the optimum thickness for conduction would be required. The temperature distributions on the inner and outer walls in the liquid-cooled length are shown in Figure 3-68 for the three configurations. It is clear from the figure that the temperature potential, and consequently the heat flux at the injector end, is increased with increasing thickness of the section. This in effect helps to reduce the high heat flux at the end of the cooled length.

The radial temperature profiles have been analytically determined and are shown in Figure 3-69. These data reveal the isothermal nature of the radial temperature in the nozzle region (for this wall geometry) due to the high thermal conductivity of copper. These results also reveal that radial gradients occur at the head end region of the chamber where the heat is rejected back into the film coolant.

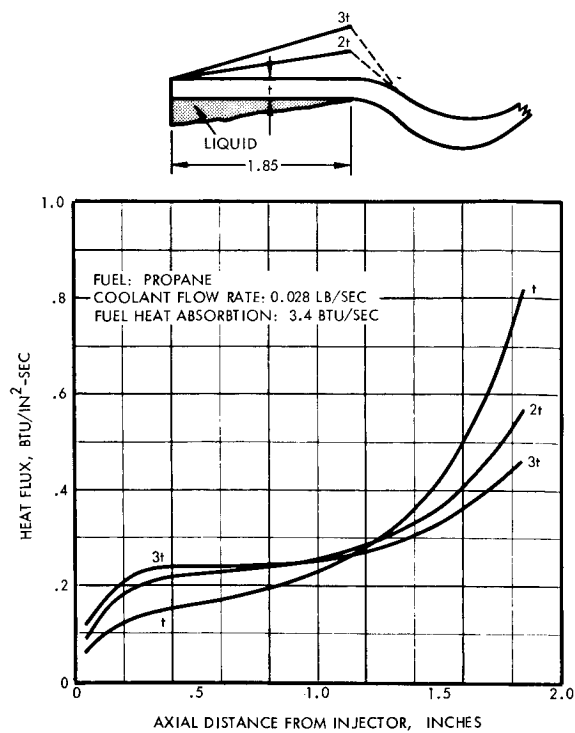


Figure 3-67. Effect of Chamber Thickness on Heat Flux Distribution

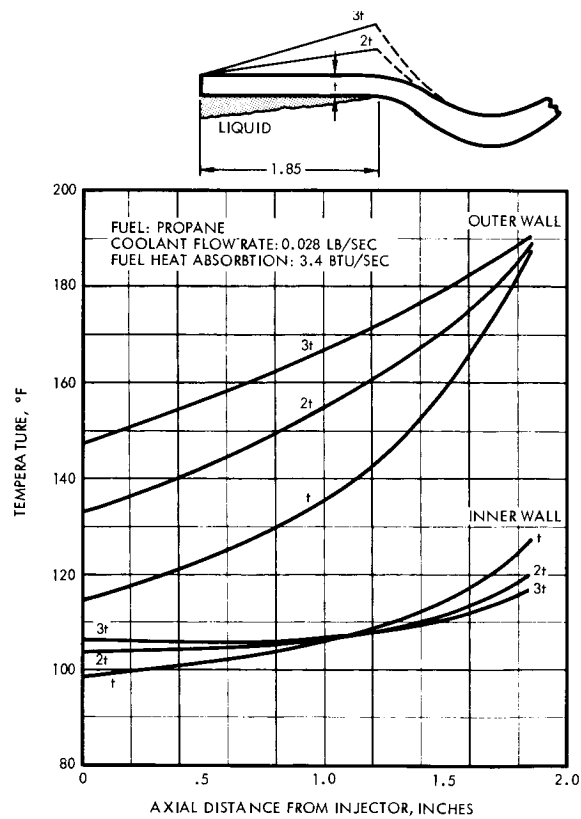


Figure 3-68. Effect of Chamber Thickness on Temperature Distribution

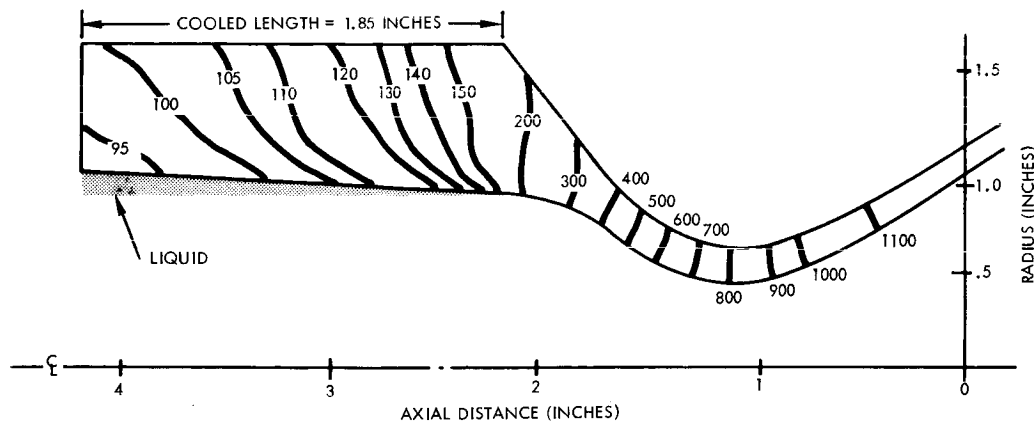


Figure 3-69. Steady-State Isothermal Profiles

The chamber thickness in the region covered by combustion gases (i.e., nozzle) should also be increased. However, this increase can not be made without an additional modification. In addition to the increased nozzle thickness, an isolation slot should be machined into the chamber, as seen in Figure 3-70. This slot acts in two ways: (1) to isolate the nozzle from the chamber, thereby forcing the nozzle to achieve a higher temperature, and (2) to meter the conducted heat flow from the nozzle to the chamber. The increased nozzle operating temperatures and temperature uniformity act to decrease the heat load into the nozzle region due to a decrease in the thermal driving potential. The gap left by the isolation slot is sized so that the heat conducted through it is equal to the heat entering the nozzle. Figure 3-71 shows the nozzle temperature profiles for each configuration. As can be seen there is little difference between the chamber with slots acting to meter on the inside or the outside; however, with the conduction metering gap at the outside the conducted heat is spread more evenly for input to the film-cooled layer. Figure 3-71 also shows a comparison between the thick nozzle with slots and the contoured thin nozzle. The more uniform temperature distribution of the slotted nozzle results in a 5% decrease in the heat input to the nozzle over the contoured shape.

The analytical methods used for the film cooling analysis are valid independently of the method of film-coolant injection. It can be injected at the beginning of the chamber or injected through the chamber walls as is the case for transpiration cooling. The basic difference between the two schemes is in the value of the film-cooling efficiency. Based on these observations, some conclusions were made with respect to transpiration cooling. Due to the higher film-cooling efficiency (near 100%) the transpiration-cooled thruster would require less fuel for cooling under the same chamber conditions. A problem area associated with this cooling concept is the possibility of coolant orifices plugging with carbon from the fuel decomposition. An additional problem would be associated with pulse mode operation. However, each of these areas was not investigated since they did not fall within the scope of the subject program.

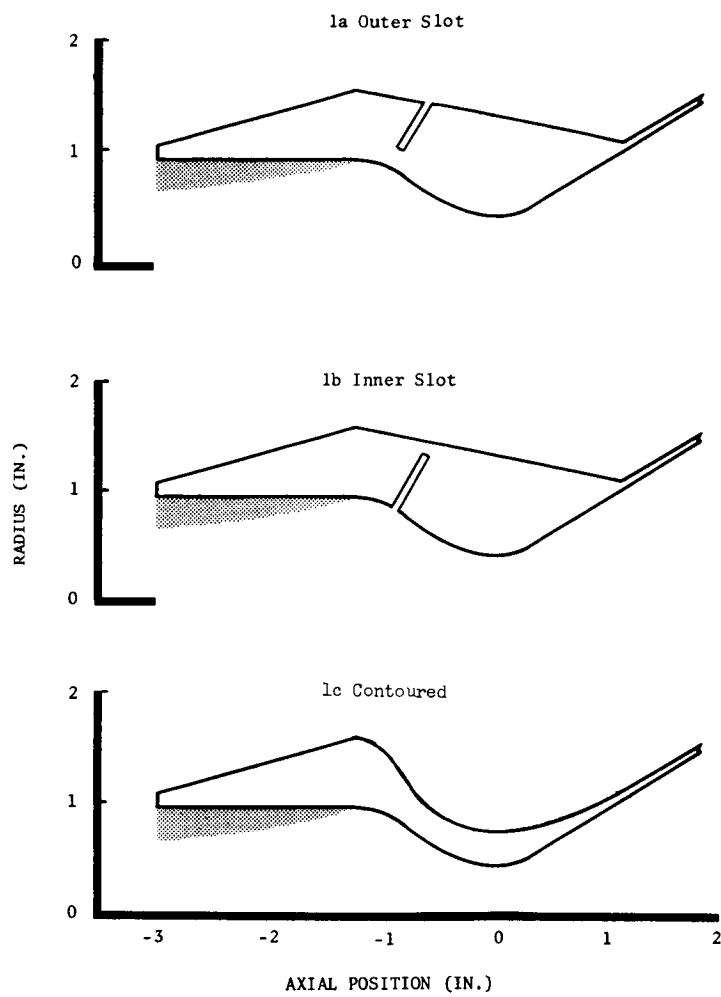


Figure 3-70. Film-Conduction Cooled Thruster Configuration with Isolation Slots

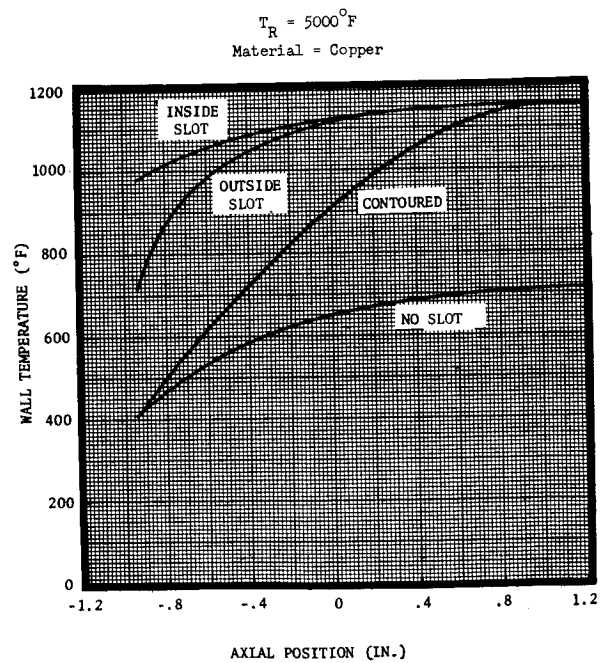


Figure 3-71. Effect of Isolation Slots on Nozzle Temperature Distribution

The configuration best suited for a film-conduction cooled chamber would be one that minimizes the throat region surface area (or the area subjected to high heat flux) and decreases the entrainment losses. From the work of Graham (Reference 19), it is evident that the chamber diameter must be relatively large to increase the film-cooling efficiency, η_{FC} . The chamber should also be tapered to provide a radial acceleration vector that would tend to hold the liquid against the wall. In summary, some of the thermal considerations that are of importance in the design of the film-conductively cooled chambers are as follows:

- Relatively large chamber diameter at the injector with a tapered chamber to the convergence section to decrease entrainment losses
- Short chamber section to allow the coolant to reach the convergence section
- Large convergence angle and small convergent section and throat blend radii to reduce the total heat load
- Maximum allowable wall temperature distribution to decrease the total heat load
- Small overall mixture ratio such that a relatively large amount of fuel is available for film coolant
- Fuels with large peak heat fluxes such that film binding (film boiling) is not a problem

While film-conduction cooled thrusters have been built and successfully tested, it is noted that these engines used MMH as a film coolant. The peak nucleate boiling heat flux of the MMH is at least an order of magnitude higher than those for methane and propane. In addition these engines were operated at mixture ratios of approximately 1.6 such that a large amount of fuel (30%) was available to cool the chamber. It should also be pointed out that the peak nucleate boiling heat flux was the factor that limited the range of operation of the film-conduction cooled chambers investigated in this report. Therefore, lowering the overall mixture ratio apparently would not increase the range of operation by making more fuel available for cooling. The increased fuel flow would only serve to create a lower boundary layer mixture ratio after the point of film binding. The lowered mixture ratio, however, might improve the performance since the main core gases would be at a more optimum mixture ratio.

Transient Behavior

Using the contoured configuration shown in Figure 3-57, transient analyses were performed for two duty cycles. The first duty cycle was a 60-second 100% burn followed by a soak period until the chamber reached equilibrium. Two cases of a 33% burn duty cycle were analyzed with pulses of 1.0 second on and 2.0 seconds off; the first case was at an initial temperature of 70°F while the second was at -300°F.

The temperature response of the chamber for the 100% burn duty cycle is shown in Figure 3-72 for three locations along the uncooled portion of the nozzle (B, C, and D) and at the point at the end of the cooled section (A). The chamber reaches steady state at the end of the 60-second burn period and does not exceed the peak nucleate boiling heat flux at the end of the cooled length. However, using criteria previously discussed for determining the point at which the liquid film makes the transition from nucleate boiling to film boiling, it is obvious from the soak temperature of 220°F that the coolant would be in the film boiling regime if an engine restart were attempted after the short soak period. The probable result of this would be a more rapid increase in the temperature response of the uncooled chamber section. The peak temperatures would then probably exceed those shown in Figure 3-72.

Using the soak temperature of the chamber as seen in Figure 3-72 the effective soakback temperature of the injector/chamber system was calculated from the heat capacities of each section. The chamber has an average temperature of about 250°F. These temperatures would result in a final average temperature of 50°F for the injector and chamber. This assumes no radiation loss as would be the case in a buried configuration. Subsequent injector startup from this temperature would probably result in some erratic operation due to vaporization of incoming propellants. This case would be particularly severe for pulsed mode operation. Some period of operation would be required before flow stability would be achieved.

The temperature responses for the two cases of the 33% burn duty cycle are shown in Figure 3-73 for the same locations as shown in Figure 3-72. In each case the chambers began to operate in the film boiling regime before steady-state operation could be achieved, however the length of time before this happened was considerably different for each case. The chamber that began at an initial temperature of -300°F made the transition between nucleate boiling and film boiling approximately 110 seconds into the duty cycle, while the chamber beginning at 70°F could operate for only slightly over 10 seconds. Here again, as with the 100% burn duty cycle, the temperatures in the uncooled chamber section would begin to rise more rapidly after film boiling began to occur, with eventual overheating of the uncooled portion.

The particular film-conduction cooled chamber that was analyzed for both of the duty cycles (100 and 33% burn) was a configuration primarily designed for a 100% burn duty cycle at a recovery temperature of 3500°F; i.e., it was designed to yield the minimum heat flux to the coolant under this condition. Since the pulsed duty cycle results in lower wall temperatures, the heat flux to the film coolant can increase as much as 20% over the 100% burn duty cycle. In essence, this points out that film-conduction cooled chambers would probably have to be designed for particular cycles in order to achieve the minimum coolant requirement. Operation of a chamber at other than the design duty cycle would require an increase in the coolant requirement.

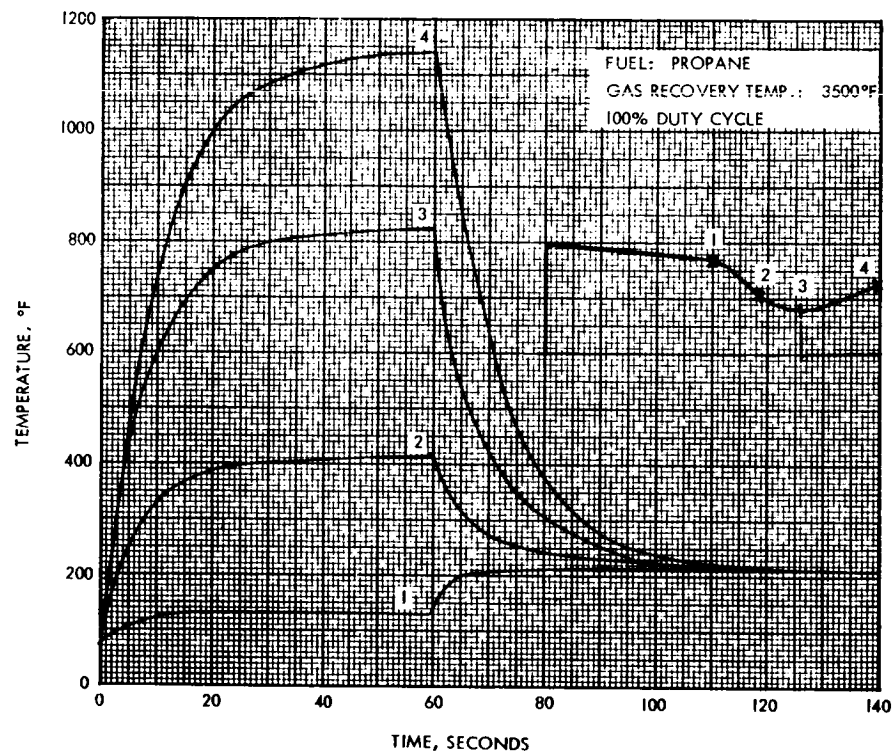


Figure 3-72. Transient Temperature Response of a Propane Cooled Thruster

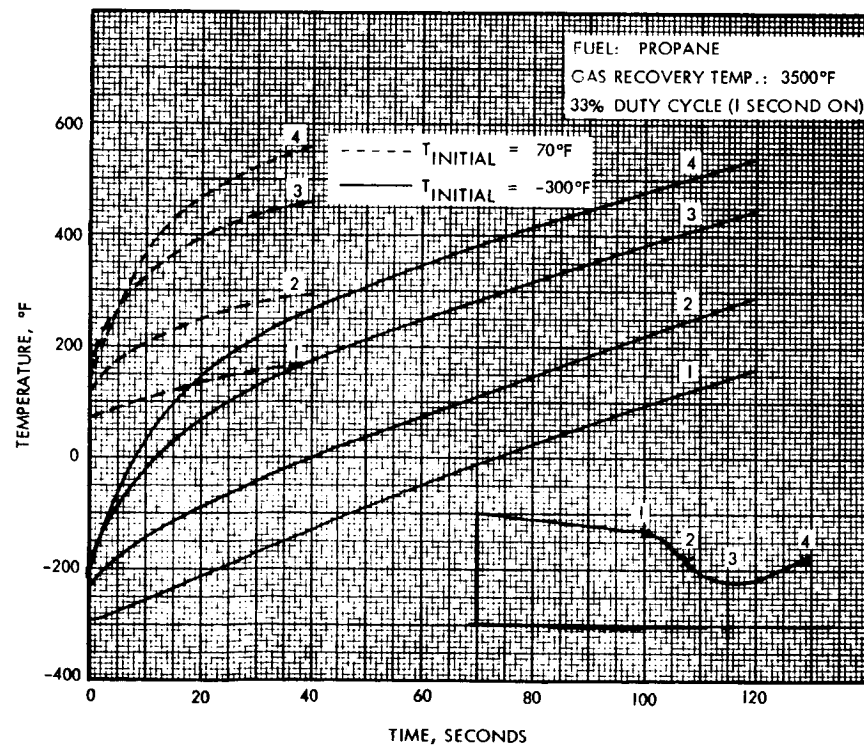


Figure 3-73. Effect of Initial Temperatures on Transient Response of a Propane Conductively Cooled Thruster

3.2.2.3 Thermal Analysis Summary

In summary of the thermal analysis, the following comparison of the different LPG fuels is made for the thruster configuration with conduction length = 1.85 inches, contraction ratio = 5.0, and expansion ratio = 6.0. Each propellant is rated on the basis of its delivered specific impulse including zonal losses resulting from film cooling. There are several cases which can be considered in the thermal analysis. These include:

- No film binding of the liquid film coolant; no recovery temperature axial gradient; no increase carbon deposition with higher film coolant flow rate
- Same as above but including peak heat flux limits
- Including all effects

This program included the first two cases but could not include the third because of lack of experimental information.

Case 1: For the same recovery temperature (5000°F), the delivered specific impulse was determined for each of the propellant combinations at this peak mixture ratio. Figure 3-59 is used to determine the flow rates of each fuel necessary to cool the thruster. These flow rates represent a film coolant percentage based on the optimum mixture ratio in the core of the thruster. For these film coolant percentages, a zonal loss can be determined from Table 3-3. Table 3-13 gives the results of this comparison.

Table 3-13. Comparison of LPG Fuels

	$T_o = 5000^\circ\text{F}$		
	Methane	Methane-Ethane	Propane
$(O/F)_{opt}$	5.75	5.2	4.5
\dot{w}_o core	0.25	0.26	0.26
\dot{w}_f core	0.045	0.05	0.058
$\dot{w}_{f.c.}$ (required)	0.084	0.057	0.041
%FC	65	53	41
ΔI_{sp}	-5.1%	-5.2%	-3.5%
I_{sp}	325	325	319
I_{sp} (del)	308	308	308

From this it can be seen that each of the propellant combinations are equivalent in delivered I_{sp} . However, as will be seen in Case 2, this result is deceiving.

Case 2: If the effects of a peak boiling heat flux are included, final flow rate increases beyond a certain limit can no longer be used to remove heat, however, they may be used to increase carbon deposition and/or decrease the throat recovery temperature. As outlined in Section 3.2.2.1, the film coolant flow rate required is the sum of the conducted heat load divided by the liquid heat absorption capability and the convected heat load divided by the total heat absorption capability. For equal recovery temperatures, the heat loads into the chamber and the nozzle can be determined by the gas convection coefficient and the effective gas convection coefficient, respectively. The liquid and total heat absorption capabilities can be determined from Table 3-9. From these values, the required film coolant flow rates are found. Now employing the peak boiling heat fluxes, or since the areas are equal, the peak boiling heating rates and the equivalent overall heat absorption capability can be determined as seen in Table 3-14, with all values related to those of propane.

Table 3-14. Effective Heat Absorption Capability of LPG Fuels

	Methane	Methane-Ethane	Propane
Nozzle heat load	1.82	1.69	1.0
Chamber heat load	1.0	1.0	1.0
Total heat absorption	1.29	1.10	1.0
Liquid heat absorption	.76	.86	1.0
$\dot{w}_{f.c.}$ (required)	1.58	1.44	1.0
Nucleat boiling	1.06	1.63	1.0
Effective heat absorption	.67	1.13	1.0

This table indicates that with the inclusion of a peak boiling criteria, the methane-ethane fuel blend becomes better than the propane. Using the peak boiling limits the flow rate limits for each fuel can be determined and hence the maximum recovery temperature limits. Table 3-15 gives these results as well as the predicted delivered specific impulses for each combination.

Table 3-15. Comparison of LPG Fuels

	Methane	Methane-Ethane	Propane
$\dot{w}_{f.c.}$ (limit)	0.040	0.055	0.029
Nozzle heat load limit	4.3	7.7	4.1
T_o (limit) ($^{\circ}F$)	2700	4900	3700
% FC	47	53	34
Δ Isp	-6.3%	-5.1%	-3.7%
Isp	325	325	319
Isp (del)	305	308	307

Thus, it can be seen that the propellants give about the same delivered performance, however, the methane-ethane blend can operate up to a recovery temperature of 4900°F while the others must operate much lower.

The inclusion of Case 3 would result in the use of additional film coolant for the methane and propane to bring the throat recovery temperatures down, but this would result in further performance losses.

The final conclusion to be drawn is that the methane-ethane blend is the best film coolant fluid for the inner regeneratively cooled thruster with propane not too much worse and methane showing poorly. However, it is noted that the low temperatures of operation and high volatility of the fuels may result in operational design requirements somewhat more stringent than previously experienced in inner regeneratively cooled designs with earth storable propellants.

3.3 OTHER MATERIAL DESIGN CONSIDERATIONS

3.3.1 Heat Transfer Properties

Physical property effects on heat transfer can be obtained by considering the transient conduction equation for variable properties

$$\rho C_p \frac{\partial T}{\partial t} = \nabla \cdot k \nabla T \quad (3-51)$$

Considering only transient effects first, the time gradients in any one direction are approximately given by

$$\frac{\partial T}{\partial t} = \frac{k_i}{\rho C_p} \sum \frac{\partial^2 T}{\partial x_i^2} \quad (3-52)$$

where it is seen that the term of primary importance is the thermal diffusivity $[\alpha = k/(\rho C_p)]$, which is a measure of diffusive ability of the material to locally redistribute a heat pulse. The conductivity term, k , is also important, both in a transient sense and in a steady-state sense, and the interaction between diffusivity and conductivity can be quickly assessed by use of an approximate one-dimensional transient solution of Equation (3-51) with constant properties and step heat input at the surface,

$$(T_s - T_i) = \frac{\frac{h}{k} \sqrt{3/2\alpha t}}{1 + \frac{h}{k} \sqrt{3/2\alpha t}} (T_{ad} - T_i) \quad (3-53)$$

For transient operation, high values of α are desired throughout the operating temperature range to minimize temperature spiking effects, and high conductivity values are desired for lower temperatures at the surface. For comparison purposes, $\alpha(T)$, $k(T)$ and $\sqrt{\alpha(t)}/k(t)$ are given in Figures 3-74

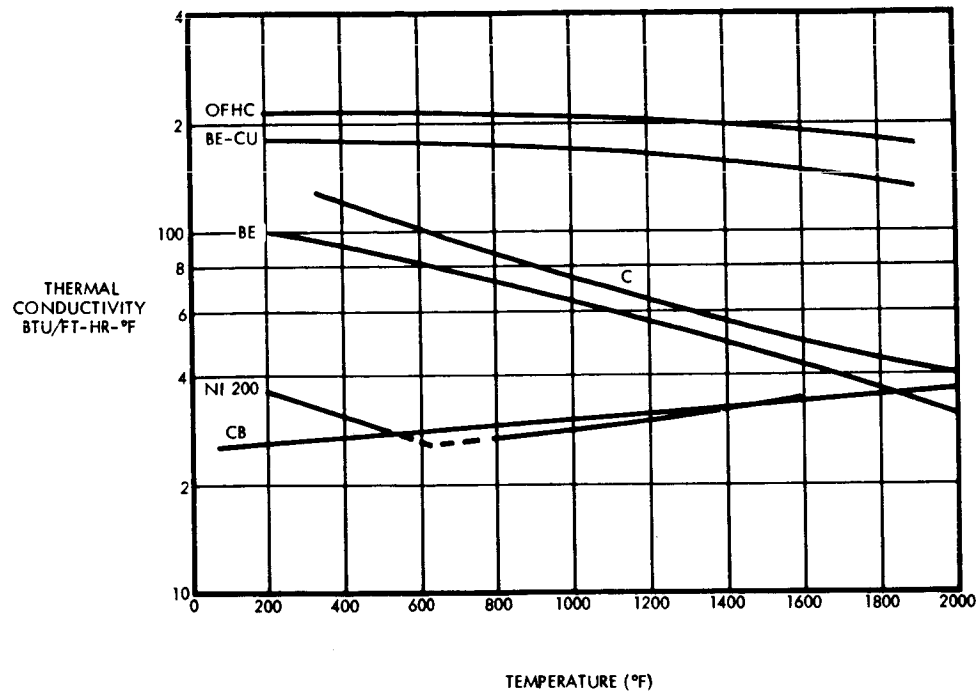


Figure 3-74. Thermal Conductivity of Candidate Conductive and Heat Sink Materials

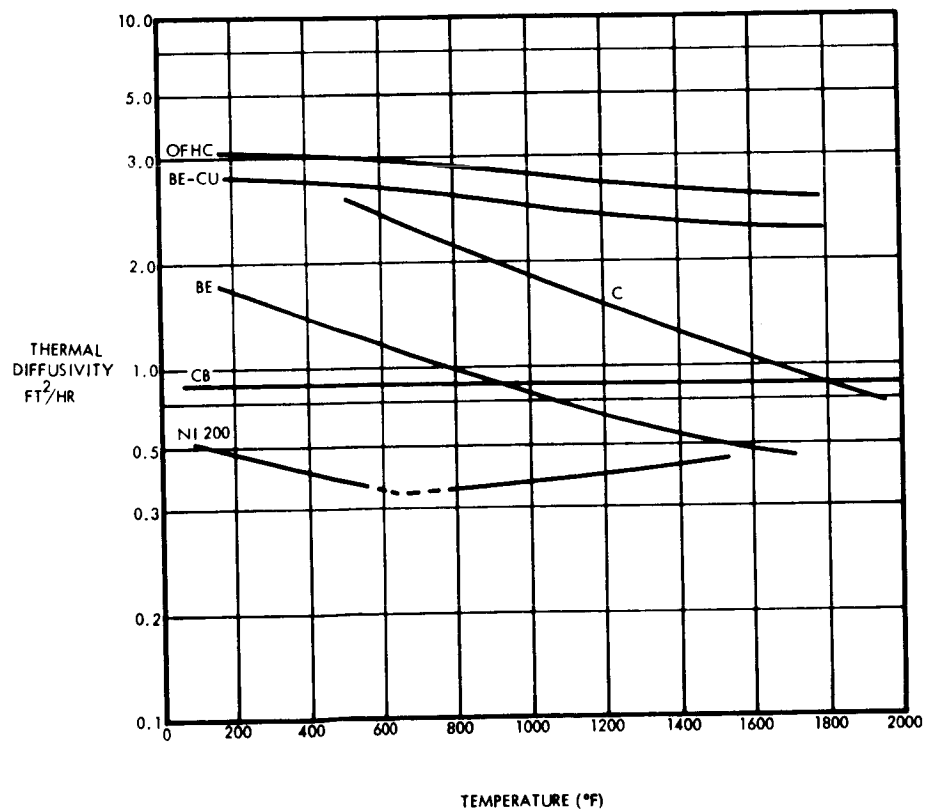


Figure 3-75. Thermal Diffusivity of Candidate Materials

through 3-76 for OFHC copper, Be-Cu alloy, and graphite. It is observed that the coppers, graphites, and beryllium materials are superior conduction materials. Only the coppers and graphitic materials have superior diffusivity values in the low to intermediate temperatures.

3.3.2 Heat Storage Effects

The selection of thrust chamber materials for heat sink type designs can be strongly influenced by potential soakback effects. Therefore, total heat storage must be considered. The product $\rho(T) C_p(T)$ serves as a figure of merit for comparing materials. Table 3-16 lists this product for several candidate materials.

Table 3-16. Heat Storage Effects for Several Candidate Thruster Materials

Material	Density* (lb/ft ³)	Specific Heat** (Btu/lb°F)	ρC_p
Cu	537	0.108	58.0
Be-Cu	533	0.112	59.8
Be**	110.6	0.72	79.6
C	106.6	0.43	45.8

* \bar{T} = 1500°R for metals
 = 2500°R for C

**1.7 percent Be-O.

From a purely soakback standpoint, graphite is superior, the high density metals second, and beryllium last. For purely heat-sink purposes, beryllium is first. The minimum heat storage factor must receive major attention since it influences the injector-combustor attachment in a major way. Further high soakback potentials can destroy film cooling effects in subsequent cycles by causing wall temperatures which are too high to allow nucleate boiling for designs wherein film cooling and conduction are important.

3.3.3 Chemical Compatibility Factors

An important factor in the life requirements for a thrust chamber utilizing the given propellants is the chemical compatibility of the materials with the exhaust products.. All of the materials considered useful for thrust chamber design theoretically are subject to some exhaust specie attack for some propellants. It is known that graphite can operate satisfactorily in an HF environment, but cannot tolerate an oxidizing atmosphere.

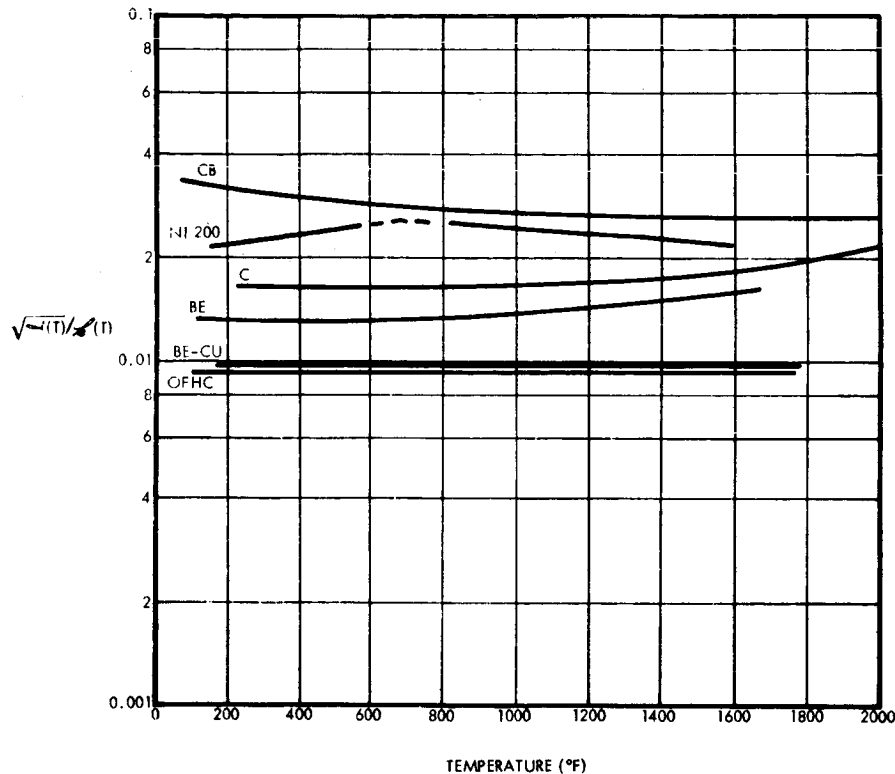


Figure 3-76. Measure of Response of Candidate Materials

Beryllium fluorides have relatively low melting temperatures and, therefore, impose wall environment control. The copper fluorides are not physically matched to parent copper in terms of specific volume and, therefore, are porous to continued attack at elevated temperatures. Nickel can withstand attack up to considerably higher temperatures. Nickel thermally diffusion bonded on copper can effectively block chemical attack in the coppers. Design attention must be given to proper matching of injector to chamber to assure a proper and uniform peripheral mixture ratio control for all these materials.

3.3.4 Mechanical Property Considerations

The mechanical property considerations fall into two categories: those which are of a primary strength nature, and those which affect life of the thrust chamber from a fatigue standpoint. Other factors of interest are resistance to creep and metallurgical stability of the material as it is subjected to either pulsing or long steady durations of operation. The factors influencing basic strength are those of importance to pressure vessel design: tensile (ultimate and yield), compressive, and shear as a function of temperature. Those affecting life and creep primarily are tensile and compressive ultimate and yield strengths and ductility. All of these are reflected in terms of combustor and throat dimensional stability. The effects of thermal plastic stresses are particularly important to life and the throat size.

Since performance is influenced most by throat area changes, attention should be directed primarily to this zone of the thrust chamber. With

mono-material metal construction, the throat effects can be analyzed with reasonable accuracy. It can be shown that throat shrinkage and expansion effects for such nozzles can be estimated for parabolic temperatures distributions to be

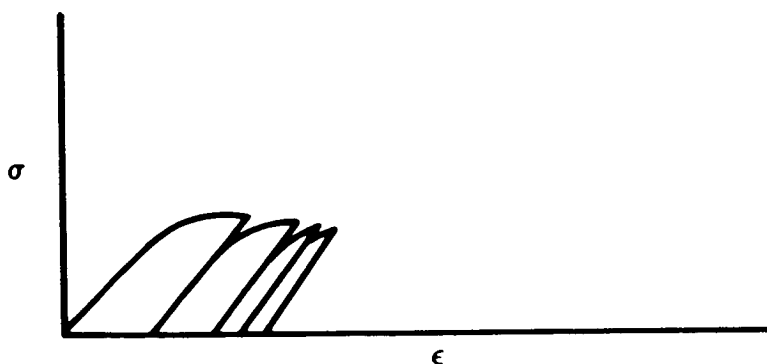
$$\Delta R_1 = \alpha \left[\frac{1+\nu}{1-\nu} \right] \frac{(T_1 - T_0)}{(R_0 - R_1)^2} \left[\frac{R_0^2 R_1}{2} - \frac{2}{3} R_0 R_1^2 + \frac{R_1^3}{4} - \frac{R_0^4}{12 R_1} \right] \quad (3-54)$$

The temperature distribution is given by

$$T = a + br + cr^2 \quad (3-55)$$

and is estimated by the integral method of Reference 20. The throat shrinkage effects manifest themselves at the initiation of firing. For long steady-state firings, the throat size may actually increase, depending upon the temperature distribution and resultant stresses. Graphitic materials are most stable here.

Thermal induced plastic damage is of particular importance for zero erosion and throat stability. Thermal fatigue effects are zero if the material does not undergo plastic strain. In the event that plastic deformation occurs, two results tend to occur. First, the material tends to "thermally ratchet" and not return to its original dimensions. This is illustrated in the stress-strain diagram below.



This effect can be analytically predicted. It can not only affect the geometrical throat size, but also can induce surface roughness effects with resultant increases in local heat transfer.

The thermal fatigue problem is of major importance to pulsing operation effects on erosion. Thermal fatigue damage occurs each time plastic strains are induced. In Reference 21, Burge provides a general engineering estimate approach to estimating thermal fatigue effects. The induced plastic strain for a given heating cycle is shown to be given by

$$\Delta \epsilon_p = 2 \epsilon_{pa} \quad (3-56)$$

where ϵ_{pa} is

$$\epsilon_{pa} = \frac{\alpha}{(1 - \nu)} \left(\frac{\partial T}{\partial r} dr \right) + \alpha \left(\frac{2T_{hg} - \frac{\partial T}{\partial r} dr}{2} - T_c \right) - \frac{\sigma_y}{E} \quad (3-57)$$

The cyclic life capability for low cycle fatigue is given by the Coffin relationship

$$N_f^k \Delta \epsilon_p = \frac{\epsilon_f}{\frac{1}{2^k + 1}} \quad (3-58)$$

Here the fracture ductility, ϵ_f , is found to be of primary importance to a materials' capability to absorb plastic strain. From these results, it is observed that reduced thermal gradients, high yields, and high fracture ductilities are conducive to long life. Thermal plastic damage here ultimately reflects itself in spalling or checking of the surface. It is of interest to note that the coppers and CARB-I-TEX materials are predicted to have superior resistance to thermal checking. Beryllium material, interestingly enough, is predicted to thermally check in a relatively few number of cycles.

The graphites can be improved in cyclic life capability by placing them in prestressed conditions; however, the maintenance of the prestress in actual thruster configurations for numerous duty cycles is at the present time difficult. Once the prestress is lost, the graphite can be expected to fail rapidly from a stress standpoint.

3.3.5 Summary of Material Property Considerations

Table 3-17 gives a summary of properties at their mean expected operating temperatures, along with a fatigue rating. For the conductively cooled thruster, only the coppers and the graphitic materials are considered to be satisfactory.

3.4 THRUSTER VALVE SELECTION EVALUATION

As a part of the overall program activities, an evaluation was conducted of candidate bipropellant valves suitable for operation with the FLOX/LPG thruster. This valve evaluation was conducted to provide the basis for the selection of a valve for subsequent integration into the later experimental phases of the program effort. The program guidelines limited the valve selection to an existing or slightly modified propellant valve. The final basis for the valve selection included: (1) availability, (2) design, (3) reliability, and (4) cost.

Table 3-17. Summary of Thruster Material Considerations

	k	ρ	ρC_p	$\frac{\sqrt{\alpha}}{k}$	α	W/W_{cu}	$N_f/N_f (B_e C_u)$
Graphite	22	106.6	45.8	0.0314	.480	1.178	0.018
C-I-T	40	93.5	17.5	0.378	2.28	1.878	
Copper (fine grained)	190	537	58.0	0.00953	3.28	1.000 (0.428)	1.000 (0.428)
Be-Copper	165	533	59.8	0.0107	2.76	1.145	1.000
Beryllium	42	110.6	79.8	0.0173	.527	.938	0.184
Nickel 200	34.5	555	57.2	0.0224	.603	5.73	0.278

$$\frac{T_s - T_o}{T_{ad} - T_o} = \frac{h/k \sqrt{3/2\alpha t}}{1 + h/k \sqrt{3/2\alpha t}} \quad \delta(t) = \sqrt{6\alpha t}$$

The valve design consideration is of the most importance and a thorough valve evaluation must include the following areas:

- Heat Soakback and Dribble Volume Considerations. Fluorine exists in liquid form at atmospheric pressure only in the narrow temperature range of -306° to -363°F . From the standpoint of propellant isolation, the retention of constant inlet conditions and minimizing of heat soakback effects should be given serious consideration. Thus, tradeoffs can be made between proximity of the valving and dribble volume downstream of the valves as determined by overall engine start transient response requirements.
- Materials Compatibility. Fluorine is a powerful, reactive oxidizing agent. Its low liquid temperature and tendency to build up protective fluoride films tend to offset its extreme chemical reactivity. Many metals, therefore, are considered to be compatible for use in liquid fluorine systems. However, low temperature mechanical properties limit the use of a number of materials, e.g., martensitic stainless steels become brittle at cryogenic temperatures. Relative coefficients of thermal contraction are also important material property considerations.
- Valve Seal Material Selection. This presents a critical problem area to fluorine service. Teflon, which is used extensively in storable propellant systems, has been found to be unsatisfactory mainly because of polymer breakdown and formation of unsaturated, low molecular weight fluor-carbons which do not adhere to the surface. Metallic seals afford the highest probability of success. Copper, for instance, has been found to be a satisfactory seat material in a variety of fluorine applications. In most cases, the development of hard metallic seats entails considerable experimental work in the proper balance between the amount of strain loading required for sealing versus the yield point of the seat material. Dissimilar metals are generally used to prevent binding or galling during operation. Effective sealing for fluorine is especially critical since the propellant represents potential toxic, fire, and explosion hazards. Under these conditions, the prospects of redundant valve seats may be considered for future work. The ability of other parts, such as bellows, to withstand prolonged duty cycles is also cited as a major problem area.
- Duty Cycle Requirements. Under the metal-to-metal sealing concept generally employed in cryogenic valve applications, duty cycle requirements under both wet and dry conditions become critical. It is conceivable that the cumulative cycles of operation conducted under checkout conditions would adversely affect the long-term sealing capability of the valve. Realistic life cycle requirements need to be

established as a reliability factor with respect to the mission requirements of an intended application.

Efforts during the initial industry survey were concentrated on the three generally recognized manufacturers of bipropellant valves; Moog, Parker Aircraft, and HR&M. The final evaluation was primarily conducted with the Parker Aircraft and HR&M valves.

Parker Aircraft had produced three bipropellant valves and supplied them to NASA-MSC (Houston) for evaluation with the conventional earth storable propellants. During the period of investigation, extensive communications were conducted with Parker to determine the rework/modification required on one of these valves to permit satisfactory operations with the cryogenic FLOX/LPG propellants. Since these valves employ a soft seal arrangement, Parker indicated that extensive modifications would be required with the resultant cost and delivery being incompatible with the basic program requirements.

The HR&M valve design had a hard seal arrangement, but required rework to meet the thruster flow rate and cryogenic operating temperature requirements. The cost and schedule necessary for these modifications was compatible with the overall program objectives. This modified HR&M bipropellant valve was thus procured and a test evaluation conducted as reported in Section 5.4.

4. HARDWARE DESCRIPTION

4.1 HARDWARE DESIGN SUMMARY

The nominal engine design conditions for the test hardware were 100 lbf (vacuum) thrust with a specified nozzle expansion ratio of 60 and a chamber pressure of 100 psia. The engine hardware was designed for operation with the 80% fluorine/20% oxygen oxidizer and the fuel blend consisting of 55% methane and 45% ethane; with the propellants delivered to the injector at nominal liquid nitrogen temperatures.

The injectors utilized during the program were based on the TRW single element coaxial design approach. Inherent with this injector design approach is a high degree of flexibility, thus permitting a large number of systematic variations in injection parameters within the same basic hardware.

4.1.1 Injector Design

During the initial design efforts on the program, the importance of overall injector hardware flexibility was emphasized based on the program performance goal of 92% of equilibrium C* and the desired chamber wall environment control. Figure 4-1 shows the basic assembly drawing for the subject 100 lbf FLOX/LPG injector design. The overall view of the chamber side of the assembled continuous sheet coaxial injector is shown in Figure 4-2. The disassembled view of this injector showing the four basic components (plus adjustment shims) is seen in Figure 4-3. The four basic injector components are the body, sleeve, pintle, and adapter plate. All injector components exposed to the combustion gas environment (i.e., the body, pintle, and sleeve) were fabricated from nickel 200; other components were fabricated from stainless steel.

Assembly of the injector is accomplished by inserting the pintle into the injector sleeve the required amount for obtaining the desired injection gap setting. The pintle is held in position by the mechanical interference between the pintle lands and the sleeve inner diameter. The sleeve/pintle assembly is then inserted into the injector body, employing the proper set of shims to obtain the desired outer propellant injection gap setting. The adapter plate supports the sleeve/pintle assembly (with appropriate seals) in the injector body. Pressure tap parts are provided on the injector body for measuring head end chamber pressure.

The four basic coaxial injector orifice configurations investigated during the initial sea-level testing are shown in Figure 4-4. In all cases, the outer propellant was injected axially as a continuous annular sheet. Variations were made in the sleeve tip OD to provide different injector gaps (sheet thickness) for the same fluid injection velocities. The centrally injected propellant orifice configurations included continuous sheets, swirl nozzles and slotted ring elements. Figure 4-5 shows the injector face view with the final slotted ring element installed. The slotted ring is removable in this design and is held to the sleeve tip by the pintle which has been modified internally to provide a more positive pintle support.

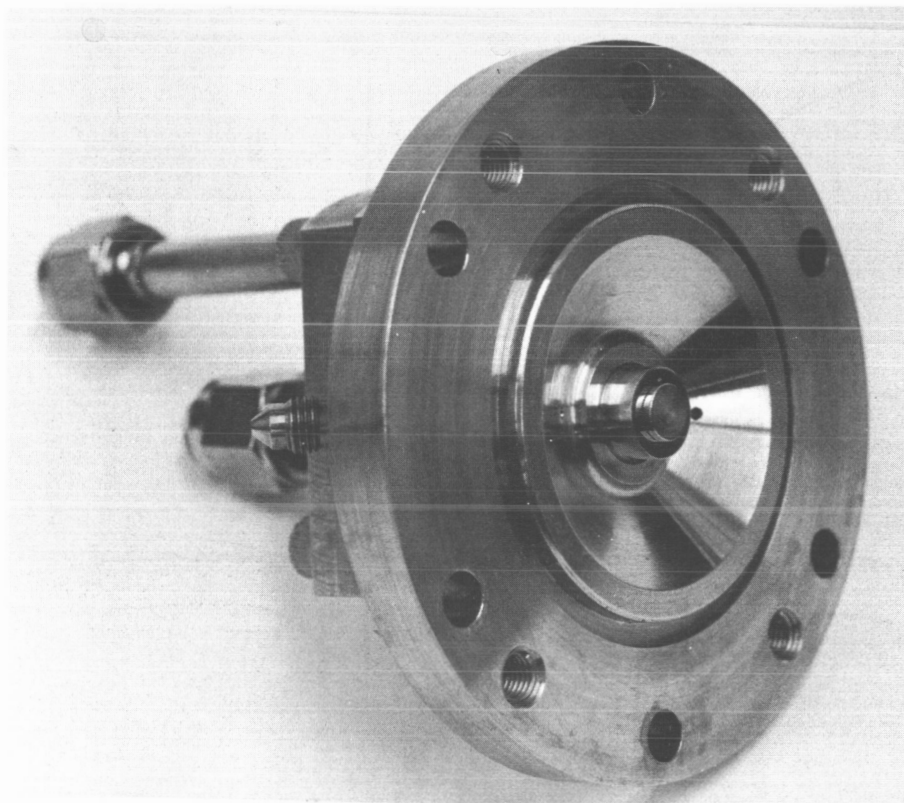


Figure 4-2. Assembled 100 lbf FLOX/LPG Injector

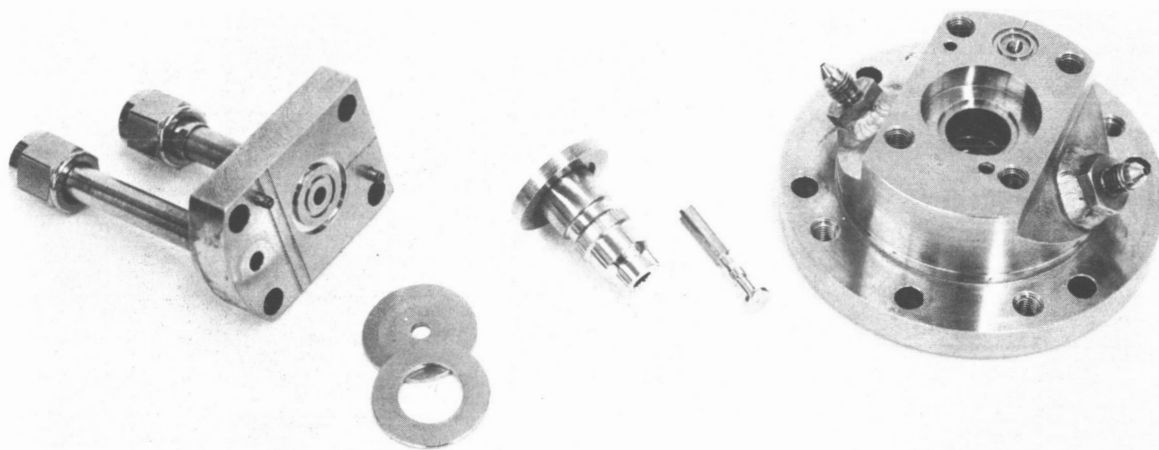


Figure 4-3. Disassembled View of 100 lbf FLOX/LPG Injector

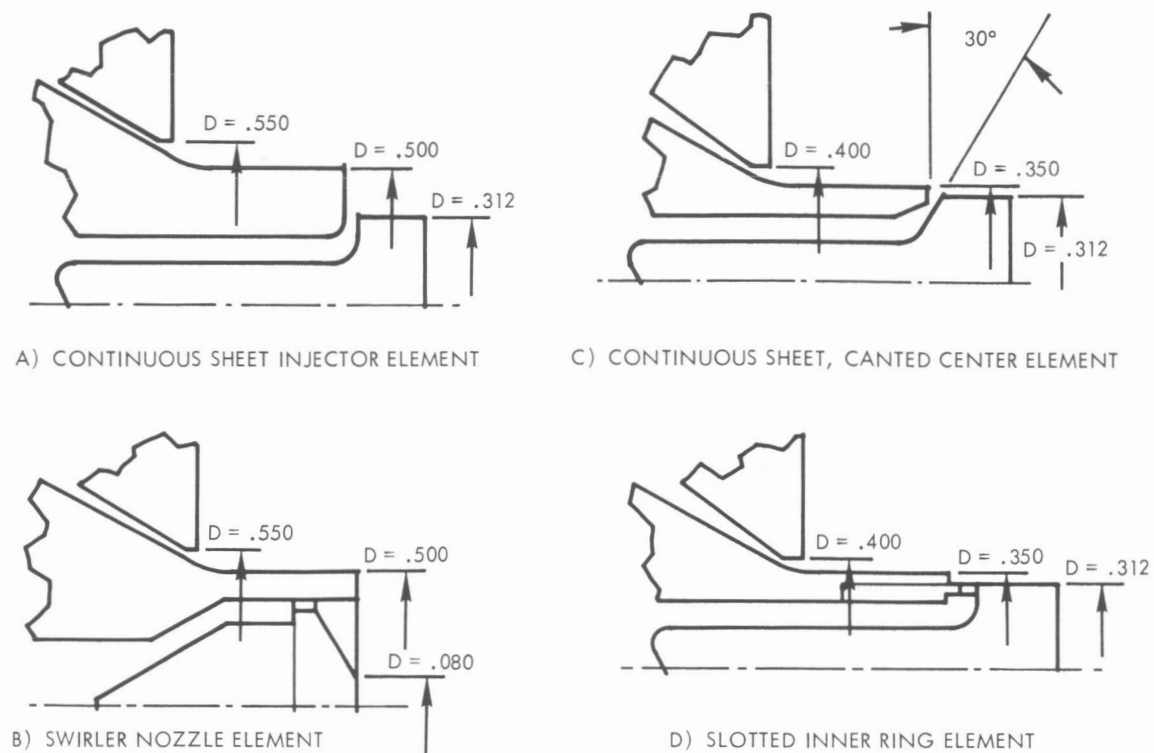


Figure 4-4. Injector Orifice Configurations

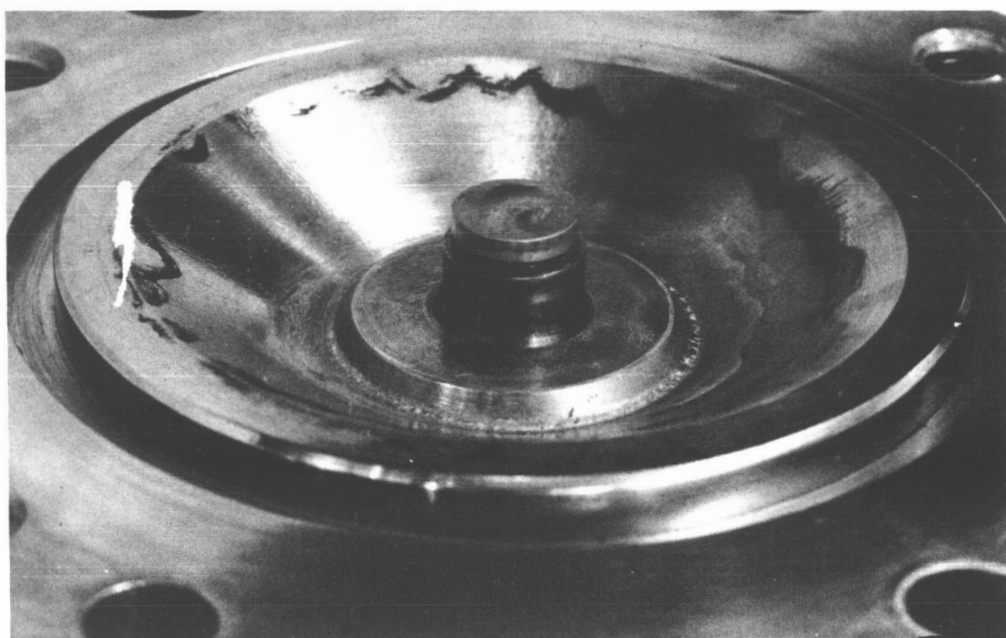


Figure 4-5. Close-up View of Final Orifice Configuration

Modifications to the basic injector design to incorporate fuel film coolant injection are shown in Figure 4-6. Also shown in this drawing is the modified pintle support design. The final selected slotted ring design consisted of 30 slots, 0.015 inch long by 0.014 inch wide. This injector configuration met the defined program performance goals and was employed for all subsequent film cooled designs. Figure 4-7 shows the integral injector/film-coolant hardware prior to assembly. The film-coolant injection ring shown has 20 orifices of 0.020-inch diameter angled 15 degrees with respect to the chamber axis. During the experimental test efforts, the desired fuel film-coolant flow rate was plumbed externally to the film-coolant manifold. This manifold could easily be fed internally within the injector body as shown in Figure 4-6.

Figures 4-8 and 4-9 show the separate film-coolant manifold design also utilized. This design had the same number and size film-coolant injection orifices, but injected the fuel parallel to the chamber wall. The separate film-coolant design was used with the grooved chamber designs (as shown in Figure 4-8), which were shortened axially to maintain the desired injector/throat dimensions.

4.1.1.1 Injection/Combustion Design Considerations

The TRW coaxial injector configuration is basically different from the various flat faced, multiorifice injector designs. The central propellant injection of the coaxial design results in propellant distribution (mass and mixture ratio) being obtained by methods widely different than the more commonly employed multiorifice injector designs. Since both performance and chamber wall environments are very sensitive to propellant distribution, particular attention must be paid to factors within the coaxial injector design which affect propellant mixing/distribution. Prime consideration must be given, with the highly reactive propellants, on the initial stream impingement effects which inhibit complete liquid phase mixing. Previous studies (References 22 and 23) indicate that performance can be maximized when the liquid phase mixing occurs at essentially the overall design mixture ratio, resulting in individual droplets being of mixed constituents at the desired mixture ratio.

Once proper attention has been given to the design factors which affect propellant distribution, the additional combustion processes (i.e., atomization, vaporization, and chemical reactions) with the coaxial design are very similar to other multiorifice injectors. Factors such as stream momentum ratios and basic jet characteristics must be optimized.

The injector design factor involves stream momentum ratio as a measure of the inherent propellant (hydraulic) energy available for mixing and atomization. This ratio is

$$\frac{F_o}{F_f} = \frac{\dot{\omega}_o V_o}{\dot{\omega}_f V_f} \quad (4-1)$$

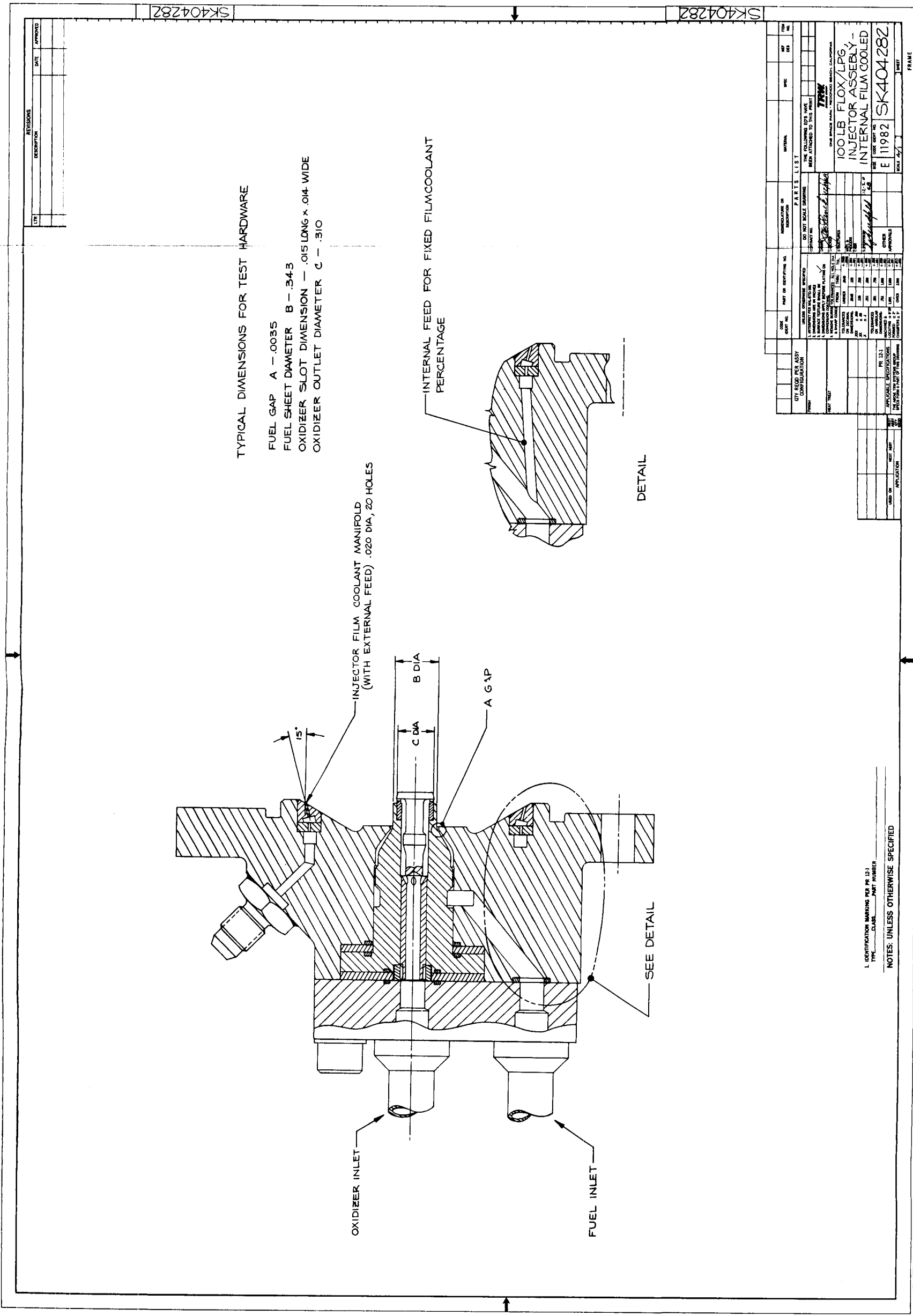


Figure 4-6. 100 lbf FLOX/LPC Injector Assembly with Integrated Film Coolant

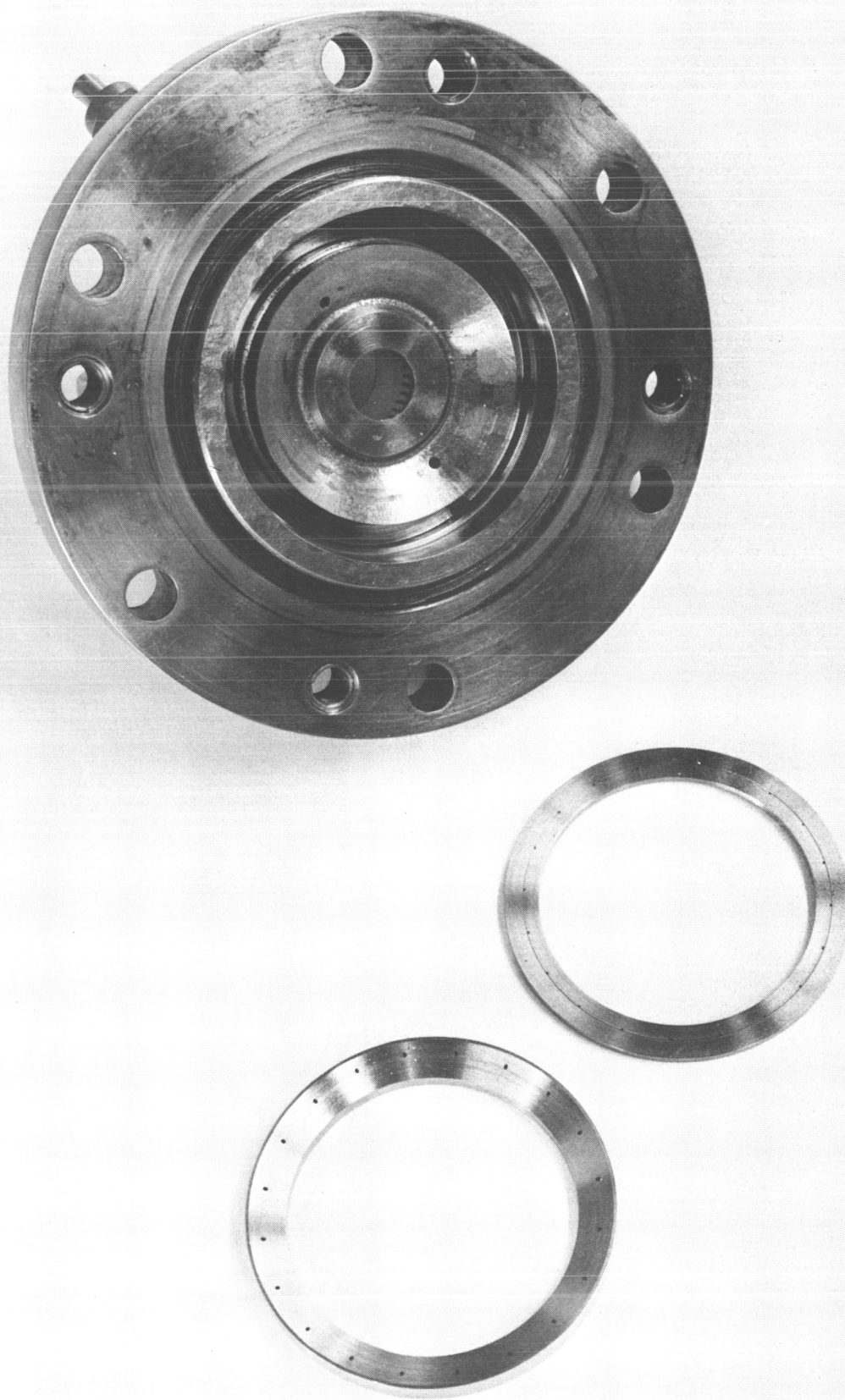
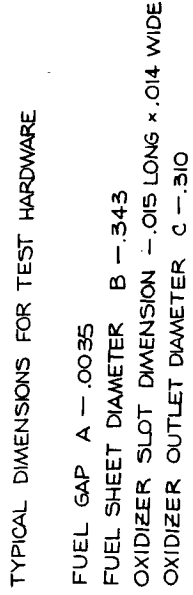


Figure 4-7. Film Coolant Injector Body Prior to Final Assembly



1. IDENTIFICATION MARKING PER PR 12-1
TYPE _____ CLASS _____ PART NUMBER _____

NOTES: UNLESS OTHERWISE SPECIFIED

107

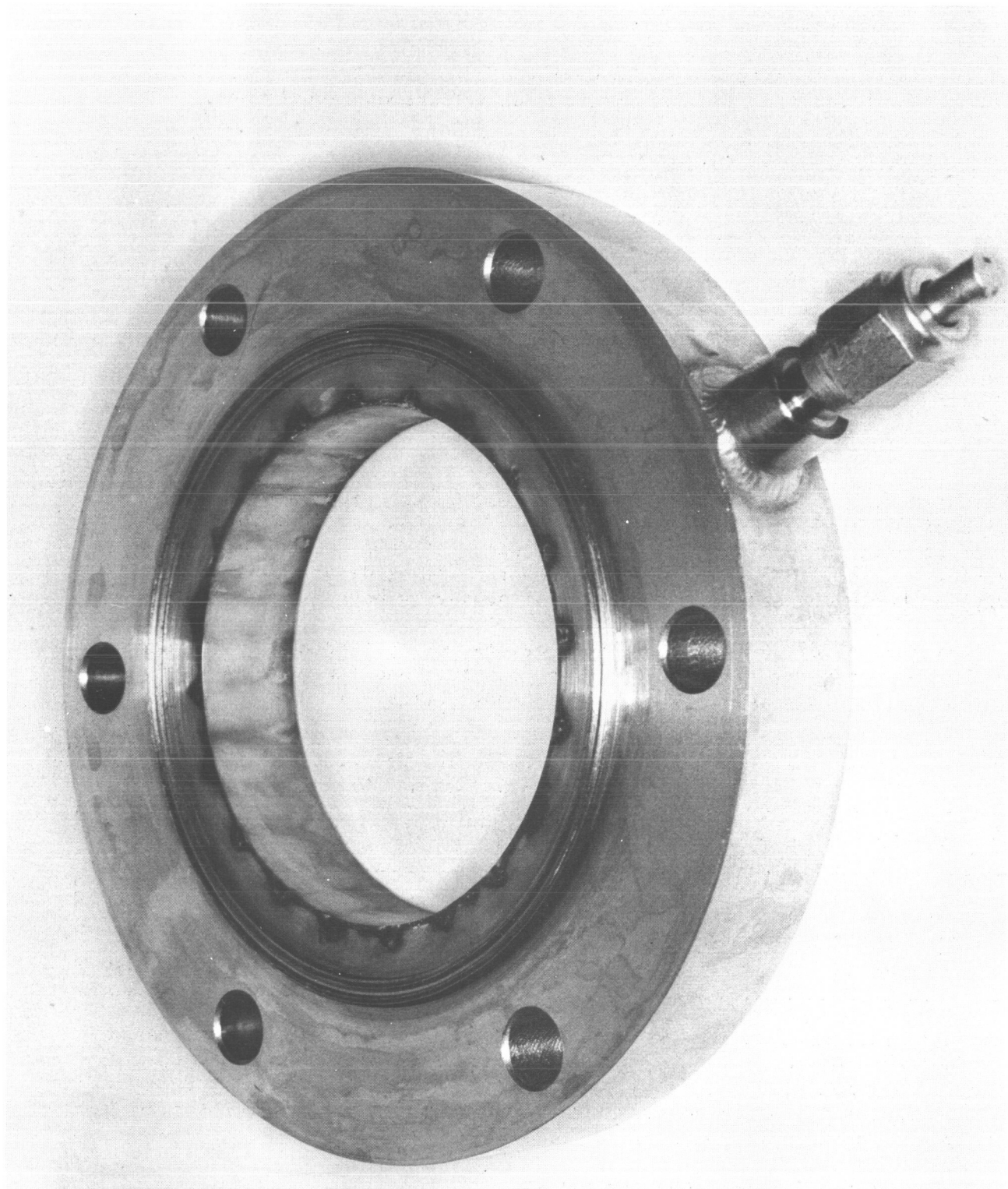


Figure 4-9. Overall View of External Film Coolant Manifold

One criteria for obtaining optimum mixing states that the ratio of dynamic interaction of oxidizer and fuel streams at impingement equals one.

$$\frac{F_o}{F_f} = \frac{\rho_o V_o^2 A_o}{\rho_f V_f^2 A_f} = 1 \quad (4-2)$$

On the basis of this design approach, it was established that the optimum velocity ratio for these propellants at the peak equilibrium mixture ratio is

$$\frac{V_o}{V_f} = \frac{1}{\dot{\omega}_o/\dot{\omega}_f} = 0.192 \quad (4-3)$$

Contrasted with the earth storable type propellants which have velocity ratios of 0.6 to 0.7, it is seen that the gross fuel momentum interchange (with the oxidizer) is considerably less with the FLOX/LPG propellant. Therefore, attention must be given to control the oxidizer dispersion early in the injection/mixing process for achieving high performance.

Using Equation (4-2) design calculations were performed for the subject 100 lbf injection assuming two different oxidizer and fuel stream energy levels. Table 4-1 presents a summary of these calculations.

Table 4-1. Summary of Injector Design Calculations
(FLOX/55% Methane-45% Ethane, O/F = 5.2)

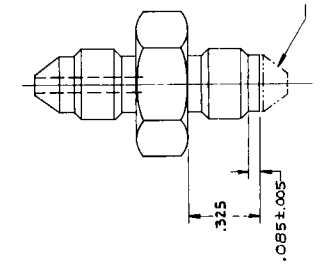
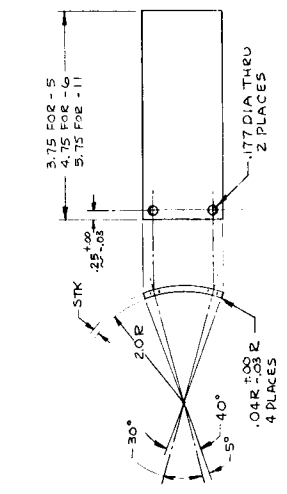
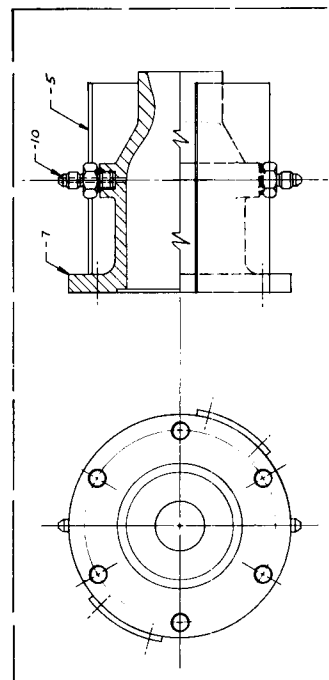
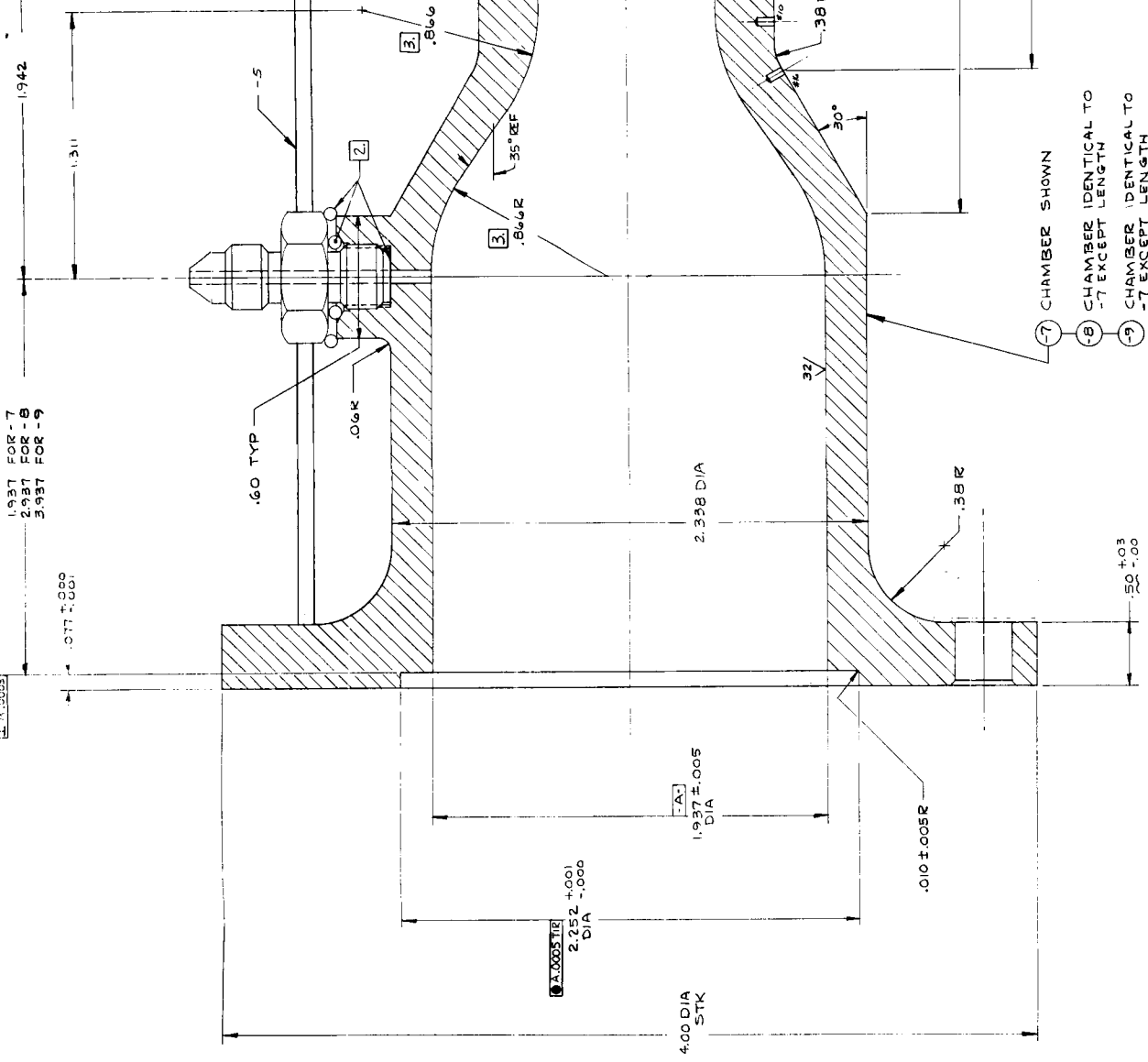
V_{ox} (ft/sec)	V_f (ft/sec)	ΔP_{ox} (psi)	ΔP_f (psi)	A_{ox} (in ²)	A_f (in ²)
7.5	4.0	0.6	5.4	.0585	.00558
40	210	16.0	159.0	.00905	.00089

These calculations indicate very small fuel injection areas and for reasonable fuel stream energy levels, and low oxidizer injection P's. These criteria were modified, based on previous 100 lbf coaxial injector designs and practical fabrication considerations, to form the basis for the previously discussed injection orifice configurations.

4.1.2 Experimental Thrust Chamber Designs

The thrust chamber hardware designs were employed during the experimental testing tasks for evaluating both thruster performance and resultant chamber heat flux characteristics. Basically, the chamber hardware was a thin-walled copper design with thermocouples imbedded axially and circumferentially to obtain the required wall heat flux data. Two basic chamber configurations were utilized; the straight wall and tapered wall geometrics shown in Figures 4-10 and 4-11, respectively. As can be seen in these

THE INFORMATION AND TECHNICAL DATA DISCLOSED BY THIS DOCUMENT MAY BE USED WITHOUT LIMITATION BY ANY OTHER PERSON OR ENTITY FOR ANY PURPOSE, INCLUDING BUT NOT LIMITED TO, RESEARCH, DEVELOPMENT, PRODUCTION, AND OPERATION, AND MAY BE DISCLOSED TO ANY OTHER PERSON OR ENTITY WITHOUT THE WRITTEN CONSENT OF THE DISCLOSING PARTY. THIS DOCUMENT IS THE PROPERTY OF THE DISCLOSING PARTY AND IS NOT TO BE REPRODUCED OR TRANSMITTED IN ANY FORM OR BY ANY MEANS, ELECTRONIC OR MECHANICAL, INCLUDING PHOTOCOPYING, RECORDING, OR BY ANY INFORMATION STORAGE AND RETRIEVAL SYSTEM, WITHOUT THE WRITTEN CONSENT OF THE DISCLOSING PARTY.



5G

-5 PLATE SHOWN

-6 PLATE IDENTICAL TO -5 EXCEPT LENGTH

-11 PLATE IDENTICAL TO -5 EXCEPT LENGTH

SCALE 1/1

-1 ASSY SHOWN

SCALE 1/1

folded

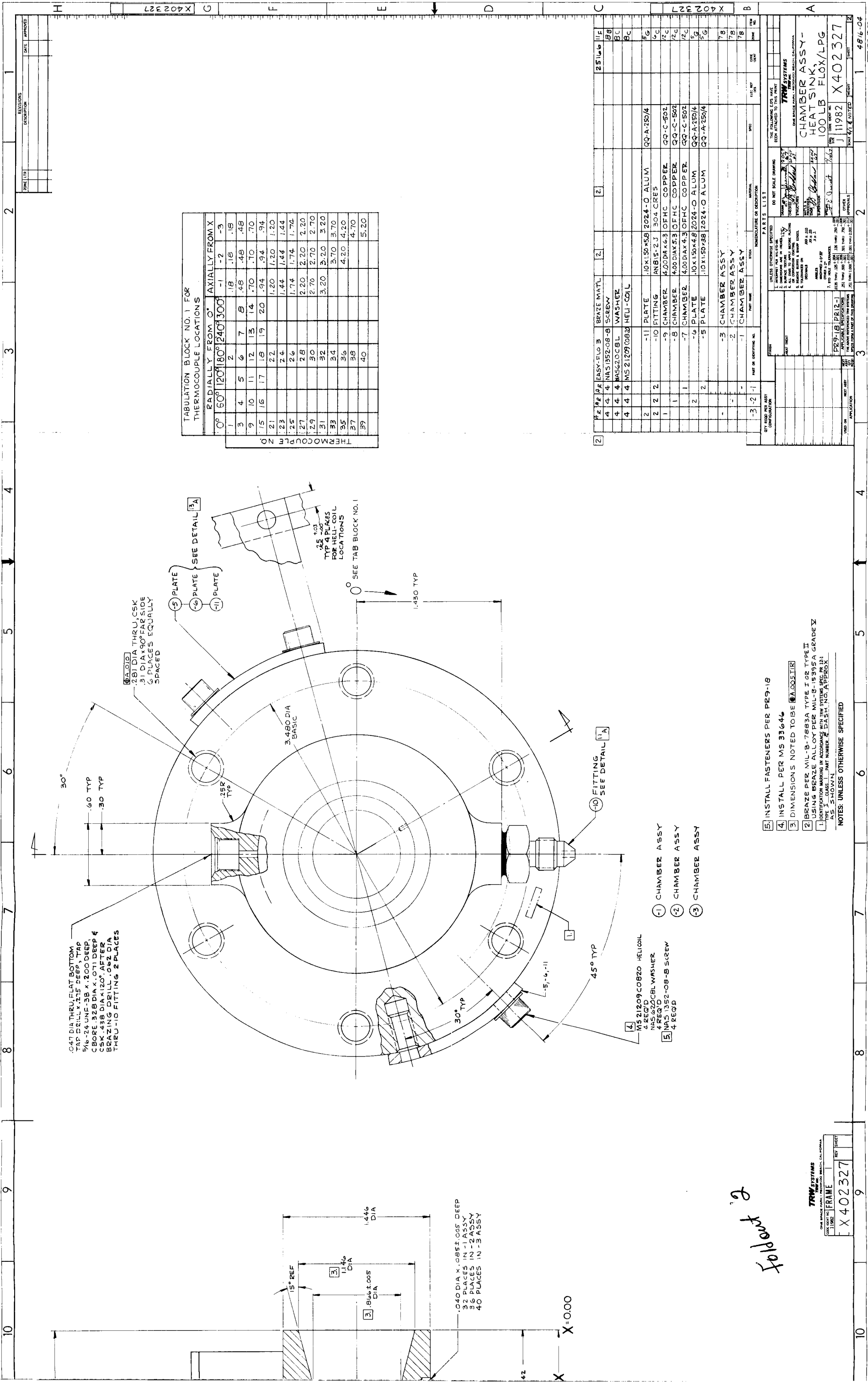
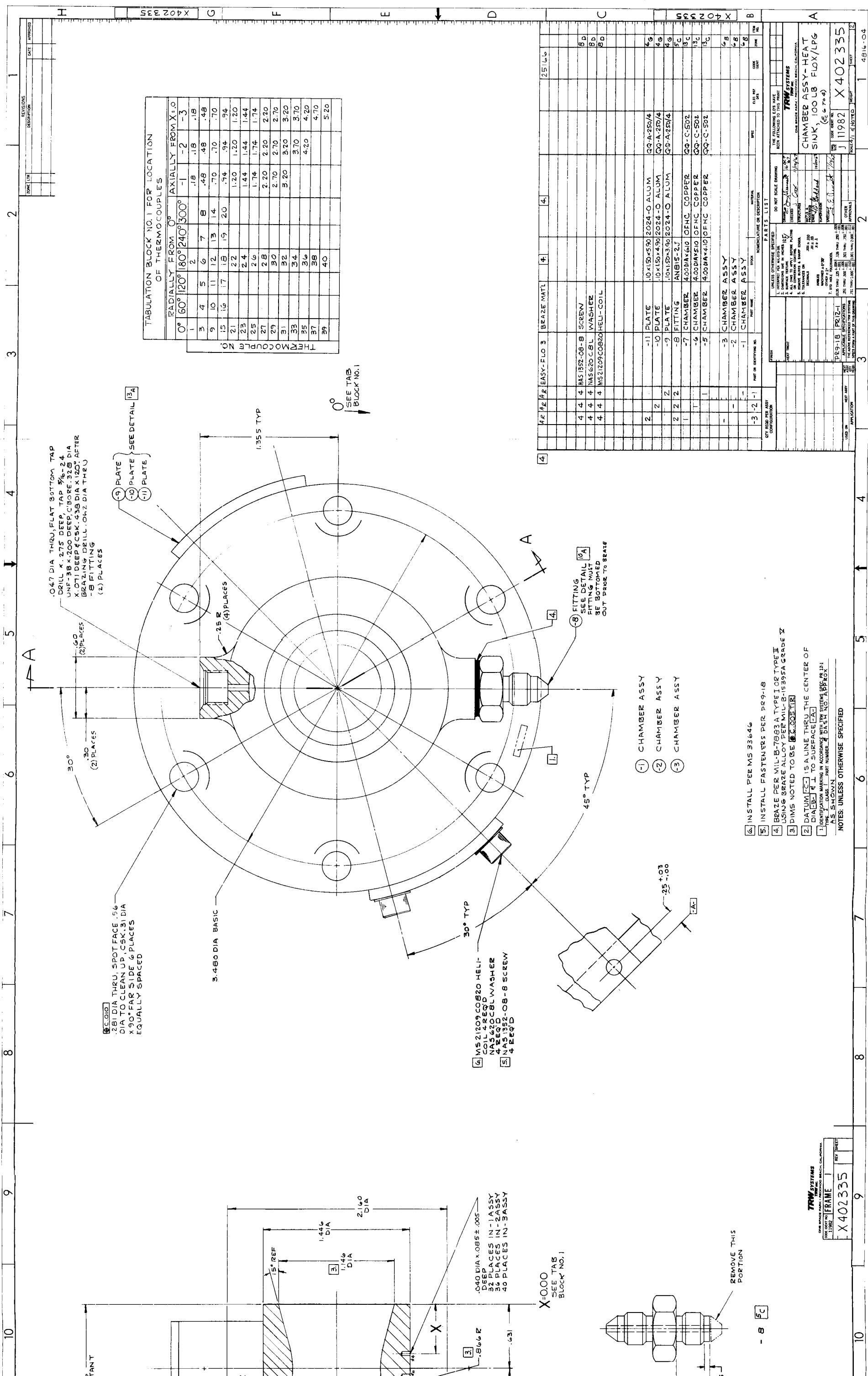


Figure 4-10. Thin Wall Copper Heat Sink Chamber Assembly (Cylindrical)

foldout 1



113 Figure 4-11. Thin Wall Copper Heat Sink Chamber Assembly (Tapered)

figures, and in the overall chamber view shown in Figure 4-12, pressure tap ports were provided for obtaining the desired chamber pressure measurements. The chambers were attached to the injectors through a bolt-on/flange design employing a serrated seal configuration. Three basic chamber lengths were designed and fabricated; providing for a chamber L^* variation of 9, 15, and 22 inches. Grooved inner-wall versions of the basic tapered wall design were also employed in an effort to increase the overall film coolant efficiency. Figure 4-13 shows one of these chambers and also illustrates the method of thermocouple installation. A thicker walled copper chamber (similar to that shown in Figure 4-13) was used during the final experimental testing as discussed in Section 5.

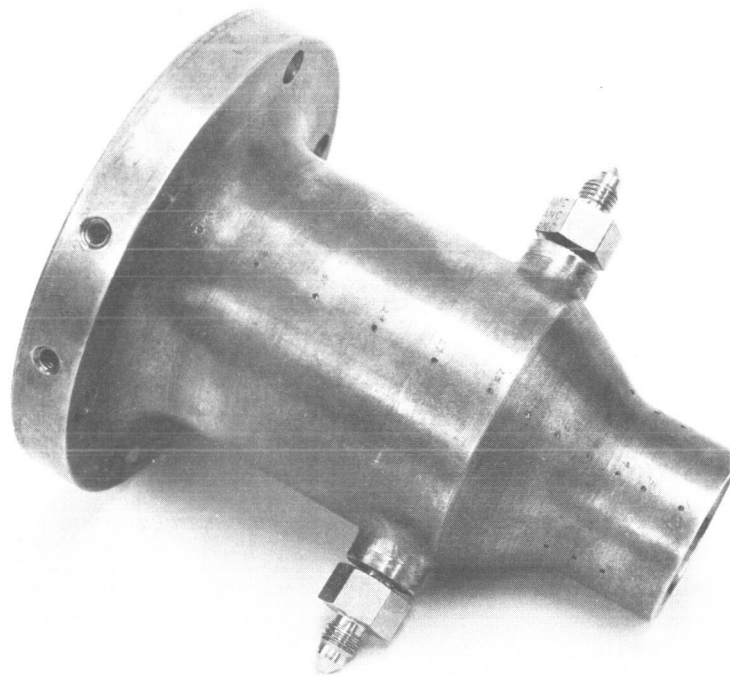


Figure 4-12. Overall View of Typical Heat Sink Chamber

4.1.3 Altitude Thruster Designs

The design of the altitude thruster was accomplished based on the thermal analysis discussed in Section 3.2 plus the program experimental results and the resultant design reevaluation covered in Section 6. The design criteria for the subject thruster were to minimize the nozzle region heat load and to control (meter) the conduction heat transfer to the chamber barrel region where it is absorbed by the film coolant.

Figures 4-14 and 4-15 show the two design versions of the subject altitude thruster. Both designs employ the OFHC copper conduction liner which extends to a nozzle expansion ratio (A_e/A^*) of 6:1 with stainless steel enclosure cans and Haynes 25 nozzle extensions. The attachment point

for the bolt-on nozzle extension was selected based on experimental heat flux data and a maximum design operating temperature for the Haynes 25 of 2000°F. The stainless steel container is brazed to the copper liner (in both designs) for sealing purposes and is provided with a bolt/seal flange for injector attachment.

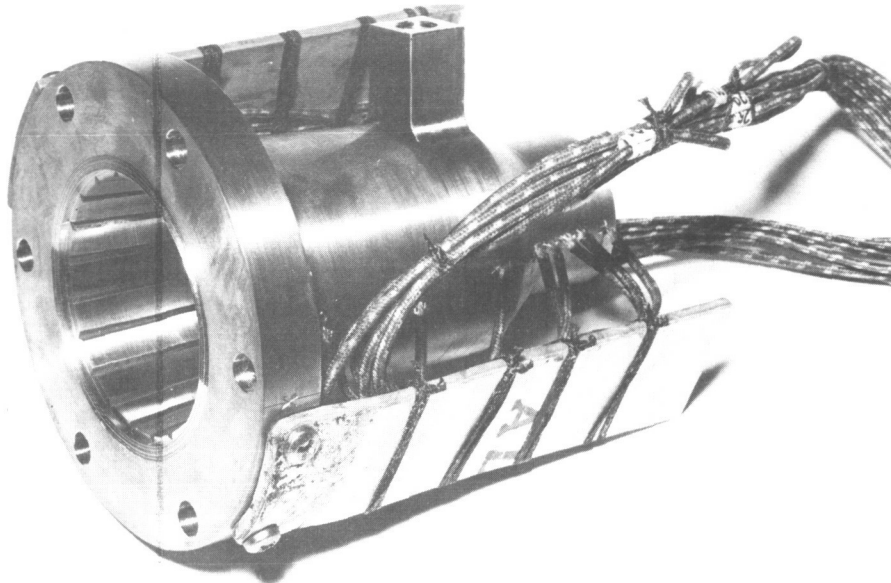


Figure 4-13. Overall View of Heat Sink Chamber Showing Internal Grooving and Thermocouple Installation

The primary difference between the two thruster designs shown is the method of controlling axial heat flow from the throat region to the chamber film-cooled cylindrical region. The thruster design, shown in Figure 4-14, controls the axial heat flow by the copper wall thickness in the convergent nozzle region. The thicker wall design (Figure 4-15) accomplishes this with a thermal isolation slot, which meters the heat load into the barrel region through the gap between the slot and outer chamber wall. This design results in more uniform nozzle wall temperatures (less axial temperature drop), thereby decreasing the overall nozzle heat transfer. The metering slot, as shown, is located to provide for a more even spreading of the resultant heat flux over the barrel portion of the chamber. The metering slot is simply a region of low conductivity. Analysis indicates that the resistance of the slot should be three or four times greater than that of the conduction metering section. This means that the gap can be either a void space of small thickness or a gap filled with a low conductivity material (such as RTV) with sufficient thickness to provide the required resistance.

The altitude thruster designs shown have bolt-on/flanged injector and nozzle extension attachments. These designs, however, can easily be modified to permit for welded attachment of both the nozzle extension and injector. The utilization of a low thermal conductivity shell over the copper chamber liner permits welded injector attachment and controlled heat soakback to the injector components.

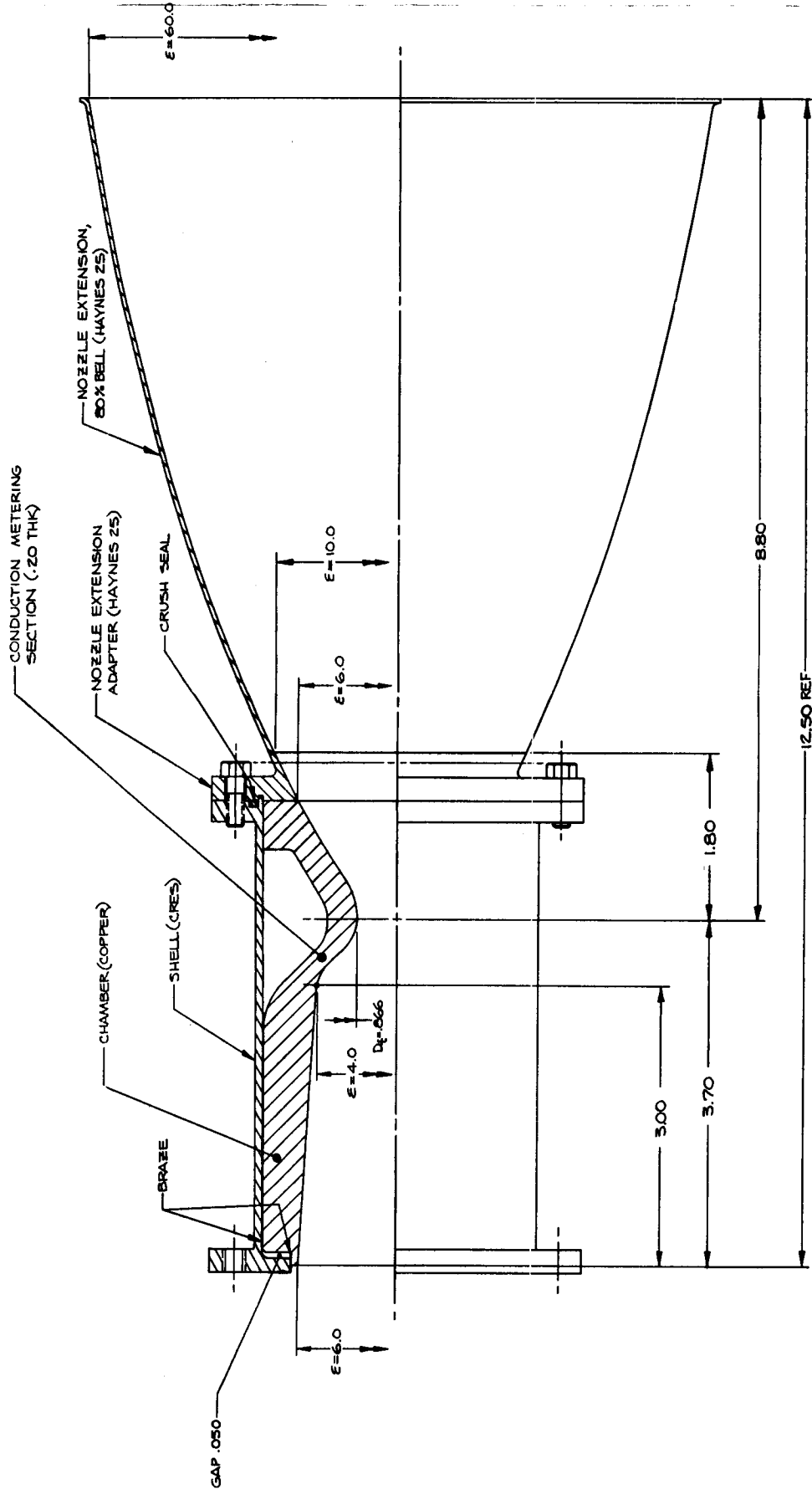
ON DRAWING

SHEET

REVISIONS		DATE	APPROVED
1	DESCRIPTION		
2			
3			

SK404298

SK404298

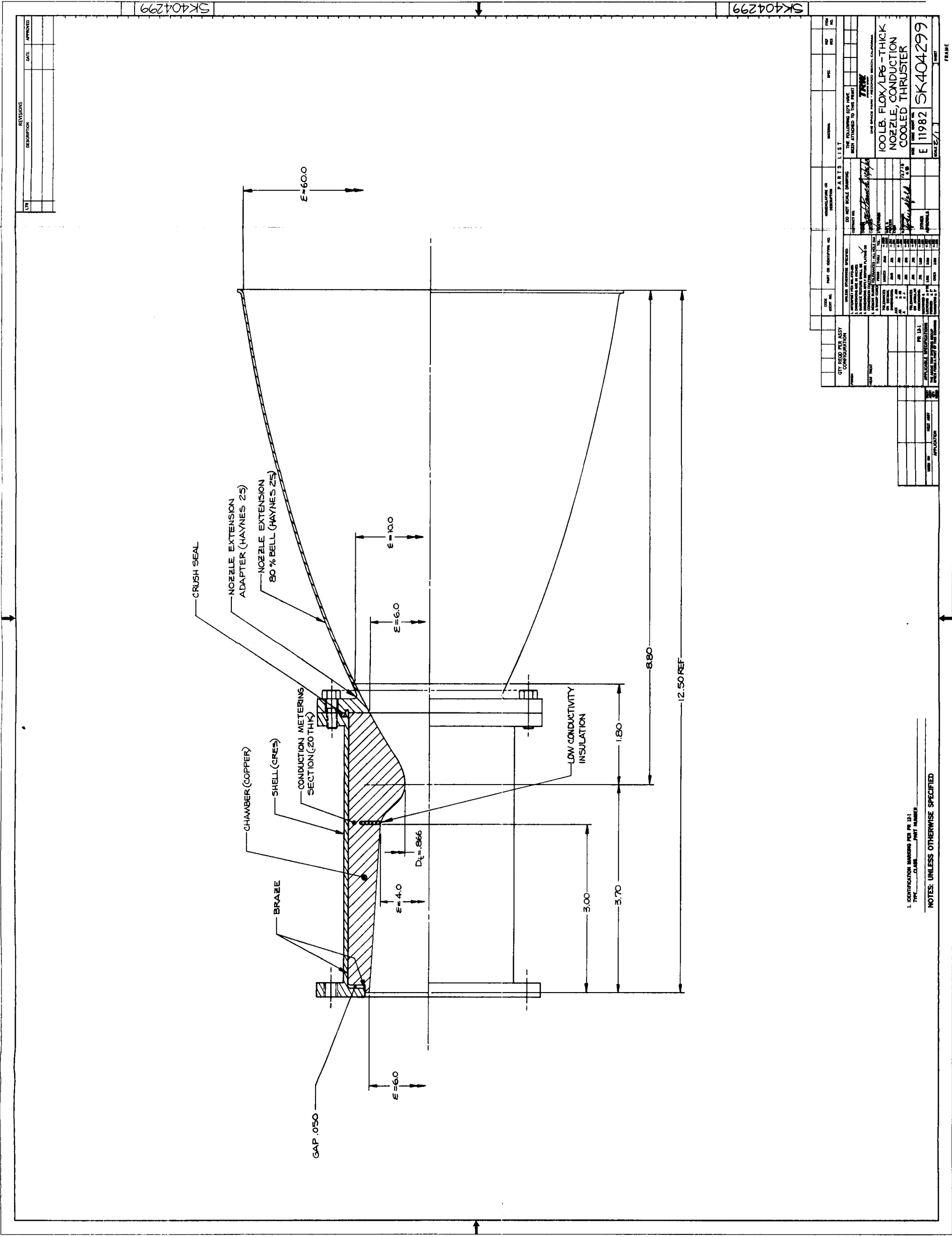


1. IDENTIFICATION MARKING PER FIG. 12-1
TYPE _____ PART NUMBER _____

NOTES: UNLESS OTHERWISE SPECIFIED

QTY. REQD PER ASSY CONFIGURATION	DATE	BY	CHKD	APP'D
1	11/19/82	SK404298		
2				
3				
4				
5				
6				
7				
8				
9				
10				
11				
12				
13				
14				
15				
16				
17				
18				
19				
20				
21				
22				
23				
24				
25				
26				
27				
28				
29				
30				
31				
32				
33				
34				
35				
36				
37				
38				
39				
40				
41				
42				
43				
44				
45				
46				
47				
48				
49				
50				
51				
52				
53				
54				
55				
56				
57				
58				
59				
60				
61				
62				
63				
64				
65				
66				
67				
68				
69				
70				
71				
72				
73				
74				
75				
76				
77				
78				
79				
80				
81				
82				
83				
84				
85				
86				
87				
88				
89				
90				
91				
92				
93				
94				
95				
96				
97				
98				
99				
100				

Figure 4-14. 100 lb FLOX/LPG Altitude Thruster Design (Thin Wall)



119 Figure 4-15. 100 lbf FLOX/LPG Altitude Thruster Design (Thick Wall)

5. EXPERIMENTAL RESULTS

Upon completion of the analytical effort, a basic TRW coaxial injector and sea-level operating thrust chamber were fabricated to provide test hardware for obtaining both combustion performance and heat transfer data with the selected nominally 80% FLOX/55% methane-45% ethane fuel blend. As described earlier, the injector was designed to provide capability for ready modification, and the chamber test hardware approximated the expected desired thin wall configuration.

The initial experimental efforts were directed toward the development of an injector capable of at least 92% of the theoretical equilibrium C^* . This effort consisted of basic cold flow studies and hot firing runs. Following this, the final design high performance injector was tested in detail to determine its resultant chamber heat transfer characteristics. After this determination, film coolant injection designs were fabricated and tested with various percentages of film coolant.

5.1 INJECTOR DEVELOPMENT COLD FLOW STUDIES

The cold flow studies encompassed two parts. The basic hydraulic operating characteristics were determined from pressure drop, mass flow, and visual observations. In the second part, cold flow characterization for the purpose of correlating with hot firing results was attempted. With respect to the latter effort, this effort marked an initial effort to provide such characterization. Efforts in the past with conventional injectors have been reasonably successful. The TRW coaxial injector requirements for high performance follow basically those of conventional injectors, atomization, and mass and mixture ratio distribution uniformity; however, whereas impinging jet injectors may require heavy emphasis on atomization, the TRW coaxial injector requires more emphasis on mass and mixture ratio uniformity.

To obtain these data, the coaxial injector requires a different approach to collection of cold flow simulants than is normally used for conventional injectors. Both circumferential and longitudinal distributions must be determined.

The cold flow experimental program was performed to determine flow rate-pressure drop characteristics, mass and mixture ratio distributions and overall impingement characteristics. The flow rate-pressure drop characteristics were determined using water, with the results appearing in Figure 5-1 for the oxidizer flow and in Figure 5-2 for the fuel flow. Also plotted on these figures are the equivalent curves for the actual propellants. In addition to overall pressure drop data, the various pressure drops associated with the overall drop were determined. These included: 1) oxidizer distribution, and 2) oxidizer and fuel injection gaps. This was necessary so that actual injection ΔP 's and, hence, injection velocities could be determined. Figure 5-3 shows the effect of the oxidizer distribution orifices on the overall pressure drop.

The mass and mixture ratio distributions were obtained with the use of the apparatus shown in Figure 5-4. This equipment collects the flow from

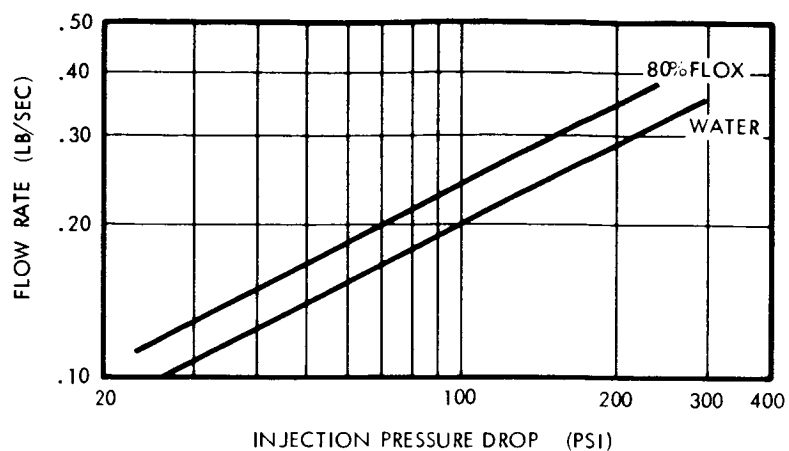


Figure 5-1. Oxidizer Orifice Hydraulic Characteristics

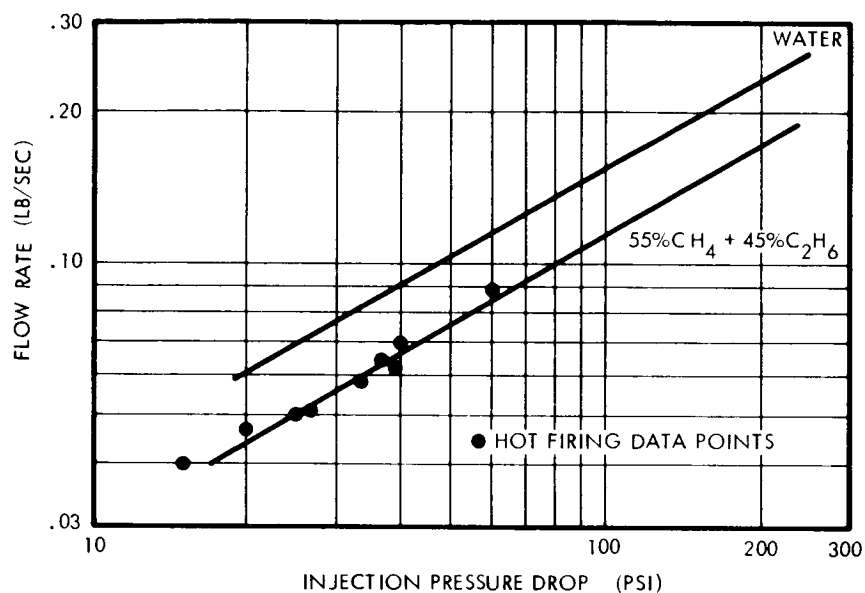


Figure 5-2. Fuel Gap Hydraulic Characteristics

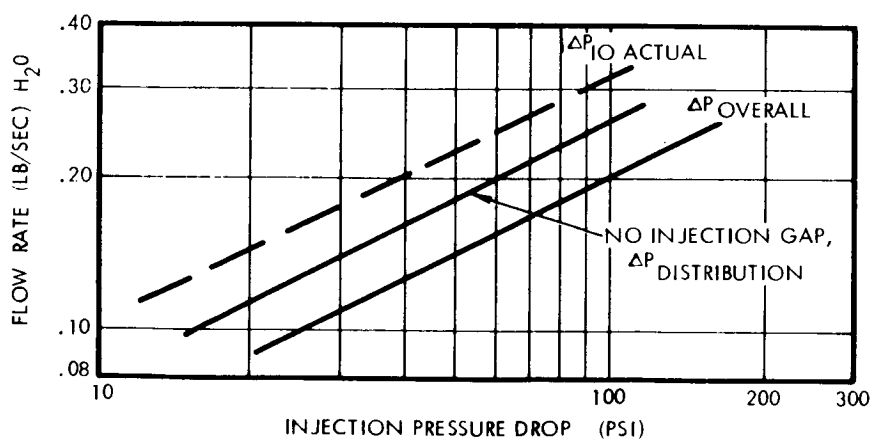
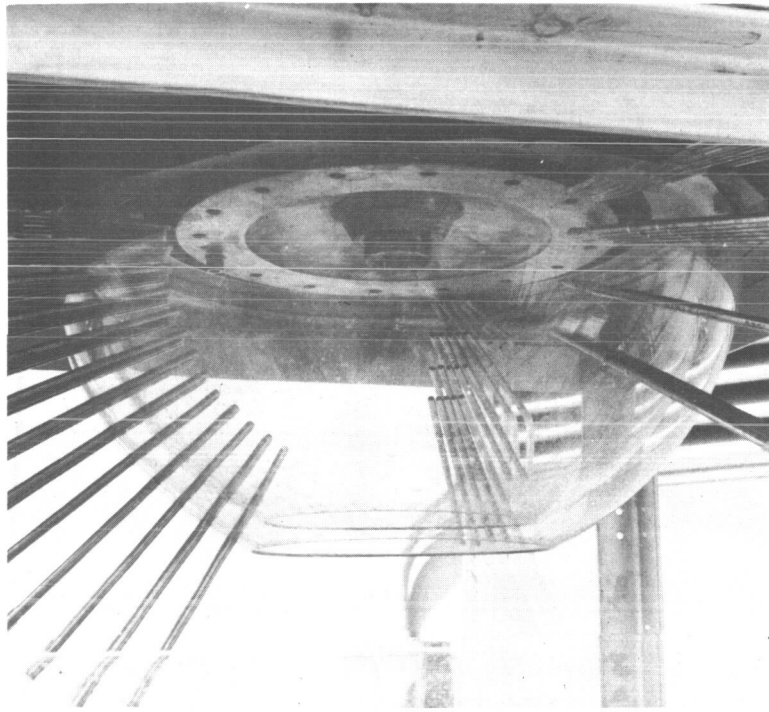
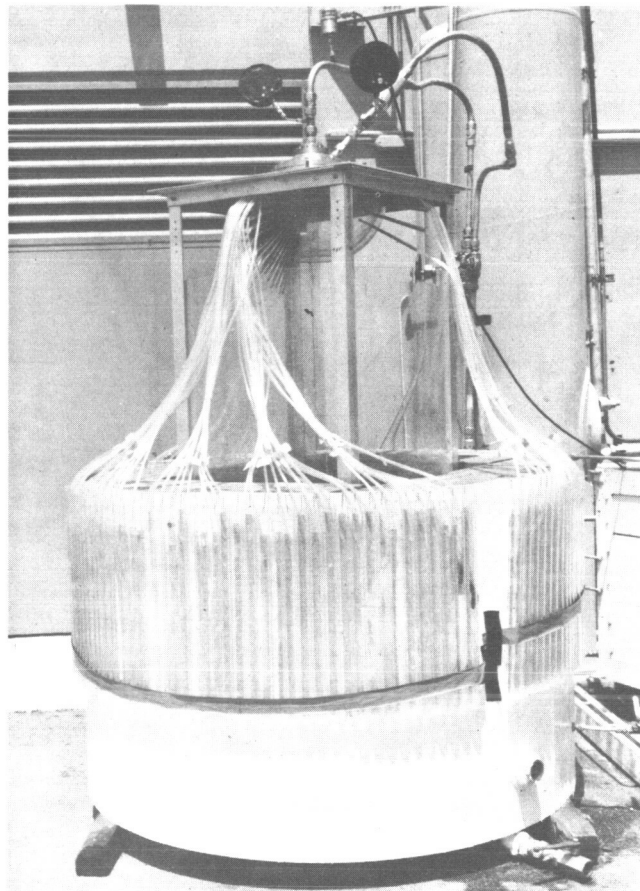


Figure 5-3. Oxidizer Passage Hydraulic Characteristics



(a)



(b)

Figure 5-4. Coaxial Injector Cold Flow Collector

the injector in tubes spaced both circumferentially and longitudinally, resulting in a determination of the circumferential uniformity of the spray and in the mass and mixture ratio gradients through the spray fan. Mixture ratio was measured by flowing kerosene through the fuel side and water through the oxidizer side.

The more conventional fluids of trichloroethylene and water were also investigated, since they are reportedly immiscible; however, the TRW coaxial flow injectors of high performance quality provided such intimate mixing and atomization that both the trichloroethylene and kerosene were virtually emulsified into the water. Since the results were the same on both simulants, kerosene was used for the bulk of the testing. The translation to actual propellants is made by

$$(MR)_{\text{propellants}} = (MR)_{\text{sim}} \left[\left(\frac{\rho_o}{\rho_f} \right)_{\text{prop}} \left(\frac{\rho_f}{\rho_o} \right)_{\text{sim}} \right]^{1/2} \quad (5-1)$$

Circumferential distribution is found to be easily achieved with the radial flow coaxial injector and minor nonuniformities do not severely affect either the performance or wall thermal environment. Prior to hot firing, each injector was water flowed to insure basic circumferential uniformity. However, the longitudinal distribution of both mass and mixture ratio is found to be of primary importance to both performance and thermal environment. The collector used has tubes spaced 5 degrees in the range from 30 to 90 degrees from the centerline. This provides for a detailed measurement of the gradients through the resulting spray fan.

A stream tube analysis can be used to determine the combustion efficiency of any injector design from the cold flow data. Several assumptions are implicit in the case of cold flow data to predict hot firing results. These are:

- 1) No reaction effects on mixing
- 2) No propellant vaporization effects on mixing
- 3) No secondary mixing downstream

In addition to these, if the γ variation is small for wide mixture ratio variation, the cold flow-hot firing correlation is quite simple. Each collector tube is taken as a stream tube having mass, \dot{w}_i , and mixture ratio, r_i . The mass in each tube is normalized with respect to the total mass sample collected, \dot{w}_i/\dot{w}_t . The tube mixture ratio can be equated to a C^* for that tube. The total predicted C^* is the sum of the predicted C^* 's. from each tube, $\dot{w}_i/\dot{w}_t C^*_i$.

$$C^* = \sum_i \frac{\dot{w}_i}{\dot{w}_t} C^*_i \quad (5-2)$$

The predicted combustion efficiency is the ratio of the predicted C^* and the theoretical equilibrium C^* for the nominal injector mixture ratio.

$$\eta_{C^*} = \frac{C^*}{C^*_{theo}} \quad (5-3)$$

Both the continuous sheet and slotted oxidizer elements were cold flow tested to determine the predicted combustion efficiency and expected wall environment. The mass and mixture ratio distribution for these elements, simulating a MR of 5.2, are shown in Figures 5-5 and 5-6, respectively. Using the stream tube analysis predicted combustion efficiencies of 98.3% and 92.9% were determined. From past TRW experience with earth storable propellants, it was expected that the continuous sheet injector would be best due to the thin sheet thicknesses for small thrusters. However, as will be seen later, the continuous sheet injector could not be made to operate at greater than 82% combustion performance during the hot firings, while the slotted injector had an efficiency as high as 93.8%. Thus, we see that excellent agreement was obtained for the slotted injector but very poor agreement for the continuous sheet injector.

It would appear that the reaction nature of the propellants strongly influence the results. The slotted type results in a fuel-oxidizer interlock system where the highly volatile fuel is confined within the initial reacting zone.

The overall impingement characteristics are determined visually. Figure 5-7 shows photographs of the resultant spray pattern and reveals the high degree of atomization and also shows good circumferential uniformity.

Two different schemes were designed and fabricated for the film coolant tests as discussed earlier. Each, however, involved the same criteria for number of injection holes and injection velocity. One technique used a film coolant manifold incorporated into the injector and impingement of the film coolant on the chamber wall. The second design was a film coolant manifold independent of the injector with the film coolant being directed parallel to the chamber wall. The fuel required for the film cooling was taken from the main fuel propellant feed line with suitable orificing used to determine the percentage of film coolant. Cold flow tests were made on the film coolant manifolds to insure straight flow and even distribution and also to determine the pressure drop-flow rate relationship for the total fuel system. Figures 5-8 through 5-10 give the results of these tests.

Prior to finalizing the design of the first film-coolant injector, a cold flow test series was made to determine the effects of impingement angle and injection velocity on the spreading width of the streams (Figure 5-11). This was necessary to insure that the film coolant completely covered the chamber wall.

Mass distribution studies on this configuration were unnecessary since the injector and film-coolant injection were independently made uniform. A mixture ratio study to determine the new effective wall mixture ratio could not be made due to limitations of the collector apparatus; however, with the use of film coolant the wall mixture ratio could be reduced below the level of 3.0 necessary for carbon deposition, as indicated from calculation.

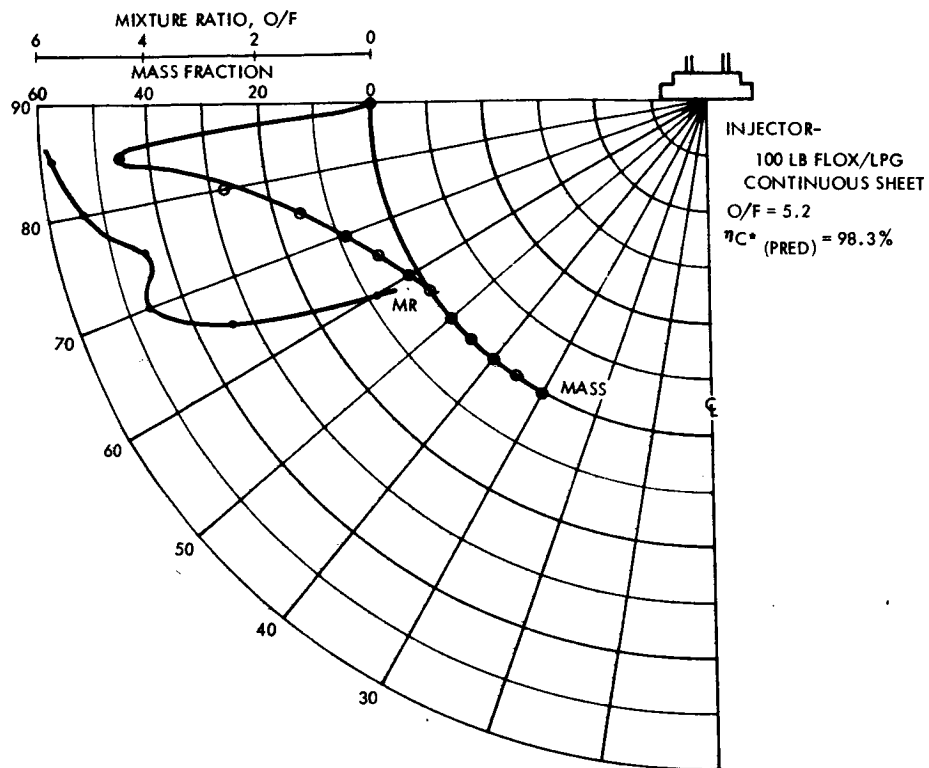


Figure 5-5. Longitudinal Mass and Mixture Ratio Distribution

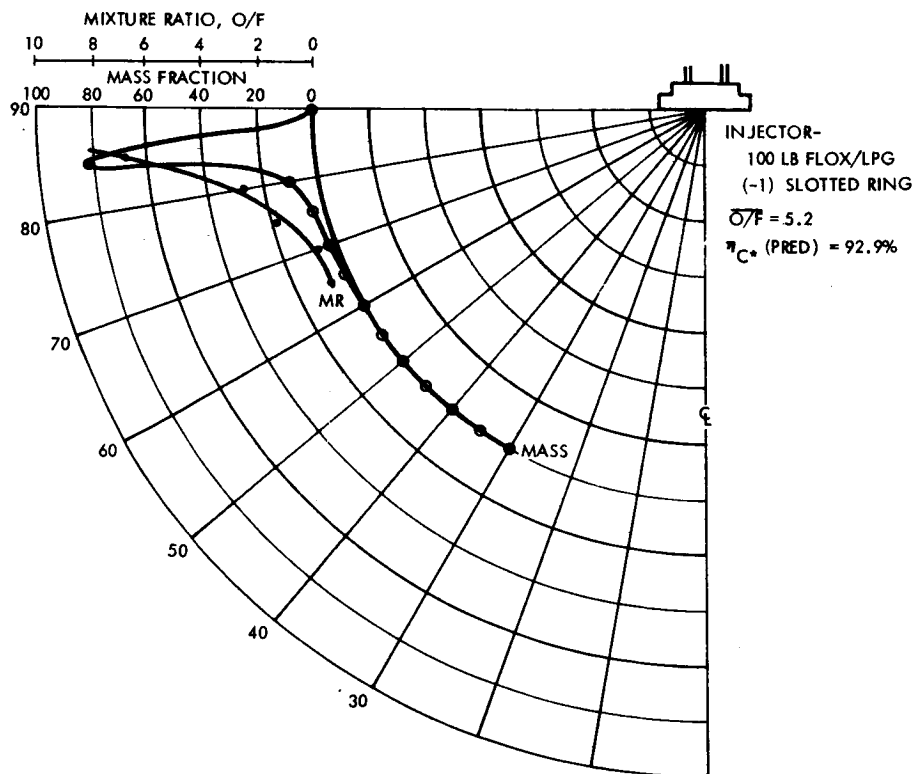


Figure 5-6. Longitudinal Mass and Mixture Ratio Distribution

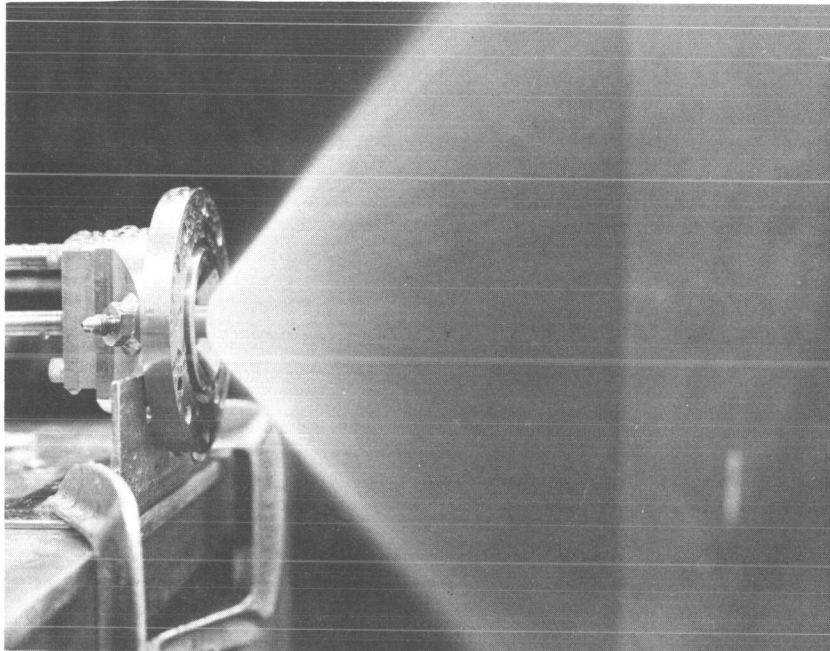


Figure 5-7a. Resulting Impingement Flow at
Optimum Force Balance

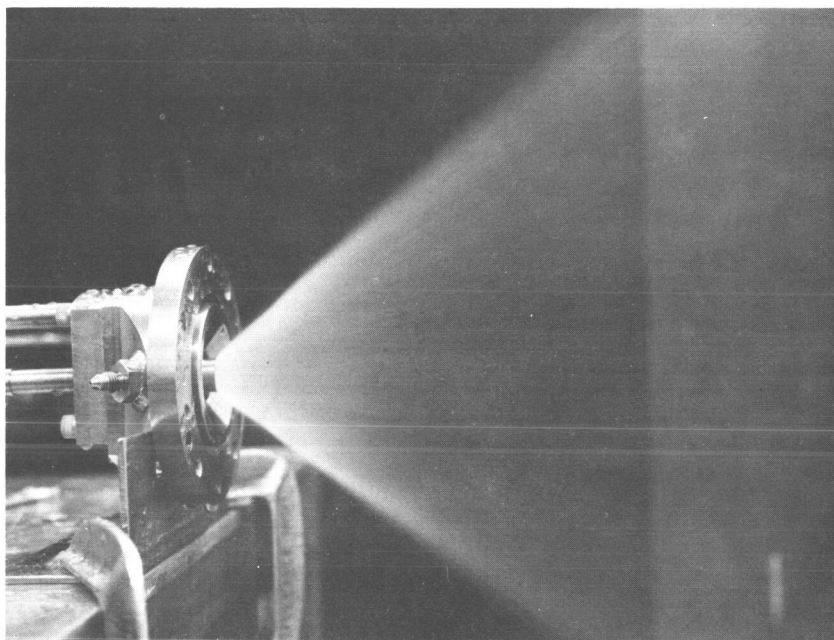


Figure 5-7b. Resulting Impingement Flow at
Rated Volumetric Flow Rates

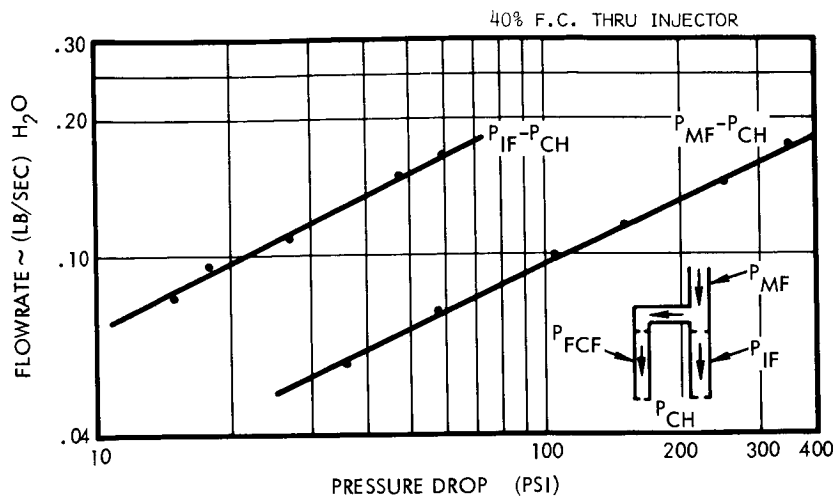


Figure 5-8. Film Coolant Manifold Hydraulic Characteristics

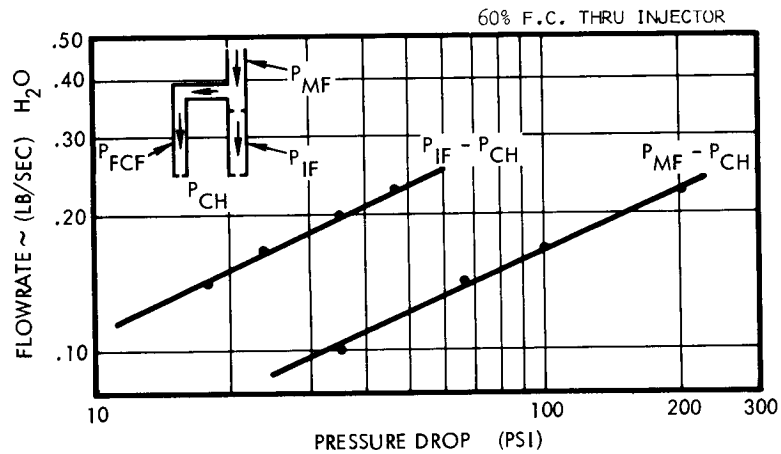


Figure 5-9. Film Coolant Manifold Hydraulic Characteristics

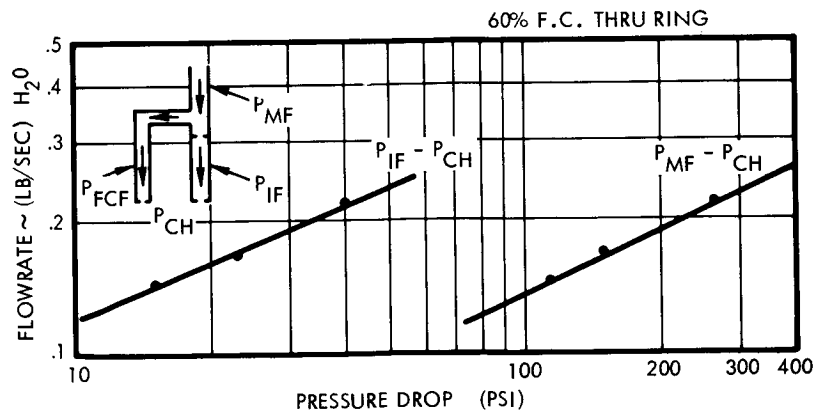
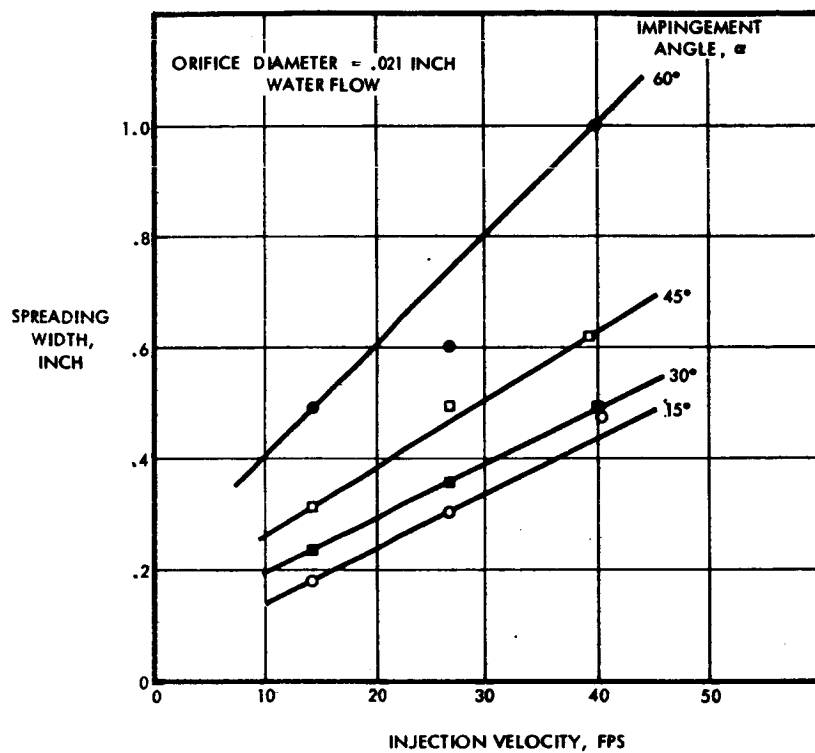
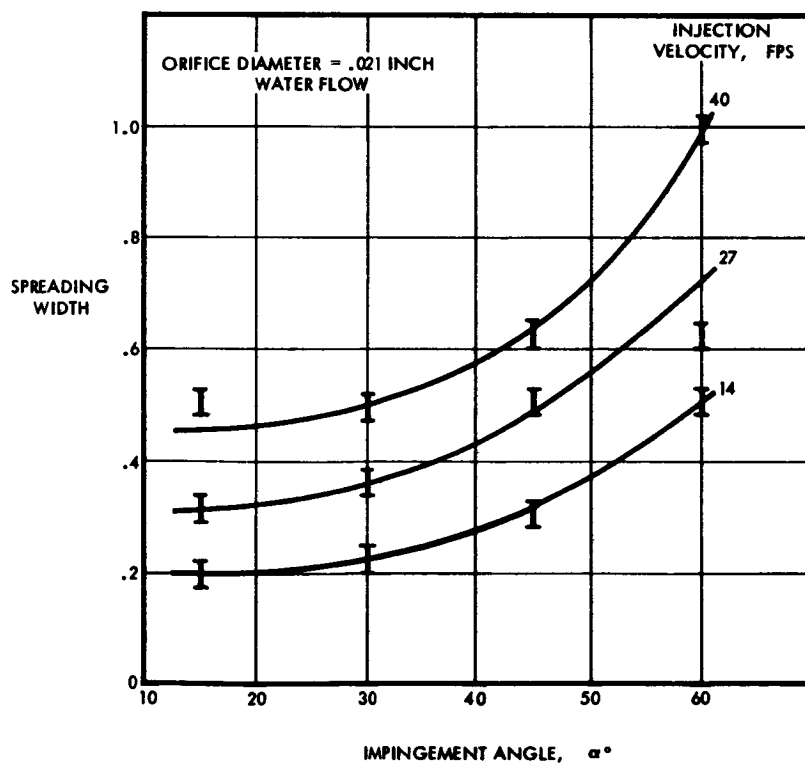


Figure 5-10. Film Coolant Manifold Hydraulic Characteristics



A



B

Figure 5-11. Film Coolant Impingement Characteristics

5.2 HOT FIRING PROGRAM

5.2.1 Test Facility

The test facility used in this program is shown schematically in Figure 5-12 and Figure 5-13 shows an overall view of the TRW FLOX/LPG facility. Propellant conditioning was accomplished with liquid nitrogen. Flow control was maintained through the use of cavitating venturi elements. The thrust stand with a thin wall copper engine mounted on it (Figure 5-14) is a basic altitude facility. Figure 5-15 shows the stand with the capsule removed. The load cell calibration is a remote calibration system. The cell is connected to a steam driven ejector.

5.2.2 Basic Injector Development

The initial effort of the experimental hot firing program was concerned with the development of an injector capable of at least 92% of theoretical equilibrium C^* performance. Initial tests were conducted with the continuous sheet injector, based upon initial cold flow results. Follow-up tests were conducted with swirl type flow and the slotted type oxidizer injector. Table 5-1 gives a summary of all tests performed during the injector performance evaluation phases of the program. A brief explanation of each test sequence follows. All development tests were conducted with an L^* of 15-inch chamber ($CR = 5.0$, barrel length of 1.85 inches, convergent angle of 35 degrees).

Test (001-004): Based upon existing TRW data with continuous sheet coaxial flow injectors with earth storable propellants, a fuel center configuration was initially used. This was attractive because it enabled a larger fuel slot to be used in the fuel center configuration. Earth storable tests showed proper fuel penetration to the wall for wall environmental control. These FLOX/LPG tests were the first tests with cryogenic type propellants in a small thruster at TRW. Performance was low and the tests were discontinued.

Test (005-009): In these tests, the propellants were switched with oxidizer in the center. Only a small increase in performance was obtained.

Test (010-012): Following the above tests, it appeared that low performance might be occurring because of propellant separation at impingement. To allow partial fuel penetration into the oxidizer, a swirl on the oxidizer center was employed. The resulting performance was still low.

Test (013-021): Examination of the flow-rate pressure-drop characteristics in the above listed tests showed a partial decay in flow rate in the oxidizer during the tests. The test series 013-021 was conducted to determine the source of this problem. It was ultimately traced to reaction occurring within the valve bellows, and the resulting residue plugging the oxidizer slots.

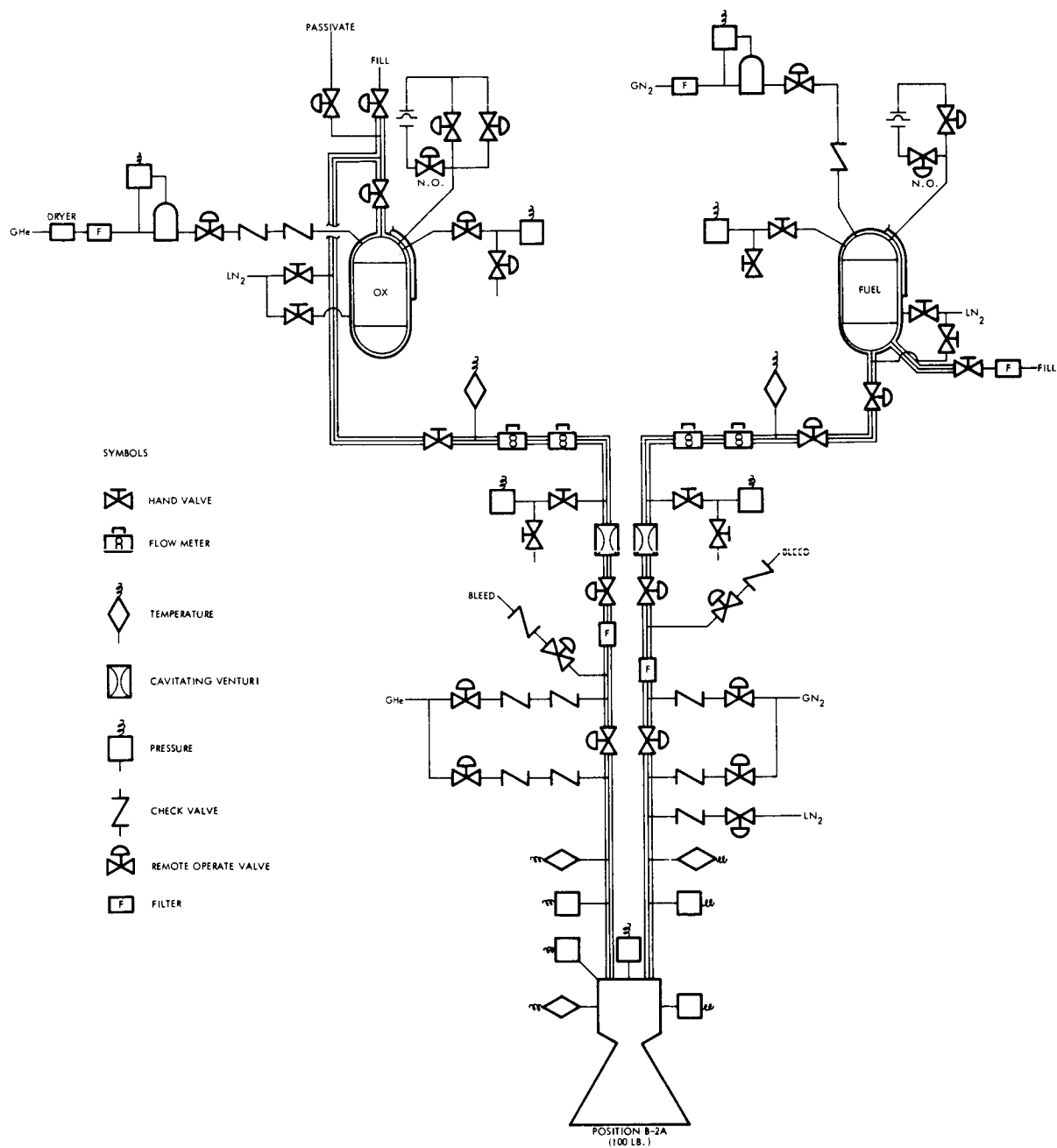


Figure 5-12. Schematic of FLOX/LPG Facility



Figure 5-13. Overall View of FLOX/LPG Facility

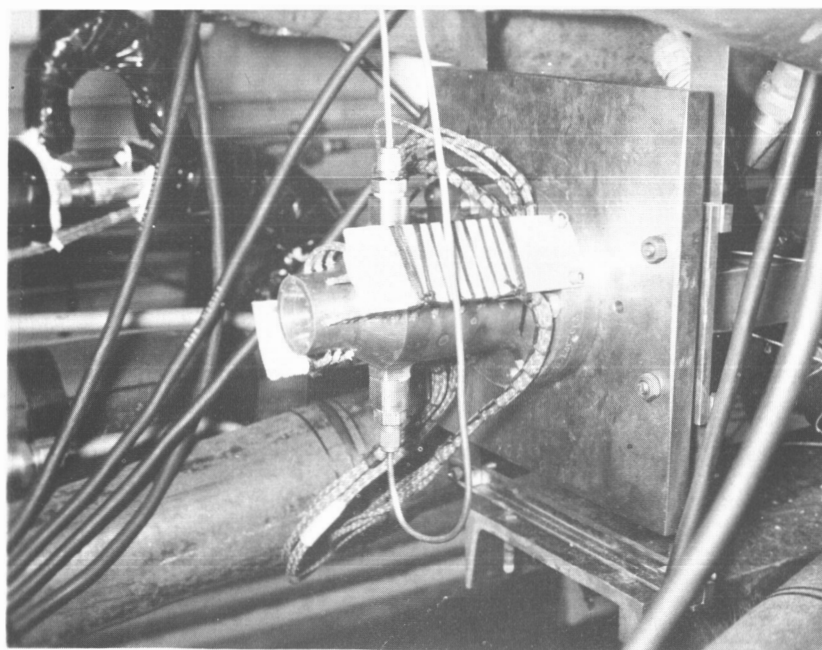


Figure 5-14. Thrust Chamber Mount

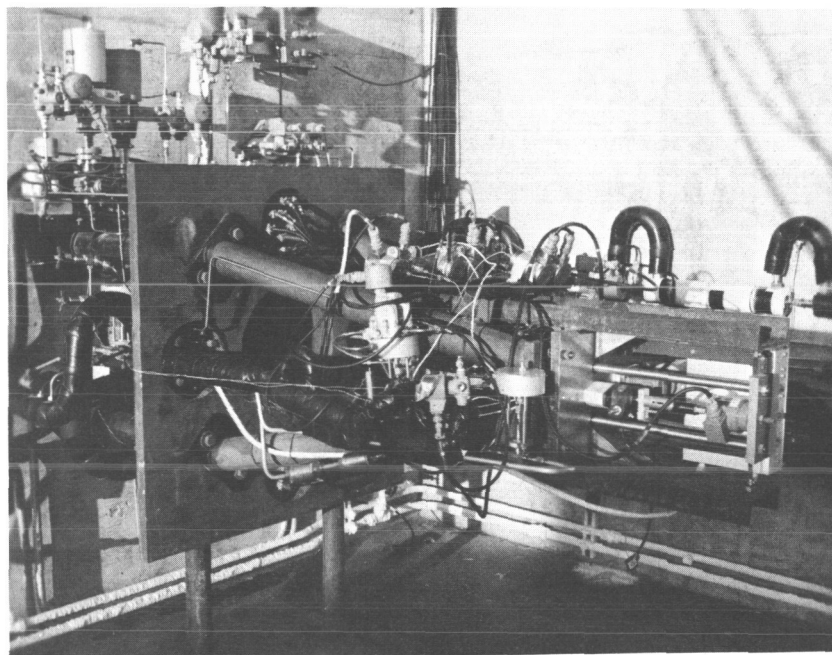


Figure 5-15. 100 Pound FLOX/LPG Thrust Stand

Test (022-029): In these tests, with the system operating satisfactorily, the oxidizer was canted downward 30 degrees to provide more free-flight time for vaporization. Also, the fuel pressure drops were varied to provide momentum ratio evaluation. Performance remained low; however, reduced fuel ΔP indications showed a possibility of performance increase.

Test (030-033): Reduced fuel pressure drops with the noncanted oxidizer center sheet resulted in increased performance.

Test (034-036): The continuous oxidizer sheet was modified to accept a slotted ring (identified as -1) containing 30 slots (0.015-inch long by 0.014-inch wide) for the oxidizer orifice. These were the first tests to provide position interlocking control of the propellants upon impingement. The oxidizer pressure drop was low and the resulting performance was low. Subsequent data analysis indicated the oxidizer ring to be leaking.

Test (037-039): The -1 injector was used in an increased length chamber ($L^* = 22$ inches) with slightly reduced fuel gaps. Performance increased to greater than 90% of equilibrium C^* .

Test (040-042): The above tests were repeated with a reduced length chamber ($L^* = 15$ inches). Performance decreased slightly but was still high.

Test (043-044): The number of oxidizer slots was increased to 40 to investigate the effect of increasing the fineness of interlock mixing. The performance decreased with this change.

Table 5-1. Basic Injector Development Data

	Duration (sec)	(O/F) Overall	(O/F) Core	$\dot{\omega}_t$	$\dot{\omega}_o$	$\dot{\omega}_f$	$\dot{\omega}_{fc}$	%F.C.	C^*_{theo}	P_o	C^*_P measured	$\eta_{c^*_P}$ measured	F_{corr}	C^*_F measured	$\eta_{c^*_F}$ measured	ΔP_{io}	ΔP_{if}	\dot{Q}_{total}	\dot{Q}_{nozzle}		
001	10.0	6.25	6.25	.271	.234	.0374	0	0	6688	65.9	4608	68.9	56.2	--	--	95.6	451.3	--	--	fuel center, L* = 15	
002	6.5	5.10	5.10	.291	.243	.048	0	0	6885	66.7	4365	63.4	57.1	--	--	117.4	21.6	--	--		
003	7.0	4.04	4.04	.335	.268	.066	0	0	6740	59.4	3424	50.8	51.6	--	--	180.8	35.7	--	--		
004	7.0	3.03	3.03	.358	.269	.089	0	0	6601	82.2	4429	67.1	71.3	4286	64.9	152.7	115.2	--	--		
005	5.5	3.92	3.92	.330	.262	.067	0	0	6750	92.2	5400	80.0	77.9	5213	77.2	28.3	23.3	--	--	oxidizer center, L* = 15	
006	5.5	2.96	2.96	.352	.263	.089	0	0	6552	84.2	5552	84.2	78.9	5043	76.5	27.0	37.5	--	--		
007	6.0	3.94	3.94	.333	.265	.067	0	0	6763	94.7	5498	81.3	80.8	5388	79.7	48.4	127.8	--	--		
008	5.5	3.03	3.03	.358	.269	.089	0	0	6599	86.2	4646	70.4	71.8	4366	66.2	40.6	150.2	--	--		
009	4.5	3.35	3.35	.294	.226	.068	0	0	6655	82.4	5404	81.2	76.0	5563	83.6	29.3	106.0	--	--	oxidizer center, swirl L* = 15	
010	5.0	3.93	3.93	.333	.266	.068	0	0	6754	86.5	5032	74.5	73.0	4775	70.7	153.2	130.1	--	--		
011	5.5	2.99	2.99	.355	.266	.089	0	0	6588	85.8	4648	71.1	72.6	4446	67.5	226.5	225.0	--	--		
012	5.5	3.59	3.59	.311	.243	.068	0	0	6703	82.2	5121	76.4	69.7	4823	72.0	141.1	50.0	--	--		
013	4.0	3.30	3.30	.288	.221	.067	0	0	6655	90.7	5976	89.8	75.6	5842	87.8	58.3	25.7	--	--	oxidizer center, L* = 15	
014	4.5	3.71	3.71	.310	.244	.066	0	0	6770	81.4	4986	74.2	69.6	4819	71.7	403.9	23.5	--	--		
015	4.5	3.96	3.96	.325	.260	.066	0	0	6756	78.2	4790	70.9	67.1	4376	64.8	138.3	24.2	--	--		
016	4.5	4.00	4.00	.328	.262	.065	0	0	6756	78.6	4797	71.0	--	--	--	96.8	24.4	--	--		
017	5.0	4.79	4.79	.302	.250	.052	0	0	6899	94.1	5885	85.3	76.3	5602	81.2	42.4	15.0	--	--	oxidizer center, L* = 15	
018	5.0	3.16	3.16	.329	.250	.079	0	0	6632	94.4	5412	81.6	75.9	5119	77.2	37.7	32.1	--	--		
019	5.0	3.01	3.01	.265	.199	.066	0	0	6569	50.6	3580	54.5	39.6	--	--	13.0	23.8	--	--		
020	5.0	4.10	4.10	.331	.266	.065	0	0	6792	92.3	5237	77.1	76.2	5087	74.9	52.5	22.6	--	--		
021	5.5	4.96	4.96	.384	.320	.064	0	0	6912	86.4	4223	61.1	69.7	3954	59.7	154.9	22.6	--	--	oxidizer center, canted L* = 15	
022	5.5	3.19	3.19	.271	.206	.064	0	0	6620	64.5	4528	68.4	52.7	--	--	52.5	265.9	--	--		
023	5.5	4.09	4.09	.330	.265	.064	0	0	6779	85.4	4915	72.5	71.1	4681	69.0	100.2	481.1	--	--		
024	5.5	3.08	3.08	.354	.267	.087	0	0	6595	61.5	3304	50.1	51.5	--	--	76.8	594.7	--	--		
025	5.5	4.97	4.97	.384	.320	.064	0	0	6922	93.3	4610	66.6	76.6	4417	63.8	90.5	508.5	--	--	oxidizer center, L* = 15	
026	5.5	2.97	2.97	.251	.192	.065	0	0	--	44.5	3292	--	35.9	--	--	46.2	33.9	--	--		
027	5.0	5.00	5.00	.309	.257	.051	0	0	6910	83.5	5148	74.5	69.1	4850	70.2	70.3	21.7	--	--		
028	5.0	5.21	5.21	.315	.264	.051	0	0	6906	79.7	4827	69.9	67.0	4529	65.6	69.2	21.5	--	--		
029	4.0	5.63	5.63	.301	.255	.045	0	0	6825	77.2	4900	71.8	64.0	4486	65.7	53.0	17.3	--	--	oxidizer center, L* = 15	
030	4.5	5.04	5.04	.307	.256	.051	0	0	6920	90.6	5619	81.2	75.3	5398	78.0	71.7	25.7	--	--		
031	4.0	3.88	3.88	.327	.260	.067	0	0	6746	86.2	5019	74.4	71.4	4753	70.5	86.7	38.1	--	--		
032	4.0	3.04	3.04	.346	.261	.086	0	0	6608	88.7	4877	73.8	73.3	4640	70.2	77.7	62.9	--	--		
033	4.5	4.74	4.74	.387	.319	.067	0	0	6912	112.0	5516	79.8	93.0	5495	79.5	125.3	41.0	--	--	oxidizer center, slots (-1), L* = 15	
034	5.0	5.28	5.28	.321	.260	.051	0	0	6915	94.8	5629	81.4	79.0	5465	79.0	89.9	18.8	--	--		
035	4.0	4.17	4.17	.334	.269	.064	0	0	6792	81.3	4646	68.4	68.5	4399	64.8	54.3	28.4	--	--		
036	Run Invalid - Lost Pintle Tip																				oxidizer center, slots (-1), L* = 22
037	5.0	5.10	5.10	.312	.261	.051	0	0	6933	102.4	6288	90.7	81.9	5914	85.3	143.0	20.5	--	--	oxidizer center, slots (-1), L* = 22	
038	5.0	3.98	3.98	.328	.263	.066	0	0	6782	107.6	6280	92.6	85.7	5937	87.5	144.5	34.2	--	--		
039	5.5	2.91	2.91	.347	.258	.089	0	0	6573	106.9	5903	89.8	84.0	5496	83.6	139.8	61.2	--	--		
040	5.0	4.60	4.60	.381	.314	.067	0	0	6916	126.9	6384	92.3	101.4	6200	89.7	208.0	33.3	--	--		
041	4.5	3.98	3.98	.329	.263	.066	0	0	6767	98.2	5975	88.3	84.7	5756	85.1	145.1	29.6	--	--	oxidizer center, slots (-1), L* = 15	
042	5.0	5.15	5.15	.315	.264	.051	0	0	6926	94.4	6005	86.7	81.1	5713	82.5	149.3	20.1	--	--		
043	4.0	5.70	5.70	.313	.262	.051	0	0	6929	98.5	5938	85.7	80.7	5769	83.3	122.0	26.8	46.1	15.4		
044	5.5	3.86	3.86	.328	.261	.068	0	0	6749	94.7	5440	80.6	73.0	5280	78.2	120.4	40.7	37.2	10.6		

5.2.2.1 Development Summary

At this point, the performance development tests were terminated. The performance goal of 92% equilibrium C* performance had been demonstrated with the -1 injector with 30 oxidizer slots (0.015 inch high by 0.014 inch wide) and a continuous 0.0039 inch fuel gap.

5.2.3 Basic Injector Heat Transfer Characterization

Following the development of a high performance injector, detailed studies were performed to determine its resultant heat transfer characteristics. Cold flow tests contributed to a better understanding of the injection interactions while hot firing data gave experimental data on the thermal environment produced by the injector. The method of data acquisition is discussed in Appendix C.

A comprehensive set of tests was made on the selected injector configuration to determine its heat transfer characteristics as well as performance. The principal heat transfer parameter considered was the heat input to the nozzle and the total heat input to the chamber as in Figure 5-16 below. Principal variables were mixture ratio and chamber length. Table 5-2 gives a summary of measured data taken in the injector characterization tests. Following is a brief description of each test sequence under this phase of the effort. All tests were made with the (-1) oxidizer ring and with a fuel gap of .0039 inch.

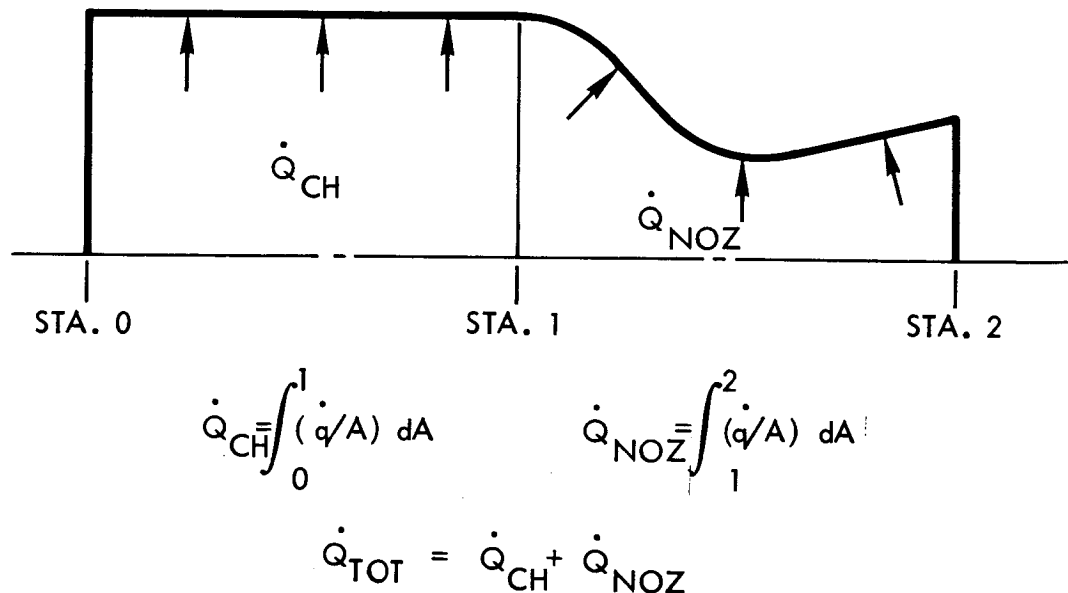


Figure 5-16. Schematic Representation of Chamber Showing Convective Heat Load Components



Run	Duration (sec)	(O/F) Overall	(O/F) Core	$\dot{\omega}_t$	$\dot{\omega}_o$	$\dot{\omega}_f$	$\dot{\omega}_{fc}$	%F.C.	C_{theo}^*	P_o	C_P^*	$\eta_{C_P}^*$ measured	F_{corr}	C_F^*	$\eta_{C_F}^*$ measured	ΔP_{io}
045	4.5	4.00	4.00	.316	.253	.063	0	0	6782	101.7	6065	89.4	82.5	5883	86.7	135.2
046	4.5	4.49	4.49	.317	.259	.058	0	0	6782	100.7	5974	86.9	81.4	5766	83.9	139.2
047	4.5	5.15	5.15	.313	.262	.051	0	0	6932	99.0	5947	85.8	81.5	5822	84.0	146.4
048	4.5	5.58	5.58	.307	.261	.047	0	0	6871	98.4	6025	87.8	81.5	5930	86.4	146.3
049	4.5	4.94	4.94	.381	.317	.064	0	0	6943	125.8	6214	89.5	103.0	6294	90.6	215.8
050	4.5	4.86	4.86	.334	.194	.040	0	0	6884	73.1	5886	85.5	60.4	5428	78.8	91.2
051	5.0	4.07	4.07	.323	.259	.064	0	0	6846	100.4	5983	87.4	83.1	5776	84.4	131.8
052	5.0	4.45	4.45	.317	.259	.058	0	0	6865	100.0	6014	87.6	83.0	5875	85.6	143.3
053	4.5	5.00	5.00	.308	.256	.051	0	0	6928	99.6	6180	89.2	81.1	5904	85.2	145.2
054	4.5	5.71	5.71	.311	.265	.046	0	0	6847	98.9	6058	88.6	81.7	5882	86.0	148.9
055	4.5	4.04	4.04	.318	.255	.063	0	0	6780	93.4	5627	83.0	77.3	5383	79.4	138.5
056	5.0	4.55	4.55	.320	.263	.058	0	0	6864	86.5	5773	84.1	77.2	5255	76.6	131.7
057	5.0	5.21	5.21	.320	.269	.052	0	0	6913	83.2	5551	80.3	70.7	4771	69.0	129.1
058	5.0	5.81	5.81	.319	.272	.047	0	0	6805	83.8	5614	82.5	73.0	4948	72.7	138.0

Foldout #1

Table 5-2. Basic Injector Characterization
Data (No Film Cooling)

ΔP_{if}	\dot{Q}_{total}	\dot{Q}_{nozzle}	
37.6	52.8	19.1	oxidizer center, slots (-1), $L^* = 15$, straight, smooth wall chamber
33.5	47.8	18.0	
27.3	40.3	15.8	
19.7	45.1	14.9	
36.8	52.1	19.5	
15.0	37.6	14.0	
37.3	66.2	15.1	oxidizer center, slots (-1), $L^* = 22$
33.2	74.6	19.9	
28.1	72.4	20.3	
21.9	70.0	19.4	
40.7	35.1	15.2	oxidizer center, slots (-1), $L^* = 9$
33.8	29.4	14.3	
28.8	26.0	17.8	
25.5	23.2	11.2	

Foldout #2

Test (045-048): A mixture ratio survey was performed in the $L^* = 15$ inches chamber. Nozzle heat loads were uniformly high across the MR range (Figure 5-17). Of interest was the flatness of the performance versus the MR variations. The MR variations were accomplished through ΔP variations only.

Test (049-050): Chamber pressure variations of $\pm 25\%$ were made in these tests. Performance remained the same with only minor nozzle heat load variations (Figure 5-18).

Test (051-054): For comparison purposes, tests were repeated in a longer length chamber ($L^* = 22$ inches). The nozzle heat loads increased somewhat (Figure 5-19).

Test (055-058): The above tests were repeated in a short chamber ($L^* = 9$ inches) and the resulting nozzle heat loads were still high (Figure 5-20).

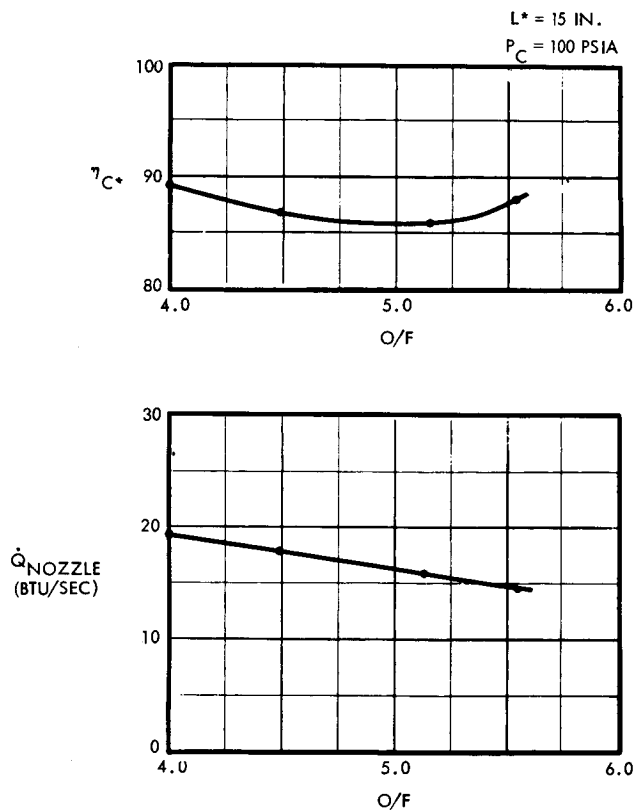


Figure 5-17
Baseline Injector Performance
and Heat Transfer Data Without
Film Cooling

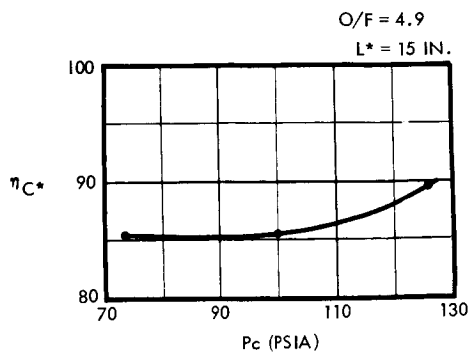


Figure 5-18

Baseline Injector Performance
and Heat Transfer Data Without
Film Cooling

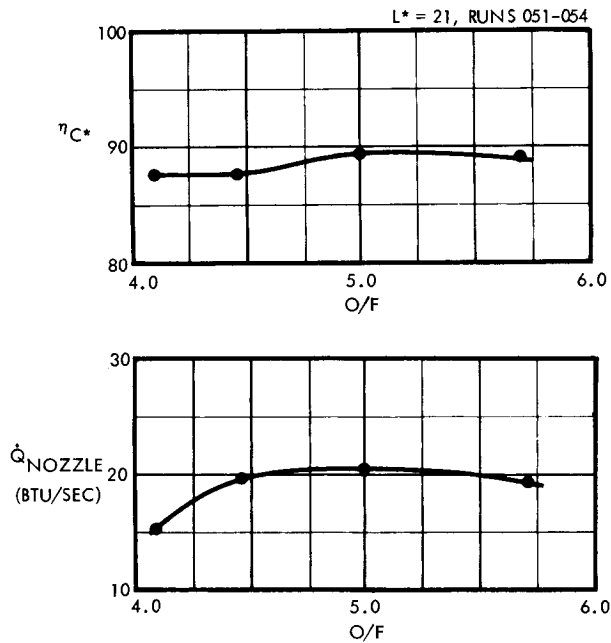
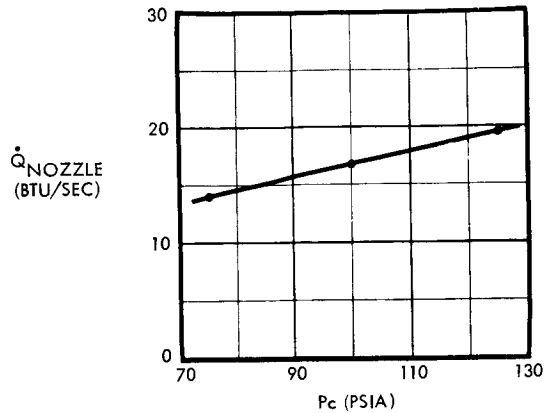


Figure 5-19. Baseline Injector
Performance and
Heat Transfer Data
Without Film Cooling

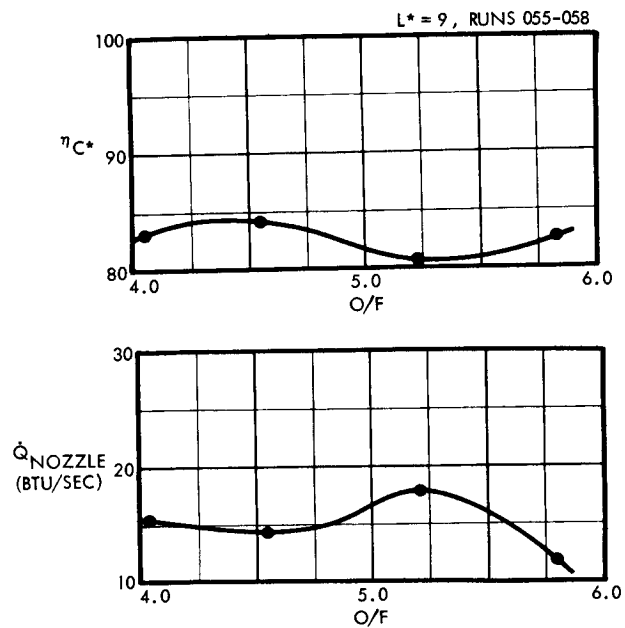


Figure 5-20. Baseline Injector
Performance and
Heat Transfer Data
Without Film Cooling

5.2.3.1 Heat Transfer Summary

Figure 5-21 gives a summary of the test results as a function of chamber L^* . A complete data evaluation showed that corrected performance levels in excess of those required were achieved on all but the shortest chamber. However, the heat transfer data indicated that nozzle heat loads were at least twice as high as was necessary to achieve conduction cooling based on the analytical results. This indicated that the wall environment was much too severe with the basic injector. Another indication was the lack of any appreciable carbon deposition on the nozzle walls. (It is noted that the thermal analysis showed a need for carbon resistance to reduce the resulting heat load to the coolant.) This meant that the theoretical wall mixture ratio was in excess of 3.0. Whereas the coaxial flow injector had demonstrated a capability of achieving inner-regeneration cooling in thin wall chambers with earth storable propellants, it appeared that this would not be achieved here with the more volatile space storable propellants. At this point in the program, no injector durability or adverse streaking problems had been encountered.

Following the above tests, the evaluation of the film coolant part of the program was initiated.

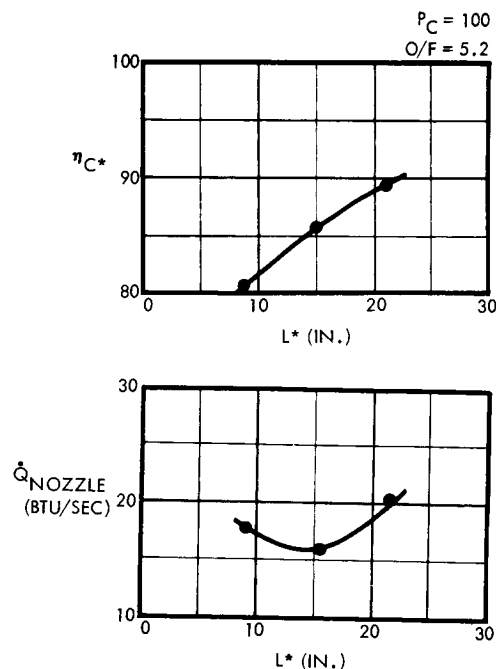


Figure 5-21
Baseline Injector Performance
and Heat Transfer Data Without
Film Cooling

5.2.4 Injector/Film Cooling Characterization

Based upon the previous tests, auxiliary film-cooling injection was evaluated. The primary goals were: (1) the achievement of a liquid layer of fuel upon the wall to provide a cooling sink for heat conducted from the nozzle, and (2) a reduction of the total nozzle heat load to a tolerable limit to allow inner-regeneration operation.

Table 5-3 gives a summary of test results from the film-coolant tests. As can be seen, a wide variety of configurations were tested in order to achieve the desired nozzle heat loads. All tests were performed with the (-1) oxidizer ring. A description of each test sequence follows.

Test (059-064): These baseline tests were performed at 40% film coolant with the $L^* = 15$ inch chamber, in order to provide a direct comparison to the nonfilm cooled tests. The 40% figure also represents a nominal percentage similar to that used in current day thrusters with earth storables. Performance decreased slightly. A marked reduction in heat load occurred (Figures 5-22 to 5-24). The temperature data indicated that no liquid was on the chamber walls.

Test (065-066): Since the possibility of wall shear forces stripping of the light fuel liquid existed, initial tests with a tapered chamber were conducted. This resulted in some additional heat load reduction as well as a slight performance increase (Figure 5-25 through 5-27).

Test (067-068): To further decrease the heat loads, the film-coolant percentage was increased to 60% with no detectable performance loss (Figures 5-28 through 5-30). (Incomplete performance data exist here because of emphasis on heat transfer data acquisition).

Test (069-070): These tests were aborted due to a fuel leak on the test stand. The problem was traced to a faulty fire valve and corrected.

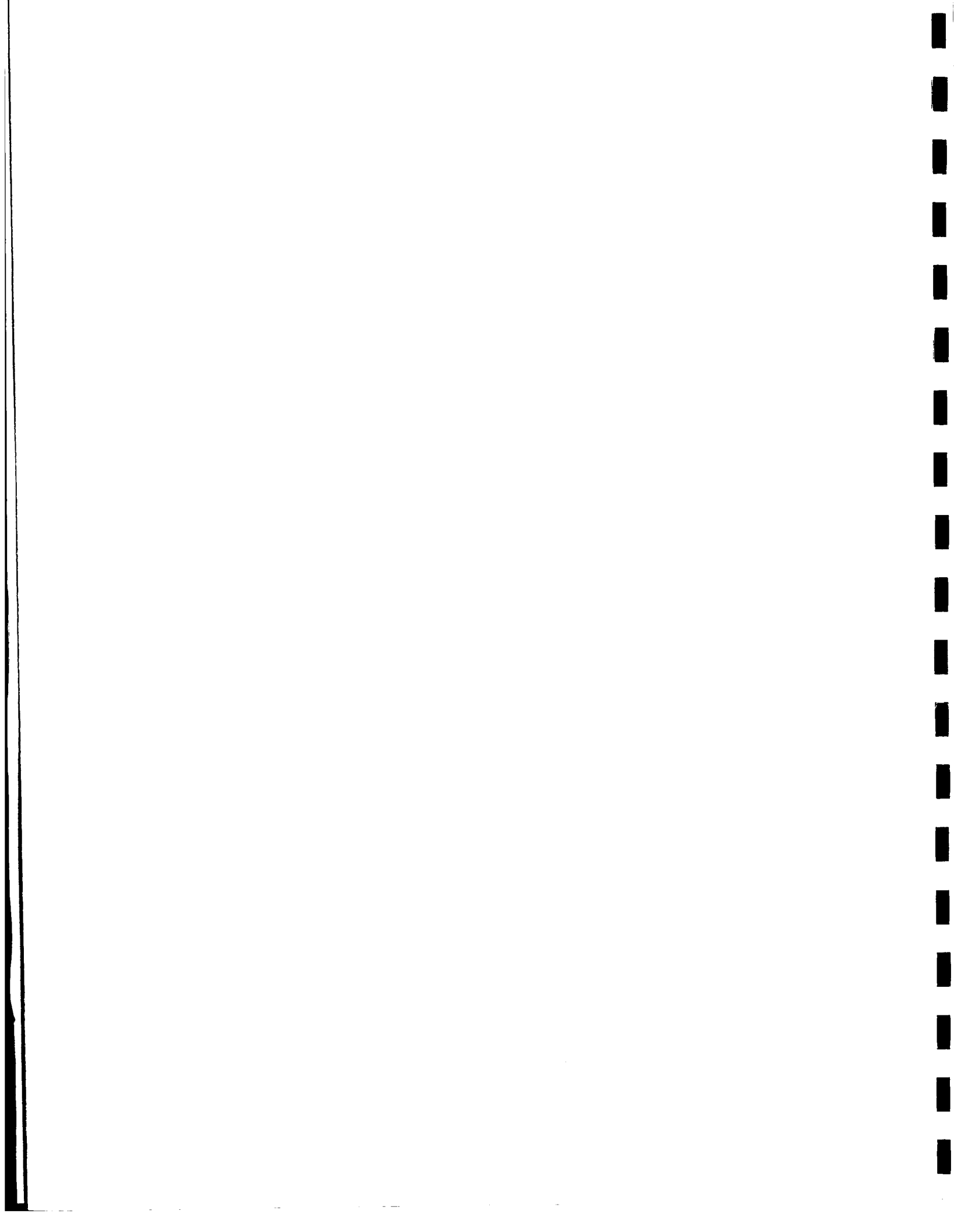
Test (071-072): The tapered chamber had grooves added to the walls which were aligned with the film-coolant streams. The purpose of the grooves was to increase the efficiency of the film-coolant layer by keeping it on the chamber walls and also to increase the heat transfer area from the chamber to the film coolant. Test results showed a significant nozzle heat load reduction to a level at which conduction cooling might be possible (~ 5 Btu/sec). Also, carbon deposition occurred. However, as can be seen in the temperature profiles of these tests, a hot spot occurred in the barrel section of the chamber. Without the elimination of this, no conduction back to the film-coolant zone could occur (Figures 5-31 through 5-33).

Test (073-074): Based upon the above tests, it was felt that the hot spot might be removed by injecting with a separate manifold which provided parallel injection with the chamber walls. No significant improvement was noted (Figures 5-34 through 5-36). Again, it was determined that liquid was not existing on the chamber walls.

Test (075): A repeat test of the previous configuration was made with a shroud covering the film coolant until it reached the hot spot location (Figure 5-37). No particular improvement was noted, and the wall temperature profiles indicated that liquid was not being maintained on the wall (all temperatures substantially above the liquid saturation temperature). Figure 5-38 shows the wall temperature profile.

Table 5-3. Film Coolant/Injector Data

P_{if}	\dot{Q}_{total}	\dot{Q}_{nozzle}	
.1	42.7	12.2	} $L^* = 15$, straight, smooth wall chamber
.1	57.3	16.8	
.5	37.1	11.7	
.1	45.9	13.6	
.9	39.8	10.7	
.5	53.0	14.2	} $L^* = 15$, smooth wall tapered chamber with injector film coolant
.65	45.2	9.2	
.74	30.2	7.4	
.7	31.9	7.8	
.7	25.1	5.4	} $L^* = 15$, grooved wall tapered chamber with injector film coolant
.2	22.8	5.6	
.2	34.3	8.1	
.3	28.3	6.4	} $L^* = 15$, grooved wall tapered chamber with film coolant ring Same as 073 with shroud Same as 073 with higher P_{if}
.4	34.2	10.2	
.6	30.4	7.9	
.9	18.7	4.9	
.5	**	**	
.3	**	**	} Same as 073 with MMH film coolant
.9	**	**	
.2	**	**	} $L^* = 15$, grooved, thick wall tapered chamber with injector film coolant
.2	**	**	
.0	**	**	
.0	**	**	} Same as 082 with CARB-I-TEX splash ring
.0	**	**	



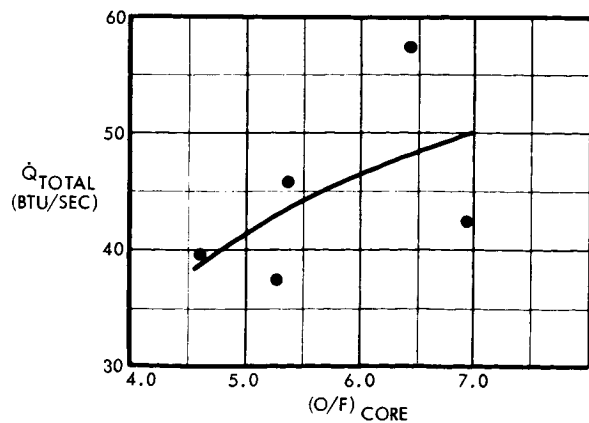
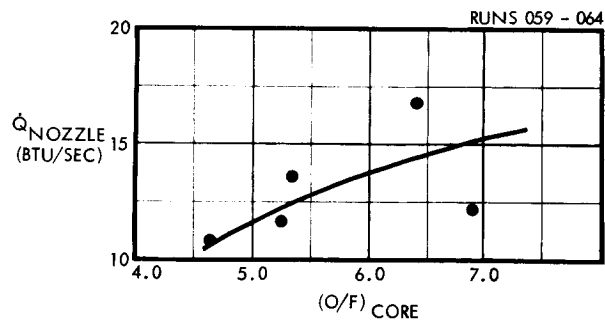
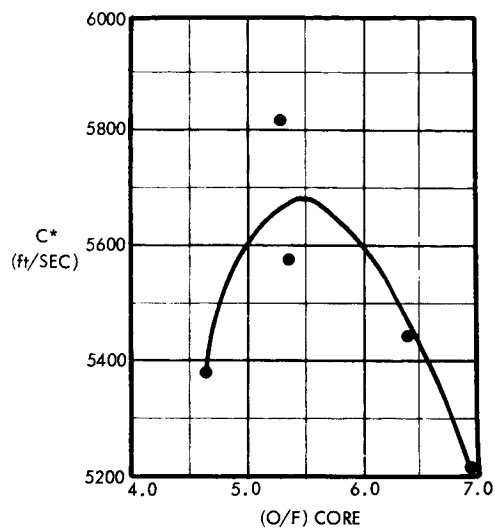
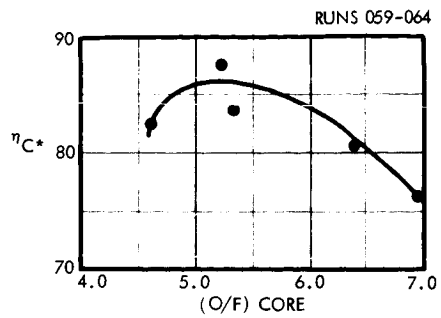


Figure 5-22

Performance Data Runs (059-064)
with 40% Film Cooling

Figure 5-23

Heat Transfer Data Runs (059-064)
with 40% Film Cooling

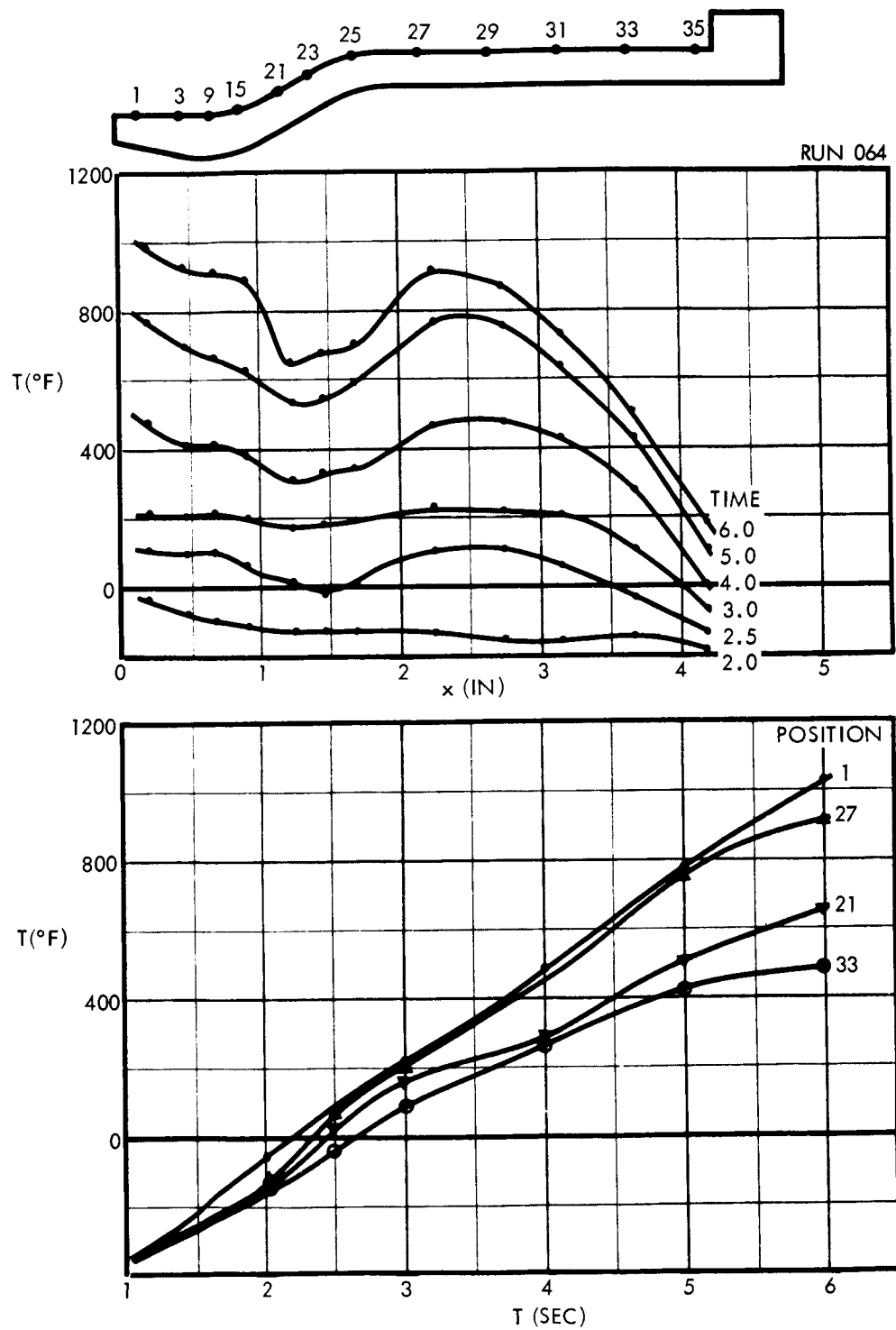


Figure 5-24. Temperature Profile Run (064)
(40% Film Cooling)

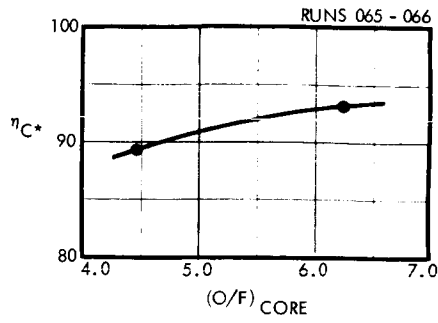


Figure 5-25
Performance Data Runs (065-066)
with 50% Film Cooling

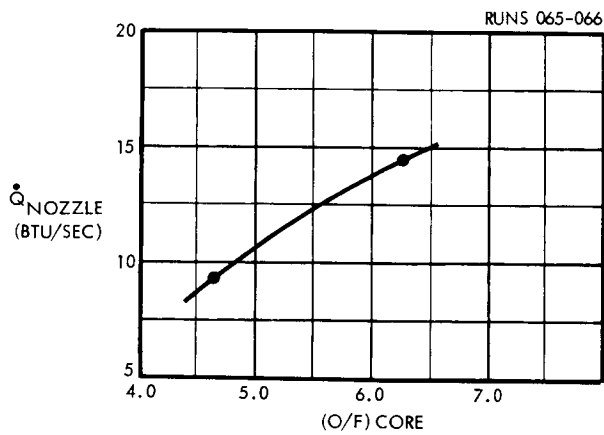
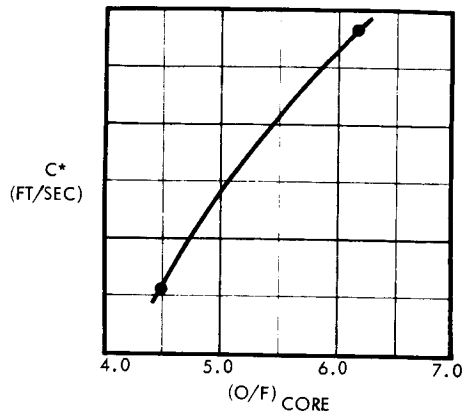
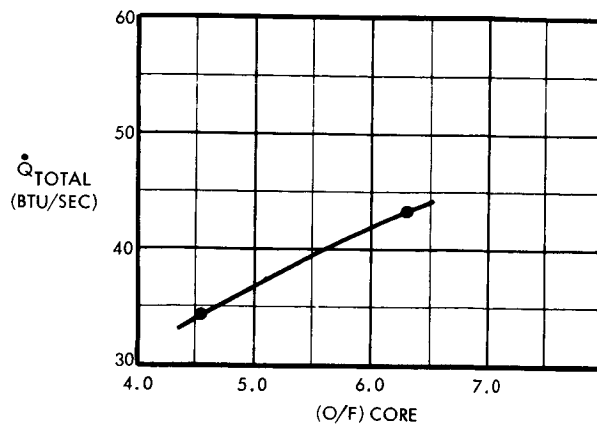


Figure 5-26
Heat Transfer Data Runs (065-066)
with 50% Film Cooling



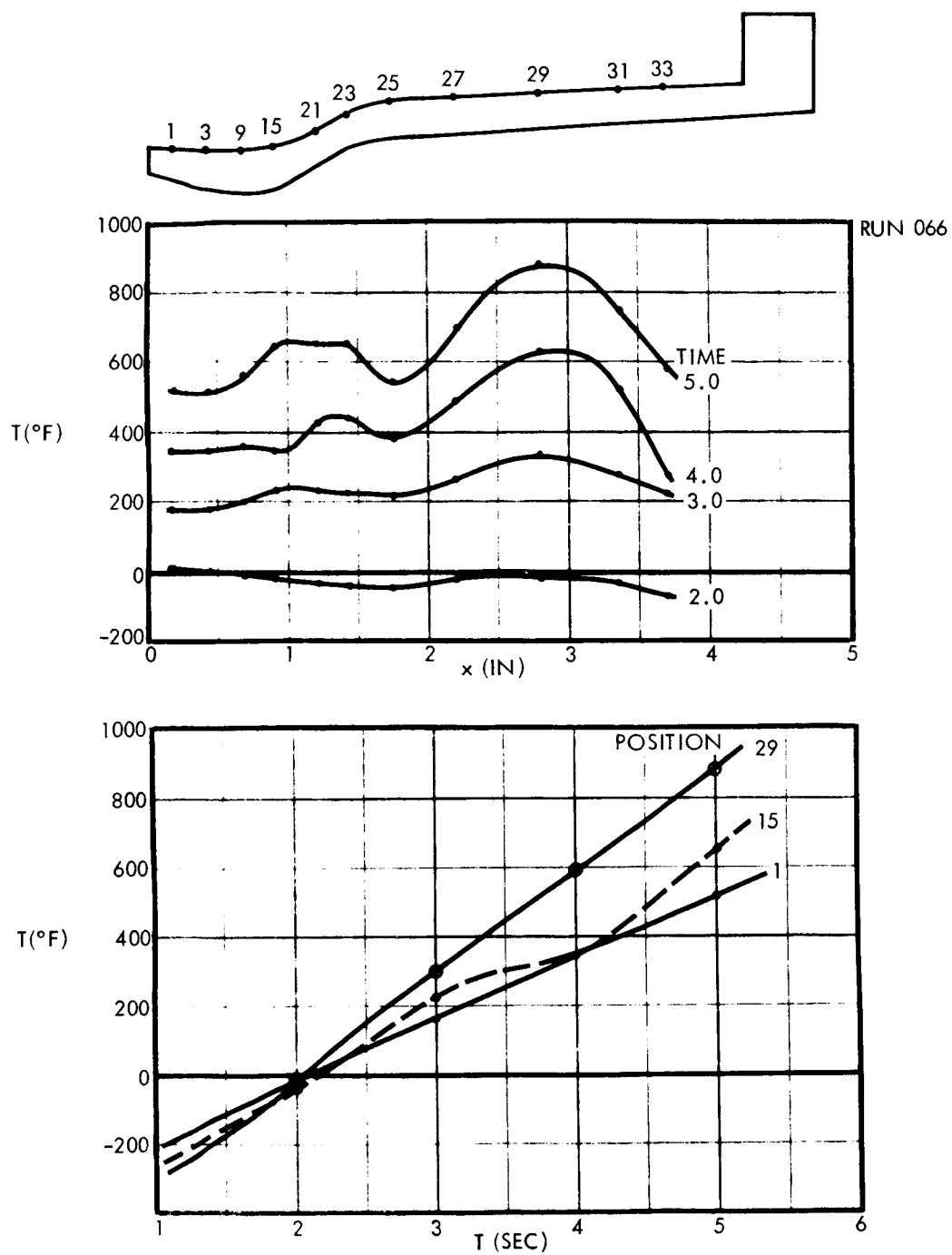


Figure 5-27. Temperature Profile Run (066)
(50% Film Cooling)

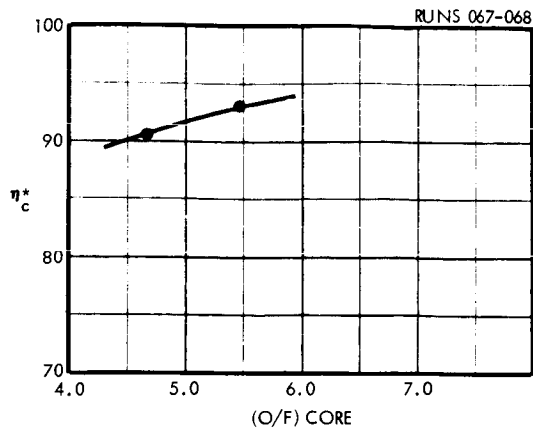


Figure 5-28
Performance Data Runs (067-068)
with 60% Film Cooling

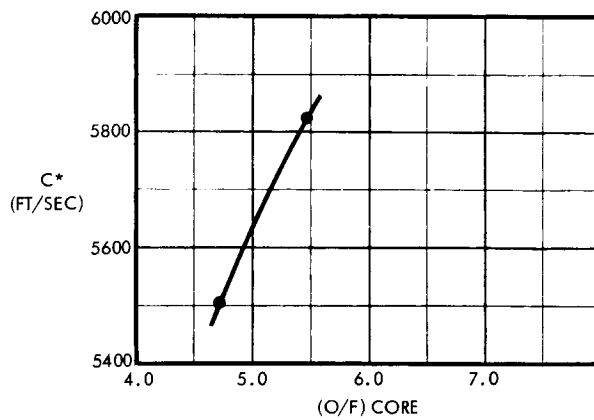
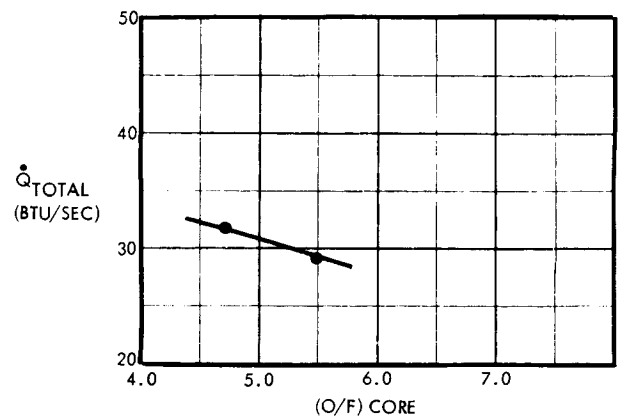
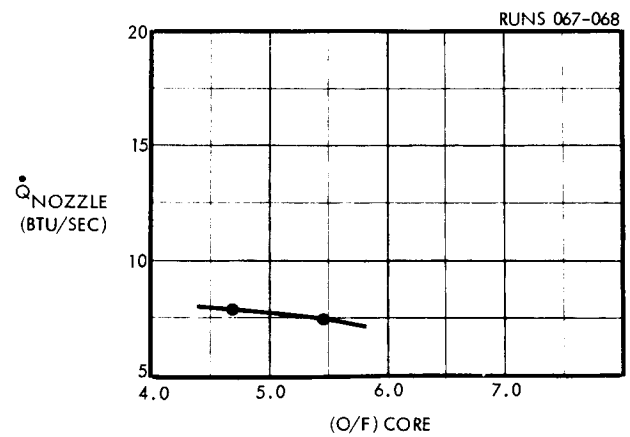


Figure 5-29
Heat Transfer Data Runs (067-068)
with 60% Film Cooling



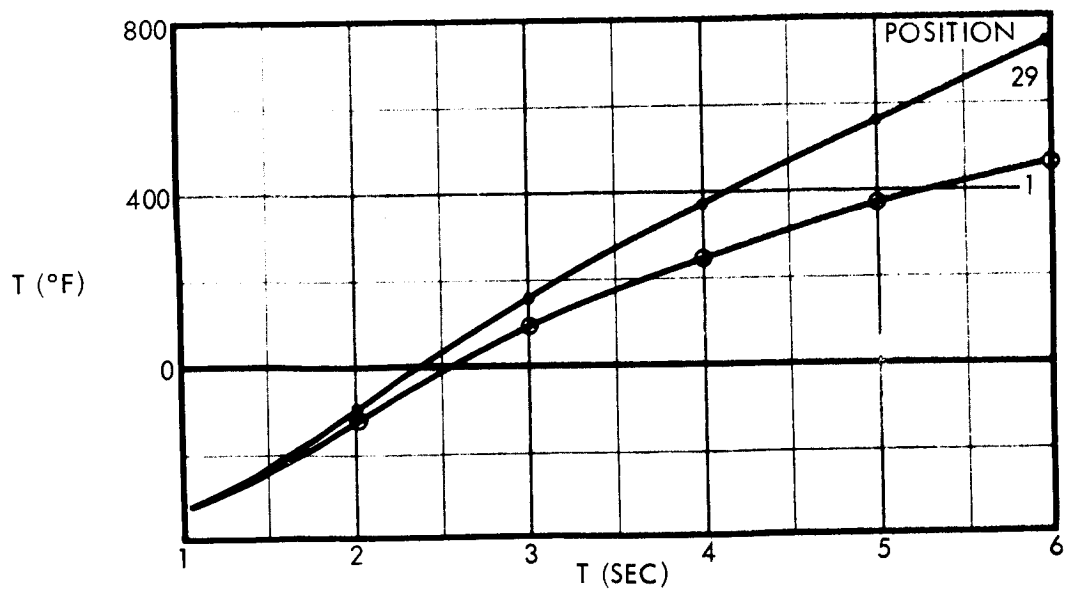
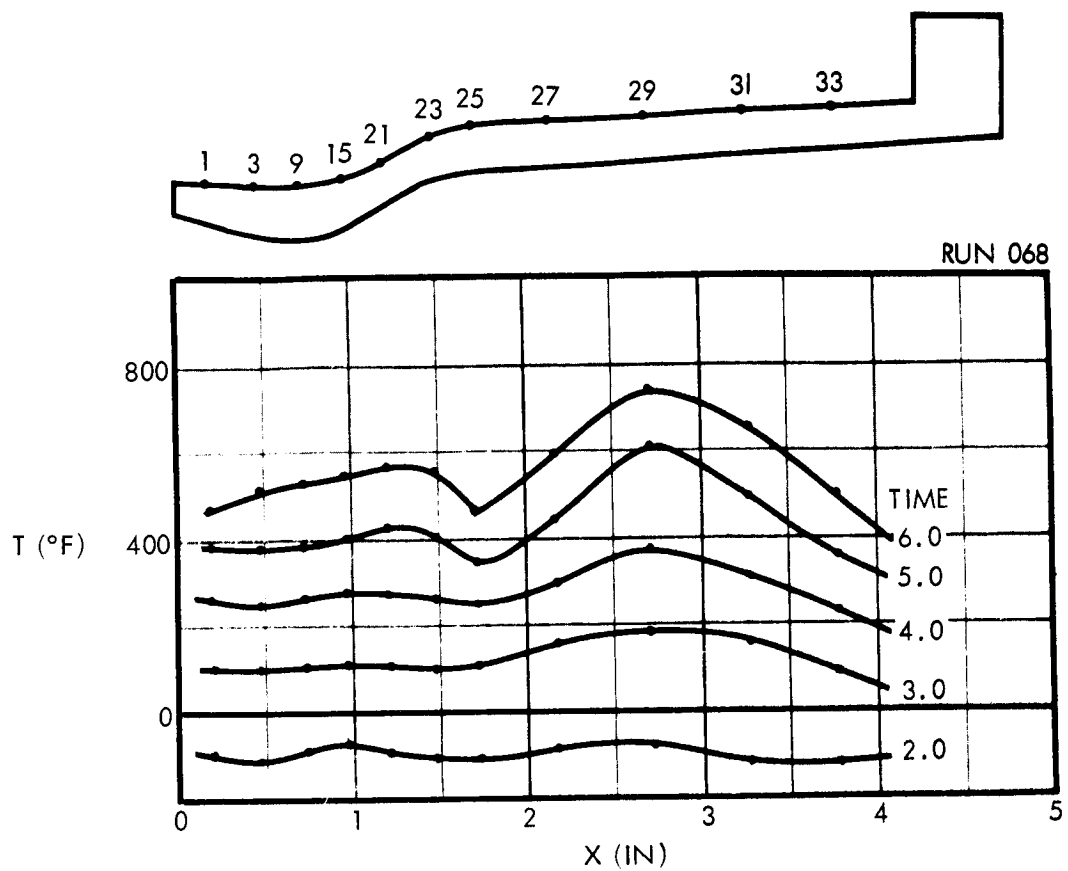


Figure 5-30. Temperature Profile Run 068
(60% Film Cooling)

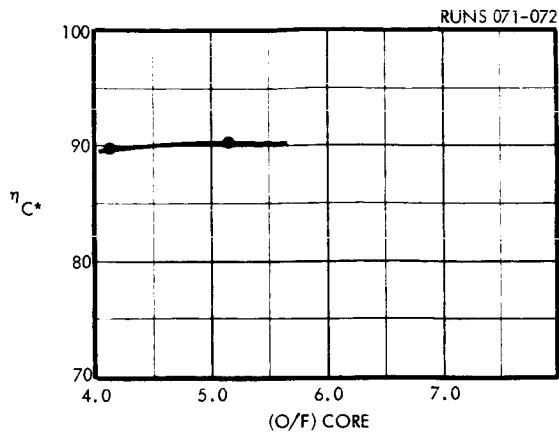


Figure 5-31

Performance Data Runs (071-072) with
60% Film Cooling and Grooved Wall

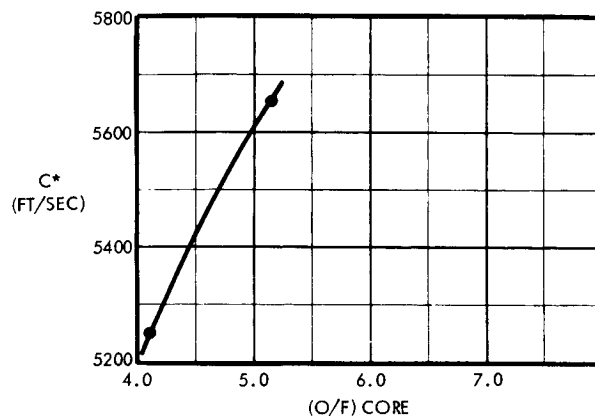
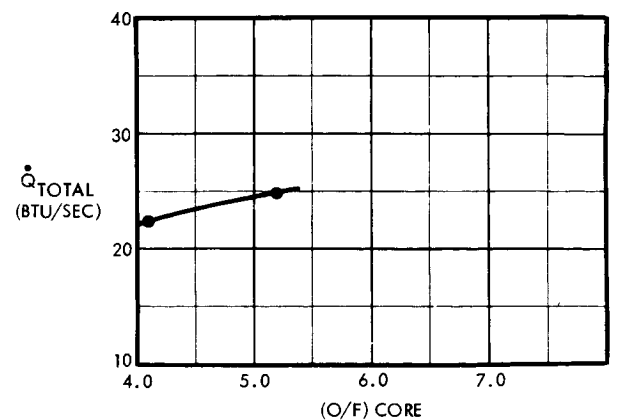
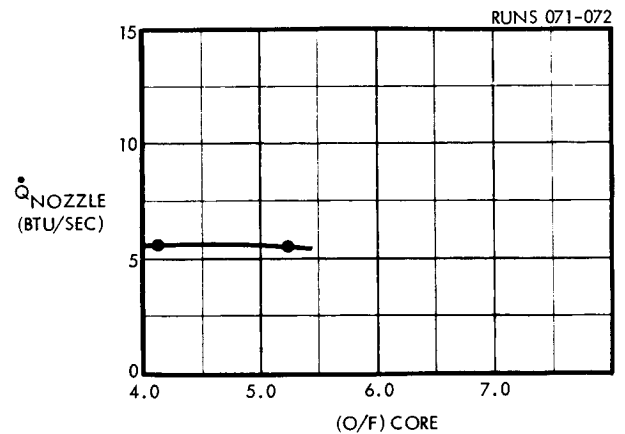


Figure 5-32

Heat Transfer Data Runs (071-072) with
60% Film Cooling and Grooved Wall



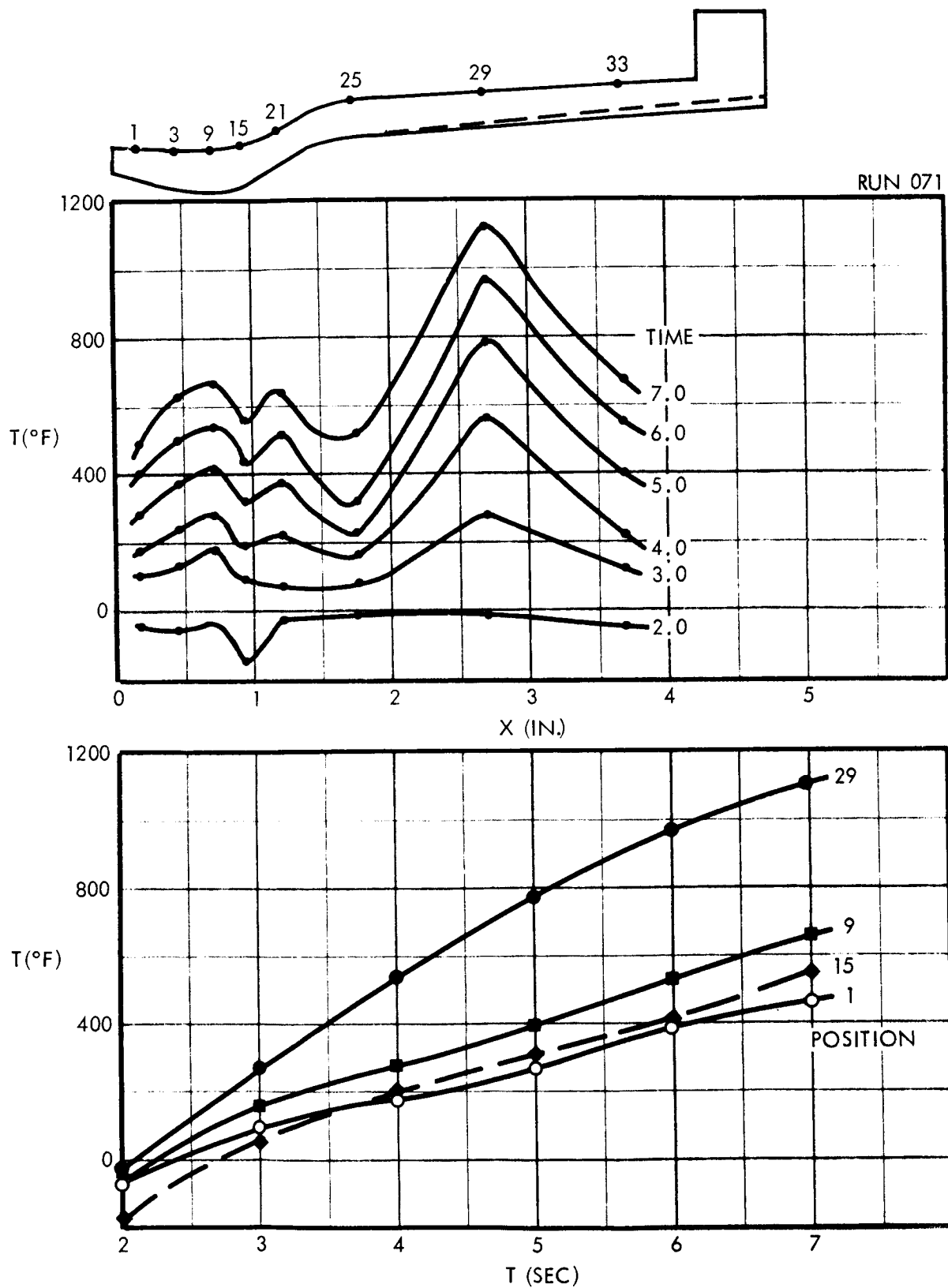


Figure 5-33. Temperature Profile Run (071)
(60% Film Cooling)

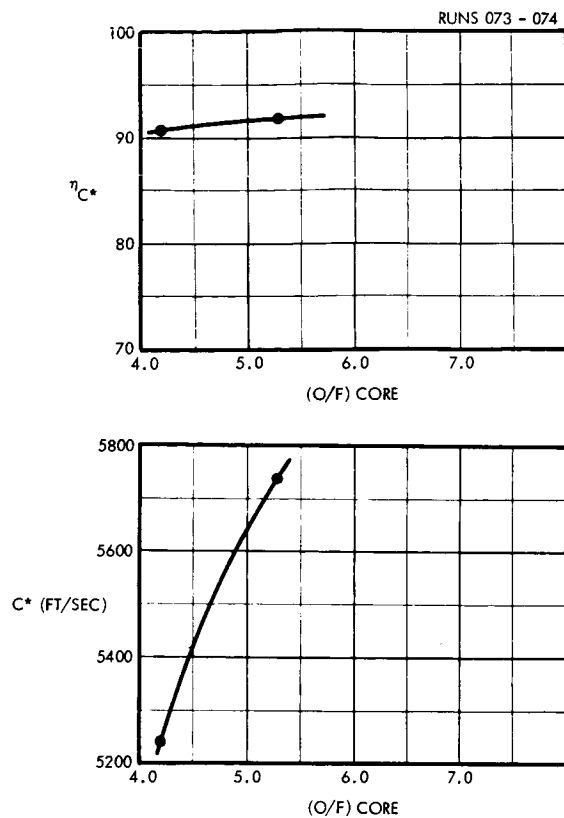
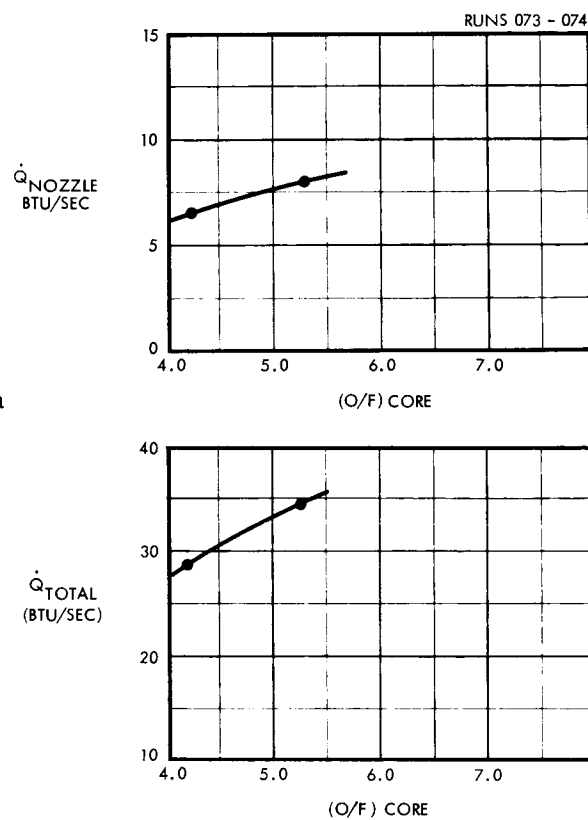


Figure 5-34
Performance Data Runs (073-074) with
60% Film Cooling

Figure 5-35
Heat Transfer Data Run (073-074) with
60% Film Cooling



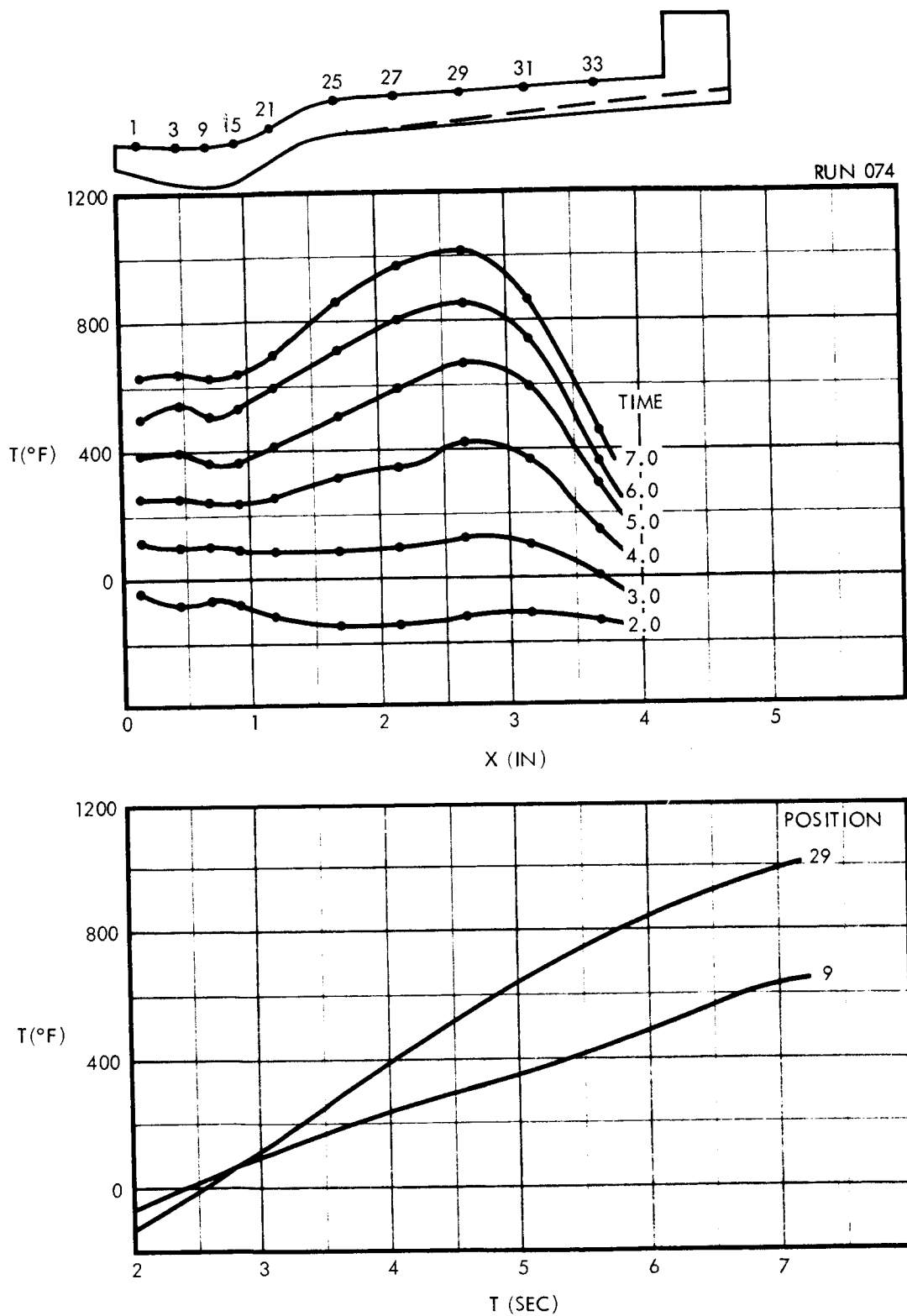
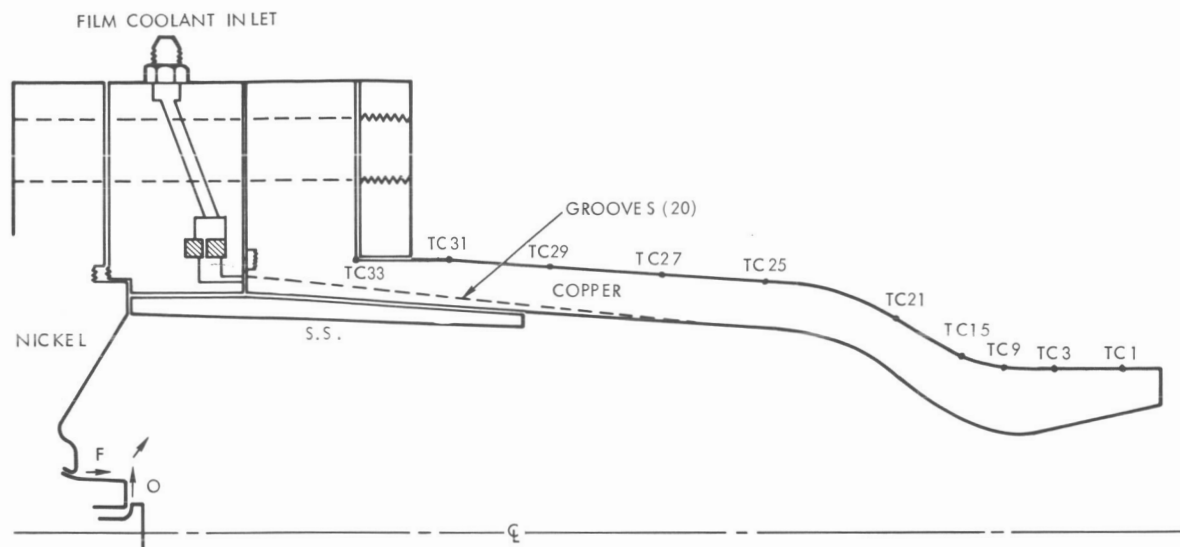
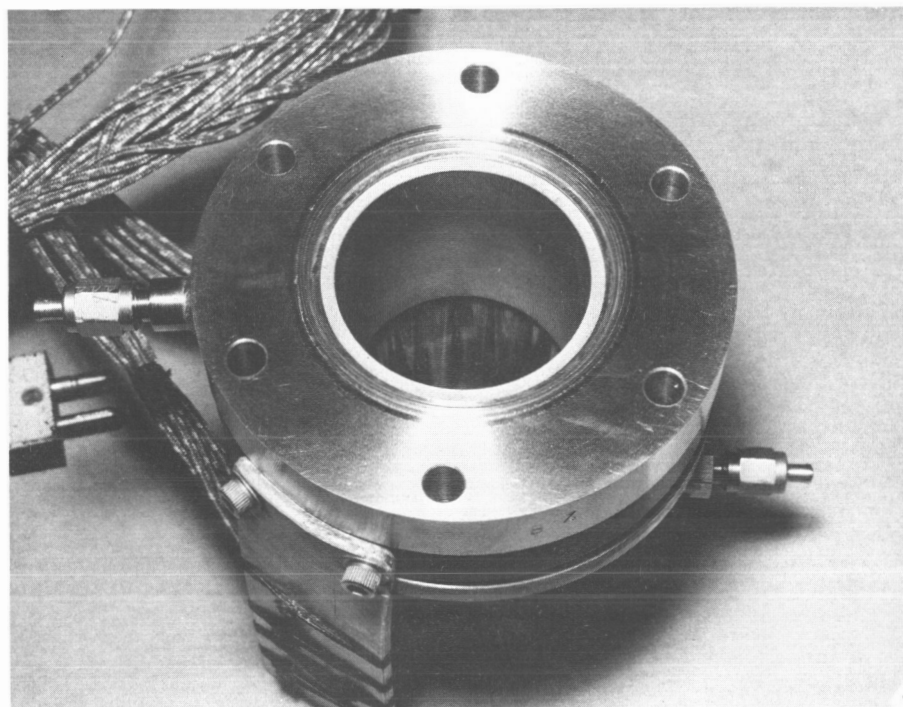


Figure 5-36. Temperature Profile Run (074)
(60% Film Cooling)



A



B

Figure 5-37. Test Hardware with Shroud

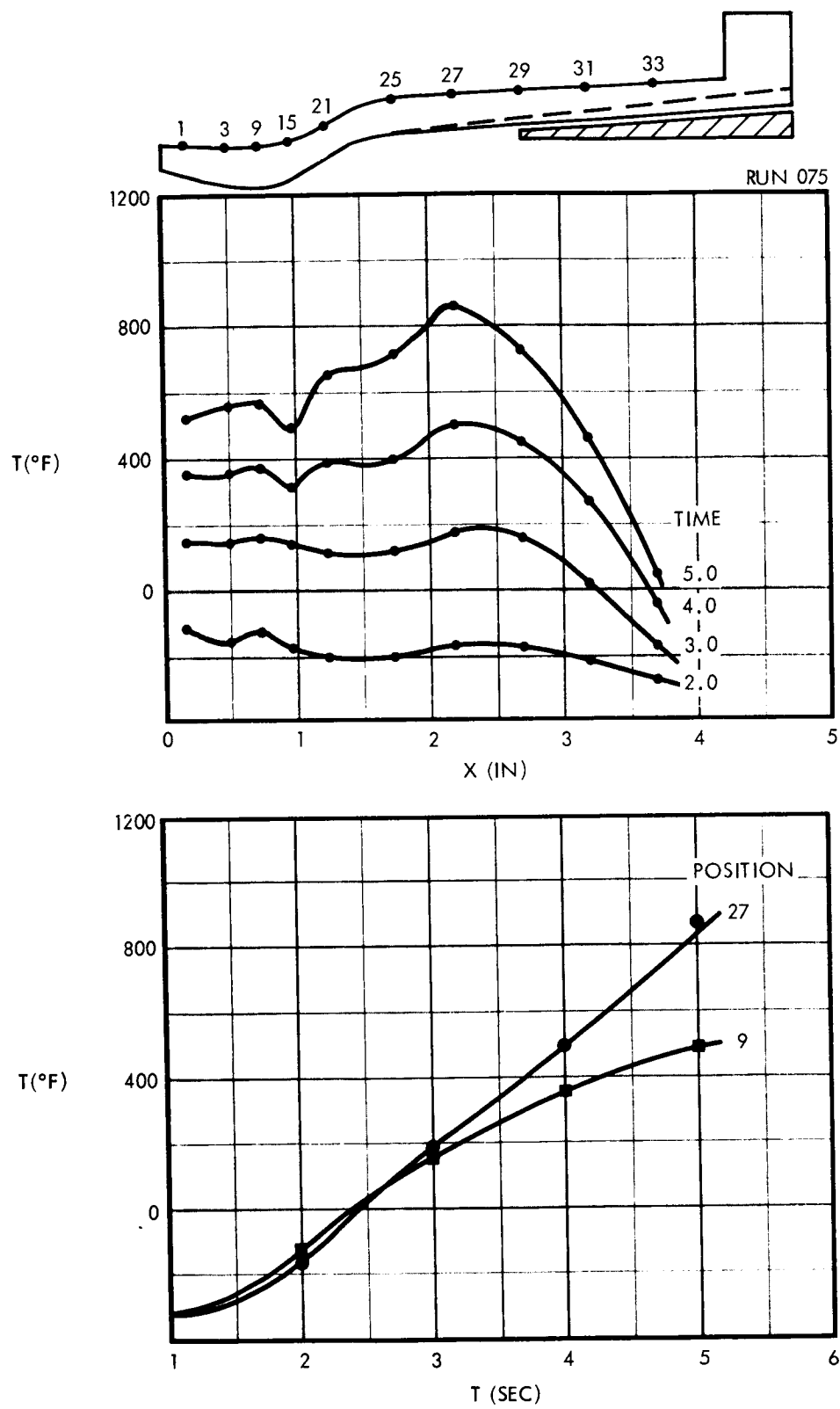


Figure 5-38. Temperature Profile Run (075)
(60% Film Cooling)

Test (076-077): To check on the possibility of primary injection interaction with the wall environmental control, tests were made with the run 073 configuration with increased fuel ΔP drop to force the resultant primary combustion downstream. As shown in Figures 5-39 to 5-41, no significant improvement occurred.

5.2.4.1 Summary of Test Results Through Run 077

The primary observation to be made in all the above runs was the non-occurrence of liquid fuel on the chamber walls. Thermal balances based upon the data showed that no inner-regeneration cooling of any significance was occurring (all heat input to the chamber was going into sensible heat storage). At this point, it was surmised that the fuel volatility and density might be such as to require special attention to minimizing combustion gas interaction effects. To check this hypothesis, a final series of tests was performed. Also, a thick wall set of tests was conducted to determine if the thin wall was inhibiting proper spreading of the heat input.

Test (078-081): To check the interaction theory and volatility aspects of the problem, a short test series was conducted with MMH introduced as the film coolant and the core operated with FLOX/LPG. The MMH represents a higher total heat capacity fluid than does the methane-ethane blend. As is seen in Figure 5-42, the chamber operated completely satisfactorily in the inner-regeneratively cooled mode with a conduction feedback heat load of 4.9 Btu/second.

Test (082-084): These tests were performed on a thick walled chamber so that conduction could take place and so that the conducted heat could be spread evenly over the chamber barrel section. System problems were encountered which limited run duration, but the test data did not indicate that anything significant was occurring (Figures 5-43 through 5-44).

Test (085-086): Following correction of the system problems, the final test runs of the program were made. These tests were designed to make every effort possible to minimize interaction between the main combustion gases and the wall coolant. For these tests, a CARB-I-TEX ring was fabricated to surround the primary injection system and to direct the primary combustion toward the center of the chamber (Figure 5-45). This figure also shows the thick wall chamber used in tests (082-086). As can be seen from the temperature profiles (Figure 5-46), successful steady-state conduction cooling was accomplished. The barrel temperature, however, indicates that no liquid fuel was present, while the temperature gradient can be used to calculate a conducted heat flow of about 5 Btu/sec. Hence, it appears that the gaseous fuel has more heat capacity than previously assumed. Successful operation was apparently due to a greatly decreased wall mixture ratio, which resulted in a decreased wall recovery temperature and increased carbon deposition. The second test run of this sequence (086) was made after the CARB-I-TEX ring was partially destroyed. This run resulted in further destruction of the ring and resultant unsuccessful conduction-cooled operation. Two effects other than the splash ring somewhat cloud the interpretation of this test result. These are the low performance level and the high fuel injection ΔP which resulted in a

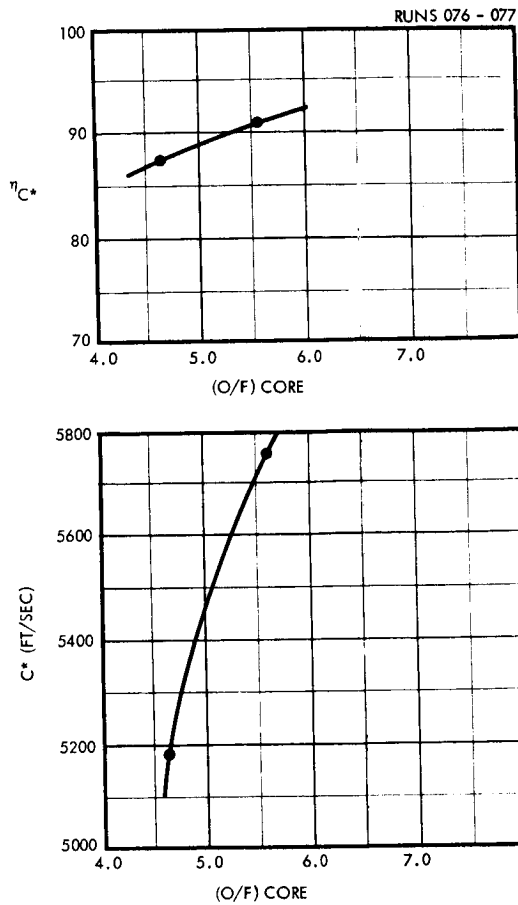
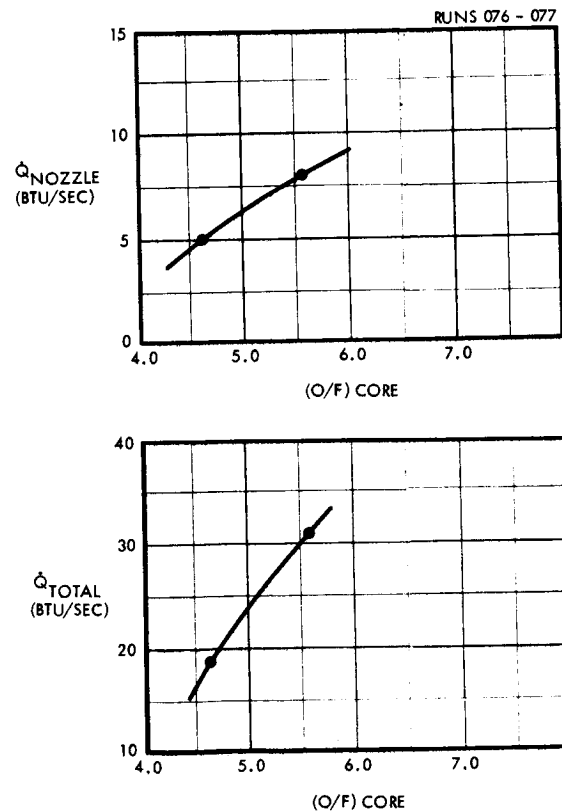


Figure 5-39
Performance Data Runs (076-077)
with 60% Film Cooling and Higher
 ΔP_{IF}

Figure 5-40
Heat Transfer Data Runs (076-077)
with 60% Film Cooling and Higher
 ΔP_{IF}



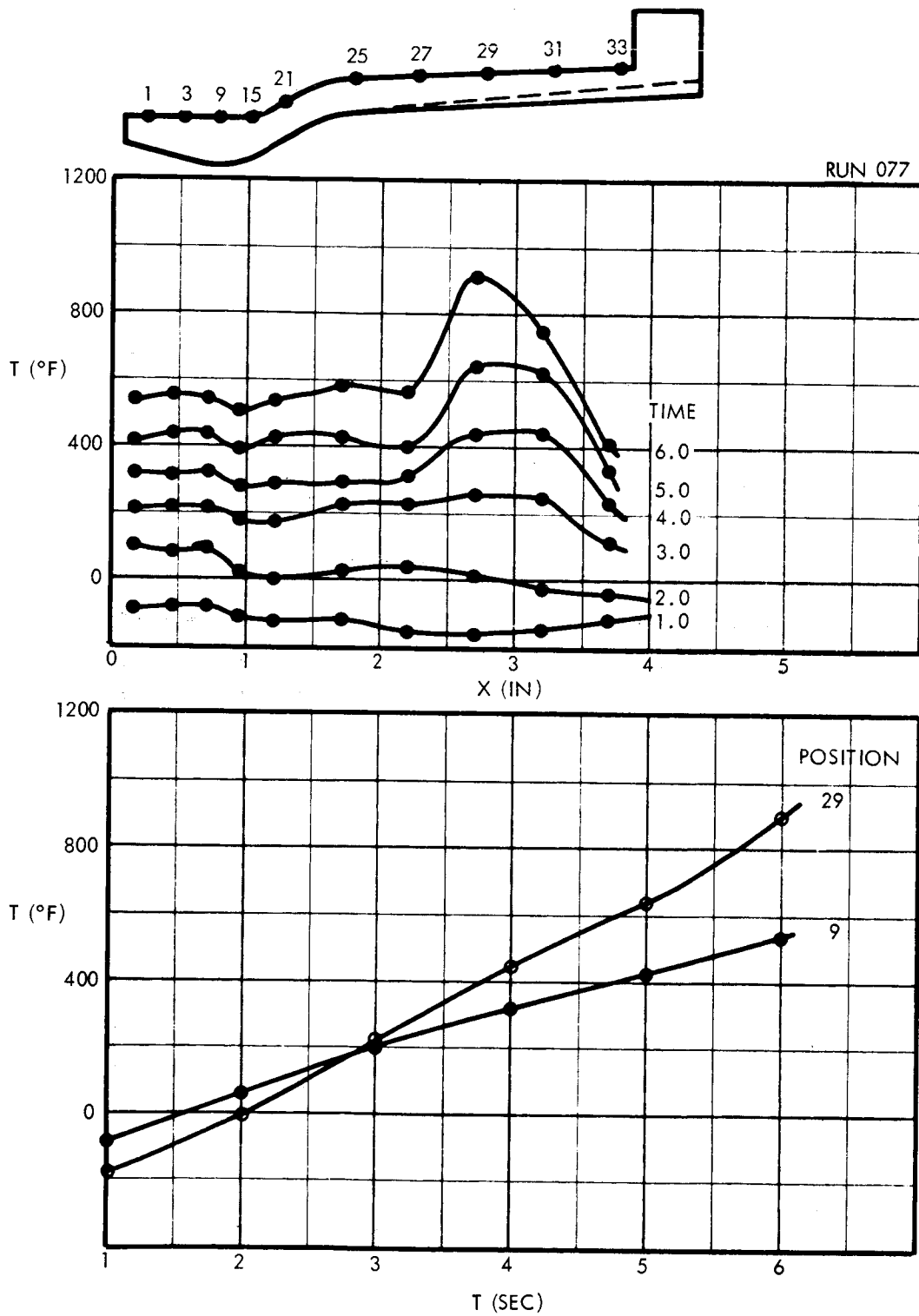


Figure 5-41. Temperature Profile Run (077)
(60% Film Cooling)

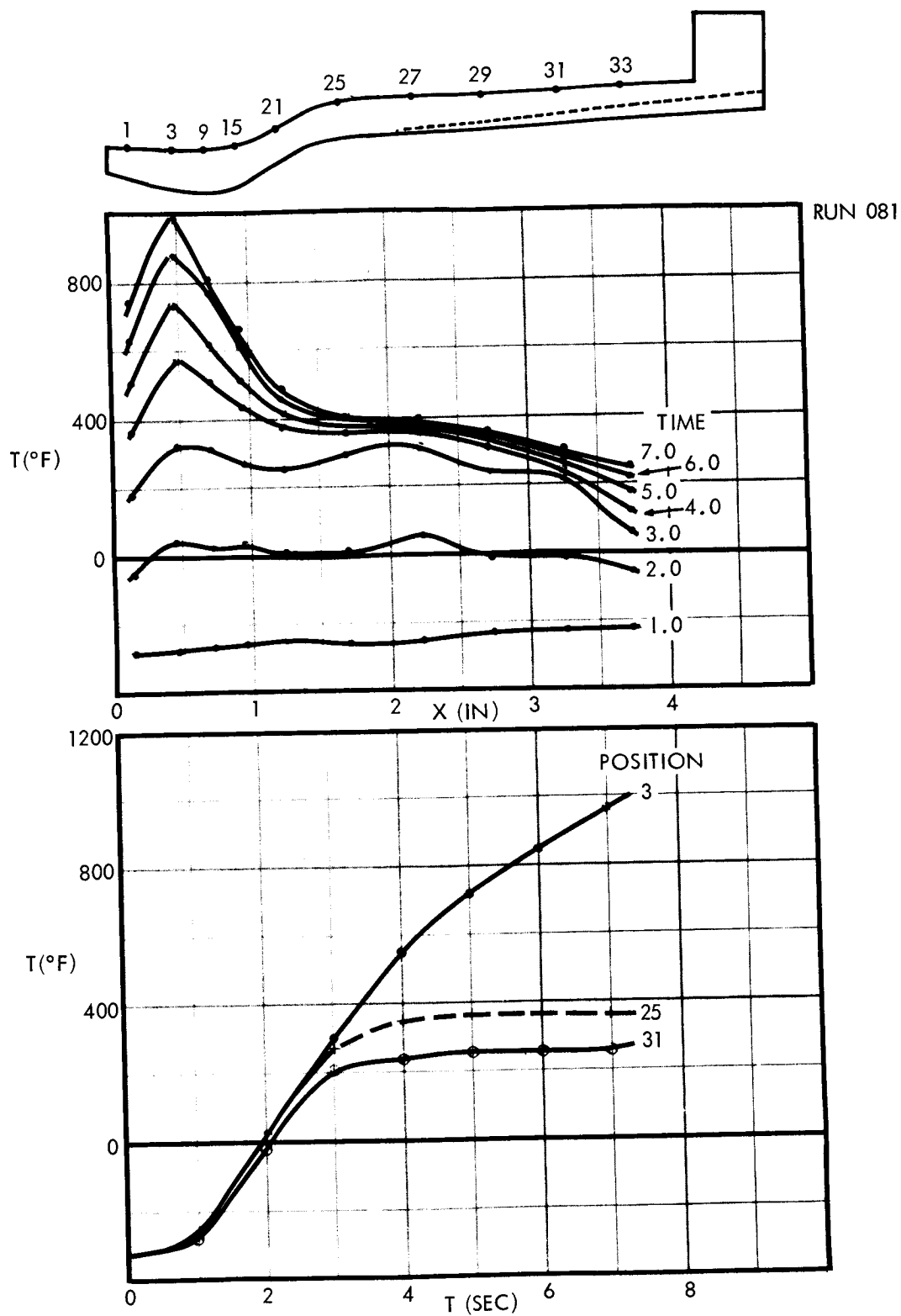


Figure 5-42. Temperature Profile Run (081)
(60% MMH Film Cooling)

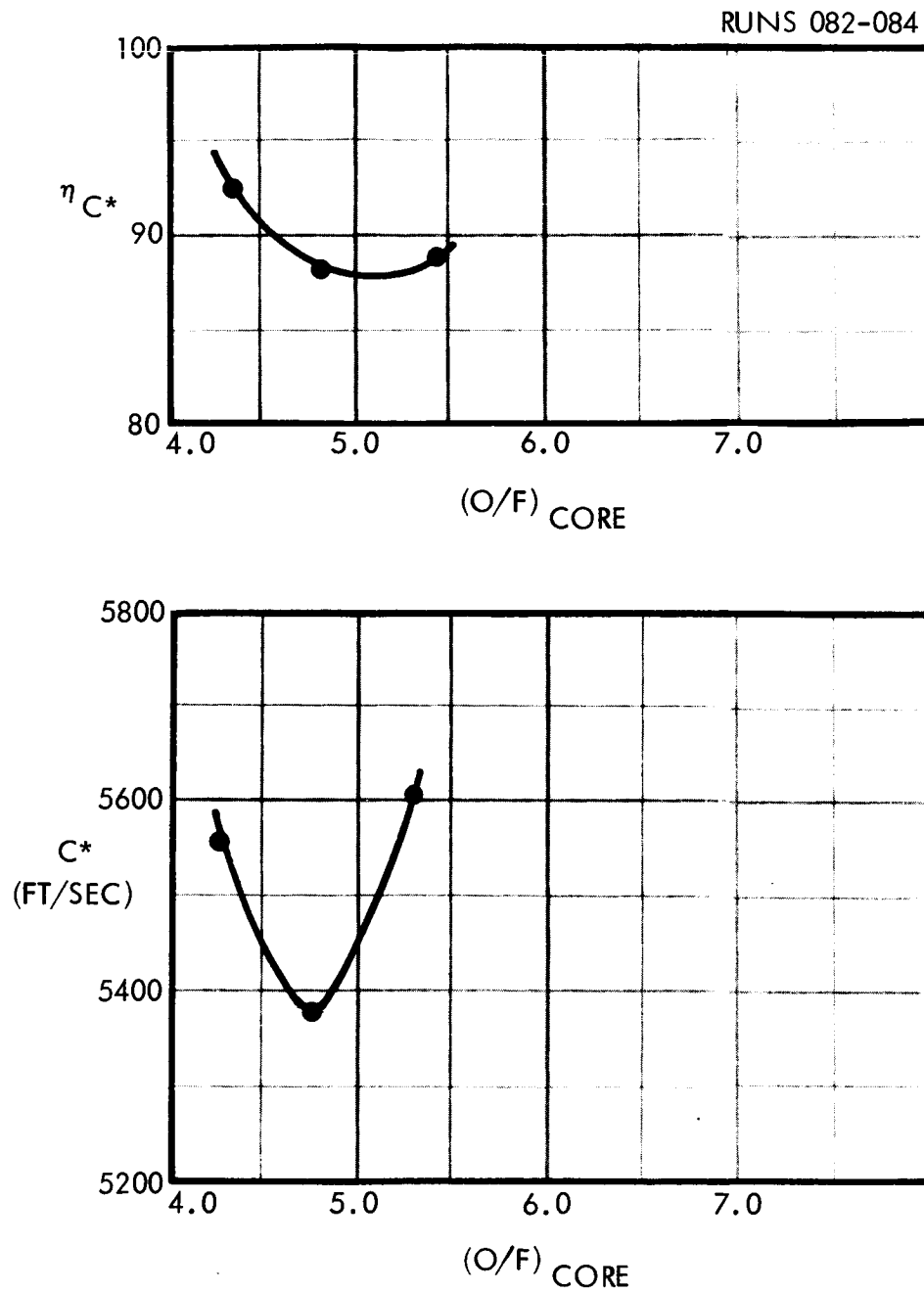


Figure 5-43. Performance Data Run (082-084) with 60% Film Cooling and Thick Walled Chamber

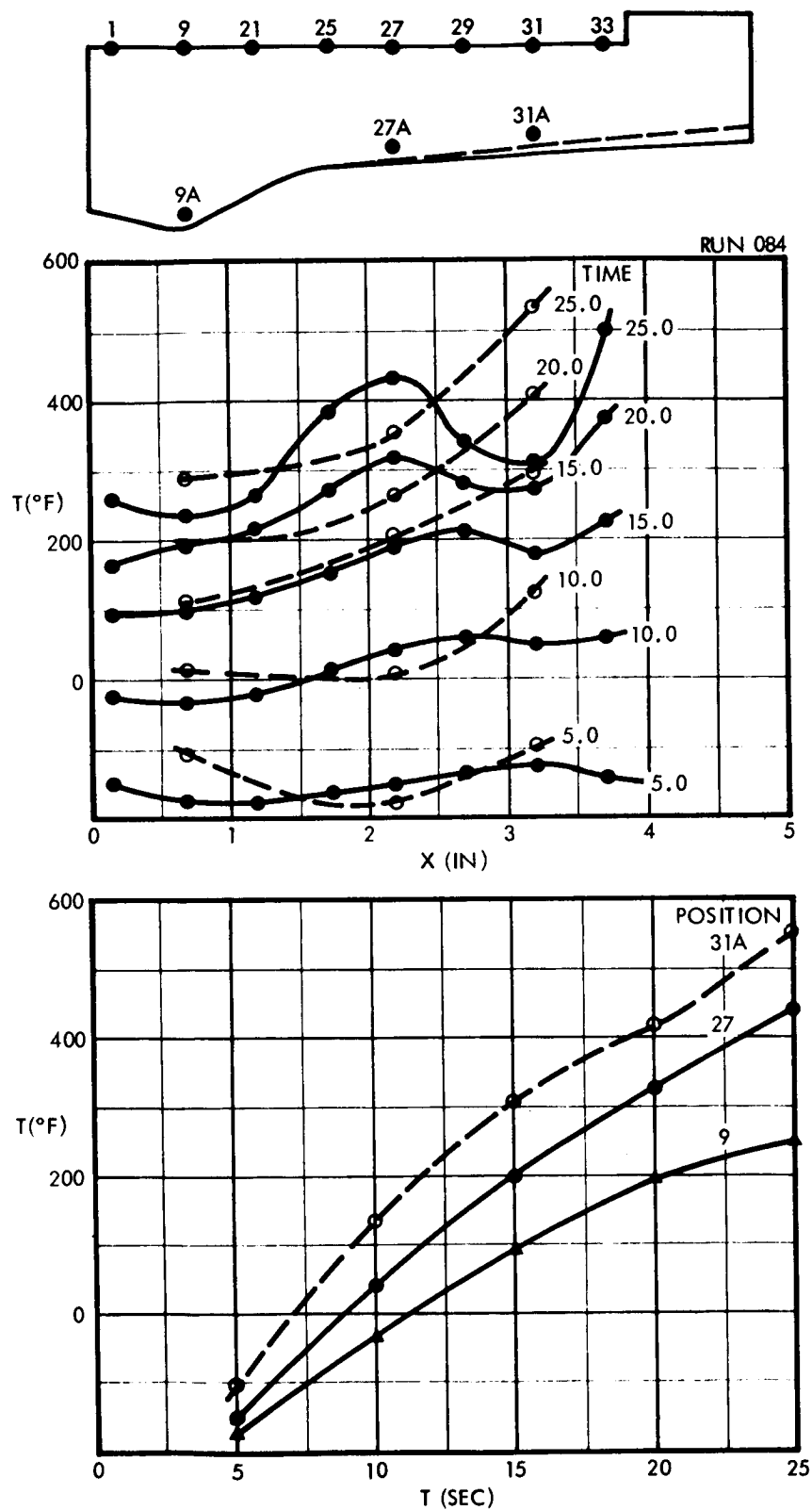
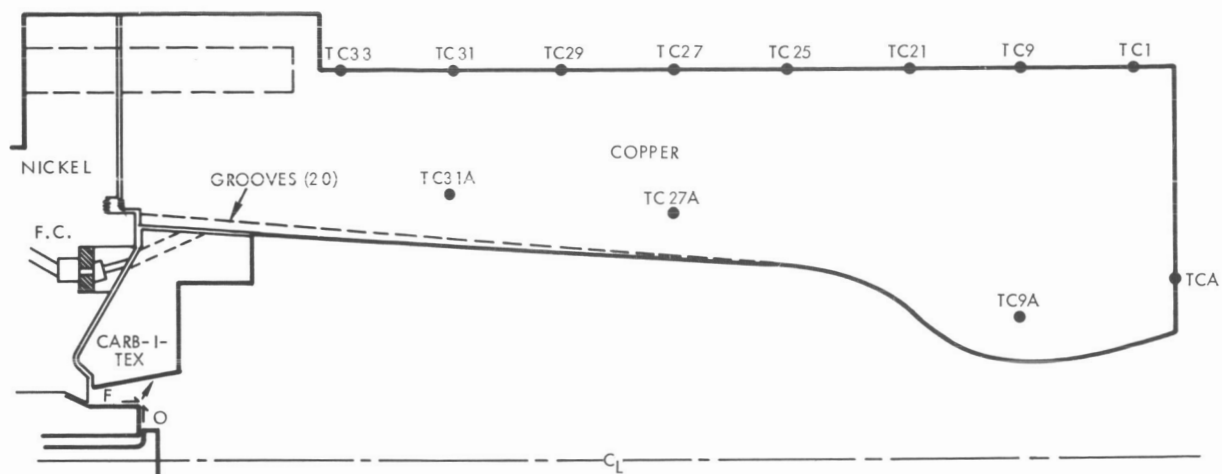
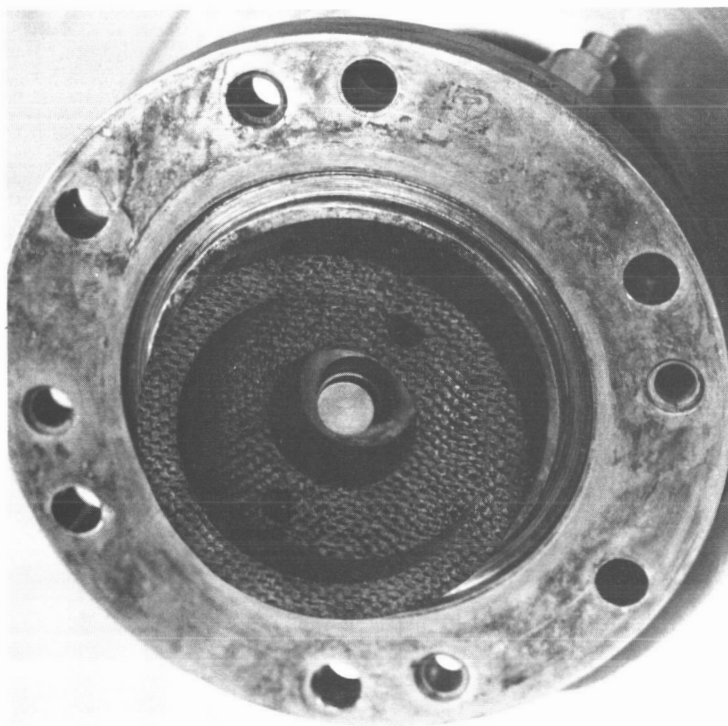


Figure 5-44. Temperature Profile Run (084)
(60% Film Cooling)



A



B

Figure 5-45 Test Hardware with Splash Ring

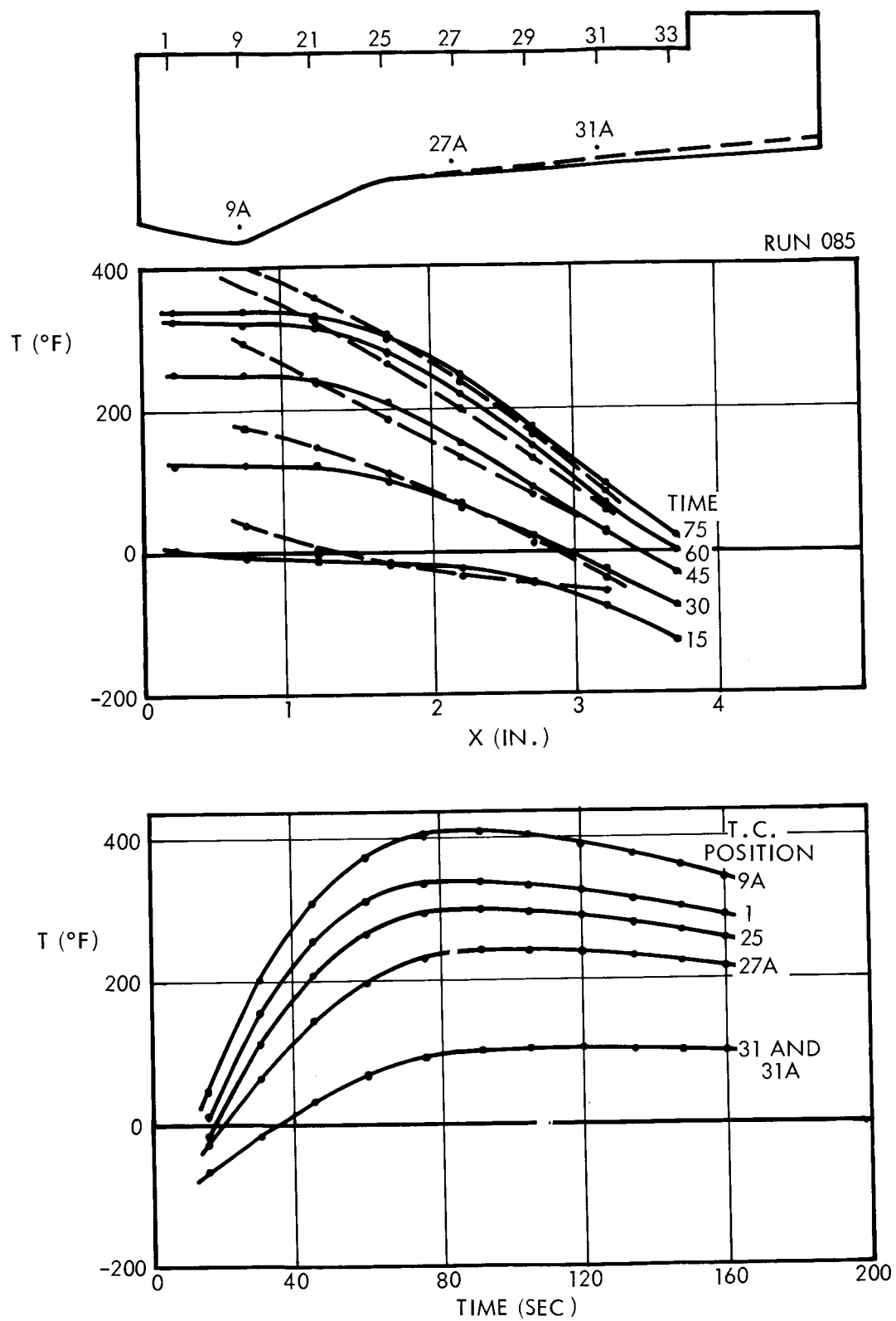


Figure 5-46. Temperature Profile Run (085)
(60% Film Cooling with Splash Ring)

higher film-coolant percentage. It appears from the results of both runs that the high fuel ΔP was responsible for the performance reduction and that the CARB-I-TEX ring was responsible for the improved thermal environment.

5.3 DATA EVALUATION

Following completion of the test program, a complete data evaluation was undertaken in order to determine the pertinent results. Table 5-4 gives a complete summary of all test results obtained during the program with performance given as measured. Table 5-5 gives corrected performance data for the last part of the experimental effort (Runs 045-074). Figure 5-47 shows the correlation between the corrected combustion efficiencies obtained by the thrust and chamber pressure measurements. Appendix D shows how performance is determined and corrected. Included also is a sample correction calculation.

5.3.1 Basic Injector Tests

The basic injector was characterized with regard to several dependent parameters and several independent parameters. The dependent parameters were the characteristic exhaust velocity, the characteristic exhaust velocity efficiency, and the nozzle and total heat loads. The independent parameters were the mixture ratio, characteristic length and chamber pressure. Figures 5-48 through 5-53 are self-explanatory summaries of the basic injector heat transfer and performance characteristics. As can be seen the heat transfer and performance show relatively weak dependence on the mixture ratio and chamber pressure while they are significantly affected by the characteristic length. The chamber pressure and characteristic length dependencies of the heat load are quite similar to the analytical results of Section 3.2.2.2. These results showed that the basic injector was operating at the desired performance levels; however, the heat transfer rates were much too high for conductive cooling.

5.3.2 Film Cooling Tests

These tests were designed to decrease the nozzle heat loads to the analytically predicted loads that a liquid fuel layer in the chamber could absorb. This was to be accomplished by providing a lower mixture ratio wall environment. Two factors resulting from the mixture ratio decrease were increased carbon deposition and decreased wall recovery temperature. Each of these acts to decrease the heat transfer to the chamber walls. Figures 5-54 through 5-57 give a summary of the film-coolant heat transfer and performance results.

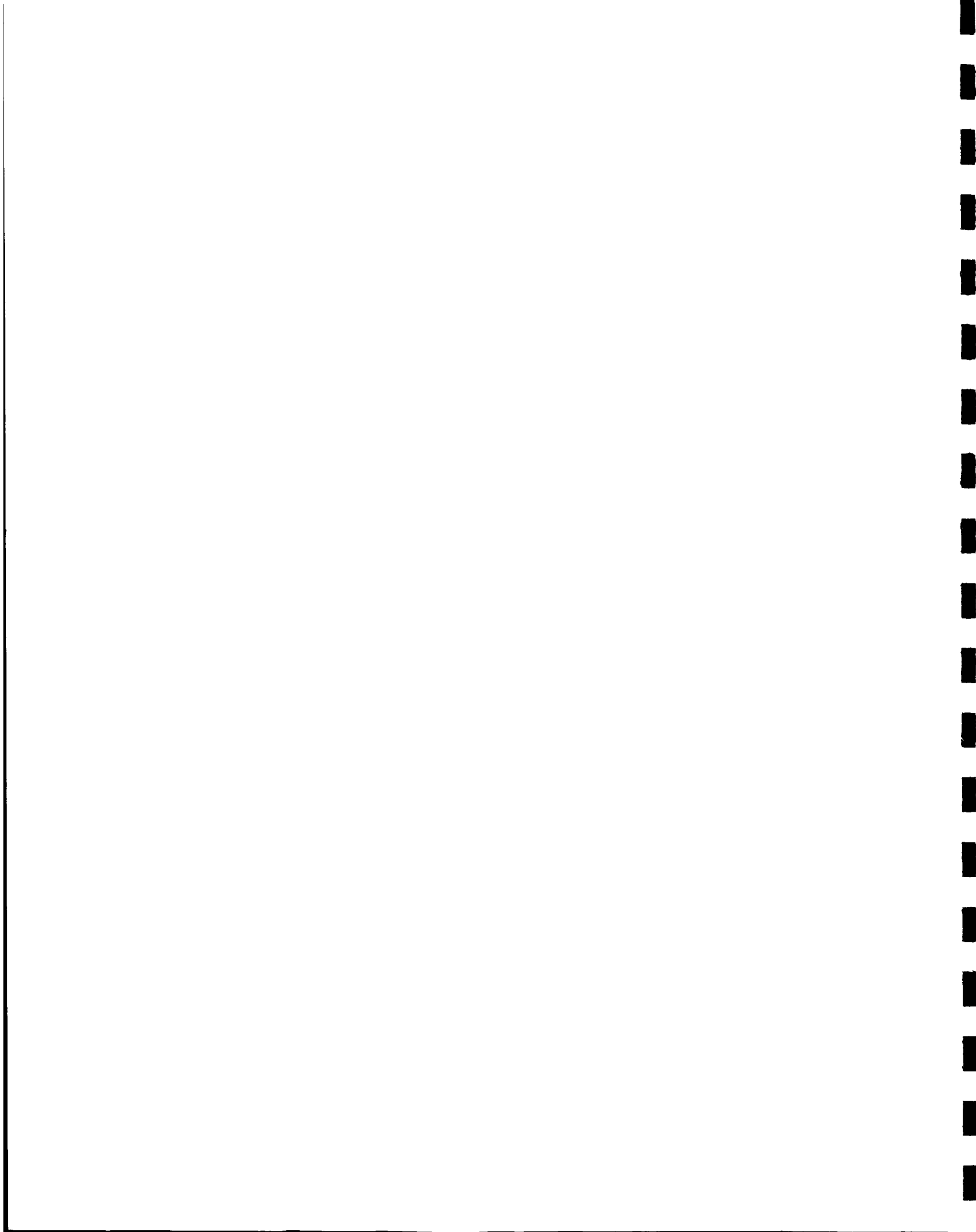


Table 5-4. Total Program Performance
and Heat Transfer Data

	Duration (sec)	(O/F) Overall	(O/F) Core	$\dot{\omega}_t$	$\dot{\omega}_o$	$\dot{\omega}_f$	$\dot{\omega}_{fc}$	%F.C.	C* _{theo}	P _o	C* _P measured	η_{c*P} measured	F _{corr}	C* _F measured	η_{c*F} measured	ΔP_{io}	ΔP_{if}	\dot{Q}_{total}	\dot{Q}_{nozzle}	
001	10.0	6.25	6.25	.271	.234	.0374	0	0	6688	65.9	4608	68.9	56.2	--	--	95.6	451.3	--	--	fuel center, L* = 15
002	6.5	5.10	5.10	.291	.243	.048	0	0	6885	66.7	4365	63.4	57.1	--	--	117.4	21.6	--	--	
003	7.0	4.04	4.04	.335	.268	.066	0	0	6740	59.4	3424	50.8	51.6	--	--	180.8	35.7	--	--	
004	7.0	3.03	3.03	.358	.269	.089	0	0	6601	82.2	4429	67.1	71.3	4286	64.9	152.7	115.2	--	--	
005	5.5	3.92	3.92	.330	.262	.067	0	0	6750	92.2	5400	80.0	77.9	5213	77.2	28.3	23.3	--	--	oxidizer center, L* = 15
006	5.5	2.96	2.96	.352	.263	.089	0	0	6594	101.1	5552	84.2	78.9	5043	76.5	27.0	37.5	--	--	
007	6.0	3.94	3.94	.333	.265	.067	0	0	6763	94.7	5498	81.3	80.8	5388	79.7	48.4	127.8	--	--	
008	5.5	3.03	3.03	.358	.269	.089	0	0	6599	86.2	4646	70.4	71.8	4366	66.2	40.6	150.2	--	--	
009	4.5	3.35	3.35	.294	.226	.068	0	0	6655	82.4	5404	81.2	76.0	5563	83.6	29.3	106.0	--	--	oxidizer center, swirl L* = 15
010	5.0	3.93	3.93	.333	.266	.068	0	0	6754	86.5	5032	74.5	73.0	4775	70.7	153.2	130.1	--	--	
011	5.5	2.99	2.99	.355	.266	.089	0	0	6588	85.8	4648	71.1	72.6	4446	67.5	226.5	225.0	--	--	
012	5.5	3.59	3.59	.311	.243	.068	0	0	6703	82.2	5121	76.4	69.7	4823	72.0	141.1	50.0	--	--	
013	4.0	3.30	3.30	.288	.221	.067	0	0	6655	90.7	5976	89.8	75.6	5842	87.8	58.3	25.7	--	--	oxidizer center, L* = 15
014	4.5	3.71	3.71	.310	.244	.066	0	0	6770	81.4	4986	74.2	69.6	4819	71.7	403.9	23.5	--	--	
015	4.5	3.96	3.96	.325	.260	.066	0	0	6756	78.2	4790	70.9	67.1	4376	64.8	138.3	24.2	--	--	
016	4.5	4.00	4.00	.328	.262	.065	0	0	6756	78.6	4797	71.0	--	--	--	96.8	24.4	--	--	
017	5.0	4.79	4.79	.302	.250	.052	0	0	6899	94.1	5885	85.3	76.3	5602	81.2	42.4	15.0	--	--	oxidizer center, L* = 15
018	5.0	3.16	3.16	.329	.250	.079	0	0	6632	94.4	5412	81.6	75.9	5119	77.2	37.7	32.1	--	--	
019	5.0	3.01	3.01	.265	.199	.066	0	0	6569	50.6	3580	54.5	39.6	--	--	13.0	23.8	--	--	
020	5.0	4.10	4.10	.331	.266	.065	0	0	6792	92.3	5237	77.1	76.2	5087	74.9	52.5	22.6	--	--	
021	5.5	4.96	4.96	.384	.320	.064	0	0	6912	86.4	4223	61.1	69.7	3954	59.7	154.9	22.6	--	--	oxidizer center, canted L* = 15
022	5.5	3.19	3.19	.271	.206	.064	0	0	6620	64.5	4528	68.4	52.7	--	--	52.5	265.9	--	--	
023	5.5	4.09	4.09	.330	.265	.064	0	0	6779	85.4	4915	72.5	71.1	4681	69.0	100.2	481.1	--	--	
024	5.5	3.08	3.08	.354	.267	.087	0	0	6595	61.5	3304	50.1	51.5	--	--	76.8	594.7	--	--	
025	5.5	4.97	4.97	.384	.320	.064	0	0	6922	93.3	4610	66.6	76.6	4417	63.8	90.5	508.5	--	--	oxidizer center, L* = 15
026	5.5	2.97	2.97	.251	.192	.065	0	0	--	44.5	3292	--	35.9	--	--	46.2	33.9	--	--	
027	5.0	5.00	5.00	.309	.257	.051	0	0	6910	83.5	5148	74.5	69.1	4850	70.2	70.3	21.7	--	--	
028	5.0	5.21	5.21	.315	.264	.051	0	0	6906	79.7	4827	69.9	67.0	4529	65.6	69.2	21.5	--	--	
029	4.0	5.63	5.63	.301	.255	.045	0	0	6825	77.2	4900	71.8	64.0	4486	65.7	53.0	17.3	--	--	oxidizer center, L* = 15
030	4.5	5.04	5.04	.307	.256	.051	0	0	6920	90.6	5619	81.2	75.3	5398	78.0	71.7	25.7	--	--	
031	4.0	3.88	3.88	.327	.260	.067	0	0	6746	86.2	5019	74.4	71.4	4753	70.5	86.7	38.1	--	--	
032	4.0	3.04	3.04	.346	.261	.086	0	0	6608	88.7	4877	73.8	73.3	4640	70.2	77.7	62.9	--	--	
033	4.5	4.74	4.74	.387	.319	.067	0	0	6912	112.0	5516	79.8	93.0	5495	79.5	125.3	41.0	--	--	oxidizer center, slots (-1), L* = 15
034	5.0	5.28	5.28	.321	.260	.051	0	0	6915	94.8	5629	81.4	79.0	5465	79.0	89.9	18.8	--	--	
035	4.0	4.17	4.17	.334	.269	.064	0	0	6792	81.3	4646	68.4	68.5	4399	64.8	54.3	28.4	--	--	
036	Run Invalid - Lost Pintle Tip																			
037	5.0	5.10	5.10	.312	.261	.051	0	0	6933	102.4	6288	90.7	81.9	5914	85.3	143.0	20.5	--	--	oxidizer center, slots (-1), L* = 22
038	5.0	3.98	3.98	.328	.263	.066	0	0	6782	107.6	6280	92.6	85.7	5937	87.5	144.5	34.2	--	--	
039	5.5	2.91	2.91	.347	.258	.089	0	0	6573	106.9	5903	89.8	84.0	5496	83.6	139.8	61.2	--	--	
040	5.0	4.60	4.60	.381	.314	.067	0	0	6916	126.9	6384	92.3	101.4	6200	89.7	208.0	33.3	--	--	
041	4.5	3.98	3.98	.329	.263	.066	0	0	6767	98.2	5975	88.3	84.7	5756	85.1	145.1	29.6	--	--	oxidizer center, slots (-1), L* = 15
042	5.0	5.15	5.15	.315	.264	.051	0	0	6926	94.4	6005	86.7	81.1	5713	82.5	149.3	20.1	--	--	
043	4.0	5.70	5.70	.313	.262	.051	0	0	6929	98.5	5938	85.7	80.7	5769	83.3	122.0	26.8	46.1	15.4	
044	5.5	3.86	3.86	.328	.261	.068	0	0	6749	94.7	5440	80.6	73.0	5280	78.2	120.4	40.7	37.2	10.6	

Table 5-4. Total Program Performance
and Heat Transfer Data
(Continued)

Run	Duration (sec)	(O/F) Overall	(O/F) Core	\dot{w}_t	\dot{w}_o	\dot{w}_f	\dot{w}_{fc}	%F.C.	C* _{theo}	P _o	C* _P measured	η_{C^*P}	F _{corr}	C* _F measured	η_{C^*F}	ΔP_{io}	ΔP_{if}	\dot{Q}_{total}	\dot{Q}_{nozzle}	
045	4.5	4.00	4.00	.316	.253	.063	0	0	6782	101.7	6065	89.4	82.5	5883	86.7	135.2	37.6	52.8	19.1	oxidizer center, slots (-1), L* = 15, straight, smooth wall chamber
046	4.5	4.49	4.49	.317	.259	.058	0	0	6875	100.7	5974	86.9	81.4	5766	83.9	139.2	33.5	47.8	18.0	
047	4.5	5.15	5.15	.313	.262	.051	0	0	6932	99.0	5947	85.8	81.5	5822	84.0	146.4	27.3	40.3	15.8	
048	4.5	5.58	5.58	.307	.261	.047	0	0	6871	98.4	6025	87.8	81.5	5930	86.4	146.3	19.7	45.1	14.9	
049	4.5	4.94	4.94	.381	.317	.064	0	0	6943	125.8	6214	89.5	103.0	6294	90.6	215.8	36.8	52.1	19.5	oxidizer center, slots (-1), L* = 22
050	4.5	4.86	4.86	.334	.194	.040	0	0	6884	73.1	5886	85.5	60.4	5428	78.8	91.2	15.0	37.6	14.0	
051	5.0	4.07	4.07	.323	.259	.064	0	0	6846	100.4	5983	87.4	83.1	5776	84.4	131.8	37.3	66.2	15.1	
052	5.0	4.45	4.45	.317	.259	.058	0	0	6865	100.0	6014	87.6	83.0	5875	85.6	143.3	33.2	74.6	19.9	
053	4.5	5.00	5.00	.308	.256	.051	0	0	6928	99.6	6180	89.2	81.1	5904	85.2	145.2	28.1	72.4	20.3	oxidizer center, slots (-1), L* = 9
054	4.5	5.71	5.71	.311	.265	.046	0	0	6837	98.9	6058	88.6	81.7	5882	86.0	148.9	21.9	70.0	19.4	
055	4.5	4.04	4.04	.318	.255	.063	0	0	6780	93.4	5627	83.0	77.3	5383	79.4	138.5	40.7	35.1	15.2	
056	5.0	4.55	4.55	.320	.263	.058	0	0	6864	86.5	5773	84.1	77.2	5255	76.6	131.7	33.8	29.4	14.3	
057	5.0	5.21	5.21	.320	.269	.052	0	0	6913	83.2	5551	80.3	70.7	4771	69.0	129.1	28.8	26.0	17.8	L* = 15, straight, smooth wall chamber
058	5.0	5.81	5.81	.319	.272	.047	0	0	6805	83.8	5614	82.5	73.0	4948	72.7	138.0	25.5	23.2	11.2	
059	5.5	4.09	6.94	.3343	.2686	.0657	.027	41.1	6794	92.3	5211	76.75	78.8	5200	76.6	153.3	30.1	42.7	12.2	
060	5.0	3.79	6.42	.3416	.2702	.0713	.029	40.7	6743	98.5	5442	80.74	84.7	5548	81.7	148.6	28.1	57.3	16.8	
*061																				
062	4.0	3.11	5.28	.3454	.2614	.0840	.034	40.5	6625	97.2	5429	81.9	85.7	5540	81.6	154.7	43.5	37.1	11.7	L* = 15, smooth wall tapered chamber with injector film coolant
063	5.0	3.16	5.36	.3504	.2661	.0843	.035	41.5	6632	94.5	5571	84.00	84.1	5326	80.3	154.0	41.1	45.9	13.6	
064	4.5	2.72	4.63	.3668	.2682	.0986	.040	40.6	6507	95.6	5381	82.74	85.4	5180	79.7	151.0	54.9	39.8	10.7	
065	5.0	3.13	6.21	.3447	.2613	.0834	.041	49.4	6637	111.6	6162	92.85	92.2	6116	92.16	147.6	19.5	53.0	14.2	
066	4.5	2.38	4.49	.3692	.2602	.1091	.051	46.8	6396	110.9	5717	89.38	90.1	5580	87.3	144.6	31.65	45.2	9.2	L* = 15, grooved wall tapered chamber with injector film coolant
067	5.5	2.08	5.44	.3862	.2608	.1253	.077	61.5	6294	118.0	5817	92.42	95.5	5708	90.7	152.4	28.74	30.2	7.4	
068	5.5	1.75	4.73	.4015	.2556	.1459	.092	63.0	6083	116.2	5511	90.6	95.6	5484	90.2	143.1	47.7	31.9	7.8	
*069																				
*070																				
071	6.0	2.04	5.14	.3837	.257	.1264	.076	60.3	6277	113.7	5652	90.04	95.7	5681	90.4	130.6	22.7	25.1	5.4	L* = 15, grooved wall tapered chamber with film coolant ring Same as 073 with shroud Same as 073 with higher ΔP_{if}
072	7.5	1.60	4.14	.4192	.258	.1611	.099	61.4	5862	113.9	5258	89.7	96.1	5250	89.6	124.0	35.2	22.8	5.6	
073	5.5	2.00	5.30	.3842	.256	.128	.079	61.7	6262	117.1	5742	91.7	96.0	5755	91.9	130.0	32.2	34.3	8.1	
074	6.5	1.55	4.19	.4197	.2554	.1644	.1024	62.3	5798	116.9	5247	90.5	94.6	5191	89.5	124.4	46.3	28.3	6.4	
075	5.0	2.17	5.46	.3902	.2673	.1229	.074	60.1	6327	119.7	5785	91.43	98.5	5830	92.1	130.4	28.4	34.2	10.2	same as 073 with MMH film coolant
076	5.5	2.14	5.58	.3849	.2623	.1226	.0756	61.6	6314	117.2	5743	90.44	96.3	5762	90.7	126.5	44.6	30.4	7.9	
077	6.5	1.67	4.65	.4231	.2649	.1582	.101	63.8	5970	116.0	5191	87.1	94.5	5137	86.2	125.3	71.9	18.7	4.9	
078	6.0	2.32	5.14	.3756	.2623	.1133	.0622	54.9	--	124.3	6245	--	102.6	--	--	127.1	20.5	**	**	
*079																				
*080																				
081	7.0	1.77	4.04	.4176	.267	.1506	.0845	56.1	--	134.0	6053	--	110.9	--	--	131.2	35.3	**	**	L* = 15, grooved, thick wall tapered chamber with injector film coolant same as 082 with CARB-I-TEX splash ring
082	20.5	2.13	5.39	.3878	.2641	.1237	.075	60.4	6314	114.7	5607	88.8	93.9	5557	88.0	137.7	51.9	**	**	
083	16.0	1.77	4.75	.4165	.2662	.1503	.094	62.7	6065	118.0	5369	88.5	97.7	5406	89.1	129.3	50.2	**	**	
084	28.0	1.63	4.3	.4262	.2644	.1618	.100	62.3	5930	125.5	5553	93.8	104.3	5697	96.2	131.1	47.2	**	**	
085	166.5	1.59	5.63	.4212	.2590	.162	.116	71.7	5880	107.6	4819	82.1	84.6	4560	77.5	108.4	187.0	**	**	
086	66.5	2.06	8.06	.3834	.2579	.1255	.094	74.5	6230	107.1	5217	83.8	83.9	4980	80.0	96.0	131.0	**	**	
* Run Invalid																				

** No Heat Load Data Available

Table 5-5. Space Storable Thruster Corrected Performance

Run	O/F	C_{theo}^*	C_P^*		$\eta_{C_P}^*$		C_P^*		$\eta_{C_P}^*$		C_F^*		$\eta_{C_F}^*$	
			measured	corrected	measured	corrected	measured	corrected	measured	corrected	measured	corrected	measured	corrected
045	4.00	6782	6065	6168	89.4	90.9	5883	5883	86.7	86.7	6148	6148	90.6	90.6
046	4.49	6881	5974	6034	86.9	87.8	5766	5766	83.9	83.9	6008	6008	87.4	87.4
047	5.15	6932	5947	6018	85.8	86.8	5822	5822	84.0	84.0	6049	6049	87.3	87.3
048	5.58	6871	6025	6121	87.8	89.2	5930	5930	86.4	86.4	6179	6179	90.0	90.0
059	4.09	6794	5211	5258	76.8	77.5	5200	5200	76.6	76.6	5392	5392	79.4	79.4
060	3.79	6743	5442	5535	80.7	82.1	5548	5548	81.7	81.7	5775	5775	85.0	85.0
062	3.11	6625	5429	5467	81.9	82.5	5540	5540	81.6	81.6	5728	5728	83.4	83.4
063	3.16	6632	5571	5649	84.0	85.2	5326	5326	80.3	80.3	5539	5539	83.5	83.5
064	2.72	6507	5381	5419	82.7	83.3	5180	5180	89.7	89.7	5361	5361	82.5	82.5
065	3.13	6637	6162	6316	92.8	95.1	6116	6116	92.1	92.1	6373	6373	96.0	96.0
066	2.38	6396	5717	5797	89.5	90.8	5580	5580	87.3	87.3	5792	5792	90.6	90.6
067	2.08	6294	5817	5875	92.4	93.3	5708	5708	90.7	90.7	5885	5885	93.5	93.5
068	1.75	6083	5511	5550	90.6	91.2	5484	5484	90.2	90.2	5659	5659	93.1	93.1
071	2.04	6277	5652	5697	90.0	90.7	5681	5681	90.4	90.4	5846	5846	93.0	93.0
072	1.60	5862	5258	5295	89.7	90.3	5250	5250	89.6	89.6	5397	5397	92.1	92.1
073	2.00	6262	5142	5204	91.7	92.8	5755	5755	91.9	91.9	5945	5945	94.9	94.9
074	1.55	5798	5247	5268	90.5	90.9	5191	5191	89.5	89.5	5347	5347	92.2	92.2

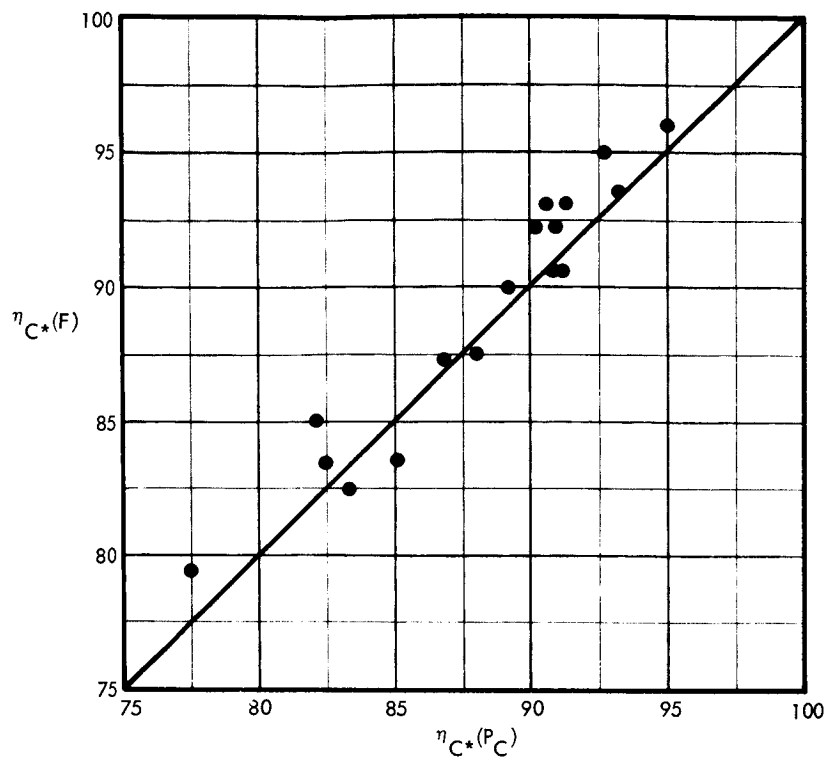


Figure 5-47. Comparison of Thrust and Chamber Pressure C^* Measurements

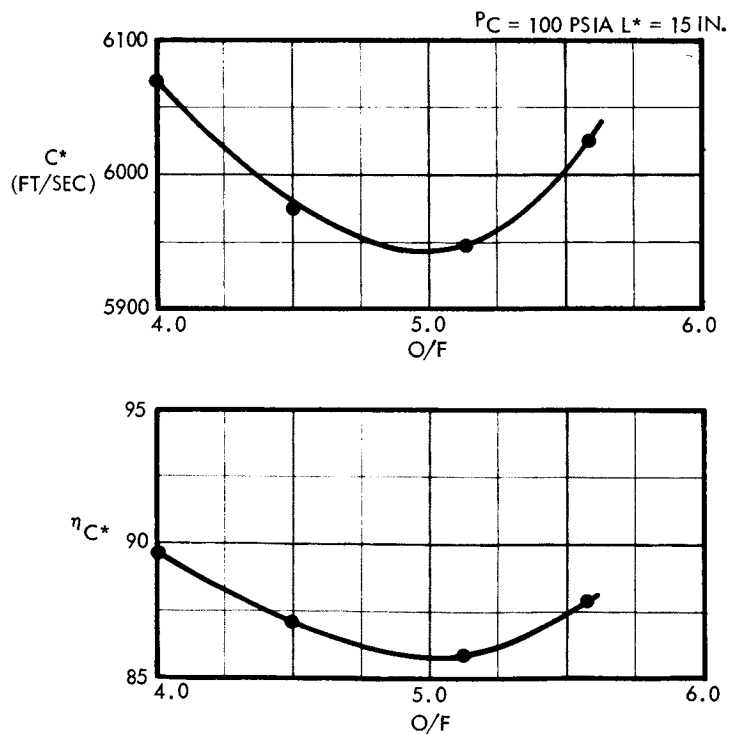


Figure 5-48. Basic Injector Performance Summary (O/F Variation)

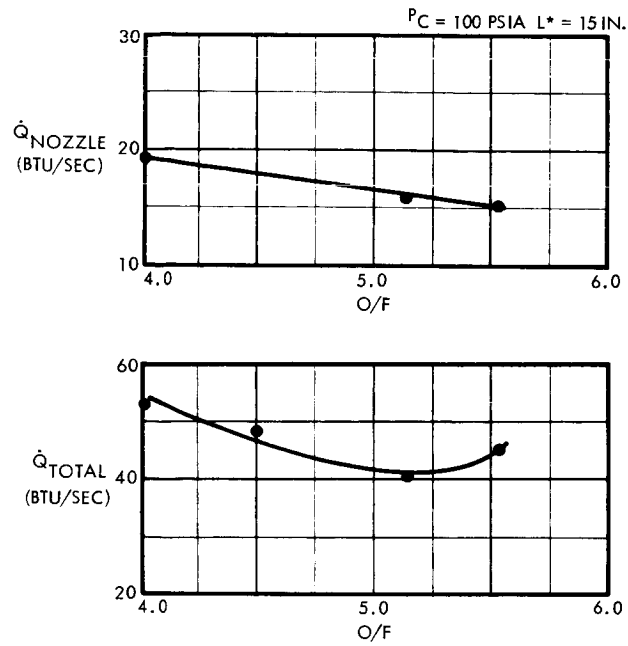


Figure 5-49. Basic Injector Heat Transfer Summary (O/F Variation)

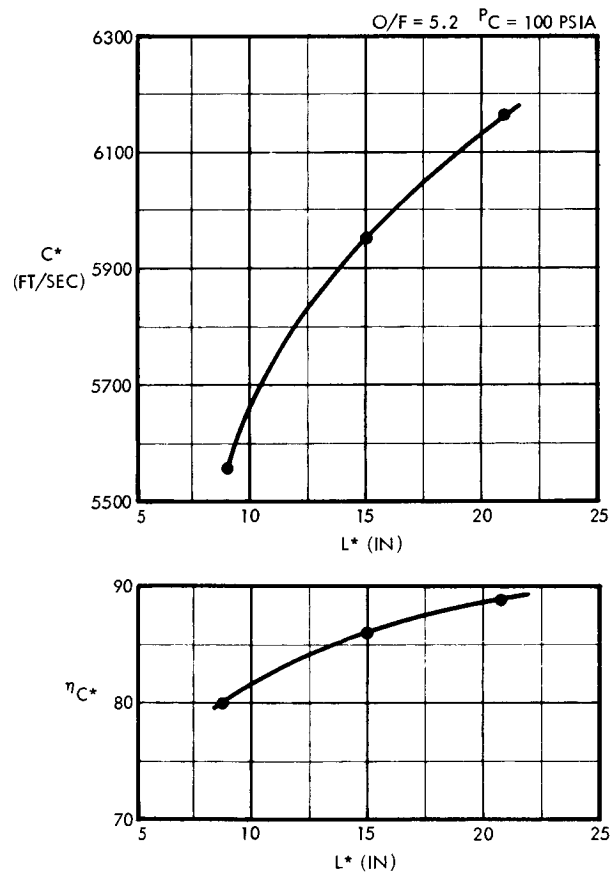


Figure 5-50. Basic Injector Performance Summary (L^* Variation)

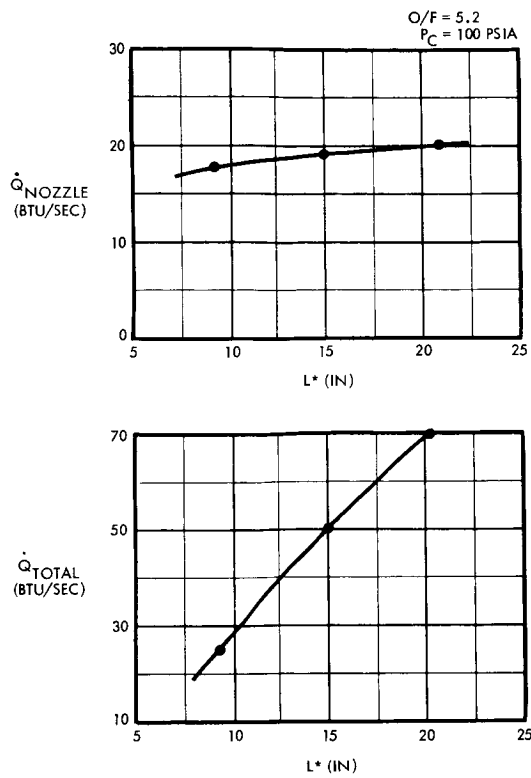


Figure 5-51
Basic Injector Heat Transfer
Summary (L* Variation)

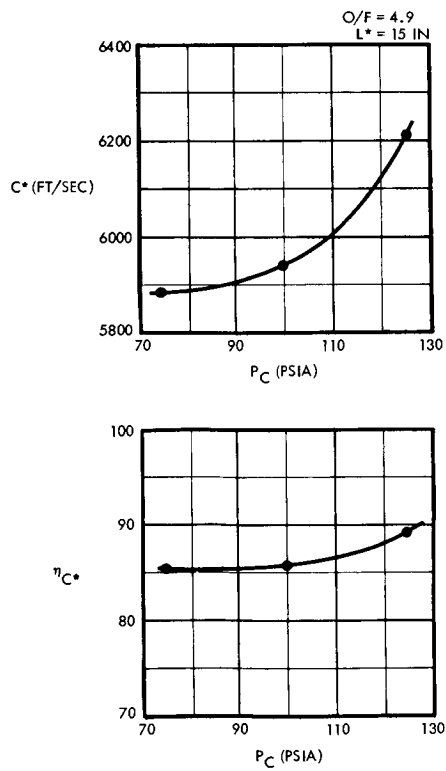


Figure 5-52
Basic Injector Performance
Summary (P_C Variation)

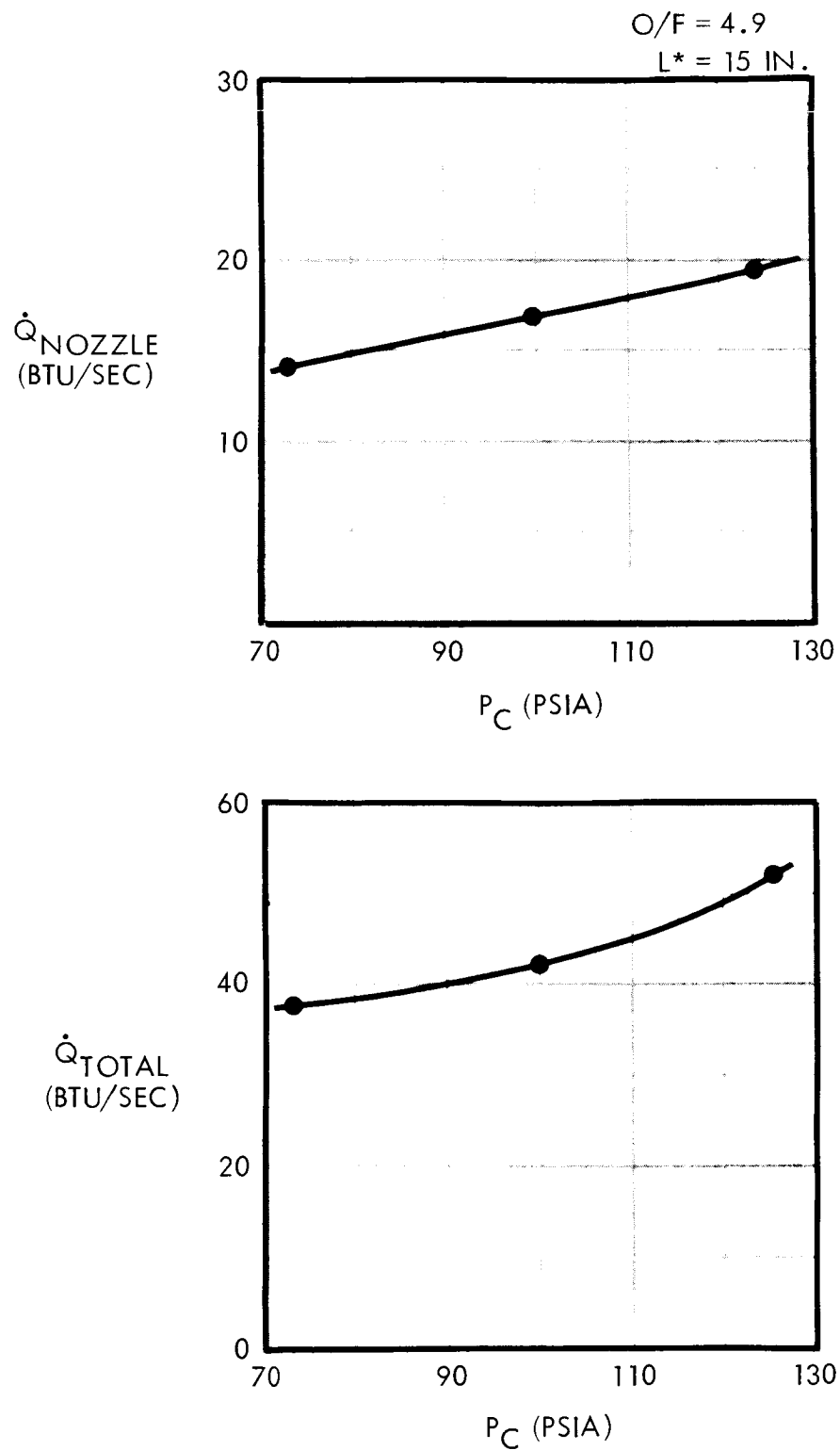


Figure 5-53. Basic Injector Heat Transfer Summary (P_C Variation)

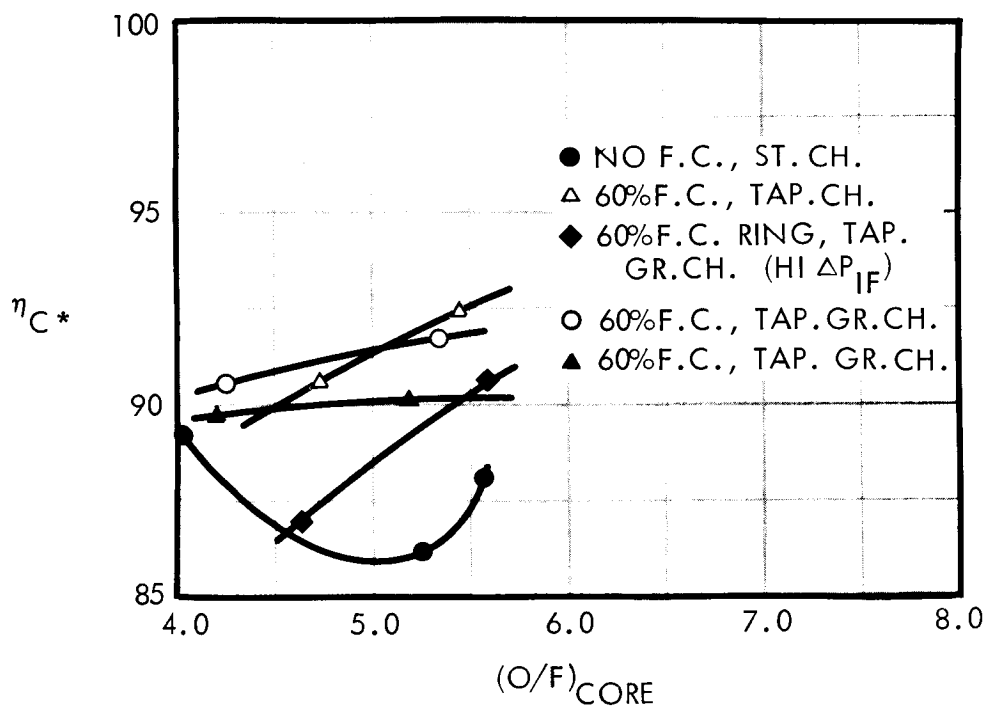
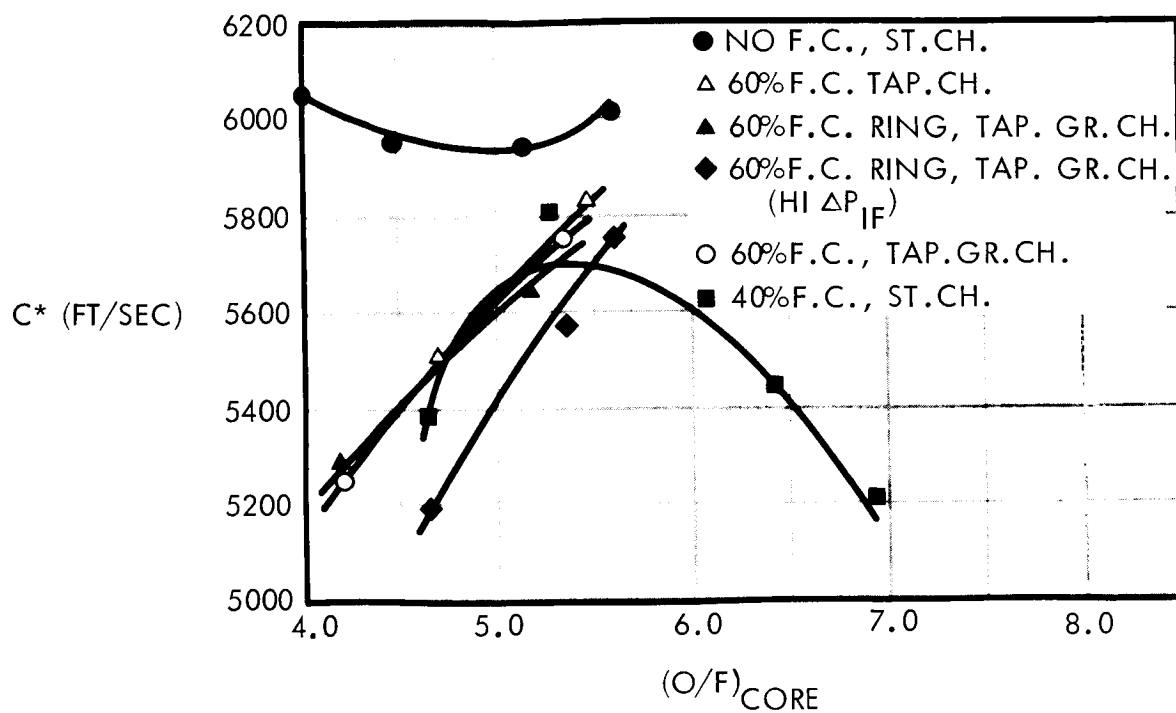


Figure 5-54. Film Cooling Performance Summary (O/F Variation)

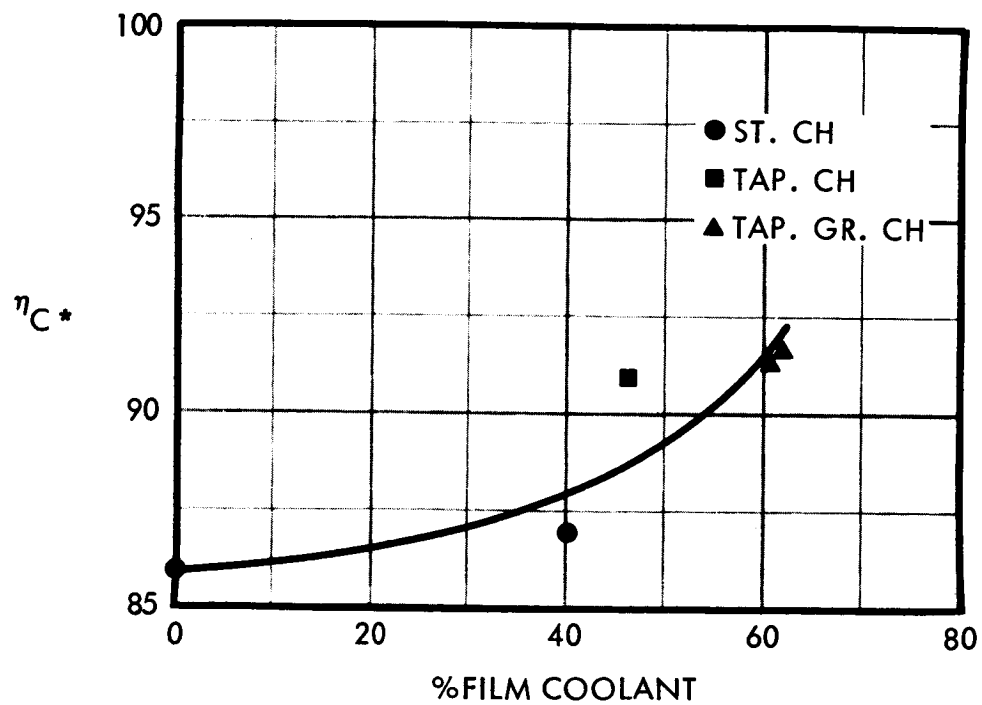
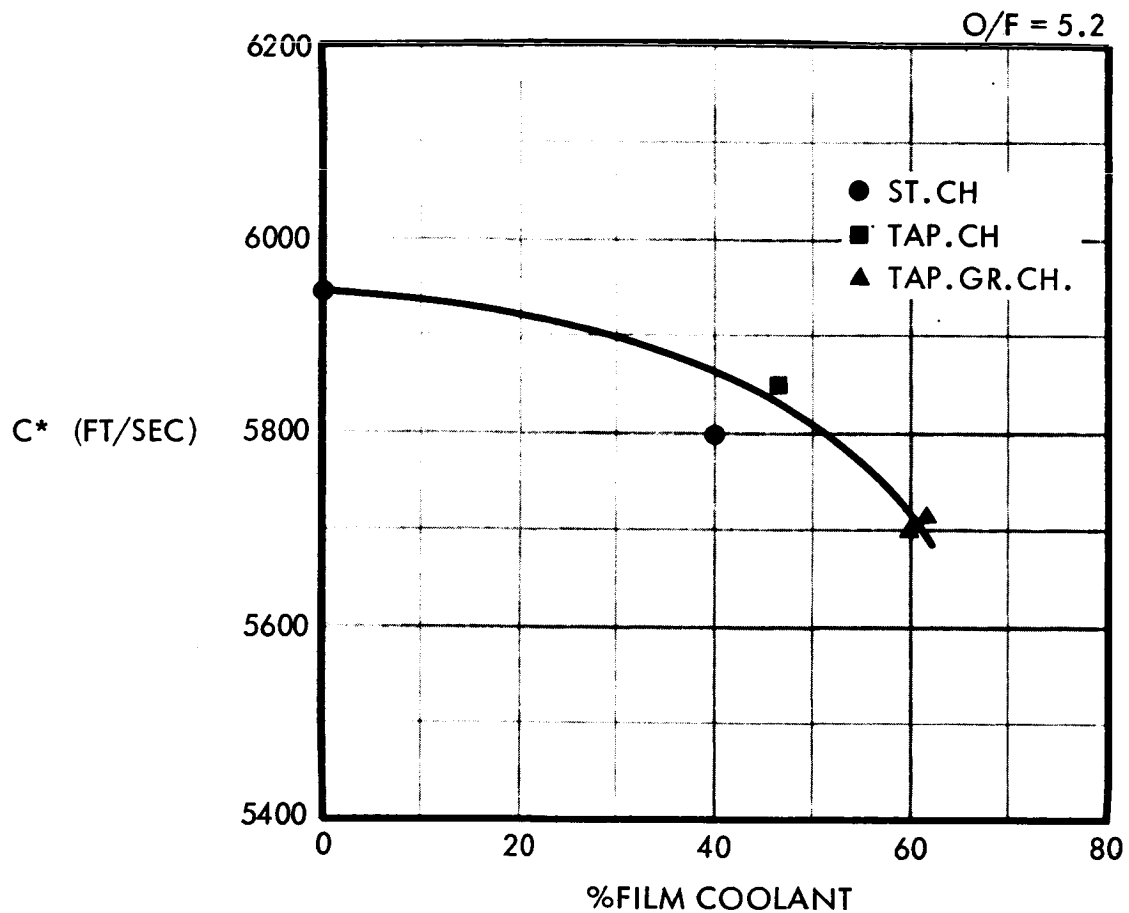


Figure 5-55. Film Cooling Performance Summary
(% F.C. Variation)

HEAT TRANSFER TEST SEQUENCE SYMBOLS

<u>Symbol</u>	<u>Run Numbers</u>	<u>Conditions</u>
■	045-048	No film cooling smooth wall, straight chamber
□	059-064	40% film cooling smooth wall, straight chamber
●	067,068	60% film cooling smooth wall, tapered chamber
○	071,072	60% film cooling grooved wall, tapered chamber
◆	073,074	60% film cooling with ring grooved wall, tapered chamber
▲	076,077	60% film cooling with ring grooved wall, tapered chamber high ΔP_{IF}
◇	075	60% film cooling with ring grooved wall, tapered chamber shroud over film coolant
▽	078-081	60% MMH film cooling with ring grooved wall, tapered chamber
○	085	60% film cooling grooved wall, tapered chamber splash cup on injector

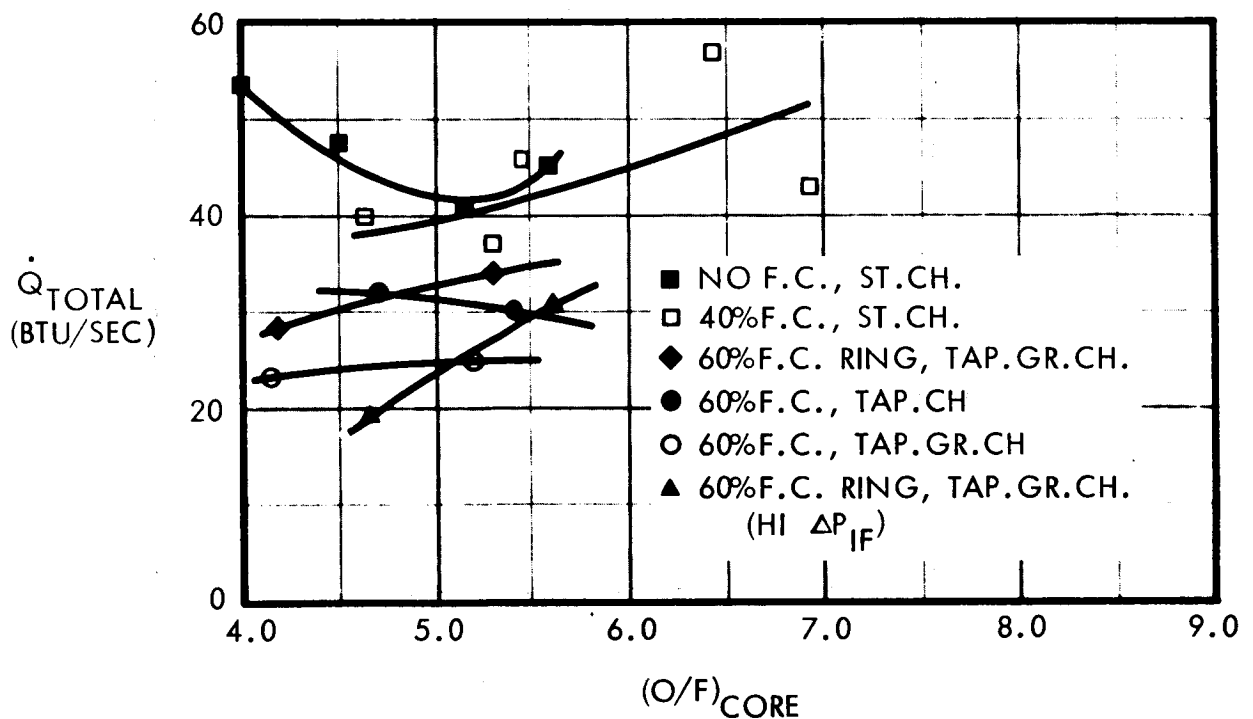
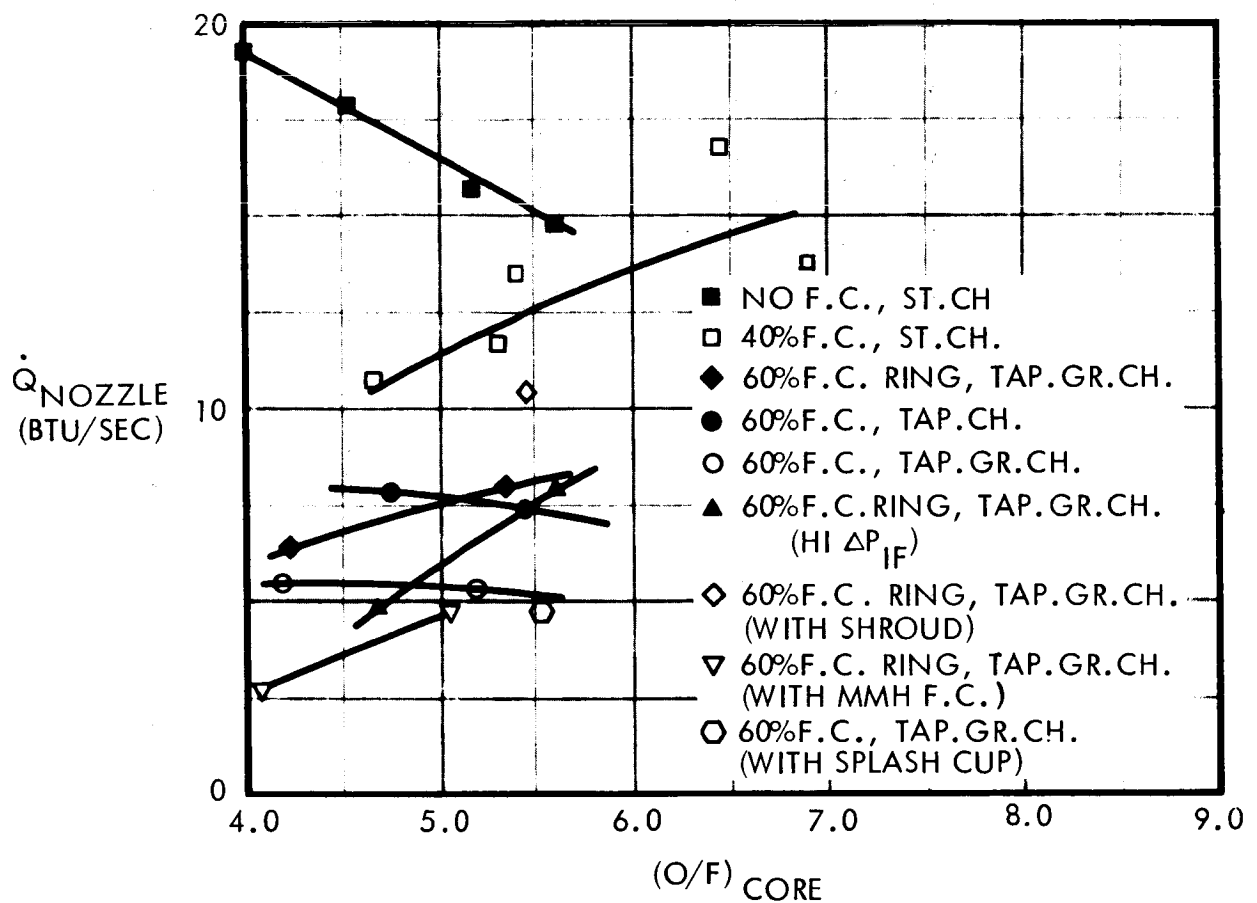


Figure 5-56. Film Cooling Heat Transfer Summary (O/F Variation)

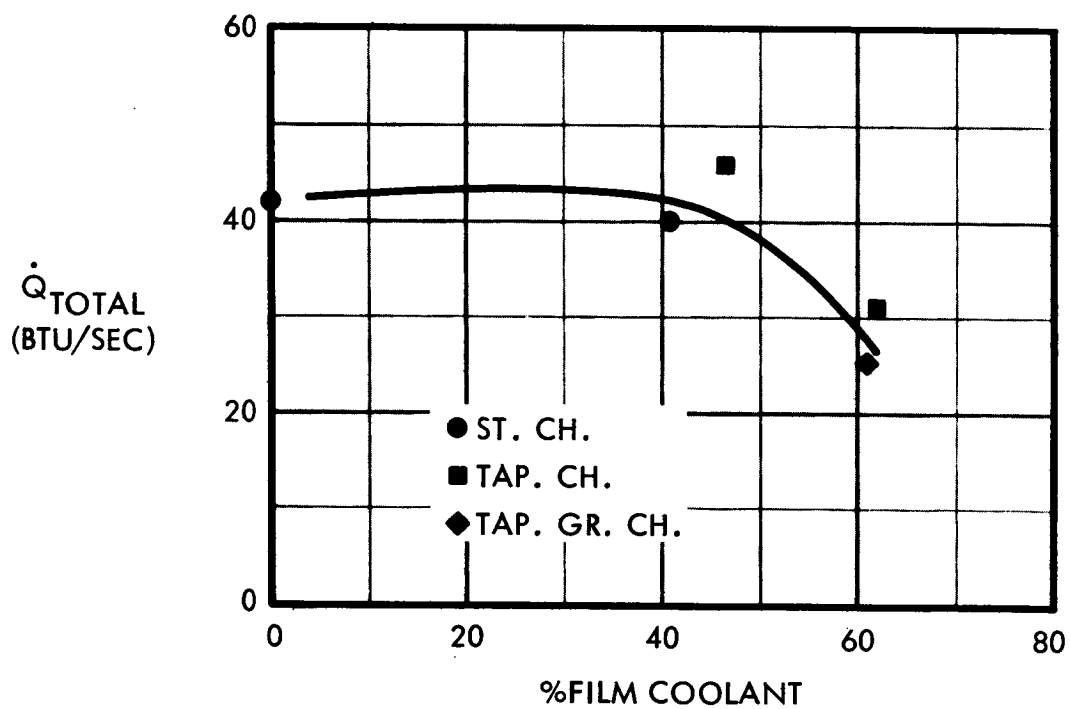
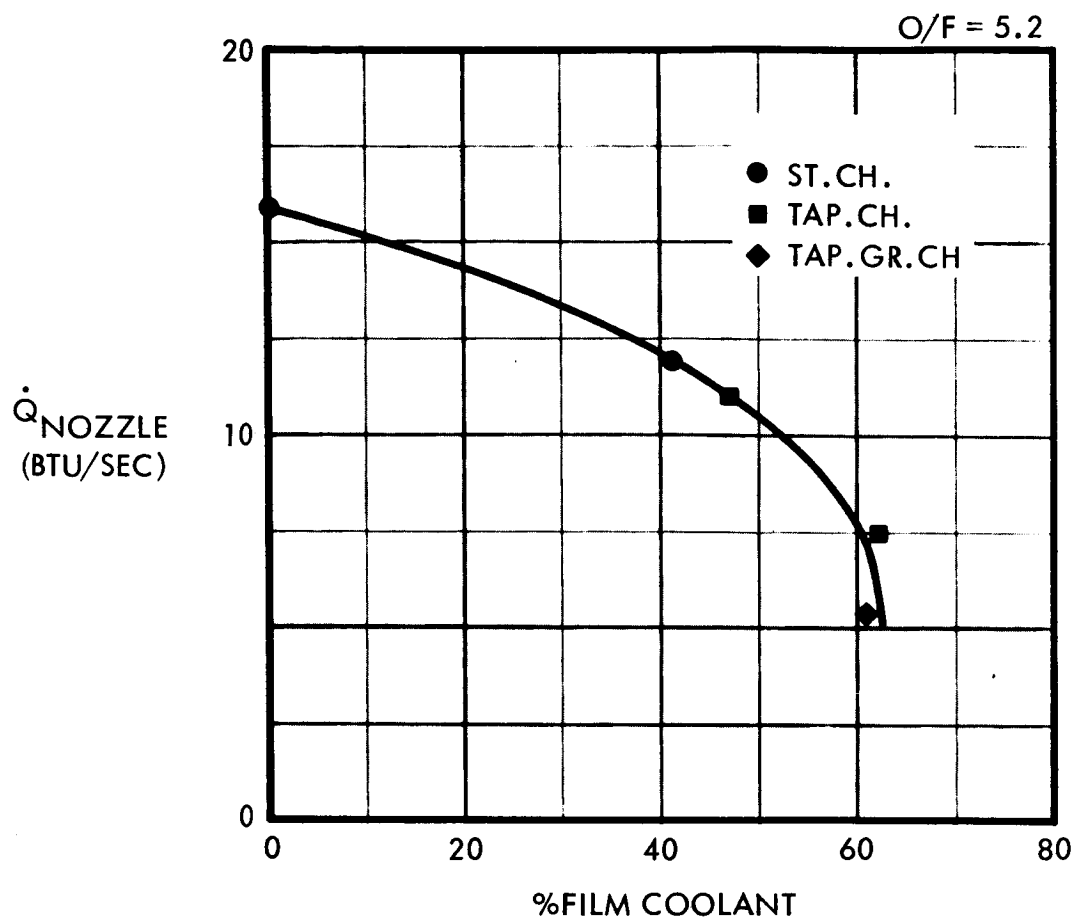


Figure 5-57. Film Cooling Heat Transfer Summary
(% F.C. Variation)

5.3.2.1 Film-Coolant Injection Techniques

Two different injection techniques were evaluated in the test program. The technique using film-coolant injection from the main injector and impinging the film coolant on the wall resulted in a heat transfer 20 percent lower and a performance 1 percent higher than the other technique where the film coolant was injected parallel to the chamber walls. This is apparently due to more complete covering of the chamber walls when the fuel is impinged on the wall.

5.3.2.2 Chamber Configuration

Significant differences were noted in the heat transfer and performance of the three chamber configurations studied. Of these, the grooved, tapered chamber exhibited the lowest nozzle heat load while the smooth, tapered chamber exhibited the highest performance. Two possibilities arise as the cause of the decreased heat loads associated with the tapered chamber designs. The axially accelerating gases have an increasing radial velocity vector which results in a pressure gradient having a strong stabilizing effect on the film-coolant layer and a corresponding increase in the film-coolant efficiency. Previous investigations (Reference 24) have also indicated a heat load reduction in the nozzle throat region with tapered chamber designs. Another possible explanation of the tapered chamber heat load reduction is due to increased carbon deposition, principally due by the radial forces maintaining the fuel rich gases adjacent to the chamber walls. Figure 5-58 shows the axial temperature profiles from three different test runs with and without film cooling and for both the cylindrical and tapered chamber contours. As can be seen, the addition of film cooling to the cylindrical chamber causes a distinct break in the axial wall temperature distribution moving the temperature peak upstream into the nozzle convergent section. By tapering the chamber the resultant wall temperature peak is shifted further upstream. These results indicate the carbon is appearing on the chamber walls at different locations for the various cases. The increased carbon deposition coverage by the tapered chamber results in a decreased heat load.

5.3.2.3 Film Coolant Fluid

Following initial failures to maintain the methane-ethane fuel blend as a film coolant, two tests were made using MMH as the film coolant fluid. MMH has been used successfully in the past for conduction cooling and offers a much greater film coolant capability than the methane-ethane since it has a much higher boiling point, peak boiling heat flux, and heat absorption capability. These tests resulted in successful film conduction cooling, thus indicating that most of the problem associated with conductive cooling with methane-ethane lies in the properties of the propellant.

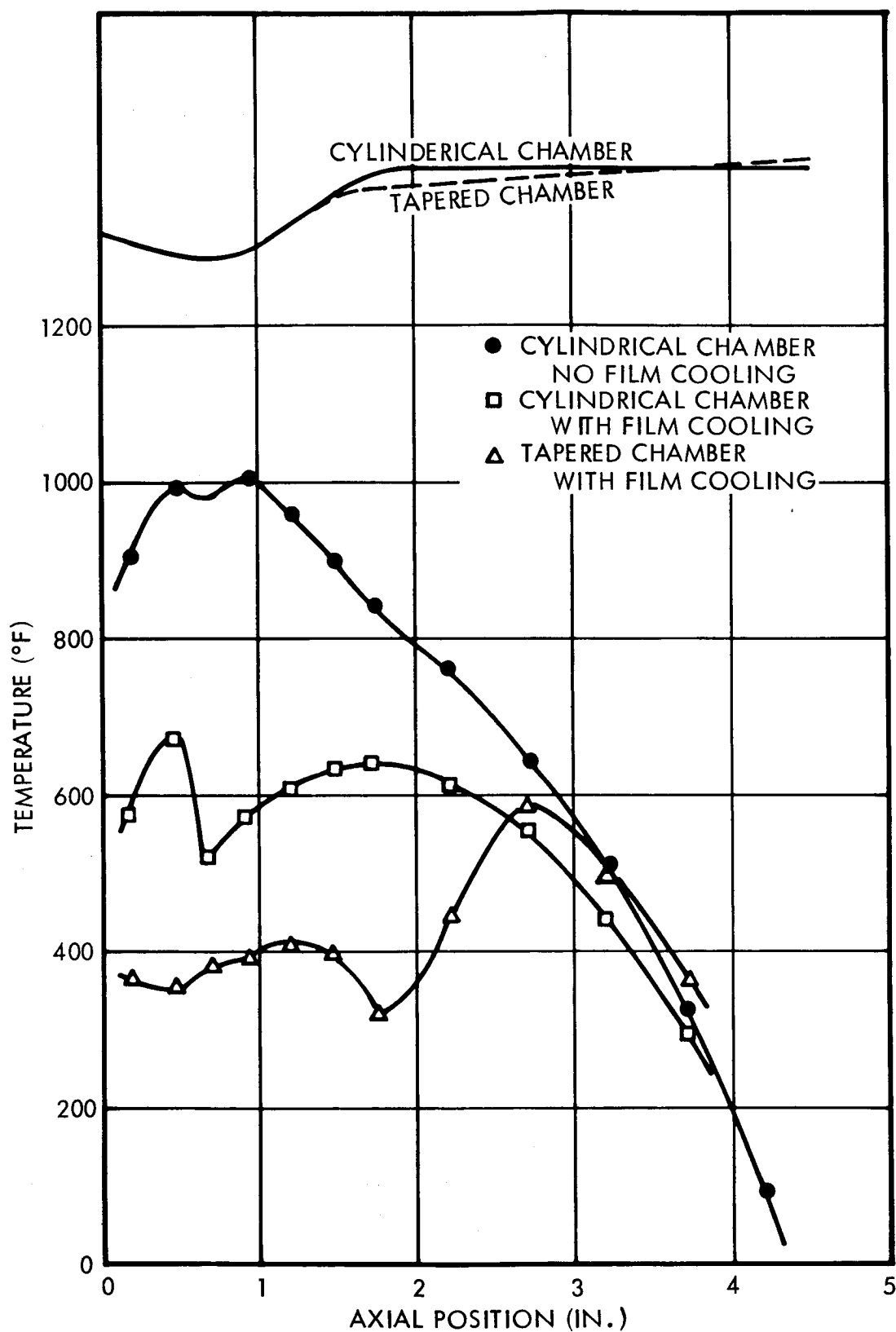


Figure 5-58. Effect of Chamber Contour and Film-Cooling on Initiation of Carbon Deposition

Using the dT/dX measured for the MMH film coolant runs, a conducted heat load can be determined to be about 4.9 Btu/sec. This is not significantly lower than the nozzle heat load measured in Runs 071-072. The principal difference in these test cases is the existence of the "hot spot" encountered in the methane-ethane runs. This appears to be the result of the LPG fuel volatility which apparently acts to mix the film-coolant layer with the main combustion gases, whereas, the MMH maintains its separation from the core gases and, hence, protects the wall.

A simplified analysis for the rate of shear from a film-coolant layer can be utilized as an indication of the effects of the film-coolant fluid properties on the film-cooling stability. This analysis yields the result that the mass loss rate from the film-coolant layer (in a gas shearing environment) is given by

$$\dot{w}_s \sim \frac{1}{\mu l} \left(\frac{\rho l}{\sigma l} \right)^{1/4} \quad (5-4)$$

Thus, we see that high viscosity is of principle importance in increasing the film-coolant stability. Using the above analytical result, a comparison can be made between the methane-ethane film coolant and MMH film coolant. The loss ratio is given by

$$\left(\frac{\dot{w}_{ME}}{\dot{w}_{MMH}} \right)_{\text{SHEAR}} = \frac{\mu_{MMH}}{\mu_{ME}} \left(\frac{\rho_{ME} \sigma_{MMH}}{\rho_{MMH} \sigma_{ME}} \right)^{1/4} = 3.35 \quad (5-5)$$

The corresponding heating loss rate ration is given by

$$\left(\frac{\dot{w}_{ME}}{\dot{w}_{MMH}} \right)_{\text{HEATING}} = \frac{Q_{ME}}{Q_{MMH}} \frac{\Delta H_{MMH}}{\Delta H_{ME}} = 1.46 \quad (5-6)$$

Thus, the total effectiveness ratio is

$$\left(\frac{\dot{w}_{ME}}{\dot{w}_{MMH}} \right)_{\text{TOTAL}} = 4.81 \quad (5-7)$$

It was experimentally found (Figure 5-42) that MMH film coolant remained liquid for a length of approximately 1.75 inches. This means (based on the above analysis) that the methane-ethane fuel-blend film coolant should persist as a liquid for only about 0.36 inch, a value close to the actual experimental results as determined from the experimental wall temperature data and heat patterns on the copper chamber walls.

It thus appears the liquid-film cooling with the LPG fuels would be very difficult, if not impossible, however, gaseous-film cooling still remains an attractive design approach.

5.3.2.4 Primary Injection

From previous results, it appeared that the possibility of maintaining liquid methane-ethane on the chamber wall was remote due to the propellant's low boiling point (-140°F at 100 psia). However, it was felt that either gas or liquid-film coolant would have a better chance of remaining on the wall if the primary combustion could be isolated from the film coolant. The hot spot in the barrel portion of the chamber was evidence that the desired two-zone nature of the flow was not being achieved. Two injector modifications were made in an attempt to promote the desired separation of primary combustion from film-coolant layer. The first of these was to increase the primary fuel injection energy by decreasing the fuel gap. This change resulted in some improvement but also resulted in lower performance. The second modification was the addition of the CARB-I-TEX ring to the injector face. The primary propellants, after impinging on themselves and traveling radially toward the wall, splash against the ring and are directed axially. The test result indicated that this technique did indeed act to isolate the primary combustion gases from the film-coolant layer. As a result of this isolation, the film coolant can absorb heat from the chamber as it is conducted from the throat toward the injector. Calculations indicate that the necessary gaseous film-coolant flow rate will be proportional to the heat load. This means that lower film-coolant flow rates could be used. This would result in higher temperatures, but with 60 percent film coolant the maximum temperatures were only 400°F , while 1200°F would be acceptable for a copper chamber. The lower flow rate would also result in a lower overall mixture ratio and consequently a higher characteristic exhaust velocity.

5.4 BIPROPELLANT VALVE EVALUATION

Preliminary valve evaluations were carried out in this program for providing a basis for future valve selection in final integrated thruster-valve assemblies. The selected valve was a HR&M (Hydraulic Research and Manufacturing, Inc.) bipropellant valve. This valve has design features of interest for use with the space storable propellants (tungsten carbide (K-96 seats) and has been used in some fluorinated propellant research at Edwards Air Force Base. The TRW program was to perform the following with the selected valve: (1) clean and assemble, (2) leak check with GN_2 , (3) cold flow with LN_2 , (4) leak check with GN_2 , (5) passivate with GF_2 , (6) leak check with GN_2 , (7) cold flow with FLOX and methane-ethane, and (8) leak check with GN_2 . Steps (1) and (2) were undertaken after receipt of the valve with the results verifying the data given by HR&M. The cold flow with LN_2 was then performed and the valve cycled several times. The leak check following this resulted in a leak several orders of magnitude larger than before the LN_2 flows. After an evaluation of the data, the conclusion was reached that the leak was occurring around the seats following the thermal compression and expansion cycle. The valve is now being redesigned by HR&M to eliminate this problem. No further tests were performed on the valve.

6. CONCLUDING REMARKS

This section discusses the basic results of the analytical and experimental studies as well as the reevaluation of the analytical results based on the information obtained during the experimental tests. Also given are some basic recommendations for further investigations deemed necessary.

6.1 ANALYTICAL RESULTS

Parametric analyses of both radiation-cooled and conductively cooled thrust chamber designs were made to determine the applicability of each as passive thrust chamber cooling concepts. The basic analytical approach was to determine the chamber operating conditions for various chamber configurations and heating rates. The heating rates were changed by varying the local recovery temperature. As a parallel effort with the heat transfer analysis, numerous studies were made on the basic chamber environment. These included theoretical performance studies including gas species determination, fuel pool boiling effects, film cooling effects on performance, and carbon deposition.

Since experimental tests were planned for the conduction-cooled designs, the majority of the analytical studies were made on conductive cooling designs. Conventional conductive cooling with the earth storable propellants required the presence of liquid fuel on the wall for successful operation. Therefore the conduction-cooling analysis was based on this premise. The analysis showed that the liquid fuel on the wall could absorb heat from the chamber up to a certain limit determined by the peak boiling heat flux. This heat absorption limit results in a fuel coolant flow rate limitation. The heat absorption limit also defines the amount of heat that can be conducted from the throat to the coolant layer, which in terms of throat heat flux means that the throat recovery temperature and overall convection coefficient are limited. These factors are in turn related to the wall mixture ratio, since this directly affects the recovery temperature and carbon deposition. The final conclusion drawn from this analysis was that carbon deposition was necessary for successful operation, which resulted in the selection of propane as the superior coolant. However, with the inclusion of peak boiling limits in the analysis it was found that both propane and the methane-ethane fuel blend were of nearly equal capability, with the blend being somewhat superior due to its high peak heat flux limit.

In terms of passive cooling material rating in a pulsed mode duty cycle environment attention must be given to thermal fatigue. Both copper and CARB-I-TEX designs can be shown to be duty-cycle insensitive from a thermal fatigue standpoint. On the other hand, beryllium has a serious thermal fatigue limit. Pulsed duty cycle operation also represents a possible problem due to soakback effects which may result in the inability to insure liquid fuel on the chamber walls.

Analytical performance evaluation shows the FLOX/LPG propellants to have expected delivered performance of about 354 seconds Isp versus 420 seconds Isp equilibrium due to large kinetic losses. The analytically determined

performance for small thrusters indicates expected delivered performance to be relatively insensitive to mixture ratio, thus making off-design operation possible for more advantageous thermal design.

6.2 EXPERIMENTAL RESULTS

Although the experimental effort was principally concerned with thermal effects important results were obtained with respect to injector performance. The injector development effort indicated that the reactivity and volatility of the propellants requires that the propellants be properly confined to provide high performance. The sheet-on-sheet injector tests indicated that reaction blow apart can occur and tends to be quite strong with these propellants. The typical TRW slotted injector configuration with a continuous fuel sheet impinging with the slotted oxidizer flow provides such confinement and results in high performance.

Injector durability appears to be fully established. A large number of firings with over 400 seconds of accumulated time have been accomplished with no problems. Injector operation does not seem to be greatly affected by mixture ratio variation. In pulsed mode operation two-phase flow effects may affect injector operation but this was not investigated during this program.

Of primary importance are the experimental heat transfer results. These tests were made to determine the thermal environment within the thrust chamber and the effects of film cooling on the environment. After several tests it became apparent that the film coolant was not remaining on the wall as a liquid. Several attempts were made to induce liquid fuel to stay on the chamber walls. These included: (1) tapering the chamber, (2) placing grooves in the tapered chamber, (3) parallel injection of the film coolant into the grooves, and (4) a shroud placed over the film coolant from the injector to the midpoint of the chamber. However, none of them were successful in the maintenance of liquid fuel, but they did indicate effects on the cooling efficiency. This indicated the propellant volatility was prohibiting the maintenance of a liquid layer. A further test was made with MMH as the film coolant to determine injector interaction effects. This test resulted in conduction-cooled operation with a liquid fuel layer on the wall. It is now felt that a combination of propellant volatility and injector interaction was responsible for unsuccessful conductive-cooling operation. The use of a splashring injector resulted in successful conduction cooling but without liquid fuel on the wall. This means that with these volatile fuels the gaseous phase can absorb the required heat loads, if the gaseous film-coolant layer is suitably isolated from the primary combustion gases.

6.3 ANALYTICAL REEVALUATION

Based on the experimental conclusion that gaseous fuel can absorb the required heat loads an analytical reevaluation was made to determine the affects of this information on the previous analytical results. The basic analytical results which did not include peak heat flux limits should nearly hold for the case of gaseous film coolant since more than 90% of the total heat absorption capability lies in the fuel decomposition energy. If an

analysis similar to that described in Section 3.2.2.3 is made to compare the three fuels on a gaseous film coolant bases with propane = 1.0, the methane fuel is found to be superior with respect to flow rate requirements as seen in Table 6-1.

Table 6-1. Comparison of Three Fuels

	<u>Methane</u>	<u>Methane-Ethane</u>	<u>Propane</u>
Heat Absorption	1.337	1.127	1.0
Total Heat Load	1.146	1.050	1.0
$\dot{w}_{F.C.}$ (required)	0.858	0.932	1.0

This is, of course, only a comparative analysis and more detailed analyses would be warranted to determine more precise rankings for each candidate fuel on a basis of delivered specific impulse, including zonal losses.

Analysis of the successful conduction-cooled test (Run 085) has given considerable insight into the basic operational mode of conduction cooling with the LPG fuel, methane-ethane blend. As previously seen the LPG fuels have considerably lower liquid heat absorption capability than does MMH and a much lower resistance to gas stripping (i.e., resulting in a lower film cooling efficiency). These factors coupled with the higher mixture ratios and hence lower fuel flow rates severely limit the ability of the LPG fuels to conductively cool small thrusters. Present indications are that the LPG coolants must rely mainly on liquid boiling and gas heating as heat absorption mechanisms. In addition, some heat absorption is obtained in the purely liquid regime in a short region at the beginning of the chamber. Blockage of heat into the thruster is obtained from vapor downstream of the primary heat absorption region. Carbon deposition in the nozzle region also helps to block heat input. All of these mechanisms are illustrated schematically in the revised thruster thermal model shown in Figure 6-1.

This revised model has been checked by generating the chamber wall temperature profiles and comparing them with the experimental results obtained during Run 085. In addition, the cumulative thruster heat load was determined. These results are shown in Figure 6-2. As seen the isotherms resulting from the revised model agree quite well with the experimentally determined temperatures.

Examination of the cumulative heat load demonstrates the various regions of heat input discussed previously. Beginning in the throat region, the heat load can be seen to increase rapidly up to a point slightly upstream of the nozzle convergence section. This is the region where the carbon is deposited on the chamber wall and it coincides with the rapid rise in the vapor temperatures caused by its diffusion into the core gases. As is also evident from the slope of the heat load curve, a large portion of the tapered chamber section is virtually isolated from any heat input or output. This coincides with the region where relatively cool vapors still exist. Near the injector, heat is transferred (removed) at a high rate over the last 0.75 to 1.0 inch section of the chamber where 90 percent of the heat is absorbed into the coolant.

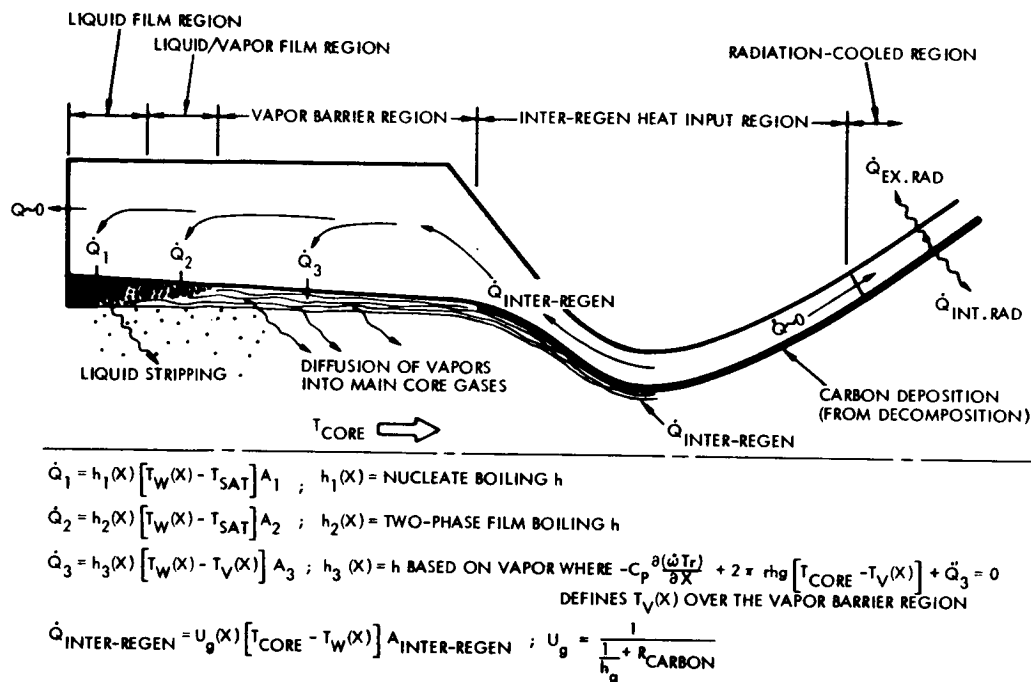


Figure 6-1. Inter-Regen Thermal Model

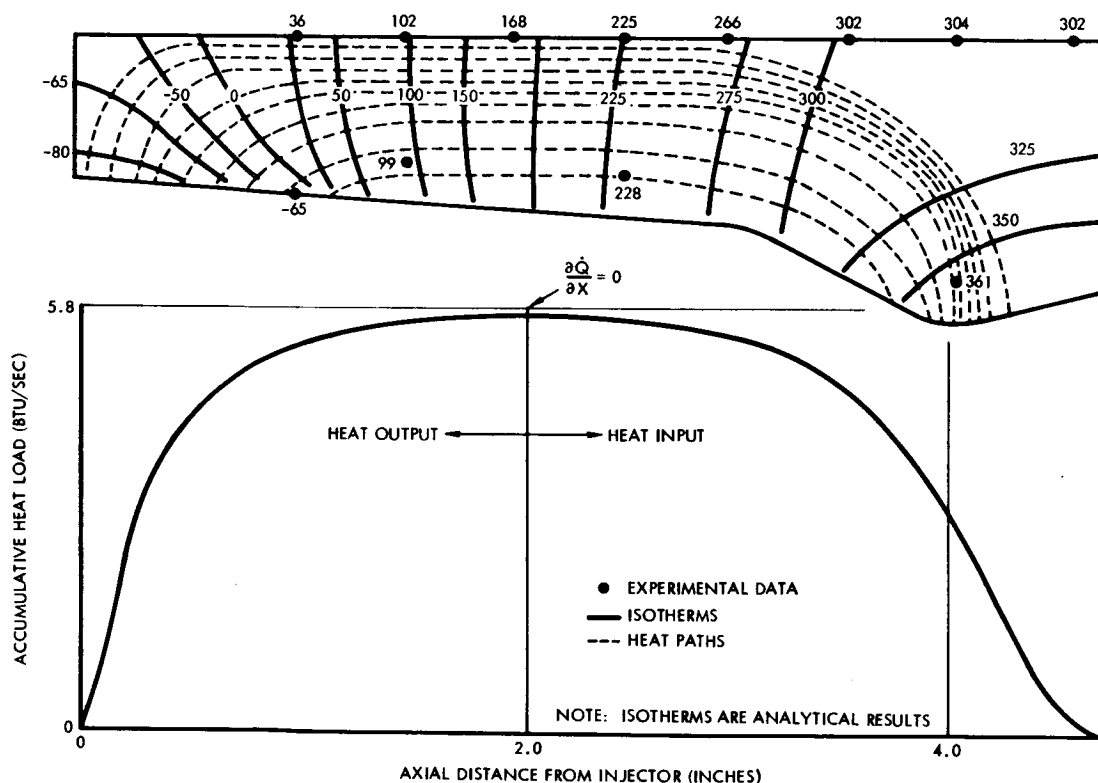


Figure 6-2. Isotherms and Accumulative Heat Load for a Steady-State Inter-Regen Thruster Test

From the stripping calculations performed, the liquid coolant layer length was determined to be of the order of 0.40 inch. This is very close to the length of the region of high heat absorption shown in Figure 6-2. Calculation of the average heat flux over this region also indicates that a large portion was in the liquid/vapor film boiling region where the coefficient is greatly reduced; however, the wall temperature can increase to compensate for the reduction in coefficient. A resultant liquid film-coolant efficiency calculated from these test results indicates an efficiency value of from 7 to 10 percent, considerably lower than that expected for most conventional liquids.

6.4 RECOMMENDATIONS

The accomplishments of this program have provided considerable data on the application of the FLOX/LPG propellants to low thrust altitude control rocket engine designs. The extensive analytical program effects have investigated the performance and operating characteristics of selected LPG fuels and chamber design approaches, with emphasis as the inter-regen cooling concept. The experimental activities have demonstrated the high combustion performance characteristics (with the pintle injector design) and excellent overall injector durability. Film cooling and chamber contour evaluations have resulted in successful thruster operation in the partially liquid/gaseous inter-regen cooling mode.

These efforts have demonstrated the basic feasibility of inter-regen cooling of the FLOX/LPG thruster operating in the liquid/gaseous conduction cooling mode. Additional investigations are required, however, to further refine and optimize these design approaches from both a cooling effectiveness and thruster performance standpoint. This will require minimizing the interaction between the primary combustion gases and the gaseous film coolant through additional injector refinements and/or inwall ducted coolant approaches. Further work is also recommended with the graphitic chamber materials; both for improved conduction as well as other chamber design approaches (radiation cooling, heat sink, etc). With these design concepts, additional attention must be given to the injector designs employed to maintain defined liquid propellant injection and overall injector durability under the higher imposed heat loads. Another area warranting investigation is the carbon deposition buildup (particularly in the nozzle throat) during long duration firings. Analytical studies of gaseous film (conduction) cooling should also be continued to determine basic operating characteristics for the various LPG fuels of current and future interest.

REFERENCES

1. TRW Report No. 4811.4.66-009, "Rocket Chemistry Computer Program," 20 June 1966.
2. TRW Report No. 9852.21-29, "The Rao Method Optimum Nozzle Contour Program," 1 October 1964.
3. NAS CR-72038 (Rocketdyne R-6636-2), Final Report, "Fluorine-Hydrogen Performance Evaluation, Phase I, Part II: Nozzle Performance Analysis and Demonstration," prepared for National Aeronautics and Space Administration under Contract NASW-1229, by Rocketdyne, North American Aviation, Inc., April 1967.
4. NASA CR-72162 (UARL E910370-13), "Investigation of Nonequilibrium Flow Effects in Hydrogen-Fluorine Rocket Nozzles," First Technical Report, prepared for National Aeronautics and Space Administration under Contract NASW-1293 by United Aircraft Research Laboratories, 8 September 1966.
5. TRW Systems Report 02874-6003-R000, "One-Dimensional Reacting Gas Nonequilibrium Performance Program," 1 March 1967 (revised September 1967).
6. TRW Systems Report 08832-6001-T000, "Phase I Final Report - Screening of Reaction Rates," 22 May 1967.
7. TRW Systems Report 08832-6002-T000, Phase II Final Report, "Screening of Reaction Rates," Vol. I - Technical Analysis, 2 December 1967.
8. JPL Technical Report No. 32-387 "Calculation of Turbulent Boundary-Layer Growth and Heat Transfer in Axisymmetric Nozzles," 15 February 1963.
9. J. R. Priem, and M. F. Heidman, Propellant Vaporization as a Design Criterion For Rocket-Engine Combustion Chambers, NASA TR R-67, 1960.
10. H. Schmidt, "Handling and Use of Fluorine and Fluorine-Oxygen Mixtures in Rocket Systems," NASA SP-3037, 1967.
11. P. M. O'Donnell, "Kinetics of the Fluorination of Beryllium," NASA TN D-3992, July, 1967.
12. N. R. Balling, "Evaluation Testing of Protective Coatings on Refractory Metals," Interim Report 07587.6004-T000, TRW Systems Group, October 1968.
13. J. D. Batchelor, J. A. Simmons, and W. E. Wist, "Chemical Reactions Between Composite Materials and Propellant Exhaust Products," Report No. ASD-TRD-63-737, Vol. 1, Contract AF 33(657)-8475, August 1963.

14. D. R. Bartz, "A Simple Equation for Rapid Estimation of Rocket Nozzle Convective Heat Transfer Coefficients," Jet Propulsion, January, 1957.
15. TRW Systems IOC 4711.6.67-60, "A Formula for Predicting Heat Transfer Coefficients in Nozzles with Carbon Deposition," 3 August 1967.
16. TRW Systems IOC 68.4711.8-3, "Impact of Experimental Pool Boiling Data on the Methane-Ethane Film-Conduction Thrustor," 11 January 1968.
17. TRW Systems Report No. 09588.6001-R000, "Preliminary Thermal Analyses - Space Storable Thruster Investigation," 1 December 1967.
18. TRW Systems IOC 68.4711.8-77, "Reduction in the Throat Heat Load of a Film-Conduction Cooled Thruster," 17 October 1968.
19. "Film Cooling, Its Theory and Application," Purdue University Rocket Laboratory, Report TM 57-3, October, 1957.
20. "Performance Characteristics of Compound A/Hydrazine Propellant Combination," Technical Documentary Report No. TR-65-107, Vol. 1, May, 1965.
21. H. L. Burge, and D. Kuyper, "Simplified Thermal Fatigue Analysis for Liquid Rocket Combustion Chambers," Journal of Spacecraft and Rockets, January, 1967.
22. J. Rupe, "An Experimental Correlation of the Nonreactive Properties of Injection Schemes and Combustion Effects in a Liquid Propellant Rocket Engine," JPL TR 32-255, July 15, 1965.
23. G. Elverum, and P. Staudhammer, "The Effect of Rapid Liquid-Phase Reactions on Injector Design and Combustion in Rocket Motors," Progress Report 30-4, Jet Propulsion Laboratory.
24. "Investigation of Space Storable Propellants - $\text{OF}_2/\text{B}_2\text{H}_6$," Thiokol Chemical Corporation, NASA CR-54741, 10 June 1966.

APPENDIX A

PROPELLANT PHYSICAL PROPERTY AND THEORETICAL
PERFORMANCE SUMMARY

APPENDIX A

PROPELLANT PHYSICAL PROPERTY AND THEORETICAL PERFORMANCE SUMMARY

1.0 PROPELLANT PHYSICAL PROPERTY DATA

The physical property data for the propellants used during this program are summarized. The summary of the fuel properties is given in Table A-1. Table A-2 contains similar property data for the nominal 80% FLOX oxidizer.

Liquid density/temperature data for both the LPG and subject oxidizer components and mixtures are shown in Figures A-1 and A-2. Figures A-3 and A-4 show the fuel and oxidizer vapor pressure data, respectively.

2.0 THEORETICAL PROPELLANT PERFORMANCE

The theoretical performance characteristics for the three (3) subject FLOX/LPG propellant combinations are presented in the following series of figures. Included in these figures are the equilibrium, frozen, kinetic, zonal and associated performance data over a range of engine design/operating conditions. These data represent the information generated and utilized during the Task I design and analyses efforts.

Table A-1. LPG Physical Property Summary

PROPERTY	LPG Fuel			
	METHANE	ETHANE	55% METHANE 45% ETHANE	PROPANE
Chemical Formula	CH ₄	C ₂ H ₆	---	C ₃ H ₈
Molecular Weight	16.042	30.068	22.42	44.094
Normal Freezing Point, °R	163.2	161.9	133.0	154.0
Normal Boiling Point, °R	200.8	331.7	209.0	415.9
Liquid Density at NBP lb/ft ³	26.48	34.15	30.40	36.4
Liquid Density at 140°R, lb/ft ³	---	---	35.28	---
Critical Temperature, °R	343.4	549.8	---	666.0
Critical Pressure, psia	673	708	---	618.7
Critical Volume, ft ³ /lb	0.0989	0.0789	---	.0709
ΔH _{vaporization} at NBP, Btu/lb	219.22	210.41	---	183.05
ΔH _{fusion} , Btu/lb	25.25	40.88	---	34.38
Viscosity at NBP, lb/ft-sec	7.0x10 ⁻⁵	1.2x10 ⁻⁴	---	1.1x10 ⁻⁴
Thermal Conductivity at NBP Btu/ft-hr-°R	0.1075	.088	---	.058
Specific Heat at NBP, Btu/lb-°R	0.81	0.57	.70	.532

Table A-2. Oxidizer Physical Property Summary

Property	Oxidizer		
	Fluorine	Oxygen	80% FLOX
Chemical Formula	F_2	O_2	---
Molecular Weight	38.00	32.00	---
Normal Freezing Point, °R	96.372	97.833	---
Normal Boiling Point, °R	153.036	162.302	154.5
Liquid Density at NBP, lb/ft ³	93.96	71.27	89.42
Liquid Density at 140°R, lb/ft ³	96.7	75	92.36
Critical Temperature, °R	259.128	277.848	---
Critical Pressure, psia	808.	730.	---
Critical Volume, ft ³ /lb	0.0398	0.03725	---
$\Delta H_{\text{vaporization}}$ at NBP, Btu/lb	71.514	91.627	---
ΔH_{fusion} at NBP, Btu/lb	5.778	5.979	---
Vapor Pressure at 140°R, psia	5.6	3.1	---
Viscosity at NBP, lb/ft-sec	.000165	.000128	---
Thermal Conductivity at NBP, Btu/ft-hr-°R	.0915	.0852	---
Specific Heat at NBP, Btu/lb-°R	.367	.405	.374

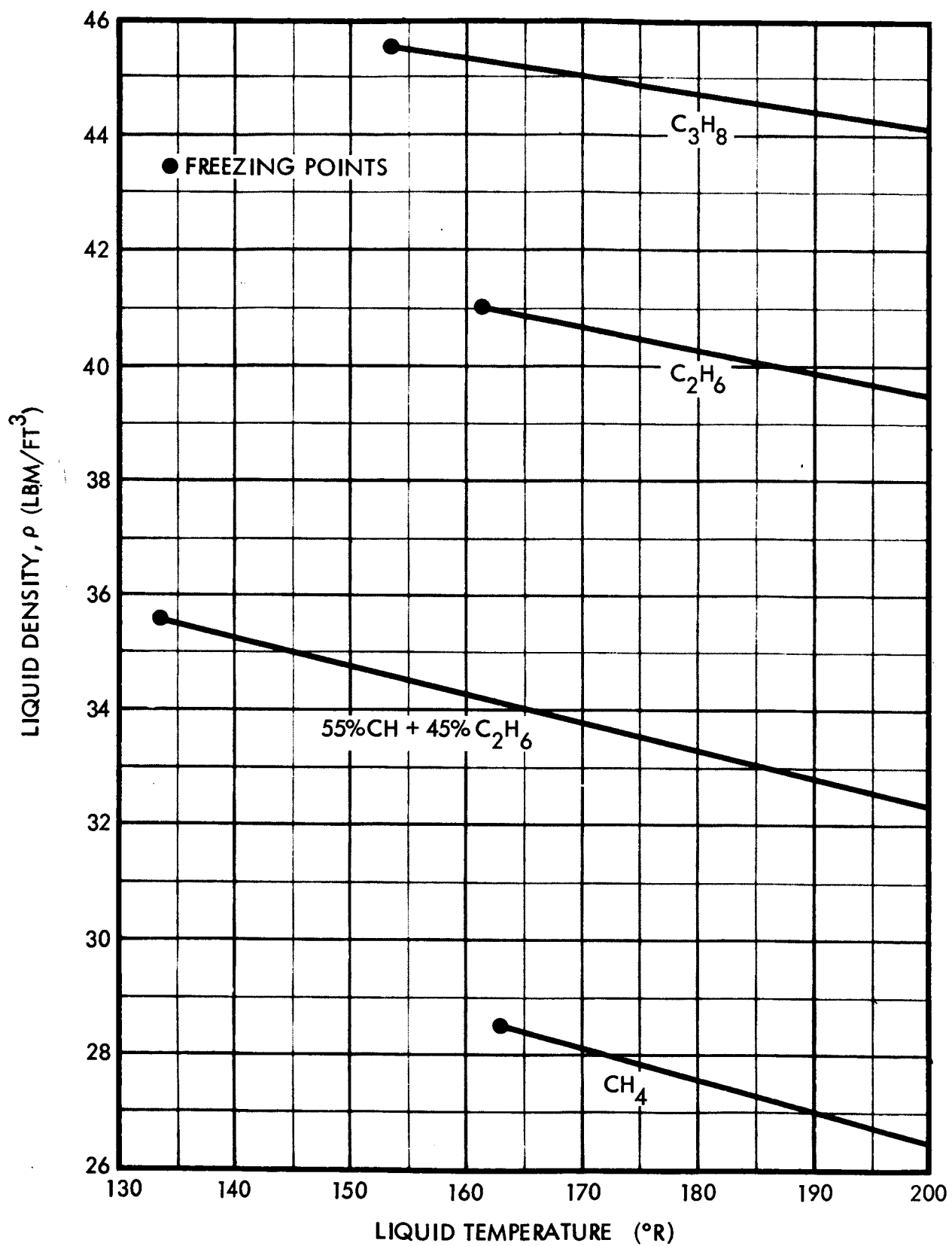


Figure A-1. LPG Liquid Density Variation with Temperature

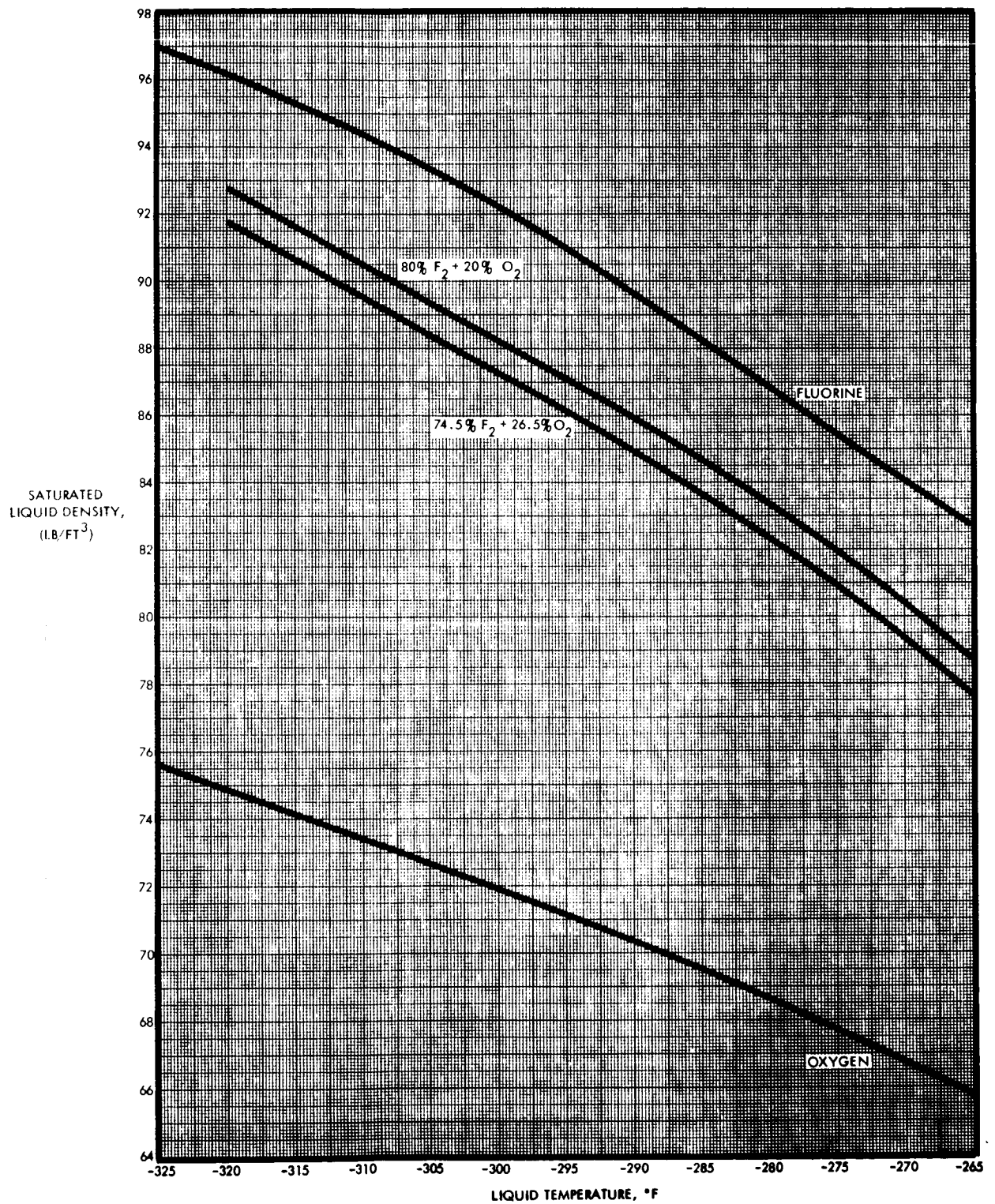


Figure A-2. Oxidizer Liquid Density Variation with Temperature

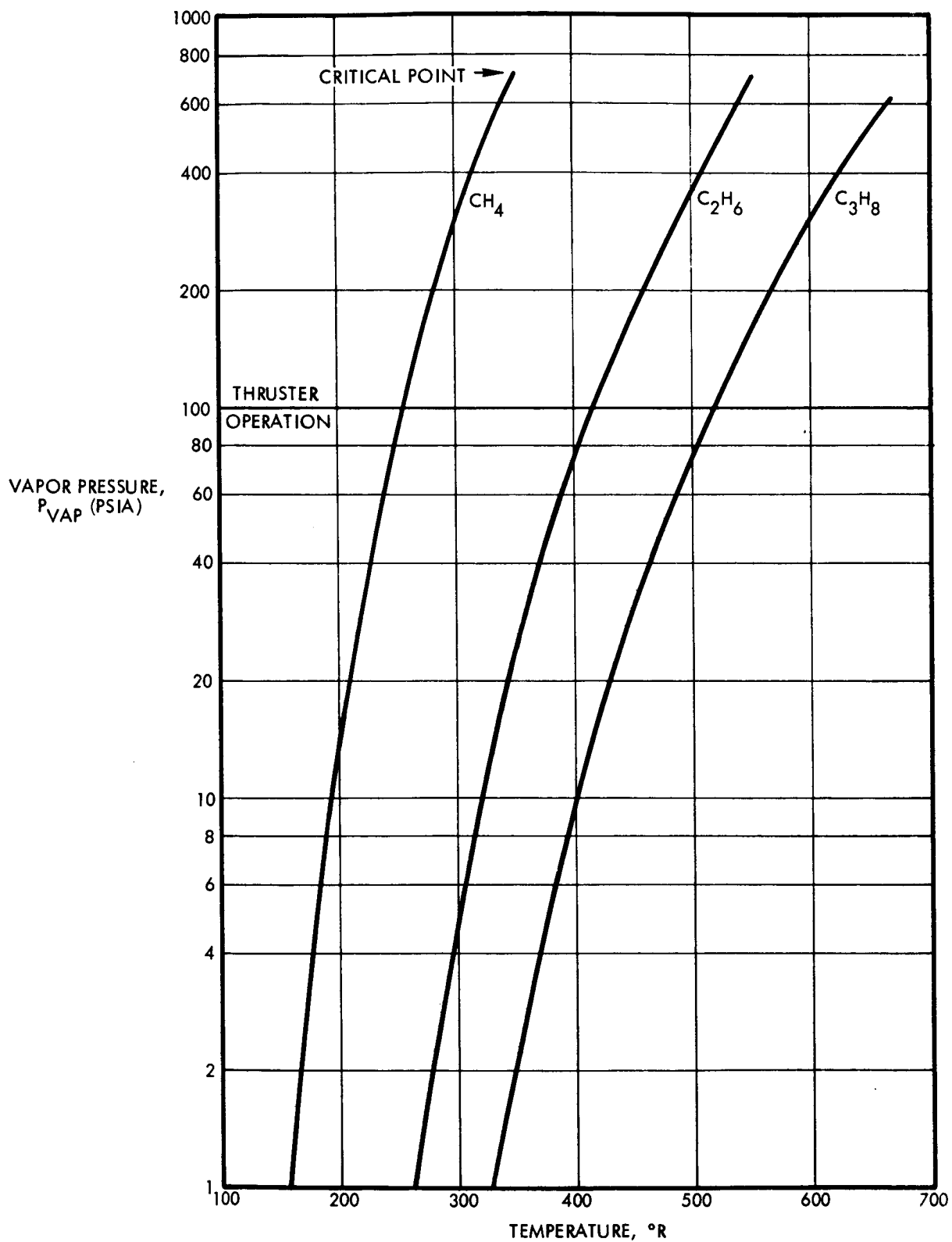


Figure A-3. LPG Vapor Pressure Variation with Temperature

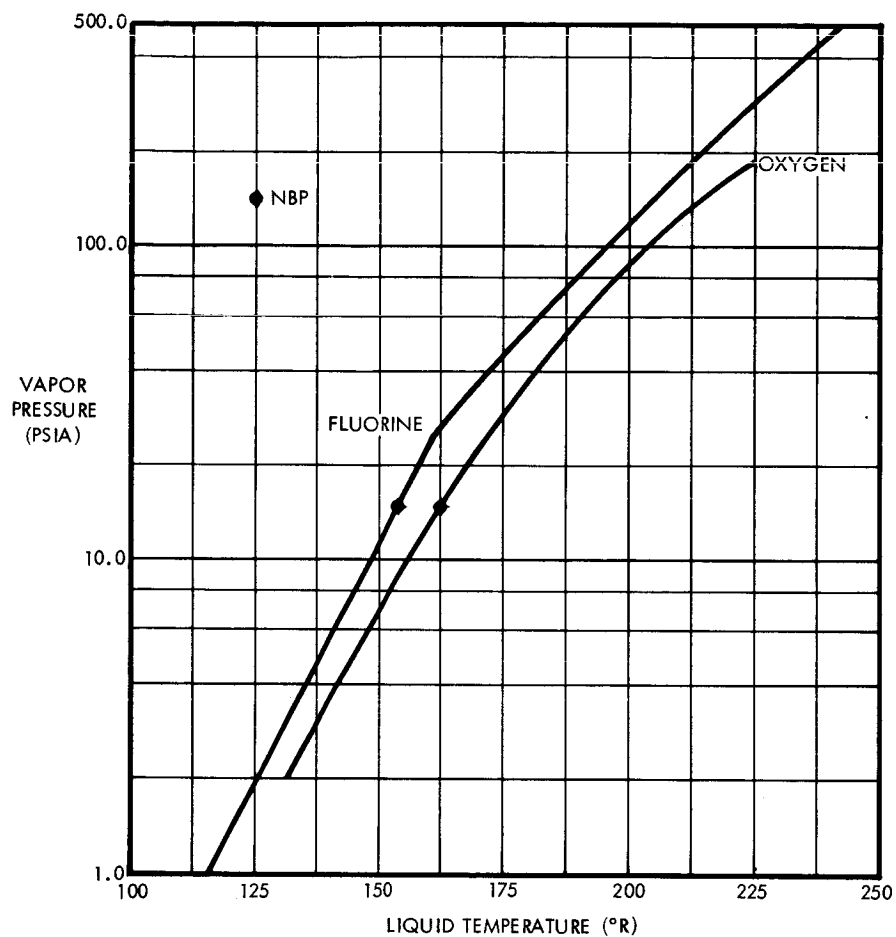


Figure A-4. Oxidizer Vapor Pressure Variation with Temperature

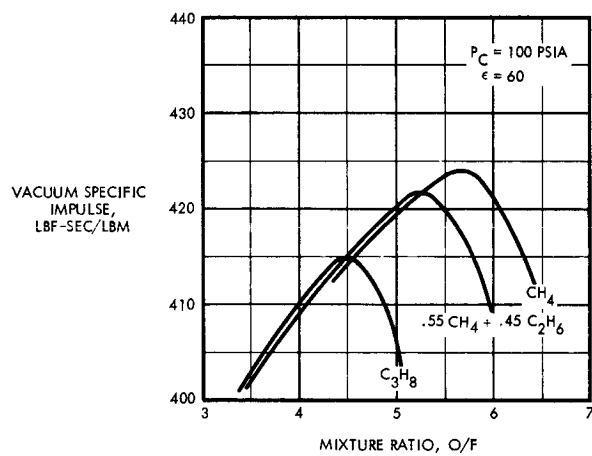


Figure A-5. Comparison of Theoretical Thrust Chamber Performance

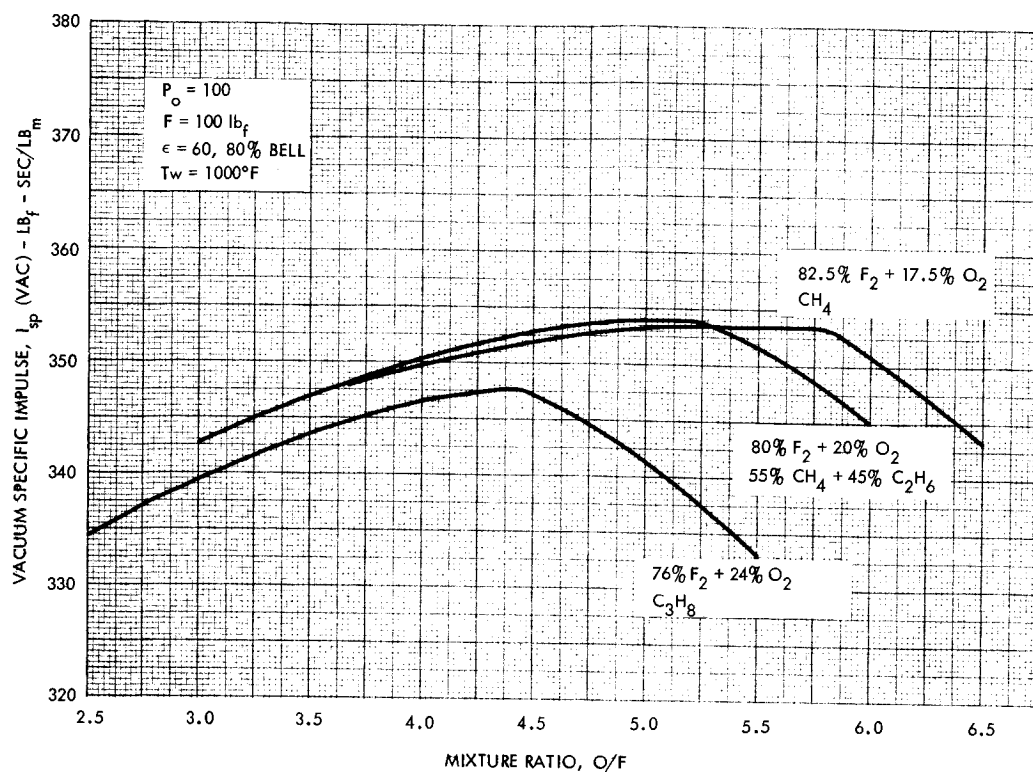


Figure A-6 Comparison of Estimated Delivered Thrust Chamber Performance

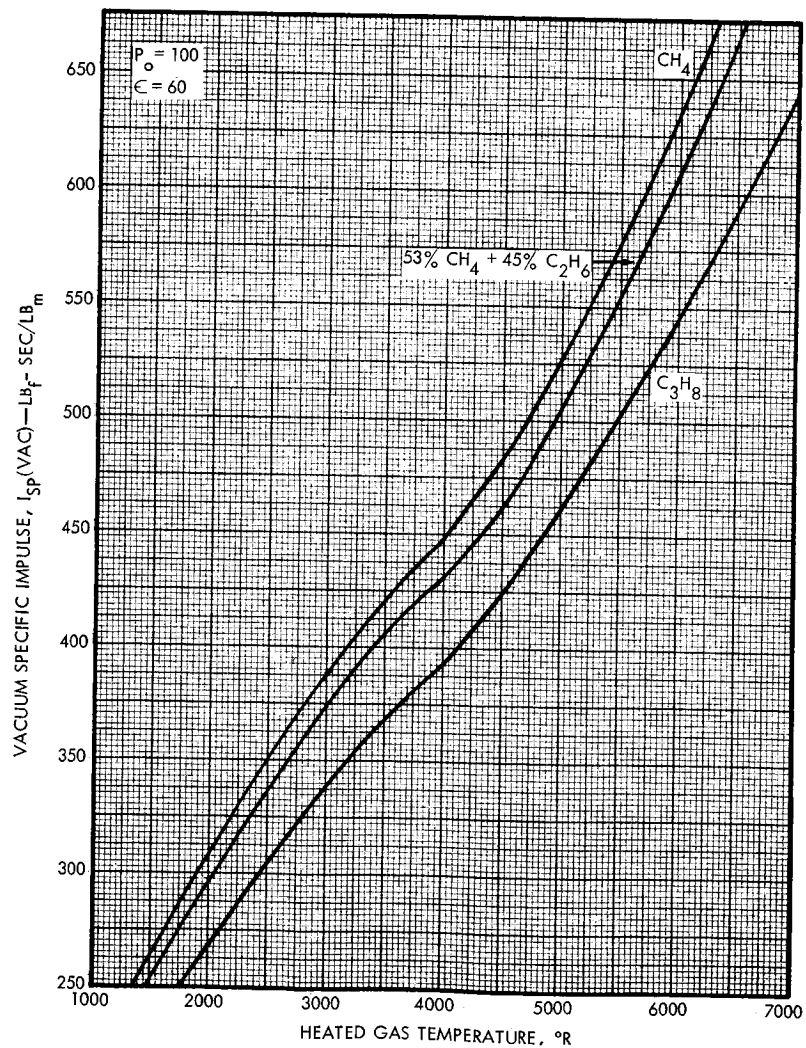


Figure A-7. LPG Monopropellant Performance

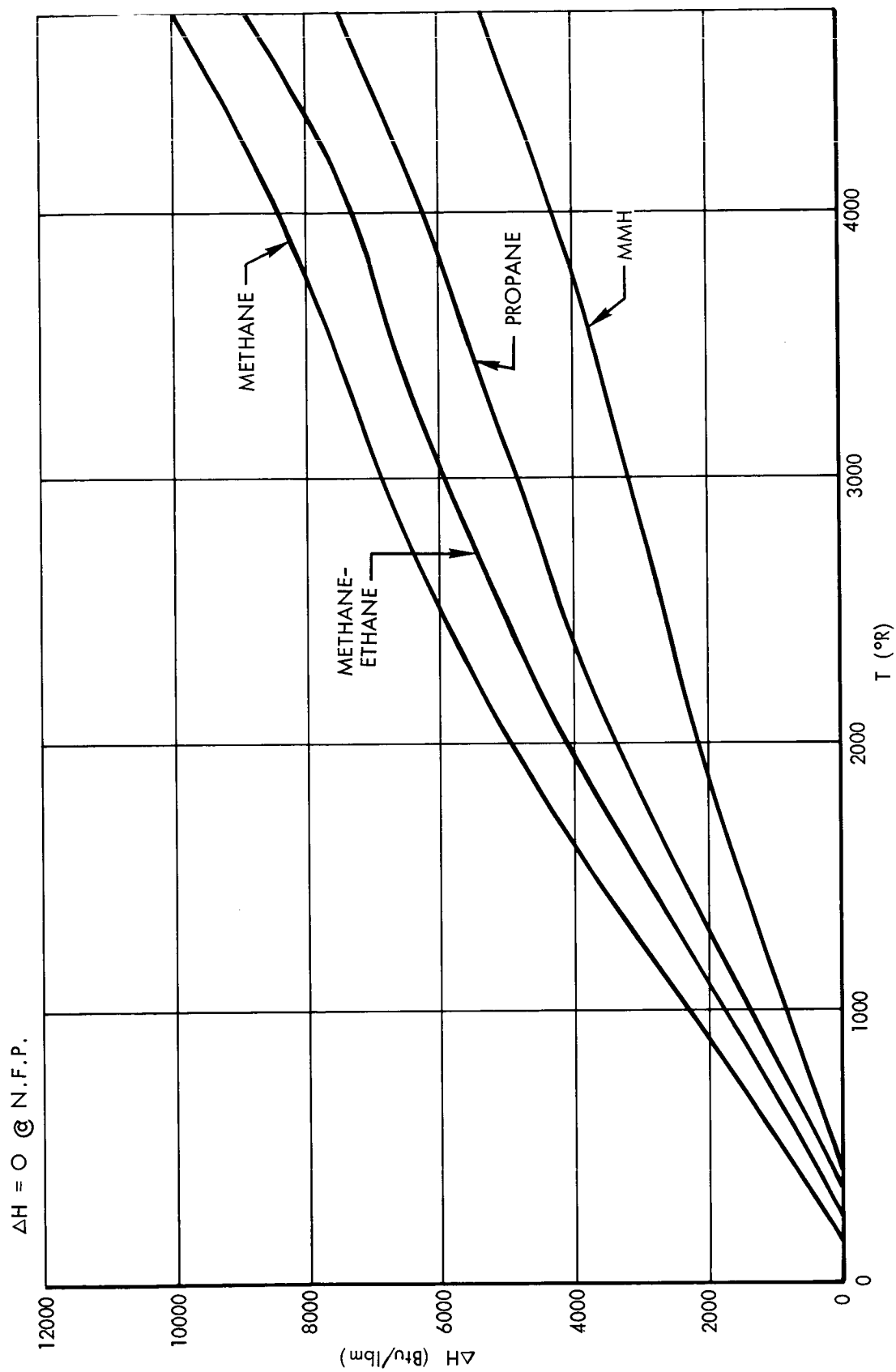


Figure A-8. LPG Heat Absorption Capability

Table A-3. 80% F₂ + 20% O₂ / 55% CH₄ + 45% C₂H₆ Equilibrium C*
as a Function of Chamber Pressure and Mixture Ratio

% FLOX	$\frac{T_o}{^{\circ}R}$	$\frac{C^*}{fps}$	$\epsilon = 60$		$\epsilon (1.84)$	
			$\frac{I_{sp}(vac)}{sec}$	$C_F(vac)$	$C_F(s1)$	$C_F(vac)$
70	7176.	6697.	414.0	1.9888	1.1771	1.4482
75	7356.	6816.	418.3	1.9744	1.1766	1.4475
80	7542.	6931.	421.8	1.9578	1.1765	1.4476
82.5	7489.	6869.	421.2	1.9728	1.1766	1.4486
85	7445.	6802.	419.0	1.9819	1.1767	1.4492
87.5	7408.	6737.	416.4	1.9888	1.1768	1.4497
90	7373.	6669.	413.5	1.9949	1.1770	1.4502
100	7267.	6413.	402.3	2.0183	1.1782	1.4560

Table A-4. Equilibrium Performance as a Function of Fluorine
Concentration 80% FLOX/55% CH₄ + 45% C₂H₆
O/F = 5.2 P_o = 100 psia

MIXTURE RATIO	NOZZLE STAGNATION PRESSURE, psia				CHARACTERISTIC VELOCITY, ft/sec			
	50	75	100	125	150	200	300	400
2.0	6247	6257	6263	6268	6272	6277	6283	6287
3.0	6569	6591	6606	6617	6626	6639	6655	6666
3.5	6664	6684	6699	6705	6711	6720	6739	6754
4.0	6720	6756	6780	6800	6815	6839	6872	6894
4.5	6811	6849	6875	6896	6913	6939	6974	6999
5.0	6861	6902	6931	6953	6972	7000	7039	7066
5.2	6860	6902	6931	6954	6972	7001	7041	7069
5.5	6808	6850	6879	6904	6922	6951	6991	7019
5.9	6734	6775	6803	6825	6843	6871	6910	6937
6.0	6715	6755	6783	6805	6822	6850	6888	6915
7.0	6496	6530	6553	6571	6585	6607	6638	6659

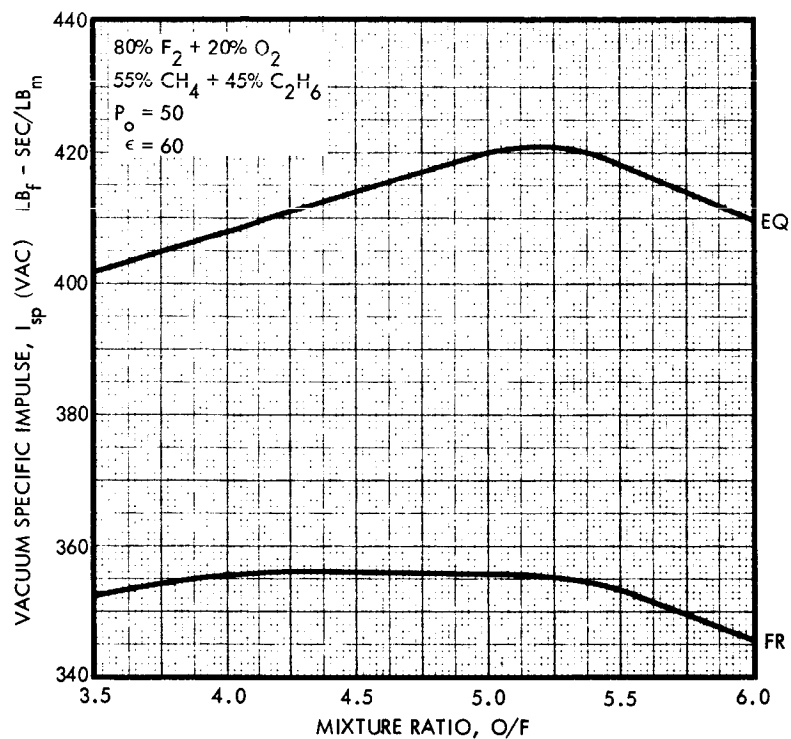


Figure A-9. Vacuum Specific Impulse Variation with Mixture Ratio (80% FLOX/methane-ethane) $P_0 = 50$ psia

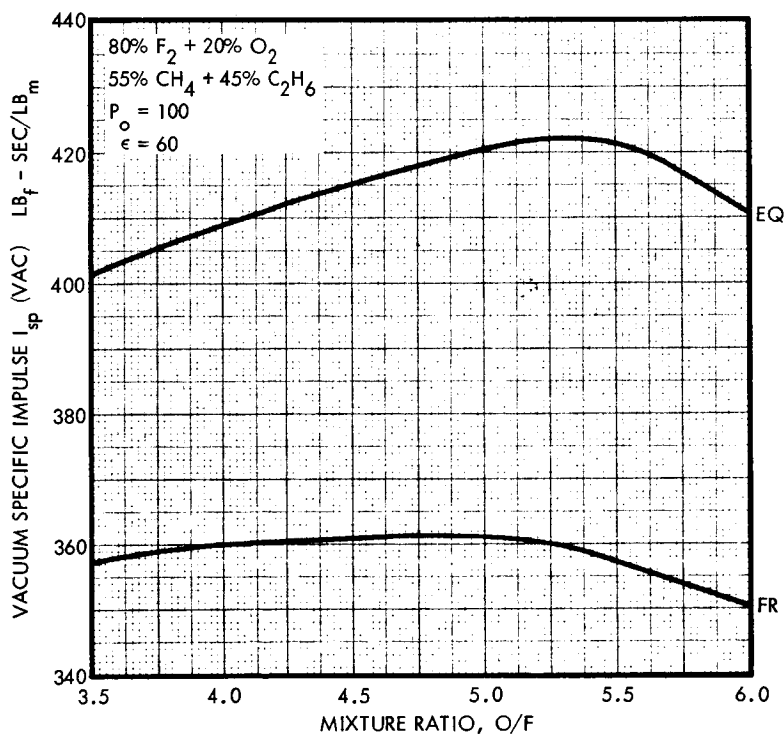


Figure A-10. Vacuum Specific Impulse Variation with Mixture Ratio (80% FLOX/methane-ethane) $P_0 = 100$ psia

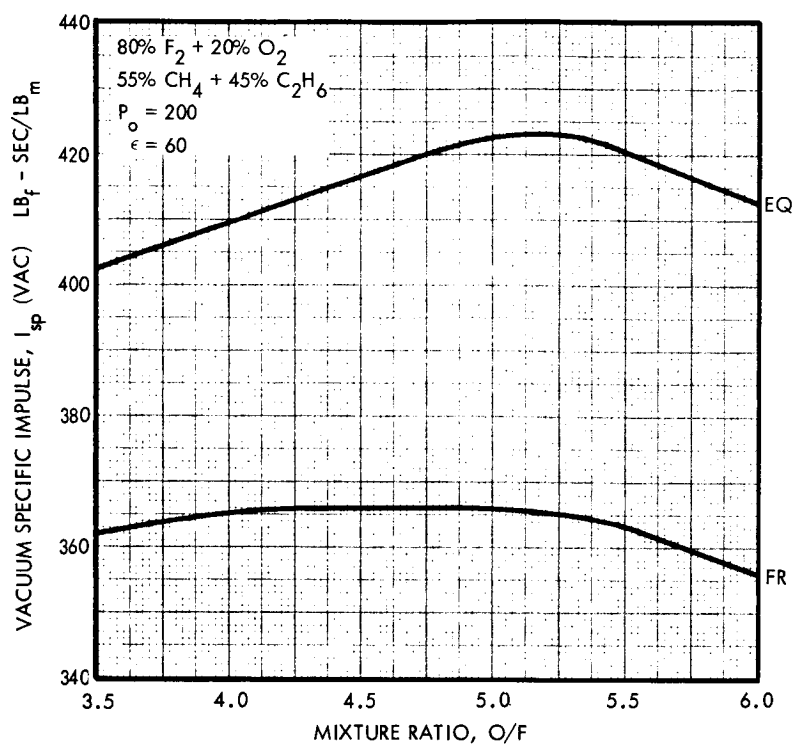


Figure A-11. Vacuum Specific Impulse Variation with Mixture Ratio
 (80% FLOX/methane-ethane) $P_0 = 200$ psia

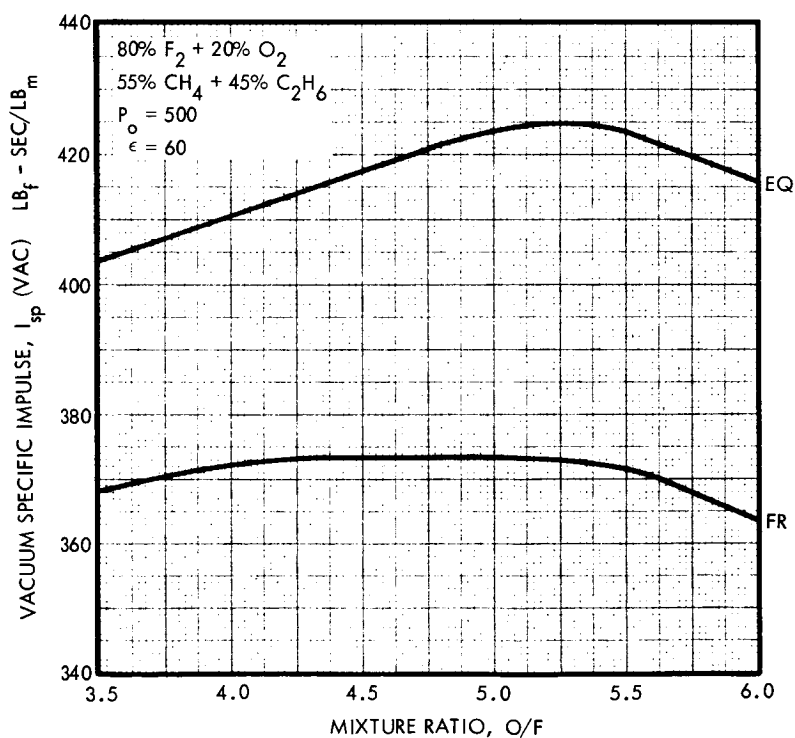


Figure A-12. Vacuum Specific Impulse Variation with Mixture Ratio
 (80% FLOX/methane-ethane) $P_0 = 500$ psia

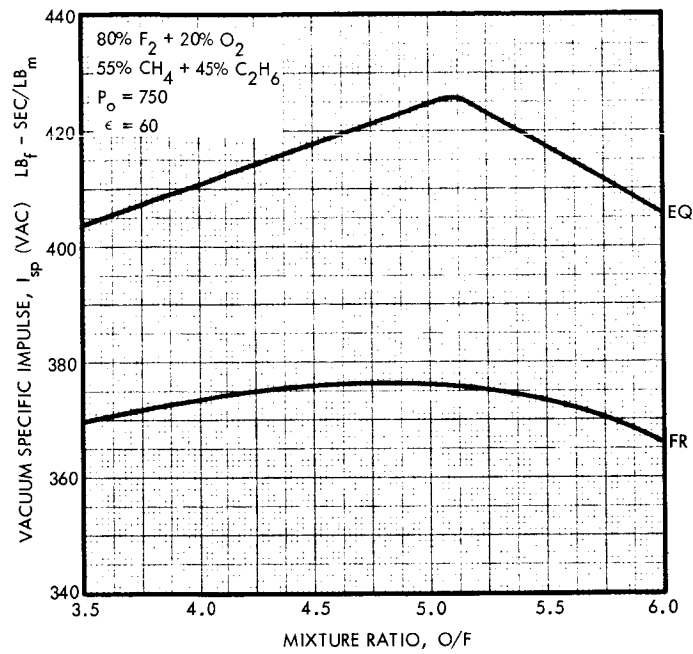


Figure A-13. Vacuum Specific Impulse Variation with Mixture Ratio (80% FLOX/methane-ethane) $P_o = 750$ psia

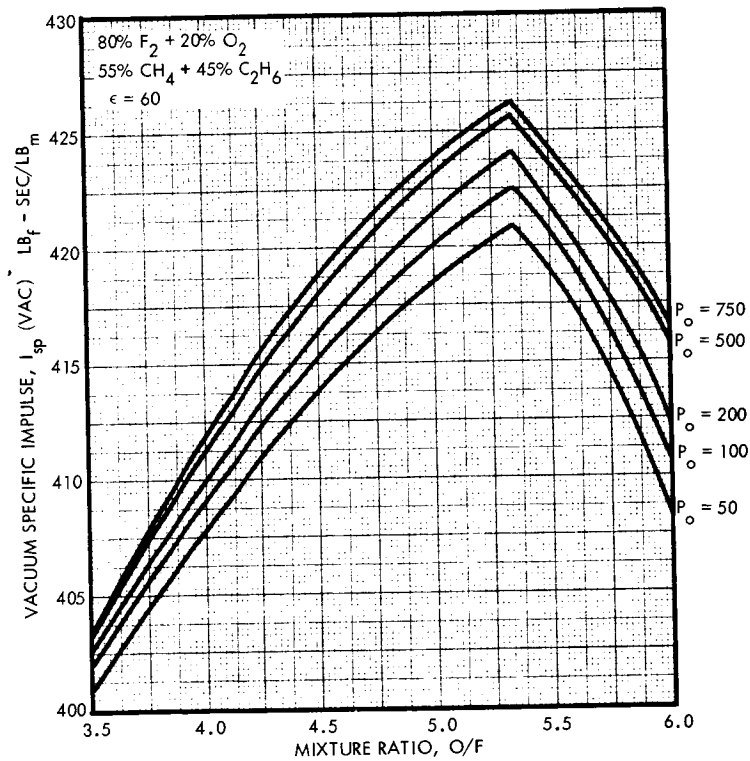


Figure A-14. Summary of Vacuum Specific Impulse Variation with Mixture Ratio (80% FLOX/methane-ethane)

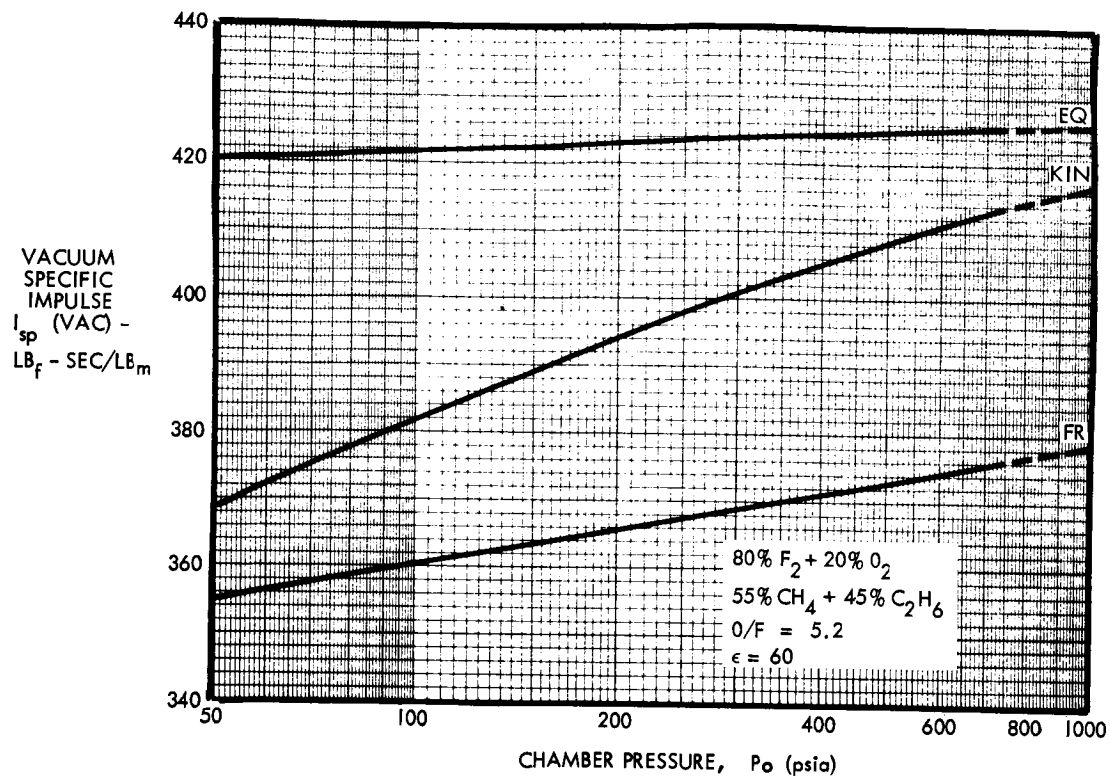


Figure A-15. Vacuum Specific Impulse Variation with Chamber Pressure (80% FLOX/methane-ethane)

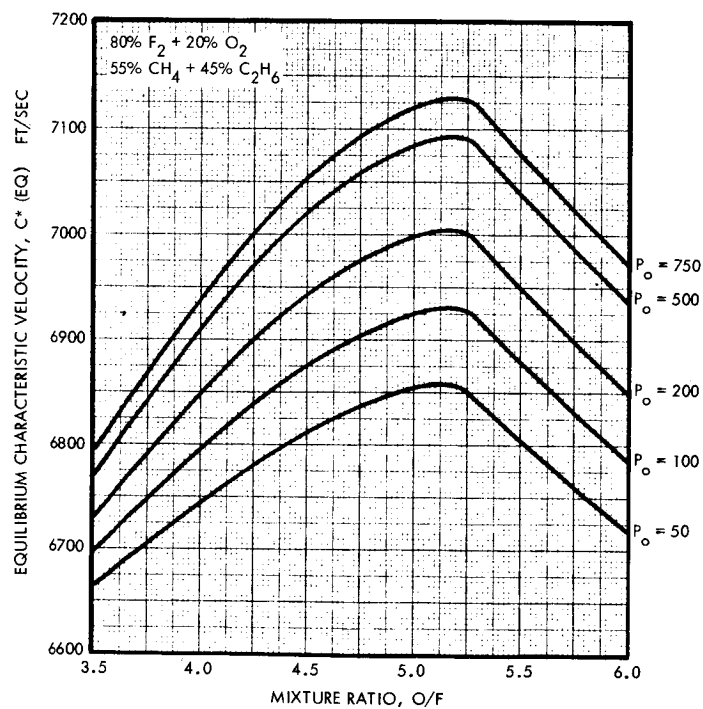


Figure A-16. Summary of Equilibrium Characteristics Velocity Variation with Mixture Ratio (80% FLOX/methane-ethane)

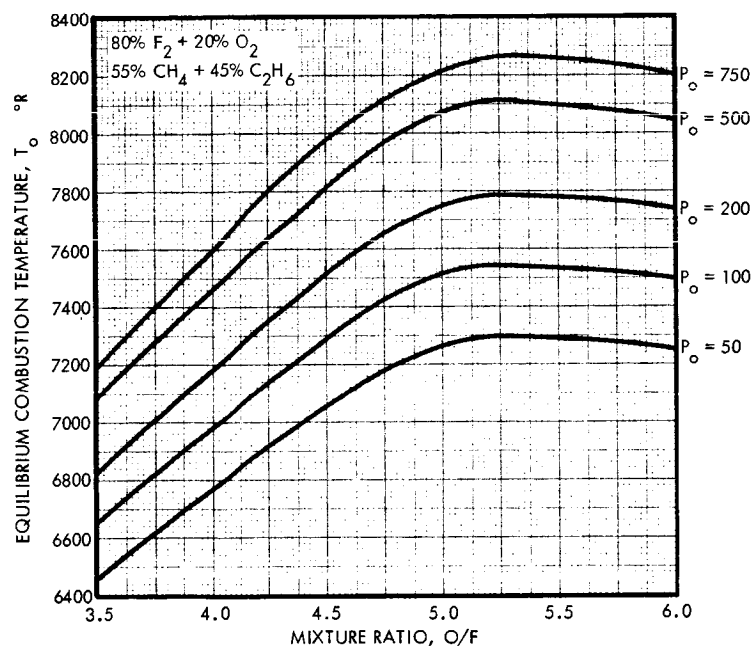


Figure A-17. Summary of Equilibrium Combustion Temperature Variation with Mixture Ratio (80% FLOX/methane-ethane)

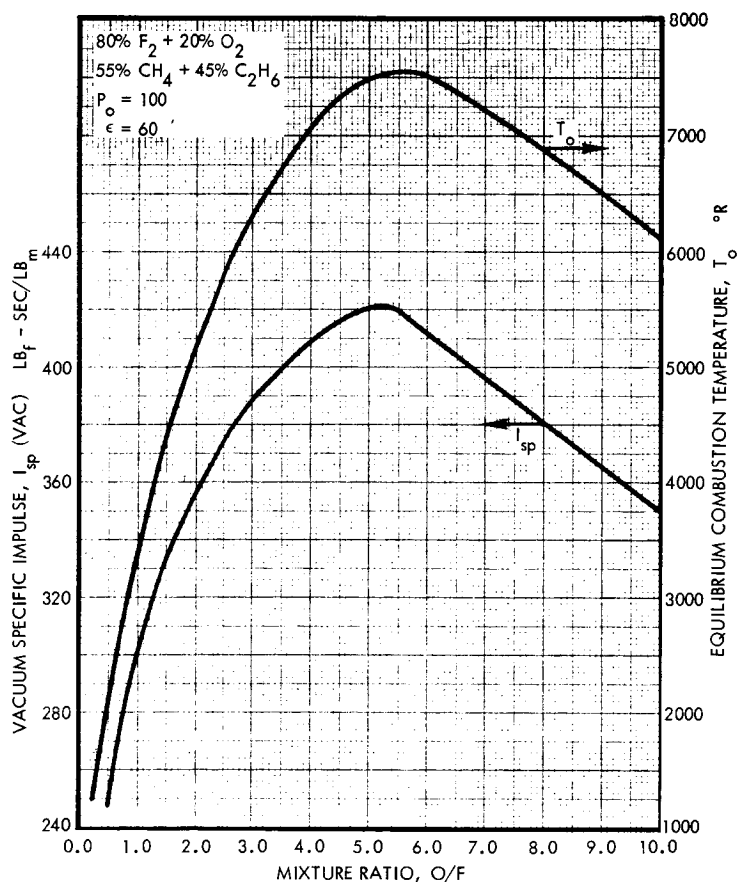


Figure A-18. Vacuum Specific Impulse and Equilibrium Combustion Temperature Variation with Mixture Ratio (80% FLOX/methane-ethane)

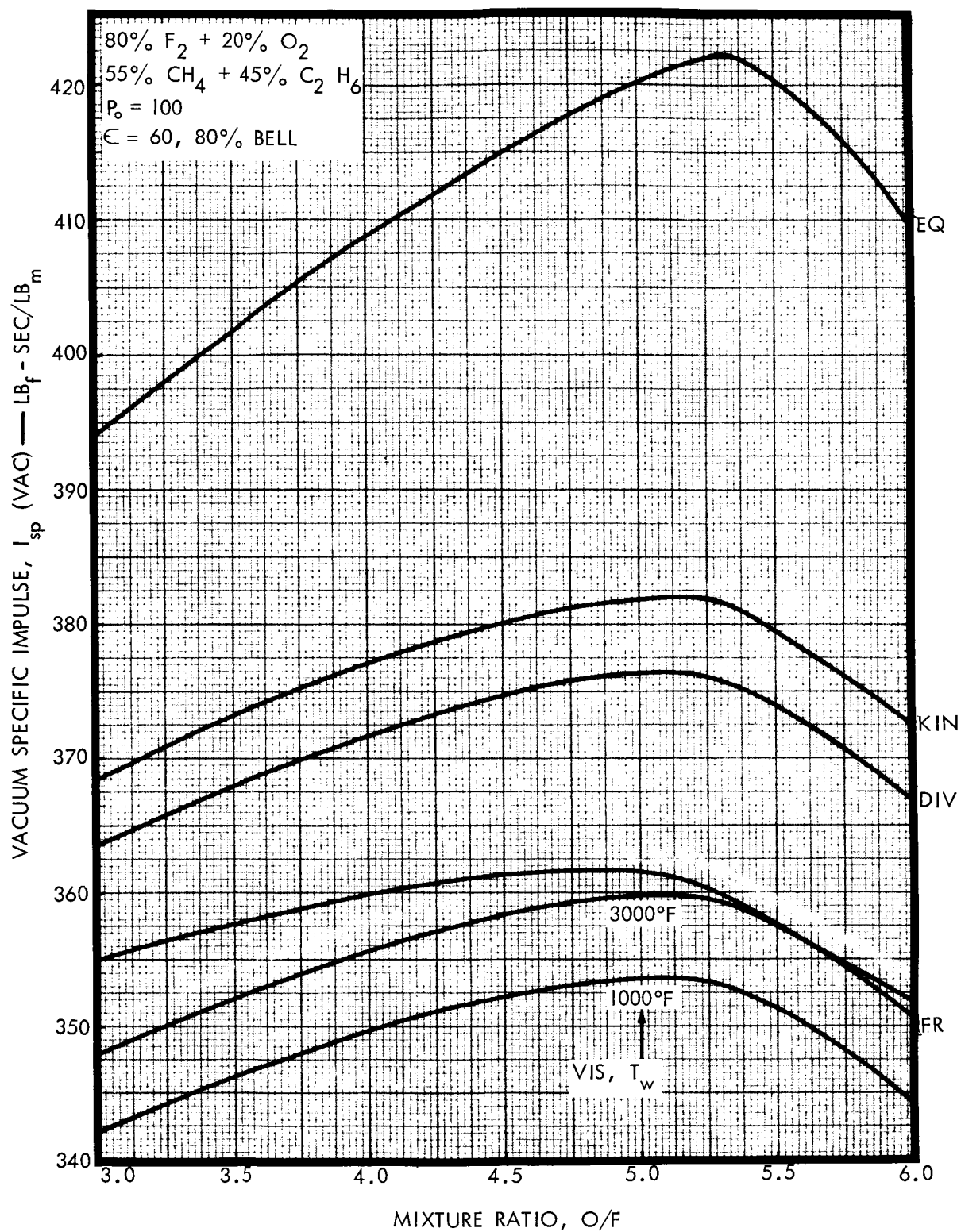


Figure A-19. Vacuum Specific Impulse with Losses
(80% FLOX/methane-ethane)

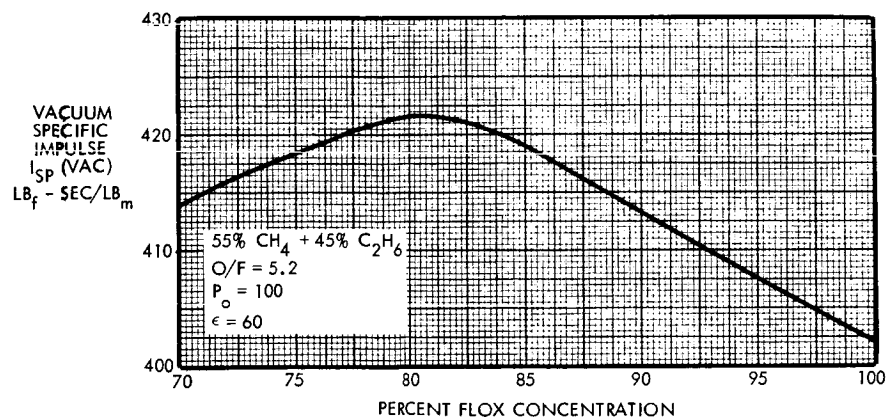


Figure A-20. Vacuum Specific Impulse Variation with Fluorine Concentration (80% FLOX/methane-ethane)

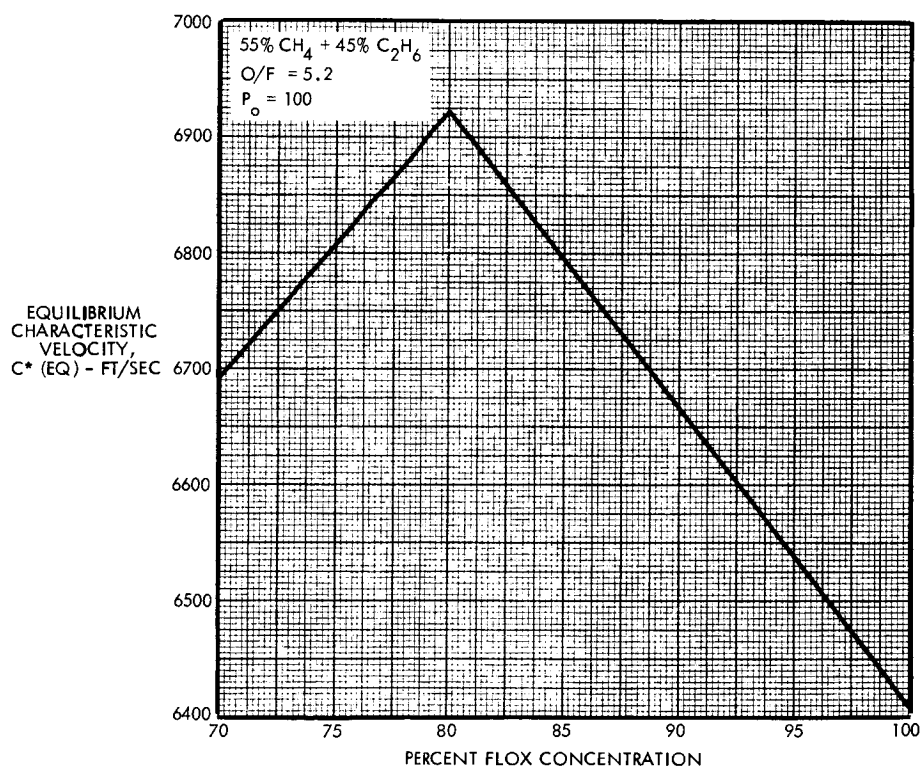


Figure A-21. Equilibrium Characteristic Velocity Variation with Fluorine Concentration (80% FLOX/methane-ethane)

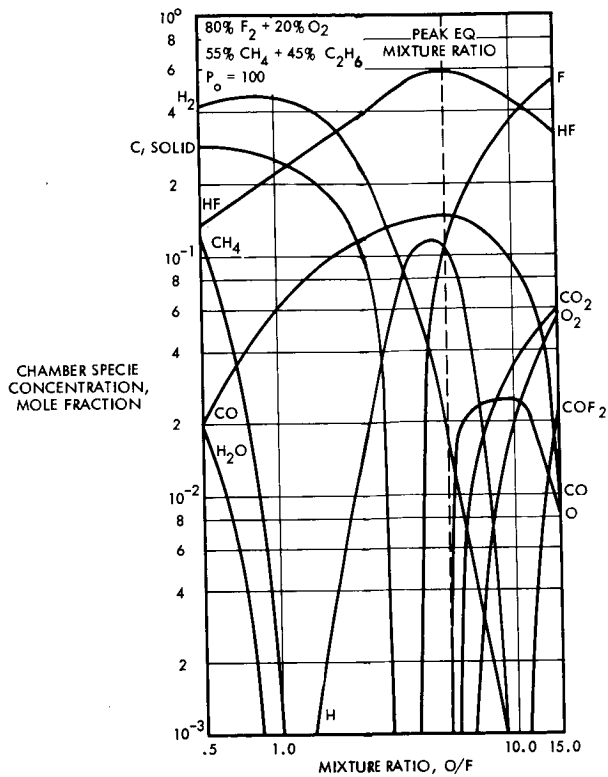


Figure A-22
Chamber Specie Concentration Variation
with Mixture Ratio
(80% FLOX/methane-ethane)

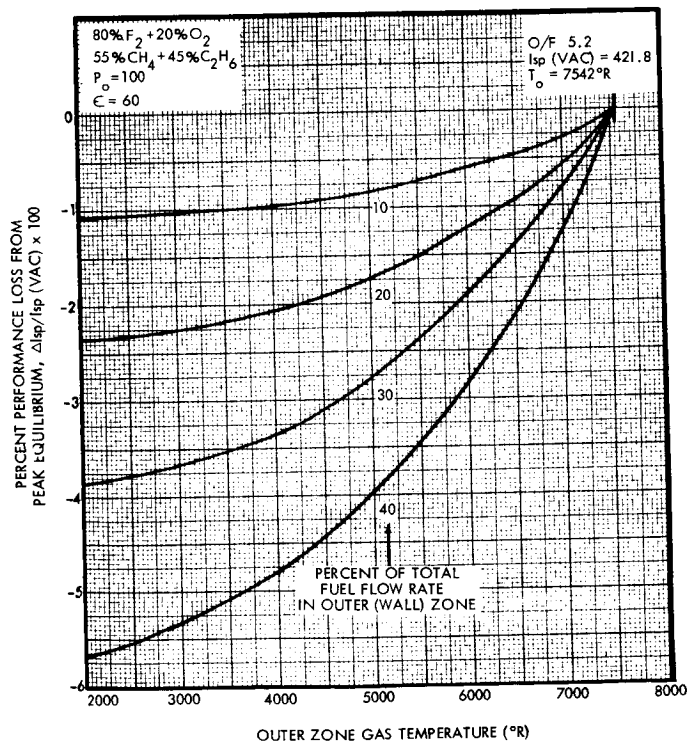


Figure A-23. Vacuum Specific Impulse Zonal Loss with Fixed Core
Mixture Ratio (80% FLOX/methane-ethane)

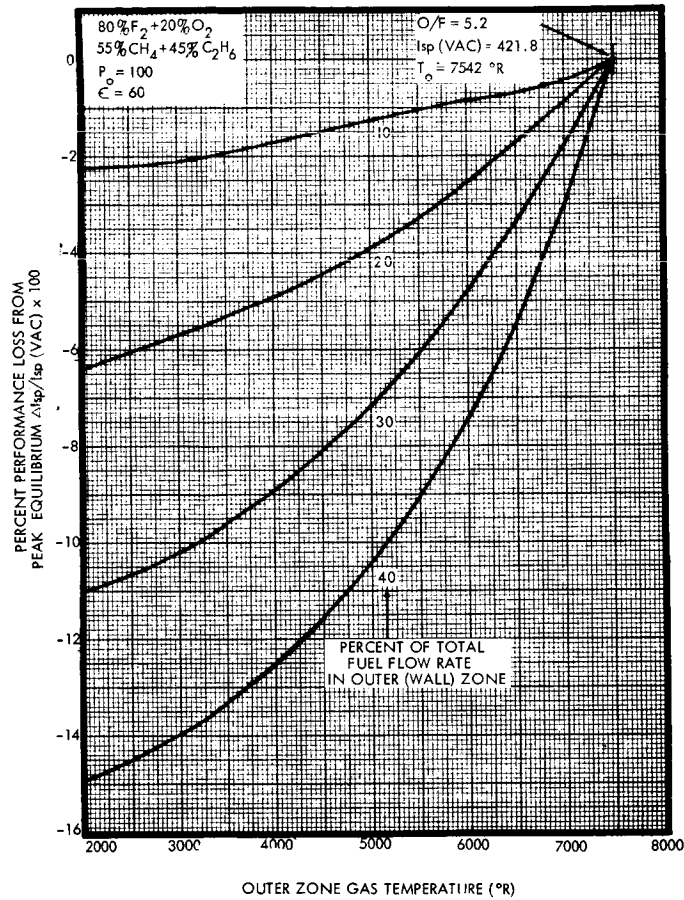


Figure A-24. Vacuum Specific Impulse Zonal Loss with Fixed Overall Mixture Ratio (80% FLOX/methane-ethane)

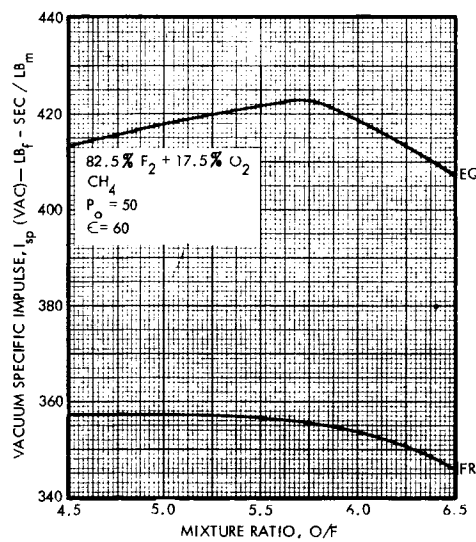


Figure A-25. Vacuum Specific Impulse Variation with Mixture Ratio (82.5% FLOX/methane) $P_o = 50$ psia

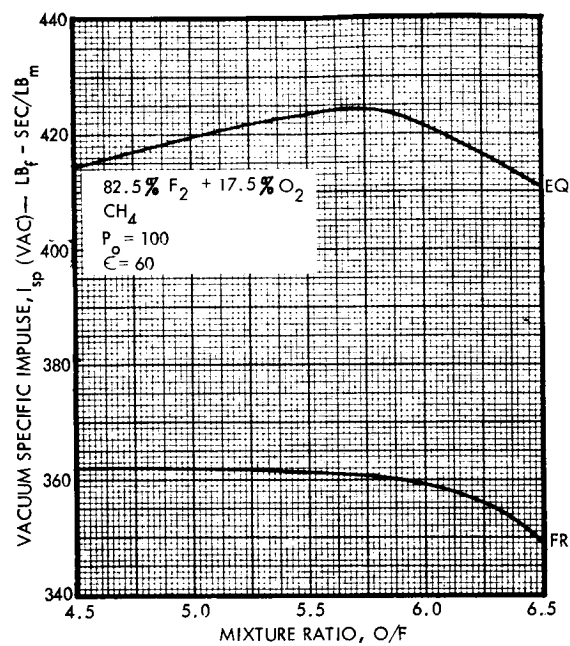


Figure A-26. Vacuum Specific Impulse Variation with Mixture Ratio
(82.5% FLOX/methane) P₀ = 100 psia

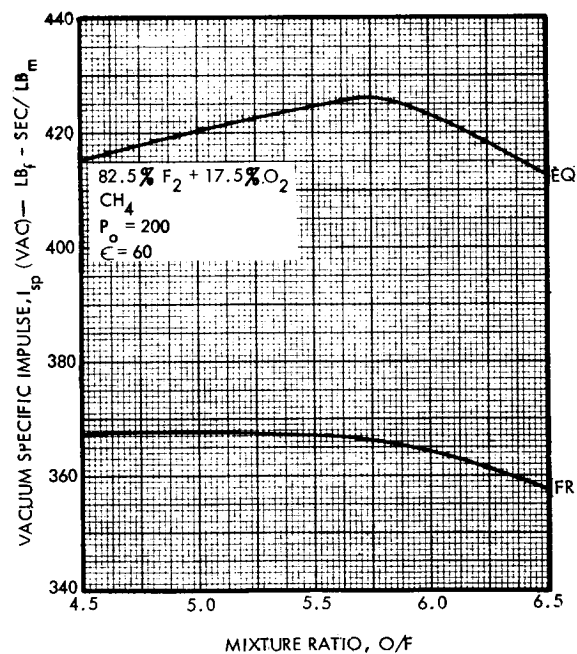


Figure A-27. Vacuum Specific Impulse Variation with Mixture Ratio
(82.5% FLOX/methane) P₀ = 200 psia

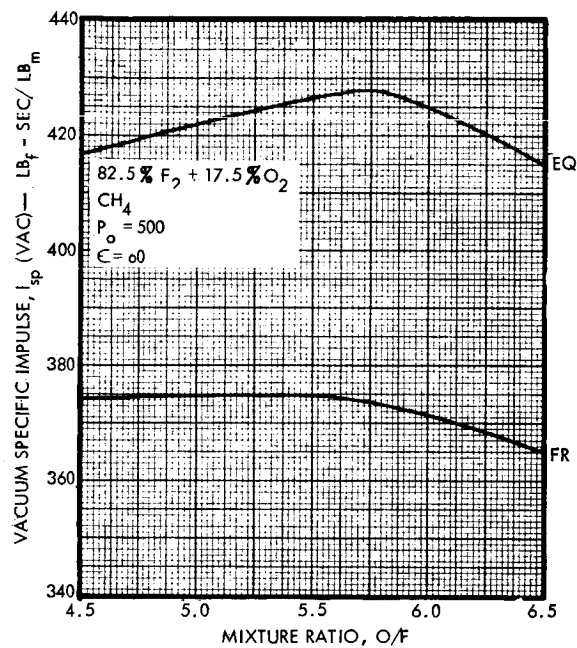


Figure A-28. Vacuum Specific Impulse Variation with Mixture Ratio (82.5% FLOX/methane) $P_0 = 500$ psia

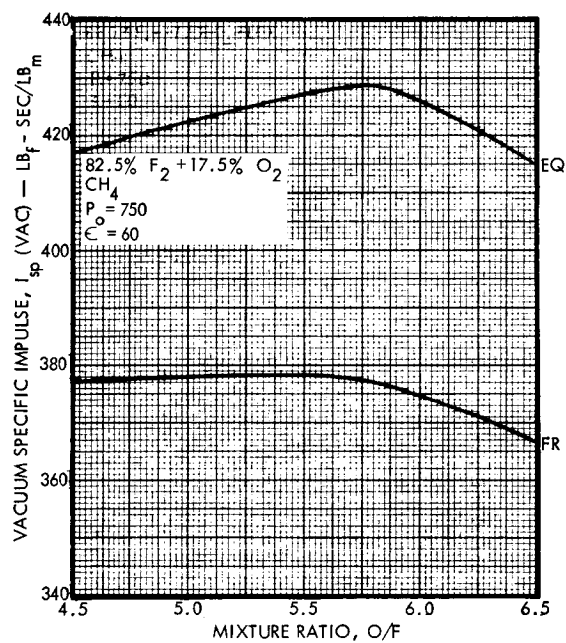


Figure A-29. Vacuum Specific Impulse Variation with Mixture Ratio (82.5% FLOX/methane) $P_0 = 750$ psia

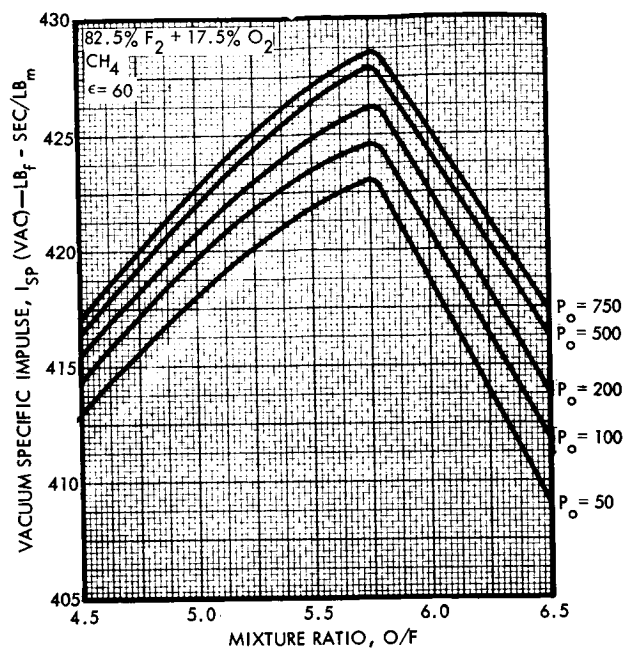


Figure A-30. Summary of Vacuum Specific Impulse Variation with Mixture Ratio (82.5% FLOX/methane)

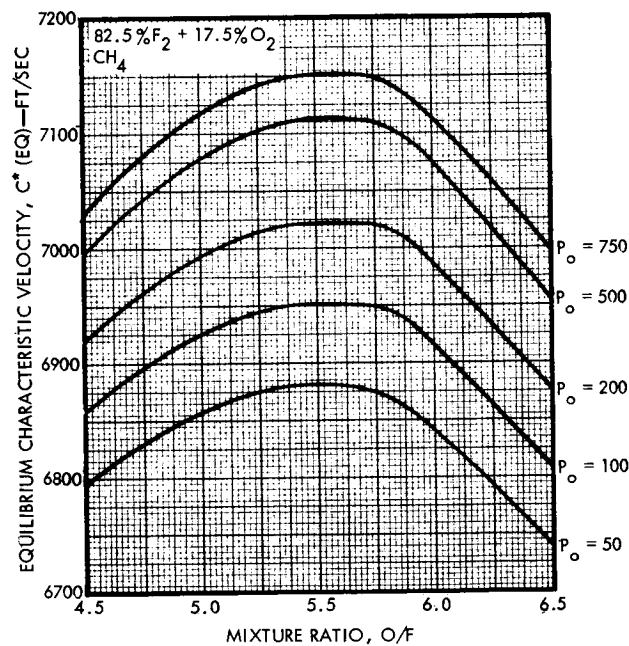


Figure A-31. Summary of Equilibrium Characteristic Velocity Variation with Mixture Ratio (82.5% FLOX/methane)

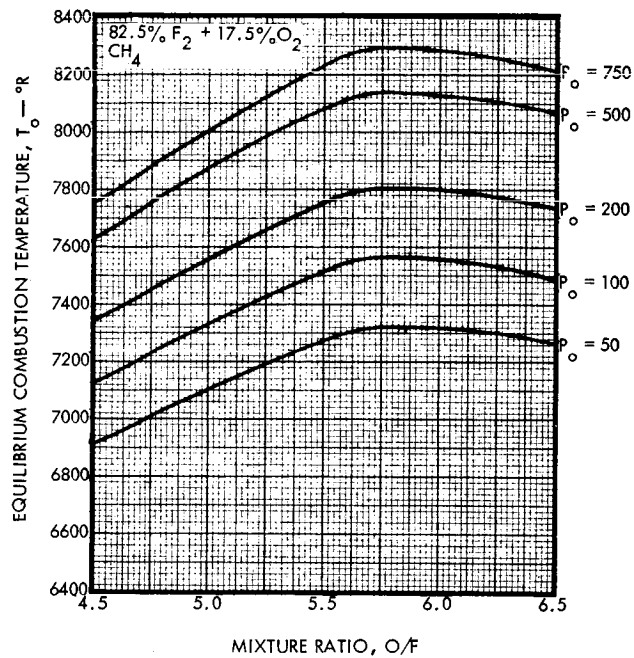


Figure A-32. Summary of Equilibrium Combustion Temperature Variation with Mixture Ratio (82.5% FLOX/methane)

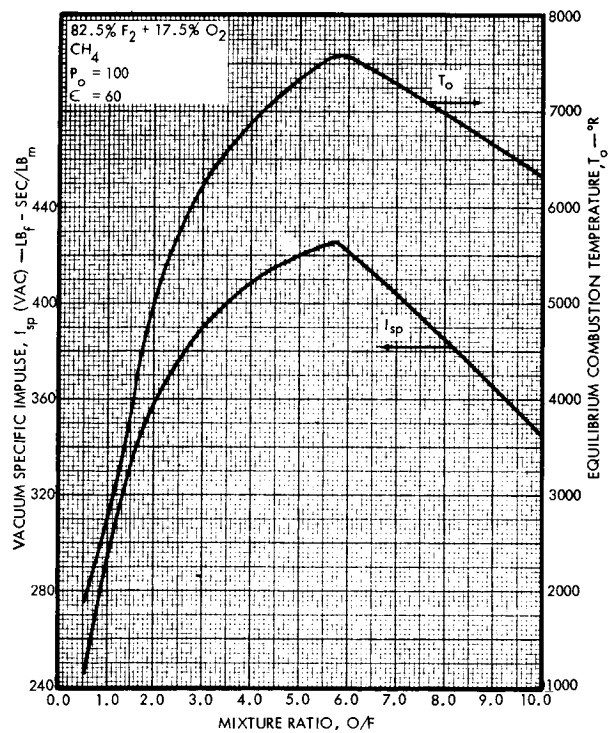


Figure A-33. Vacuum Specific Impulse and Equilibrium Combustion Temperature Variation with Mixture Ratio (82.5% FLOX/methane)

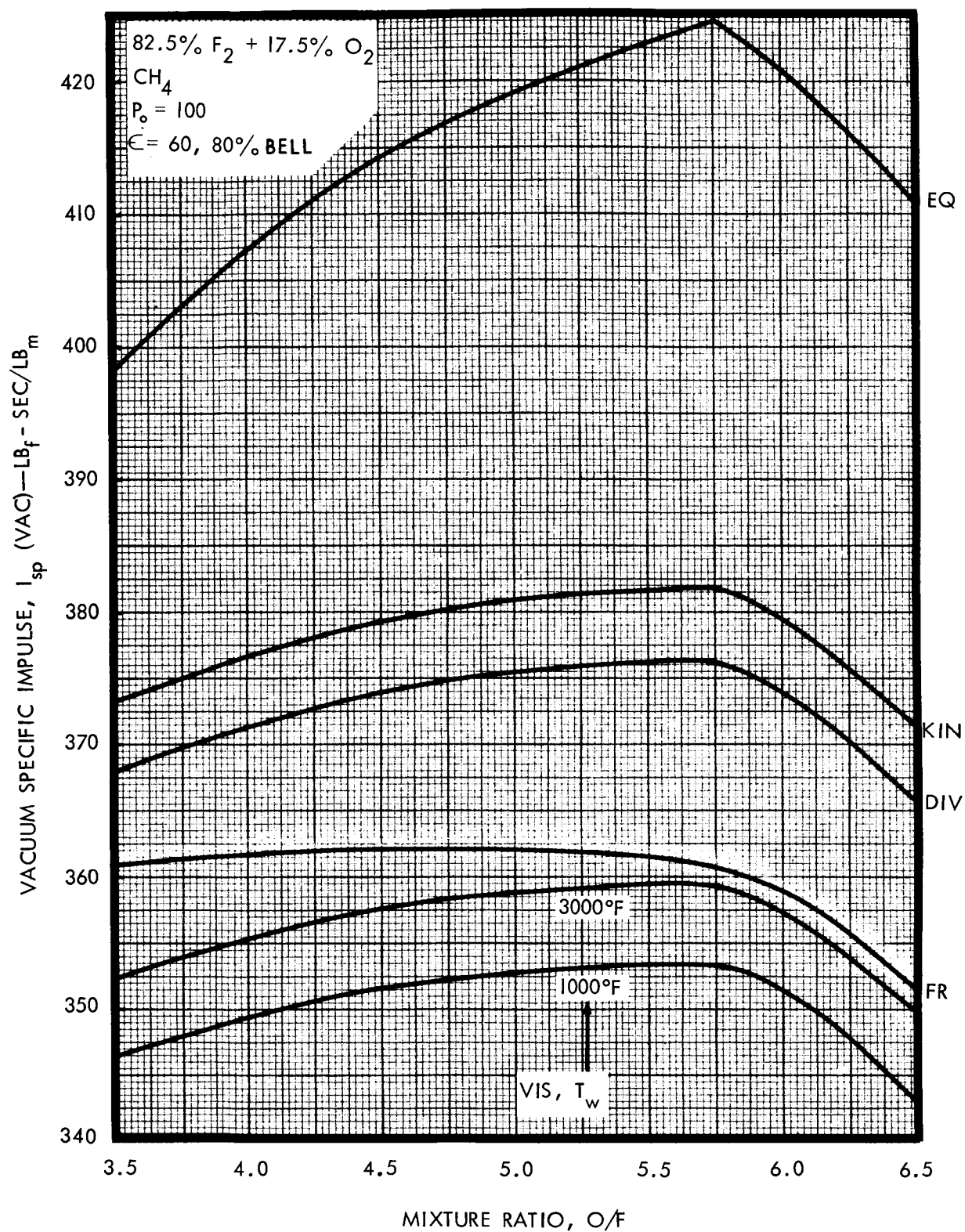


Figure A-34. Vacuum Specific Impulse with Losses
 (82.5% FLOX/methane)

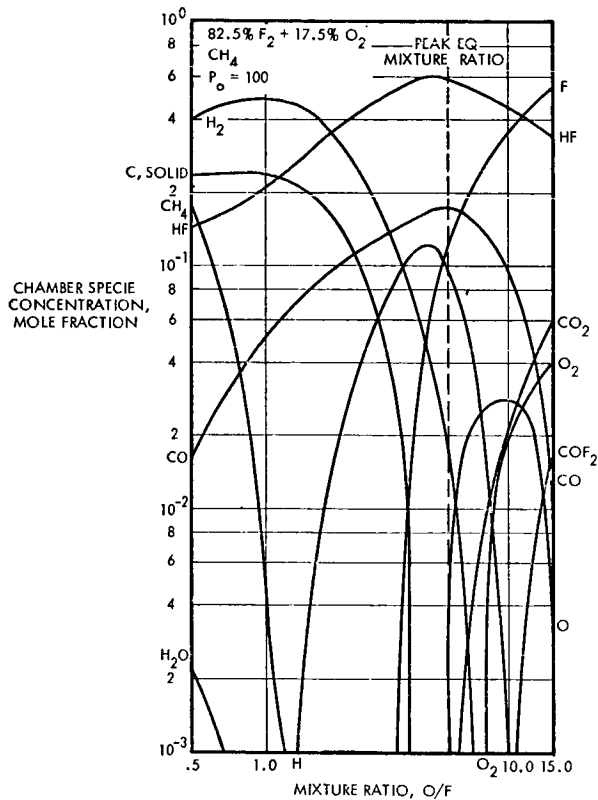


Figure A-35. Chamber Species Concentration Variation with Mixture Ratio (82.5% FLOX/methane)

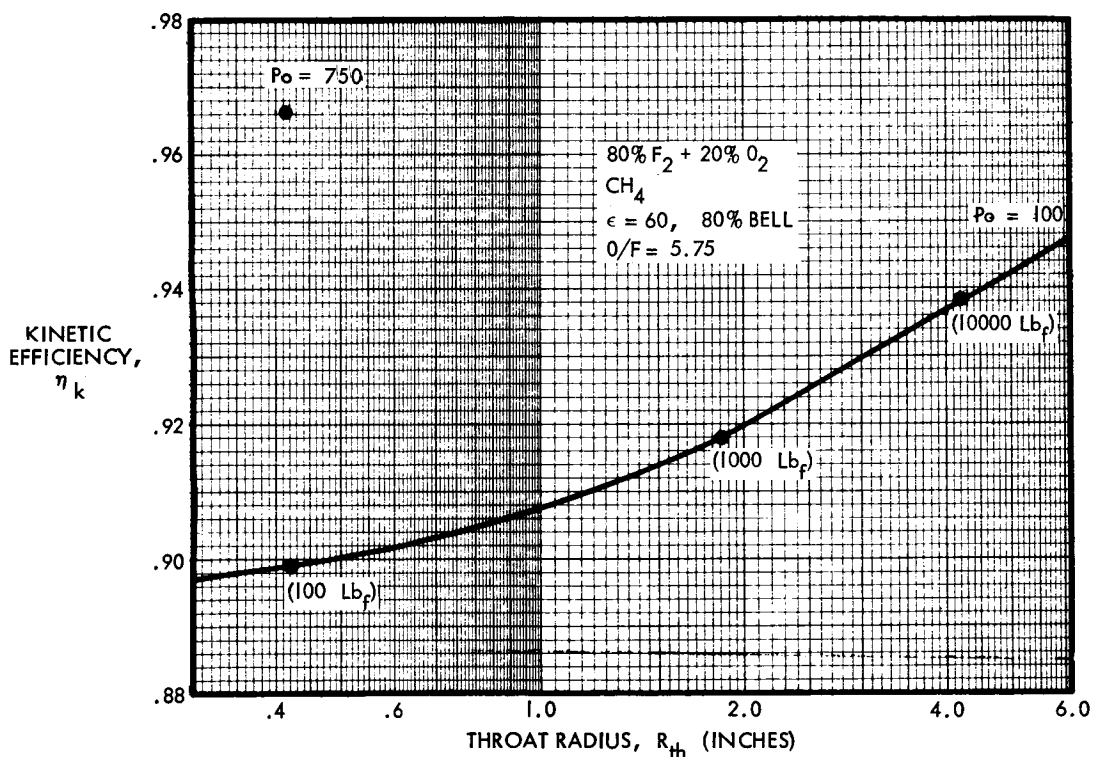


Figure A-36. Variation of Kinetic Efficiency with Throat Radius (82.5% FLOX/methane)

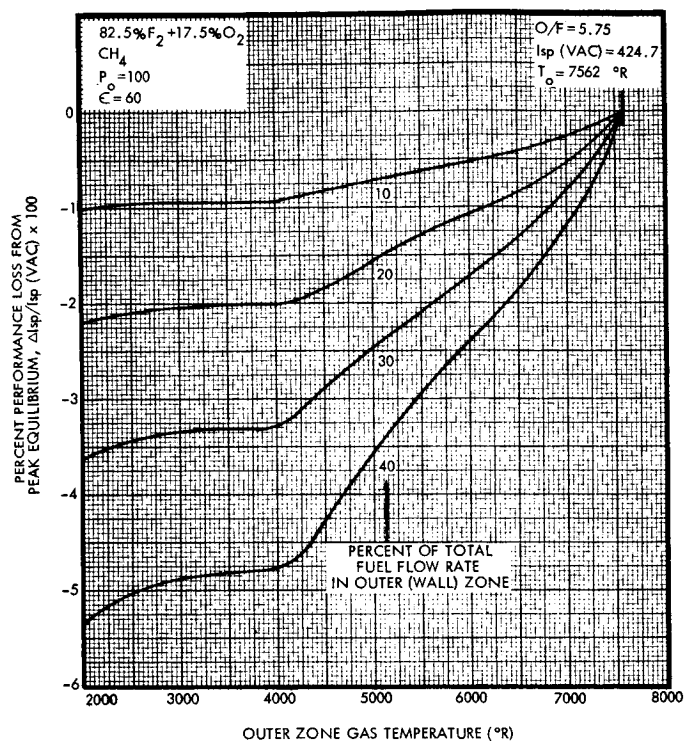


Figure A-37. Vacuum Specific Impulse Zonal Loss with Fixed Core Mixture Ratio (82.5% FLOX/methane)

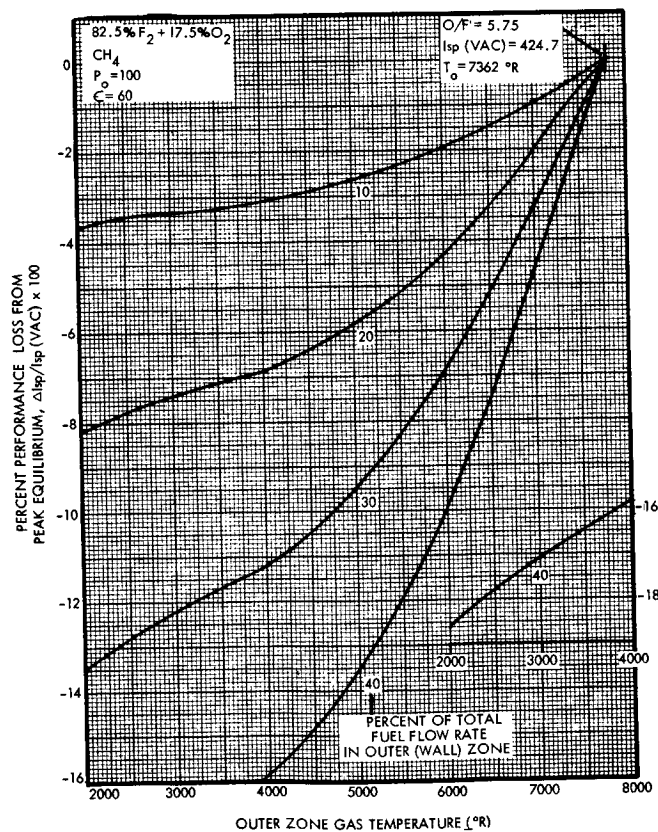


Figure A-38. Vacuum Specific Impulse Zonal Loss with Fixed Overall Mixture Ratio (82.5% FLOX/methane)

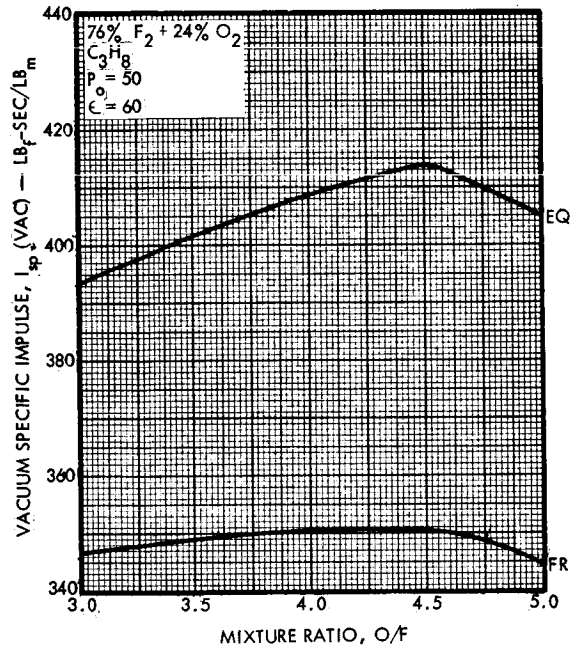


Figure A-39. Vacuum Specific Impulse Variation with Mixture Ratio
 (76% FLOX/propane) $P_0 = 50$ psia

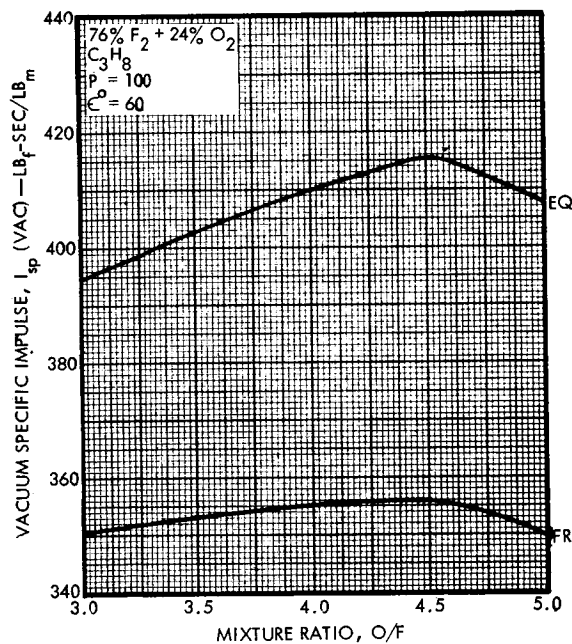


Figure A-40. Vacuum Specific Impulse Variation with Mixture Ratio
 (76% FLOX/propane) $P_0 = 100$ psia

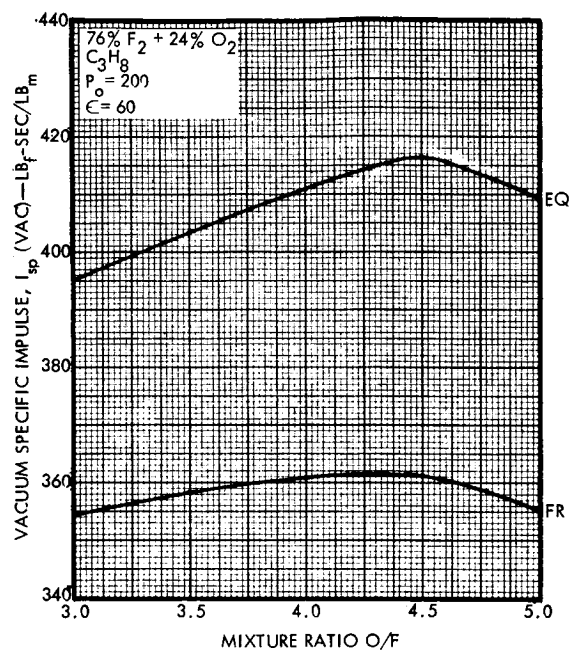


Figure A-41. Vacuum Specific Impulse Variation with Mixture Ratio (76% FLOX/propane) $P_0 = 200$ psia

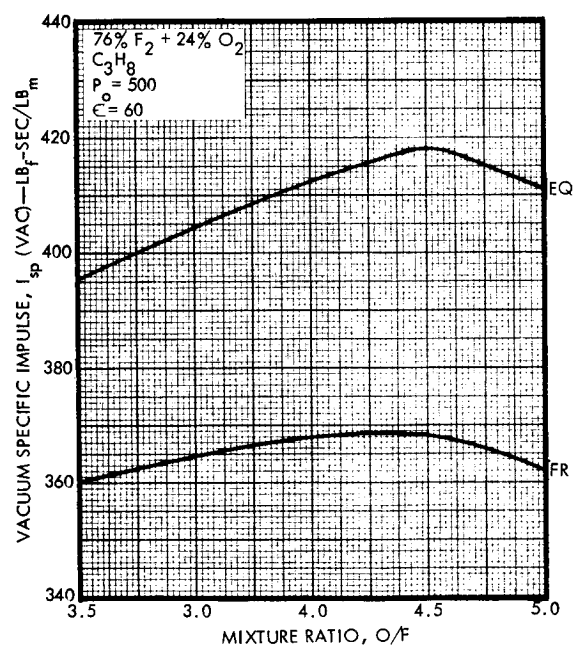


Figure A-42. Vacuum Specific Impulse Variation with Mixture Ratio (76% FLOX/propane) $P_0 = 500$ psia

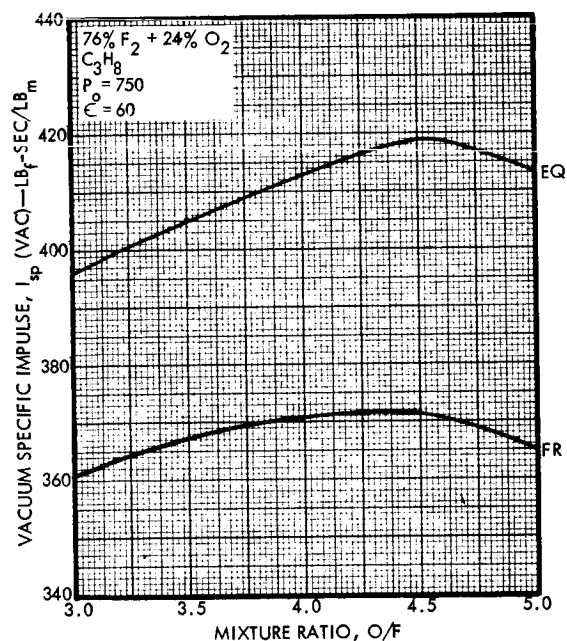


Figure A-43. Vacuum Specific Impulse Variation with Mixture Ratio (76% FLOX/propane) $P_o = 750$ psia

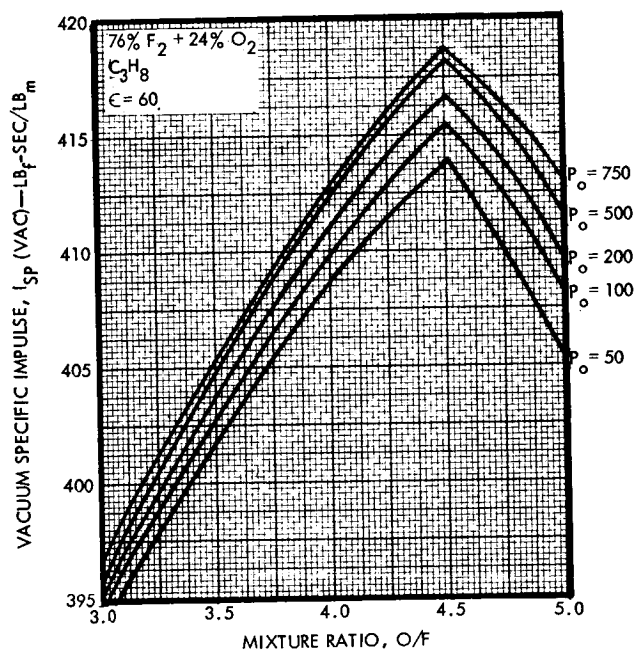


Figure A-44. Summary of Vacuum Specific Impulse Variation with Mixture Ratio (76% FLOX/propane)

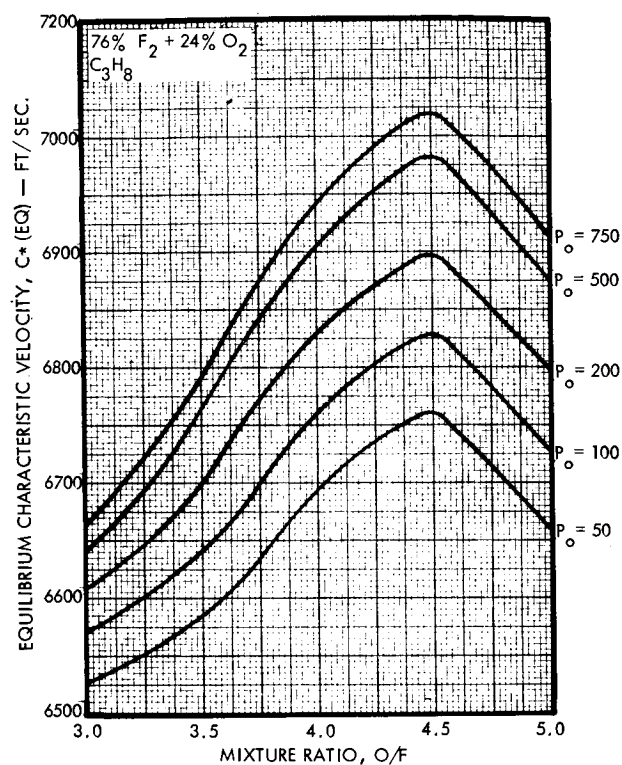


Figure A-45. Summary of Equilibrium Characteristic Velocity Variation with Mixture Ratio (76% FLOX/propane)

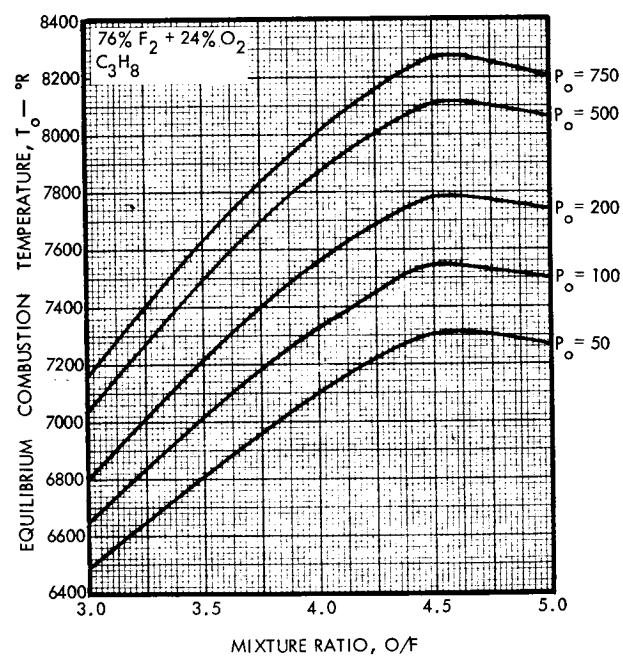


Figure A-46. Summary of Equilibrium Combustion Temperature Variation with Mixture Ratio (76% FLOX/propane)

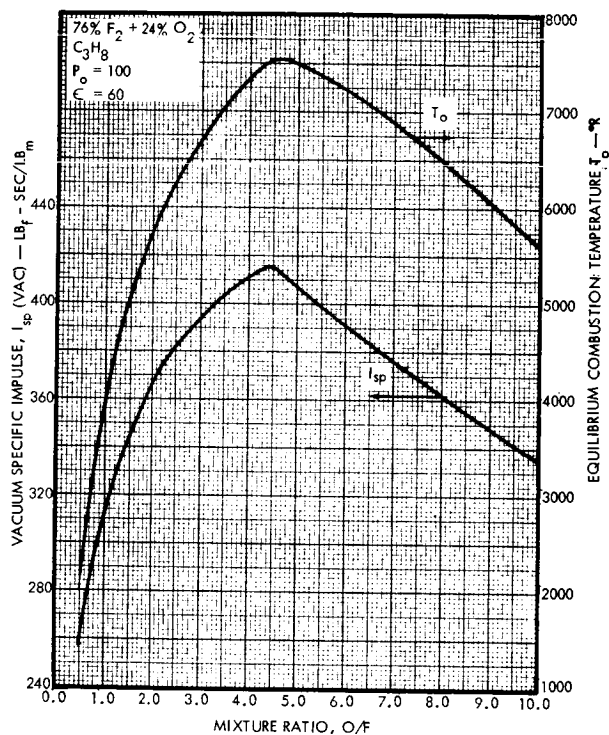


Figure A-47. Vacuum Specific Impulse and Equilibrium Combustion Temperature Variation with Mixture Ratio (76% FLOX/propane)

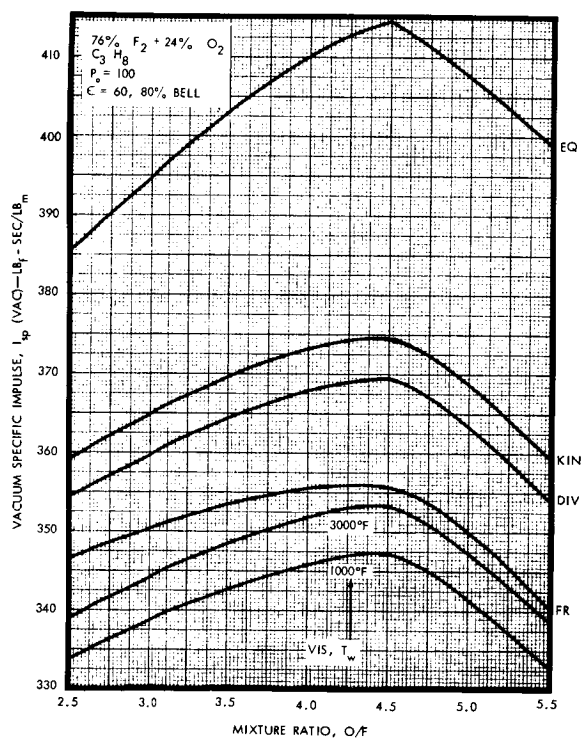


Figure A-48. Vacuum Specific Impulse with Losses (76% FLOX/propane)

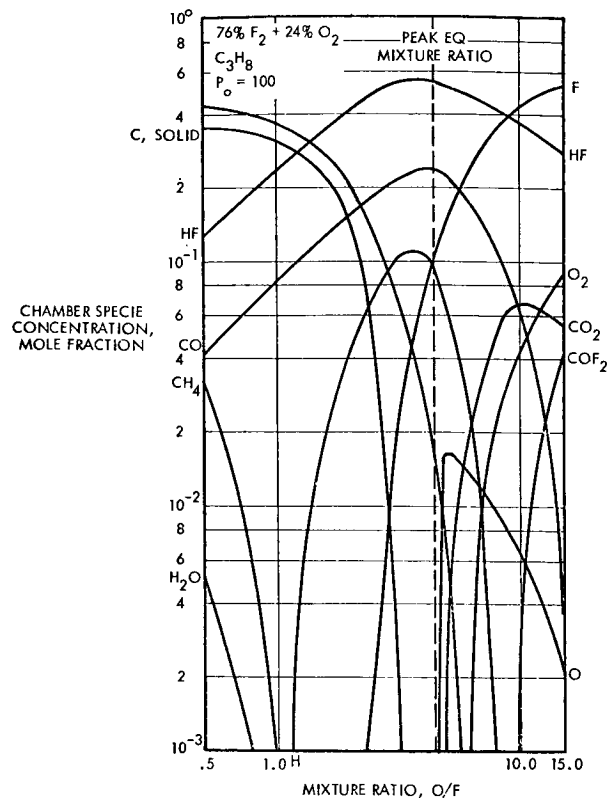


Figure A-49. Chamber Specie Concentration Variation with Mixture Ratio (76% FLOX/propene)

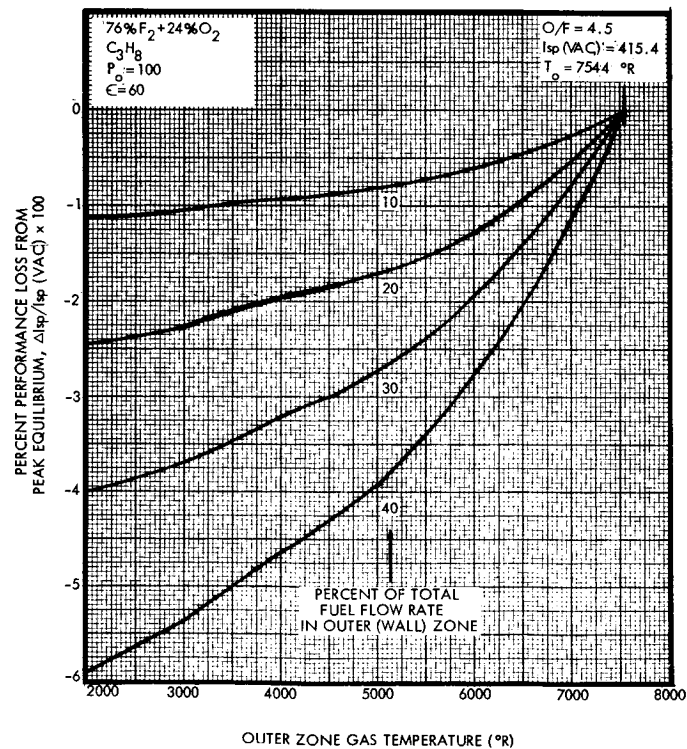


Figure A-50. Vacuum Specific Impulse Zonal Loss with Fixed Core Mixture Ratio (76% FLOX/propene)

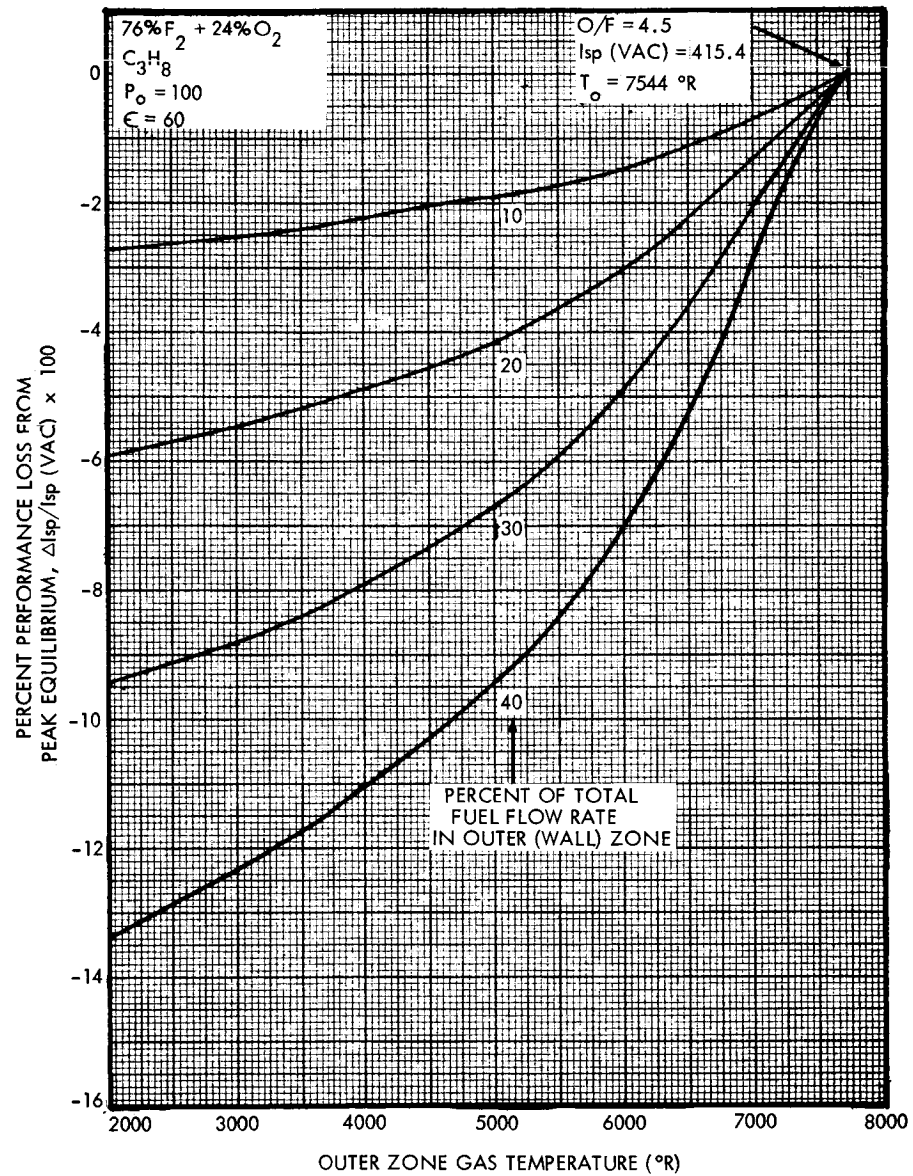


Figure A-51. Vacuum Specific Impulse Zonal Loss with Fixed Overall Mixture Ratio (76% FLOX/propane)

APPENDIX B

LPG POOL BOILING EXPERIMENTS

APPENDIX B

LPG POOL BOILING EXPERIMENTS

1.0 INTRODUCTION

Limited data exist on the nucleate boiling characteristics of the LPG's. Although the data of Reference B-1 were useful for the neat liquids, no data are available for the eutectic blend of 55% methane + 45% ethane. Accurate knowledge of the burnout heat flux for each of the fuels at saturated propellant conditions was required to evaluate design limits for the film-conduction cooled thruster. The data of Reference B-1 indicated that under saturated propellant conditions there was essentially no dependence of the burnout heat flux with velocity for the range of velocities of interest ($V < 40$ ft/sec). It was therefore concluded that valid pool boiling experiments could be performed with propane, methane and a 55% methane/45% ethane blend at atmospheric pressure in both the subcooled and saturated states. The primary purpose of the experiments was to determine the peak nucleate boiling heat flux, which is used in determining the maximum operating limits of liquid film-conduction cooled thruster designs. In addition to peak heat flux information, data were also obtained in both the nucleate boiling and unstable pool boiling regimes (Reference B-2).

The experiments were performed using a transient calorimetric technique in which a heated calibrated mass of OFHC copper was emersed into the liquified fuel and the thermal response recorded. In each test, heat transfer began well into the stable film-boiling regime, made the transition into the unstable film-boiling regime through the peak heat flux and finally passed into the nucleate boiling regime.

2.0 EXPERIMENTAL APPARATUS

The schematic of the test setup to obtain the pool boiling data is shown in Figure B-1. The primary test apparatus consisted of a double jacketed glass dewar, a high-speed oscillograph and a calibrated OFHC copper calorimeter. The test setup is shown photographically in Figure B-2.

The glass dewar was specifically designed for the LPG boiling experiments such that thermal gradients in the test liquid would not affect the

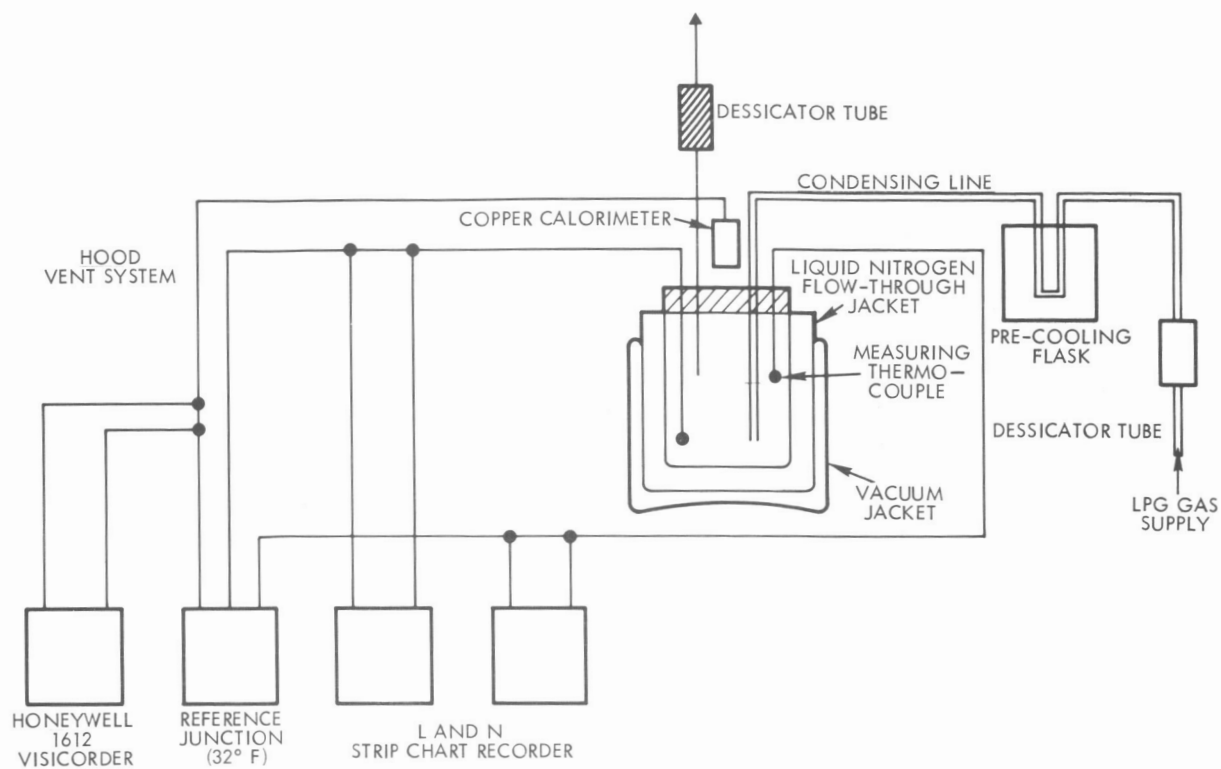


Figure B-1. Schematic of Pool Boiling Test Setup

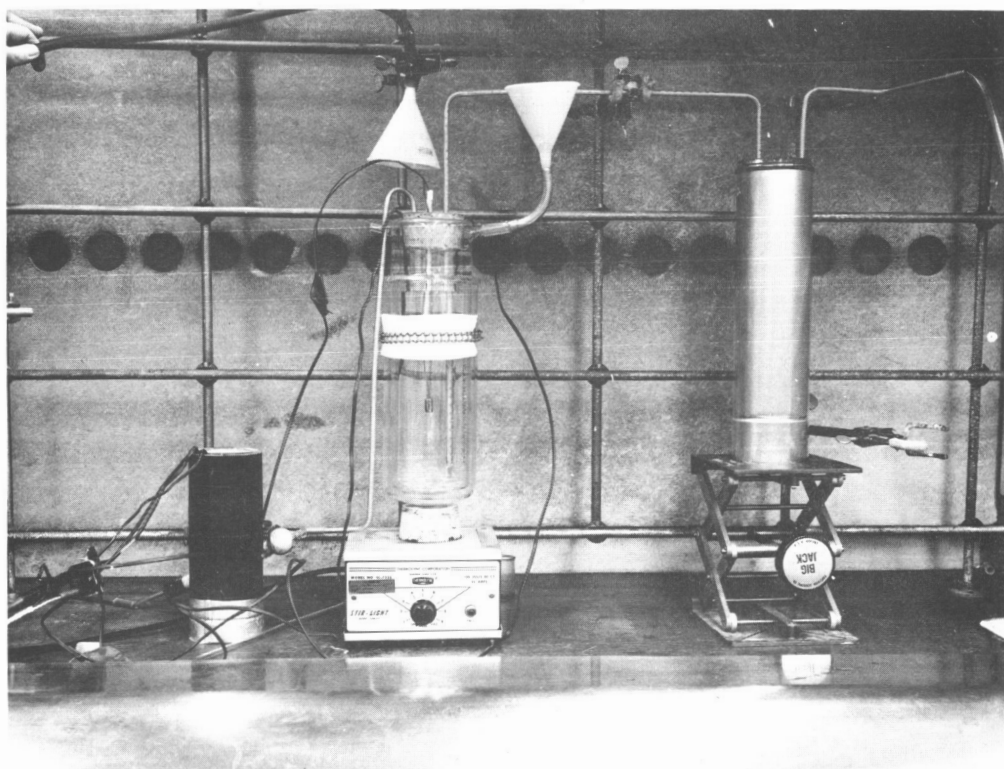


Figure B-2. Experimental Apparatus for LPG Nucleate Boiling Experiments at NBP

heat flux measurements. The L/D of the dewar was large enough to prevent stratification from influencing the liquid bulk temperature near the calorimeter. A magnetic stirrer was incorporated in the dewar to mix the liquid between tests; however, this later proved to be inefficient due to the large L/D of the dewar. The liquid was consequently agitated with a glass rod to eliminate any stratification that might have occurred during the test. The bulk temperature of the LPG was measured at two locations within the dewar with copper/constantan thermocouples: one located near the bottom of the dewar and one near the top of the dewar. These were recorded on two L & N strip chart recorders.

The calorimeter used to obtain the pool boiling data is shown in Figure B-3. To assure that the thermal mass responded as a calorimeter, the diameter of the slug was sized according to the criteria

$$B_i = \frac{hr}{k_o} \leq 0.1 \quad (B-1)$$

where

- Bi = Biot modulus
- h = convection coefficient
- r = characteristic thermal dimension
- k_o = thermal conductivity of slug material

The radius of the slug was sized on the basis of the Biot modulus being equal to 0.1. Thus, the heat balance given by Equation (B-1) could be used to determine the heat flux to the slug.

$$q/A = \rho C_p \frac{V}{A} \frac{dT}{d\theta} \quad (B-2)$$

where

- q/A = average heat flux
- $\rho C_p V$ = the thermal mass of the slug
- A = area of the slug
- dT/dθ = measured temperature response of the slug

The slug sized according to this criteria would give a peak heat flux error of less than 2 percent. At heat fluxes below the peak heat flux, the error would be much less than 1 percent.

For recording purposes, it was necessary that the transient time be as long as possible. The time from the inception of unstable film boiling to the end of nucleate boiling should be in the order of 3 to 4 seconds. It is obvious from Equation (B-2) that the time would increase with an increase in the volume to surface area ratio, V/A . For a calorimeter configuration similar to that shown in Figure B-3, the ratio V/A is

$$V/A = \frac{D(\frac{1}{6} D + \frac{1}{4})L}{D + L} \quad (B.3)$$

Holding D constant and varying L , it can be seen that the expression for V/A does not have a maximum value at a finite value of L . However, in the limit as L approaches infinity,

$$\left. V/A \right|_{L=\infty} = \lim_{L \rightarrow \infty} \frac{D(\frac{1}{6} D + \frac{1}{4})L}{D + L} = \frac{D}{4} \quad (B.4)$$

Therefore, the maximum increase in the transient time of this calorimeter over the transient time of a spherical mass of the same diameter is approximately 50 percent. The design length of $L = .45$ inches was chosen as it resulted in a transient time of approximately 60 percent of the maximum time. It was found that relatively large increases in length above $L = .45$ yielded very small increases in V/A (or transient time).

A .032 inch constantan thermocouple wire was swaged into the copper mass along the axis of symmetry and a .032 inch copper thermocouple wire was swaged into the mass slightly off center from the constantan wire (see Figure B-3). This essentially made the copper mass the thermocouple junction, and the measured temperature represented the average temperature of the calorimeter mass. The exposed thermocouple wires were stripped of their insulation so that they would more rapidly come to the temperature of the LPG and therefore not enter into the calculation of the heat flux by influencing the $\rho C_p V/A$ of the calorimeter. The thermocouple response was recorded on a Honeywell 1612 Visicorder which operated at a speed of 20 inches per second with a deflection of approximately 45°F per inch. All thermocouples used a 32°F reference junction.

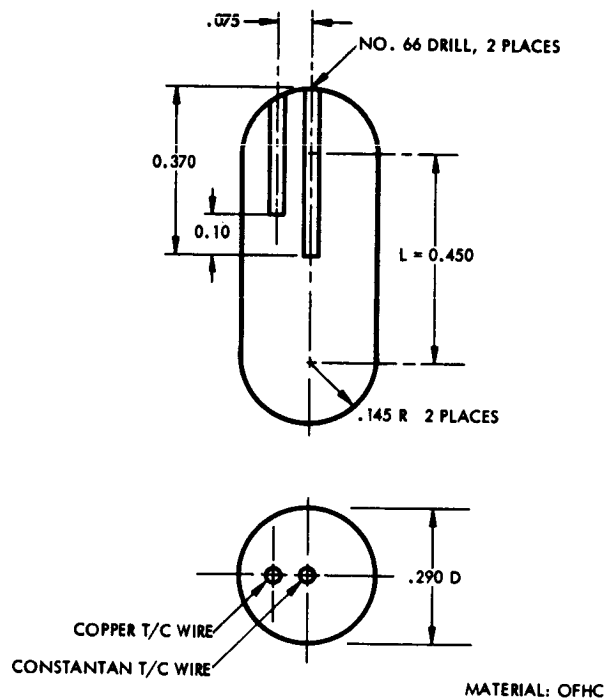


Figure B-3. Schematic of Copper Slug Calorimeter

3.0 EXPERIMENTAL PROCEDURE

Approximately 880 millimeters of the test gas was first condensed into the dewar and then brought to the desired bulk temperature by evaporating LN_2 in the dewar inner jacket. In the case of the methane-ethane blend the dewar was calibrated for the 55% methane/45% ethane ratio on a volumetric basis. The methane was first condensed into the dewar, and then the ethane was condensed into the dewar to bring the blend to the desired 55/45 ratio.

Originally, it was intended to continuously evaporate LN_2 in the inner jacket keeping the LN_2 level at the same level as the LPG. However, early in the testing of the propane this technique resulted in solidification of the propane. The same result occurred with the methane and the methane-ethane blend. The alternate procedure used to bring the bulk temperature of the LPG to the desired level was to partially fill the inner jacket and evaporate all of the LN_2 . The LPG was then agitated to bring it to a constant temperature. Following this, the pool boiling tests were performed in rapid succession so that the bulk temperature did not vary more than 5°F during a test series.

For each test, the calorimeter was first brought to a constant temperature well above the saturation temperature of the particular LPG used, i.e., 80°F for methane and the methane-ethane blend and 212°F for the propane. The calorimeter was then rapidly emersed in the liquid and the temperature response recorded while it cooled to a temperature near the bulk temperature of the liquid. Using this method of testing, data were obtained in all heat transfer regimes from stable film boiling to nucleate boiling. One advantage of testing in this manner rather than electrically heating a copper specimen is that data in the peak heat flux region are more easily obtained; i.e., delicate power input adjustments are not necessary to keep the specimen out of the unstable film boiling regime.

4.0 EXPERIMENTAL RESULTS

The millivolt output from the copper calorimeter was used in a heat flux computer program to generate the heat flux versus wall superheat ($T_{\text{wall}} - T_{\text{saturation}}$) by calculating the $\frac{dT}{d\theta}$ term in Equation (B-2). The data of interest was primarily in the peak heat flux region. Consequently, data from all of the tests were reduced only in this range, i.e., from the unstable film boiling regime to the nucleate boiling regime.

Only two bulk temperatures were tested with the methane and methane-ethane blend due to the relatively small range between the freezing temperature (approximately -320°F) and the boiling temperature (approximately -260°F). Due to the method of achieving the desired bulk temperature in the LPG, bulk temperatures could not be obtained close to the freezing point. With propane, the range of temperatures between freezing and boiling is much greater (-320°F to -42°F) and consequently tests were conducted at more bulk liquid temperatures.

Tests were performed with the methane-ethane blend at bulk temperatures of -314°F (approximately 55°F subcooled) and at the saturation temperature of methane (-260°F) at one atmosphere. The experimental results for the subcooled condition are shown in Figure B-4, and the results at the saturated condition are shown in Figure B-5. At atmospheric pressure, the peak pool boiling heat flux is from 0.24 to 0.33 Btu/in²-sec. (Figure B-5). With 55°F subcooling, the peak heat flux increases to approximately 0.38 Btu/in²-sec (Figure B-4).

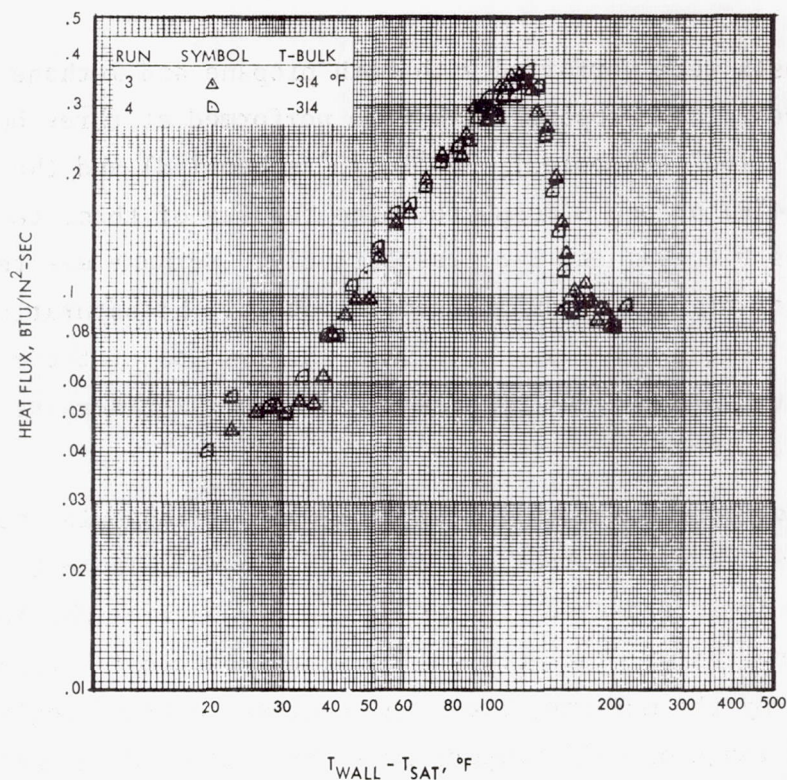


Figure B-4. Subcooled Pool Boiling of 55% Methane-45% Ethane Fuel Blend ($T_{\text{Bulk}} = -314^{\circ}\text{F}$)

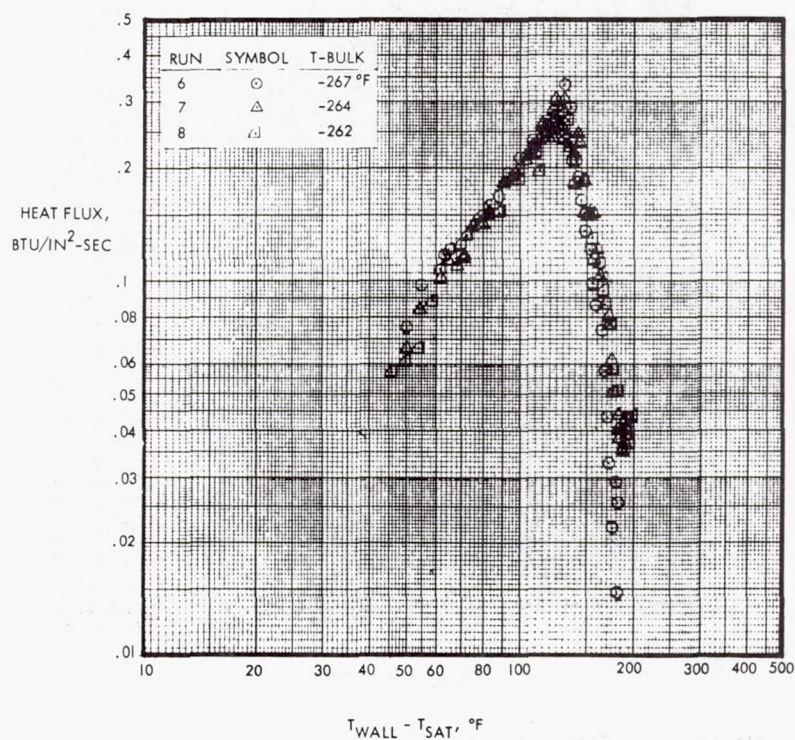


Figure B-5. Saturated Pool Boiling of 55% Methane-45% Ethane Fuel Blend ($T_{\text{Bulk}} = -265^{\circ}\text{F}$)

Similar tests were performed with both propane and methane at various bulk temperatures. The propane tests were performed at three bulk temperatures: -140°F (100° subcooled), -80°F (40° subcooled) and the saturation temperature (-44°F) at one atmosphere. The results of these tests are shown in Figures B-6, B-7 and B-8, respectively. Methane was tested at bulk temperatures of -300°F (40° subcooled) and at the saturation temperature (-260°F). Figures B-9 and B-10 show the results of these tests. As expected, both the propane and methane showed the same increase in peak heat flux with an increase in the subcooling.

The range of the peak heat fluxes from the boiling point to near the freezing point was obtained from the tests as shown in Table B-1. An interesting result is obtained by comparing the data from the methane-ethane blend and methane tests. The nucleate boiling characteristics of the blend were controlled by the methane, i.e., the nucleate boiling regime did not extend into the range of wall temperatures that exceeded the saturation temperature of ethane. The peak heat flux of the blend seemed to be strongly

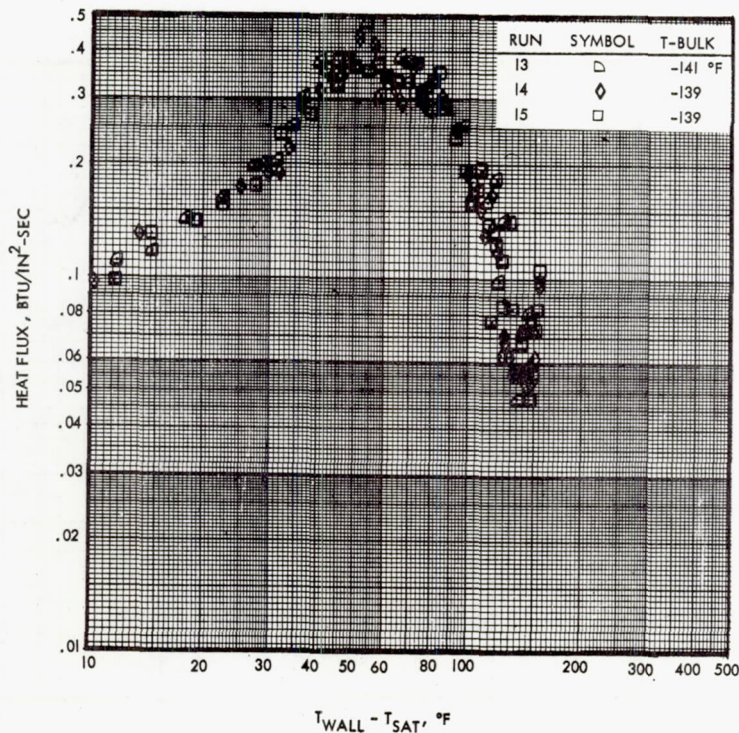


Figure B-6. Subcooled Pool Boiling of Propane Fuel ($T_{\text{Bulk}} = -140^{\circ}\text{F}$)

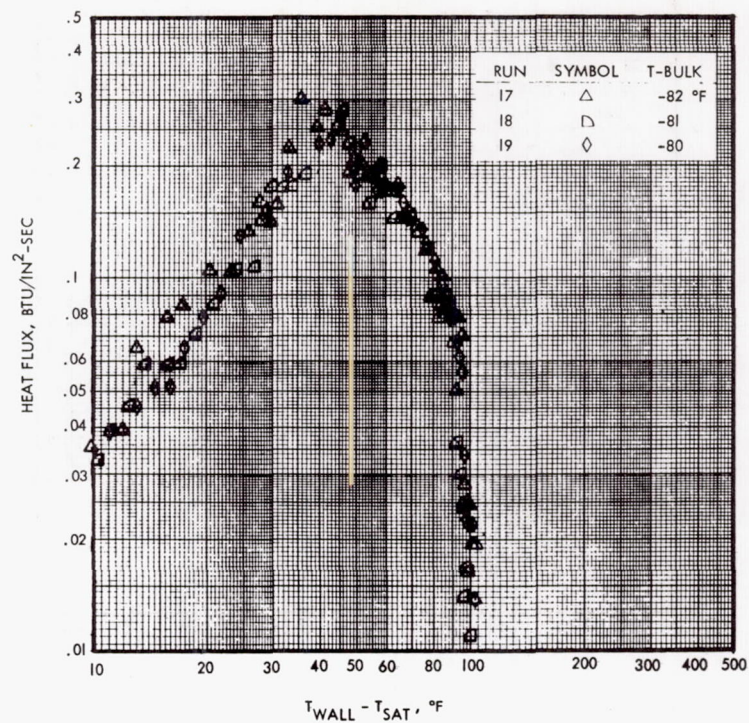


Figure B-7. Subcooled Pool Boiling of Propane Fuel ($T_{\text{Bulk}} = -80^{\circ}\text{F}$)

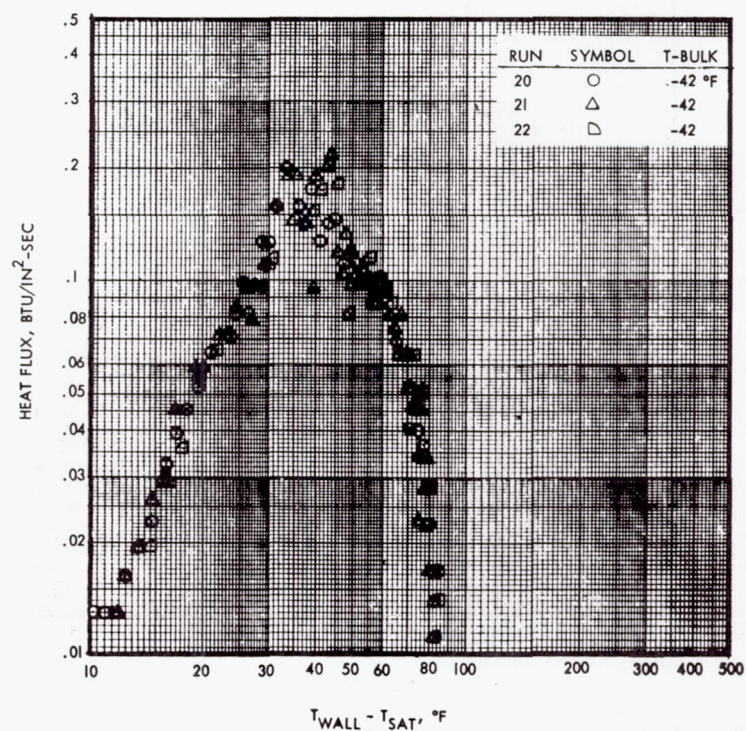


Figure B-8. Saturated Pool Boiling of Propane Fuel ($T_{\text{Bulk}} = -42^{\circ}\text{F}$)

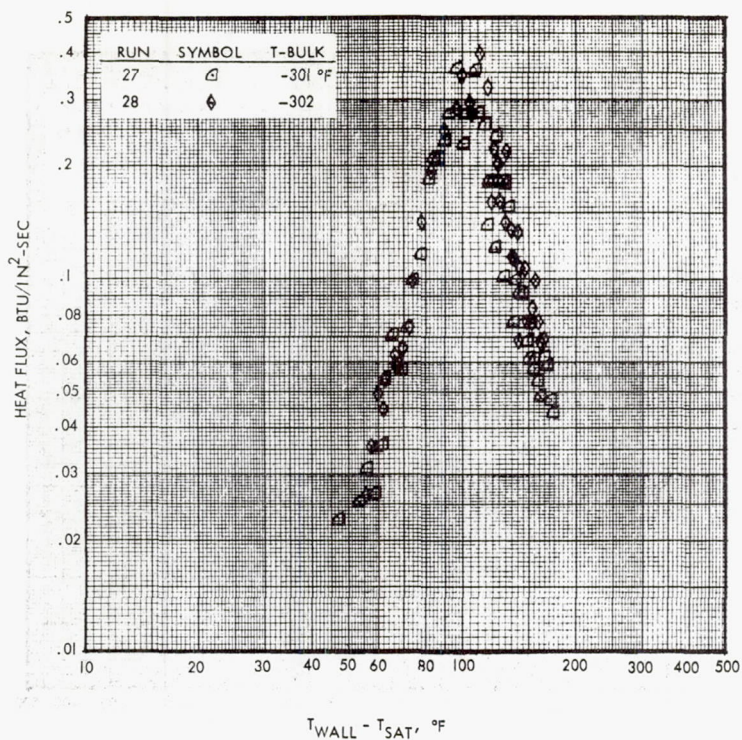


Figure B-9. Subcooled Pool Boiling of Methane Fuel (T Bulk = -300°F)

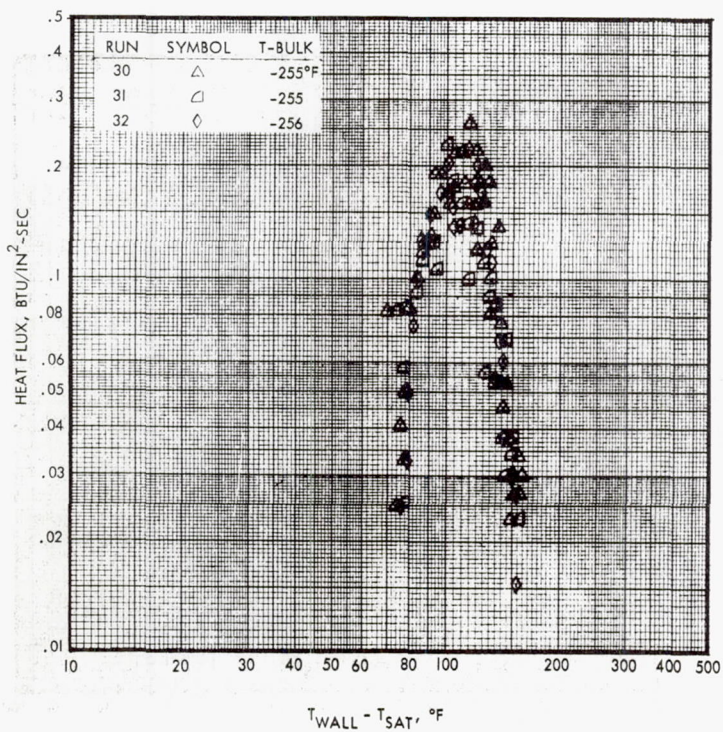


Figure B-10. Saturated Pool Boiling of Methane Fuel (T Bulk = -255°F)

Table B-1. Comparison of Burnout Heat Flux For Various Degrees of Subcooling

<u>Fuel</u>	<u>Bulk Temperature</u> (°F)	<u>Measured (Q/A)_{max}</u> at 14.7 psia (Btu/in ² -sec)
55% Methane/ 45% Ethane	-313	.32 - .38
	-260 (saturated)	.24 - .33
Propane	-140	.35 - .45
	-80	.24 - .28
	-44 (saturated)	.14 - .21
Methane	-300	.28 - .35
	-260 (saturated)	.14 - .23

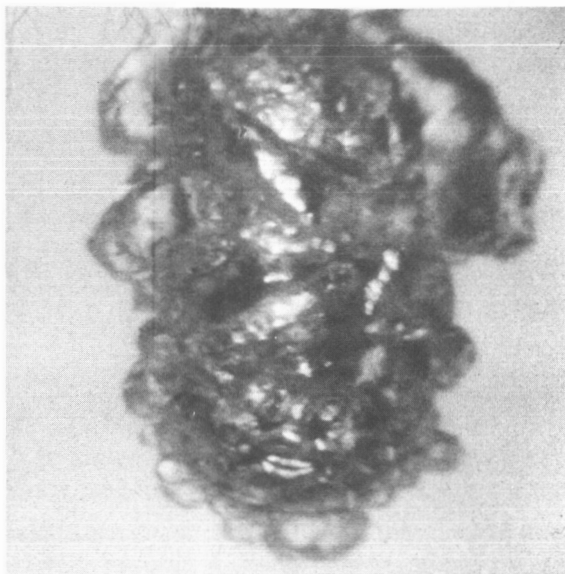
influenced by the ethane in that the peak heat flux was higher than the methane alone. In addition, the peak heat flux occurred within 4°F of the saturation temperature of the ethane. With methane alone, the peak heat flux occurred at a wall superheat about 20°F higher than for the blend; however, the heat flux was about 30% lower than with the blend.

The reduced data from the tests shown in Figures B-4 through B-10 can be found in Section 6.0.

Figures B-4 to B-10 demonstrate that the repeatability of the tests was extremely good with most scatter in the data occurring at the peak heat flux. This is to be expected since boiling is most violent at that condition.

High speed movies were made of the propane tests at bulk temperatures of -80°F and -42°F. Figure B-11 shows a frame of each of these at a point very near the peak heat flux. In both cases, the boiling was so violent that the generated vapor extended as much as 0.3 inch from the surface of the calorimeter. This was more pronounced in saturated boiling since the vapor could not collapse.

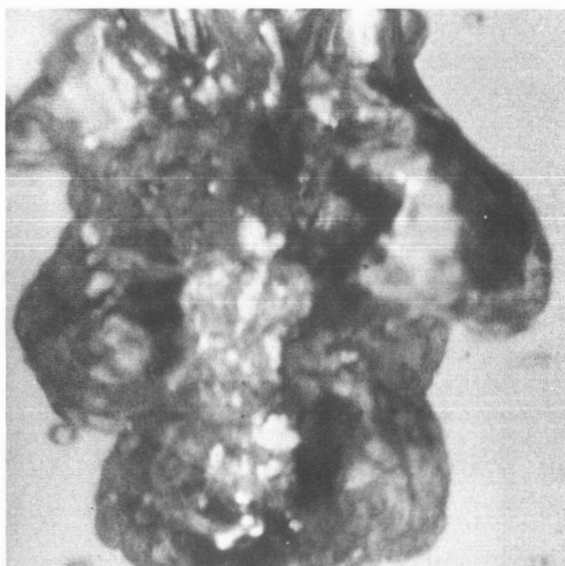
The various states of vapor generation are shown in Figure B-12 from film boiling to nucleate boiling. In the film boiling regime, distinct waves can be seen traveling up the calorimeter walls. This is at present unexplained, however, it is felt to be associated with the film stability.



SUBCOOLED (-80°F)



CALORIMETER
SIZE



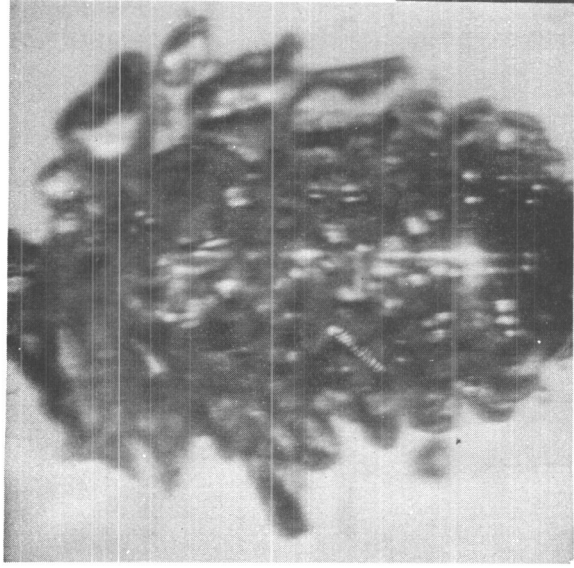
SATURATED (-44°F)



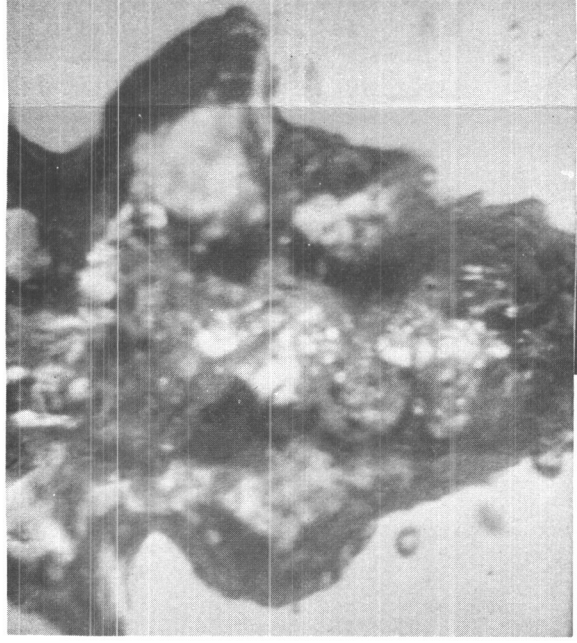
CALORIMETER
SIZE

Figure B-11. Subcooled and Saturated Bubble Characteristics of Propane at Peak Heat Flux

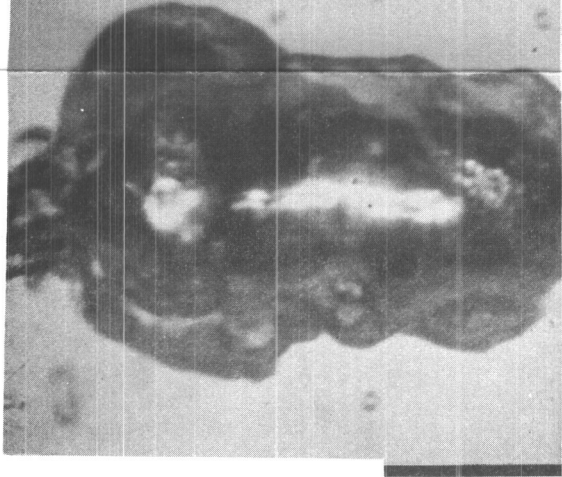
NUCLEATE



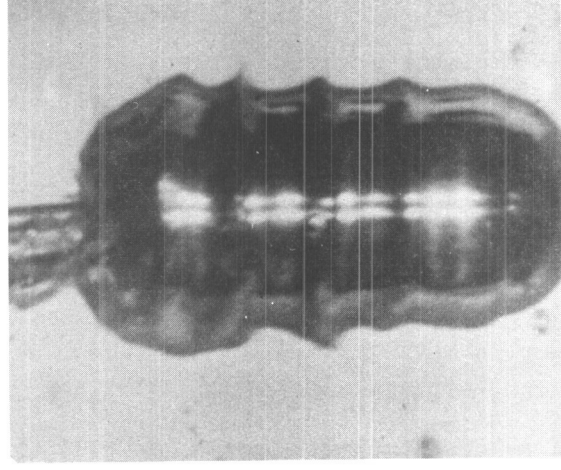
PEAK



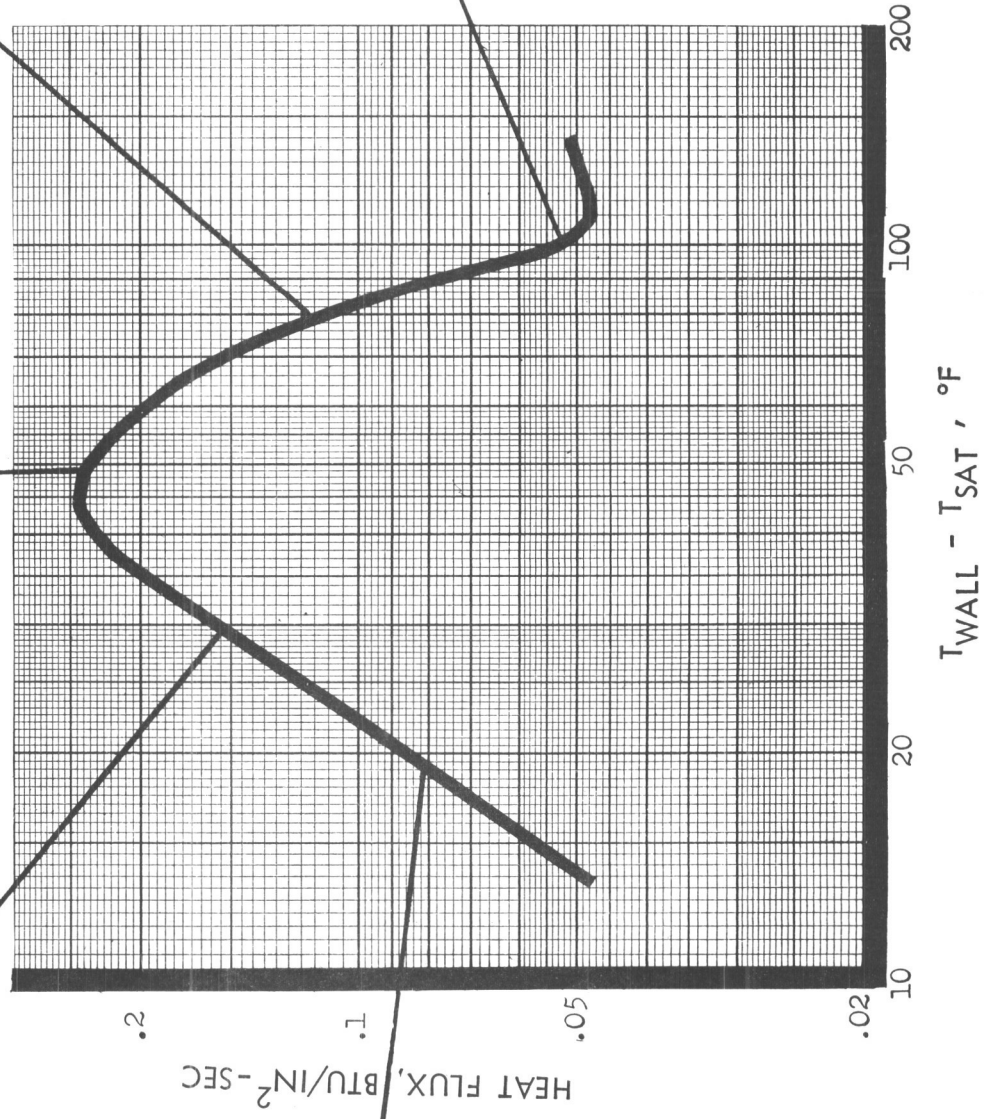
UNSTABLE FILM



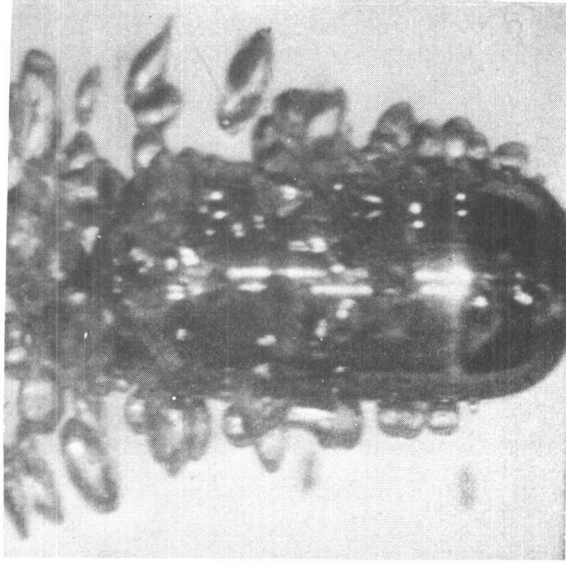
STABLE FILM



($\Delta T > 200^{\circ}\text{F}$)



NUCLEATE



UNSTABLE FILM

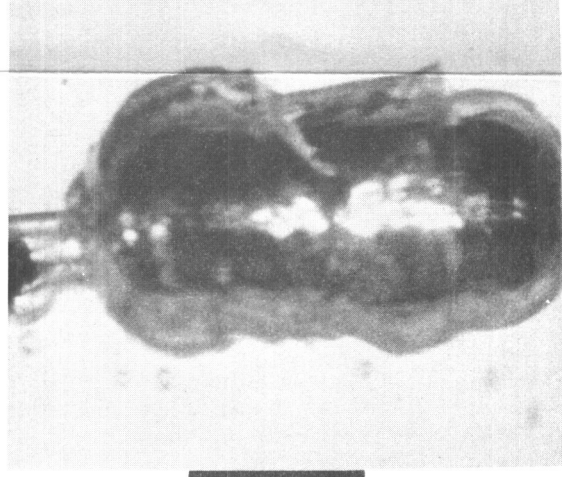


Figure B-12. Typical Bubble Characteristics of Saturated Propane Fuel

As heat transfer rates approach the unstable region, the film begins to break up, and the liquid comes in contact with the calorimeter surface. In the peak boiling region, very large bubbles are generated at the calorimeter surface and completely engulf the calorimeter. In contrast to the peak nucleate boiling region, definite nucleation sites can be seen in the nucleate boiling regime.

5.0 CONCLUSIONS

In general, the method employed for obtaining the LPG pool boiling peak heat flux data proved to be a simple and rapid technique. In addition, data in all of the boiling regions could be obtained with ease during the same experiment. The repeatability of the tests was surprisingly good in light of the relative simplicity of the technique. As was shown earlier, the data accuracy is felt to be quite good. The correlation of Ciechelli and Bonilla, Reference B-3, was used to scale the peak heat flux data of the atmospheric pool boiling tests to other system pressures of interest. The experimental data of Reference B-3 was represented within +10 percent by the following expression:

$$\frac{(q/A)_{\max}}{\rho_v h_{fg}} = 14.3 \left(\frac{\rho_l}{\rho_v} - 1 \right)^{0.6}$$

6.0 EXPERIMENTAL TEST RESULTS

The test results obtained from the pool boiling experiments are presented in the following listings of data. The following system of units apply to the data:

Time	-	seconds
Temperature	-	degrees Fahrenheit
Heat Flux	-	Btu/in ² -sec
Superheat	-	(T _w - T _{sat})

REFERENCES

- B-1. NASA CR-54445 (PWA FR-1443), Final Report, "Investigation of Light Hydrocarbon Fuels with FLOX Mixtures as Liquid Rocket Propellants," prepared for National Aeronautics and Space Administration under Contract NAS 3-4195 by Pratt & Whitney Aircraft, Division of United Aircraft Corporation, 1 September 1965.
- B-2. TRW Systems Group, IOC 4811.7.68-008, "Experimental Method for the Determination of the Boiling Characteristics of Liquid Petroleum Gases (LPG) at the Surface of a Copper Plug Calorimeter," 12 January 1968.
- B-3. C. F. Bonilla, and M. T. Ciechelli, "Heat Transfer to Liquids Boiling Under Pressure," AIChE Transactions, Vol. 41, 1945.

METHANE/ETHANE TEST DATA

RUN NO. 3
BULK TEMP. -314.4

TIME	TEMP.	SUPERHEAT	HEAT FLUX
.1	-57.386	201.814	8.33654 E-2
.2	-61.8716	197.328	.08316
.3	-66.731	192.469	9.09258 E-2
.4	-72.128	187.072	9.18901 E-2
.5	-77.14	182.06	8.46969 E-2
.6	-81.76	177.44	9.56738 E-2
.7	-88.06	171.14	.106182
.8	-93.94	165.26	9.59341 E-2
.9	-99.116	160.084	.102279
1	-105.776	153.424	.125938
1.05	-109.772	149.428	.152161
1.1	-114.656	144.544	.198343
1.15	-121.393	137.807	.263754
1.2	-130.194	129.006	.289983
1.22	-133.556	125.644	.322895
1.24	-137.879	121.321	.341412
1.26	-141.722	117.478	.35972
1.28	-146.525	112.675	.357501
1.3	-150.368	108.832	.335963
1.32	-154.691	104.509	.336544
1.34	-158.593	100.607	.285827
1.36	-161.712	97.4875	.275063
1.38	-165.379	93.8213	.296637
1.4	-169.065	90.1345	.296012
1.42	-172.752	86.4478	.252479
1.44	-175.386	83.8144	.223636
1.5	-184.339	74.8608	.22509
1.55	-191.186	68.014	.195897
1.6	-196.909	62.2915	.160307
1.65	-201.553	57.6468	.151637
1.7	-206.778	52.4216	.12397
1.75	-209.681	49.5187	9.70086 E-2
1.8	-213.165	46.0352	9.69651 E-2
1.85	-216.068	43.1323	8.81937 E-2
1.9	-218.973	40.2265	7.95531 E-2
1.95	-221.307	37.8927	6.20103 E-2
2	-223.058	36.1424	5.31517 E-2
2.1	-226.558	32.6417	5.35132 E-2
2.2	-230.107	29.0933	5.20211 E-2
2.3	-233.411	25.7892	5.01675 E-2
2.4	-236.715	22.485	4.51508 E-2

METHANE/ETHANE TEST DATA

RUN NO. 4
BULK TEMP. -314.4

TIME	TEMP.	SUPERHEAT	HEAT FLUX
.1	-58.1336	201.066	8.33413 E-2
.2	-66.731	192.469	.120589
.3	-71.736	187.464	-.239991
.4	-39.554	219.646	9.38135 E-2
.5	-82.18	177.02	.417479
.6	-87.22	171.98	9.15976 E-2
.7	-92.68	166.52	.091757
.8	-97.784	161.416	9.02422 E-2
.85	-100.448	158.752	9.96489 E-2
.9	-103.556	155.644	9.17546 E-2
.95	-105.776	153.424	.091591
1	-108.884	150.316	.114202
1.05	-112.436	146.764	.144647
1.1	-117.344	141.856	.183191
1.15	-123.193	136.007	.250377
1.2	-132.116	127.084	.331982
1.22	-136.438	122.762	.362161
1.24	-140.761	118.439	.340155
1.26	-144.604	114.596	.318567
1.28	-148.446	110.754	.316989
1.3	-152.289	106.911	.315411
1.32	-156.132	103.068	.278681
1.34	-159.113	100.087	.290454
1.36	-163.272	95.928	.317388
1.38	-166.959	92.2412	.275639
1.4	-170.119	89.0812	.244923
1.45	-177.492	81.7076	.234153
1.5	-184.866	74.3341	.21527
1.55	-191.186	68.014	.187688
1.6	-196.909	62.2915	.169284
1.65	-202.134	57.0662	.160427
1.7	-207.359	51.841	.132717
1.75	-210.842	48.3575	.114595
1.8	-214.907	44.2935	.10578
1.85	-217.809	41.3906	7.94659 E-2
1.9	-220.14	39.0596	.079684
1.95	-223.058	36.1424	7.97276 E-2
2	-225.391	33.8086	6.20103 E-2
2.1	-228.892	30.3079	5.08462 E-2
2.2	-232.089	27.1108	5.93876 E-2
2.3	-236.715	22.485	5.51843 E-2
2.4	-239.358	19.8417	.040134

METHANE/ETHANE TEST DATA

RUN NO. 6
BULK TEMP. -266.9

TIME	TEMP.	SUPERHEAT	HEAT FLUX
.1	-75.46	183.74	2.58864 E-2
.2	-76.3	182.9	1.47825 E-2
.3	-77.14	182.06	2.58523 E-2
.4	-79.24	179.96	2.94966 E-2
.5	-80.5	178.7	2.21005 E-2
.6	-81.76	177.44	2.20786 E-2
.7	-83.02	176.18	2.57327 E-2
.8	-84.7	174.5	2.93698 E-2
.9	-86.38	172.82	3.29971 E-2
1	-88.48	170.72	4.39229 E-2
1.1	-91.42	167.78	5.84273 E-2
1.2	-95.2	164	7.44095 E-2
1.3	-100.004	159.196	8.74915 E-2
1.35	-102.668	156.532	9.94717 E-2
1.4	-105.776	153.424	.122121
1.45	-109.772	149.428	.136945
1.5	-113.768	145.432	.163298
1.52	-115.994	143.206	.19076
1.54	-118.244	140.956	.210561
1.56	-120.943	138.257	.210099
1.58	-123.193	136.007	.290245
1.6	-127.793	131.407	.336126
1.62	-131.155	128.045	.283092
1.64	-134.517	124.683	.28231
1.66	-137.879	121.321	.26108
1.68	-140.761	118.439	.260118
1.7	-144.124	115.076	.266965
1.75	-151.809	107.391	.237697
1.8	-158.593	100.607	.212372
1.85	-164.852	94.348	.194619
1.9	-170.646	88.5545	.168794
1.95	-175.386	83.8144	.15934
2	-180.652	78.5476	.14156
2.1	-188.026	71.174	.118139
2.2	-195.747	63.4526	.118241
2.3	-203.295	55.9051	9.78804 E-2
2.4	-208.52	50.6799	7.50837 E-2

METHANE/ETHANE TEST DATA

RUN NO.	7		
BULK TEMP.	-264.2		
TIME	TEMP.	SUPERHEAT	HEAT FLUX
.1	-62.993	196.207	3.65585 E-2
.2	-65.2358	193.964	3.98125 E-2
.3	-67.4786	191.721	4.02266 E-2
.4	-69.776	189.424	3.76534 E-2
.5	-71.736	187.464	.035358
.6	-73.78	185.42	4.02386 E-2
.7	-76.3	182.9	4.43474 E-2
.8	-78.82	180.38	4.05713 E-2
.9	-80.92	178.28	4.41864 E-2
1	-83.86	175.34	6.24523 E-2
1.1	-88.06	171.14	8.05522 E-2
1.2	-93.1	166.1	.102111
1.25	-96.46	162.74	.104193
1.3	-99.116	160.084	.122637
1.35	-103.556	155.644	.152924
1.4	-107.996	151.204	.152379
1.42	-109.772	149.428	.152161
1.44	-111.548	147.652	.189928
1.46	-114.212	144.988	.228181
1.48	-116.894	142.306	.248361
1.5	-120.043	139.157	.229367
1.52	-122.293	136.907	.228947
1.54	-125.442	133.758	.252938
1.56	-128.273	130.927	.30187
1.58	-132.596	126.604	.302954
1.6	-135.478	123.722	.241737
1.62	-138.36	120.84	.240849
1.64	-141.242	117.958	.259958
1.66	-144.604	114.596	.258836
1.68	-147.486	111.714	.238038
1.7	-150.368	108.832	.229245
1.75	-157.092	102.108	.210522
1.8	-163.272	95.928	.193752
1.85	-169.065	90.1345	.177607
1.9	-174.332	84.8677	.151167
1.95	-178.546	80.6543	.141963
2	-183.286	75.9142	.141056
2.05	-187.499	71.7007	.115499
2.1	-190.659	68.5406	.110532
2.15	-194.586	64.6138	.114954
P2.2	-198.07	61.1303	.103075
2.3	-204.456	54.7439	8.43962 E-2
2.4	-209.101	50.0993	6.61963 E-2

METHANE/ETHANE TEST DATA

RUN NO. 8
BULK TEMP. -262.4

TIME	TEMP.	SUPERHEAT	HEAT FLUX
.1	-64.1144	195.086	4.31678 E-2
.2	-66.3572	192.843	4.32539 E-2
.3	-68.992	190.208	4.41314 E-2
.4	-71.344	187.856	3.85842 E-2
.5	-73.36	185.84	4.37091 E-2
.6	-76.3	182.9	5.17387 E-2
.7	-79.24	179.96	5.16191 E-2
.8	-82.18	177.02	5.88567 E-2
.9	-85.96	173.24	7.70188 E-2
1	-91.	168.2	8.76702 E-2
1.05	-93.52	165.68	9.47857 E-2
1.1	-96.46	162.74	.112299
1.15	-100.004	159.196	.114882
1.2	-103.112	156.088	.130032
1.25	-107.552	151.648	.152434
1.3	-111.992	147.208	.184291
1.36	-119.593	139.607	.184165
1.38	-121.393	137.807	.229115
1.4	-124.992	134.208	.270782
1.42	-127.793	131.407	.239875
1.44	-130.675	128.525	.262975
1.46	-134.037	125.163	.262249
1.48	-136.919	122.281	.2614
1.5	-140.281	118.919	.2803
1.52	-143.643	115.557	.239222
1.54	-146.045	113.155	.198735
1.56	-148.446	110.754	.21793
1.58	-151.328	107.872	.217116
1.6	-153.73	105.47	.216438
1.62	-156.612	102.588	.198484
1.64	-158.593	100.607	.187018
1.7	-166.432	92.7679	.181647
1.75	-171.172	88.0278	.151808
1.8	-175.912	83.2877	.150847
1.85	-180.652	78.5476	.149887
1.9	-185.393	73.8074	.132379
1.95	-189.079	70.1207	.12555
2	-193.425	65.7749	.121646
2.05	-196.909	62.2915	.10773
2.1	-200.392	58.808	8.93425 E-2
2.2	-205.037	54.1633	6.65745 E-2
2.3	-209.101	50.0993	6.17832 E-2
2.4	-213.165	46.0352	5.72975 E-2

PROPANE TEST DATA

RUN NO. 13
BULK TEMP. -140.5

TIME	TEMP.	SUPERHEAT	HEAT FLUX
.4	108.761	152.861	7.35868 E-2
.5	104.547	148.647	7.63447 E-2
.6	100.634	144.734	8.19277 E-2
.7	95.818	139.918	7.34534 E-2
.8	92.7994	136.899	4.83045 E-2
.9	90.6623	134.762	6.57575 E-2
1	85.7775	129.878	.142794
1.05	80.5874	124.687	.142626
1.1	78.145	122.245	9.87588 E-2
1.15	75.2995	119.4	.184301
1.2	68.2705	112.371	.160752
1.25	66.673	110.773	.135211
1.3	61.012	105.112	.171622
1.35	57.448	101.548	.166825
1.4	52.0376	96.1376	.25264
1.45	43.8404	87.9404	.29256
1.5	36.2504	80.3504	.280667
1.52	33.2144	77.3144	.326789
1.54	29.1726	73.2726	.374612
1.56	25.0885	69.1885	.3326
1.58	21.9469	66.0469	.389982
1.6	16.6062	60.7062	.345955
1.62	14.407	58.507	.30246
1.64	10.0088	54.1088	.480906
1.66	3.89992	47.9999	.382751
1.68	1.62688	45.7269	.322343
1.7	-3.1652	40.9348	.377326
1.72	-6.6584	37.4416	.301863
1.74	-9.80228	34.2977	.253897
1.76	-12.2475	31.8525	.206099
1.78	-14.3434	29.7566	.20658
1.8	-16.8029	27.2971	.196736
1.85	-21.5102	22.5898	.163758
1.9	-25.8554	18.2446	.143868
1.95	-29.4764	14.6236	.117547
2	-32.3732	11.7268	.110801
2.05	-35.627	8.473	.103506
2.1	-38.126	5.974	9.03563 E-2
2.2	-43.1816	.9184	8.22314 E-2
2.3	-47.2934	-3.1934	7.36486 E-2
2.4	-51.4052	-7.3052	6.35046 E-2

PROPANE TEST DATA

RUN NO. 14
BULK TEMP. -139.2

TIME	TEMP.	SUPERHEAT	HEAT FLUX
.1	110.868	154.968	9.62744 E-2
.2	106.052	150.152	6.22278 E-2
.3	104.246	148.346	5.37204 E-2
.4	100.333	144.433	5.93229 E-2
.5	97.925	142.025	.053644
.6	94.614	138.714	5.66268 E-2
.7	91.8835	135.984	5.70351 E-2
.8	88.5252	132.625	5.71529 E-2
.9	85.7775	129.878	6.28292 E-2
1	81.8086	125.909	7.13328 E-2
1.05	79.9768	124.077	6.84511 E-2
1.1	78.145	122.245	6.34866 E-2
1.15	76.5775	120.678	.11874
1.2	71.785	115.885	.166838
1.25	67.6315	111.732	.130964
1.3	64.756	108.856	.150904
1.35	59.527	103.627	.1801
1.4	55.072	99.172	.18991
1.45	49.3052	93.4052	.247829
1.5	41.7152	85.8152	.309288
1.55	32.6072	76.7072	.282235
1.56	31.3717	75.4717	.316941
1.58	26.9734	71.0734	.361777
1.6	23.5177	67.6177	.289046
1.62	20.6902	64.7902	.317613
1.64	16.6062	60.7062	.345955
1.66	13.1504	57.2504	.418569
1.68	7.47184	51.5718	.437832
1.7	3.5752	47.6752	.358074
1.72	-.37064	43.7294	.339146
1.74	-3.86384	40.2362	.318088
1.76	-7.35704	36.743	.2859
1.78	-10.1516	33.9484	.22213
1.8	-12.2475	31.8525	.190245
1.82	-14.3434	29.7566	.190159
1.84	-16.4408	27.6592	.13332
1.9	-18.9755	25.1245	.175937
1.95	-26.5796	17.5204	.209204
2	-30.5627	13.5373	.130553
2.05	-33.8216	10.2784	9.76088 E-2
2.1	-35.984	8.116	8.70685 E-2
2.2	-41.339	2.761	8.80957 E-2
2.3	-45.7982	-1.6982	7.01049 E-2
2.4	-49.1624	-5.0624	6.02145 E-2
2.5	-52.5266	-8.4266	5.34544 E-2
2.6	-55.1432	-11.0432	5.00628 E-2
2.7	-58.1336	-14.0336	4.66711 E-2

PROPANE TEST DATA

RUN NO. 15
BULK TEMP. -138.6

TIME	TEMP.	SUPERHEAT	HEAT FLUX
.1	111.771	155.871	.10479
.2	107.557	151.657	8.20554 E-2
.3	103.042	147.142	5.65325 E-2
.4	101.537	145.637	4.80364 E-2
.5	97.925	142.025	7.34076 E-2
.6	93.711	137.811	6.80593 E-2
.7	90.6623	134.762	5.71402 E-2
.8	87.6093	131.709	8.28545 E-2
.9	81.8086	125.909	8.55993 E-2
1	78.4503	122.55	.114082
1.05	74.0215	118.122	.124368
1.1	71.785	115.885	7.74607 E-2
1.15	69.868	113.968	.136986
1.2	64.4365	108.537	.192533
1.25	59.527	103.627	.157588
1.3	55.963	100.063	.189948
1.35	49.3052	93.4052	.236195
1.4	43.2332	87.3332	.281268
1.42	39.59	83.69	.351272
1.44	35.6432	79.7432	.336724
1.46	32.3036	76.4036	.298652
1.48	29.1726	73.2726	.31814
1.5	25.4026	69.5026	.376027
1.52	21.0044	65.1044	.33209
1.54	18.177	62.277	.331736
1.56	13.7787	57.8787	.374385
1.58	10.0088	54.1088	.362974
1.6	5.84824	49.9482	.368195
1.62	1.9516	46.0516	.379406
1.64	-2.46656	41.6334	.360393
1.66	-5.95976	38.1402	.27016
1.68	-8.405	35.695	.269909
1.7	-11.8982	32.2018	.241036
1.75	-16.4408	27.6592	.174216
1.8	-21.5102	22.5898	.157208
1.85	-25.1312	18.9688	.143908
1.9	-29.4764	14.6236	.130608
1.95	-32.3732	11.7268	9.78469 E-2
2	-34.9079	9.1921	8.42592 E-2
2.05	-37.055	7.045	.077128
2.1	-39.197	4.903	8.43575 E-2
2.2	-44.303	-.203	7.59447 E-2
2.3	-47.6672	-3.5672	7.02908 E-2
2.4	-52.1528	-8.0528	6.34863 E-2
2.5	-54.7694	-10.6694	.043394
2.6	-57.0122	-12.9122	4.33563 E-2

PROPANE TEST DATA

RUN NO. 17
BULK TEMP. -82.4

TIME	TEMP.	SUPERHEAT	HEAT FLUX
.1	60.715	104.815	1.42311 E-2
.2	61.309	105.409	8.28864 E-3
.3	59.824	103.924	1.93336 E-2
.4	59.23	103.33	1.38079 E-2
.5	58.339	102.439	1.38051 E-2
.6	57.745	101.845	1.93245 E-2
.7	56.26	100.36	2.48374 E-2
.8	55.072	99.172	2.51224 E-2
.9	53.5556	97.6556	2.81782 E-2
1	52.0376	96.1376	7.04582 E-2
1.05	49.0016	93.1016	7.88587 E-2
1.1	47.7872	91.8872	5.06809 E-2
1.15	46.2692	90.3692	7.88096 E-2
1.2	43.5368	87.6368	9.00121 E-2
1.25	41.4116	85.5116	.101215
1.3	38.072	82.172	.106726
1.35	35.6432	79.7432	8.97931 E-2
1.4	33.2144	77.3144	.119502
1.45	29.1726	73.2726	.138258
1.5	25.7168	69.8168	.150428
1.55	21.0044	65.1044	.17904
1.6	15.9778	60.0778	.178701
1.62	14.0929	58.1929	.201616
1.64	11.5796	55.6796	.187037
1.66	10.0088	54.1088	.18801
1.68	7.47184	51.5718	.205092
1.7	5.52352	49.6235	.207719
1.72	2.92576	47.0258	.163048
1.74	1.9516	46.0516	.246053
1.76	-2.46656	41.6334	.280828
1.78	-4.21316	39.8868	.254437
1.8	-8.05568	36.0443	.301703
1.82	-10.8502	33.2498	.222071
1.84	-12.9462	31.1538	.158496
1.86	-14.3434	29.7566	.14257
1.88	-16.09	28.01	.160688
1.9	-17.8892	26.2108	.133954
1.95	-20.786	23.314	.104834
2	-23.6828	20.4172	.104718
2.05	-26.5796	17.5204	8.49892 E-2
2.1	-28.3901	15.7099	7.83972 E-2
2.15	-30.9248	13.1752	6.52675 E-2
2.2	-32.0111	12.0889	3.91442 E-2
2.3	-34.1837	9.9163	3.57604 E-2
2.4	-35.984	8.116	3.54605 E-2
2.5	-38.126	5.974	3.20852 E-2
2.6	-39.554	4.546	2.24473 E-2
2.7	-40.625	3.475	2.25027 E-2

PROPANE TEST DATA

RUN NO. 18
BULK TEMP. -80.7

TIME	TEMP.	SUPERHEAT	HEAT FLUX
.1	58.042	102.142	.016565
.2	57.151	101.251	1.10411 E-2
.3	56.854	100.954	1.10403 E-2
.4	55.963	100.063	1.65571 E-2
.5	55.072	99.172	1.95431 E-2
.6	53.8592	97.9592	1.69021 E-2
.7	53.252	97.352	1.40955 E-2
.8	52.3412	96.4412	2.53667 E-2
.9	50.5196	94.6196	3.09909 E-2
1	49.0016	93.1016	.036613
1.05	47.7872	91.8872	6.75745 E-2
1.1	45.3584	89.4584	8.44214 E-2
1.15	43.2332	87.3332	8.43805 E-2
1.2	40.8044	84.9044	8.43338 E-2
1.25	38.6792	82.7792	7.86582 E-2
1.3	36.554	80.654	8.98237 E-2
1.35	33.8216	77.9216	.118944
1.4	30.115	74.215	.132122
1.45	26.6593	70.7593	.144694
1.5	22.261	66.361	.144455
1.55	18.8053	62.9053	.144267
1.6	14.407	58.507	.195879
1.62	11.8938	55.9938	.187059
1.64	10.323	54.423	.158187
1.66	8.438	52.538	.189831
1.68	6.17296	50.273	.222245
1.7	3.5752	47.6752	.19274
1.72	1.9516	46.0516	.227868
1.74	-1.4186	42.6814	.28094
1.76	-4.21316	39.8868	.254437
1.78	-7.00772	37.0923	.190625
1.8	-8.405	35.695	.142893
1.82	-10.1516	33.9484	.174531
1.84	-12.2475	31.8525	.174392
1.86	-13.9941	30.1059	.174276
1.88	-16.09	28.01	.143699
1.9	-17.165	26.935	.107746
1.95	-20.4239	23.6761	.104849
2	-22.9586	21.1414	8.51071 E-2
2.05	-25.1312	18.9688	7.19539 E-2
2.1	-26.9417	17.1583	5.88305 E-2
2.15	-28.3901	15.7099	5.87979 E-2
2.2	-30.2006	13.8994	5.87571 E-2
2.25	-31.649	12.451	4.56746 E-2
2.3	-32.7353	11.3647	3.91333 E-2
2.35	-33.8216	10.2784	3.25975 E-2
2.4	-34.5458	9.5542	3.24048 E-2
2.5	-36.698	7.402	3.21946 E-2

PROPANE TEST DATA

RUN NO. 19
BULK TEMP. -80.2

TIME	TEMP.	SUPERHEAT	HEAT FLUX
.1	62.839	106.939	.014238
.2	61.309	105.409	2.80474 E-2
.3	59.824	103.924	1.65717 E-2
.4	59.527	103.627	5.52352 E-3
.5	59.23	103.33	1.38079 E-2
.6	58.042	102.142	2.20866 E-2
.7	56.854	100.954	2.20807 E-2
.8	55.666	99.766	2.21825 E-2
.9	54.4664	98.5664	2.24216 E-2
1	53.252	97.352	3.38293 E-2
1.05	52.0376	96.1376	5.63666 E-2
1.1	50.216	94.316	6.19776 E-2
1.15	48.698	92.798	6.75885 E-2
1.2	46.5728	90.6728	7.88151 E-2
1.25	44.4476	88.5476	7.87769 E-2
1.3	42.3224	86.4224	.084363
1.35	39.8936	83.9936	9.55569 E-2
1.4	37.1612	81.2612	.112305
1.45	33.8216	77.9216	.124357
1.5	30.4292	74.5292	.135036
1.56	25.7168	69.8168	.144643
1.58	24.146	68.246	.144557
1.6	22.5752	66.6752	.158919
1.62	20.6902	64.7902	.173244
1.64	18.8053	62.9053	.173121
1.66	16.9203	61.0203	.172998
1.68	15.0354	59.1354	.172875
1.7	13.1504	57.2504	.172752
1.72	11.2654	55.3654	.187015
1.74	9.06632	53.1663	.232997
1.76	6.17296	50.273	.176758
1.78	5.1988	49.2988	.192859
1.8	1.9516	46.0516	.270074
1.82	-.71996	43.38	.233244
1.84	-3.1652	40.9348	.228024
1.9	-10.8502	33.2498	.192462
1.95	-15.0421	29.0579	.153915
2	-19.3376	24.7624	.130216
2.05	-22.2344	21.8656	9.16792 E-2
2.1	-24.407	19.693	7.85169 E-2
2.15	-26.5796	17.5204	6.53763 E-2
2.2	-28.028	16.072	.052272
2.25	-29.4764	14.6236	.052243
2.3	-30.9248	13.1752	4.56873 E-2
2.4	-33.0974	11.0026	3.91279 E-2
2.5	-35.27	8.83	2.91838 E-2
2.6	-36.341	7.759	2.56858 E-2

PROPANE TEST DATA

RUN NO. 20
BULK TEMP. -42.4

TIME	TEMP.	SUPERHEAT	HEAT FLUX
.1	40.1972	84.2972	1.68644 E-2
.2	39.2864	83.3864	1.12394 E-2
.3	38.9828	83.0828	8.42863 E-3
.4	38.3756	82.4756	1.40445 E-2
.5	37.4648	81.5648	1.68477 E-2
.6	36.554	80.654	2.24559 E-2
.7	35.036	79.136	.028054
.8	33.518	77.618	.036742
.9	31.0575	75.1575	.040094
.95	30.115	74.215	4.63621 E-2
1	28.5442	72.6442	4.63348 E-2
1.05	27.6018	71.7018	4.05286 E-2
1.1	26.3451	70.4451	5.20837 E-2
1.15	24.7743	68.8743	6.36203 E-2
1.2	22.8894	66.9894	6.35752 E-2
1.25	21.3186	65.4186	6.93138 E-2
1.3	19.1194	63.2194	8.07992 E-2
1.35	16.9203	61.0203	9.22655 E-2
1.4	14.0929	58.1929	8.64068 E-2
1.45	12.2079	56.3079	8.63454 E-2
1.5	9.38048	53.4805	.104517
1.55	6.49768	50.5977	.112078
1.6	3.25048	47.3505	.111183
1.64	.97744	45.0774	.145198
1.66	-1.06928	43.0307	.141049
1.68	-2.11724	41.9828	9.54898 E-2
1.7	-3.1652	40.9348	.127269
1.72	-4.9118	39.1882	.174879
1.74	-7.00772	37.0923	.142969
1.76	-8.05568	36.0443	.158791
1.78	-10.5009	33.5991	.206236
1.8	-12.5968	31.5032	.158517
1.82	-13.9941	30.1059	.126746
1.84	-15.3914	28.7086	.127323
1.86	-16.8029	27.2971	9.67599 E-2
1.88	-17.5271	26.5729	8.20038 E-2
1.9	-18.6134	25.4866	9.83637 E-2
1.92	-19.6997	24.4003	8.19358 E-2
1.94	-20.4239	23.6761	7.09914 E-2
2	-22.9586	21.1414	6.43759 E-2
2.05	-24.407	19.693	5.23446 E-2
2.1	-25.8554	18.2446	4.57761 E-2
2.15	-26.9417	17.1583	3.92204 E-2
2.2	-28.028	16.072	.03267
2.3	-29.4764	14.6236	2.28563 E-2
2.4	-30.5627	13.5373	.019583
2.5	-31.649	12.451	1.63123 E-2
2.6	-32.3732	11.7268	1.30462 E-2
2.7	-33.0974	11.0026	1.30426 E-2
2.8	-33.8216	10.2784	.013039

PROPANE TEST DATA

RUN NO. 21
BULK TEMP. -42.4

TIME	TEMP.	SUPERHEAT	HEAT FLUX
.1	39.8936	83.9936	.011242
.2	39.2864	83.3864	1.12394 E-2
.3	38.6792	82.7792	8.42767 E-3
.4	38.3756	82.4756	8.42671 E-3
.5	37.7684	81.8684	8.42480 E-3
.6	37.4648	81.5648	8.42384 E-3
.7	36.8576	80.9576	1.68439 E-2
.8	35.6432	79.7432	3.36724 E-2
.85	34.4288	78.5288	3.36571 E-2
.9	33.8216	77.9216	2.80412 E-2
.95	32.9108	77.0108	4.52407 E-2
1	31.3717	75.4717	3.42033 E-2
1.05	31.0575	75.1575	2.31892 E-2
1.1	30.115	74.215	4.63621 E-2
1.15	28.5442	72.6442	4.63348 E-2
1.2	27.6018	71.7018	4.63184 E-2
1.25	26.031	70.131	5.20775 E-2
1.3	24.7743	68.8743	6.36203 E-2
1.35	22.5752	66.6752	8.09044 E-2
1.4	20.3761	64.4761	7.50634 E-2
1.45	18.4911	62.5911	8.07801 E-2
1.5	15.9778	60.0778	9.22328 E-2
1.55	13.4646	57.5646	9.21454 E-2
1.6	10.9513	55.0513	9.78586 E-2
1.65	8.12128	52.2213	9.92995 E-2
1.7	5.52352	49.6235	.121664
1.72	3.89992	47.9999	.133452
1.74	2.60104	46.701	.103745
1.76	1.62688	45.7269	.119644
1.78	-.02132	44.0787	.2185
1.8	-3.1652	40.9348	.190904
1.82	-4.21316	39.8868	9.54139 E-2
1.84	-5.26112	38.8389	9.53759 E-2
1.86	-6.30908	37.7909	.143007
1.88	-8.405	35.695	.190524
1.9	-10.5009	33.5991	.190372
1.92	-12.5968	31.5032	.158517
1.94	-13.9941	30.1059	.110903
1.96	-15.0421	29.0579	.110924
1.98	-16.4408	27.6592	9.61942 E-2
2	-17.165	26.935	7.87345 E-2
2.05	-19.6997	24.4003	8.52132 E-2
2.1	-21.8723	22.2277	7.20436 E-2
2.15	-23.6828	20.4172	.058904
2.2	-25.1312	18.9688	5.88713 E-2
2.25	-26.9417	17.1583	4.57571 E-2
2.3	-27.6659	16.4341	2.94071 E-2
2.4	-29.4764	14.6236	2.61215 E-2
2.5	-30.5627	13.5373	.019583
2.6	-31.649	12.451	1.63123 E-2
2.7	-32.3732	11.7268	1.30462 E-2

PROPANE TEST DATA

RUN NO. 22
BULK TEMP. -42.4

TIME	TEMP.	SUPERHEAT	HEAT FLUX
.1	42.626	86.726	1.12492 E-2
.2	42.0188	86.1188	1.12476 E-2
.3	41.4116	85.5116	8.43455 E-3
.4	41.108	85.208	8.43396 E-3
.5	40.5008	84.6008	1.40547 E-2
.6	39.59	83.69	1.40509 E-2
.7	38.9828	83.0828	1.12382 E-2
.8	38.3756	82.4756	1.68534 E-2
.9	37.1612	81.2612	2.80763 E-2
.95	36.2504	80.3504	2.80667 E-2
1	35.6432	79.7432	2.24483 E-2
1.05	35.036	79.136	.028054
1.1	34.1252	78.2252	3.36533 E-2
1.15	33.2144	77.3144	5.08528 E-2
1.2	31.3717	75.4717	5.14024 E-2
1.25	30.4292	74.5292	4.63676 E-2
1.3	28.8584	72.9584	6.37179 E-2
1.35	26.9734	71.0734	6.36728 E-2
1.4	25.4026	69.5026	6.36353 E-2
1.45	23.5177	67.6177	6.35902 E-2
1.5	21.9469	66.0469	6.35527 E-2
1.55	20.0619	64.1619	8.66013 E-2
1.6	17.2345	61.3345	9.51601 E-2
1.62	16.292	60.392	.100892
1.64	15.0354	59.1354	.100844
1.66	14.0929	58.1929	8.64068 E-2
1.68	13.1504	57.2504	.100772
1.7	11.8938	55.9938	.115114
1.72	10.6371	54.7371	.100677
1.74	9.69464	53.7946	.100641
1.76	8.438	52.538	.101676
1.78	7.47184	51.5718	.10357
1.8	6.17296	50.273	9.64648 E-2
1.84	4.54936	48.6494	8.15739 E-2
1.86	3.5752	47.6752	.118609
1.88	1.9516	46.0516	.18005
1.9	-.37064	43.7294	.201424
1.92	-2.46656	41.6334	.175041
1.94	-4.21316	39.8868	.153722
2	-9.10364	34.9964	.143913
2.05	-12.9462	31.1538	.114117
2.1	-15.3914	28.7086	9.61936 E-2
2.15	-18.2513	25.8487	.097709
2.2	-20.786	23.314	7.20735 E-2
2.25	-22.2344	21.8656	6.54851 E-2
2.3	-24.407	19.693	5.56161 E-2
2.4	-26.2175	17.8825	.035962
2.5	-28.3901	15.7099	2.93989 E-2
2.6	-29.4764	14.6236	1.95911 E-2
2.7	-30.5627	13.5373	.019583

METHANE TEST DATA

RUN NO. 27
BULK TEMP. -300.7

TIME	TEMP.	SUPERHEAT	HEAT FLUX
.1	-83.86	175.34	4.40839 E-2
.2	-86.38	172.82	4.76625 E-2
.3	-89.32	169.88	5.85248 E-2
.4	-93.1	166.1	.061996
.5	-96.46	162.74	4.82517 E-2
.6	-98.672	160.528	5.36643 E-2
.7	-102.668	156.532	5.73875 E-2
.75	-104.	155.2	6.11479 E-2
.8	-106.22	152.98	7.62986 E-2
.85	-108.44	150.76	6.09298 E-2
.9	-109.772	149.428	6.84724 E-2
.95	-112.436	146.764	9.11002 E-2
1	-115.1	144.1	7.60562 E-2
1.05	-116.894	142.306	9.18811 E-2
1.1	-120.493	138.707	9.93559 E-2
1.15	-122.743	136.457	7.62876 E-2
1.2	-124.992	134.208	.15656
1.22	-127.793	131.407	.179045
1.24	-129.234	129.966	.101264
1.26	-130.194	129.006	6.07104 E-2
1.28	-130.675	128.525	.182059
1.3	-134.517	124.683	.24198
1.32	-136.438	122.762	.12072
1.34	-137.399	121.801	.180859
1.36	-140.761	118.439	.180082
1.38	-141.722	117.478	.139891
1.4	-144.124	115.076	.258996
1.42	-147.966	111.234	.277538
1.44	-150.848	108.352	.355503
1.46	-156.612	102.588	.274431
1.48	-157.572	101.628	.229088
1.5	-162.232	96.9677	.358906
1.52	-166.432	92.7679	.275281
1.54	-169.065	90.1345	.232581
1.56	-172.226	86.9744	.210548
1.58	-174.332	84.8677	.209955
1.6	-177.492	81.7076	.183978
1.65	-181.179	78.0209	.116496
1.7	-184.866	74.3341	9.93552 E-2
1.75	-187.499	71.7007	7.42496 E-2
1.8	-189.606	69.594	5.75837 E-2
1.85	-191.186	68.014	5.95211 E-2
1.9	-193.425	65.7749	7.08714 E-2
1.95	-195.747	63.4526	5.39513 E-2
2	-196.909	62.2915	3.59099 E-2
2.1	-199.231	59.9691	3.57946 E-2
2.2	-201.553	57.6468	2.67595 E-2
2.3	-202.714	56.4857	.031169
2.4	-205.617	53.5828	3.54776 E-2

METHANE TEST DATA

RUN NO. 28
BULK TEMP. -301.7

TIME	TEMP.	SUPERHEAT	HEAT FLUX
.1	-68.992	190.208	6.09935 E-2
.2	-72.128	187.072	7.93456 E-2
.3	-77.98	181.22	8.09502 E-2
.4	-81.34	177.86	5.52147 E-2
.5	-84.28	174.92	7.34488 E-2
.6	-89.74	169.46	P.087758
.7	-94.36	164.84	6.92201 E-2
.75	-96.04	163.16	6.70137 E-2
.8	-98.228	160.972	.068557
.85	-100.004	159.196	7.66803 E-2
.9	-102.668	156.532	9.94717 E-2
.95	-105.776	153.424	8.39584 E-2
1	-107.552	151.648	7.62167 E-2
1.05	-110.216	148.984	7.60532 E-2
1.1	-111.992	147.208	.106524
1.15	-116.444	142.756	.106544
1.2	-118.244	140.956	6.89109 E-2
1.22	-119.143	140.057	.133895
1.24	-121.393	137.807	.114557
1.26	-121.843	137.357	9.54296 E-2
1.28	-123.643	135.557	.114347
1.3	-124.542	134.658	.135
1.32	-126.832	132.368	.218487
1.34	-129.714	129.486	.141713
1.36	-130.194	129.006	.141658
1.38	-133.076	126.124	.161511
1.4	-134.037	125.163	.20173
1.42	-137.879	121.321	.220914
1.44	-139.32	119.88	.160369
1.46	-141.722	117.478	.319751
1.48	-147.005	112.195	.396976
1.5	-151.328	107.872	.27633
1.52	-153.73	105.47	.297614
1.54	-158.593	100.607	.346089
1.56	-162.232	96.9677	.28582
1.6	-169.065	90.1345	.247107
1.65	-175.912	83.2877	.192749
1.7	-181.179	78.0209	.141459
1.75	-184.866	74.3341	9.93552 E-2
1.8	-187.499	71.7007	7.42496 E-2
1.85	-189.606	69.594	6.58099 E-2
1.9	-191.713	67.4873	5.94781 E-2
1.95	-193.425	65.7749	6.26882 E-2
2	-195.747	63.4526	5.39513 E-2
2.05	-196.909	62.2915	4.48874 E-2
2.1	-198.65	60.5497	4.92572 E-2
2.2	-201.553	57.6468	3.56793 E-2
2.3	-203.295	55.9051	2.66947 E-2
2.4	-205.037	54.1633	2.21915 E-2

METHANE TEST DATA

RUN NO. 30			
BULK TEMP. -255.4			
TIME	TEMP.	SUPERHEAT	HEAT FLUX
.1	-99.56	159.64	.030683
.2	-101.78	157.42	2.67999 E-2
.3	-102.668	156.532	3.44325 E-2
.4	-105.776	153.424	3.05303 E-2
.5	-106.22	152.98	2.67045 E-2
.6	-108.884	150.316	.030454
.7	-109.772	149.428	2.28241 E-2
.75	-110.66	148.54	3.80129 E-2
.8	-111.992	147.208	3.03776 E-2
.85	-112.436	146.764	1.51834 E-2
.9	-112.88	146.32	3.03558 E-2
.95	-114.212	144.988	5.31665 E-2
1	-115.994	143.206	5.33925 E-2
1.05	-117.344	141.856	4.59742 E-2
1.1	-118.693	140.507	7.65396 E-2
1.15	-121.843	137.357	.138097
1.2	-126.832	132.368	.124898
1.22	-127.793	131.407	8.11067 E-2
1.24	-128.753	130.447	.182347
1.26	-132.116	127.084	.202049
1.28	-133.556	125.644	.161448
1.3	-135.958	123.242	.181191
1.32	-137.879	121.321	.120498
1.34	-138.84	120.36	.220643
1.36	-143.163	116.037	.259317
1.38	-145.084	114.116	.159185
1.4	-147.005	112.195	.178639
1.42	-149.407	109.793	.217659
1.44	-152.289	106.911	.216845
1.46	-154.691	104.509	.176864
1.48	-156.612	102.588	.15928
1.5	-158.593	100.607	.122981
1.52	-159.633	99.5669	.126787
1.54	-161.712	97.4875	.190215
1.56	-164.325	94.8746	.190665
1.58	-166.432	92.7679	.148525
1.6	-168.012	91.1879	.131275
1.65	-172.226	86.9744	.117907
1.7	-175.386	83.8144	.100636
1.75	-178.546	80.6543	8.35076 E-2
1.8	-180.652	78.5476	4.99622 E-2
1.85	-181.706	77.4942	3.32607 E-2
1.9	-182.759	76.4408	4.15166 E-2
1.95	-184.339	74.8608	4.14277 E-2
2	-185.393	73.8074	.024821
2.05	-185.919	73.2808	1.65355 E-2
2.1	-186.446	72.7541	1.23927 E-2
2.2	-186.973	72.2274	1.65118 E-2
2.3	-188.553	70.6474	1.64762 E-2
2.4	-189.079	70.1207	8.23217 E-3

METHANE TEST DATA

RUN NO. 31
BULK TEMP. -255.4

TIME	TEMP.	SUPERHEAT	HEAT FLUX
.1	-104.444	154.756	2.29223 E-2
.2	-105.776	153.424	2.28977 E-2
.3	-107.108	152.092	3.04976 E-2
.4	-109.328	149.872	3.42485 E-2
.5	-111.104	148.096	3.79993 E-2
.6	-113.768	145.432	.030334
.65	-114.212	144.988	3.03231 E-2
.7	-115.544	143.656	6.87592 E-2
.75	-118.244	140.956	5.35973 E-2
.8	-118.693	140.507	3.82698 E-2
.85	-120.493	138.707	5.34994 E-2
.9	-121.843	137.357	5.34406 E-2
.95	-123.643	135.557	8.45326 E-2
1	-126.832	132.368	.102602
1.05	-129.714	129.486	.089077
1.1	-132.116	127.084	5.65737 E-2
1.15	-133.076	126.124	.113058
1.2	-138.84	120.36	.136397
1.22	-139.801	119.399	.16027
1.24	-142.683	116.517	.159678
1.26	-143.643	115.557	9.96756 E-2
1.28	-145.084	114.116	.139287
1.3	-147.005	112.195	.158791
1.32	-148.927	110.273	.158396
1.34	-150.848	108.352	.118501
1.36	-151.809	107.391	8.87649 E-2
1.4	-154.21	104.99	.127815
1.42	-156.132	103.068	.178994
1.44	-158.593	100.607	.227172
1.46	-161.712	97.4875	.189661
1.48	-163.272	95.928	.105704
1.5	-164.325	94.8746	.106386
1.52	-165.905	93.2946	.127396
1.54	-167.485	91.7146	.127129
1.56	-169.065	90.1345	.126862
1.58	-170.646	88.5545	.126595
1.6	-172.226	86.9744	.113696
1.65	-175.386	83.8144	9.22497 E-2
1.7	-178.019	81.181	8.35669 E-2
1.75	-180.652	78.5476	5.82893 E-2
1.8	-181.706	77.4942	3.32607 E-2
1.85	-182.759	76.4408	.02491
1.9	-183.286	75.9142	1.65948 E-2
1.95	-183.813	75.3875	1.65829 E-2
2	-184.339	74.8608	1.65711 E-2
2.05	-184.866	74.3341	1.65592 E-2
2.1	-185.393	73.8074	1.24105 E-2
2.2	-185.919	73.2808	8.26775 E-3
2.3	-186.446	72.7541	1.65236 E-2
2.4	-188.026	71.174	2.06101 E-2

METHANE TEST DATA

RUN NO. 32
BULK TEMP. -256.3

TIME	TEMP.	SUPERHEAT	HEAT FLUX
.1	-104.888	154.312	1.52761 E-2
.2	-105.332	153.868	1.52706 E-2
.4	-107.996	151.204	2.66663 E-2
.5	-109.772	149.428	3.04322 E-2
.6	-111.548	147.652	3.79857 E-2
.7	-114.212	144.988	3.79039 E-2
.75	-115.1	144.1	3.80786 E-2
.8	-116.444	142.756	3.82389 E-2
.85	-117.344	141.856	6.12989 E-2
.9	-120.043	139.157	6.88101 E-2
.95	-121.393	137.807	5.34602 E-2
1	-123.193	136.007	5.33818 E-2
1.05	-124.542	134.658	8.60146 E-2
1.1	-128.273	130.927	.111614
1.15	-131.155	128.045	.121325
1.2	-135.478	123.722	.173245
1.22	-137.879	121.321	.200831
1.24	-140.281	118.919	.180193
1.26	-142.202	116.998	.139805
1.28	-143.643	115.557	.159481
1.3	-146.045	113.155	.218608
1.32	-148.927	110.273	.158396
1.34	-149.887	109.313	.138424
1.36	-152.289	106.911	.177419
1.38	-154.21	104.99	.137647
1.4	-155.651	103.549	.157865
1.42	-158.074	101.126	.204543
1.44	-160.673	98.5272	.168818
1.46	-162.232	96.9677	.169303
1.48	-164.852	94.348	.169546
1.5	-166.432	92.7679	.127307
1.52	-168.012	91.1879	.12704
1.54	-169.592	89.6078	.147902
1.56	-171.699	87.5011	.147487
1.58	-173.279	85.9211	.126151
1.6	-174.859	84.341	.104903
1.65	-177.492	81.7076	7.52635 E-2
1.7	-179.599	79.6009	5.00334 E-2
1.75	-180.652	78.5476	3.33082 E-2
1.8	-181.706	77.4942	3.32607 E-2
1.85	-182.759	76.4408	.02491
1.9	-183.286	75.9142	1.65948 E-2
1.95	-183.813	75.3875	1.65829 E-2
2	-184.339	74.8608	1.65711 E-2
2.05	-184.866	74.3341	1.65592 E-2
2.1	-185.393	73.8074	1.24105 E-2
2.2	-185.919	73.2808	1.24016 E-2
2.3	-186.973	72.2274	1.65118 E-2
2.4	-188.026	71.174	.012366

APPENDIX C

HEAT TRANSFER DATA REDUCTION PROCEDURES

APPENDIX C

HEAT TRANSFER DATA REDUCTION PROCEDURES

1. INTRODUCTION

A simplified computer program was developed for calculating the heat transfer rates obtained with the thin wall copper chamber designs employed during the program experimental tasks. The copper chamber designs were instrumented with wall thermocouples at selected axial and circumferential locations. These transient wall temperature data were employed as input information for the subject computer program.

2. PROGRAM FORMULATION

The chamber is divided into nodes located at the thermocouple points. The total surface heat flux at node m at any time is

$$\dot{Q}_{in} = \dot{Q}_{stored} + \dot{Q}_{loss} \quad (C. 1)$$

For a nearly adiabatic back wall the only mode of heat loss at node m will be due to axial and circumferential conduction. By utilizing a segmented chamber design (circumferential grooving) the axial conduction between the various nodes is minimized with respect to the total heat stored in a node. This modified heat sink copper chamber design thus provides for a more detailed definition of axial heat transfer profiles, but employs the same basic modeling approach (with only changes in internodal thermal resistances). Thus,

$$\dot{Q}_{loss} = \dot{Q}_{cond} = \sum_{j=1}^N \frac{T_m - T_j}{R_{m,j}} \quad (C. 2)$$

where N equals the number of nodes in contact with node m . $R_{m,j}$ is the value of the resistance between nodes m and j and is given by

$$R_{m,j} = \frac{\Delta X}{kA_{m,j}} \quad (C. 3)$$

where

ΔX = length between nodes m and j

$A_{m,j}$ = cross-sectional area of heat transfer

k = thermal conductivity

The heat storage term, \dot{Q}_{stored} , is given by

$$\dot{Q}_{\text{stored}} = \rho C_p V_m \frac{dT}{d\theta} \quad (\text{C. 4})$$

where

ρ = density

C_p = specific heat

V_m = volume of node m

θ = time

T = temperature

The numerical computation involves an average of the forward and backward time steps; i. e., the derivative $\frac{dT}{d\theta}$ is evaluated at the forward slope of the temperature-time response and at the backward slope of the temperature-time response according to

$$\left. \frac{dT}{d\theta} \right|_{i+1/2} = \frac{T_{i+1} - T_i}{\theta_{i+1} - \theta_i} \quad (\text{C. 5})$$

$$\left. \frac{dT}{d\theta} \right|_{i-1/2} = \frac{T_i - T_{i-1}}{\theta_i - \theta_{i-1}} \quad (\text{C. 6})$$

Thus,

$$\dot{Q}_{\text{stored}} = \frac{\rho C_p V \left. \frac{dT}{d\theta} \right|_{i+1/2} + \rho C_p V \left. \frac{dT}{d\theta} \right|_{i-1/2}}{2} \quad (\text{C. 7})$$

The thermal properties are evaluated at the average temperature. The thermal conductivity, $K_{m,j}$, is evaluated at $(T_m + T_j)/2$, and the heat capacity, ρC_p , is evaluated at $(T_{\theta+1} + T_\theta)/2$ for $i+1/2$ and at $(T_\theta + T_{\theta-1})/2$ for $i-1/2$.

3. PROGRAM OPERATING PROCEDURE

3.1 Program Capabilities and Restrictions

- 1) Thermal conductivities (k) and volumetric heats (ρC_p) must be input as functions of temperature. The dependent and independent variables are input in pairs with up to 15 pairs allowed for each table. Linear interpolation between points is used, and when the independent variable is outside the bounds of the table input, the end points are assumed. At least two pairs of entries must be made for each table, even if thermal properties are constant with temperature.
- 2) Up to 50 thermocouples and 60 resistances may be used. Thermocouples do not need to be numbered in sequence and may be numbered greater than 50 as long as only 50 thermocouple numbers are input.
- 3) A thermocouple may be connected to as many resistances as desired, or may not be connected to a resistance at all. In the latter case, the heat flux will be determined only from the heat storage term.
- 4) If the resistance connections use numbers other than the thermocouple numbers input, an error message will be typed out and the case will be terminated.
- 5) The program will use any set of units for time, temperature and length as long as they are consistent in each set of input data.
- 6) The amount of data is limited to approximately 2400 characters, including decimals, commas and spaces. Thus, if a large number of nodes and time points is required, the number of significant figures in input data should be limited to the number needed for accuracy in the solution. A typical case of 20 thermocouples with input temperature data to 4 significant places would have enough storage to input approximately 20 time points.

3.2 Program Input Data

Data is input to the program starting at data location 800 and must be completed before data location 999. The user must enter the data in the order shown below and must not delete an item even if its value is zero. The quantities underlined are the numbers which must be entered.

- 1) N1, N2, N3, N4

N1 = total number of nodes or thermocouples

N2 = total number of resistances

N3 = number of pairs of entries in C_p table

N4 = number of pairs of entries in K table

- 2) C(1), A(1), V(1), C(2), A(2), V(2), ----- C(m), A(m), V(m)

C(m) = thermocouple number associated with node m

A(m) = heating surface area of node m

V(m) = volume of node m

NOTE: There must be a total of N1 nodes entered.

- 3) X(1), Y(1), R(1), X(2), Y(2), R(2), ----- X(m), Y(m), R(m)

X(m) = number of first thermocouple connected to resistor m

Y(m) = number of second thermocouple connected to resistor m

R(m) = value of geometric resistance, X/AREA

NOTE: There must be a total of N2 resistances entered.

- 4) T(1), $C_p(1)$, T(2), $C_p(2)$, ----- T(m), $C_p(m)$

T(m) = temperature associated with $C_p(m)$

$C_p(m)$ = volumetric heat capacity at temperature T(m)

NOTE: A total of N3 pairs must be entered.

- 5) T(1), K(1), T(2), K(2), ----- T(m), K(m)

T(m) = temperature associated with K(m)

K(m) = thermal conductivity at T(m)

NOTE: A total of N4 pairs must be entered.

- 6) θ_1 , T(1), T(2), T(3), ----- T(m)

.
.
.

θ_n , T(1), T(2), T(3), ----- T(m)

θ_n = nth time point

T(m) = temperature of node m at nth time point

NOTE: Each time point must be followed by a total of N1 temperatures.

3.3 Output Data

Data output occurs at each time point and consists of the following values:

- 1) Total surface heat rate, $\Sigma \dot{Q}$
- 2) Total surface area, ΣA
- 3) Temperature at each node, T
- 4) Surface heat flux at each node, \dot{Q}/A

There is no output at the initial and final time points.

4. PROGRAM LISTING AND SAMPLE PROBLEM

A flow diagram (Figure C-1), program listing and program nomenclature are included in the following. The program listing is in G. E. "Basic" language.

Also included is a sample problem. The model is shown in Figure C-2. It consists of a thin-walled chamber instrumented with six thermocouples, and has both axial and radial conduction. The thermal properties and table of temperature versus time are also shown. Following this is the input to and the resultant output from QDOT/A. This sample problem is an illustration only and is not meant to show actual results of real test data.

4.1 Program Nomenclature

- A(N) Surface care of node N.
- A1 Temperature average used in ρC_p subroutine.
- A3 Interpolated value of ρC_p at temperature A1.
- A5 Temperature average used in K subroutine.
- A7 Interpolated value of K at temperature A5.
- A9 Temperature difference over resistance, $\frac{T_{B3} - T_{C3}}{R_{B3, C3}}$
- B(N) Volume of node N.
- B3 Number of first node or thermocouple corrected to a resistance.
- B4 Temporary variable; number of first node connected to a resistance.
- B6 Counts number of lines already printed on each page.

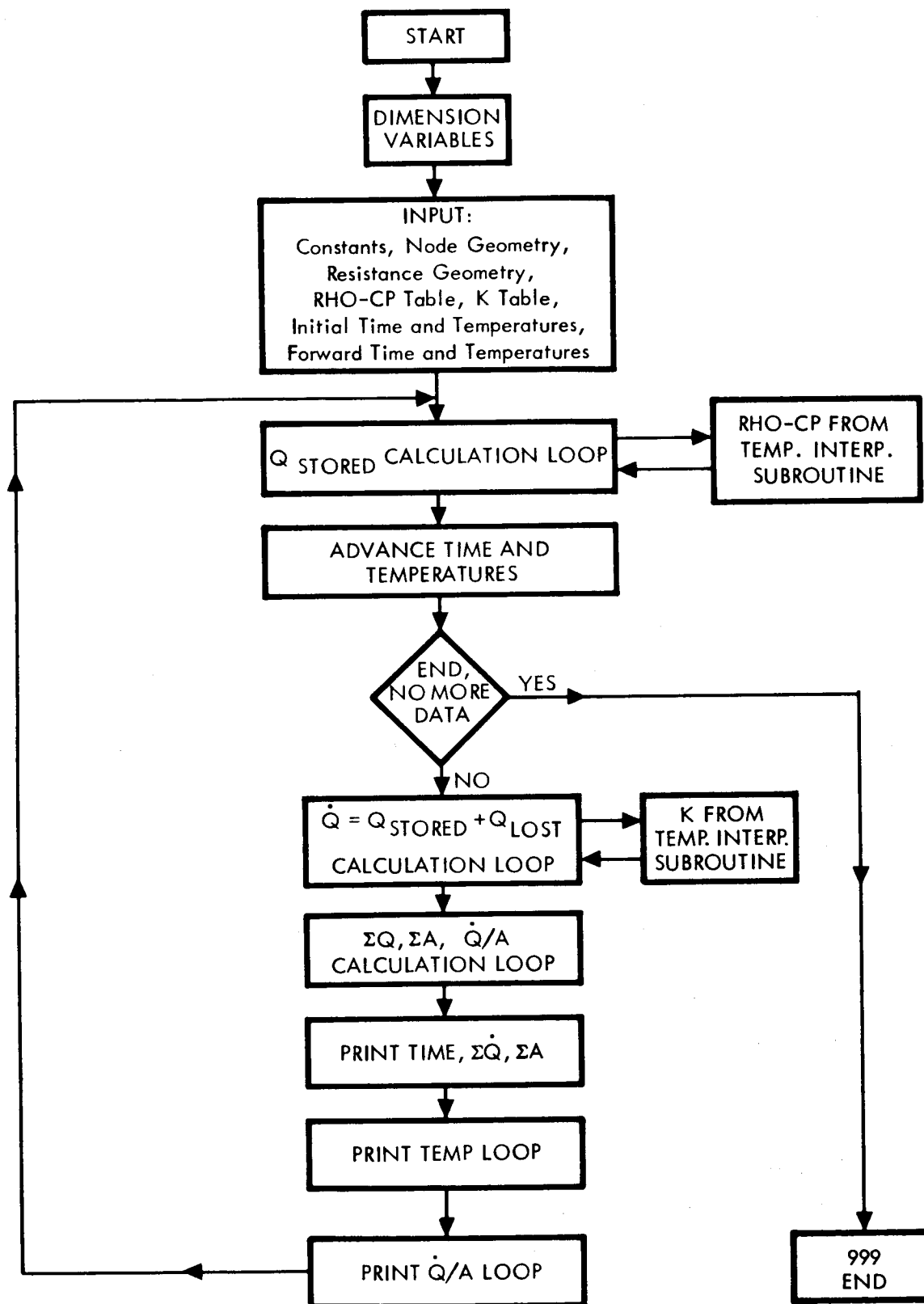


Figure C-1. Overall Flow Diagram

C(N)	Thermocouple number associated with node N.
C1	Counter used in some loops requiring a constant counter.
C3	Number of second node or thermocouple connected to a resistance.
C4	Temporary variable; number of second node connected to a resistance.
C6	Counter used in printing blank lines at end of each page.
D(M)	Value of temperature at point M in ρC_p table.
E(L)	Integer used for storage of node numbers connected to resistance L.
F(M)	Value of ρC_p at point M in ρC_p table.
G(M)	Value of temperature at point M in K table.
H(M)	Value of K at point M in K table.
J1	Counter used in $\rho C_p V \frac{dT}{d\theta}$ calculation loop.
L	Used as counter of total number of resistances in all loops requiring a resistance counter.
M	Counter used in K and ρC_p interpolation subroutines. Counts number of pairs of entries in each table.
N	Used as counter of total number of nodes in all loops requiring a node counter. Also used for blank line spacing at start of problem.
N1	Total number of nodes.
N2	Total number of resistances.
N4	Number of pairs of entries in ρC_p table.
N5	Number of pairs of entries in K table.
Q(N)	Current value of heat rate of node N and final heat flux at node N.
R(L)	Value of geometric resistance L; $\frac{\Delta AX}{A_L}$
S(N)	Temperature at node N for forward time step.
T(N)	Temperature at node N at present time step.
W1	Sum of all heat rates for any time step; $\Sigma \dot{Q}(N)$.
W2	Sum of all surface areas; $\Sigma A(N)$.
X1	Present time.
X2	Forward time.

4.2 QDOT/A Program Listing

```
3   For N=1 to 8
4   Print
5   Next N
10  Dim A(50), B(50), C(50), T(60), S(50), Q(50)
15  Dim R(60), E(60), D(15), F(15), G(15), H(15)
20  Read N1, N2, N4, N5
25  For N=1 to N1
28  Read C(N), A(N), B(N)
30  Next N
33  For L=1 to N2
35  Read B3, C3, R(L)
37  Let C1=0
40  For N=1 to N1
42  If C(N)=B3 then 50
43  If C(N)=C3 then 55
45  If C1>1 then 65
47  Next N
48  Print "Error in numbering resistance connectors"
49  Go to 999
50  Let B4=N
51  Let C1=C1+1
52  Go to 43
55  Let C4=N
57  Let C1=C1+1
60  Go to 45
65  Let E(L) = 100*B4+C4
70  Next L
75  For M=1 to N4
80  Read D(M), F(M)
85  Next M
90  For M=1 to N5
95  Read G(M), H(M)
100 Next M
120 Read X1
```

```

125   For N=1 to N1
130   Read T(N)
135   Next N
140   Read X2
145   For N=1 to N1
150   Read S(N)
155   Next N
365   Let B6=0
370   For J1=1 to 2
375   For N=1 to N1
380   If J1<2 then 440
385   If N>1 then 390
388   Read X2
390   Read S(N)
395   Let A1 = (T(N) + S(N))/2
397   Go Sub 660
400   Let Q(N)=Q(N)+(A3*B(N)*(S(N)-T(N))/((X2-X1)*2))
405   If J1>1 then 415
410   Let T(N)=S(N)
415   Next N
420   If N1>1 then 430
425   Let X1=X2
430   Next J1
435   Go to 460
440   Let Q(N)=0
445   Go to 395
460   For L=1 to N2
465   Let B3=Int(E(L)/100)
470   Let C3=E(L)-100*Int(E(L)/100)
482   Let A5=(T(B3)+T(C3))/2
484   Go Sub 720
485   Let A9=(T(B3)-T(C3))*A7/R(L)
490   Let Q(B3)=Q(B3)+A9
495   Let Q(C3)=Q(C3)-A9
496   Next L

```

```

498   Let W1=0
499   Let W2=0
500   For N=1 to N1
502   Let W1=Q(N)+W1
503   Let W2=A(N)+W2
510   Let Q(N)=Q(N)/A(N)
512   Next N
514   If B6<58 then 520
517   Go Sub 780
520   Print "Time ="; X1, "Total Q-Dot ="; W1, "Total Area ="; W2
523   Print
525   Print "Temperatures"
528   Let B6=B6+3
530   If B6<58 then 535
532   Go Sub 780
535   Go Sub 600
540   Print "Q-Dot/A, BTU/in. 2=sec. "
541   Let B6=B6+1
542   If B6<58 then 545
543   Go Sub 780
545   Let C1=3.5
550   For N=1 to N1
555   If N>C1 then 570
560   Print C(N); Q(N)
565   Go to 580
570   Print C(N);Q(N)
572   Let B6=B6+1
573   If B6<58 then 575
574   Go Sub 780
575   Let C1=C1+4
580   Next N
583   Print
584   Print
585   Print
586   If N<C1 then 592
587   Let B6=B6+3

```

```

588   If B6<58 then 590
589   Go Sub 780
590   Go to 370
592   Print
594   Let B6=B6+4
596   Go to 588
600   Let C1=3.5
605   For N=1 to N1
610   If N>C1 then 630
620   Print C(N); T(N),
625   Go to 640
630   Print C(N); T(N)
632   Let B6=B6+1
633   If B6<58 then 635
634   Go Sub 780
635   Let C1=C1+4
640   Next N
645   Print
646   If N<C1 then 653
647   Let B6=B6+1
648   If B6<58 then 650
649   Go Sub 780
650   Return
653   Print
655   Let B6=B6+2
657   Go to 648
660   If A1<=D(1) then 695
665   If A1>=D(N4) then 705
670   For M=2 to N4
675   If A1< D(M) then 685
680   Next M
685   Let A3=F(M-1)+((A1-D(M-1))*(F(M)-F(M-1))/(D(M)-D(M-1)))
690   Return
695   Let A3=F(1)
700   Go to 690

```

```

705   Let A3=F(N4)
710   Go to 690
720   If A5<=G(1) then 755
725   If A5>=G(N5) then 765
730   For M=2 to N5
735   If A5<G(M) then 745
740   Next M
745   Let A7=H(M-1)+((A5-G(M-1))*(H(M)-H(M-1))/(G(M)-G(M-1)))
750   Return
755   Let A7=H(1)
760   Go to 750
765   Let A7=H(N5)
770   Go to 750
780   For C6=1 to 9
782   Print
785   Next C6
788   Let B6=0
790   Return
999   End

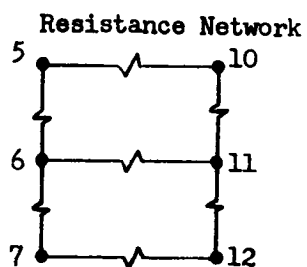
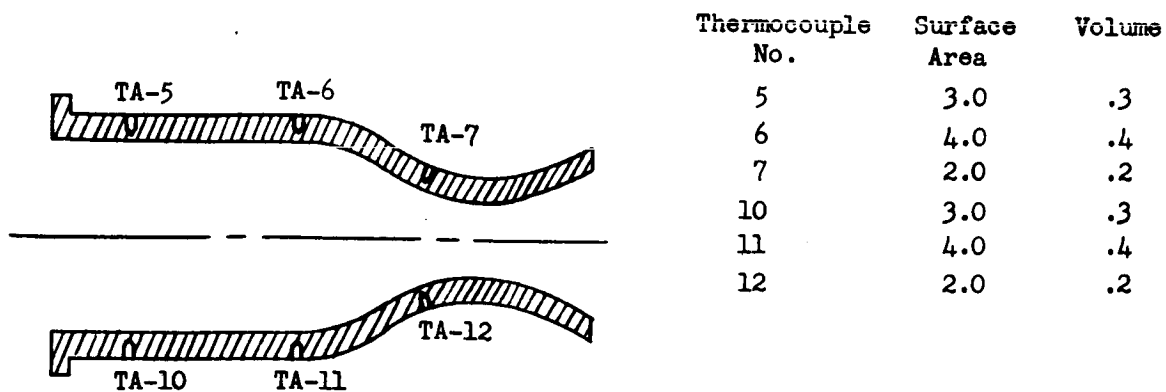
```

4.3 Sample Problem Input

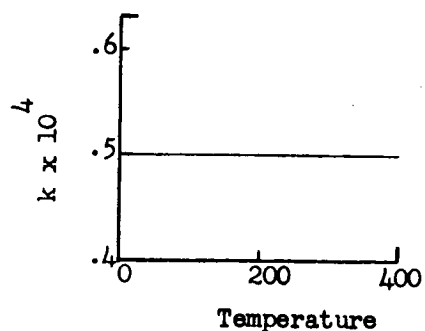
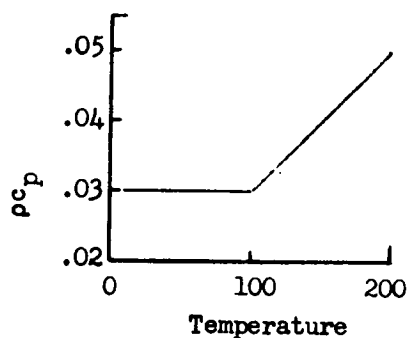
```

800 DATA 6, 7, 3, 2
801 DATA 5, 3, . 3,    6, 4, . . 4,    7, 2, . . 2,    10, 3, . . 3,    11, 4, . . 4
802 DATA 12, 2, . . 2
805 DATA 5, 10, . 5,    6, 11, . 5,    7, 12, . 4,    5, 6, . 2,    6, 7, . 2
806 DATA 10, 11, . 2,    11, 12, . 2
810 DATA 0, . 03,    100, . 03,    200, . 05
815 DATA 0, . 5E-4,    400, . 5E-4
820 DATA 0,    100, 100, 100, 100, 100, 100
821 DATA . 1,    120, 125, 125, 125, 125, 125
822 DATA . 2,    140, 150, 150, 145, 150, 155
823 DATA . 3,    170, 180, 180, 170, 180, 190
824 DATA . 4,    190, 195, 200, 190, 200, 210
825 DATA . 5,    210, 210, 210, 205, 210, 215
826 DATA . 6,    220, 215, 220, 220, 215, 220

```



Resistance Connections	$\frac{\Delta X}{A}$
5-10	.5
6-11	.5
7-12	.4
5-6	.2
6-7	.2
10-11	.2
11-12	.2



Time	Temperature					
	TA-5	TA-6	TA-7	TA-10	TA-11	TA-12
0	100	100	100	100	100	100
.1	120	125	125	120	125	125
.2	140	150	150	145	150	155
.3	170	180	180	170	180	190
.4	190	195	200	190	200	210
.5	210	210	210	205	210	215
.6	220	215	220	220	215	220

Figure C-2. Sample Model

4.4 Sample Problem Output

TIME = .1 TOTAL Q-DOT = 15.0713 TOTAL AREA = 18

TEMPERATURES

5	120	6	125	7	125	10	120
11	125	12	125				

Q-DOT/A, BTU/IN. 2=SEC.

5	.679583	6	.875313	7	.875	10	.775833
11	.875313	12	.97625				

TIME = .2 TOTAL Q-DOT = 19.685 TOTAL AREA = 18

TEMPERATURES

5	140	6	160	7	150	10	145
11	150	12	155				

Q-DOT/A, BTU/IN. 2=SEC.

5	.974	6	1.11438	7	1.11344	10	.97475
11	1.11375	12	1.34969				

TIME = .3 TOTAL Q-DOT = 19.4738 TOTAL AREA = 18

TEMPERATURES

5	170	6	180	7	180	10	170
11	180	12	190				

Q-DOT/A, BUT/IN. 2=SEC.

5	1.07417	6	1.00188	7	1.12438	10	.977917
11	1.125	12	1.28063				

TIME = .4 TOTAL Q-DOT = 13.9288 TOTAL AREA = 18

TEMPERATURES

5	190	6	195	7	200	10	190
11	200	12	210				

Q-DOT/A, BTU/IN. 2=SEC.

5	.959583	6	.731125	7	.73	10	.830417
11	.730125	12	.626875				

TIME = .5 TOTAL Q-DOT = 9.48875 TOTAL AREA = 18

TEMPERATURES

5	210	6	210	7	210	10	205
11	210	12	215				

Q-DOT/A, BTU/IN. 2=SEC.

5	.750167	6	.5	7	.499688	10	.745667
11	.375	12	.250938				

APPENDIX D

CALCULATION OF C* EFFICIENCY

APPENDIX D

CALCULATION OF C* EFFICIENCY

The index of injector performance used in the experimental program was the corrected C* efficiency. This parameter was calculated by two independent methods, one based on measurement of chamber pressure and the other on measurement of thrust. Details of the computational procedures and of the applied corrections are given in the following sections. The procedures and nomenclature format are essentially those as developed in NASA sponsored programs at Rocketdyne.

1.0 CHAMBER PRESSURE TECHNIQUE

Characteristic velocity efficiency based on chamber pressure is defined by the following:

$$\eta_{C^*} = \frac{(P_c)_o (A_t)_{\text{eff}} g_c}{(\dot{w}_T) (C^*)_{\text{theo}}}$$

D-1

where

- $(P_c)_o$ = stagnation pressure at the throat
- $(A_t)_{\text{eff}}$ = effective thermodynamic throat area
- g_c = conversion factor (32.174 lbf-ft/lbf-sec²)
- \dot{w}_T = total propellant weight flow rate
- $(C^*)_{\text{theo}}$ = theoretical characteristic velocity based on shifting equilibrium

Values calculated from Equation (D-1) are referred to as "corrected" C* efficiencies, because the factors involved are obtained by application of suitable influence factor corrections to measured parameters. Stagnation pressure at the throat is obtained from measured static pressure at start of nozzle convergence by assumption of isentropic expansion, effective throat area is estimated from measured geometric area by allowing for geometrical radius changes during firing and for nonunity discharge coefficient, and chamber pressure is corrected to allow for energy losses from combustion

gases to the chamber wall by heat transfer and friction. Equation (D-1) may therefore be written as follows:

$$\eta_{C^*} = \frac{P_c A_t g_c f_p f_{TR} f_{DIS} f_{FR} f_{HL} f_{KE}}{(\dot{w}_o + \dot{w}_f) (C^*)_{theo}} \quad (D-2)$$

where

- P_c = measured static pressure at start of nozzle convergence, psia
- A_t = measured geometric throat area, in²
- g_c = conversion factor (32.174 lbf-ft/lbf-sec²)
- \dot{w}_o = oxidizer weight flow rate, lb/sec
- \dot{w}_f = fuel weight flow rate, lb/sec
- $(C^*)_{theo}$ = theoretical C* based on shifting equilibrium calculations, ft/sec
- f_p = influence factor correcting observed static pressure to throat stagnation pressure
- f_{TR} = influence factor correcting for change in throat radius during firing
- f_{DIS} = influence factor correcting throat area for effective discharge coefficient
- f_{FR} = influence factor correcting measured chamber pressure for frictional drag of combustion gases at chamber wall
- f_{HL} = influence factor correcting measured chamber pressure for heat losses from combustion gases to chamber wall
- f_{KE} = influence factor correcting C* values to account for finite chemical reaction rates

Methods of estimation of the various correction factors are described in the following paragraphs.

1.1 PRESSURE INFLUENCE FACTOR (f_p)

Measured static pressure at start of nozzle convergence is converted to stagnation pressure at the throat by assumption of effectively no

combustion in the nozzle and application of the isentropic flow equations, with contraction ratio (A_c/A_t) and shifting-equilibrium specific heat ratios (γ). Frozen-equilibrium specific heat ratios usually make the influence correction factor about 1/2 percent larger. Hence the value employed with shifting-equilibrium is the more conservative. Figure D-1 shows the influence factor as a function of contraction ratio.

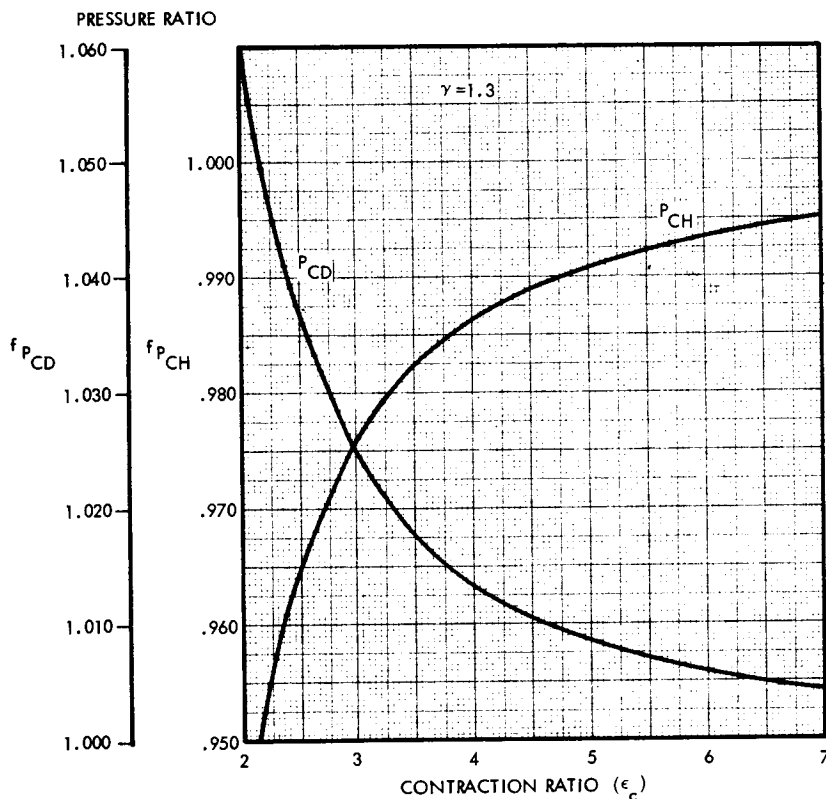


Figure D-1. Momentum Correction

1.2 THROAT RADIUS INFLUENCE FACTOR (f_{TR})

Temperature gradients produced in the solid metal nozzle wall result in thermal stresses which affect throat radius, with the result that the geometric throat diameter ambient measurement is not the same as that which exists during firing.

In the chamber type employed during the experimental effort (i.e. thin throat wall thickness), the throat area change is computed from the thermal growth of the throat based on temperature changes from ambient temperature. The change in throat area can be written as:

$$A_{th} = \frac{\pi}{4} (2 + \alpha \Delta T) (\alpha \Delta T) D^2 \quad (D-3)$$

where

ΔA^* = change in throat area due to thermal growth

α = average thermal expansion coefficient

ΔT = temperature rise from ambient conditions

D = throat diameter at ambient conditions

The throat area correction factor is as follows:

$$\begin{aligned} f_{TR} &= 1 + \frac{\Delta A_{th}}{A_{th}} \\ &= [1 + \alpha \Delta T]^2 \end{aligned} \quad (D-4)$$

The thermal expansion coefficient for copper is $\alpha_{Cu} = 9.8 \times 10^{-6}$ in/in-°F, assuming an ambient temperature of 70°F, the throat area correction factor becomes

$$f_{TR} = [1 + 9.8 \times 10^{-6} (T_{th} - 70)]^2 \quad (D-5)$$

This equation was used to generate the curve in Figure D-2.

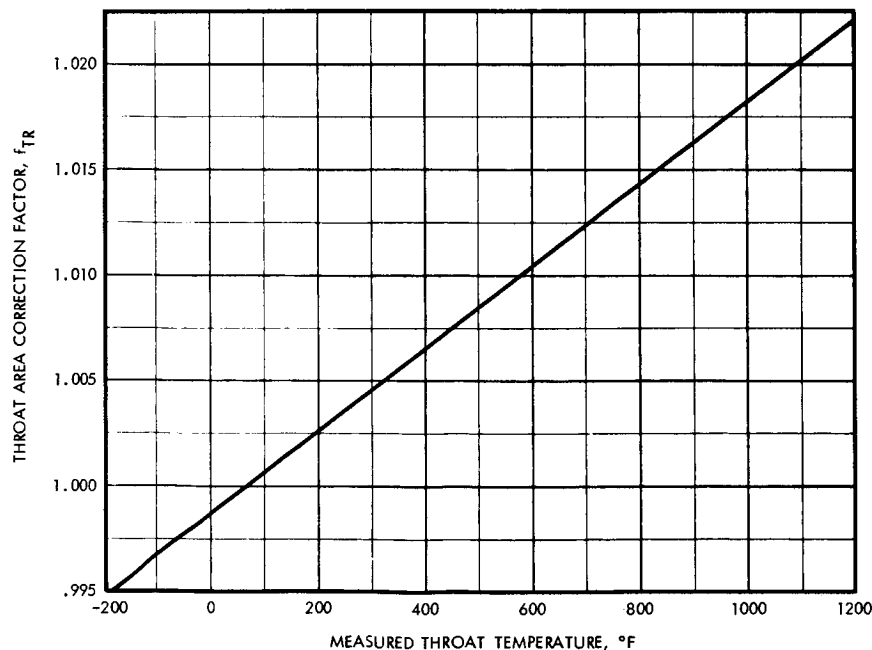


Figure D-2. Throat Area Correction Factor

1.3 THROAT DISCHARGE COEFFICIENT INFLUENCE FACTOR (f_{DIS})

The discharge coefficient is defined as the ratio of actual flow rate through the throat to the theoretical maximum, based on geometric throat area and ideal, uniform, one-dimensional flow with no boundary layer. The discharge influence coefficient may be estimated in two ways: one based on calculations made from a theoretical, inviscid flow model of combustion products, and the other based on a correlation of results obtained in various experimental study results of air flow through nozzles of similar geometry.

1.3.1 Theoretical Model

Total mass flow rate is given by

$$\dot{m} = \int_0^A \rho V dA \quad (D-6)$$

where:

- ρ = gas density
- V = gas velocity
- A = cross-sectional area

Theoretical maximum flow rate at the throat is

$$\dot{m}_{max} = \int_0^{A_t} \rho^* V^* dA \quad (D-7)$$

where:

- A_t = geometric area of the throat
- ρ^* = sonic gas density
- V^* = sonic gas velocity

For ideal, uniform, parallel flow, Equation (D-7) becomes

$$\dot{m}_{max} = \rho^* V^* A_t \quad (D-8)$$

The discharge coefficient is then

$$C_D = \frac{\dot{m}}{\dot{m}_{\max}} = \int_0^A \left(\frac{\rho}{\rho^*} \right) \left(\frac{V}{V^*} \right) \left(\frac{dA}{A_t} \right) \quad (D-9)$$

1.3.2 Empirical Value

Experimental conical nozzle discharge coefficients obtained with air by various investigators are plotted in Figure D-3 against the indicated geometric parameter. Data sources also are listed in Figure D-3.

The values obtained by both methods are found to be in excellent agreement.

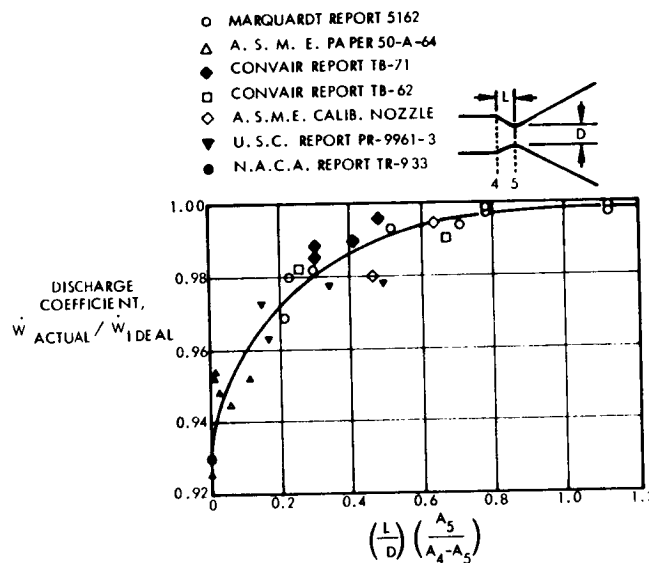


Figure D-3. Conical Nozzle Discharge Coefficient

1.4 FRICTIONAL DRAG INFLUENCE FACTOR (f_{FR})

Calculations of C^* based on chamber pressure are concerned with chamber phenomena up to the nozzle throat. Drag forces to this point are small enough to be considered negligible, so that the factor f_{FR} may be taken to be unity.

1.5 ENERGY LOSS INFLUENCE FACTOR (f_{HL})

Chamber pressure and thrust are decreased by heat transfer from the combustion gases to the walls of a thrust chamber. This enthalpy loss is substantially reduced in ablative chambers and is effectively recovered in a regeneratively cooled chamber.

The effect on C^* of enthalpy loss by heat transfer can be estimated from a loss of chamber enthalpy. This is determined from a two station energy balance, one at the start of nozzle convergence and the other at the throat.

$$\frac{1}{2} V_c^2 + H_c = \frac{1}{2} V_t^2 + H_t + \dot{Q}_{conv} \quad (D-10)$$

where:

- V_c = gas velocity at chamber exit
- V_t = gas velocity at nozzle throat
- H_c = gas enthalpy at chamber exit
- H_t = gas enthalpy at nozzle throat
- \dot{Q}_{conv} = heat loss in nozzle convergence

Velocity at the throat is given by:

$$V_t = [V_c^2 + 2(H_c - H_t - \dot{Q}_{conv})]^{1/2} \quad (D-11)$$

With negligible nozzle inlet velocity

$$V_t = [2(H_c - H_t - \dot{Q}_{conv})]^{1/2} \quad (D-12)$$

Logarithmic differentiation of Equation (D-12) gives

$$\frac{dV_t}{V_t} = \frac{1}{2} \frac{d(H_c - H_t - \dot{Q}_{conv})}{(H_c - H_t - \dot{Q}_{conv})} = \frac{1}{2} \left(\frac{dH_c - dH_t}{H_c - H_t - \dot{Q}_{conv}} \right) \quad (D-13)$$

Substitution of enthalpy definition into Equation (D-13) gives:

$$\frac{dV_t}{V_t} = \frac{1}{2} \left(\frac{c_{pc} dT_c - c_{pt} dT_t}{H_c - H_t - \dot{Q}_{conv}} \right) \quad (D-14)$$

With constant \dot{C}_p between the two stations,

$$\frac{dv_t}{v_t} = 1/2 \left(\frac{c_p dT_c}{H_c - H_t - \dot{Q}_{conv}} \right) \left(1 - \frac{dT_t}{dT_c} \right) \quad (D-15)$$

If the specific heat ratio, γ , is assumed constant,

δ

$$\frac{dT_t}{dT_c} = \frac{T_t}{T_c} \quad (D-16)$$

Substituting Equation (D-16) into Equation (D-15), replacing differentials by incrementals, and noting that C^* is proportional to gas velocity at the throat gives:

$$\frac{\Delta v_t}{v_t} = \frac{\Delta C^*}{C^*} = 1/2 \left(\frac{c_p \Delta T_c}{H_c - H_t - \dot{Q}_{conv}} \right) \left(1 - \frac{\Delta T_t}{T_c} \right) \quad (D-17)$$

Total heat loss to the chamber walls, in Btu per pound of propellant, is obtained by summation of observed heat fluxes over the appropriate areas:

$$\text{Heat loss} = \frac{\Sigma(q/A) A}{\dot{w}_T} \quad (D-18)$$

where:

q/A = experimentally observed heat flux

A = area applicable to each q/A value

\dot{w}_T = total propellant flow rate

If this heat loss is equated to the change in enthalpy of the gas in the combustion chamber, $c_p \Delta T_c$, then substitution in Equation (B.19) gives:

$$\frac{\Delta C^*}{C^*} = 1/2 \left[\frac{\Sigma(q/A) A}{\dot{w}_T} \right] \left[\frac{1 - (T_t/T_c)}{H_c - H_t - \dot{Q}_{conv}} \right] \quad (D-19)$$

The applicable influence factor is:

$$f_{HL} = 1 + \frac{\Delta C^*}{C^*} = 1 + 1/2 \left[\frac{\Sigma(q/A) A}{\dot{w}_T} \right] \left[\frac{1 - (T_t/T_c)}{H_c - H_t - \dot{Q}_{conv}} \right] \quad (D-20)$$

An alternate expression can be obtained from the basic C^* definition:

$$C^* = \frac{\sqrt{RT_c}}{\Gamma} \quad (D-21)$$

Logarithmic differentiation of this yields:

$$\frac{dc^*}{c^*} = \frac{1}{2} \frac{dT_c}{T_c} \quad (D-22)$$

Substituting incrementals from differentials in Equation (D-22) gives:

$$\frac{\Delta c^*}{c^*} = \frac{1}{2} \frac{\Delta T_c}{T_c} \quad (D-23)$$

Equating ΔT_c with the heat loss from Equation (D-18) results in the following:

$$\frac{\Delta c^*}{c^*} = \frac{1}{2} \left[\frac{\Sigma(q/A)A}{\dot{w}_t} \right] \left[\frac{1}{c_p T_c} \right] \quad (D-24)$$

The applicable influence factor is:

$$f_{HL} = 1 + \frac{1}{2} \left[\frac{\Sigma(q/A)A}{\dot{w}_t} \right] \left[\frac{1}{c_p T_c} \right] \quad (D-25)$$

where

c_p = specific heat at constant pressure

Although derived independently it can be shown that these two expressions, Equations (D-20) and (D-25), are nearly equivalent.

1.6 INFLUENCE FACTOR FOR CHEMICAL KINETICS (f_{KE})

The effect of finite chemical reaction rates is to produce a C^* less than the corresponding theoretical equilibrium values. A TRW Systems Group developed one-dimension nonequilibrium reacting gas computer program was employed with reaction rate constants selected for the propellant system. The fluid mechanical and chemical equations were integrated from the inlet section by an implicit technique. It was determined that the effect of nonequilibrium chemistry produced a C^* loss of 1.2% compared to the shifting equilibrium limits.

2. CALCULATIONS BASED ON THRUST

The alternate determination of C^* efficiency is based on thrust:

$$\eta_{C^*} = \frac{F_{vac} g_c}{(C_F)_{vac} \dot{w}_T C^*_{theo}} \quad (D-26)$$

where:

- F_{vac} = measured thrust corrected to vacuum conditions
by the equation: $F_{vac} = F + P_a A_e$
- F = measured thrust, lbf
- P_a = ambient pressure, psia
- A_e = area of nozzle exit, in²
- g_c = conversion factor (32.174 lbf-ft/lbf-sec²)
- $(C_F)_{vac}$ = theoretical shifting thrust coefficient (vacuum)
- \dot{w}_T = total propellant flow rate, lbf/sec
- C^*_{theo} = theoretical shifting-equilibrium characteristic
velocity, ft/sec

Values of vacuum thrust are obtained by applying corrections to sea-level measurements. With these values, which include allowances for all important departures from ideality, theoretical thrust coefficients may be used for calculation of C^* . C_F efficiency is taken as 100 percent if there is no combustion in the nozzle, if chemical equilibrium is maintained in the nozzle expansion process, and if energy losses from the combustion gases are accounted for.

Applicable influence factors for measured thrust are specified in the following equation:

$$\eta_{C^*} = \frac{(F + P_a A_e) g_c \phi_{FR} \phi_{DIV} \phi_{HL} \phi_{KE}}{(C_F)_{theo} (\dot{w}_o + \dot{w}_f) (C^*)_{theo}} \quad (D-27)$$

where:

- F = measured thrust, lbf
- P_a = ambient pressure, psia
- A_e = area of nozzle exit, in²
- g_c = conversion factor (32.174 lbf-ft/lbf-sec²)

$(C_F)_{\text{theo}}$	=	theoretical shifting thrust coefficient (vacuum)
\dot{w}_o	=	oxidizer weight flow rate, lbm/sec
\dot{w}_f	=	fuel weight flow rate, lbm/sec
$(C^*)_{\text{theo}}$	=	theoretical shifting equilibrium characteristic velocity, ft/sec
ϕ_{FR}	=	influence for frictional losses
ϕ_{DIV}	=	influence factor for nozzle divergence
ϕ_{HL}	=	influence factor for heat losses to chamber and nozzle walls
ϕ_{KE}	=	influence factor correcting C^* and C_F values to account for finite chemical reaction rates

The influence factors in Equation (D-27) are applied to vacuum thrust $(F + P_a A_e)$ instead of to measured site thrust (F) because, for convenience, the factors are readily calculated as changes in efficiency based on theoretical vacuum parameters. The total influence factor is then of the form $\Delta F/F_{\text{vac}}$.

Implicit in the use of theoretical C_F values are corrections to geometric throat area and to measured static chamber pressure at start of nozzle convergence. Therefore, calculation of corrected C^* efficiency from thrust measurement includes all the previously described corrections plus an additional one to account for nonparallel nozzle exit flow. However, because $(C_F)_{\text{theo}}$ is essentially independent of small changes to chamber pressure and contraction ratio which are involved in corrections to P_c and A_t , these corrections are of no practical significance in calculation of C^* from thrust measurements.

2.1 INFLUENCE FACTOR FOR FRICTIONAL DRAG (ϕ_{FR})

This factor corrects for energy losses caused by viscous drag forces on the thrust chamber walls. Its magnitude is estimated by a boundary layer analysis utilizing the integral momentum equation for turbulent flow, which accounts for boundary layer effects from the injector to the nozzle exit by suitable description of the boundary layer profile and local skin friction coefficient. A computer program is used to carry out a numerical

integration of the equation, including effects of pressure gradient, heat transfer, and surface roughness. The program requires a potential nozzle flow solution obtained from variable-property, axisymmetric method of characteristics calculation of the flow field outside the boundary layer; corresponding properties for the subsonic combustion chamber flow field are also calculated.

2.2 INFLUENCE FACTOR FOR NOZZLE DIVERGENCE (ϕ_{DIV})

The one-dimensional theoretical performance calculations assume that flow at the nozzle exit is uniform and parallel to the nozzle axis. The influence factor, ϕ_{DIV} , allows for nozzle divergence (i.e., for nonaxial flow) and for nonuniformity across the nozzle exit plane. It is calculated by a computer program which utilizes the axisymmetric method of characteristics for a variable-property gas. Computation begins with a transonic input near Mach 1, providing a characteristic line for use in the analysis of the supersonic portion of the nozzle. The resulting pressures are integrated over the given geometry to give the geometric efficiency.

2.3 INFLUENCE FACTOR FOR HEAT LOSS (ϕ_{HL})

To obtain the heat loss influence factor from measured thrust the approach is identical to that taken previously from the pressure measurement, except that the nozzle losses must also be included. With constant specific heat and gamma from start of nozzle convergence to exit, Equation (D-20) becomes

$$\phi_{HL} = 1 + \frac{1}{2} \left[\frac{\sum \left(\frac{q}{A} \right) A}{\dot{w}_T} \right] \left[\frac{1 - T_e/T_c}{H_c - H_e - \dot{Q}_{nozzle}} \right] \quad (D-2)$$

when "e" corresponds to the exit condition, and the summation occurs over the entire combustion.

An alternate can also be derived as in Equation (D-25). This equation becomes

$$\phi_{HL} = 1 + \frac{1}{2} \left[\frac{(q/A)A}{\dot{w}_T} \right] \left[\frac{1}{c_p T_e} \right] \quad (D-29)$$

2.4 INFLUENCE FACTOR FOR CHEMICAL KINETICS (ϕ_{KE})

The effect of finite chemical reaction rates is to produce a C^* and C_F less than the corresponding theoretical equilibrium values. A TRW Systems Group developed one dimensional nonequilibrium reacting gas computer program was employed with reaction rate constants selected for the FLOX methane-ethane blend propellant system. The fluid mechanical and chemical equations were integrated from the inlet section by an implicit technique. It was determined that the effect of nonequilibrium chemistry produced a C^* loss of $\sim 1.2\%$ and a C_F loss of $\sim 2.4\%$ compared to the shifting equilibrium limits.

3. SAMPLE COMPUTATION WITH EXPERIMENTAL DATA

Presented here is a sample calculation for a selected test to illustrate the above methods. The physical properties and theoretical data utilized in the program are given in Appendix A. The descriptions of the computer programs used in the performance computations are given in Appendix G. The selected run is 065 of Table 5-4.

3.1 INFLUENCE FACTOR EVALUATION

The influence factors, f_i and ϕ_j , of Equations (D-2) and D-27) are summarized here for run number 065.

3.1.1 Momentum

The momentum correction is a standard correction to either combustion head end or start of convergence static pressures to compute an indicated nozzle stagnation pressure. This correction is a function of contraction ratio and gas gamma ratio only. The correction factor for this program and selected contraction ratios is given in Figure D-1. For run 065 the start of convergence static pressure was

$$P_{CD} = 110.6 \text{ psia}$$

Using Figure D-1, the momentum correction gives the stagnation pressure as

$$\begin{aligned} f_p &= 1.0088 \\ P_o &= 111.6 \text{ psia} \end{aligned}$$

The other pertinent data for subsequent calculations are:

$$\dot{w}_T = .345 \text{ lbs/sec}$$

$$MR = 3.13$$

$$F_{vac} = 92.2 \text{ lb}_f$$

3.1.2 Throat Radius Effects

Using Figure D-2, the throat radius change influence factor is found to be 1.014 for a throat wall temperature of 770°F.

3.1.3 Throat Discharge Coefficient

From Figure D-3, f_{dis} is taken as

$$f_{dis} = .989$$

3.1.5 Kinetic Effects

The kinetic effects were computed and presented in Figure D-4 for this program. Since there is a finite expansion effect it must be recognized that in computing C^* values from either P_c or F measurements that kinetic effects must include this expansion. This factor was not utilized here in the performance reduction because of its lack of previous use; however, its value is

$$f_{KE} = 1.012$$

$$\phi_{KE} = 1.024$$

3.1.6 Energy Loss

The heat loss effect on the P_c computation technique is easily accomplished when the \dot{q}/A axial distributions are known. In this case

$$\begin{aligned} f_{HL} &= 1 + \frac{1}{2} \left(\frac{49}{.34} \right) \left(\frac{1 - 5580/6385}{-598 + 998 - 10} \right) \\ &= 1.023 \end{aligned}$$

For the thrust measurement

$$\begin{aligned} \phi_{HL} &= 1 + \frac{1}{2} \left(\frac{53}{.34} \right) \left(\frac{1 - 4105/6385}{-598 + 1733 - 14} \right) \\ &= 1.027 \end{aligned}$$

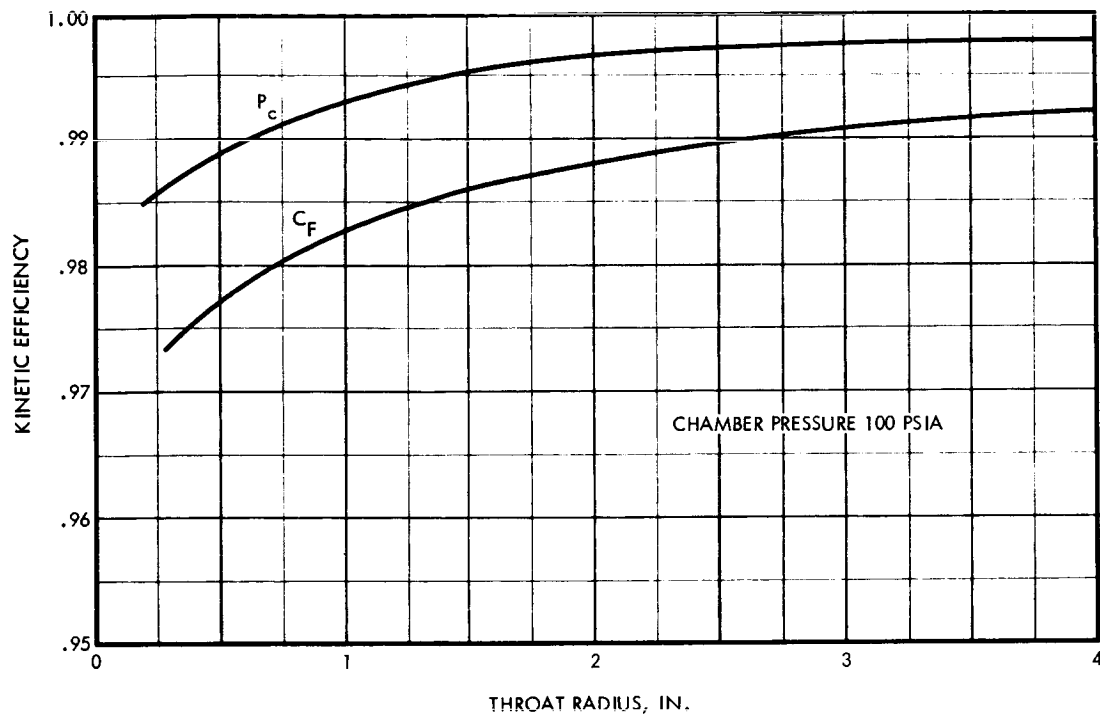


Figure D-4. Kinetic Efficiency

3.1.7 Total Corrections

The total product correction for the P_c computation is

$$f_{pc} = 1.035$$

and for the F computational technique is

$$f_F = 1.044$$

3.1.8 C* Calculation

The substituted quantities for the C^* computation based on the two techniques are summarized below:

$$\begin{aligned} \eta_{C^*} (P_c) &= \frac{(110.6)(.591)(32.17)(1.0088)(1.014)(.989)(1.023)}{(.345)(6637)} \\ &= .951 \end{aligned}$$

$$\begin{aligned} \eta_{C^*} (F) &= \frac{(92.2)(32.17)(1.017)(1.027)}{(1.41)(.345)(6637)} \\ &= .960 \end{aligned}$$

APPENDIX E

CARBON DEPOSITION EFFECTS ON GAS
SIDE HEAT TRANSFER COEFFICIENTS

APPENDIX E

CARBON DEPOSITION EFFECTS ON GAS SIDE HEAT TRANSFER COEFFICIENTS

1. INTRODUCTION

When rocket engines that use hydrocarbon fuels are fired, carbon is deposited on the interior surface of the engine. The formation of this carbon layer greatly reduces the heat flux from the combustion gas and thus protects the nozzle walls from reaching excessively high temperatures. It has been observed that the carbon buildup is cyclic; i. e., the carbon layer or a fraction of it flakes off the wall surface periodically.

In the present study, a simple empirical equation is derived which can be utilized to estimate the effects of carbon deposition on the resultant heat transfer in nozzles. The results based on this equation show very close agreement with currently available experimental data (Ref. E-1).

2. ANALYSIS

The time variation of the carbon resistance is assumed to be representable by the form

$$R = \frac{\Delta X}{k} = R_o (1 + \alpha \sin \omega t) \quad (\text{E-1})$$

From Reference B-1, one may deduce the approximate values of

$$\alpha = 0.4 \quad (\text{E-2})$$

$$\omega = \pi \text{ (period} = 2 \text{ sec)} \quad (\text{E-3})$$

The periodic time variation of the resistance is useful in analyzing the stress in the nozzle material. For heat transfer purposes, the main interest is concerned with the mean resistance R_o . As pointed out in Reference B-1, the mean effective carbon thickness is about 0.0022 inch, corresponding to $R_o = 2500 \text{ in}^2\text{-sec-}^\circ\text{F/Btu}$ and assuming $k_{\text{carbon}} = 8.8 \times 10^{-7} \text{ Btu/sec-in-}^\circ\text{F}$. It is not desired to evaluate R_o as a function of the mass flow rate, type of fuel and oxidizer, mixture ratio, and possibly other parameters.

It is assumed that the mean resistance may be given by

$$R_o = F_G F_A F_r F K \quad (E-4)$$

where F_G , F_A , and F_r represent factors due to variations in the local mass flow rate, the atomic ratio of hydrogen to carbon in the fuel, and the mixture ratio, respectively, while F is a factor due to other parameters and K is a constant.

It is reasonable to expect that the thickness of the carbon layer is related to the local shearing stress, which in turn is related to the local mass flow rate. It was found in Reference E-3, p. 82, that the variation in resistance with mass flow velocity is approximately given by

$$R_G = e^{10 - 0.51G}$$

Normalizing this value with respect to the results of Reference E-2, which are estimated to be for $G = 2.52 \text{ lb/in}^2\text{-sec}$, one obtains

$$F_G = \frac{R_G}{R_G(G=2.52)}$$

or

$$F_G = e^{1.285 - 0.51G} \quad (E-5)$$

The atomic ratio of hydrogen to carbon is believed to be a significant parameter since the carbon layer thickness should increase when there are more carbon atoms present. The increase in resistance with increase in carbon atoms has been experimentally verified in Reference E-4, p. 128, and in Reference E-5, p. V-20.

From these experimental data, one may deduce

$$\left(\frac{Q_e}{Q_t} \right)_A = C_1 + C_2 (A-2)$$

where C_1 is the value of Q_e/Q_t for $A = 2$ and C_2 is the slope of the curve of Q_e/Q_t versus A for optimum mixture ratios. Now suppose

$$\frac{Q_e}{Q_t} = \frac{h_e}{h_g} = \frac{R_g}{R_g + R_A}$$

Then

$$\frac{1}{1 + \frac{R_A}{R_g}} = C_1 + C_2 (A-2)$$

or

$$R_A = \left[\frac{1}{C_1 + C_2 (A-2)} - 1 \right] R_g$$

Normalizing with respect to the results of Reference E-2 where $A = 2$, one obtains

$$F_A = \frac{R_A}{R_2}$$

or

$$F_A = \frac{C_1}{(1 - C_1)} \frac{1 - [C_1 - C_2 (A-2)]}{[C_1 + C_2 (A-2)]} \quad (E-6)$$

Equation (E-6) applies for $2 \leq A \leq 4$.

The constants C_1 and C_2 seem to depend on the test conditions such as presence or absence of cooling, injector design, etc. From the experimental data of Reference E-4, p. 128, which appear to be more consistent than the data of Reference E-5, one may take $C_1 = 0.16$ and $C_2 = 0.21$.

To consider the effect of mixture ratio, it is observed from Reference E-4, p. 126 and 127 and Reference E-5, p. V-20 that an approximately linear relation exists between Q_e/T_t and the mixture ratio r for

r near r_m where r_m is the mixture ratio corresponding to maximum specific impulse. The relation may be represented by

$$\left(\frac{Q_e}{Q_t}\right)_r = C_3 + C_4 (r - r_m)$$

where C_3 is the value of Q_e/Q_t for $r = r_m$ and C_4 is the slope of the curve of Q_e/Q_t is r . Now suppose

$$\frac{Q_e}{Q_t} = \frac{h_e}{h_g} = \frac{R_g}{R_g + R_r}$$

Then

$$\frac{1}{1 + \frac{R_r}{R_g}} = C_3 + C_4 (r - r_m)$$

or

$$R_r = \left[\frac{1}{C_3 + C_4 (r - r_m)} - 1 \right] R_g$$

Normalizing with respect to r_m , one obtains

$$F_r = \frac{R_r}{R_{rm}}$$

or

$$F_r = \frac{C_3 [1 - C_3 - C_4 (r - r_m)]}{(1 - C_3) [C_3 + C_4 (r - r_m)]} \quad (E-7)$$

It is noted that C_3 is not a new constant. At $r = r_m$, $(Q_e/Q_t)_A = (Q_e/Q_t)_r$; therefore C_3 is related to C_1 , C_2 , and A by

$$C_3 = C_1 + C_2 (A-2) \quad (E-8)$$

The values of C_4 and r_m seem to depend on the fuel, and the experimental data for C_4 do not seem to be consistent, which indicates that C_4 probably depends also on the test conditions such as method of cooling, injector design, etc. For the time being, the following values appear to be typical: Methane: $r_m = 5.75$ and $C_4 = 0.07$; Propane: $r_m = 4.5$ and $C_4 = 0.08$; Pentant Blend: $r_m = 4.3$ and $C_4 = 0.04$; Butene-1: $r_m = 3.9$ and $C_4 = -0.01$. It should be emphasized that the available experimental data for C_4 are not consistent. Fortunately, C_4 is generally small and consequently F_r has a value close to 1.0.

Equation (E-7) applies for r near r_m , say $-r_1 r - r_m r_2$, where r_1 and r_2 have values of order 1.0. Outside this range, a constant should be used for F_r . Furthermore, for r very close to r_m , Equation (E-7) may be expanded in Taylor series and approximated by

$$F_r = 1 - \frac{C_4}{C_3(1 - C_3)} (r - r_m)$$

From Equation (E-7), it is observed that F_r depends on C_3 , which in turn depends on A . It appears that the factors F_A and F_r may be combined if one considers the percentage of carbon present in the propellant rather than just the hydrogen/carbon atomic ratio of the fuel. It appears reasonable that the carbon resistance should depend on the local free stream mass velocity, the atomic ratio of the sum of all chemical elements to carbon in the boundary layer, and the carbon affinity to the wall which probably is a function of the local wall temperature. The development of such a relation requires further detail study, however. For the present time, Equations (E-1) through (E-8) may be applied with the factor F set equal to 1.0. Then for a given nozzle and given propellant, the values of F_A and F_r are constant; thus the variation in R_0 along the nozzle wall is influenced only by the factor F_G which accounts for the variation in local mass velocity. The constant K is determined from Reference E-2. Since F_G and F_A are normalized with respect to this

reference ($F_G = F_A = 1$) and F_r is approximately equal to 1.0 there, the value of K is

$$\begin{aligned} K &= 2500 \text{ in}^2\text{-sec-}^\circ\text{F/Btu} \\ &= 0.00482 \text{ ft}^2\text{-hr-}^\circ\text{F/Btu} \end{aligned} \quad (\text{E-9})$$

The final formula has the form

$$R = R_o (1 + 0.4 \sin \pi t) \quad (\text{E-10})$$

where

$$R_o = F_G F_A F_r F K \quad (\text{E-11})$$

$$F_G = e^{1.285 - 0.51G} \quad (\text{E-12})$$

$$F_A = \frac{C_1 [1 - C_1 - C_2 (A-2)]}{(1 - C_1) [C_1 + C_2 (A-2)]} \quad (\text{E-13})$$

$$F_r = \frac{C_3 [1 - C_3 - C_4 (r-r_m)]}{(1 - C_3) [C_3 + C_4 (r-r_m)]} \quad (\text{E-14})$$

$$F = 1 \text{ (This may be modified later)} \quad (\text{E-15})$$

$$\begin{aligned} K &= 2500 \text{ in}^2\text{-sec-}^\circ\text{F/Btu} \\ &= 0.00482 \text{ ft}^2\text{-hr-}^\circ\text{F/Btu} \end{aligned} \quad (\text{E-16})$$

where

$$C_3 = C_1 + C_2 (A-2) \quad (\text{E-17})$$

and the values of C_1 , C_2 , C_4 and r_m have been discussed in previous pages.

3. COMPARISON WITH EXPERIMENTAL DATA

A comparison between the experimental results shown on pages 84-104 of Reference E-4 and the results calculated using the derived formula and the constants given in this memo is shown on Tables E-1 and E-2. The experimental heat transfer coefficients he_1 , he_2 , and he_3 , corresponding to the nozzle entrance, throat, and exit, respectively, are tabulated in Table E-1. The calculated coefficients hp_1 , hp_2 , and hp_3 for the three corresponding nozzle locations are given in Table E-2.

In calculating for h_p , the following equation is used

$$h_p = \frac{1}{\frac{1}{h_g} + R_o} \quad (E-18)$$

where h_g is the local heat transfer coefficient with no carbon deposition and is obtained using Bartz simple equation. Besides h_p , the factors F_A , F_r , and F_G as well as the calculated carbon resistances R_o are also shown in Table E-2.

The comparison of the predicted heat transfer coefficients h_p with the experimental coefficients h_e shows surprisingly good agreement, especially at the throat and exit sections of the nozzle. In fact, if one plots h_p on the figures of Reference E-4, one observes that the differences between h_p and h_e are generally smaller than the scatter of the experimental data. The experimental data of Reference E-5 are not analyzed here since the injector and the non-uniform mixing of oxidizer and fuel in Reference E-5 cause excessively high heat flux in some cases reported there.

Table E-1. Results Deduced from Reference E-4

Fuel	Page	Test #	Injector	(psia) P_c	% F_2	r	lb/sec \dot{w}	$(ft^2-hr-^\circ F/Btu \times 10^2)$			$(Btu/ft^2-hr-^\circ F)$		
								R_{g1}	R_{g2}	R_{g3}	h_{e1}	h_{e2}	h_{e3}
Methane	86	13	4	104	82.6	4.03	14.1	0.602	0.260	0.980	160	176	58
	84	2	1	97	82.6	4.11	14.1	0.649	0.278	1.087	194	158	43
	85	10	3	102	82.6	4.34	13.9	0.658	0.283	1.111	197	122	53
	89	21	6	103	82.6	5.35	14.1	0.746	0.320	1.389	68	176	62
	90	24	6	107	82.6	5.73	14.8	0.741	0.323	1.370	62	179	56
Propane	92	28	7	108	75	4.0	14.8	0.704	0.305	1.265	58	85	53
	93	29	7	105	75	4.36	14.6	0.610	0.263	0.847	55	91	61
	94	30	7	103	75	4.68	14.6	0.694	0.246	2.702	116	194	164
	95	31	7	103	75	5.02	14.8	0.813	0.353	1.492	48	104	70
Pentane Blend	97	34	7	104	75	3.05	15.5	0.735	0.321	1.333	22	59	40
	96	33	7	101	75	3.32	15.0	0.658	0.281	0.934	28	70	44
	98	35	7	101	75	3.80	15.2	0.757	0.330	1.449	20	60	40
	99	36	7	102	75	4.0	15.4	0.833	0.364	1.492	18	70	45
	100	37	7	106	75	4.444	16.2	0.769	0.345	1.316	13	77	47
Butene 1	102	39	7	115	70.4	2.45	16.6	0.512	0.218	0.787	33	66	40
	101	38	7	119	70.4	2.73	16.8	0.538	0.230	0.862	60	71	35
	103	42	7	117	70.4	2.82	16.6	0.559	0.239	0.917	24	71	42
	104	43	7	120	70.4	3.67	16.7	0.625	0.270	1.111	20	59	40

Table E-2. Results Obtained from Derived Formulas

Fuel	r	F _A	F _r	F _{G1}	F _{G2}	F _{G3}	(ft ² -hr-°F/Btux10 ²)			(Btu/ft ² -hr-°F)		
							R ₀₁	R ₀₂	R ₀₃	h _{p1}	h _{p2}	h _{p3}
Methane	4.03	0.138	1.624	3.29	2.78	3.34	0.353	0.298	0.359	105	179	75
	4.11	0.138	1.588	3.29	2.78	3.34	0.345	0.292	0.350	101	175	70
	4.34	0.138	1.489	3.30	2.79	3.35	0.324	0.273	0.329	101	180	69
	5.35	0.138	1.121	3.29	2.78	3.34	0.243	0.206	0.248	101	190	61
	5.73	0.138	1.001	3.27	2.76	3.32	0.218	0.184	0.221	104	197	63
Propane	4.00	0.443	1.186	3.27	7.76	3.32	0.828	0.699	0.841	65	100	56
	4.36	0.443	1.047	3.28	2.77	3.33	0.731	0.617	0.742	76	113	71
	4.68	0.443	0.943	3.28	2.77	3.33	0.658	0.556	0.668	74	125	49
	5.02	0.443	0.848	3.27	2.76	3.32	0.592	0.500	0.601	71	117	57
Pentane Blend	3.05	0.59	1.330	3.26	2.75	3.31	1.236	1.044	1.256	51	73	44
	3.32	0.59	1.246	3.27	2.76	3.32	1.159	0.978	1.176	55	79	52
	3.80	0.59	1.119	3.27	2.76	3.32	1.040	0.878	1.056	56	83	46
	4.00	0.59	1.065	3.26	2.75	3.31	0.990	0.836	1.006	55	83	46
	4.44	0.59	0.970	3.25	2.74	3.30	0.902	0.761	0.916	60	90	52
Butene-1	2.45	1.0	0.893	3.24	2.73	3.29	1.407	1.188	1.429	52	71	49
	2.73	1.0	0.913	3.24	2.73	3.29	1.439	1.215	1.461	51	69	47
	2.82	1.0	0.919	3.24	2.73	3.29	1.448	1.222	1.471	50	68	46
	3.67	1.0	0.981	3.24	2.73	3.29	1.546	1.305	1.570	46	63	41

APPENDIX E SYMBOLS

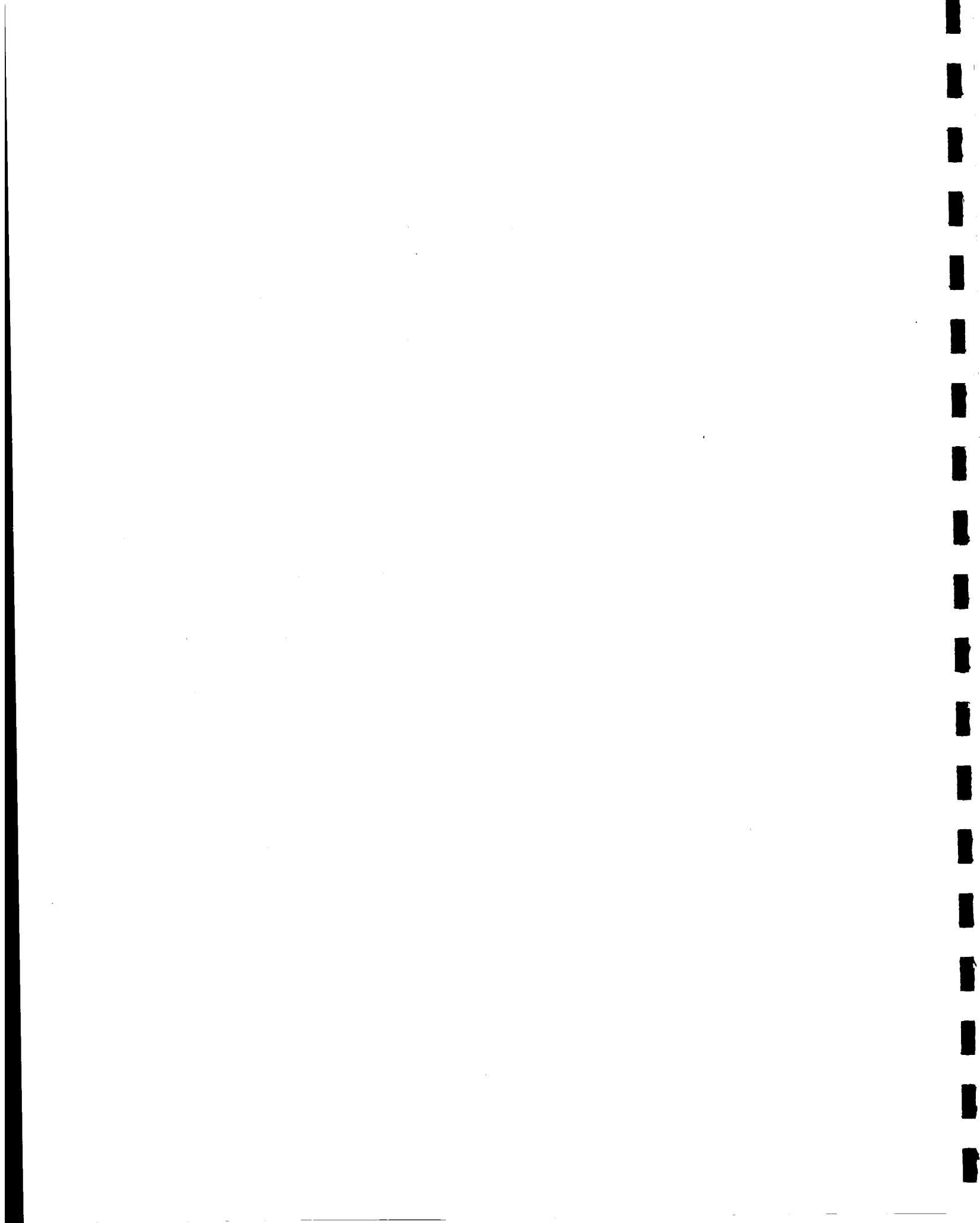
- A = atomic ratio of hydrogen to carbon in the fuel, dimensionless
 C_1 = value of Q_e/Q_t for $A=2$ in the curve of Q_e/Q_t versus A , dimensionless
 C_2 = gradient of the curve of Q_e/Q_t versus A , dimensionless
 C_3 = constant given by Equation (E-8), dimensionless
 C_4 = gradient of the curve Q_e/Q_t versus r , dimensionless
 F = factor in Equation (E-4), dimensionless
 F_A = factor given by Equation (E-6), dimensionless
 F_G = factor given by Equation (E-5), dimensionless
 F_r = factor given by Equation (E-7), dimensionless
 G = mass flow velocity, $\text{lb/in}^2\text{-sec}$
 h = heat transfer coefficient, $\text{Btu/in}^2\text{-sec-}^\circ\text{F}$ or $\text{Btu/ft}^2\text{-hr-}^\circ\text{F}$
 K = constant given by Equation (E-16), $\text{in}^2\text{-sec-}^\circ\text{F/Btu}$ or $\text{ft}^2\text{-hr-}^\circ\text{F/Btu}$
 k = effective conductivity of carbon, $\text{Btu/in-sec-}^\circ\text{F}$ or $\text{Btu/ft-hr-}^\circ\text{F}$
 P = pressure, lb/in^2 absolute
 Q = heat rate, Btu/sec or Btu/hr
 R = resistance, $\text{in}^2\text{-sec-}^\circ\text{F/Btu}$ or $\text{ft}^2\text{-hr-}^\circ\text{F/Btu}$
 r = mass ratio of oxidizer to fuel (mixture ratio), dimensionless
 t = time, sec
 w = mass flow rate, lb/sec
 ΔX = effective thickness of deposited carbon layer, in. or ft
 α = constant in Equation (E-1), dimensionless
 ω = constant in Equation (E-1), sec^{-1}

Subscripts:

- c = chamber condition
- e = experimental value
- g = gas value (without presence of deposited carbon)
- m = mixture ratio for maximum specific impulse
- o = time-mean value
- p = value predicted by Equation (E-18)
- t = theoretical value for the condition of no deposited carbon

REFERENCES

- E-1. TRW Systems IOC 4711.6-67-60, "A Formula for Predicting Heat Transfer Coefficients in Nozzles with Carbon Deposition, " 3 August 1967
- E-2. J. P. Sellers Jr., "Effect of Carbon Deposition on Heat Transfer in a LOX/RP-1 Thrust Chamber, " ARS Journal, May 1961, p. 662
- E-3. "Investigation of Cooling Problems at High Chamber Pressure, " Final Report R-3999, Rocketdyne, May 1963
- E-4. "Investigation of Light Hydrocarbon Fuels with FLOX Mixtures as Liquid Rocket Propellants, " Final Report PWA FR-1443, Pratt and Whitney Aircraft, September 1965
- E-5. "Investigation of Light Hydrocarbon Fuels with Fluorine-Oxygen Mixtures as Liquid Rocket Propellants, " Final Report PWA FR-2227, Pratt and Whitney Aircraft, Preliminary Copy



APPENDIX F

CHEMICAL ANALYSIS OF CARBON DEPOSITION LAYER

APPENDIX F

CHEMICAL ANALYSIS OF CARBON DEPOSITION LAYER

A brief study was undertaken to determine the mechanism for the formation of an adherent carbon layer on the copper chamber walls. Since carbon is not soluble in, and forms no compounds with copper, the adherence of the layer indicates the presence of one or more other elements. Identification of these reaction layer constituents was necessary to determine the feasibility of intentionally applying a similar deposit prior to test firing to provide a thermal barrier. Electron microprobe analysis was employed for this identification. The general area of the nozzle on which the analysis was conducted is shown in Figure F-1. The following procedure was used:

- Samples containing the deposited reaction layer on copper were cut from two locations in the nozzle area and mounted for analysis. Deposits on the specimens were different in appearance; one was predominantly black, the other white. Each specimen was mounted in orientations with the surface deposit parallel to the surface of the mount and normal to the surface of the mount.
- Spectral scans were run on specimens with deposits parallel to the mount surface to determine which elements were present in the deposit.
- Spatial scans were run across the thickness of each specimen to determine the distribution of elements through and adjacent to the deposits.
- By using electron beam scanning techniques, oscilloscope images generated by back scattered electrons and horizontal line profiles of X-ray intensities of each element present across the deposited layer were photographed.

Results of the spectral scans indicated the presence of only copper, carbon and fluorine in the specimens examined.* A spectral scan on a sodium fluoride standard specimen over a wavelength corresponding to the fluorine

* Hydrogen, helium, lithium and beryllium cannot be detected by microprobe analysis. Oxygen in small quantities (<5 wt %) can be detected only when carbon is absent.

K α line is shown in Figure F-2. A corresponding scan on the white reaction deposit is shown in Figure F-3. The intensity (height) of the peak in the specimen is nearly as high as that in the standard, indicating the fluorine concentration is only slightly lower in the reaction layer than in NaF (42.5 wt % F in NaF). A lower fluorine K α X-ray intensity was observed in the black deposit.

Results of the spatial scans show the fluorine containing zone is about 28 μ (0.0011 inch) thick in the white layer and about 1 μ (0.00004 inch) thick in the black layer. The carbon containing zone is about 4 μ (0.00015 inch) thick in the white layer and about 3 μ (0.00012 inch) in the black layer.

Figures F-4 and F-5 are photographs of X-ray line intensity profiles of C, Cu, and F superimposed on back scattered electron images. An arrow indicates the line of traverse of the electron beam (horizontal line with subdivisions) which is also the area analyzed on the specimen. The intensity plots (vertical scale) representing the relative concentration of each element are projected one on top of the other to avoid crossover. There is a straight horizontal line underneath each intensity curve representing the zero intensity line. However, the zero concentration line could be above the zero intensity line depending on the background. Note that the zero intensity line for F K α is out of the field in Figure F-5.

Thus, Figures F-4 and F-5 can be used to indicate qualitatively or semi-quantitatively, the quantity of each element present in a given location. One can pick any point on the center horizontal line (line of beam traverse) and project vertically to each intensity curve to obtain the relative concentration of each element. For example, an abrupt increase in fluorine concentration of each element. For example, an abrupt increase in fluorine concentration in the reaction zone is evident in both samples. The copper content remains quite uniform throughout. There is indication of a slight rise in carbon in the reaction zone. However, the intensity of the carbon K α lines rise rapidly beyond the edge of the specimen due to high carbon content in the mounting material.

The analysis shows that chemically combined fluorine is present to varying degrees in the reaction layer deposited on the copper nozzle surface. The quantity present is too high to be completely accounted for by CuF or CuF₂, and is probably partially or completely in the form of fluorocarbon compounds.

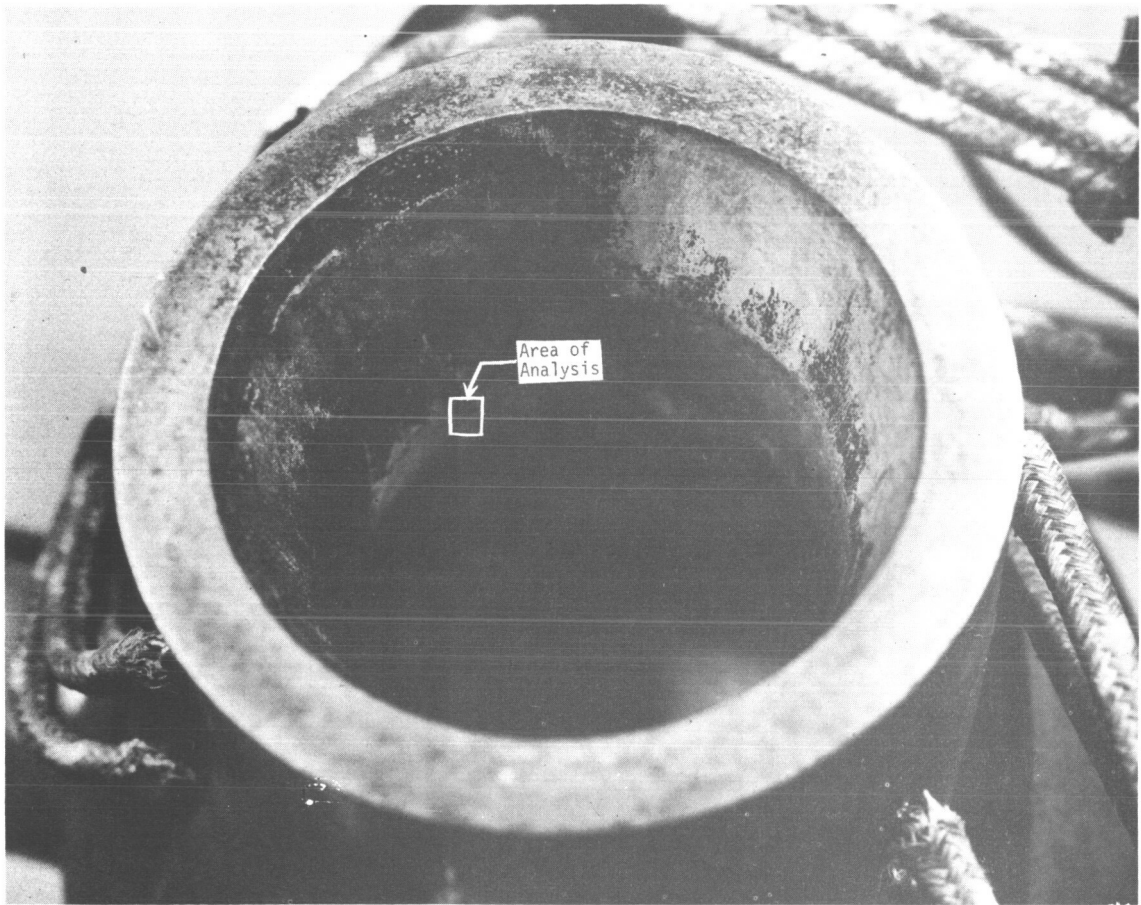


Figure F-1. Small Rocket Engine Nozzle Showing Area on which Microprobe Analysis was Conducted

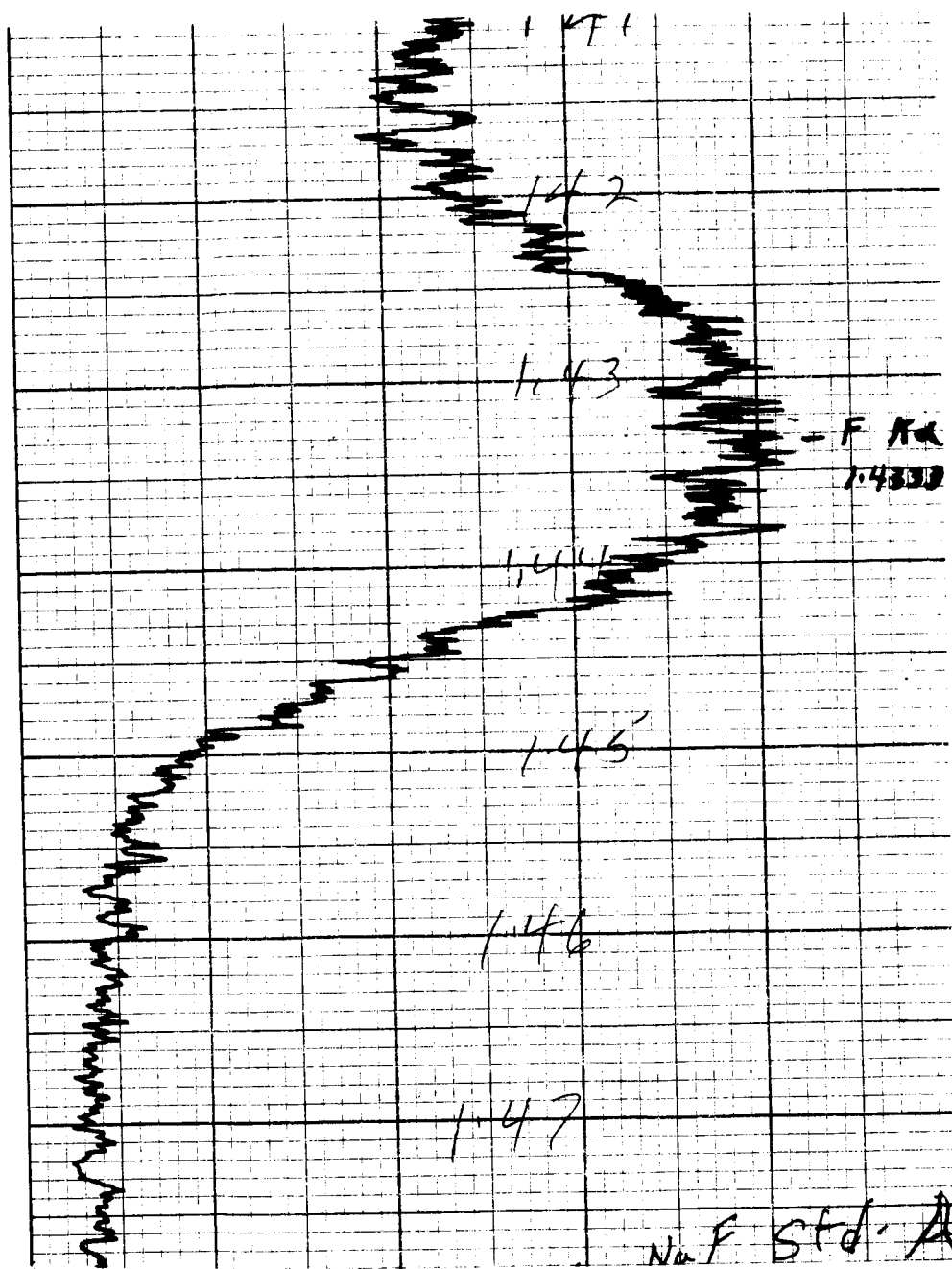


Figure F-2. Spectral Scan on NaF Standard over Wavelength Range that Includes Fluorine K α Line

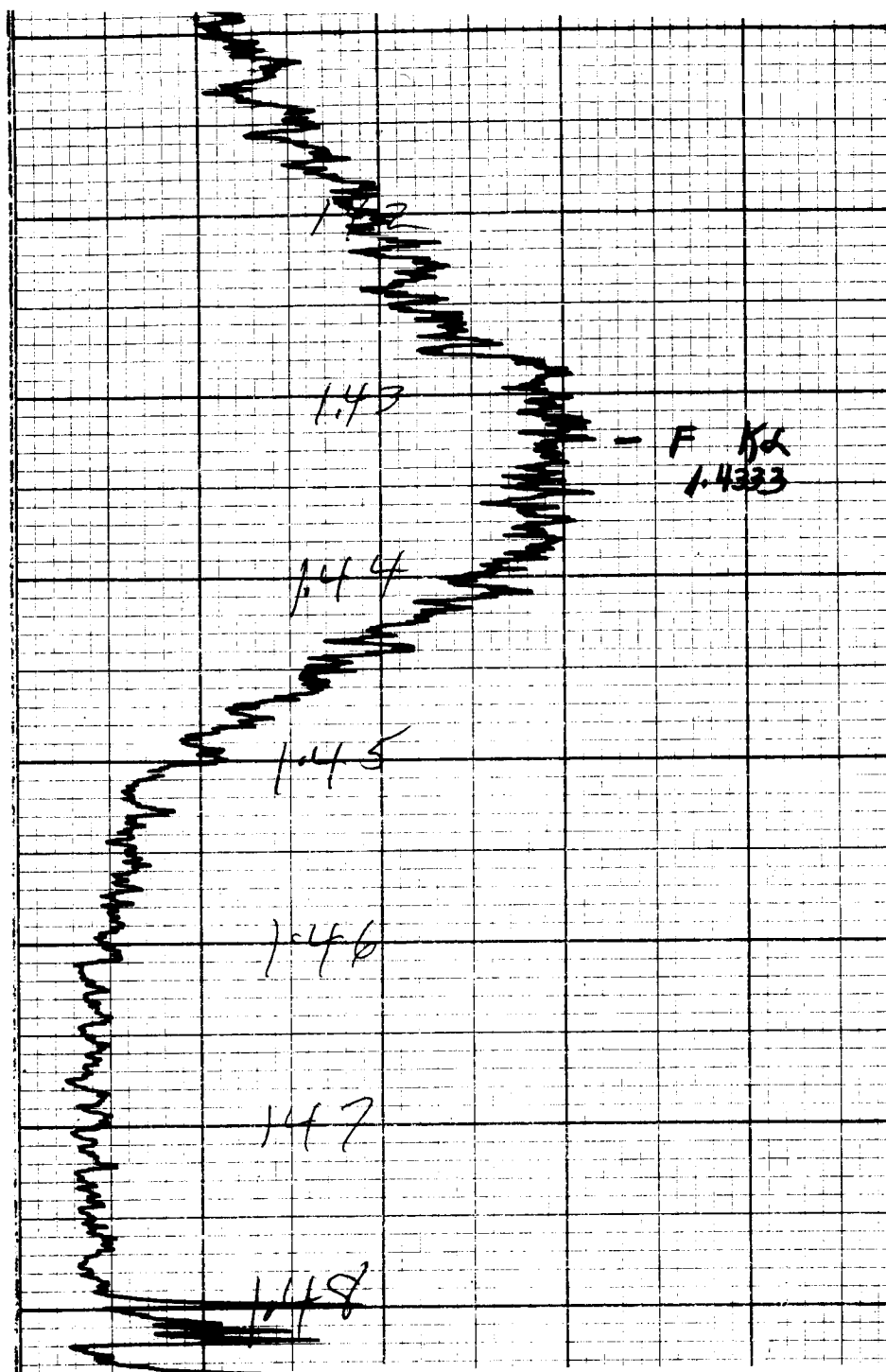


Figure F-3. Spectral Scan on White Deposit over Wavelength Range that Includes Fluorine K α Line

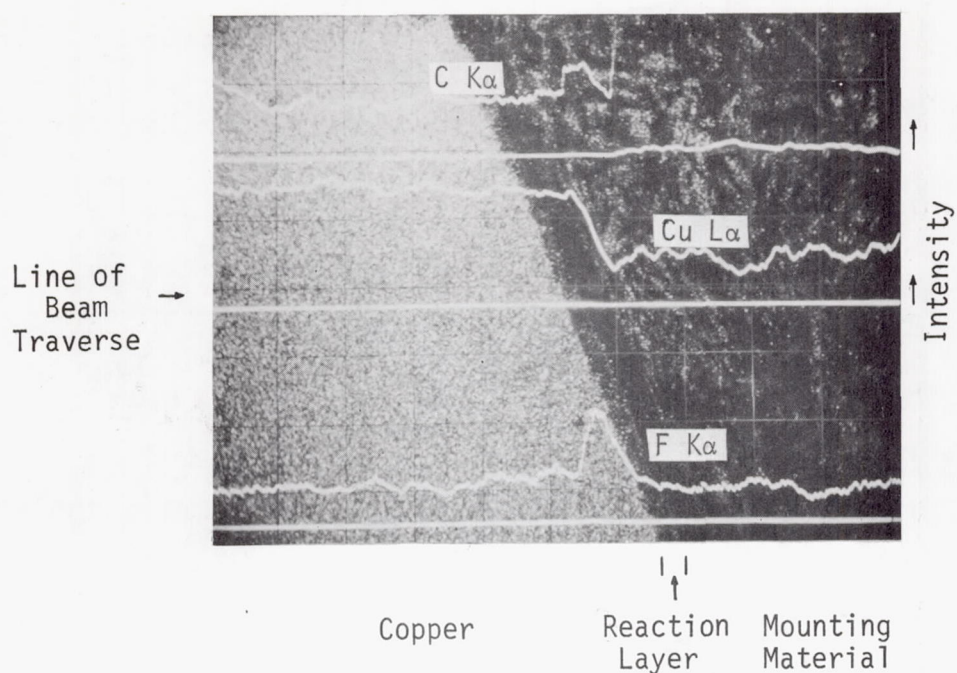


Figure F-4. Horizontal Line Profile of C K α , Cu L α , and F K α X-ray Intensities across Section of Region Containing White Reaction Layer (300X magnification)

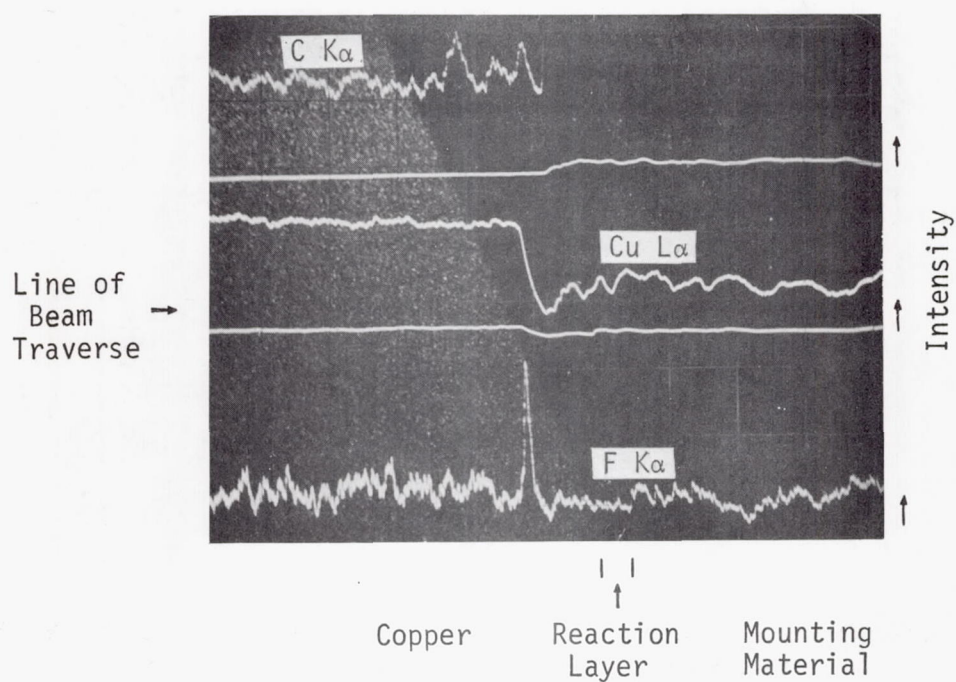
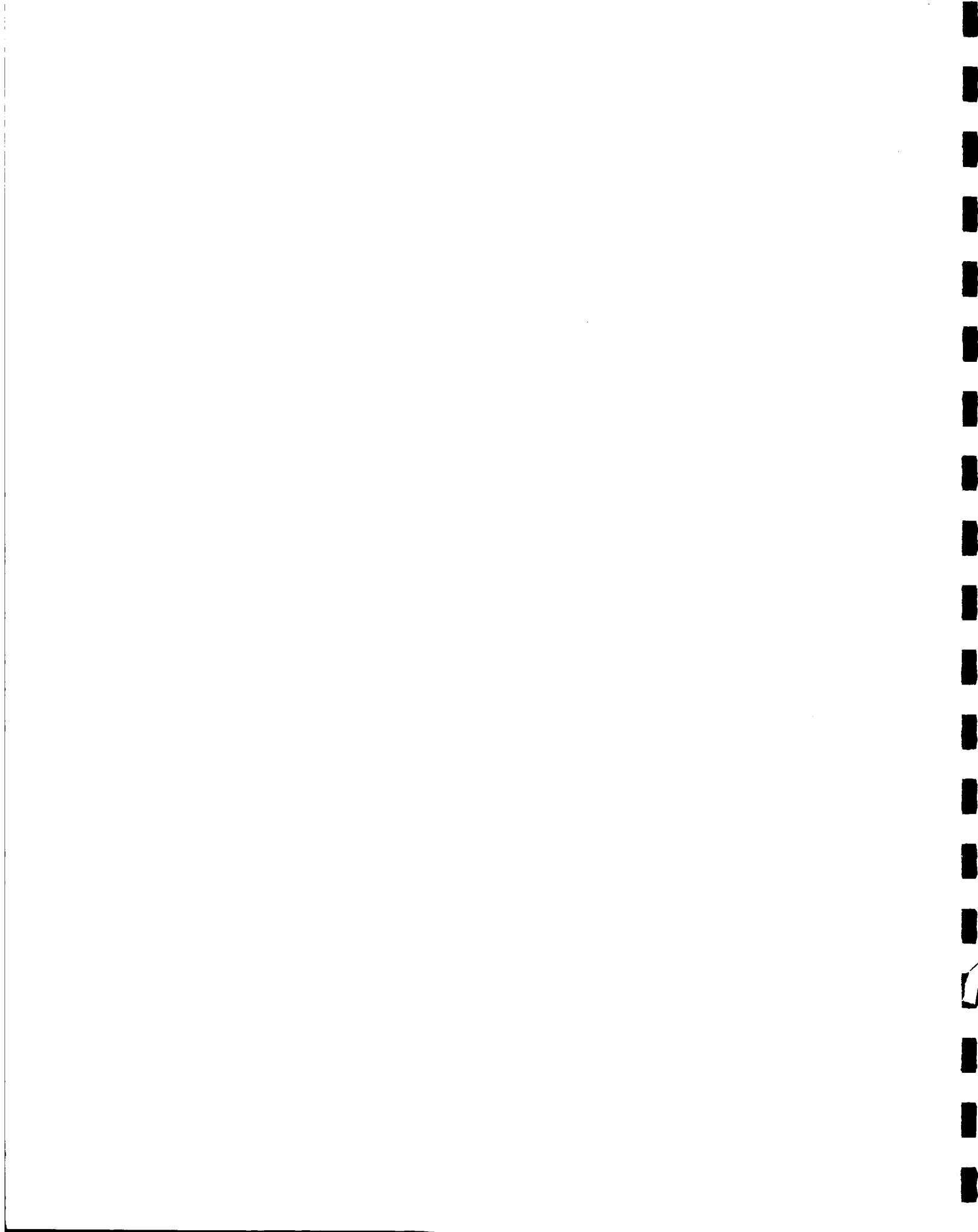


Figure F-5. Horizontal Line Profile of C K α , Cu L α , and F K α X-ray Intensities across Section of Region Containing Black Reaction Layer (300X magnification)

APPENDIX G
COMPUTER PROGRAMS



APPENDIX G

COMPUTER PROGRAMS

The following computer programs were used to facilitate performance and heat transfer analysis during various phases of this program. An additional computer program is shown in Appendix C for specific data reduction of chamber heat transfer experimental data.

1.0 ROCKET CHEMISTRY PROGRAM

The generalized equilibrium chemistry program solves a wide range of thermodynamic problems requiring only the composition and two of the following system properties to be specified: pressure, volume, temperature, enthalpy, entropy or internal energy. The program calculates composition, either from a pair of compounds with a specified weight mixture ratio, or from a series of compounds and their respective weight percents. In addition to the usual pure condensed phases, it is possible to submit a series of ideal chemical solutions composed of selected combinations of the condensed phases; the program will determine whether or not these solutions are formed by the reaction. The possible reaction products are obtained by searching a prepared master inventory tape containing entropy and enthalpy curve fit coefficients for all elements and compounds of interest. Nongaseous phases and ionized species are treated as distinct and separate compounds. The program initially assumes an ideal all-gas system. The equilibrium gas pressures of all possible gaseous species are calculated. Using these partial pressures as initial estimates, nongaseous phases and solutions are then considered. Upon convergence of the calculations, the program eliminates all but the actual gases, condensed phases, and ideal solutions present at equilibrium. Rocket performance is computed for isentropic sonic flow through a throat by specifying exit pressures, temperatures, or area ratios. Chemical reactions only, or chemical reactions and phase changes, may be stopped at any point in the expansion. Equilibrium or frozen composition, thermodynamic parameters, and the usual rocket parameters are given in the program output.

2.0 ONE-DIMENSIONAL, ONE-PHASE EXACT KINETIC COMPUTER PROGRAM

TRW Systems had developed under contract to the National Aeronautics and Space Administration Manned Spacecraft Center (Contract NAS 9-4358), a One-Dimensional, One-Phase (1D, 1P) Reacting Gas Nonequilibrium Performance Program. The computer program calculates the inviscid one-dimensional equilibrium, frozen and nonequilibrium nozzle expansion of propellant exhaust mixtures containing the six elements: carbon, hydrogen, oxygen, nitrogen, fluorine and chlorine.

The computer program considers all significant gaseous species (19) present in the exhaust mixtures of propellants containing these elements and all gas phase chemical reactions (48) which can occur between the exhaust products. In order to reduce the computation times per case to a minimum, the program utilizes a second-order implicit integration method. This integration method has reduced the computation time, per case, several orders of magnitude compared to the computation time required when utilizing standard explicit integration methods such as fourth order Runge-Kutta or Adams-Moulton methods.

The throat size is determined for each combination of propellant system and mixture ratio through use of the given chamber pressure, thrust level, and the value of the one-dimensional thrust coefficient, C_F , computed by the Rocket Chemistry Program. The reverse reaction rate constant, $k_r = AT^{-n}e^{-B/T}$, is employed in the Kinetics Program and forms a portion of the input data to the computer program. It is usually input in chemist's units; i.e., cm^3 , gm, $^\circ\text{K}$, sec., and is converted internally into units consisting of ft^3 , lb, $^\circ\text{R}$, sec.

3.0 ONE-DIMENSIONAL, TWO-PHASE EXACT KINETIC COMPUTER PROGRAM

TRW Systems has also developed, under contract to the National Aeronautics and Space Administration Manned Spacecraft Center (Contract NAS 9-4358), a One-Dimensional, Two-Phase (1D, 2P) Reacting Gas Nonequilibrium Performance Program. This program calculates the inviscid one-dimensional equilibrium, frozen and nonequilibrium nozzle expansion of propellant exhaust mixtures containing the six elements: carbon, hydrogen, oxygen, nitrogen, fluorine and chlorine; and one metal element, either aluminum, beryllium,

boron or lithium. Energy and momentum transfer is considered between the two phases but interphase mass transfer is not considered.

In all 79 species related by 763 reactions are handled with a maximum of 46 species and 380 reactions for the boron metal element. In addition, provision is made for eight condensed species with a maximum of four condensed species at any time. Furthermore, the condensed phase can be allocated to one (or more) size group.

All the species and reactions of importance to the proposed program can be accommodated by the TRW Systems developed One-Phase and/or Two-Phase Kinetics Programs.

4.0 VISCOUS EFFECTS COMPUTER PROGRAM.

The method of Bartz for computing boundary-layer thicknesses, skin-friction, and heat flux in axisymmetric nozzles has been revised and programmed for digital computer solution. The method solves, simultaneously, the integral momentum and energy equations for thin axisymmetric boundary layers. Boundary-layer shape parameters are approximated from one-seventh power profiles of velocity and stagnation temperature; and skin-friction coefficient and Stanton number are evaluated as functions of boundary-layer thickness from the best available semiempirical relations.

This program either employs a given wall Mach number distribution as generated by, for example, the Two-Dimensional Kinetics Computer Program, or can generate internally a one-dimensional Mach number distribution as a function of local area ratio and (constant) γ , the ratio of specific heats. In addition, the program requires a wall temperature, T_w , distribution. This distribution can be produced, by an iterative procedure, from a thermal analysis of the nozzle. A constant wall temperature may be assumed in lieu of such data.

The program computes the local parameters: convective heat transfer coefficient (h_g), heat flux (\dot{q}/A), where A is the nozzle surface area, skin-friction coefficient (C_f), boundary-layer thickness (δ), displacement thickness (δ^*) and momentum thickness (θ). The total heat rejection load, \dot{q} , is found from numerical integration of \dot{q}/A versus A .

5.0 BASIC ONE-DIMENSIONAL HEAT TRANSFER PROGRAM

This program, designated 84040 on TRW's IBM 7070, computes the change in temperature of each of a number of points (called nodes) in a slab of material, at specified intervals of time, during which the slab is to be heated and/or cooled. The heating and cooling is accomplished by convection and radiation, at the slab boundaries. The program is general enough so that it can handle heat transfer through both flat plate and cylindrical sections, regardless of size, thickness, and material layer composition. Most commonly, the program is used to simulate rocket engine firing duty cycles.

Preparation of the input for this program requires the following:

- 1) Convective heat transfer coefficients on the inside and outside surfaces
- 2) Inside and outside adiabatic wall temperatures
- 3) Initial temperatures of the node points
- 4) Thermal conductivities and diffusivities of the materials in the slab
- 5) Thicknesses of the material layers

The output consists of temperature profiles in the slab at specified time intervals.

6.0 THREE-DIMENSIONAL PROGRAM

This is a high-speed digital program for transient problems involving all nodes or combinations of nodes of heat transfer (i.e., convection, conduction, and radiation). This program can be used for any thermal problem whose finite difference equation is analogous to the differential equation for a lumped RC electrical network and can, therefore, be visualized as an electrical circuit.

The number of connecting flux paths to any node is arbitrary. This program can handle as many as 250 node point and capacitances with approximately 800 resistances.

Four valuable features are incorporated into this program:

- 1) Variable thermal properties are simulated when a table showing values of each property versus temperature is entered in the input.
- 2) This program can hold any node at a constant temperature for a period of time and thus simulate phase transition.
- 3) Erosion rate schedule is entered in the input in the form of a table.
- 4) A cathode follower is used for the purpose of transferring a temperature from one node in the network to another with zero transfer of energy.

7.0 GAS PROPERTIES COMPUTER PROGRAM

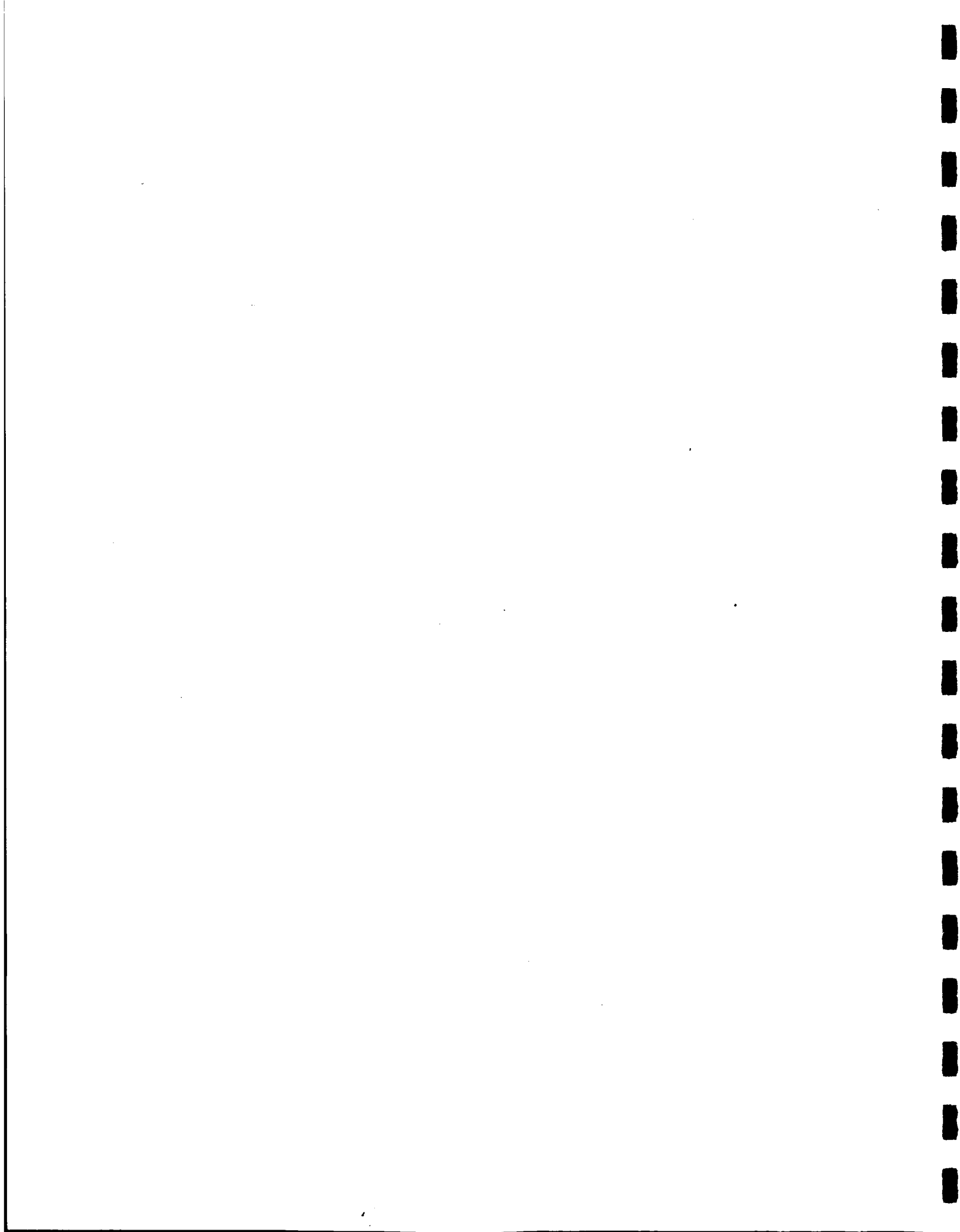
This program is used to rapidly determine the following:

- 1) Nozzle thrust coefficient as a function of pressure ratio
- 2) Nozzle area ratio as a function of pressure ratio
- 3) Nozzle area ratio as a function of Mach number
- 4) Ratio of local to critical temperature as a function of Mach number
- 5) Ratio of isentropic temperature drop to inlet temperature as a function of pressure ratio

The range of values covered for each of the basic parameters is:

Mach number:	1 - 10
Pressure ratio:	$3.5 - 10^4$
Ratio of specific heats:	1.1 - 1.67

The effect of the ratio of specific heats is included in all the plots.



FINAL REPORT DISTRIBUTION LIST (NASA CR-72495)

"SPACE STORABLE THRUSTER INVESTIGATION"

NAS3-11184

	<u>Copies</u>
National Aeronautics and Space Administration Lewis Research Center 21000 Brookpark Road Cleveland, Ohio 44135	
Attention: Contracting Officer, MS 500-313	1
Liquid Rocket Technology Branch, MS 500-209	8
Technical Report Control Office, MS 5-5	1
Technology Utilization Office, MS 3-16	1
AFSC Liaison Office, MS 4-1	1
Library	2
National Aeronautics and Space Administration Washington, D. C. 20546	
Attention: Code MT	1
RPX	2
RPL	2
SV	1
Scientific and Technical Information Facility P. O. Box 33 College Park, Maryland 20740	
Attention: NASA Representative Code CRT	6
National Aeronautics and Space Administration Ames Research Center Moffett Field, California 94035	
Attention: Library	1
C. A. Syvertson	1

Copies

National Aeronautics and Space Administration
Flight Research Center
P. O. Box 273
Edwards, California 93523
Attention: Library

1

National Aeronautics and Space Administration
Goddard Space Flight Center
Greenbelt, Maryland 20771
Attention: Library

1

National Aeronautics and Space Administration
John F. Kennedy Space Center
Cocoa Beach, Florida 32931
Attention: Library

1

National Aeronautics and Space Administration
Langley Research Center
Langley Station
Hampton, Virginia 23365
Attention: Library

1

National Aeronautics and Space Administration
Manned Spacecraft Center
Houston, Texas 77001
Attention: Library

1

National Aeronautics and Space Administration
George C. Marshall Space Flight Center
Huntsville, Alabama 35812
Attention: Library
Keith Chandler, R-P&VE-PA

1

1

National Aeronautics and Space Administration
Western Operations Office
150 Pico Boulevard
Santa Monica, California 90406
Attention: Library

1

Jet Propulsion Laboratory
4800 Oak Grove Drive
Pasadena, California 91103
Attention: Library

1

Office of the Director of Defense Research & Engineering
Washington, D. C. 20301
Attention: Office of Asst. Dir.
(Chem. Technology)

1

	<u>Copies</u>
Defense Documentation Center Cameron Station Alexandria, Virginia 22314	1
Arnold Engineering Development Center Air Force Systems Command Tullahoma, Tennessee 37389 Attention: AEOIM	1
Advanced Research Projects Agency Washington, D. C. 20525 Attention: D. E. Mock	1
Aeronautical Systems Division Air Force Systems Command Wright-Patterson Air Force Base Dayton, Ohio Attention: D. L. Schmidt, Code ASRCNC-2	1
Air Force Missile Test Center Patrick Air Force Base, Florida Attention: L. J. Ullian	1
Air Force Rocket Propulsion Laboratory (RPR) Edwards, California 93523	1
Air Force Rocket Propulsion Laboratory (RPM) Edwards, California 93523	1
U. S. Army Missile Command Redstone Scientific Information Center Redstone Arsenal, Alabama 35808 Attention: Chief, Document Section Dr. W. Wharton	1 1
Bureau of Naval Weapons Department of the Navy Washington, D. C. Attention: J. Kay, Code RTMS-41	1
Commander U. S. Naval Weapons Center China Lake, California 93557 Attention: Code 45 Code 753 W. F. Thorm, Code 4562	1 1 1
Director (Code 6180) U. S. Naval Research Laboratory Washington, D. C. 20390 Attention: H. W. Carhart	1

	<u>Copies</u>
Picatinny Arsenal Dover, New Jersey Attention: I. Forsten, Chief Liquid Propulsion Laboratory	1
Air Force Aero Propulsion Laboratory Research & Technology Division Air Force Systems Command United States Air Force Wright-Patterson AFB, Ohio 45433 Attention: APRP (C. M. Donaldson)	1
Aerojet-General Corporation P. O. Box 296 Azusa, California 91703 Attention: Librarian	1
Aerojet-General Corporation 11711 South Woodruff Avenue Downey, California 90241 Attention: F. M. West, Chief Librarian	1
Aerojet-General Corporation P. O. Box 1947 Sacramento, California 95809 Attention: Technical Library 2484-2015A Dr. C. M. Beighley D. T. Bedsole	1 1 1
Aeronutronic Division of Philco Corporation Ford Road Newport Beach, California 92600 Attention: Dr. L. H. Linder, Manager D. A. Carrison Technical Information Department	1 1 1
Aerospace Corporation P. O. Box 95085 Los Angeles, California 90045 Attention: J. G. Wilder, MS-2293 Library-Documents	1 1
Astropower, Laboratory McDonnell-Douglas Astronautics Co. 2800 Campus Drive Newport Beach, California Attention: Dr. George Moe Director, Research	1

	<u>Copies</u>
Chrysler Corporation Space Division New Orleans, Louisiana Attention: Librarian	1
Curtiss-Wright Corporation Wright Aeronautical Division Woodridge, New Jersey Attention: G. Kelley	1
McDonnell-Douglas Corporation Missiles & Space Systems Division 3000 Ocean Park Blvd. Santa Monica, California 90405 Attention: J. L. Waisman R. W. Hallet G. W. Burge	1 1 1
Fairchild Stratos Corporation Aircraft Missiles Division Hagerstown, Maryland Attention: J. S. Kerr	1
General Dynamics/Astronautics P. O. Box 1128 San Diego, California 92112 Attention: F. Dore Library & Information Services (128-00)	1 1
Convair Division General Dynamics Corporation P. O. Box 1128 San Diego, California 92112 Attention: Mr. W. Fenning Centaur Resident Project Office	1
General Electric Company Re-Entry Systems Department P. O. Box 8555 Philadelphia, Pennsylvania 19101 Attention: F. E. Schultz	1
General Electric Company Flight Propulsion Lab. Department Cincinnati 15, Ohio Attention: D. Suichu	1
Grumman Aircraft Engineering Corporation Bethpage, Long Island, New York Attention: Joseph Gavin	1

	<u>Copies</u>
Astrosystems, Incorporated 1275 Bloomfield Avenue Caldwell Township, New Jersey Attention: A. Mendenhall	1
ARO, Incorporated Arnold Engineering Development Center Arnold AF Station, Tennessee 37389 Attention: Dr. B. H. Goethert Chief Scientist	1
Atlantic Research Corporation Shirley Highway & Edsall Road Alexandria, Virginia 22314 Attention: A. Scurlock Security Office for Library	1 1
Beech Aircraft Corporation Boulder Facility Box 631 Boulder, Colorado Attention: J. H. Rodgers	1
Bell Aerosystems, Inc. Box 1 Buffalo, New York 14205 Attention: T. Reinhardt W. M. Smith	1 1
Bendix Systems Division Bendix Corporation Ann Arbor, Michigan Attention: John M. Bureger	1
The Boeing Company Aero Space Division P. O. Box 3707 Seattle, Washington 98124 Attention: Ruth E. Peerenboom (1190) J. D. Alexander	1 1
Chemical Propulsion Information Agency Applied Physics Laboratory 8621 Georgia Avenue Silver Spring, Maryland 20910	1
Chrysler Corporation Missile Division Warren, Michigan Attention: John Gates	1

Copies

IIT Research Institute Technology Center Chicago, Illinois 60616 Attention: C. K. Hersh, Chemistry Division	1
Kidde Aero-Space Division Walter Kidde & Company, Inc. 675 Main Street Belleville 9, New Jersey Attention: R. J. Hanville, Director of Research	1
Lockheed Missiles & Space Company P. O. Box 504 Sunnyvale, California Attention: Y. C. Lee, Power Systems R&D Technical Information Center	1 1
Lockheed Missiles & Space Company Propulsion Engineering Division (D. 55-11) 1111 Lockheed Way Sunnyvale, California 94087	1
Marquardt Corporation 16555 Saticoy Street Box 2013 - South Annex Van Nuys, California 91404 Attention: Librarian	1
Martin-Marietta Corporation Martin Division Baltimore 3, Maryland Attention: John Calathes (3214)	1
McDonnell Aircraft Corporation P. O. Box 6101 Lambert Field, Missouri Attention: R. A. Herzmark	1
North American Rockwell Space & Information Systems Division 12214 Lakewood Boulevard Downey, California 90242 Attention: Technical Information Center, D/096-722 (AJ01) H. Storms	1 1
Northrop Space Laboratories 1001 East Broadway Hawthorne, California Attention: Dr. William Howard	1

Copies

Radio Corporation of America
Astro-Electronics Division
Defense Electronic Products
Princeton, New Jersey
Attention: S. Fairweather

1

Republic Aviation Corporation
Farmingdale, Long Island
New York
Attention: Dr. William O'Donnell

1

Rocket Research Corporation
Willow Road at 116th Street
Redmond, Washington 98052

1

Rocketdyne Division of
North American Rockwell
6633 Canoga Avenue
Canoga Park, California 91304
Attention: Library, Department 596-306

1

Rohm and Haas Company
Redstone Arsenal Research Division
Huntsville, Alabama 35808
Attention: Librarian

1

Space-General Corporation
777 Flower Street
Glendale, California
Attention: C. E. Roth

1

Stanford Research Institute
333 Ravenswood Avenue
Menlo Park, California 94025
Attention: Thor Smith

1

Thiokol Chemical Corporation
Alpha Division, Huntsville Plant
Huntsville, Alabama 35800
Attention: Technical Director

1

Thiokol Chemical Corporation
Reaction Motors Division
Denville, New Jersey 07834
Attention: Librarian

1

Thiokol Chemical Corporation
Redstone Division
Huntsville, Alabama
Attention: John Goodloe

1

Copies

TRW, Inc.
TAPCO Division
23555 Euclid Avenue
Cleveland, Ohio 44117
Attention: P. T. Angell

1

United Aircraft Corporation
Corporation Library
400 Main Street
East Hartford, Connecticut 06118
Attention: Dr. David Rix

1

United Aircraft Corporation
Pratt & Whitney Division
Florida Research & Development Center
P. O. Box 2691
West Palm Beach, Florida 33402
Attention: R. J. Coar
Library

1

1

United Aircraft Corporation
United Technology Center
P. O. Box 358
Sunnyvale, California 94088
Attention: Librarian

1

Vought Astronautics
Box 5907
Dallas 22, Texas
Attention: Warren C. Trent

1